UNIVERSITAT POLITÈCNICA DE CATALUNYA BARCELONATECH

Development of novel instruments and techniques for passive microwave remote sensing

Joan Francesc Muñoz Martin

UNIVERSITAT POLITÈCNICA DE CATALUNYA
BARCELONATECH
Departament de Teoria del Senyal
i Comunicacions

Development of Novel Instruments and Techniques for Passive Microwave Remote Sensing

Author

Joan Francesc Muñoz Martin

Thesis Advisor

Prof. Adriano José Camps Carmona

A thesis submitted to the
Universitat Politècnica de Catalunya - BarcelonaTech (UPC)
in partial fulfillment of the requirements for the degree of
DOCTOR OF PHILOSOPHY

PhD program on Signal Theory and Communications
Remote Sensing Laboratory (RSLAB) Group
Barcelona, July 2021

Development of Novel Instruments and Techniques for Passive Microwave Remote Sensing, *J.F. Munoz-Martin*, PhD thesis, UPC, Barcelona, 2021.

Author IDs
IEEE Member: 94639303
ORCID: 0000-0002-6441-6676
WOS ResearcherID: AAA-2214-2019
GitHub: juan0fran
LinkedIn: https://www.linkedin.com/in/joan-francesc-munoz-martin

The author of this PhD thesis received financial support from the grant for the recruitment of early-stage research staff FI-DGR 2018 of the AGAUR / Generalitat de Catalunya, he has been also supported by the 2017 ESA S3 challenge and Copernicus Masters overall winner award ("FSSCat" project) and ESA project "FSSCat Validation Experiment in MOSAIC". Part of the instrumentation has been developed within the SPOT project: Sensing with Pioneering Opportunistic Techniques grant RTI2018-099008-B-C21 / AEI / 10.13039/501100011033, and by EU EDRF funds and the Spanish Ministry of Science, Innovation and Universities, and by the Unidad de Excelencia Maria de Maeztu MDM-2016-0600.

To my parents, this is your heritage.

Acknowledgments

I want to start this section by expressing my gratitude to my advisor Adriano. Since we met during my Bachelor's degree, he has always supported me, advised me, and gave me the freedom to do what I like to do. I have been lucky to form part of his team, and I really appreciate all the effort he makes to make the NanoSat-Lab a great place to learn and work. I could say hundreds of compliments, but I would not even finish in a page. I can only say that you should be the "role model" for all Professors and Investigators in this entire world.

I would also like to thank the reviewers for all the time they dedicated to reviewing my dissertation. I really appreciate the time you have devoted to reading it and the kind comments you have sent to me.

Many people from the NanoSat-Lab have contributed in some way to this dissertation. From a piece of advice at the right time, to helping building a 3-meter antenna, without them it wouldn't be possible. The list of NanoSat-Lab members that have "intersect" my path is endless, and I really appreciate all people I have been able to interact with. I would like to thank all of them. Specifically, I would like to thank my three closest colleagues that have been very important during my stage at the NanoSat-Lab. To Lara Fernández for her work on the antenna design, mechanical support, and the AIV of all our missions. To Joan Adrià Ruiz-de-Azúa for his fruitful discussions, brainstormings, and support during all hardware and software developments carried out during my thesis. To Adrián Pérez, for being a great person, always willing to help others, even when he says "I told you" when you do something wrong. To Carles Araguz, Pol Via, Jaume Jané, Arnau Solanellas, and Ricard Castellà for their work in ^{3}Cat-1 and ^{3}Cat-4, and for the great moments while building the VHF/UHF Montsec antenna. To Marc Badía, Marco Sobrino, Amadeus Gonga, and Albert Marton for their generous and selfless help while building the S-band Montsec antenna. To Hyuk Park for always being there to help and for being a great person. To Christoph Herbert, David Llavería, and Miriam Pablos for the efforts done to process FMPL-2 data. I am also very grateful to other UPC Ph.D. students that I had the pleasure to work and share my time with them, giving a special mention to Jorge Querol, whose advice has always been wise and pleasant.

I would also like to thank all people out that are not members of the NanoSat-Lab for the efforts and patience they had with me and our team. To the ESA Educational Office staff had with the ^{3} Cat-4 team. Especially, to Cristina, Lily, and Josh. To the FSSCat consortium, with a special mention to Massimiliano Pastena and Bernardo Carnicero. They have always been willing to help and solve the problems we have faced during the

project. It has been very difficult, but we did it. I would also like to thank the great work that Balamis S.L. staff Dr. Roger Jové, Dr. Adrià Amezaga, and Mr. Ricard Gonzálvez have carried out. I am also very thankful to Daniel Pascual and Raul Onrubia for developing MIR, and for helping me with the LaTeX template. A large part of this dissertation would not be possible without your previous work. I am also very grateful to Serni Ribó and Estel Cardellach for their support to develop the GNSS-R instruments for the MOSAiC expedition, and to all the MOSAiC staff who operate our instrument.

Last, but not least, I want to give my thanks to a set of people who in one way or the other, have also taken part in the thesis. The technicians Joaquim, Ruben, Eric for all soldering, manufacturing, and helping me with everything I needed, to the department secretary Aynie for everything she did, and to Sergi and Pere for their help and positivism spirit they have shared with me.

Finally, I want to thank all my beloved ones and people who have shared part of their time with me while doing this thesis. Special thanks to all my family for educating me to become what I actually am. To my partner-in-crime Elena, who understands and motivates me to seek for my dreams. To my closest friends from Mallorca, especially to the Balle-Llabrés family for welcoming me as one of them, specially to Joan for designing me the cover of the thesis book, to the Oliver-Sans family, and to Mar Merino. To all my friends and colleagues from the C.M.U. Ramón Llull (and relatives) that have been part of my life, especially the ones that have shared flats, travels, or rooms with me: Marta Bofill, Rovi, Tomeu, Bouns, Jurgi, Jon, Estela, Toni, Amelia, Neus, Emilia, Moragón, Elena C., Claudia, Sara and to the rest of the "shordakens" group. To my mates of "Ausias Marc" (and relatives) Galian, Amanda, Enric, Sergi, Pau, Ignacio, Nil, Andrea, Andreu, and Pascu, who have shared with me during almost the entire thesis.

Abstract

Earth Observation using satellites has helped to better understand our planet. The goal of such systems is to provide large data sets to help to understand the effects of our actions on the climate, to predict storms in near real-time, to prevent forest fires, or to prevent desertification, among others. Nowadays, Earth Observation missions embark large and expensive instruments, such as radars, which out-perform on their task, providing very good resolution, but moderate to low revisit times. In the last years, thanks to the miniaturization of electronics a new type of satellite have become popular, the CubeSat, a small spacecraft weighing from 1 to 10 kg, which can carry different types of instruments. Thanks to the cost reduction of these new platforms, new techniques can be easily evaluated, and the concept of a "mesh" of sensors surrounding the Earth is becoming a reality. Besides, the suitability of new techniques is being proven for such small spacecraft, such as GNSS reflectometry (GNSS-R). GNSS-R instruments are typically cheaper, more efficient (in terms of power consumption), and smaller than their "traditional" equivalent ones (either altimeter, scatterometer, or synthetic aperture radiometer), as they work as radar, but without the need of a transmitter. New GNSS-R instruments are based on Software Defined Radio (SDR) concept, and they can be adapted for a CubeSat platform thanks to the recent evolution in this field. Although GNSS-R is a relatively new technique, it is showing promising results to retrieve several geophysical parameters, but still requires further investigations to maximize its performance. On this path, thanks to the evolution of data-driven algorithms, such as neural networks, new applications are being derived from GNSS-R data, aiming to break the trade-off between radiometric, temporal, and spatial resolutions.

This Ph.D. thesis is devoted to the development of passive microwave remote sensing instruments for CubeSats. However, before entering into the instrument design, several field experiments were conducted to model and validate the use of GNSS-R under different conditions. This Ph.D. thesis is divided in three main parts.

The first part is devoted to assessing the capabilities of GNSS-R to retrieve different geophysical parameters through a different set of field experiments. First, an analysis of different GNSS-R signals retrieved by the Microwave Interferometric Reflectometer (MIR) is performed. The achievable spatial resolution of L1 and L5 GNSS-R signals is analyzed under different conditions. Some considerations on the incoherent integration time to enhance the spatial resolution of the GNSS-R observable are provided. Second, taking into account the incoherent integration limits previously analyzed, the coherency of the GNSS-R signal collected by MIR over the ocean is analyzed at L1 and L5 bands. It is shown that the coherent part of the GNSS-R signal under short integration times is mostly equivalent to the total power waveform. Third, thanks to the use of short integration times, multiple reflections received in the GPS L5 reflected signal could be identified as multiple individual peaks, thanks to the narrower auto-correlation function of L5 signals. Over the ocean, these multiple peaks are analyzed and linked to the sea state. Over the Australian rainforest, these multiple peaks at L5 are linked to multiple reflections on top

of the vegetation canopy and in the bare soil. The peaks can be easily differentiated if the canopy height is larger than half the width of the L5 auto-correlation function. Fourth, a methodology to estimate soil moisture content over land using GNSS-R signals is proposed. The methodology combines statistical properties of the GNSS-R signal with a neural network algorithm to correct the surface roughness and the speckle noise effect. Finally, the use of GNSS-R signals to estimate sea-ice thickness and snow content over the sea-ice is examined thanks to the data collected by a circular polarization GNSS-R instrument part of the Multidisciplinary drifting Observatory for the Study of Arctic Climate (MOSAiC) expedition. A four-layer dielectric model is proposed, consisting of a first air layer, a snow layer, a sea-ice layer, and the water underneath. Dual-polarization and dual-band measurements are used to estimate both parameters from this ground-based instrument results and validated using ground-truth data collected by MOSAiC researchers.

The second part of this dissertation is devoted to the design, implementation, and test of three passive microwave instruments for CubeSats. First, the Flexible Microwave Payload -1 (FMPL-1) is proposed as part of the European Space Agency (ESA) Fly Your Satellite! ^{3}Cat-4 mission. The instrument includes three experiments in a single platform: a total power L-band radiometer with frequent internal calibration, an L1/L2 GNSS reflectometer, and an AIS receiver. This novel instrument is integrated into a 1-unit CubeSat (10x10x10 cm^3 and $\sim$1.33 kg), and aims at proving the capabilities of 1U CubeSats for Earth Observation. The instrument also serves as technology boosts for the two next instruments developed within this Ph.D. thesis. Second, the FMPL-2 instrument is proposed as the main payload of the ^{3}Cat-5/A, one of the two instruments composing the ESA FSSCat mission, the first third-party mission based on CubeSats contributing to the Copernicus system. This second instrument is the evolved version of FMPL-1 to be integrated into a 6-unit CubeSat (30x20x10 cm^3 and $\sim$8 kg), which can provide synchronous GNSS-R and L-band radiometry data. Finally, a third instrument, the FMPL-3, is proposed for the GNSSaS mission of the National Space Science and Technology Center from the United Arab Emirates. This third instrument includes the first-ever GNSS-R receiver at L5, and aims at proving the capabilities of L5 signals from space.

Finally, in the third part, the first results of FMPL-2 are presented and analyzed. The instrument was successfully launched into a Low Earth Orbit on September the 3^{rd}, 2020, during the Vega VV16 flight, and commissioned in less than three weeks. First, the results of FMPL-2 during the first two weeks of in orbit validation are presented. The sensitivity and accuracy of the L-band radiometer are analyzed, showing an accuracy better than 1 K, and sensitivity better than 2 K. Then, different GNSS-R reflections over ocean, land, and sea-ice are presented, showing the capabilities of GNSS-R even at very short integration times. Furthermore, several algorithms are proposed to estimate different geophysical parameters using FMPL-2 data in combination with other data sets. Data-driven algorithms to estimate sea-ice concentration, thickness and soil moisture content over land are implemented using L-band microwave radiometry data and GNSS-R data retrieved by FMPL-2 during the period comprising October the 1^{st} and December the 4^{th}, 2020. It is presented how the combination of GNSS-R and L-band radiometry data improves both the radiometric and the spatial resolutions of the estimated geophysical parameters.

Contents

List of Tables

List of Figures

Glossary

ACF Auto-Correlation Function

ACL Active Cold Load

ADC Analog-to-Digital Converter

ADCS Attitude Determination and Control System

AGB Above-Ground Biomass

AIS Automatic Identification System

ANN Artificial Neural Network

AVHRR Advanced very-high-resolution radiometer

BEC Barcelona Expert Center on Remote Sensing

BOC Binary Offset Carrier

BPSK Binary Phase-Shift Keying

C&DH Command and Data Handling

CAF Cross Ambiguity Function

CAN Controller Area Network

CCT Communication and Control Thread

cGNSS-R Conventional Global Navigation Satellite System - Reflectometry

CH Canopy Height

CIMR Copernicus Imaging Microwave Radiometer

COMMS Communications System

COTS Commercial-off-the-Shelf

CSK Complex Signal Kurtosis

CSP CubeSat Space Protocol

CSV Comma-separated value

CYGNSS Cyclone Global Navigation Satellite Systems

DAC Digital-to-Analog Converter

DDM Delay Doppler Map

DMA Direct Memory Access

DOC Degree of Coherence

DPU Data Processing Unit

DR Dicke Radiometer

DTC Distributed Thermistor Chain

ECMWF European Centre for Medium-Range Weather Forecasts

ECV Essential Climate Variable

EM Engineering Model

EO Earth Observation

EPS Electrical and Power System

ESA European Space Agency

ETSETB Escola Tècnica Superior d'Enginyeria de Telecomunicacions de Barcelona

FFT Fast Fourier Transform

FIR Flat Impulse Response

FLL Frequency Locked Loop

FM Flight Model

FPGA Field Programmable Gate Array

FSPL Free-space propagation losses

GCOS Global Climate Observing System

GFCH Global Forest Canopy Height

GIS Geographical Information System

GMSK Gaussian Minimum Shift Keying

GNSS Global Navigation Satellite System

GNSS-R Global Navigation Satellite System - Reflectometry

GNSS-RO Global Navigation Satellite System - Radio Occultations

GPU Graphics Processing Unit

GT GNSS-R Thread

HDLC High-Level Data Link Control

HF High Frequency

HT Housekeeping Thread

I/Q In-phase and Quadrature Compontents

IB Interface Board

ICE/CSIC Institute of Space Sciences / Spanish National Research Council

IEEC Institud d'Estudis Espaials de Catalunya

IFFT Inverse Fast Fourier Transform

iGNSS-R Interferometric Global Navigation Satellite System - Reflectometry

IP Interference Pattern

IPT Interference Pattern Technique

IT Ionosphere Thread

ITU International Telecommunication Union

JPL Jet Propulsion Laboratory

LAEA Lambert-Azimuthal-Equal-Area

LDO Low-dropout regulator

LEO Low Earth Orbit

LNA Low Noise Amplifier

LO Local Oscillator

LST Land Surface Temperature

LUT Look-up Table

MAE Mean Absolute Error

MEO Medium Earth Orbit

MIR Microwave Interferometer Reflectometer

MIRAS Microwave Imaging Radiometer by Aperture Synthesis

ML Matched Load

MODIS Moderate Resolution Imaging Spectroradiometer

MOSAiC The Multidisciplinary Drifting Observatory for the Study of Arctic Climate

MWR Microwave Radiometer

NADS Nadir Antenna and Deployment Subsystem

NASA National Aeronautics and Space Administration

NDVI Normalized Difference Vegetation Index

NIR Noise Injection Radiometer

NNI Nearest Neighbor Interpolation

NOAA National Oceanic Atmospheric Administration

NSR Noise-to-Signal Ratio

NSSTC National Space Science and Technology Center

OBC On-board Computer

OSI SAF Satellite Application Facility on Ocean and Sea-Ice

PAU Passive Advanced Unit for Earth Observation

PCB Printed-Circuit Board

PCPS Parallel Code Phase Search

PFM Proto-Flight Model

PLL Phase Locked Loop

PPP Point-to-Point Protocol

PRN Pseudo-Random Noise

PRS Passive Remote Sensing

PYCARO P(Y) and C/A Reflectometer

QM Qualification Model

RF Radio Frequency

RF-FE Radio-Frequency Front-End

RFI Radio Frequency Interference

RMS Root-mean-square

RMSD Root-mean-square differences

RMSE Root-mean-square error

S^3 Sentinel Small Sat

SAR Synthetic Aperture Radar

SAW Surface Acoustic Wave

SDR Software Defined Radio

SEU Single Event Upset

SGR-ReSi Space GNSS Receiver – Remote Sensing Instrument

SIC Sea-ice Concentration

SIE Sea-ice Extent

SIT Sea-ice Thickness

SKT Skin Surface Temperature

SM Soil Moisture

SMAP Soil Moisture Active Passive

SMD Surface Mount Device

SMOS Soil Moisture and Ocean Salinity

SNR Signal-to-Noise Ratio

SoC System on Chip

SoOp Signals of Opportunity

SP3T Single Pole Three Throw

SSDL Space Systems Development Laboratory

SSMS Small Satellite Mission Service

TDMA Time Division Multiple Access

TDS-1 TechDemoSat-1

TID Total Ionizing Dose

TPR Total Power Radiometer

TVAC Thermal Vacuum Chamber

UAE United Arab Emirates

UK-DMC United Kingdom Disaster Monitoring Constellation

UN United Nations

UPC Universitat Politècnica de Catalunya

VOD Vegetation Optical Depth

WAF Woodward Ambiguity Function

WF Waveform

ZADS Zenith Antenna and Deployment Subsystem

Part I

Introduction and Theoretical Background

1

Chapter 1
Introduction

This Chapter presents the introduction, motivation, goals, and outline of this Ph.D. thesis. The framework in which this Ph.D. thesis has been developed is described. First, a brief introduction to nano-satellites is presented, with the focus on Remote Sensing for Earth Observation. Then, the CubeSat, a specific type of nano-satellite is presented. The Universitat Politècnica de Catalunya (UPC) Nano-Satellite and Small Payload laboratory, where this Ph.D. thesis has been conducted, is also introduced. Finally, the motivation of the thesis is presented, together with the goals, and the outline of the thesis.

1.1 A new Earth Observation paradigm

The United Nations (UN) and all their Member States defined 17 Sustainable Development Goals to end poverty, protect the planet, and ensure peace and prosperity by the end of 2030. The objective number 13 is "to take urgent actions to combat Climate Change and its impacts on the planet". To understand the climate change impact, the UN established in 1992 the Global Climate Observing System (GCOS). Through this initiative, up to 54 essential climate variables (ECV) were defined [1]. Each of these variables studies a particular aspect of our planet. ECV monitoring is needed to understand the climate and to mitigate and predict the effects of global warming [2]. ECVs are classified into three main groups: atmosphere, land, and ocean variables, and most of them are monitored through remote sensing techniques.

1.1.1 Remote Sensing for Earth Observation

Remote Sensing is the ability to retrieve information from an object without physical contact. The term was coined in the 1950s by Evelyn Pruitt, a US Geographer working at the US Office of Naval Research. However, the first form of Remote Sensing was conceived more than a hundred years ago, when Louis Jacques Mandé Daguerre invented the first photographic plate: the daguerreotype. This process was the first commercial photographic process (1839), where the captured images were "printed" over a polished silver surface. From this point, the use of cameras grows up not only to capture people's movements but to show the Earth from a falcon-eye perspective. In 1840 cameras were attached to balloons to provide the first-ever aerial photography; during the First and Second World Wars, aerial images were used to plan attacks [3]; in 1935 the Explorer II balloon took pictures of the Earth curvature at a height of 20 km; and in the 1960s the first image from space was taken from TIROS-1, a 120 kg spacecraft carrying the first imagery instrument onboard [4].

Photography is the technique of capturing photons in the visible range of the electromagnetic spectrum, emitted by a natural source of light, and then collided into a photographic plate or into an optical sensor. In the case of modern sensors, photons induce an electric charge that is collected by electronic circuitry, and then converted into counts. Under proper illumination (i.e., a bulb or the Sun), cameras receive the light scattered from the target object. Thus, cameras do not transmit any kind of energy, and they are classified as passive remote sensing instruments. Other sensors work with a similar physical principle, but at other frequencies different than the visible range of the spectrum, such as infrared, ultraviolet, or X-ray radiation (see Fig. 1.1).

Capturing photons reflected by an object is not the only way to perform remote sensing. All bodies at a physical temperature higher than 0 K emit energy without the need for interaction of an external source (i.e., light). This emission is produced at longer wavelengths (i.e., IR and microwaves in Fig. 1.1), and can be captured by means of antennas and then processed by an instrument called *radiometer*. This type of instrument is a passive remote sensing instrument that is able to sense the emitted electromagnetic radiation of a given object at a given frequency of the radio spectrum.

Aside from optical imagers or radiometers, the third remote sensing technique used nowadays is based on emitting a signal from a given source, let it "bounce" over a given surface, and capture the reflection. In this case, the instrument can be either active, if the

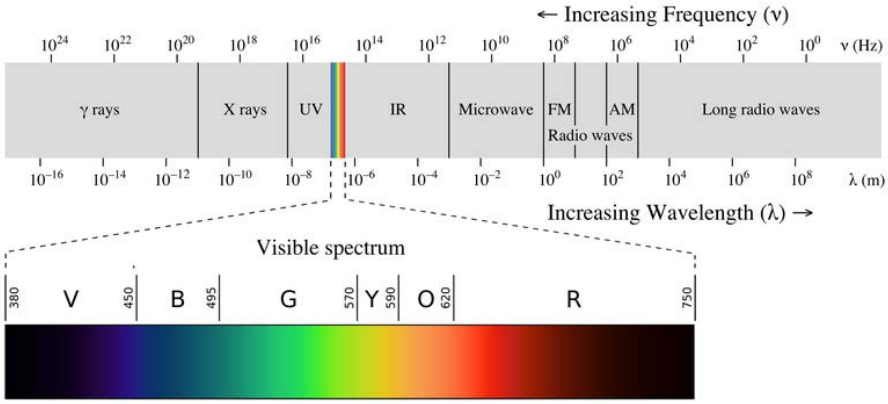

Figure 1.1: Distribution of the electromagnetic waves with respect to frequency and wavelength, highlighting visible part of the electromagnetic spectrum (Philip Ronan, Gringer, CC BY-SA 3.0, via Wikimedia Commons).

instrument itself emits the signal; or passive, if the instrument uses an already existing signal transmitted for another purpose.

Therefore, depending on the transmitter-receiver configuration, active remote sensing can be conducted through a mono-static radar, where transmitter and receiver are in the same location, or a bi-static (or multi-static) radar, where the transmitter and receiver are in different locations. A particular case of bi-static or multi-static radars is when the transmitted signal is used for other purposes that are not remote sensing. This is called passive remote sensing using Signals of Opportunity (SoOp).

One particular case of passive remote sensing using SoOp is the Global Navigation Satellite Systems - Reflectometry (GNSS-R), where the GNSS signals transmitted by the different GNSS satellites. An example of this concept is presented in Fig. 1.2.

Remote sensing instruments have been widely used for scientific purposes, including a variety of applications such as medical imaging, material research, astronomy, or Earth Observation (EO). In this last topic, the development of new instruments is key to monitor ECVs with sufficient coverage, accuracy, and spatial and time resolutions.

1.1.2 CubeSats for Earth Observation

In 1957 *Sputnik 1* was launched, reaching a major goal: being the first object ever orbiting the Earth. The 83 kg satellite was launched into a Leo Earth Orbit (LEO) at an altitude of 938 km, and since then the space industry has launched a large variety of satellites for a variety of applications: communications, Earth observation, remote sensing, etc.

First operational satellites were very expensive due -to a large extent- to the use of non-standarized platforms and equipment. Technology has drastically evolved over the last two decades. The miniaturization of electronics thanks to the computer and phone industry had an impact on the space industry. Large spacecraft, such as the Hubble

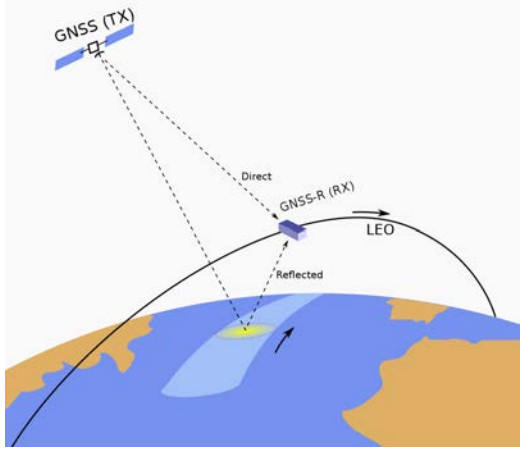

Figure 1.2: Remote Sensing from a Leo Earth Orbit satellite collecting GNSS transmitted signals to perform GNSS-R (Carlos Molina, CC BY-SA 4.0, via Wikimedia Commons).

Space Telescope ($\sim$ 12 tons), or smaller ones, as the Soil Moisture and Ocean Salinity (SMOS) mission ($\sim$ 600 kg) are now part of a world called "Old Space". For some particular applications, these satellites are being replaced by smaller ones implemented in a "different way". This is the "NewSpace" industry. This new type of industry is commonly linked to a very specific type of spacecraft: the nano-satellite. This type of satellite weighs from 1 to 10 kg, with capabilities to perform communication links, to carry out scientific experiments, and to sense the Earth. A particular type of nano-satellite has become popular since 1999: the CubeSat. This type of satellite was proposed as a de facto "standard" [5] by Prof. Jordi Puig-Suari from California Polytechnic State University (Cal-Poly), San Luis Obispo, and by Prof. Bob Twiggs from Stanford University's Space Systems Development Laboratory (SSDL), to develop a quick and cost-effective solution to make space accessible to universities and research institutes, aiming a satellite design, manufacturing, launch, and operations in less than 4 years.

A one-unit CubeSat is a 10 cm sized cube that weights up to 1.33 kg and includes all the necessary systems to operate from space, normally in LEO orbit. A CubeSat is specified by its "units", being a one-unit CubeSat (1U) a 10x10x10cm^3 satellite, a 2U CubeSat is 20x10x10cm^3 (with the weight doubled as well), as detailed in Fig. 1.3. Nowadays the largest standarized CubeSats has the 6U form factor, 30x20x10cm^3 and it weights about 8 kg, but larger standards are being developed.

Governments and space agencies start to look at CubeSats, as a cheap way to test new technologies and to prove new scientific concepts. The CubeSat philosophy aims at using Commercial-off-the-Shelf (COTS) components, benefiting from the continuous developments in mobile phone, robotics, and sensing industry. In the end, a CubeSat is a sensing system, somehow similar to an "Internet of Things" sensor. However, instead of being placed on the ground, it is orbiting at a given height above the surface of the Earth.

The number of nano-satellites launched is rising since 2010 (see Fig. 1.4), and it is expected that the number of nano-satellites will significantly increase in the next few

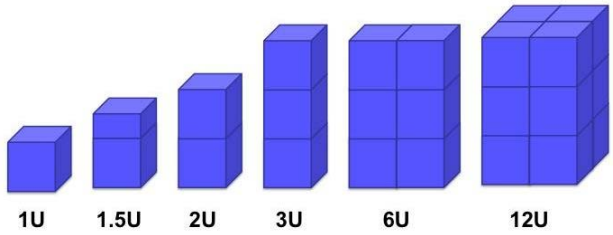

Figure 1.3: Different CubeSat sizes, from 1 unit to 12 units [6]

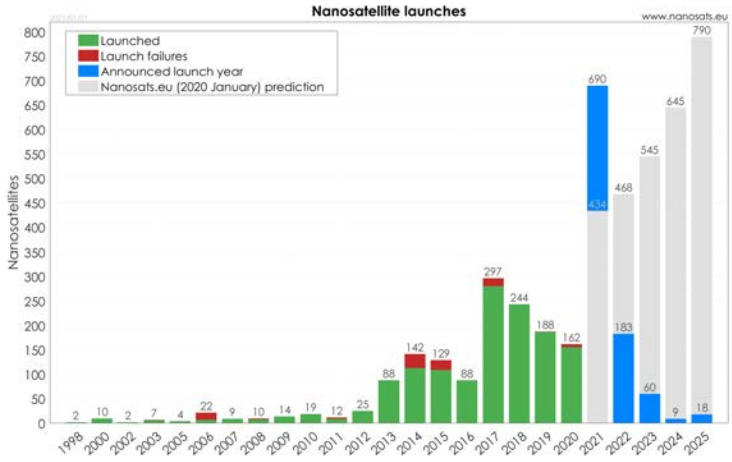

Figure 1.4: Number of nano-satellites launched since 1999, including the forecast for the next 5 years [11].

years. In the last five years, the use of CubeSats for to Remote Sensing, and especially to EO has been dominant [7]. Half of the CubeSats launched between 2015 and 2019 are Remote Sensing CubeSats [8], as is the case of the Planet Labs [9] or the Spire [10] constellations, with more than 320 and 125 CubeSats already launched, respectively.

1.1.3 From Old Space to NewSpace: a New Earth Observation paradigm

So far, EO has been mostly carried out by "Old Space" satellites. To provide some examples: the SMOS mission, the first European Space Agency (ESA) EO mission designed to measure soil moisture, ocean salinity, and sea-ice thickness using an L-band radiometer; the NASA Terra and Aqua missions carrying the Moderate Resolution Imaging Spectroradiometer (MODIS) instrument, a multispectral imager of 228 kg weight; or DEIMOS-1, a 91 kg spacecraft carrying an optical payload.

Due to the high cost, and long development time, the operations performed by "Old Space" EO missions are mostly carried out with a single-spacecraft. However, a few constellations (same type of satellite) and trains (different types of satellites) do exist

today. The single-spacecraft approach has the inconvenience of large revisit times over selected target areas, which may differ from the type of sensor used (i.e., a camera with a very narrow footprint will have very large revisit times). The role of a CubeSat is to decrease both costs and development time at the expense of lowering, in some cases, the performance of the sensors (e.g., you cannot "easily" put a 20-meter antenna on a CubeSat). Despite that, the CubeSat enables the concept of massive-constellations, with hundreds of satellites orbiting around the Earth with a set of instruments capable of producing near real-time data of the Earth.

Despite the growing use of CubeSats for EO, their size and power limitations often limit their choice of instruments to optical imagers, such as the 3-unit CubeSat that form the Planet Labs constellation. However, while cameras are often suitable instruments for CubeSat-based platforms, they tend to be largely affected by cloud cover, causing irrecoverable scientific loss. Furthermore, many other geophysical parameters cannot be measured by means of optical sensors.

Aside from imagers, other CubeSat missions have included either active or passive microwave or millimeter-wave remote sensing payloads. One example is RainCube, the first CubeSat mission carrying a mono-static radar [12], developed by the National Aeronautics and Space Administration (NASA) Jet Propulsion Laboratory (JPL). Moreover, a number of CubeSat missions have included millimeter-wave radiometers, such as MiRaTa [13], working at 56, 180, and 207 GHz bands; MicroMAS-2 [13], working at 90, 118, 183, and 206 GHz; CubeRRT [14], working between 6 GHz and 40 GHz; TEMPEST-D [15], working at five frequencies between 89 GHz and 182 GHz; and TROPICS [16], working at 90 GHz, 118.75 GHz, 183 GHz, and 205 GHz. Additionally, Spire Global, Inc. is using 3-unit CubeSats to deploy a constellation of nano-satellites to perform EO using SOOP. In this case, Spire Global, Inc. is focused on using Global Navigation Satellite System (GNSS) signals to remotely sense the Earth. Two types of GNSS receivers for EO are currently used: a Global Navigation Satellite System - Radio Occultations (GNSS-RO) receiver [10, 17], and a Global Navigation Satellite System - Reflectometry (GNSS-R) [17, 18] receiver.

1.1.4 CubeSats for EO at UPC: the UPC NanoSat-Lab

The *Universitat Politècnica de Catalunya* is pioneering the development of such small systems through the Nano-Satellite and Small Payload Laboratory (NanoSat-Lab). This laboratory is a cross-department initiative part of the Barcelona School of Telecommunications Engineering (ETSETB), and part of the UPC Passive Remote Sensing Laboratory / CommSensLab - UPC Centre Especific de Recerca (Maria de Maeztu Excellence Research Unit 2016-2020).

The laboratory focuses on two main objectives: to educate future aerospace and telecommunication engineers, and to develop high-quality novel remote sensing missions and instruments for CubeSats. Until now, the UPC NanoSat-Lab has been involved in several nano-satellite projects (see Fig. 1.5), including the launch of the first Catalan satellite, the ^{3}Cat-2 in 2016; the development of the first educational-based satellite, the ^{3}Cat-1, entirely designed and developed by university students; and the FSSCat mission, launched on the 3 September 2020, as the first ESA third-party mission contributing to the Copernicus system and based on CubeSats [19]. Aside from those, the UPC NanoSat-Lab is also part of the ESA Fly Your Satellite! program with the ^{3}Cat-4 mission, and is

also cooperating with the National Space Science Technology Center (NSSTC) of United Arab Emirates (UAE) with the ^{3}Cat-7/GNSSaS mission, and the ^{3}Cat-6/RITA mission on board the AlAinSat-1.

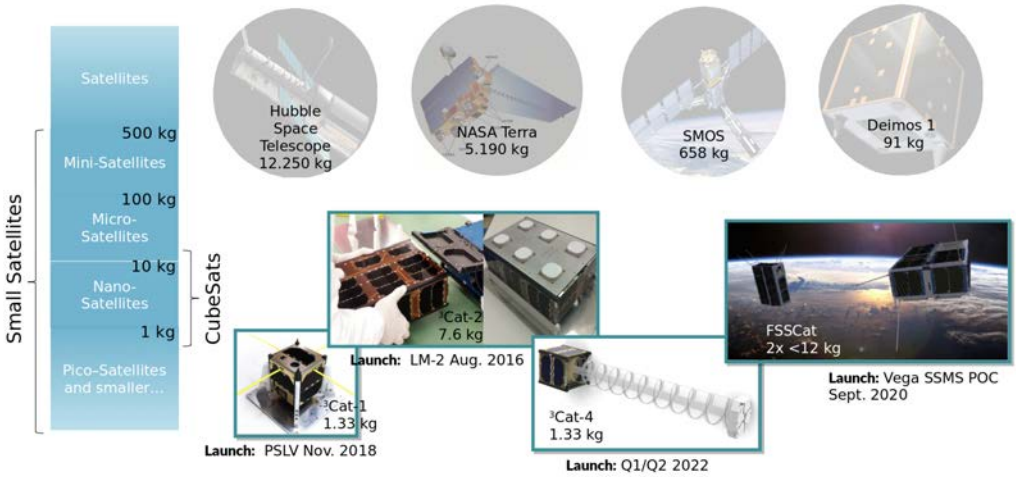

Figure 1.5: Weight comparison between UPC NanoSat-Lab former missions and other sample remote sensing "Old Space" missions.

Finally, it is important to remark that UPC NanoSat-Lab is one of the main contributors to the recently approved "Pla Estatègic del NewSpace a Catalunya" [CD1]. This plan is a road-map to create a "NewSpace" hub in Catalonia. The goal is to provide Barcelona a new aerospace industry based on CubeSat technology. Thus, this plan includes the development of several CubeSats from which the first two of them are already contracted: the first one is a 3U CubeSat carrying an "Internet of Things" technology demonstrator, and the second one is a 6U CubeSat carrying a multispectral optical imager for EO.

1.2 Motivation

I joined the NanoSat-Lab in 2013 during my Bachelor's degree, as part of a practical course given by Prof. Adriano Camps entitled "Projecte Avançat d'Enginyería". The course was given in the "old" NanoSat-Lab facilities in the A2 building basement. The course objective was to develop a communication system for a nano-satellite. The idea that some of my work could reach the space fascinated me. After taking the course, I joined the NanoSat-Lab, and who could have imagined at that time, that would have ended doing my Ph.D. with them? - So, here we are. During my early stage in the NanoSat-Lab, I contributed to the development of the communication system of the ^{3}Cat-1. I also joined the BEXUS 19 TORMES 2.0 team, traveled to the ESA headquarters, and to Kiruna (North of Sweden), to perform a stratospheric balloon experiment as part of this team . Finally, I ended up doing my B.Sc. thesis finalizing the development of the communication system of ^{3}Cat-1, together with its ground segment. By that time, I

already joined the ^{3}Cat-2 team, where I was working on the development of the command and data handling (C&DH) system, the ground segment, and the control software of the entire spacecraft.

I decided to stay in the NanoSat-Lab, and I got a grant from Prof. Adriano Camps while I was coursing my M.Sc. in Telecommunications Engineering. During that period, I kept working in ^{3}Cat-2, up to the point it ended up being half of my M.Sc. thesis. The other half was, again, the communication system of our next spacecraft: the ^{3}Cat-4. I had also started to *play* with remote sensing as part of the work I was doing at the laboratory: we launched a camera to the "space" using a stratospheric balloon! And I have to admit it, I have always been fascinated by Earth-curvature images. I cannot imagine the feelings of the first person looking at the first image from space...

At that time, right by the end of my M.Sc. thesis, ^{3}Cat-2 was launched. That satellite contained tons of hours of my work, and I remember the first time its signal was received. It was the 23^{rd} of August, 2016. The satisfaction of being able to contribute to something that is orbiting the Earth is astonishing. However, after 2 months of operations, the satellite had an unidentified error, and it never woke up again. I was devastated. At that moment, Prof. Adriano Camps told me: American's required 11 rockets to land on the moon, we have not failed, we are just learning, and we will do it better... And he was right. One year after that moment, the NanoSat-Lab was selected by the ESA Academy to be part of the Fly Your Satellite! program. This event gave me the push to go one step further. I finally enrolled in the Ph.D. program with Prof. Adriano Camps.

1.3 Goals

The main goal of this dissertation is **to develop the necessary instruments, techniques, and algorithms to retrieve some essential climate variables using a passive microwave instrument onboard a CubeSat**. The two remote sensing techniques covered in this Ph.D. thesis are the L-band microwave radiometry, a well-known technique that is being studied since 1968 thanks to the launch of Cosmos 243 spacecraft [20]; and the GNSS-R technique, a novel technique whose first measurement from space was conducted by the UK Disaster Monitoring Constellation (UK-DMC) mission in 2004 [17]. This last technique is not as mature as L-band microwave radiometry is. Therefore, there is still a lot of work in this area that must be conducted.

In this context, this Ph.D. thesis contributes to the GNSS-R technique by means of different preparatory field experiments from a ground-based and an airborne GNSS-R instrument. **The goal is to study three essential climate variables** [21] using GNSS-R data: **sea ice, sea state, and soil moisture**. Then, a set of **instruments are developed to study these ECVs from a CubeSat-based platform**. The goal of those instruments is to study the **synergy between GNSS-R and L-band microwave radiometry measurements**, as from an electromagnetic point of view the emissivity (i.e. collected by a radiometer) and the reflectivity (i.e. collected by a GNSS-R instrument) are complementary measurements (see p. 136 from [3]).

To fulfill the first goal, data collected by the Microwave Interferometer Reflectometer (MIR) is used. The MIR instrument is an airborne GNSS-R instrument with high directive antennas working at L1/E1 and L5/E5a bands. The instrument is part of Dr. Raul Onrubia [22] and Dr. Daniel Pascual [23] Ph.D. theses, and it flew over Australia in

2018, over land, to study soil moisture, and over the ocean, to study the sea state. The instrument design and data collection were conducted in the frame of their Ph.D. theses, and the necessary data processing tools, algorithms, and techniques to retrieve geophysical parameters from MIR data are analyzed in this dissertation.

Furthermore, to retrieve the sea ice climate variable, a ground-based experiment was performed as part of the Multidisciplinary Drifting Observatory for the Study of Arctic Climate (MOSAiC) expedition over the Arctic sea. This campaign's primary objective is to prove the capabilities of GNSS-R to measure sea ice properties (i.e., snow content on top of the sea-ice and sea-ice thickness).

Finally, to contribute to the development of passive microwave instruments for CubeSats, a family of passive microwave instruments is proposed, named "Flexible Microwave Payloads", or "FMPL". Within this Ph.D. thesis, three instruments are developed: the FMPL-1, the FMPL-2, and the FMPL-3. The FMPL-1 is part of the ^{3}Cat-4 mission [CP1], part of the ESA Fly Your Satellite! program, and there is not a planned launch yet. The second, FMPL-2, is part of the FSSCat mission [CP2], which was launched the 3 September 2020. Finally, the FMPL-3 is part of the GNSSaS mission [24] from the NSSTC of the UAE, and there is not a confirmed launch date yet. In this dissertation, the design of these three instruments is presented. However, the validation and data results are only presented for the FMPL-2, which is the only instrument already in orbit.

From these primary goals, a set of particular objectives are defined, and described below:

- To **study** the different GNSS signals, their achievable spatial resolution, and the signal processing constrains for using them for GNSS-R applications.
- To **develop** a data processing framework for the MIR instrument.
- To **analyze** and **develop** the required algorithms to retrieve sea state using MIR data.
- To **analyze** and **develop** the required algorithms to retrieve land-related parameters using MIR data.
- To **analyze** and **develop** the required algorithms to retrieve sea-ice parameters using MOSAiC GNSS-R data.
- To **contribute to the development** of FMPL-1, FMPL-2, and FMPL-3 CubeSat-based passive microwave instruments.
- To **develop** the necessary algorithms to validate and retrieve essential climate variables using in-orbit FMPL-2 data.

Moreover, during the development of the thesis, other activities have been also carried out. To support in the development of the UHF and S-band ground stations in Sant Esteve de la Sarga (Montsec), Spain, which are used to download the data from ^{3}Cat-4 and ^{3}Cat-5/A, respectively. To support the project management of FSSCat by performing the frequency filling and coordination with the International Telecommunication Union

(ITU). To contribute to the software development of the ^{3}Cat-4 mission, and provide support to the communications, attitude, and electrical power subsystems. To contribute in the creation of the "Pla Estatègic del NewSpace a Catalunya", which is the Catalan government initiative to establish a "NewSpace" industry in Catalonia.

1.4 Outline

This Ph.D. thesis has been divided in seven parts, containing a total of thirteen chapters including the main contributions of the Ph.D. thesis, a number of Appendices with complementary information, and the bibliography and list of publications. The outline of the thesis is the following:

- Part I: Introduction and Theoretical Background
  - Chapter 1 introduces the concept of nano-satellite and the CubeSat form factor and its use for Remote Sensing. Then, remote sensing sensing and the use of CubeSats for Earth Observation is presented. After that, the different instrument precursors previously developed in the Department are briefly introduced. In addition, the motivation and goals of the thesis are presented. Finally, the outline of this Ph.D. thesis is stated.
  - Chapter 2 shows an introduction and a brief review of the different passive microwave remote sensing techniques developed within this Ph.D. thesis: GNSS-R and L-band radiometry. Applications for each sensor and current space-borne missions are presented.
  - Chapter 3 presents two theoretical studies performed for the GNSS-R technique. The first study presents the implications of selecting the optimum incoherent integration time for GNSS-R receivers at both L1 and L5 bands from an airborne point of view, and its link to space-borne missions. Finally, the second study presents the analytical results of the ripples produced when the GNSS reflection transits between two different media as land and water.
- Part II: Preparatory Field Experiments
  - Chapter 4 explains the GNSS-R signal processor developed to process the MIR experiments conducted in Australia, in 2018.
  - Chapter 5 presents the results of the MIR campaign over the Ocean. The first part of the chapter covers the potential of coherent integration over the ocean, and the second part of the chapter explains a new algorithm developed to estimate wind-driven and swell waves.
  - Chapter 6 presents the results of the MIR campaign over Land. This chapter is focused on the study of the effect of the local surface roughness in the GNSS-R signal, its link to soil moisture, and potential actions to mitigate this effect, proposing a machine-learning algorithm to retrieve soil moisture using L1 and L5 GNSS-R data. Moreover, a methodology to retrieve vegetation canopy height is also presented.
  - Chapter 7 presents the PYCARO-2 instrument. This instrument has been deployed over an ice floe in the Arctic Ocean as part of the MOSAiC campaign.

The objective of instrument is to provide ancillary data and model validation for GNSS-R over the sea-ice.

- Part III: Development of Space-borne Instrumentation
  - Chapter 8 presents the Flexible Microwave Payload -1, the passive microwave payload part of the ^{3}Cat-4 mission, part of the ESA Fly Your Satellite! program (target launch date Q4 2021, Q1 2022). The instrument comprises a GNSS-R and an L-band radiometer instrument using low-cost SDR technologies.
  - Chapter 9 presents the Flexible Microwave Payload -2, the passive microwave payload part of the FSSCat mission, winner of the 2017 ESA Sentinel Small Satellite challenge and the 2017 Copernicus Masters competition award. The instrument is simultaneously retrieving GNSS-R and L-band radiometry measurements.
  - Chapter 10 presents the Flexible Microwave Payload -3, the passive microwave payload part of the GNSSaS mission, developed by NSSTC, the United Arab Emirates technology center. The instrument will be the first L5 GNSS-R instrument deployed into the space, and it integrates a secondary experiment to study the ionosphere.
- Part IV: FMPL-2 Results
  - Chapter 11 presents the in-orbit validation results retrieved by FMPL-2 during its first two weeks of executions in LEO. This chapter includes the details and validation of the data going from level 0 (raw data) to level 1C (Geo-projected and calibrated).
  - Chapter 12 presents different algorithms to estimate Sea Ice Concentration, Sea Ice Thickness, and Soil Moisture data using FMPL-2 in-orbit data.
- Part V: Conclusions and Future Research Lines
  - Chapter 13 states the main conclusions and contributions of this Ph.D. thesis. Finally, it presents future research lines to continue with the work of this Ph.D. thesis.
- Part VI: Appendices.
- Part VII: Bibliography and list of publications.

Finally, it is important to remark that this Ph.D. thesis is composed of several peer-reviewed journal manuscripts. In particular, Chapters 3, 5, 6, 7, 9, 11, and 12 contain adapted contents from published peer-reviewed manuscripts, being the Ph.D. candidate one of the main contributors. Moreover, it is important to remark that all the manuscripts forming this Ph.D. thesis have been published under the CC-BY 4.0 license, and they are open access for everyone.

2

Chapter 2

Passive Microwave Remote Sensing

This Chapter introduces the two passive microwave remote sensing techniques that are covered in this dissertation: L-band radiometry and GNSS-Reflectometry. Section 2.2 covers the types of radiometers, explaining different techniques, calibration schemes, and applications; Section 2.3 explains the GNSS-R technique, including the definition of the observables, the nowadays available GNSS signals to perform GNSS-R, and their current applications from space. Section 2.4 introduces the basic concepts of a particular machine learning algorithm used in EO: the artificial neural network. Finally, Section 2.5 is a review of all Earth Observation instruments developed by the Passive Remote Sensing group at the UPC Remote Sensing Laboratory, including all GNSS-R instruments, microwave radiometry instruments, and other types of instruments that have been developed in the last 20 years. Note that, instruments developed in the frame of this Ph.D. thesis are also introduced in this section.

2.1 Introduction

Climate change is a reality. The world is changing, and to better understand the effects that these changes will bring, humanity must monitor and understand the ECVs [1]. Sea Ice Extent (SIE), Sea Ice concentration (SIC), Sea Ice Thickness (SIT), and Soil Moisture (SM) over land [2, 25] are four of these geophysical indicators that serve for a better understanding of the "water cycle" of our planet. On one hand, the increase of sea ice monitoring instruments, in terms of quantity and quality, is strongly required, and this is one of the 10 use cases that are not currently covered by the Copernicus program of the European Union [26]. On the other hand, SM monitoring is crucial for several reasons: as the planet's population increases, more and more resources are needed. Larger farms and plantations will be required, and sustainable irrigation policies are required to prevent desertification or flooding [27].

GNSS-R and L-band radiometry are two passive microwave techniques that have proved to work for sea-ice [28–32] and SM monitoring [28, 33–36]. Thanks to the lower power consumption, as compared to active sensors, both instruments can be adapted to smaller satellites, like CubeSats.

2.2 L-band Radiometry

Every material at a temperature different from 0 K emits a certain amount of energy per unit of time in a certain wave-length range. In case of a blackbody, an ideal absorber, all the absorbed power is then radiated isotropically, as stated by Planck's Law (Chapter 4 from [3]), and its approximation for low frequencies (e.g. L-band). The spectral brightness density is defined in Eq. 2.1.

$$B_f = \frac{2 \cdot h \cdot f^3}{c^2} \cdot \frac{1}{\frac{h \cdot f}{e^{k_B \cdot T_{ph}}} - 1} \approx \frac{2 \cdot h \cdot f^3}{c^2} \cdot \frac{k_B \cdot T_{ph}}{h \cdot f} = \frac{2 \cdot k_B \cdot T_{ph}}{\lambda^2}, \tag{2.1}$$

where B_f is called the spectral brightness density, which is the amount of power being radiated per unit of surface, per unit of spectral width, and per unit of solid angle. In Eq. 2.1 f is the frequency in Hertz, k_B is the Boltzmann's constant $k_B = 1.38 \cdot 10^{-23} J/K$, T_{ph} is the physical temperature in Kelvin, and c is the speed of light.

However, a blackbody is an idealized source, and *real* bodies do not absorb all the incident power, some part is reflected, some part is transmitted into the body, etc. In this case, a real body radiates less than a blackbody at the same physical temperature. The emitted brightness is then related to the "brightness temperature" (T_B), and it is also related to the physical temperature by means of the emissivity, as shown in Eq. 2.2.

$$e_f(\theta, \phi) = \frac{B_f(\theta, \phi)}{B_{f,blackbody}} = \frac{T_B(f, \theta, \theta, \phi)}{T_{ph}}. \tag{2.2}$$

In this case, the emissivity of perfect reflecting material is zero, while for a perfect absorber (i.e., blackbody) is one. At L-band, the sea, the ice, and the land have different emissivities, and therefore different brightness temperatures. At nadir, the sea surface has a $T_B \sim 100$ K, and the sea ice emits a range of T_B depending of its thickness ∼120-220 K.

Finally, the land emits a different brightness temperature depending on its surface water content and temperature. In this case, within a range of 180-260 K. For the land case, the drier the land surface is, the higher the emitted T_B.

At low frequencies the T_B is measured by means of antennas. As described in [3, 37], the radiation emitted by a given surface (i.e., sea or land) reaches the antenna passing through the atmosphere which, depending on the band, attenuates the emission and possibly it also scatters it (if hydrometeors are presents). At the end, the antenna receives an apparent power weighted by its radiation pattern, as shown in Eq. 2.3.

$$P = \frac{1}{2}\int_{f_0-\frac{B}{2}}^{f_0+\frac{B}{2}} \iint_{4\pi} A_{eff} \cdot B_i \cdot |F_n(\theta,\phi)|^2 \, d\Omega \, df \triangleq k_B \cdot T_A \cdot B, \tag{2.3}$$

where A_eff is the antenna effective area, B is the receiver's noise bandwidth, centered at the frequency f_0, and $|F_n(\theta,\phi)|^2$ is the normalized antenna co-polar radiation pattern.

2.2.1 Types of radiometers

As detailed in Fig 2.1, depending on the antenna configuration, two different types of radiometers are encountered: real aperture radiometers, or synthetic aperture radiometers. On the first one, half-beam antenna foot-print corresponds to the pixel size of the instrument (e.g., Fig. 2.1 (A)). In the case of synthetic aperture radiometers, the cross-correlation between the signal collected by different antennas produces different *synthetic beams*, thus, providing a complete *image* of the scanned area. As an example, a 1D synthetic aperture can be developed to implement the push-broom scanning approach (see Fig. 2.1 (F)).

The type of radiometers that are developed within this Ph.D. thesis are based on *real aperture* radiometers, and the following list summarizes, in general, the three most relevant topologies implemented for real aperture radiometers are:

- The Total Power Radiometer (TPR) is the simplest concept of a microwave radiometer (MWR). As sketched in Fig. 2.2a, the radiometer antenna collects the radiation at a given band (i.e. thermal noise). Then, the collected radiation is amplified, filtered, and the final received power is then either the input of a low-pass filter and power meter, or the signal can be IQ demodulated to baseband, sampled by an Analog-to-Digital converter (ADC), and then the received power is computed and filtered digitally. This output is then compared to some calibration values (e.g. the sky apparent temperature or a perfect absorber) to estimate the antenna temperature emitted by the "material" pointed by the antenna. This scheme is quite sensitive to thermal variations in the amplifying chain, as the power measured is the sum of the antenna received power (T'_A at Fig. 2.2a is the antenna power including the antenna ohmic losses) plus the amplifier temperature (T_R), which normally varies with temperature/voltage. Therefore, this type of radiometer may induce erroneous measurements if proper calibration techniques are not applied.

- The Dicke radiometer (DR) was conceived by Dr. Robert Dicke in 1946 [38] to minimize the effect of gain fluctuations in the TPR. The Dicke radiometer includes a radio-frequency (RF) switch to commute between the antenna, and a known and

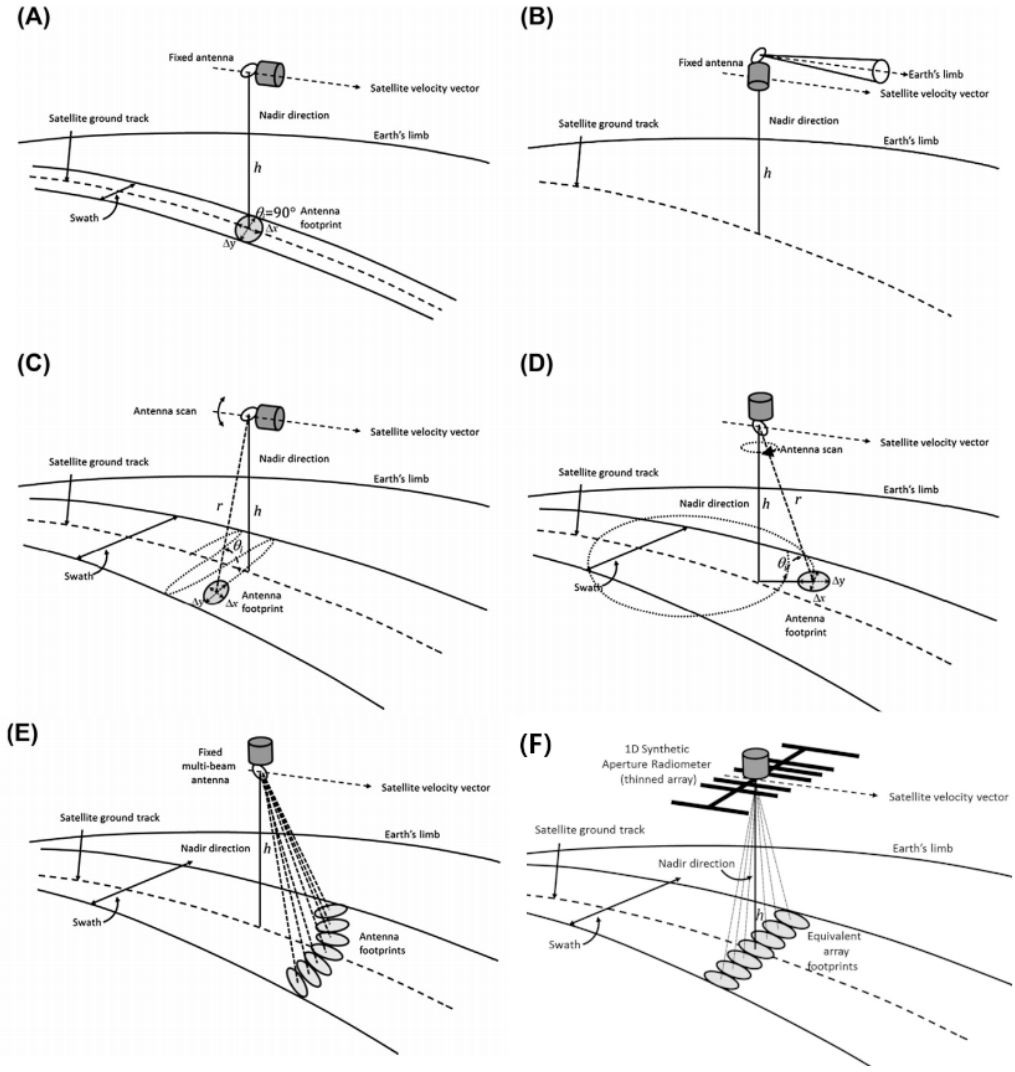

Figure 2.1: Typical microwave radiometer scanning configurations: (A) nadir looking, (B) limb sounders, (C) cross-track scanner, (D) conical scanner, (E) real aperture push-broom, and (F) 1-D synthetic aperture push-broom scanning. Adapted from Figs. 4.69 and 4.112 of [3].

thermally stable matched load. The amplifier and filter output is now multiplied by ± 1 before the power detection. Thanks to this technique, the power measured is not proportional to T_R anymore, but to the difference between the antenna temperature (T'_A, including ohmic losses), and the reference temperature T_{Ref}, as illustrated in Fig. 2.2b. This gain fluctuations are totally compensated if the antenna received temperature is equal to the reference temperature, which cannot be normally achieved, as the antenna temperature varies depending on the emission

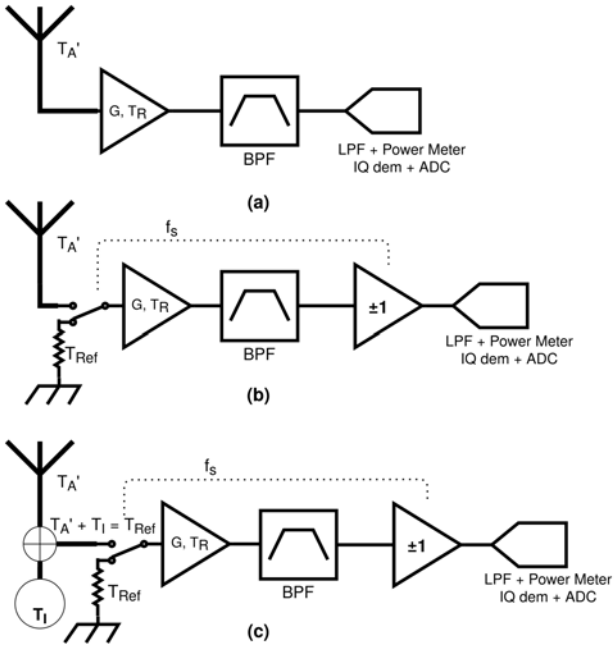

Figure 2.2: (a) RF sketch of a Total Power Radiometer, (b) RF sketch of the Dicke radiometer , and (c) RF sketch of a Noise Injected Radiometer

an a priori unknown source.

- The Noise Injection Radiometer (NIR) is an evolution of the DR where noise is injected to the antenna so that the sum of the antenna temperature (T'_R) plus this new injected noise (T_I in Fig. 2.2c) is equal to T_{Ref}. This type of radiometers are stable against gain fluctuations, but it requires that the noise source is very well characterized and stable.

There is not a rule to select the type of radiometer or the topology that should be used. It all depends on the final application, the accuracy and stability required, the surrounding environment, etc. As an example for a single measurement, the TPR has a higher sensitivity as compared to the Dicke or the Noise Injection radiometer. However, in terms of thermal stability, the TPR is the one losing, as it performs the worse if the radiometer lacks of a frequent calibration (p. 230-232 from [3]).

2.2.2 Current applications of L-band radiometers from space

L-band radiometric measurements are used for several applications, all of them related to what is known as "*the water cycle*". At L-band, the following measurements can be retrieved:

- Soil Moisture: the apparent brightness temperature of the near-surface (i.e. 5 to 20 cm) soil depends on the water content of this thin layer, being larger for dryer

soils, and smaller for moist soils. In combination to other sensors (i.e. surface temperature, vegetation opacity), near-surface soil moisture can be retrieved [36].

- Wind speed over the ocean: the ocean has an apparent brightness temperature of $\sim$ 90 K. This value varies depending on the ocean surface temperature, the wind-speed over the ocean, and the salinity of the ocean itself. If the average temperature and salinity are compensated, wind-speed over the ocean can be retrieved [39].

- Ocean salinity: analogously to the previous case, if both temperature and wind-speed are compensated, the ocean salinity can be estimated from these measurements [40].

- Sea ice extent: as compared to the ocean, the ice has a much larger brightness temperature. Thus, by looking to abrupt brightness temperature changes, sea-ice extent can be estimated [29].

- Sea ice thickness: following the previous case, from increasing ice thickness, the brightness temperature emitted by the ice core increases, and it attenuates more the water emission [29].

- Cryosphere monitoring: as a consequence of the previous measurements, cryosphere measurements can be conducted by looking to the emitted temperature of a frozen land area.

All six parameters above presented are ECVs [1]. Thus, it is clear that L-band radiometry plays an important role to understand the planet's climate. Moreover, space agencies over the world have invested in deploying missions that include L-band radiometers. The Soil Moisture and Ocean Salinity (SMOS) mission (see Fig. 2.3a) is the first EO mission from ESA, and also the first mission ever including an L-band radiometer in space [41]. The radiometer architecture is based on a Synthetic Aperture Radiometer, providing global coverage in 2-3 days. The mission was conceived to provide ocean salinity, with an accuracy of 0.2 psu at 100 km resolution, and SM measurements, with an accuracy of 0.04 m^3/m^3 at 35-55 km resolution. However, it is also delivering sea-ice thickness estimates over the Arctic ocean. The mission is still running and providing data since 2009.

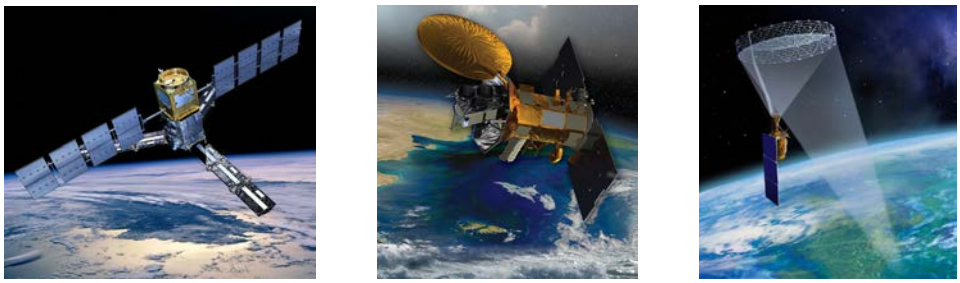

(a) **(b)** **(c)**

Figure 2.3: (a) SMOS artist's view from ESA/AOES Medialab, (b) Aquarius spacecraft artist's view from NASA, and (c) SMAP artist's view adapted from [42].

Aside from SMOS, there are two more missions that include an L-band radiometer. The first one was the Aquarius mission (see Fig. 2.3b) from NASA, including a real aperture radiometer combined with a scatterometer. The main objective was to provide ocean salinity measurements at a 100 km spatial resolution with an accuracy of 0.2 psu, providing global coverage in 7 days. In addition, a secondary objective was set after launch to provide SM estimates over land at the same coarse resolution. However, the mission had a major failure and stopped providing data in 2015.

The last mission presented here is the Soil Moisture Active Passive (SMAP) mission (see Fig. 2.3c) from NASA. This mission includes an L-band radiometer to provide SM measurements with an enhanced spatial resolution of 36 km, with the same accuracy as SMOS, 0.04 m^3/m^3. The mission also integrated an L-band radar to provide 9 km measurements, but it failed 3 months after launch. SMAP comprises a rotating deployable mesh antenna to measure the Earth using a rotating scan, providing global coverage in 2-3 days.

2.3 GNSS-R

Global Navigation Satellite Systems (GNSS) were originally designed to provide accurate position, navigation, and timing. The transmitted signals, the so-called Pseudo-Random Noise (PRN) codes, spread the power of the signals in the frequency domain and allows code multiplexing. In this way, a receiver is able to receive signals below the noise floor, and from multiple satellites and systems simultaneously.

Besides the original purposes of these systems, multiple applications have been derived [43–45]. GNSS signals are used in Remote Sensing as SoOp for Radio Occultations (GNSS-RO) [46,47] and Reflectometry (GNSS-R). The GNSS-R concept was proposed for the first time in 1988 as a multi-static scatterometer [48], and later on in 1993 for sea altimetry [49], using a method called now interferometric GNSS-R (iGNSS-R), which consists of cross-correlating the direct signal with the reflected one. In that way, military codes, which provide a better spatial resolution, could also be used without knowing them. However, iGNSS-R suffers from interferences and channel cross-talk between the different GNSS satellites. In 1996, the conventional technique (cGNSS-R) was proposed [50], which is based on the correlation of the reflected signal with a locally generated clean replica of the desired code. This replica is system dependent, and each GNSS constellation (i.e., GPS, Galileo, GLONASS, or Beidou), and band, has its own type of GNSS code, providing different type of applications, as it will be introduced in Section 2.3.1.

cGNSS-R is the second passive microwave technique covered in this Ph.D. thesis. This technique is based on the acquisition of the GNSS reflected signal on a given Earth surface, which produces multiple wavefronts being scattered depending on the reflected surface. Each wavefront has a different delay and Doppler that depends on the scenario geometry [51]. The point that has the minimum path between the satellite, the surface, and the antenna is called the Specular Reflection Point. When the surface is flat, only the wave reflected in this point is received (see Fig. 2.4). As the surface becomes rougher, more wavefronts scattered around the specular point are received by the antenna. The area from where these reflected wavefronts are received is the so-called Glistening Zone, and it depends not only on the roughness, but also on the height, and the elevation angle [50].

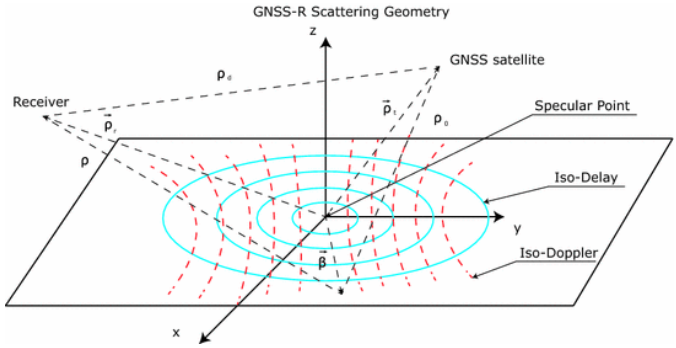

Figure 2.4: Reflection scenario adapted from [52].

The distribution of the received signals in the delay and Doppler domains can be studied with the Cross Ambiguity Function (CAF) [51], defined in Eq. 2.4.

$$Y_{xy}(\tau,\nu) = \frac{1}{T_c}\int_0^{Tc} x(t)y^*(t-\tau)e^{-j2\pi\nu t}dt, \tag{2.4}$$

where x and y are the signals to be cross-correlated, and T_c is the coherent integration time. In cGNSS-R, the reflected signal $x = s_r$ is correlated against the code $y = c$, and this is called Woodward Ambiguity Function (WAF). In iGNSS-R, the reflected signal $x = s_r$ is correlated against the direct signal $y = s_d$, and it is called CAF.

Moreover, the correlated signal is then incoherently averaged a given number of times (N) in order to increase the signal-to-noise ratio (SNR) of the observable, usually called Delay-Doppler Map (DDM), and each cell of the DDM is given by Eq. 2.5. Note that, the incoherent integration time (T_{int}) is usually given in seconds, as the product between N and T_c ($T_{int} = N \cdot T_c$).

$$DDM_{xy}(\tau,\nu) = \frac{1}{N}\sum_{i=1}^{N}\left|Y_i(\tau,\nu)\right|^2, \tag{2.5}$$

where Y_i is the i^{th} realization of Y_{xy} from Eq. 2.4.

Figure 2.5 shows two examples of DDM from a space-borne instrument, and over different scattering surfaces.

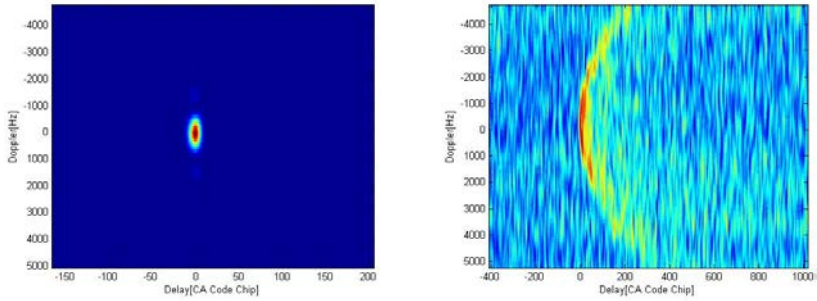

(a) **(b)**

Figure 2.5: Examples of DDMs from the UK-UK-DMC mission with coherent integration time of 1 ms, incoherent averaging time of 200 ms [53] (a) over ice, (b) over ocean.

2.3.1 GNSS signal types

There are four different types of GNSS systems, each of them with different signal types, band usages, etc. When this type of signal is used to perform GNSS-R, the intrinsic characteristics of each system must be taken into account. Overall, for GNSS-R applications the following parameters need to be considered:

- **Band**: located at L-band, GNSS systems transmit in different sub-bands inside the L-band. In general, GNSS systems are divided in the Upper L-band, ranging from 1559 MHz to 1610 MHz, and the Lower L-band, ranging from 1164 MHz to 1300 MHz (see Fig. 2.6). Each GNSS system has different sub-band definitions, with different central frequencies and bandwidths. Depending on the band used to perform GNSS-R the reflection properties will differ. For instance, the upper band has a lower penetration depth than the lower band.

- **Chip rate**: same as the band, each GNSS system has a different modulation and chip rate definition. In case of GNSS-R, the chip rate is critical, as it directly impacts the achievable spatial resolution. A chip rate of 1.023 MHz (i.e. GPS L1 C/A, Galileo E1, Beidou B1D1, or GLONASS L1) translates into a spatial resolution of $\sim$ 300 m, which is the chip length in space (see Eq. 2.6), whilst a chip rate of 10.230 MHz (i.e. Galileo E5a/E5b or GPS L5) corresponds to a spatial resolution of $\sim$ 30 m.

- **Code length**: each GNSS signal has an in-built periodicity. The PRN code used is repeated a number of times to build the different bits composing a GNSS message. The length of this code is usually specified in time units (i.e. milliseconds). As an example, the L1 C/A code is repeated every 1 ms, while the Galileo E1C is repeated every 4 ms, despite they have the same chip rate. This has a direct impact when GNSS signals are used to perform GNSS-R. If the length PRN code is larger than the coherency of the reflected surface (T_{corr}) [54], the code is not likely to work. As an example, in case that given surface has a coherence time of 1 ms (i.e. it will randomly rotate the phase of a reflected wave), and a GNSS code has a length of 4 ms, 4 "phase changes" will occur during the coherent integration (i.e. T_c in Eq. 2.4) of the PRN signal, therefore the auto-correlation value will be negligible,

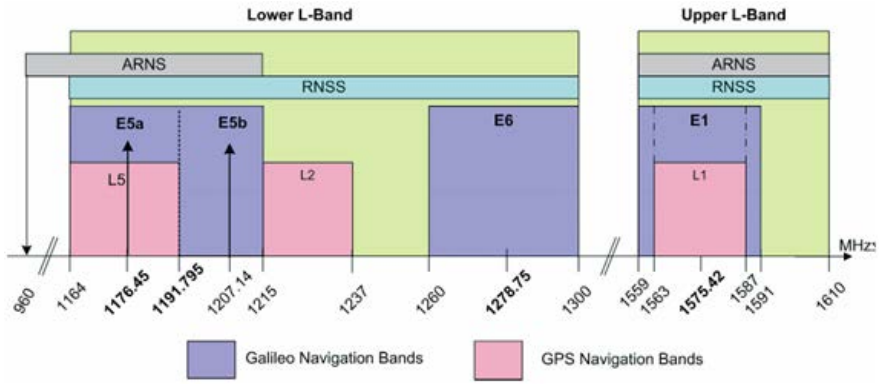

Figure 2.6: GPS and Galileo frequency band plan, including the definition of the Upper and Lower L-bands, and each of the GPS and Galileo sub-bands.

and likely masked by the noise floor[1]. In this case, the "code length" term used is the smallest code length that can be used. At the end, the code can be extended by appending N times the *base* code in order to generate a longer one up to the navigation bit period of the GNSS signal (i.e. 20 ms for GPS L1 C/A). However, most of the current applications are working with the smallest code length possible.

- **Modulation**: the first GNSS signals transmitted the information using a Binary Phase-Shift Keying (BPSK) signal, but new system use improved modulations called Binary Offset Carrier (BOC) [55]. This new type of modulation introduces subcarriers to the original ranging codes, resulting in a multi-peak auto-correlation function (ACF) (see Fig. 2.7). The BOC modulation is usually defined with two additional numbers: BOC(n, m), being m the code chipping rate, and n the subcarrier frequency. Moreover, some GNSS signals combine different BOC modulations, producing Alternative BOC modulations (AltBOC), using complex subcarriers instead of real ones; or the multiplexed BOC (MBOC), where multiple subcarriers are used. Further information on the implications for each modulation type can be found in [23, 56, 57].

$$L_{chip} = \frac{c}{R_{chip}} \tag{2.6}$$

where L_{chip} is the chip length in space (i.e. the spatial resolution), c is the speed of light, $3 \cdot 10^8$ m/s, and R_{chip} is the chip rate in Hz.

[1]This is the case of Galileo E1C signals (T_c =4 ms) for ocean applications (T_{corr} ∼1 ms) from space

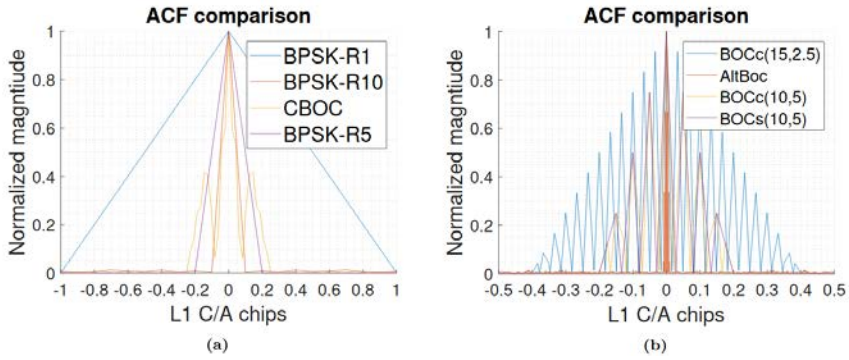

Figure 2.7: Comparison between different modulations present in modern GNSS system, (a) comparison between different BPSK modulations at different sampling times, and the CBOC modulation, and (b) comparison between different BOC modulations and the AltBoc modulation. Adapted from Fig. 2.6 of [23].

The modulation scheme of the GNSS systems is used to transmit the appropriate data sequence used to triangulate the position of a given GNSS receiver. This data sequence is formed by a binary sequence, and it is transmitted at a very low baud rate. In case that the coherent integration time, T_c, is larger than the code length, a bit transition may occur in the middle of the integration, decreasing the integration value. However, most of the modern GNSS signals contain a pilot (i.e., data-less) signal. This pilot signal is multiplexed together with the data signal, as in Galileo E5/E6 bands, or the GPS L5 pilot signal.

Tables 2.1, 2.2, 2.3, and 2.4 summarize the different GNSS service names for each GNSS system, detailing their frequencies, chip rates, and code length. Note that, only the civil codes that have been used for cGNSS-R are presented.

Table 2.1: GPS signal scheme summary for civil data and pilot signals commonly used for GNSS-R applications

Service Name	**Service Type**	**Frequency**	**Chip Rate**	**Code Length**	**Modulation**
L1 C/A	Data	1575.42 MHz	1.023 MHz	1 ms	BPSK
L1 C	Data + Pilot	1575.42 MHz	1.023 MHz	10 ms	MBOC(6,1,1/11)
L2 CM	Data	1227.60 MHz	511.5 kHz	20 ms	BPSK
L2 CL	Pilot	1227.60 MHz	511.5 kHz	1500 ms	BPSK
L5I	Data	1176.45 MHz	10.23 MHz	1 ms	BPSK
L5Q	Pilot	1176.45 MHz	10.23 MHz	1 ms	BPSK

Table 2.2: Galileo signal scheme summary for civil data and pilot signals commonly used for GNSS-R applications

Service Name	Service Type	Frequency	Chip Rate	Code Length	Modulation
E1 OS	Data + Pilot	1575.42 MHz	1.023 MHz	4 ms	MBOC(6,1,1/11) (called CBOC)
E5a	Data + Pilot	1176.45 MHz	10.23 MHz	1 ms	AltBOC(15,10)
E5b	Data + Pilot	1207.14 MHz	10.23 MHz	1 ms	AltBOC(15,10)

Table 2.3: GLONASS signal scheme summary for civil data and pilot signals commonly used for GNSS-R applications

Service Name	Service Type	Frequency	Chip Rate	Code Length	Modulation
L1 C/A	Data	1602 MHz	511.5 kHz	1 ms	BPSK
L2 C/A	Data	1246 MHz	511.5 kHz	1 ms	BPSK

Table 2.4: Beidou signal scheme summary for civil data and pilot signals commonly used for GNSS-R applications

Service Name	Service Type	Frequency	Chip Rate	Code Length	Modulation
B1I	Data	1561.10 MHz	2.046 MHz	1 ms	BPSK
B1C	Data + Pilot	1575.42 MHz	1.023 MHz	10 ms	BOC(1,1)
B2I	Data	1207.14 MHz	2.046 MHz	1 ms	BPSK

2.3.2 Current applications of GNSS-R from space

Located at L-band, GNSS-R can provide, at least, the same type of applications as L-band radiometry. The reflectivity is one of the main observables retrieved by a GNSS-R instrument. This observable is the complementary magnitude of the emissivity collected by an L-band radiometer (see p. 136 from [3]). However as opposed to the L-band radiometry technique, the GNSS-R technique shines because of two reasons. First, the huge amount of GNSS satellites currently working, as each GNSS satellite in view produces a reflection on the Earth's surface that is collected from a spacecraft[2]. Second, the spatial

[2]Assuming an average of 6-8 satellites in view per constellation and multiplied by 4 constellations, up to 24-32 reflection points can be retrieved simultaneously.

resolution is not given by the antenna size, but by the size of the Fresnel zones of the reflection, as will be analyzed in Chapter 3.

So far, up to seven missions have been launched carrying a GNSS-R instrument on board. The first mission was the UK - Disaster Monitoring Constellation (UK-DMC), launched in 2003 (see Fig. 2.8a), carrying a set of experimental payloads and technology demonstrators. Among them, the first spaceborne GNSS-R receiver was launched. The UK-DMC GNSS-R experiment was a success [58]. Even though the downlinked data set was very limited [59], preliminary results showed a correlation between the GNSS-R DDM and the sea state, resulting in the first GNSS-R application from space.

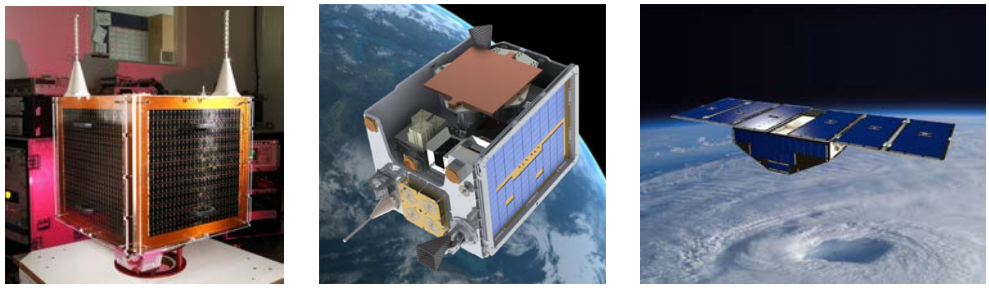

(a) **(b)** **(c)**

Figure 2.8: (a) UK-DMC artist's view, (b) UK TDS-1 artist's view, and (c) CyGNSS artist's view.

The UK-DMC satellite manufacturer, Surrey Satellite Technology Ltd., designed the first generation of a spaceborne GNSS-R receiver: the Space GPS Receiver Remote Sensing Instrument (SGR-ReSi) [60]. In 2014, the UK-TechDemoSat-1 (TDS-1), was launched with this new receiver as one of its main payloads (see Fig. 2.8b). The mission proved to retrieve GNSS-R data from the entire globe, allowing a large set of applications, such as sea ice detection [30, 32], sea ice classification [61], wind velocity over the ocean [62], above-ground biomass (AGB) retrieval [63, 64], canopy height (CH) [63], and soil moisture retrieval from ground [65, 66], airborne [67–69], and spaceborne [34, 35, 70–74] configurations.

Two years later, in December 2016, NASA launched the Cyclone GNSS (CYGNSS) mission: an 8 microsatellite constellation (see Fig. 2.8c) carrying the TDS-1 SGR-Resi as the main instrument. The mission goal is to provide near real-time wind velocity over the ocean information to detect hurricanes [75–77], showing uncertainties up to 17% for wind speeds below 20 m/s [78]. As compared to UK-DMC or TDS-1, the amount of data collected by an 8-satellite constellation allows implementing data-driven algorithms to enhance the retrieval of several ECV [75, 76]. One of the ECV that CyGNSS mission is contributing the most in the last years is in the soil moisture estimation. In this field, different machine learning models have been implemented, showing promising results to retrieve several ECVs, as they are able to recognize "hidden" patterns in large amounts of data. Furthermore, several algorithms have been applied to retrieve soil moisture using Artificial Neural Networks (ANN) [35, 79, 80]. These algorithms can easily solve complex non-linear problems, where traditional approaches often fail to address adequately. Prior to the model training, GNSS-R observations can be combined differently in terms of

preceding averaging, gridding, and the processing of time series, where multiple GNSS-R observables can be combined in different ways, such as performing multiple averages into a 36 km grid [73, 79], computing spatio-temporal averages to finer grids (achieving a resolution of 22 km), or by means of time-series analysis [81]. Recent works using such algorithms have shown great performance to retrieve SM, with root-mean-square differences (RMSD) with respect to SMAP SM ground-truth lower than 0.05-0.07 m^3/m^3 (as detailed in Table 1 from [79]).

Aside from CyGNSS, several missions carrying a GNSS-R instrument have also been launched, as the ^{3}Cat-2 mission, in 2016, whose payload was never executed due to a failure in the satellite bus. More recently, the BuFeng-1 A/B [82] mission, the two GNSS-R CubeSats from Spire [18], and the ^{3}Cat-5/A CubeSat of the FSSCat mission [CP2] have been launched, all of them including a GNSS-R payload.

2.4 Artificial Neural Networks for Remote Sensing Applications

ANNs are the revolution of this decade. The applications of ANN are diverse, from speech recognition to image detection. To predict stock values evolution, or to know if tomorrow will rain or not [83]. ANN are also being used for EO [84], showing promising results for image classification or bias correction. As it can be seen in Fig. 2.9, an ANN has been used to correct the bias of the Normalized Difference Vegetation Index (NDVI[3]) product from the National Oceanic Atmospheric Administration (NOAA) Advanced very-high-resolution radiometer (AVHRR). In this case, the AVHRR data is corrected using MODIS NDVI data.

ANNs are also used for passive microwave remote sensing instruments. For L-band radiometers, the near real-time level 2 soil moisture product from SMOS is computed using an ANN [85] since 2016. This product combines T_B data from SMOS, NDVI data from MODIS, and back-scattering coefficients from the NOAA C-band Advanced Scatterometer to derive a daily global-coverage soil moisture product. Moreover, other studies using an ANN to combine active and passive data from SMAP data [86] have shown promising results for soil moisture content retrieval. Furthermore, ANNs are also applicable to actually predict future SM values, as shown in [87], and not only to correct or enhance actual SM products.

As presented in Section 2.3.2, valuable EO products are being retrieved from GNSS-R data through the implementation of ANNs. In this case, the most recent advances in SM estimation using GNSS-R data from CyGNSS are coming from ANN-based algorithms, such as [35, 79, 80, 88, 89]. Moreover, ANNs have been used to estimate wind-speed over the ocean by means of CyGNSS measurements [90]. For TDS-1, an ANN has been implemented to estimate the sea-ice border using image detection techniques [91].

2.4.1 Neuron structure

ANNs are contributing to many recent advances in all fields. But, how are ANN actually working? As defined in [83], a neural network is a set of interconnected analog signal

[3]NDVI is one of the most used parameters captured by multi-spectral spectrometers or imagers. This index is used to monitor the quality, quantity, and vegetation growth.

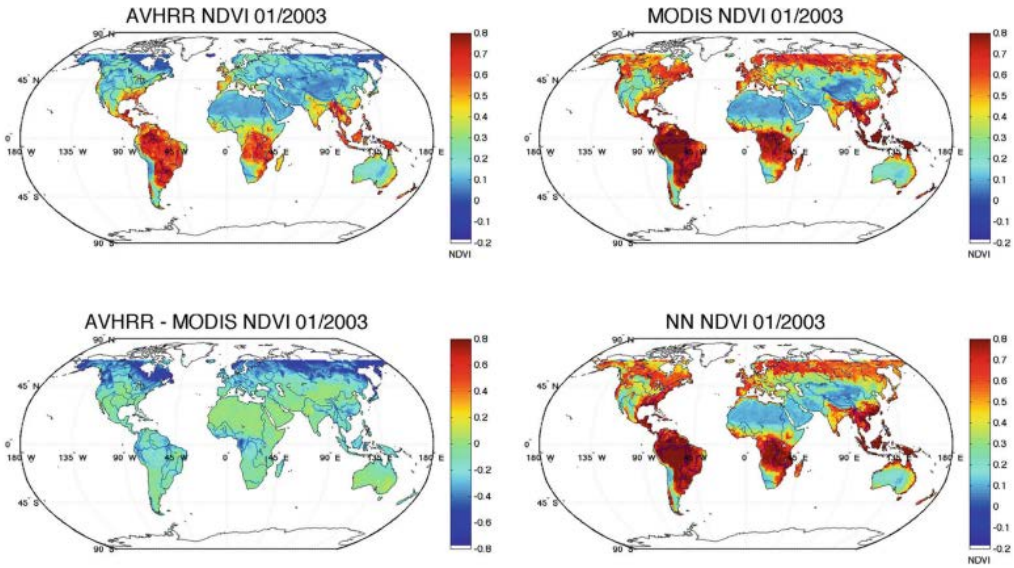

Figure 2.9: Use of ANN to correct AVHRR NDVI data using MODIS NDVI data. Reproduced from [84] (Fig. 1).

processors. These analog signal processors are called neurons [92], and they are usually interconnected in such way that they form some kind of *mesh*, similarly to how biological neurons work (Fig. 2.10a). Generally, the output of a kth neuron is:

$$y_k = f\left(\sum_{j=0}^{n} w_{kj}x_j - u\right), \tag{2.7}$$

where f is the transfer function, n is the number of inputs, x_j is the jth input signal, w_{kj} is the weight for the kth neuron applied to the jth input signal, and u is a bias or threshold term subtracted at the end of the sum operation. A graphical representation of Eq. 2.7 is presented in Fig. 2.10b. data

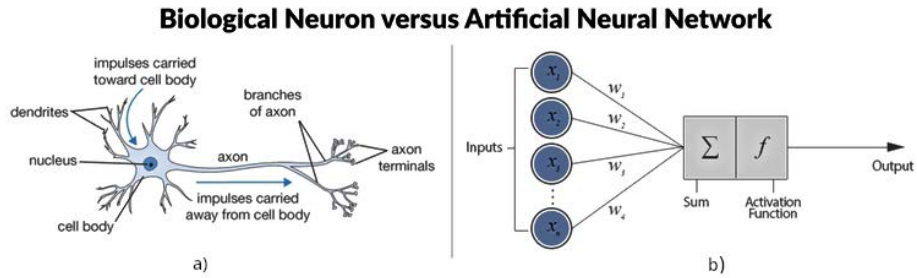

Figure 2.10: (a) Scheme of a biological neuron, as compared to (b) an artificial neuron. Credits: `https://www.datacamp.com/community/tutorials/deep-learning-python`

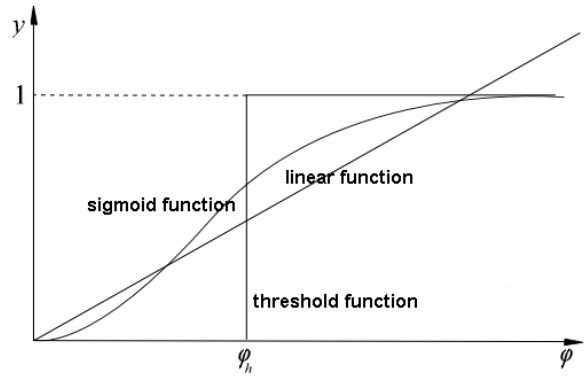

Figure 2.11: Example of different transfer functions used in ANN neurons. Reproduced from: `http://home.agh.edu.pl/~vlsi/AI/intro`.

The activation or transfer function, f is the function applied to the sum of all biases and neuron inputs. The most common functions are step functions (i.e., a binarization), linear functions, or non-linear functions, as detailed in Fig. 2.11. The most used transfer function in ANN is the *sigmoid* function, as it is a strictly smooth increasing function with "good" asymptotic properties, as described in [93].

In the end, neurons are distributed in different layers, forming the input layer, a set of hidden layers, and the output layer, as detailed in Fig. 2.12a as a Shallow network. The most basic neural network structure is composed of an input layer, a single hidden layer formed by a given number of neurons, and an output layer. Applied to EO, as the case of retrieving SM from a set of measurements, this output layer is normally a single neuron that produces a continuous output, e.g., a soil moisture value. When an ANN is computing a continuous value from the input data set, is it stated that the network is performing a *regression fit*. Furthermore, when more than one hidden layer is used inside an ANN, the network is now called a "Deep" network (as presented in Fig. 2.12b). These last type of networks are outstanding when solving complex non-linear problems with an a priori "*impossible*" solution. There are multiple network architectures, but normally the number of hidden layers (i.e., the depth of the network), and the number of neurons per layer are the most representative feature of the network.

2.4.2 Training, validation, and test of an ANN

The training process is the most critical task when implementing an ANN algorithm. The networks are trained in such a way that the output of the network has the least possible error with respect to the desired target. As an example, let's assume we have a set of meteorological measurements (e.g. for the sake of simplicity, wind speed and pressure), and an ANN is designed to infer the ambient temperature using these other two measurements. The training algorithm will collect different realitzations of wind speed and pressure and will adjust the weights and biases in Eq. 2.7 for each of the neurons composing the ANN. The output is then compared to the "target" value (i.e., temperature), and the weights and biases are adjusted in order to minimize the mean absolute error (MAE) between the ANN output and the desired target.

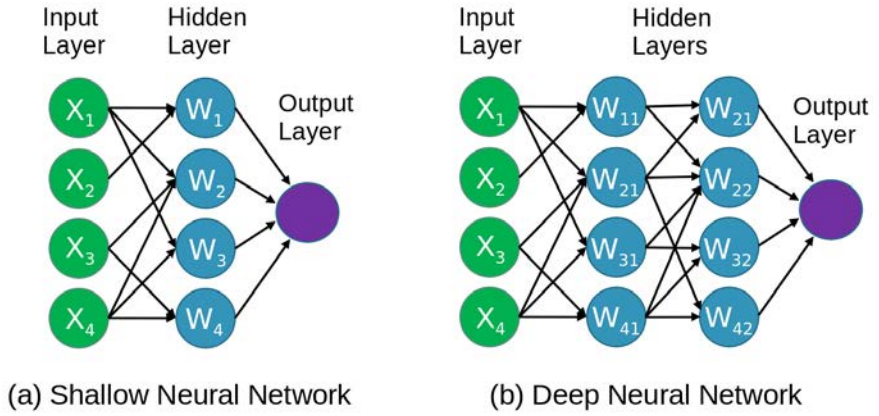

Figure 2.12: Comparison between (a) a shallow neural network, and (b) a deep neural network.

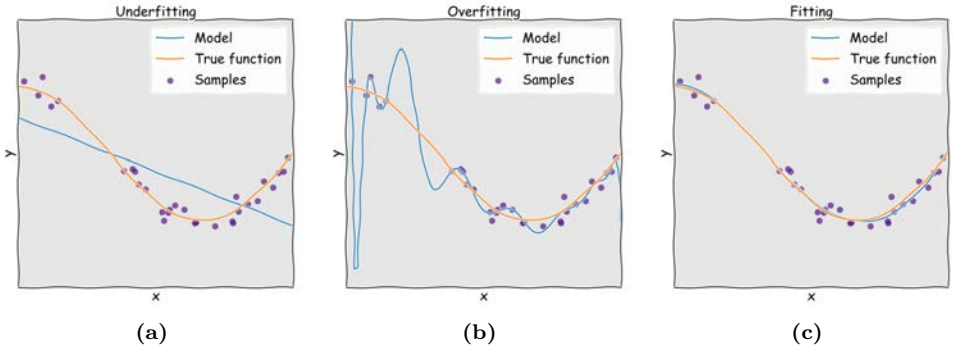

Figure 2.13: Example of an ANN (a) under-fitting, (b) over-fitting, and (c) well-fitting. Adapted from `https://keeeto.github.io/blog/bias_variance`.

After that, three situations can actually happen: the network "under-fits" the data, the network "over-fits" the data, or the network actually performs well. To illustrate that, three 1D examples are shown in Fig. 2.13.

An ANN may under-fit if the training process is too short, e.g., too few samples are introduced to the network to be trained. Going back to the meteorological example, if the training process just contained targets with high temperatures, the network does not know how to "predict" a low temperature value based on the wind speed and pressure measurements used as a input. In this case, the network will not perform for low temperature values, as it has not been trained for such purpose The network will be under-fitted. On the contrary, an ANN may over-fit when the selected model (i.e., number of hidden layers, and number of neurons per layer) is too large as compared to the size of both the data set and the number of inputs, and when the training process takes too many "examples". In this last case, the network will tend to capture the "noise" of the target values, as pictured in Fig. 2.13b.

To prevent under-fitting, the training set shall be large enough to "capture" all data dynamics (i.e., a range of all possible temperature values in the meteorological example). To prevent over-fitting, the network size shall be critically adjusted, and the training process stopped before the network starts to over-fit. To do so, a validation set of data is used for training. The training algorithm compares the MAE of the network output to the training data set with the MAE of the network output to the validation data set [94]. In case that, the validation set MAE increases to the training set MAE, the training process is stopped to prevent over-fitting. Finally, the network is tested against the test set. In case that the MAE of the three data sets is the same (with some tolerance), the network is performing a good fit. Aside from this strategy, other techniques are used to prevent over-fitting, as stopping the training process slightly before the MAE of the validation set increases [94], or pruning the network after training [95].

2.5 UPC Passive Microwave Remote Sensing Instruments

The UPC NanoSat-Lab is one of the laboratories of the UPC Passive Remote Sensing (PRS) laboratory. Both belonging to the Department of Signal Theory and Communications of the Universitat Politècnica de Catalunya, BarcelonaTech. The UPC PRS laboratory has designed and implemented a large set of Remote Sensing equipment for Earth Observation. The laboratory developed in 2001-2002 its first GNSS-R instrument, the DODEREC (DOppler-DElay RECeiver) [96], a three-channel GNSS-R instrument that was able to synchronously sample the GPS L1 C/A in-phase and quadrature components at 1-bit precision. In parallel, the laboratory was already developing L-band radiometers, but it was in 2003 where came the idea to combine an L-band radiometer with a GNSS-R, giving a technology push to the laboratory. At this point, the family of instruments called Passive Advanced Unit for Earth Observation (PAU) [54]. The expertise acquired with PAU brought the knowledge to later produce the most advanced instruments in the Remote Sensing Laboratory, including the Microwave Interferometer Reflectometer (MIR) [97], and the BEXUS 19 and ^{3}Cat-2 main payload, the P(Y) and C/A Reflectometer (PYCARO) [98, 99].

Thanks to the know-how previously acquired, it has been possible to create the new state-of-the-art miniaturized remote sensing instruments part of this thesis: the Flexible Microwave Payload family. In the following tables, all previously developed GNSS-R, MWR, or combined GNSS-R/MWR instruments previously developed are shown, grouped by their type (i.e.GNSS-R, L-band MWR, or combined GNSS-R and L-band MWR).

Table 2.5 presents all GNSS-R instruments developed by the UPC PSRL. Instruments specifically designed for space applications have some additional features highlighted, like volume and power consumption. Note that, GNSS-R instruments described below may operate following two different approaches, doing real-time processing, and thus providing a direct observable (i.e., reflectivity ratio, DDM, etc.), or by acting as a "data logger". In this last approach, the IQ data is sampled for later processing. Instruments following this approach include the I/Q sampling rate and the bit precision of the captured data.

Table 2.5: GNSS-R instruments developed by the UPC Passive Remote Sensing Laboratory, and a summary of the main instrument specifications.

Instrument Name	**Main specifications**
DODEREC (2002) [100]	• First 3 GPS channels at L1. • 20.46 MHz I/Q sampling at 1 bit. • RHCP up-looking antenna. • RHCP and LHCP down-looking antennas for polarimetry.
Passive Advanced Unit - One Receiver Airborne (PAU-ORA) (2009) [101]	• Miniature GPS L1 data sampler for unmanned platforms. • Both direct and reflected signals combined in a single channel. • Post-processed on ground following the cGNSS-R technique. • RHCP up-looking antenna. • LHCP down-looking antenna.
Light Airborne Reflectometer for GPS-R observations (LARGO) (2013) [67]	• Autonomous GPS-R instrument. • Outputs the reflectivity ratio between a RHCP up-looking antenna, and a LHCP down-looking antenna.
COmpact Reflectometer for Terrain Observations (CORTO) (2014) [69, 102]	• Miniaturized version of LARGO. • Same receiver and antenna configuration as LARGO.
DUO [53]	• Single dual polarization (RHCP + LHCP) high-directive dish antenna at L1 band. • Sequentially measuring direct and reflected signal using a rotor. • Compute reflectivity ratio between both measurements.
Soil Moisture Instrument for GNSS-R measurements Over Land (SMIGOL) (2010) [103]	• Ground-based GNSS-R instrument at L1 band. • Reception of both direct and reflected signals using a linearly polarized antenna pointing to the horizon. • Interference pattern technique.

McGiver (Monitoring of the Canopy using a GNSS-T Instrument for VEgetation Research) (2012) [102]	• Combination of the LARGO and the SMIGOL instrument. • RHCP and LHCP antennas (both up-looking). • Study polarization of GNSS waves when passing through a dense forest.
MalyGNSS (Multiband Airborne L-band reflectometrY with GNSS-R) (2013) [22, 104]	• Proof-of-concept prototype for the Microwave Interferometric Reflectometer. • Dual-band RHCP up-looking antenna and LHCP down-looking antenna. • Based on Software Defined Radio (SDR).
Microwave Interferometric Reflectometer (MIR) (2018) [97]	• L1/E1 and L5/E5a GNSS-R instrument. • High-directive RHCP up-looking antenna (21 dB at L1, 18 dB at L5). • High-directive LHCP down-looking antenna (21 dB at L1, 18 dB at L5). • Beamforming (up to 4 beams per antenna, 2 per band). • 32.736 MHz I/Q sampling at 1 bit.
P(Y) and C/A ReflectOmeter - 1 (PYCARO-1) (2013) [98]	• L1/E1/B1 GNSS-R instrument. • Dual polarization single patch up-looking antenna, and dual polarization 6-element patch antenna array (directiviy $\sim$13 dB). • Retrieves the amplitude of the GNSS signal at configurable sampling rates. • ESA Balloon Experiment for Universitiy Students (BEXUS) 17 and 19 main payload [105,106], and ^{3}Cat-2 main payload [99]. • Fits in 3 CubeSat units plus a 6-unit flat antenna. • Power consumption: $>$ 8 W.
P(Y) and C/A ReflectOmeter - 2 (PYCARO-2) (2019) [JP1]	• Evolved version of PYCARO-1 including GPS L2, Galileo E5b, and Beidou B2D1 signals. • RHCP up-looking antenna. • LHCP down-looking antenna. • Part of the MOSAiC campaign in the Arctic Ocean.

Flexible Microwave Payload - 3 (FMPL-3) (2020) [Detailed in Chapter 10]	• L5/E5a GNSS-R instrument. • 10.230 MHz I/Q sampling at 1 bit. • RHCP up-looking antenna. • LHCP down-looking antenna. • Part of the GNSSaS mission [24] and the first spaceborne L5/E5a GNSS-R instrument. • Fits in one CubeSat unit. • Power consumption: $\sim$ 5.5 W.

Table 2.6 presents the MWR developed at UPC PSRL. Note that, only those instruments that are radiometer-only instruments are presented.

Table 2.6: MWR instruments developed by the UPC Passive Remote Sensing Laboratory, and a summary of the main instrument specifications.

Instrument Name	**Main specifications**
L-band Automatic Radiometer (LAURA) (2000) [39]	• First fully polarimetric L-band radiometer. • In preparation for SMOS calibration/validation activities. • Two-channel Dicke radiometer with I/Q down-conversion.
Airborne RadIomEter at L-band (ARIEL) (2009) [107]	• Single antenna with circular polarization. • Dicke Radiometer. • Periodic external calibration required before and after. operation
The Multifrequency Experimental Radiometer with Interference Tracking for Experiments over Land and Littoral (MERITXELL) (2013) [108]	• Multi-band (L-, S-, C-, X-, K-, Ka-, and W-band). • Dual polarization antenna. • Total Power Radiometer.

Finally, Table 2.7 shows all the instruments developed by the UPC PSRL that comprises a combined GNSS-R and L-band MWR in a single instrument. Two family of instruments is presented here, the first one is the the Passive Advance Unit (PAU) family [109], with its first version developed in 2003 in the frame of the EUropean Young Investigator Awards, part of the European Science Fundation. The second family of instruments is the Flexible Microwave Payload (FMPL), previously introduced and

detailed in Part 3 (Chapters 8, 9, and 10) of this thesis. Note that, the last version of FMPL, the FMPL-3, does not include a MWR, as it is a GNSS-R technology demonstrator for L5/E5a signals in space, and hereby it is presented in Table 2.5 instead.

Table 2.7: Combined GNSS-R and MWR instruments developed by the UPC Passive Remote Sensing Laboratory, and a summary of the main instrument specifications.

Instrument Name	**Main specifications**
GPS Receiver Instrument for PAU (GriPAU) (2007) [110, 111]	• First real-time and synchronized GNSS-R (L1) and L-band MWR receiver. • Designed as a ground-based instrument to measure primary the ocean (e.g. from a cliff). • RHCP up-looking antenna. • LHCP down-looking antenna. • GNSS-R observables generated in real time in the instrument FPGA (GNSS-R). • Dicke radiometer (MWR).
PAU - Real Aperture (PAU-RA) (2007) [112]	• Dual GNSS-R (L1) and L-band MWR using a single RF front-end. • Dual polarization (vertical and horizontal) 16-element antenna array including the first ever MWR with digital beamforming. • GNSS-R observables generated in real time in the instrument FPGA (GNSS-R). • Digital dicke radiometer with external calibration (MWR).
PAU - Synthetic Aperture (PAU-SA) (2009) [113, 114]	• Ground-based technology demonstrator to improve future interferometric radiometers (digital filtering, I/Q downconversion, and power power detection, calibration using PRN signals, etc.). • Inherits some parts of the ESA SMOS instrument, the Microwave Imaging Radiometer by Aperture Synthesis (MIRAS), such as its Y-shape antenna (dual polarization). • Data logger approach with I/Q sampling at 2.2 MHz at 8 bit (GNSS-R). • 2D imager (MWR).

PAU-Spaceborne (2010) [115]	• Designed to be the secondary payload of the INTA MicroSat-1. • RHCP up-looking antenna at L1. • Dual band (1413-1575.42 MHz) 8-element LHCP down-looking antenna (∼15 dB). • Real-time GNSS-R (L1) processor, 1 s incoherent averaging time. • Total Power Radiometer at L-band with internal calibration (MWR). • Outputs generated at 0.5 Hz. • Designed for a microsat, larger than 3 CubeSat units. • Power consumption >10 W.
Flexible Microwave Payload - 1 (FMPL-1) (2018) [CP1]	• Main payload of ^{3}Cat-4 [CP3]. • RHCP zenith-looking patch antenna at L1 band. • Dual frequency (L1-L2) LHCP nadir-looking deployable helix antenna (directivity ∼12 dB). • I/Q sampling at 1.024 MHz at 1-bit (GNSS-R). • Total Power Radiometer with frequent internal calibration (MWR). • Fits in 0.3 CubeSat units. • Power consumption <2 W.
Flexible Microwave Payload - 2 (FMPL-2) (2019) [JP2]	• Main payload of FSSCat [CP2]. • RHCP single patch up-looking antenna. • Dual band (1413-1575.42 MHz) LHCP 6-element nadir-looking patch antenna array. • Real time GNSS-R processor at L1/E1. 40 ms integration time with four simultaneous satellites (GNSS-R). • Total Power Radiometer with frequent internal calibration (MWR). • Outputs generated at 2 Hz. • Fits in 1 CubeSat unit, plus 6 units to fit the flat antenna array. • Power consumption ∼7.5 W.

2.6 Conclusions

This Chapter has summarized the two passive remote sensing techniques that will be covered in this Ph.D. thesis. First, the L-band radiometry technique has been presented, with the different types of radiometers. The different radiometer configurations in space

and the types of applications covered by an L-band radiometer, such as sea-ice monitoring, sea state monitoring, or soil moisture estimations have been presented. In this case, the three latest "Old Space" satellites launched carrying an L-band radiometer have been presented.

Second, the GNSS-R technique has been presented, and its current applications from space. A review on the generation of cGNSS-R observables has been presented. In this part, the different signal types used in GNSS-R have been introduced. Moreover, all missions which have carried a GNSS-R payload have been presented, detailing the applications derived from their measurements.

Third, an introduction to machine learning applied for EO has been provided. This section included the basic concepts of ANNs used in RS to retrieve different geophysical parameters. Moreover, a review of current applications using ANN for both L-band radiometers and GNSS-R instrument has been presented.

Finally, a review of all instruments developed by the UPC PSRL is presented. Note that, instruments covered in this Ph.D. thesis have also been presented. PYCARO-2 is explained in Chapter 7, and FMPL-1, -2, and -3 are presented in Chapters 8 to 10, respectively.

3

Chapter 3

Theoretical study: GNSS-R airborne implications in the spatial resolution

This Chapter presents two theoretical studies carried out using GNSS-R data provided by the MIR instrument. The instrument performed different field experiments in Australia, collecting a large amount of I/Q data at L1 and L5 bands over different surfaces. Thus, allowing the analysis of the GNSS-R waveform statistics under different integration times. Section 3.2 presents an analytical review on the spatial resolution and the effects of varying the incoherent integration time while depending on the receiver dynamics. Section 3.3 presents an analysis of the work initially sketched by Dr. Raul Onrubia in his Ph.D. thesis (Section 8.5.4), where *ripples* are found in the evolution of the reflectivity when transitioning from different media (i.e., land to water). The analysis presented section is adapted from the peer-reviewed journal manuscript entitled "Analytical Computation of the Spatial Resolution in GNSS-R and Experimental Validation at L1 and L5" [JP3].

3.1 Introduction

The spatial resolution of GNSS-R has been already analyzed in several works. In [116], it is presented that the spatial resolution for an iGNSS-R altimeter was about 36 km to 54 km from an altitude of 450 km, at incidence angles ranging from 90º to 40º, respectively. Years later, in [117], the spatial resolution definition was re-defined as "effective" spatial resolution, now taking into account both the geometry and the delay-Doppler interval. This new definition set the spatial resolution of GNSS-R from 25 to 37 km at an altitude of 700 km.

Both definitions where assuming both an incoherent scattering and long incoherent integration times. However, with the development of advanced receivers, where coherent processing is possible, much finer features can be distinguished [118]. When the reflection is produced by coherent scattering, the spatial resolution is much improved, as the reflected power is not coming from the entire glistening zone (see Fig. 3.1), but from its center. This point is called the first Fresnel zone [119], and it is defined by an ellipse with the semi-major a (Eq. 3.1), and semi-minor axis a (Eq. 3.2) as follows:

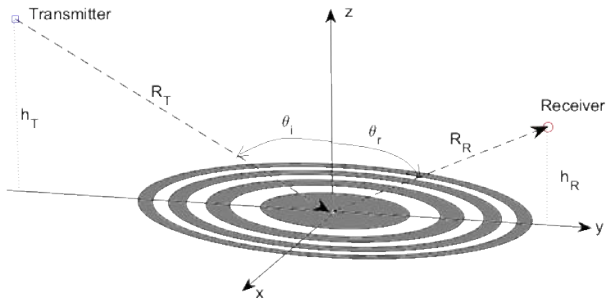

Figure 3.1: GNSS-R scattering geometry showing the transmitter, receiver, specular reflection point (origin of coordinates), and the different Fresnel zones.

$$a = \sqrt{\lambda \frac{R_T \cdot R_R}{R_T + R_R}}, \tag{3.1}$$

$$b = \frac{a}{cos(\theta_i)}, \tag{3.2}$$

where lambda is the electromagnetic wavelength, R_T and R_R are the distance from the transmitter to specular point, and from the receiver to the specular point, respectively, and θ_i is the incidence angle. In case that $R_T >> R_R$, R_R is usually approximated by $R_R \approx h_R/cos(\theta_i)$, where h_R is the platform height, as defined in Fig. 3.1.

Then, the length (i.e., the semi-minor axis) of the first Fresnel zone is simplified to:

$$l_{Fz} \approx \frac{\sqrt{\lambda \frac{h_R}{cos(\theta_i)}}}{cos(\theta_i)}. \tag{3.3}$$

Finally, in [120], the spatial resolution definition was revised under coherent scattering conditions, including the effect of the different Fresnel zones. The study concluded that up to ∼45º of incidence angle, most of the power received was coming from a region ∼0.6 times the size of the first Fresnel zone, but with significant contributions from region farther away from this area. Figure 3.2 shows two examples of the size of the first Fresnel zone for an airborne receiver at an altitude of 1 km, and for a spaceborne receiver at an altitude of 500 km.

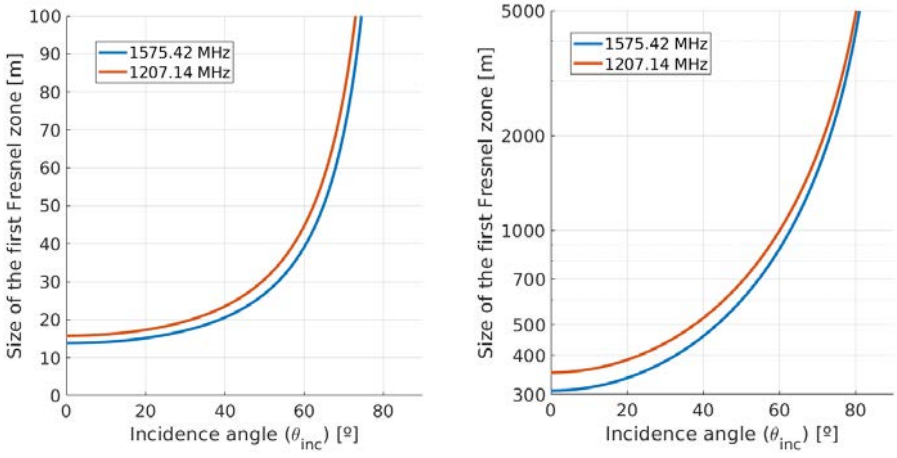

Figure 3.2: Size of the first Fresnel zone seen from (a) an airborne at an altitude of 1 km, and (b) a spaceborne GNSS-R instrument at an altitude of 500 km at both the upper L-band (1575.42 MHz), and the lower L-band (∼1207.14 MHz). Note that Y axis in (b) is set in logarithmic scale to ease its visualization.

3.2 GNSS-R Spatial Resolution and Integration Time Considerations

The integration time is one of the parameters of GNSS-R receivers that have been fixed since the launch of TDS-1 in 2014. The SGR-ReSi receiver onboard TDS-1 and CyGNSS missions had this parameter set to 1 second[1]. The selection of this parameter has several implications, as it has been discussed in [54, 121]. On the one hand, specular point re-tracking shall be performed to prevent the auto-correlation function to get blurred. As the platform moves, the relative distance between the receiver, the transmitter, and the specular point changes, producing a change in the position of the ACF. Moreover, as the position of the specular reflection point changes, the properties of the reflection surface change too, producing many uncertainties that cannot be easily modeled.

[1]In late 2020, CyGNSS science team reduced the integration time of the SGR-ReSi receiver to 0.5 s.

3.2.1 Data set description

To assess the impact of large integration times with respect to the size of the first Fresnel zone and the chip length, data from the MIR instrument is used. Selected fragments of raw data collected by MIR in different flights have been selected. The MIR instrument flew four times over New South Wales (NSW), Australia, in April-June 2018. The first flight was conducted over the Portsea peninsula, in Melbourne, Australia; the second and third flights were conducted over the Yanco-designed area covered by the OzNet soil moisture monitoring network in southern New South Wales (Australia) [122]. Being the first of these two flights conducted after a long period without rain events, and the second flight after a strong rain event. The fourth flight was conducted over the ocean, in the Bass Strait, Australia, but some portions of the plane also entered into dense vegetation areas, in the Tamboon area of the Peachtree Creek Reserve Campground.

The reflected signal is coherently integrated with a $T_c = 1$ ms for the GPS L1, and GPS L5. Up to 4000 complex waveforms have been computed at L1, and 1000 complex waveforms at L5. Thus, all complex waveforms are then appended in a vector to compute the covariance matrix, as detailed in Fig. 3.3, and based on the work on [123] (Section 4.2.1).

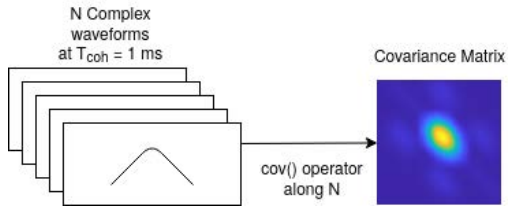

Figure 3.3: Covariance matrix of a GNSS signal formed by N complex waveforms and computing the MATLAB® *cov()* operator along the N axis.

3.2.2 Covariance matrices analysis

To conduct this study, selected waveforms are retrieved from four different sites: the first selected site corresponds to the fourth flight, in the middle of the ocean in the Bass Strait; the second and third sites correspond to a bare soil area of Yanco, both corresponding to the second (long period without rain events) and third flights (after a strong rain event), respectively; and the fourth site is a highly vegetated area near Tamboon, corresponding to the fourth flight.

The plane height varied from 500 m for the flights over land, to 1500 m for the flight conducted over the ocean. Thus, producing different sizes of the first Fresnel zone, but both are on the same order of magnitude, between 10 m and 25 m for incidence angles lower than 45º. Moreover, the plane velocity for all flights is $v_{plane} = 75$ m/s.

To illustrate the effects of increasing the integration time, the width of the GNSS ACF is considered. Following the concepts introduced in Section 2.3.1, the ACF width for the L1 C/A signal collected by MIR is 300 m (i.e., any signal coming within this 300 m just contributes to wide the peak), and the ACF width for the L5 signal is 30 m. As the plane moves at 75 m/s, up to ~ 4 s need to be integrated into the L1 case, and up to 400 ms for the L5 case (see Eq. 3.4).

$$T_{int} = \frac{L_{chip}}{v_{platform}}, \tag{3.4}$$

where L_{chip} is defined in Eq. 2.6 of Chapter 2[2].

Taking into consideration the width of the ACF and the plane speed, different integration times have been selected at L1 and L5:

- L1: 500, 1000, 2500, and 4000 ms,
- L5: 50, 150, 500, and 1000 ms.

Figures 3.4 and 3.5 present the covariance matrices at L1 and L5, respectively. Note that, the diagonal of the covariance matrix is the WAF introduced in Section 2.3.

As it can be seen, when the integration time is equivalent to the size of the first Fresnel zone divided by the plane speed (i.e., $T_{int} \sim 500$ ms [3]) the blurring of the diagonal of the covariance matrices is almost negligible for the ocean flight and for the two Yanco flights. However, a very small distortion is noticed in the Forest area. The increase of integration time produces a blurring in the diagonal direction of the covariance matrix (i.e., the waveform is blurred), which means that the reflection is coming from many different facets, in this case from an area larger than 800 m for the ocean flight, and for the Yanco flight conducted after a rain event (Wet). The first Yanco flight (Dry) showed almost no blurring, and the waveforms retrieved over the Australian rainforest show small blurring up to ∼600 m.

The ocean and Yanco (Wet) cases show a very larger dispersion when the integration time is increased. In both cases, the reflection produced is strong, with moderate reflectivity values (∼-10 dB), as compared to the other two cases. In this case, strong reflection can come from the entire glistening zone.

However, this is not the case for the first Yanco flight (Dry), where the reflection seems just to come from the first Fresnel zone. Thus, the retrieved waveform is not exhibiting this blurring. In this case, the entire zone is very dry, with very low soil moisture values, which normally produce low reflectivity values [124] (as it will be detailed in Chapter 6). Therefore, additional reflections coming from the entire glistening zone may be masked by the noise floor, and the main reflection is coming from the water table underneath the surface, which is "flatter" and more homogeneous.

Moreover, in the forest area, the waveform does not extend over 400-500 m, and the light-green color strip in the diagonal direction corresponds to the noise floor, noting that the signal SNR is poor. If looking at the power evolution at the diagonal, the resultant waveform looks like the examples provided in [64], where the volumetric scattering produced by dense forest is linked to the blurring of the waveform, even at short integration times.

Moving to the L5 case (Fig. 3.5), a similar phenomenon is detected. In this case, the delay axis has been re-scaled from -100 to 100 m, as the ACF width is 10 times narrower. In the two land cases, if one or less than one Fresnel zone is integrated (i.e., 50 or 150 ms

[2] L_{chip} is defined as the speed of light divided by the code chip rate: $L_{chip} = \frac{c}{R_{chip}}$

[3] after applying Eq. 3.4 assuming L_{chip} is the size of the first Fresnel zone

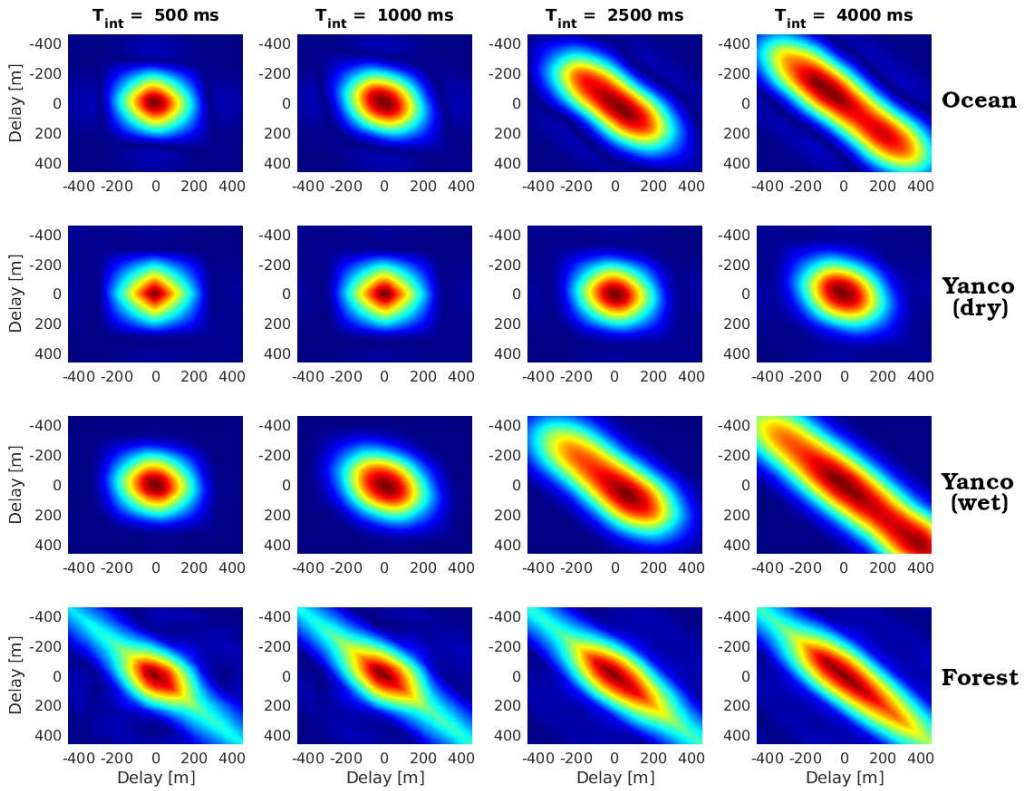

Figure 3.4: Covariance matrices of GNSS-R L1 C/A signals collected by MIR. Columns represent different integration times, and rows the different flights and areas covered

cases), there is not blurring at all. Similarly to the L1 case, the first Yanco flight (no rain) shows less waveform blurring, as reflections from the entire glistening zone might be masked because of the noise floor. Analogously to the L1 case, the first Yanco flight shows almost no blurring when the integration time is increased, but this is not the case for the second flight, where some nearby peaks (i.e., nearby reflections coming from the glistening zone) can be identified.

Moving to the Ocean and Forest cases, the same artifacts as in the second Yanco flight are detected even at 50 ms of integration. In both cases, it looks as additional "peaks" are appearing ∼50 m apart from the main peak. Those interesting artifacts are still present if the integration time is enlarged, clearly showing two large peaks when the integration time is ∼500 ms, and showing more than three peaks for 1000 ms integration.

In this airborne case, the waveform blurring is produced by two phenomena:

- Contributions from different Fresnel zones when the receiver is moving, and this seems to be mitigated when the integration time satisfies that the distance traveled by the plane during the integration does not exceed the size of the first Fresnel zone.

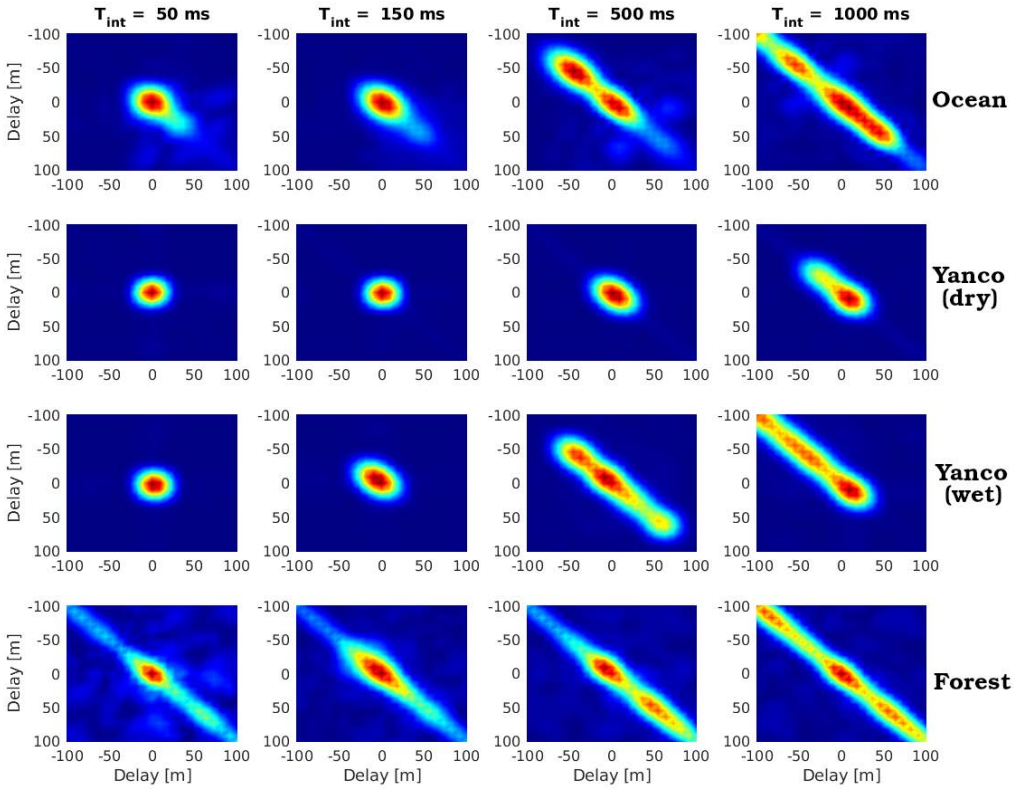

Figure 3.5: Covariance matrices of GNSS-R L5 signals collected by MIR. Columns represent different integration times, and rows the different flights and areas covered

- Multiple reflections in different areas of the glistening zone which are not due to the platform movement, and be noticed even at very short integration times. This hypothesis will be analyzed in Chapters 5 and 6.

Applying the same reasoning for the satellite case, exceeding the chip length directly produces waveform blurring if no re-tracking of the specular point is applied. In this case, if the platform has moved more than 300 m if using at L1 C/A signals, or 30 m if using at GPS L5, waveform blurring might be present. Therefore, the maximum integration time will be limited by the platform velocity as in Eq. 3.4, and introduced in [54, 121]. For all this, under general conditions, the maximum integration time without specular point re-tracking will be set by Eq. 3.5:

$$T_{int_{max}} = \frac{min|L_{chip}, L_{Fz}|}{v_{platform}}. \tag{3.5}$$

3.3 GNSS-R Spatial Resolution under Media Transition

In the previous section, the selection of the maximum integration time was based assuming the spatial resolution it the one determined by the first Fresnel zone. However, this assumed that the reflection surface is invariant (i.e., always ocean, always land, etc.). In this section, a similar analysis is performed showing the achievable spatial resolution when transitioning from different reflection surfaces or regions (i.e., from water to land). In what follows, a few principles of electromagnetism are reviewed. They will be used to compute a closed-form solution of the GNSS-R response to a step function, as in a transition from water to land.

3.3.1 Review of electromagnetic concepts

3.3.1.1 Principle of equivalence and image theory

To proceed with the analysis, some electromagnetic concepts shall be first reviewed.

The principle of equivalence [125] allows us to compute the solutions in the region of interest (half-space in front of the conducting plane) by replacing the plane conductor with the images of the dipoles. The image sources must satisfy the boundary condition that the tangential electric field at the conducting surface should be zero. The total electric field above the conducting plane (see Fig. 3.6) is then computed as the sum of the one created by the original currents and the image ones, while the total electric field below the conducting plane is zero. Applying this principle to our problem, the transmitter can be replaced by its "image" underneath the plane, as illustrated in Fig. 3.7.

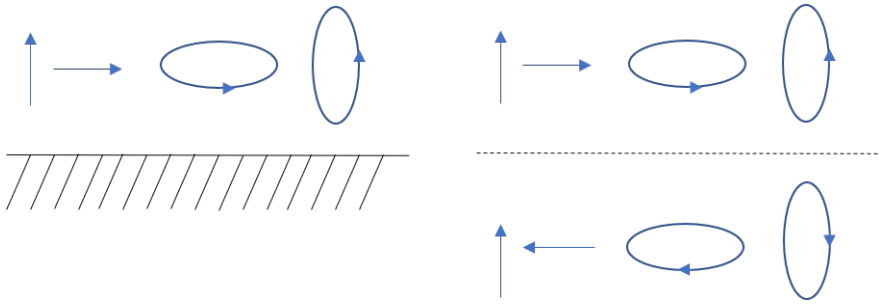

Figure 3.6: Left: linear and loop currents over a perfect conductor. Right: the conductor has been replaced by the image currents. Note that the sign reversal of the currents parallel to the conducting plane are responsible for the polarization change of the "reflected" wave.

3.3.1.2 The Huygens principle and knife-edge diffraction

The Huygens principle states that every point (red dots in Fig. 3.8) on a primary wave front (blue curve in Fig. 3.8) may be regarded as a new source of spherical secondary waves, and that at each point in space these waves propagate in every direction at a speed and frequency equal to that of the primary wave, and in such a way that the primary wave front at some later time is the envelope of these secondary waves (red curve in Fig.

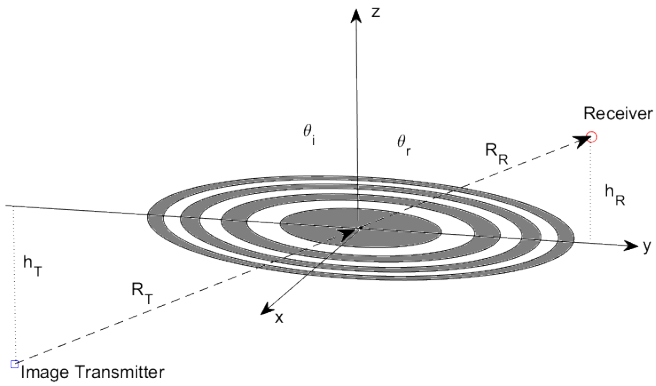

Figure 3.7: GNSS-R scattering geometry in Fig. 3.1 modified according to the principle of equivalence: the transmitter is replaced by its image. Computed electric fields are only valid in the region z > 0.

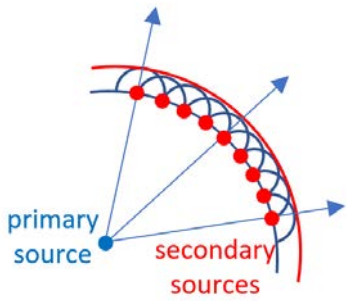

Figure 3.8: Graphical representation of the Huygens diffraction principle.

3.8). The Huygens principle can be applied to compute the electric fields when part of the trajectory is partially obstructed by a conducting plane as illustrated in Fig. 3.9, leaving a clearance h with respect to the line of sight. This academic case is known as the "knife-edge diffraction", and it is used in radio communications to assess the propagation losses with respect to the free space caused by the obstruction by a mountain, building, etc. In the latter this will represent the transition from one media to another [119].

The development of an analytical solution can be found in many text books, and only the final result is provided below:

$$E_{diff} = E_{freespace} \cdot F(v), \tag{3.6}$$

where:

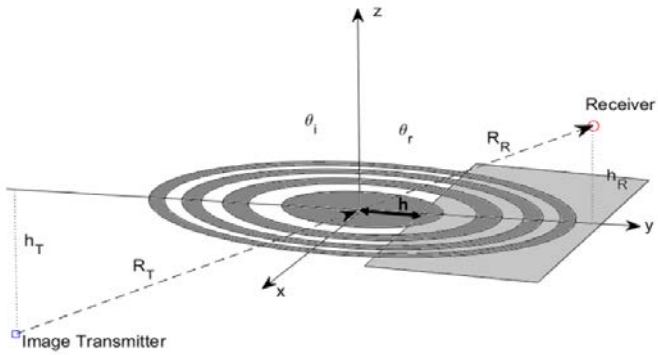

Figure 3.9: Huygens principle applied to the "knife-edge diffraction" case. The light-gray area partially blocks the propagation of the signal, hiding parts of some Fresnel zones. h is the clearance of the obstruction.

$$F(v)\hat{=}\frac{1+j}{2}\left[\int_v^\infty cos(\frac{\pi}{2}t^2)dt - j\int_v^\infty sin(\frac{\pi}{2}t^2)dt-\right] = \frac{1+j}{2}\left\{\left[\frac{1}{2}-C(v)\right]-j\left[\frac{1}{2}-S(v)\right]\right\}, \tag{3.7}$$

$C(v)$ and $S(v)$ are the so-called Fresnel integrals, which are given below:

$$C(v) = \int_v^\infty cos\left(\frac{\pi}{2}t^2\right)dt, \tag{3.8}$$

$$S(v) = \int_v^\infty sin\left(\frac{\pi}{2}t^2\right)dt, \tag{3.9}$$

and v is the Fresnel-Kirchhoff parameter:

$$v = h\cdot\sqrt{\frac{2\cdot(R_T+R_R)}{\lambda\cdot R_T\cdot R_R}}. \tag{3.10}$$

Figure 3.10 shows the absolute value of in Eq. 3.7 in linear units. When $h = 0$, half of the electric field is blocked, which translates into a power loss of 6 dB with respect to the free-space conditions. Note the ringing for $h < 0$ due to the different Fresnel zones being blocked or not, and contributing to the total electric field with different phases.

3.3.1.3 Babinet's principle

Babinet's principle [126] states that the diffraction pattern from an opaque body is identical to that from a hole of the same size and shape, except for the overall forward beam intensity. The concept is expressed graphically in Figure 3.11 [127].

Babinet's principle can be used to compute the electric field diffracted when the signal emitted by the transmitter's image is diffracted by the light-gray opaque area in the z

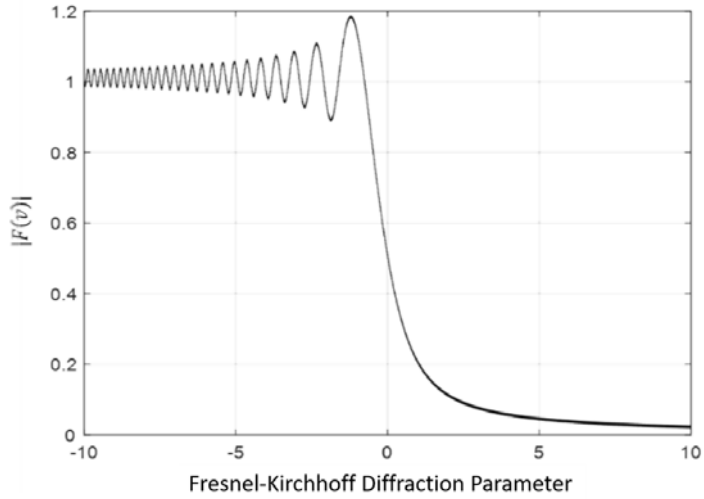

Figure 3.10: Absolute value of $F(v)$. Negative v indicates that the line-of-sight (LoS) trajectory is unobstructed, while positive v indicates an LoS obstruction (see Fig. 3.9).

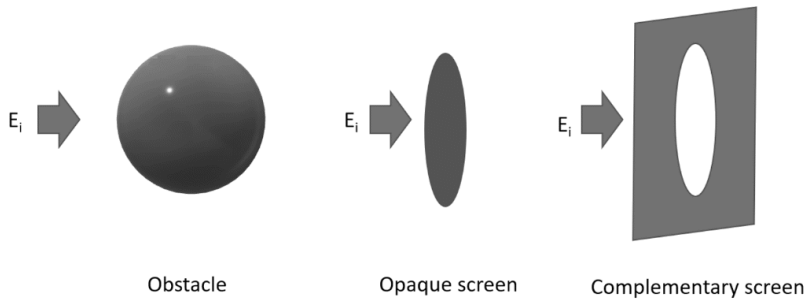

Figure 3.11: Graphical representation of the concept of Babinet's principle and the three equivalent obstacles: electric field incident on an arbitrary obstacle (left), associated opaque screen (center), and complementary screen (i.e. hole in the infinite plane; right).

= 0 plane (the white area being "transparent"), and when it is diffracted by the white opaque area in the z = 0 plane (the light-gray area now being "transparent").

3.3.1.4 Principle of superposition

Once the electric fields diffracted by the semi-plane (the white area in the plane z = 0 in Fig. 3.9) are computed, the electric fields diffracted by the complementary semi-plane (the light-gray area in the plane z = 0 in Fig. 3.9), when it is not opaque, can be computed using Babinet's principle, and then the total electric field arriving at the receiver can be computed as the sum of both.

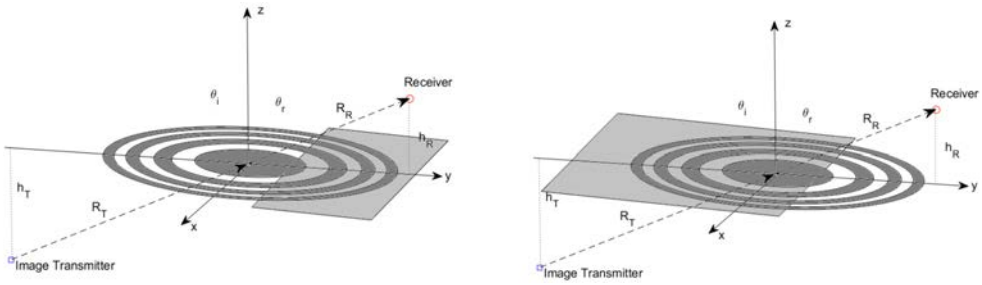

(a) **(b)**

Figure 3.12: Graphical representation of the principle of superposition and its application to the computation of the total electric field incident. Opaque screen on the (a) right and (b) left sides block radiation.

3.3.2 Computation of the electric field scattered by the discontinuity between two media

Assuming that an electromagnetic wave impinges over the $z = 0$ plane around $(x,y,z) = (0,0,0)$, where the specular reflection point is, and:

- The extension of the Fresnel reflection zones is small enough (a few hundred meters from a low Earth orbiter) so that the variations of the local incidence angle can be neglected over a few Fresnel zones;
- The plane z = 0 is composed of two flat half-planes of different materials, and thus exhibiting different reflection coefficients; and
- The transmission coefficient for the wave emitted by the image transmitter (Fig. 3.9) is equal to the reflection coefficient evaluated at the local incidence angle at the origin.

Then, as illustrated in Fig. 3.12, the total electric field can be immediately computed as the sum of the following two terms:

$$E_{diff} = E_{freespace} \cdot \left[F(v) \cdot \rho(\epsilon_{r,1}, \theta_i) + F(-v) \cdot \rho(\epsilon_{r,2}, \theta_i) \right], \tag{3.11}$$

where $\rho(\epsilon_{r,n}, \theta_i)$ is the Fresnel reflection coefficient, and $\epsilon_{r,n}$ is the dielectric constant of the half-plane n. The receiver power is then proportional to the square of the absolute value of Eq. 3.11.

$$P_{diff} = P_{freespace} \cdot \left[F(v) \cdot \rho(\epsilon_{r,1}, \theta_i) + F(-v) \cdot \rho(\epsilon_{r,2}, \theta_i) \right]^2, \tag{3.12}$$

Following Eq. 3.12, an example is shown in Fig. 3.13.

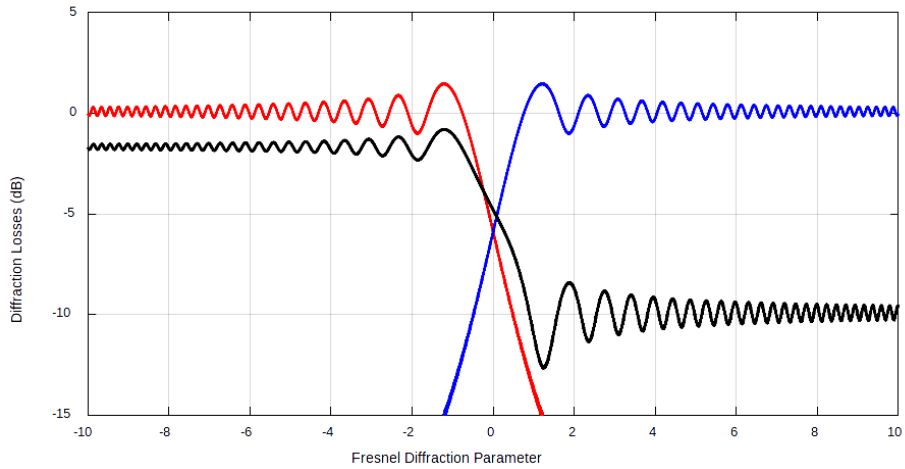

Figure 3.13: Graphical representation of the $|F(v)|$ (red) and $|F(-v)|$ (blue) functions, and total power loss computed as $|F(v) \cdot \rho(\epsilon_{r,1}, \theta_i) + F(-v) \cdot \rho(\epsilon_{r,2}, \theta_i)|$ (black) for $\rho(\epsilon_{r,1}, \theta_i) = \frac{2}{3}$ and $\rho(\epsilon_{r,2}, \theta_i) = \sqrt{0.1}$

3.3.3 Spatial resolution computation

Based on the above results the spatial resolution of a GNSS-R system can now be defined as the width of the transition from the 10% above $|\rho(\epsilon_{r,2}, \theta_i)|^2 \triangleq |\rho_{max}|^2$, and 90% of $|\rho(\epsilon_{r,1}, \theta_i)|^2 \triangleq |\rho_{min}|^2$

$$|F(v_{90\%}) \cdot \rho_{max} + F(-v_{90\%}) \cdot \rho_{min}|^2 = 0.9 \cdot |\rho_{max}|^2, \tag{3.13}$$

$$|F(v_{10\%}) \cdot \rho_{max} + F(-v_{10\%}) \cdot \rho_{min}|^2 = 1.1 \cdot |\rho_{min}|^2, \tag{3.14}$$

The solution of the above equations has to be performed numerically, and it actually depends on the values of ρ_{min} and ρ_{max}. The difference between $v_{10\%}$ and $v_{90\%}$ leads to the width of v, $\Delta v = v_{10\%} - v_{90\%}$, which is linked to the spatial resolution by means of Eq. 3.15. For the sake of simplicity, assuming an airborne GNSS-R instrument, $R_R \approx h_R/cos(\theta_i)$, and the following is an approximated formula for the spatial resolution:

$$\Delta v = \Delta x \sqrt{\frac{2 \cdot cos(\theta_i)}{\lambda \cdot h_R}} \Rightarrow \Delta x = \Delta v \sqrt{\frac{\lambda \cdot h_R}{2 \cdot cos(\theta_i)}} \tag{3.15}$$

Figure 3.14 shows the evolution of Δv as a function of $\Delta\rho = \rho min/\rho_{max}$ in decibels. It varies from 0.74 for $\rho min/\rho_{max} = -3$ dB to 1.7 for $\rho min/\rho_{max} = -20$ dB. This means that for a plane flying at $h_R = 1000$ m height, at GPS L1/Galileo E1 ($\lambda = 19$ cm), the spatial resolution ranges from 7.2 m$/\sqrt{cos(\theta_i)}$ to 16.6 m$/\sqrt{cos(\theta_i)}$, depending on the contrast of the reflection coefficients in the transition.

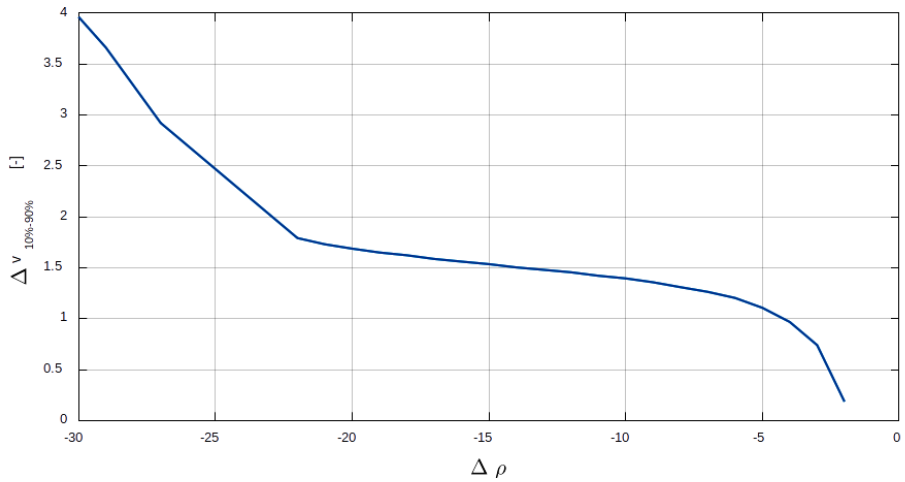

Figure 3.14: Width of the Δv parameter for a transition from 10% above ρ_{min} to 90% of ρ_{max}.

As compared to the spatial resolution approximation to selected the optimum integration time in Section 3.2, the size of the semi-major axis of the first Fresnel zone, given by Eq. 3.1 is 13.7 m/$\sqrt{cos(\theta_i)}$.

3.3.3.1 Experimental validation

Figure 3.15 shows the measured reflectivity (Γ) in a transition between land and calm water in the Devilbend Reservoir, south of Melbourne, Victoria, Australia. The data was acquired during the first flight of the MIR instrument on 30 April 2018, as introduced in Section 3.2.1. The plot at the top of the figure corresponds to one of the four beams at GPS L1, and the bottom plot corresponds to another beam receiving GNSS-R at L5. The flight speed was 75 m/s, the flight height was $h_R = 1000$ m, and the GNSS-R data was coherently integrated for 1 ms (GPS L1 C/A code), and incoherently for $T_{inc} = 20$, 40, 100, and 200 ms. At 20 ms, the blurring produced by the aircraft movement is 1.5 m, which is negligible compared to the best spatial resolution previously computed. Inspecting Figure 11, at 20 and 40 ms incoherent integration time, one can clearly observe some reflectivity ripples that are reminiscent of those seen in Fig. 3.13. At 100 ms, the blurring is 7.5 m, which is now comparable to the best spatial resolution, and the ripples can no longer be appreciated. At 200 ms the reflectivity plot is even smoother. In the land part (left part of the plots), the L5 reflections exhibit a more marked fading pattern than the L1 ones. This may be due to the fact that L5 penetrates slightly more in the land and vegetation. Although it is not very clear, the width of the reflectivity step is approximately 0.3 s, which corresponds roughly to 22.5 m, as compared to the 20.7 m predicted value using Eq. 3.15 and Fig. 3.14 for a ∼-15 dB reflectivity.

Taking a closer look to the periodicity of the ripples, it can be observed that the period in Fig. 3.15b is larger than that in Fig. 3.15a, as it can be inferred from Eq. 3.10, and Figures 3.10 and 3.10, parameterized in terms of v. In Fig. 3.15a, the separation between consecutive peaks in time is ∼100 ms, while in Fig. 3.15b it is ∼130 ms, which, for an

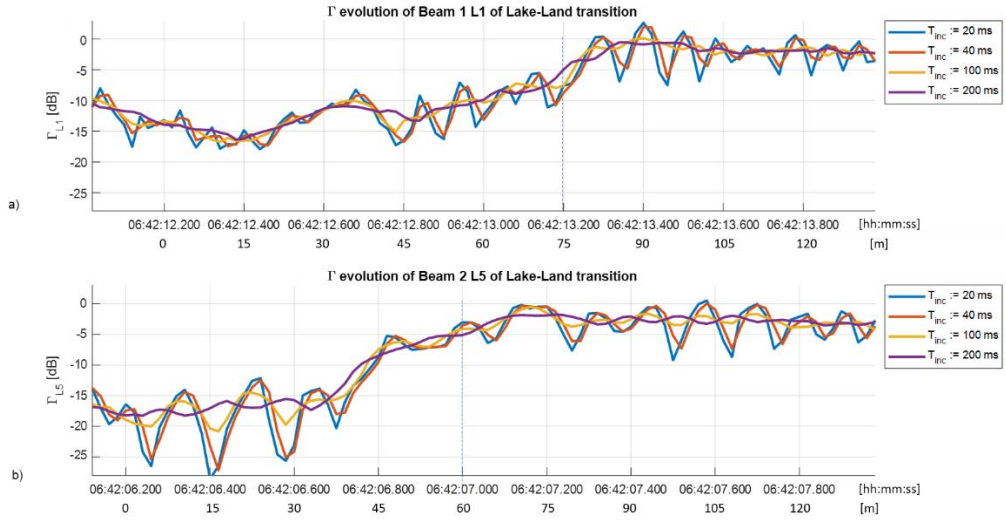

Figure 3.15: Land-to-water transition during a MIR flight over Devilbend Reservoir (38.29°S, 145.1°E): a) GPS L1, b) GPS L5. Horizontal axis units: time and distance. Vertical dashed line: land–water transition.

aircraft speed of $v_{plane} = 75$ m/s corresponds to 7.50 and 9.75 m, respectively. More detailed results are shown in Table 3.1 for several peaks. Replacing Δx by $v_\perp \cdot \Delta t$ in Eq. 3.15, where $v = v_\perp \cdot cos(\Phi)$, Φ being the angle formed between the aircraft ground-track and the coastline, one obtains:

$$\Delta v = v_\perp \cdot \Delta t \sqrt{\frac{2 \cdot cos(\theta_i)}{\lambda \cdot h_R}} \Rightarrow \Delta x = \Delta v \sqrt{\frac{\lambda \cdot h_R}{2 \cdot cos(\theta_i)}}. \tag{3.16}$$

Assuming $h_R = 1000$ m, $\theta_i = 45^o$, and substituting Δt for the time difference between consecutive peaks in Fig. 3.15 (except for round-off errors due to the discrete sampling), this ratio closely matches the squared root of the ratio of the wavelengths at L1 and L5: $\sqrt{1575.42/1176.45}$ (in MHz) $= 1.16$. Other sources of error are variations of the flight height, variations of the incidence angle, and most likely the fact that the velocity vector is not perpendicular to the coastline (as implicitly assumed in Fig. 3.9).

These results are corroborated by many other transitions. In what follows a few more examples are presented to illustrate this effect. A minimum incoherent integration time of 40 ms is used, since blurring is still negligible, and these results are almost identical to when 20 ms is used. Figure 3.16 shows a geo-located double transition from land–calm water–land, the temporal evolution of the reflection coefficient at L1, and two zooms around the transitions for different incoherent integration times. Figure 3.17 shows another example at L5. Note that for large incoherent integration times (i.e., 200 ms) the ringings cannot be identified for both the L1 and L5 examples.

Figure 3.18 presents another example on the same flight. In this case, there is an additional transition to a small portion of a peninsula being crossed by the GNSS-R

Table 3.1: Peak positions in Fig. 3.13 and peak spacing (Δv), peak positions in time for L1 and L5 beams, time spacing and estimated peak spacing in v.

v_{peaks}	$\lvert\Delta v_{peaks}\rvert$	$t_{peaks,L1}$ [s]	$\Delta t_{peaks,L1}$ [ms]	$\lvert\Delta \hat{v}_{peaks,L1}\rvert$	$t_{peaks,L5}$ [s]	$\Delta t_{peaks,L5}$ [ms]	$\lvert\Delta \hat{v}_{peaks,L5}\rvert$
–1.22	-	Not visible	-	-	7.140	-	
–2.34	1.12	13.290	-	-	7.310	170	0.95
–3.08	0.74	13.400	110	0.71	7.450	140	0.67
–3.68	0.60	13.500	100	0.65	7.570	120	0.78
–4.18	0.50	13.580	80	0.52	7.700	130	0.67

track. It can be noticed that at short integration times, some ripples are produced when changing from land to water, at the beginning and the end of the track. In addition, in the central part, when passing over the peninsula the combination of the different responses produces very large amplitude ripples. In this case, large incoherent integration times (i.e., 200 ms) are not blurring the ripples in the center of the image. However, if even larger integration times were used (i.e. 1 s) no ringings could be identified.

Finally, Fig. 3.19 shows another double transition when passing over Sorrento, South of Melbourne. The left part corresponds to an open ocean area (Sorrento ocean beach), while the right part of the image is inside Port Phillip Bay (Sorrento front beach). Looking at the ocean–land transition in Fig. 3.19c on the left-hand side, the reflectivity step is larger, but longer over time, and reflectivity values are noisy because of the increased surface roughness and speckle noise associated with a mostly incoherent scattering. The ripples described in the previous sections and illustrated in the previous examples can no longer be identified. However, as compared to the ocean side in Fig. 3.19c, in Fig. 3.19d the reflectivity step is smaller (calm water), but shorter in time (i.e. sharper), and similar ripples to the lake case can now be identified.

3.4 Achievable Spatial Resolution and Implications in the Integration Time

The analytical expression of the measured reflectivity $\hat{\Gamma}$ can be derived from Eq. 3.12:

$$\hat{\Gamma} = \left[F(v) \cdot \rho(\epsilon_{r,1}, \theta_i) + F(-v) \cdot \rho(\epsilon_{r,2}, \theta_i)\right]^2, \tag{3.17}$$

where v is given by Eq. 3.10. It shows smooth transition between $\left|\rho(\epsilon_{r,1}, \theta_i)\right|^2$ and $\left|\rho(\epsilon_{r,2}, \theta_i)\right|^2$, and ripples associated to different Fresnel zones passing from one area to the other one. The width of the transition, as measured from the 10% above the lowest reflectivity values to 90% of the highest reflectivity value, has been found to be dependent on the amplitude of the reflectivity step itself, although it is quite flat for a wide range of reflectivity steps (e.g. Fig. 3.14): $\Delta v \approx 1.5$

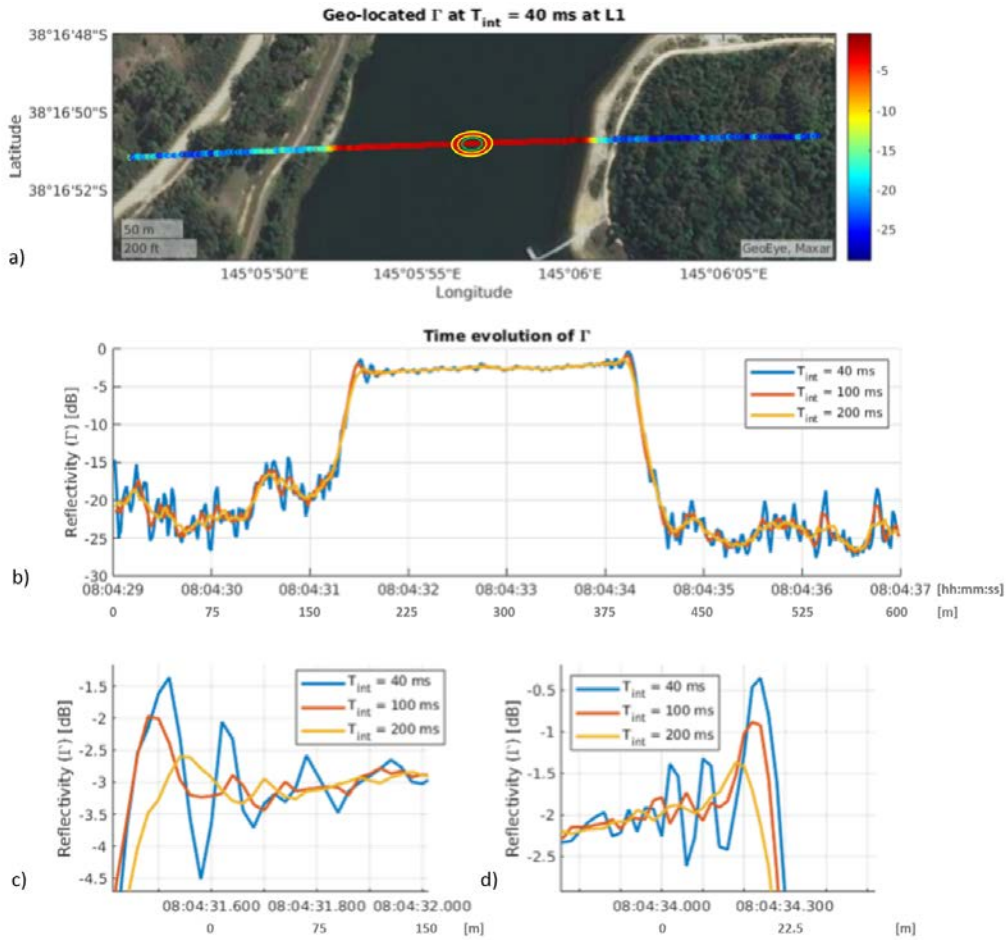

Figure 3.16: Land-to-water transition during an MIR at L1 test flight over Devilbend Reservoir (38.29°S, 145.1°E). (a) Geo-located reflectivity, and approximated representation of the first four Fresnel zones; (b) time evolution of the reflectivity, and a zoom-in of the step transition on the (c) left and (d) right.

$$\Delta x = \Delta v \sqrt{\frac{\lambda \cdot h_R}{2 \cdot cos(\theta_i)}} \approx 1.5 \sqrt{\frac{\lambda \cdot h_R}{2 \cdot cos(\theta_i)}}. \tag{3.18}$$

In this case, the achievable spatial resolution is almost equivalent to the size of the first Fresnel zone in Eq. 3.1, as $1.5/\sqrt{2} \approx 1.06$. Thus, being never smaller than the size of the first Fresnel zone.

It is worth mentioning that the theoretical analysis assumes that coherent scattering is the dominant mechanism, which is the case when transitioning from land to/from calm water. However, when transitioning into the open ocean, where incoherent scattering is more important, the presence of the ripples is not that evident, and the reflectivity

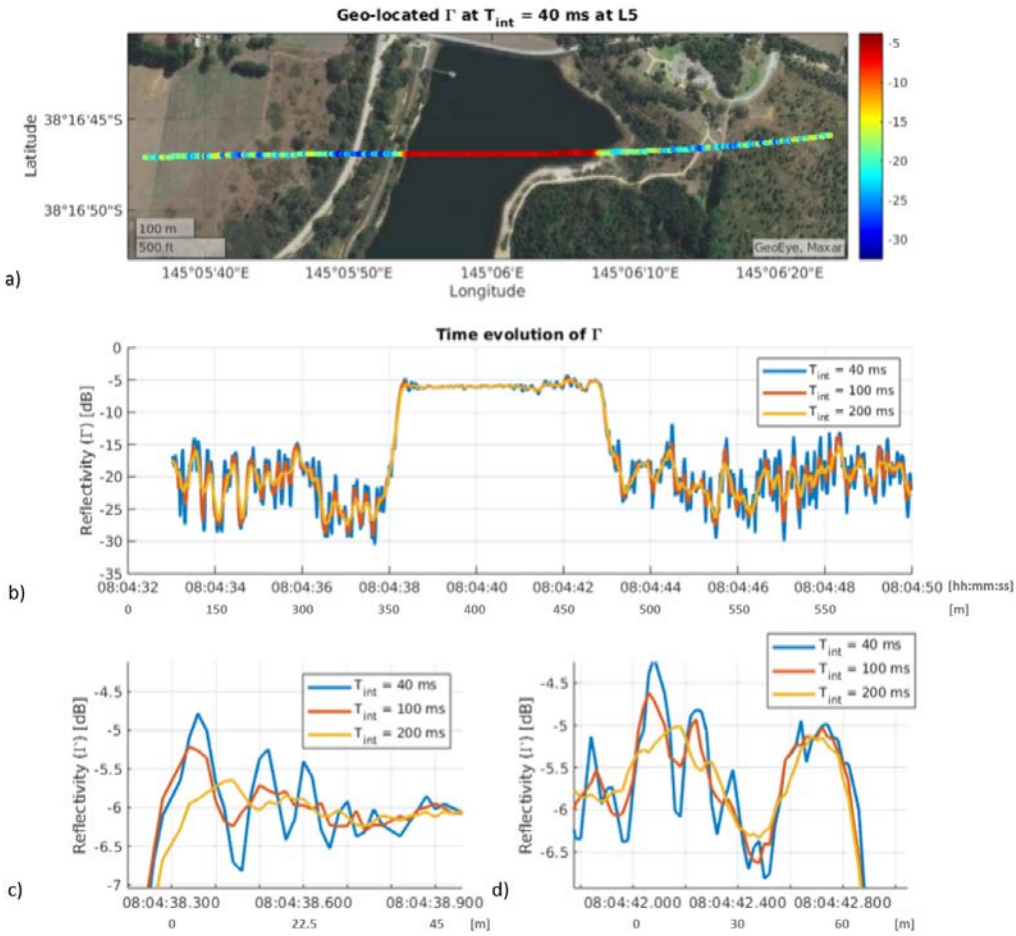

Figure 3.17: Land-to-water transition during a MIR at L5 test flight over Devilbend Reservoir (38.29°S, 145.1°E). (a) Geo-located reflectivity, (b) time evolution of the reflectivity, and a zoom-in of the step transition on the (c) left and (d) right.

exhibits random fluctuations associated mostly with the speckle noise.

3.5 Conclusions

This Chapter has addressed the achievable spatial resolution in GNSS-R from two points of view, and the optimum integration time required to maximize achieve this resolution. A first analysis has been conducted taking into consideration that most of the reflected power comes from the first Fresnel zone, as previously analyzed in [120]. Signals collected by the MIR instrument in different flights have been analyzed, showing that the WAF was blurred when the plane crosses more than one Fresnel zone, both at L1 and L5 bands. Furthermore, a second analysis has been conducted to analyze the achievable spatial resolution, under coherent scattering conditions, when transitioning from two different

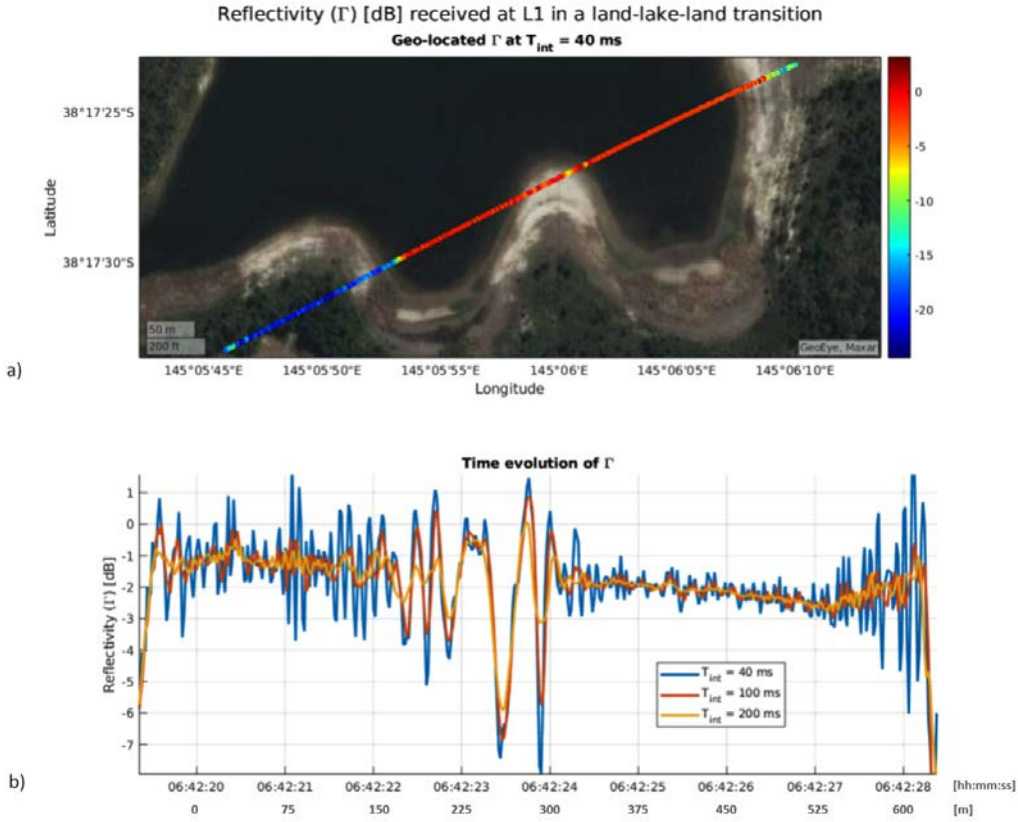

Figure 3.18: Land-to-water transition during an MIR at L1 test flight over Devilbend Reservoir (38.29°S, 145.1°E). (a) Geo-located reflectivity, and (b) time evolution of the reflectivity.

media (i.e., water-land transitions), presenting the first analytical study of the response of a GNSS-R system to a reflectivity step.

Under general conditions, the achievable spatial resolution is equivalent to the size of the first Fresnel zone. However, in some specific cases as in the transition between different media, the achievable spatial resolution (i.e., low values of v in Eq. 3.16) is smaller. This has several implications to select the optimum integration time for a GNSS-R receiver. However in general, the optimum integration time will be determined by either the code length (in meters) or the size of the first Fresnel zone (whichever is smaller), as detailed in Eq. 3.5 (reproduced below for the readers' convenience).

$$T_{int_{max}} = \frac{min|L_{chip}, L_{Fz}|}{v_{platform}}. \tag{3.5}$$

It is also important to remark that, if there is enough link budget (i.e., using high-directive antennas, having a very low receiver's noise figure, etc.), shorter integration times can be used. In such a way that oversampling is possible over the same Fresnel

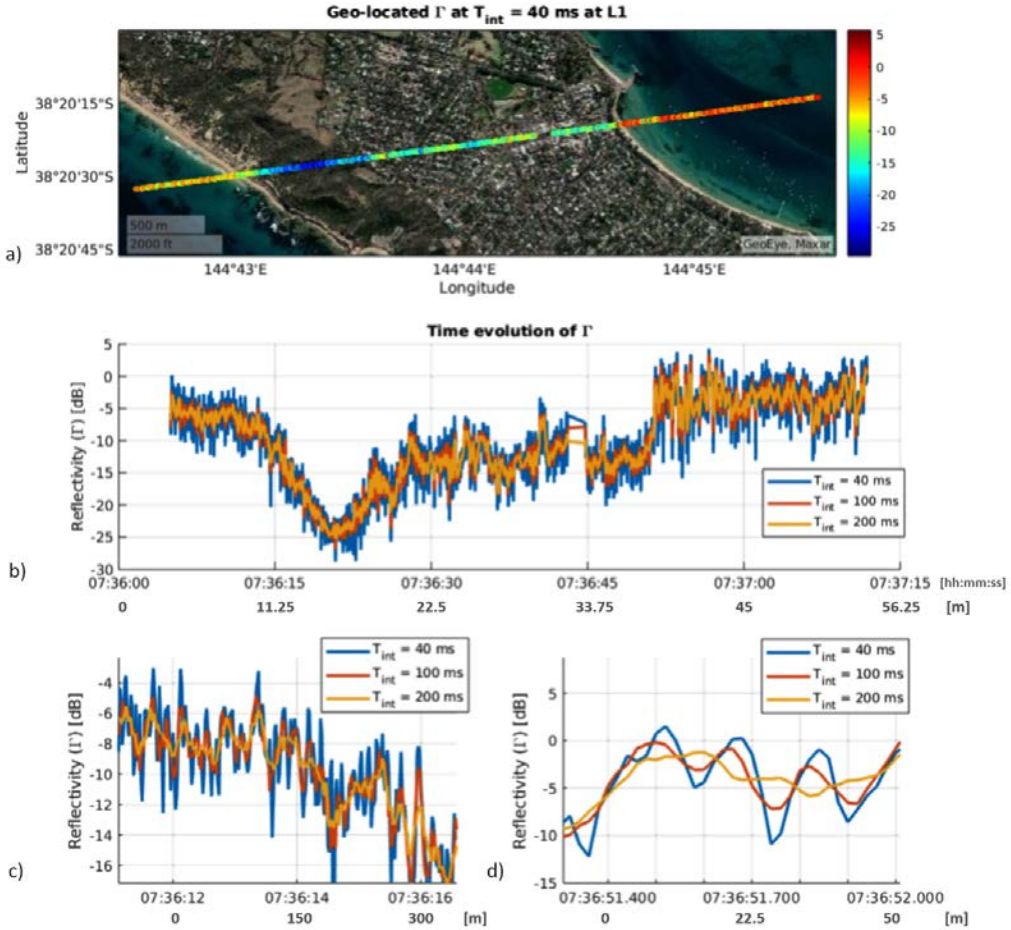

Figure 3.19: Land-to-water transition during an MIR at L1 test flight over Point Nepan, Melbourne (38.35°S, 144.74°E). (a) Geo-located reflectivity, (b) time evolution of the reflectivity, and a zoom-in of the step transition on the (c) left and (d) right.

zone. Thus, producing almost negligible blurring in the retrieved waveforms, and allowing to study other facets of the reflection, as multiple peaks due to nearby reflections in the glistening zone. This phenomena will be further analyzed in Chapters 5 and 6.

Part II

Preparatory Field Experiments

4

Chapter 4

Microwave Interferometric Reflectometer: GNSS-R processor

This Chapter explains the GNSS-R processor developed to process the raw data acquired by MIR during its four flights conducted in South Australia in 2018. The objective of this Chapter is to provide a complete overview of the GNSS-R software implemented to process MIR data, including data storage and visualization. The processor takes level 0 data (i.e., raw samples data) and processes them into valuable observables, such as reflectivity, or GNSS waveform shape. The processor has been developed to be compatible with Geographical Information Systems (GIS). The output variables are stored in a SQL database using geographic-type variables, which can be visualized using GIS software. This processor is the baseline for the UPC Remote Sensing Laboratory future missions, and it provides a common input/output interface to process and retrieve the GNSS-R data.

Some figures used in this Chapter to illustrate the MIR instrument and the GNSS-R processor have been adapted from two peer-reviewed journal publications: "Untangling the Incoherent and Coherent Scattering Components in GNSS-R and Novel Applications" [JP4], and "Experimental Evidence of Swell Signatures in Airborne L5/E5a GNSS-Reflectometry" [JP5]. Moreover, the Chapter is organized as follows: Section 4.1 introduces the MIR instrument, Section 4.2 describes the raw data generated by the MIR instrument, and how this data is re-structured for processing, Section 4.3 describes the cGNSS-R processor framework developed to process the data generated by MIR, Section 4.4 describes the structure of the processed data, providing some use-case examples, and finally Section 4.5 concludes the Chapter with some key messages and considerations for future remote sensing processing.

(a) **(b)**

Figure 4.1: (**a**) (MIR) instrument and up-looking array mounted inside the airplane, and (**b**) down-looking array covered with a radome hanging from the airplane's fuselage [128].

4.1 Introduction

The MIR instrument was developed within Dr. Raul Onrubia and Dr. Daniel Pascual Ph.D. theses, and the instrument design and characterization are available in their dissertations, as well as in journal publications [22, 23, 97]. MIR is an state-of-the-art airborne GNSS-R instrument composed by two dual-band high-directive antennas (∼21 dB at L1, ∼18 dB at L5), as detailed in Fig. 4.1. The instrument was conceived to perform iGNSS-R, and the purpose of such high-directive antennas was to improve the SNR and reduce the signal cross-talk [128], mimicking the PARIS IoD instrument. However, aside from this primary objective, the instrument was collecting raw data at 32.736 Mega-Samples per second (MS/s) at a 1-bit for post-processing. Thus, allowing offline post-processing using other techniques, such as cGNSS-R.

In short, the instrument is composed by the following elements:

- **The antenna array** is formed by an up-looking antenna and a down-looking antenna (Fig. 4.1b shows the down-looking antenna radome). Both antennas are 19-element dual-band (L1 and L5) patch antenna arrays. The up-looking is RHCP, and the down-looking is LHCP. Each antenna element is followed by a signal conditioning circuit (i.e., amplifiers and filters), that outputs the RF signal which is then injected into the beamforming unit.

- **The Beamforming unit** is composed of 19 phase shifters that change the amplitude and phase of each antenna element to produce the desired pointing. This unit is able to create four different beams per antenna, two beams at L1 and two beams at L5 per antenna array. The up-looking antenna and the down-looking antenna are configured to produce a beam that tracks the same GNSS satellite (i.e. the up-looking antenna tracks the satellite, and the down-looking antenna tracks the specular reflection point).

- **The Data Sampling and Processing unit** is composed of four dual-channel software-defined radios (SDR). Each SDR samples data for the pair of beams produced by the up-looking and the down-looking antenna so they are perfectly

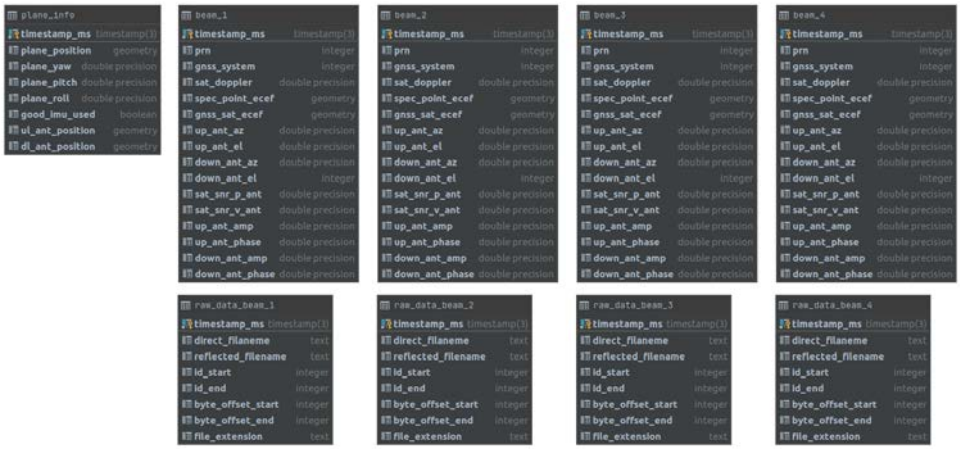

Figure 4.2: MIR input data database layout. Diagram generated by DataGrip®software.

synchronized. The radios are configured to sample IQ data at 32.736 MS/s at 1 bit. The data is stored in a hard drive, and recovered after the flight.

- **The Embedded control unit** communicates with the beamforming unit to tune the beam generation parameters at a rate of 3 Hz. This unit is composed by a GPS receiver, and an attitude determination system (i.e. inertial measurement unit) to compensate for the airplane maneuvers. The control unit takes the information of all satellites in view, filters those satellites with small incidence angles, and calculates the specular point position, which is then transmitted to the beamforming unit. Moreover, this unit keeps a log of the airplane position, and the GNSS satellites being tracked by each beam.

4.2 Input Data Definition: Handling MIR Data

As introduced in Section 3.2.1, MIR conducted four flights in Australia, collecting nearly one Terabyte of 1-bit sampled IQ data, and more than 20.000 waypoints (i.e., airplane telemetry information) per flight. To handle the large amount of data collected, a storing and processing framework was required. As explained in the previous section, the data generated by MIR is divided into two parts: the raw data part coming from the data sampling and processing unit (i.e., IQ samples), and the embedded system telemetry information.

The IQ raw data is formed by a set of binary files that are time-tagged by the embedded system. This time-tag is used to identify the plane position and beam pointing information corresponding to the raw data recorded. Thus, the "common" link between the telemetry and the IQ recording is the timestamp. For that reason, the approach followed was to organize the input data in a relational database. As presented in Fig. 4.2, a set of tables are generated in a PostgreSQL database [129]. A different PostgreSQL schema is created per flight (i.e., a database schema is an equivalent of a separate folder in a file system). In this way, each flight is logically separated from another one.

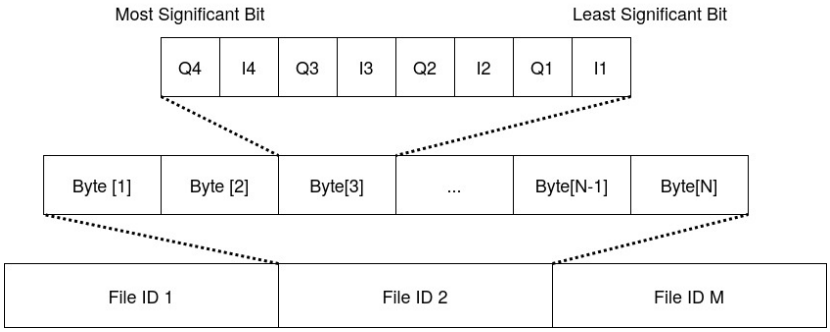

Figure 4.3: MIR raw data file description.

4.2.1 Embedded system telemetry

As it can be seen, the *plane_info* table contains the basic plane information, like the plane position, and the yaw/pitch/roll angles of the platform. Then, four tables are used to store the telemetry of each beam. The information stored in this table is the GNSS system (i.e., GPS or Galileo), the PRN of the GNSS satellite being tracked, and its estimated Doppler shift. In addition, the GNSS satellite position and the specular point position (computed in real-time during the flights) are also stored. Then, other parameters are also stored for calibration purposes, such as the amplitude of the antenna radiation pattern in the direction where the beam is pointing to. Finally, four extra tables are used to classify the raw data files. The files themselves are not stored in the database, but a file identifier and the byte offset corresponding to a given timestamp are stored. In other words, given a timestamp, the database can retrieve the plane position, the beam information, and the pointer to the raw data segment containing the GNSS-R data.

4.2.2 IQ raw data files

The raw data files generated contain the 1-bit IQ data packetized in bytes. As shown in Fig. 4.3, a MIR execution generates a set of M files, with N bytes per file, and four IQ samples per byte. Each beam produces a file with a unique identifier, whose information is stored in the corresponding *raw_data_beam* table of the database. The raw data files are stored in a hard drive, and the processing chain access to the files through the information stored in the database, as detailed in Section 4.3). Moreover, thanks to the SQL interoperability, this data can be easily accessed through any SQL software available.

4.2.3 Geographical Information System (GIS) databases

One of the benefits of SQL databases is their interoperability. SQL connections can be established in any programming language. Modern databases also allow handling "intricate" variables. As it can be seen in the "position" columns in Fig. 4.2 (i.e., plane_position variable), the variable selected to store plane positions is from a type called "geometry". This type of variable is one of the main advantages of PostGIS-enabled PostgreSQL databases [130], which allows to easily store geographical information.

(a) **(b)**

Figure 4.4: Visualizing different geometry variables stored in the PostgreSQL database using QGIS: (a) the aircraft position variable, and (b) Visualizing the evolution of the Doppler shift (Hz) of the GNSS satellite followed by the MIR instrument.

PostGIS is an extension of PostgreSQL databases to add spatial and geographic objects (i.e., variables) to the database, known as Geographical Information System (GIS). GIS is an entire ecosystem, comprising a large set of tools to organize, store, manipulate, visualize, and analyze geographical information. As previously presented, different geographical information needs to be indexed for MIR: the plane information, the specular reflection point per beam, and the GNSS satellite position. Instead of creating Lat-Lon-height columns, the information is stored in this GIS-compatible variable called "geometry". This variable contains all required features of a geographical representation, such as the projection and the geodetic reference frame of the stored position.

PostGIS-enabled databases also allow performing different operations on geometry-type variables, such as computing the distance between points, performing nearest neighbor interpolations, or doing re-projections through SQL queries (i.e., from the Lat-Lon-height projection to a cartesian X-Y-Z projection). Moreover, a large amount of GIS software is nowadays available to visualize geometry-type variables, such as QGIS [131]. As it can be seen in Fig. 4.4, a GIS visualization software connected to a database allows handling geographic-type variables. Once the data is loaded into the GIS visualization software, it can be manipulated to add different color scales, overlay additional maps, etc.

4.3 MIR GNSS-R Processor

The MIR GNSS-R processor has been developed using a modern language called *Go* [132]. *Go* is an open-source language developed by Google. It is simple to code and designed for multi-core operations, reporting a higher efficiency than C in multi-threaded applications.

In this case, the use of an efficient multi-threading language allows processing GNSS-R reflections in parallel. In the MIR case, four parallel threads are created to process each beam independently. However, in a generic case, where a GNSS-R sensor collects more

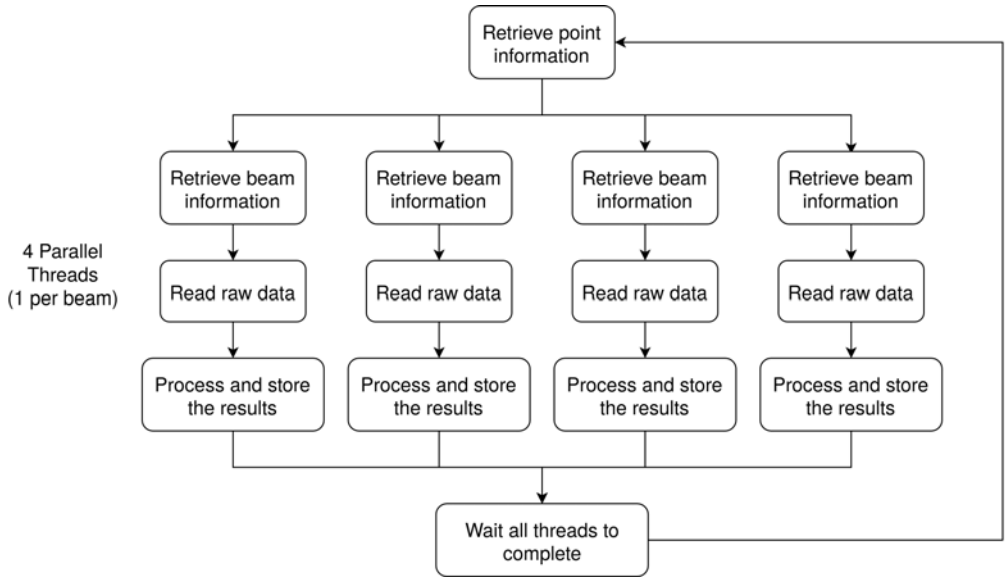

Figure 4.5: MIR GNSS-R processor flowchart

than 4-6 reflections simultaneously, the *Go* software can be easily adapted to add more threads thanks to its in-built multi-threading interface.

Aside from that, *Go* can be easily executed on any operative system, and its core already includes several applications to interface with a Graphics Processing Unit (GPU) to perform complex operations (i.e., correlations, multiplications).

4.3.1 High-level flowchart

The MIR processor needs a set of configurations to be executed. The processor input requires a list of points (i.e., platform information) to start processing. In this case, thanks to the SQL database, the list of points is delivered through a SQL query. The processing chain is connected to the database and performs the appropriate queries to process the raw data. Moreover, the processing chain requires information of the data that is going to be processed. In this case, the signal type (i.e., the code sequence: L1 C/A, L1C, L5I, L5Q, E5a, E5b, etc.) used in each beam, the incoherent integration time, and the Doppler step used in the GNSS-R processor are required as part of the processor initial configuration. Once everything is set, the processor starts the execution following the flowchart in Fig. 4.5. As it is seen, from the list of points retrieved in the first step, four threads are created, and each thread process one of the four MIR beams.

Each thread has a handle to connect to the database and loads into the processor memory the necessary information to process the GNSS-R signal. Each thread accesses the hard drive, where the IQ raw data files are stored, reading them as registered in the file pointer information specified in the database. In this process, the mutual exclusion when accessing the disk or the database are internally handled by the in-built *Go* multi-threading engine.

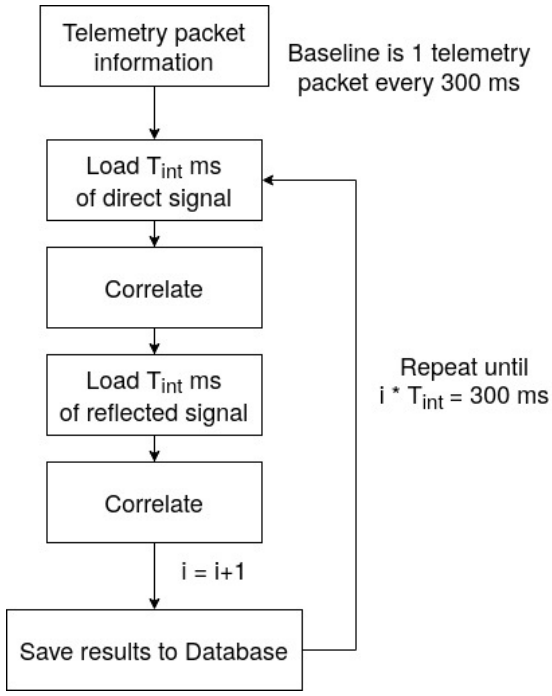

Figure 4.6: MIR cGNSS-R processor flowchart.

4.3.2 Processing the GNSS signals

This version of the MIR processor performs the cGNSS-R approach by computing the correlation between the IQ raw data with a clean replica of the PRN signal, as specified in the previous section. As detailed in Fig. 4.6, each processor thread takes as many samples as specified by the incoherent integration time (i.e., if the incoherent integration time is set to 5 ms, 163680 samples are read from the IQ file handler, which in terms of bytes is 40920 bytes). Then, the PRN clean replica is multiplied by the estimated Doppler shift from the beam.

Once all the data is loaded into the processor memory, each thread starts the correlation process for both the direct and the reflected signals, as shown in Fig. 4.6. Note that, to have aligned the correlation output with the airplane telemetry, the telemetry rate (i.e., timestamp difference) shall be evenly divisible by the selected integration time T_{int}. In this case, the telemetry rate can be easily tuned using database inherit tools, and the integration time shall not exceed the size of the first Fresnel zone, as explained in Chapter 3.

Each iteration takes T_{int} ms of signal of either the direct or the reflected signals. The MIR signal is cross-correlated with the PRN clean replica previously loaded, as described in Fig. 4.7. The correlation is performed following the Parallel Code Phase Search (PCPS) algorithm, using the Fast Fourier Transform (FFT) [133]. As the coherent integration time (T_c) is set by the PRN code length (i.e., 1 ms for GPS L1 C/A), this process is repeated N times, where $N = \frac{T_{int}}{T_c}$. The FFT and the Inverse FFT (IFFT) are both computed

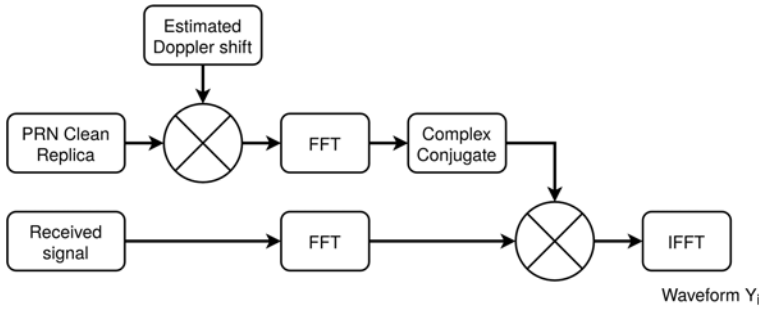

Figure 4.7: Cross-correlation process of the MIR data based on the PCPS algorithm.

inside the computer GPU. Thanks to the parallel computing capabilities of GPUs, the whole set of N waveforms are processed sychronoulsy by the GPU. Finally, all waveforms are squared and averaged following Eq. 2.5, which is reproduced below for the readers' convenience.

$$\overline{Y} = \frac{1}{N}\sum_{i=1}^{N} |Y_i(\tau,\nu)|^2 \tag{2.5}$$

4.4 Output Definition and Processor Extendibility

Once the correlation of both direct and reflected signals is finalized, all results are stored again in the database. As the *Go* multi-threading engine is able to independently manage the database access from different threads, each thread pushes its own results to the database. In this case, the "*results*" database is organized as shown in Fig. 4.8.

As it can be seen, the database is now organized into four tables, where each table contains the information out of the cross-correlation process. The *level_0_metadata* table contains the basic telemetry information, including a unique identifier (*id*), the timestamp, the coherent integration time (i.e., 1 ms for GPS L1 C/A, 4 ms for Galileo E1OS, stored as a multiple of 1 ms), the incoherent integration time, stored as a multiple of 1 ms (i.e., *inc_int* = 500 and *coh_int* = 1 means 1 ms coherent integration, and 500 ms of incoherent integration). Then, some additional telemetry, as the flight identifier (i.e., OCEAN flight, YANCO flight, etc.), and the PRN, GNSS system identifier (i.e., GPS, Galileo), and the beam identifier (i.e., 1 to 4). In this case, all beams are stored in the same table, and thanks to the SQL engine, retrieving data from a given beam is as easy as executing a query with the conditional "*where beam_id* = X", where X is the beam identifier (1 to 4).

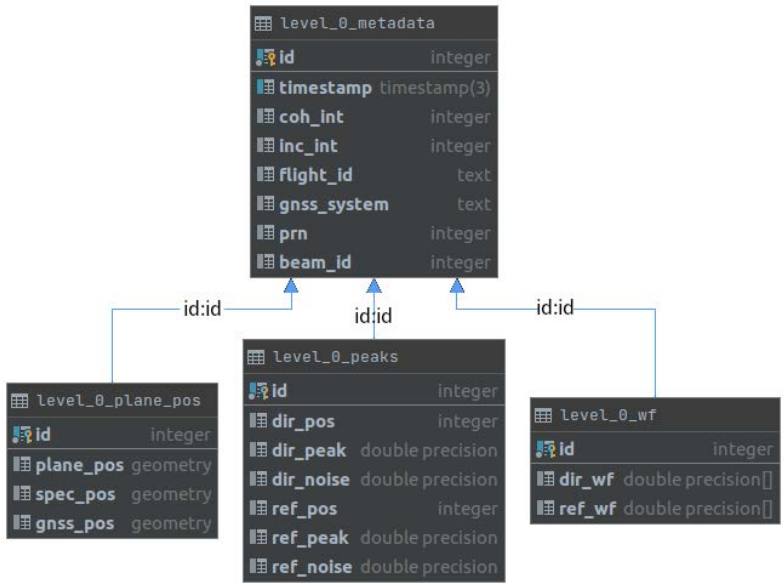

Figure 4.8: MIR output data database layout. Diagram generated by DataGrip®software.

The three remaining tables are linked with the first one using a unique identifier (*id* variable). The *level_0_plane_pos* table includes the plane position, the specular point position, and the transmitting GNSS satellite position for each *id*. Note that, the three variables are "geometry" variables so they can be easily accessed by any GIS software. Then, the *level_0_peaks* table includes basic information of the correlation output for both direct and reflected signals, including the position (in code) of the peak, the amplitude of the peak (in arbitrary units), and the noise level, computed after the correlation. By performing the appropriate queries to this table, it is possible to retrieve a GNSS-R observable, such as an un-calibrated reflectivity (i.e., *ref_peak* divided by *dir_peak*). Finally, table *level_0_wf* contains a waveform slice around the peak, stored as a floating-point array, for both direct and reflected signals.

4.4.1 Visualizing the output with QGIS

In this section, preliminary results from one MIR flight are presented as an example. The processor has been executed with an incoherent integration time of 100 ms, producing more than 300.000 entries in the database. The following SQL is executed to retrieve un-calibrated reflectivity for the four beams:

```
select a.id,timestamp,10*dlog10(b.ref_peak/b.dir_peak) as refl, c.spec_pos
from sea_flight_new.level_0_metadata as a
inner join sea_flight_new.level_0_peaks as b on a.id = b.id
inner join sea_flight_new.level_0_plane_pos as c on a.id = c.id
order by timestamp asc
```

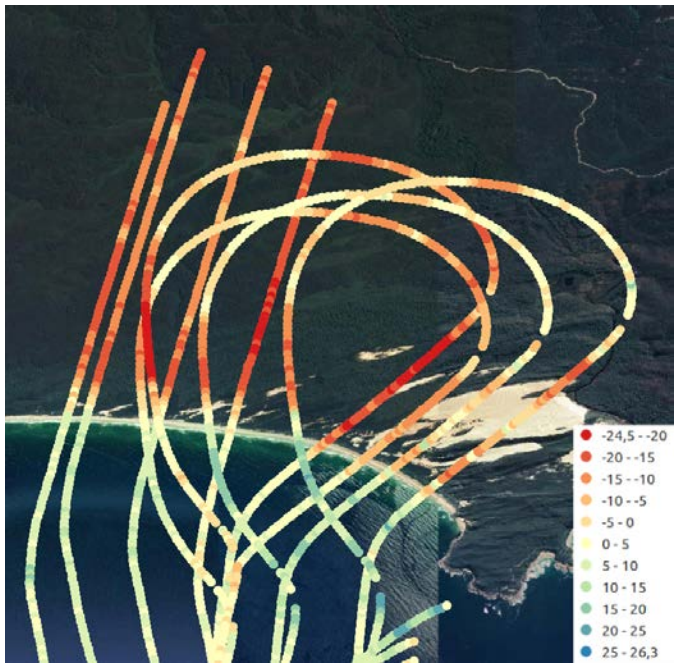

Figure 4.9: Un-calibrated reflectivity values visualized in QGIS and retrieved from the PostGIS-enabled PostgreSQL database.

In this SQL query, data from the four beams is retrieved together, and directly re-projected by the QGIS software, as it can be seen in Fig. 4.9. Despite the displayed magnitude is still not calibrated, handling such number of points is turned easy and optimized thanks to the use of a GIS-enabled software, and a well-structured output in a PostGIS-enabled PostgreSQL database.

4.4.2 Extending the processing chain

As it is seen, the processing chain is very modular. Thanks to the definition of inputs and outputs based on a SQL connection, the processing framework can be easily adapted.

In case that a different processing scheme is desired (i.e., iGNSS-R), it is as easy as changing the cGNSS-R processor shown in Fig. 4.6 by the processing shown in Fig. 4.10. Then, the database output shall be restructured to include only one correlation output instead of the direct and reflected correlation outputs. In this case, this could also be done without changing the database, as the information related to the *dir* correlation can be introduced as a *NULL*, preserving the database structure.

In this case, the GPU interface to compute the correlation is the same, but now the carrier wipe-off due to the Doppler shift is not performed (i.e., the direct signal and the reflected signal have similar Doppler shifts in the airborne case).

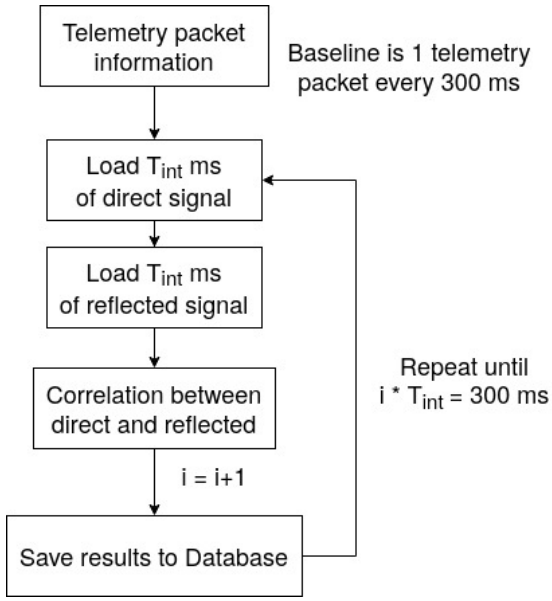

Figure 4.10: MIR iGNSS-R processor flowchart

4.5 Conclusions

This Chapter has presented the architecture of the signal processing framework to process MIR IQ raw data into observables. The presented framework follows a modular input/output approach based on a SQL database. In particular, the PostgreSQL database with the PostGIS extension has been selected. The use of GIS-enabled software brings interoperability to the system, and the algorithm inputs and outputs can be easily accessed through any interface, such as the visualization tool QGIS.

The use of *Go* as the programming language allows to easily scale the processor, as the built-in multi-threading engine allows to easily deploy more beams in case it is needed.

A clear definition of the system inputs and outputs is required to deploy advanced remote sensing products. The use of modern and well-structured databases guarantee interoperability among users all over the world.

5

Chapter 5

Microwave Interferometric Reflectometer: Ocean experiment

This Chapter explains the results of the MIR campaign over the Bass Strait, Australia, conducted in June 2018. The Chapter is divided into two main Sections aside from the introduction and the conclusions. Section 5.2 presents the results adapted from the peer-reviewed journal publication "Untangling the Incoherent and Coherent Scattering Components in GNSS-R and Novel Applications" [JP4], where the coherency of L1 and L5 GNSS-R reflections over the ocean is analyzed following a technique proposed by Dr. Francisco Martin [118]. Then, Section 5.3 presents the results adapted from the peer-reviewed journal publication "Experimental Evidence of Swell Signatures in Airborne L5/E5a GNSS-Reflectometry" [JP5], where the shape of the L5 reflected waveforms are linked to swell and wind-driven waves. Moreover, the results presented in this Chapter have also been part of the following conference proceedings [CP4, CP5].

5.1 Introduction

As introduced in Chapter 4, one of the main differences of MIR with respect to other instruments is its antenna. Thanks to the analog beam-steering and the very large directivity ($\sim$ 21 dB at L1 and $\sim$ 18 dB at L5) the instrument is able to receive reflections with a quite large SNR, allowing the use of shorter integration times. Thanks to this very short integration times, as introduced in Chapter 3, the waveform is not blurred, and there is no need of re-tracking the specular point.

As it is was presented in Chapter 3 for the Ocean case, as the integration time increases, the received GNSS reflected signal blurs. At L1, this effect is detected as a slight widening of the resulting waveform, but for the L5 case, multiple peaks appear in the retrieved waveform. Depending on the reflection geometry and the surface characteristics, this reflection might be coherent (with a large coherent component) or incoherent (with a very small coherent component), which will also be affected if the integration time increases. The larger the integration time, the more "facets" of the Ocean contributing with small portions of power into the receiver antenna.

In order to further study the effects presented in Section 3.2.1, data corresponding to the flight over the Bass Strait on 6 June 2018 is selected. The plane followed three passes over a straight line going from 37.9°S, 149.23°E to 38.9°S, 149.1°E, as shown in Fig. 5.1. The GNSS-R data used include both L1/E1 and L5/E5a bands, and also contain data from both GPS and Galileo constellations at different incidence angles and coming from different azimuths.

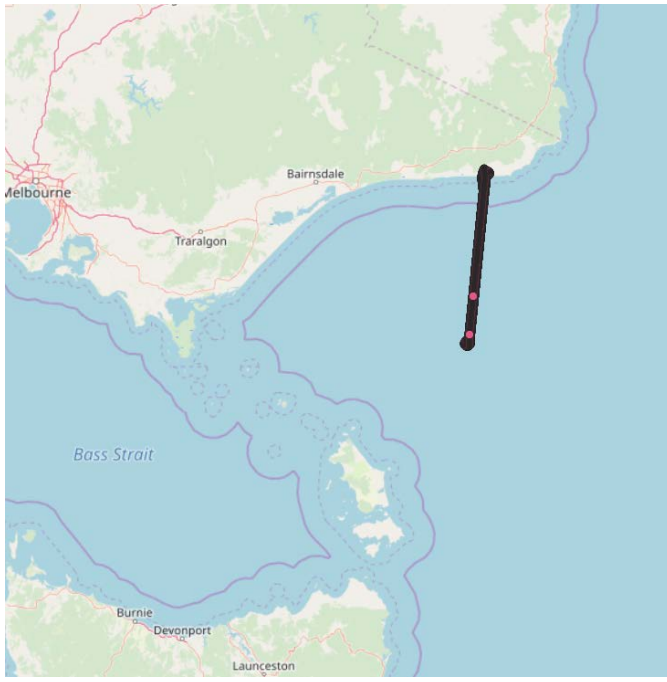

Figure 5.1: Flight path on 6 June 2018. Data retrieved from this flight is used for the coherency analysis and the swell wave study.

The plane flew at a height of $h \sim 1500$ meters at an average speed of ∼75 m/s. In that case, the specular reflection occurs in the first Fresnel zone, which is limited by the plane altitude, as it was shown in Eq. 3.3[1]

In this case, $\lambda = 19$ cm for L1, $\lambda = 25$ cm for L5, $h = 1500$ m, and θ_{inc} the wave incidence angle. Thus, at nadir $\theta_{inc} = 0°$ and $R_r = h$, which lead to a semi-major axis of the first Fresnel zone for L1 $l_{Fr_{L1}} = 17$ m, and for L5 $l_{Fr_{L5}} = 19$ m, and a Fresnel zone of $l_{Fr_{L1}} = 28$ m, and for L5 $l_{Fr_{L5}} = 33$ m for an incidence angle of $\theta_{inc} = 45°$.

Considering the plane height and both L1 and L5 antenna 3 dB beam-width, $\theta_{L1} = 18°$ and $\theta_{L5} = 25.5°$, the footprint projection (in one direction) over the Earth's surface is given by Equation (5.1),

$$L = R_r \cdot \left(cotg\left(\theta_{inc} - \frac{\theta_{3dB}}{2}\right) - cotg\left(\theta_{inc} + \frac{\theta_{3dB}}{2}\right)\right) \tag{5.1}$$

where $L = 475$ m for an incidence angle $\theta_{inc} = 0°$ and $\theta_{3dB} = \theta_{L1}$, and $L = 678$ m for $\theta_{inc} = 0°$ and $\theta_{3dB} = \theta_{L5}$, $L = 975$ m for $\theta_{inc} = 45°$ and $\theta_{3dB} = \theta_{L1}$, and $L = 1430$ m and for $\theta_{inc} = 45°$ and $\theta_{3dB} = \theta_{L5}$.

5.2 Coherence of Airborne GNSS-R at L1/L5 in the Ocean

GNSS-R has been implemented mainly by performing the incoherent integration (the sum of the modulus square presented in Eq. 2.5) of a set of coherently integrated GNSS codes over short integration times (1–4 ms at most from space). This integration removes any coherency present in the reflected signal. The presence of a coherent component in a GNSS reflection can be transferred into a surface property or a geophysical parameter.

Coherent reflections have been found from low height ground-based instruments based on the coherent interference between the direct and the reflected signals [134]. However, as shown in [135], the maximum interferometric delay is limited to about half the chip length, which puts a trade-off limit on the receiver height and the satellite elevation angle (∼150 m for L1 C/A; ∼15 m for L5/E5a). This coherent component is almost negligible (but still present) in many reflections for airborne, high stratospheric balloons [106], and spaceborne instruments [118, 136]. The use of a larger antenna (i.e., dish antenna) or an array of antennas (i.e., multiple microstrip antennas) allows a higher gain on the receiver side, and therefore a higher SNR. Therefore, using shorter integration times increases even further the SNR of the coherent component of the reflected wave. This Section analyzes in more depth the presence of a coherent component in the data acquired by the MIR instrument.

5.2.1 Coherency of the cGNSS-R signal

In most GNSS-R instruments [137, 138], the coherent integration time is limited by the code length used by the GNSS signal (i.e., $\tau_c = 1$ ms for GPS L1 C/A, $\tau_c = 1$ ms for GPS L5 without secondary codes, and $\tau_c = 20$ ms for GPS L5 including secondary codes), as

[1] $l_{Fr} = \dfrac{\sqrt{\lambda R_r}}{cos(\theta_{inc})}$, where $R_r \approx \dfrac{h}{cos(\theta_{inc})}$

it has been introduced in Chapter 2. As it has been discussed, incoherent averaging is performed to increase the Signal-to-Noise Ratio (SNR). The incoherent integration has been the most used technique to acquire GNSS signals, and to perform DDMs. However, this technique destroys the coherent part of the signal, which is the one coming from the specular reflection point, around the first Fresnel zone, and as covered in this Section, it may contain valuable information of the reflection geometry.

In [118], a method was proposed to detect and eliminate leakage of the direct signal. In this Section, this technique is applied to detect the coherent component present in a GNSS-R signals collected by the MIR instrument. The technique explained in [118] consists of the computation of the variance of the coherently integrated DDM (Y in Eq. 2.4, reproduced below for the readers' convenience), i.e., prior to the incoherent averaging, as in Eq. 5.2.

$$Y(\tau,\nu) = \frac{1}{T_c}\int_0^{Tc} x(t)y^*(t-\tau)e^{-j2\pi\nu t}dt \tag{2.4}$$

$$Var\,(Y) = E[|Y|^2] - |E\,[Y]|^2\,, \tag{5.2}$$

where $E[|Y|^2]$ is the incoherently averaged DDM. In practice, the variance term, $Var(Y)$ is computed as the mean squared of the N_{inc} samples (amount of samples incoherently averaged) minus the arithmetic mean of the samples (μ), as in Eq. 5.3. Note that Y is a complex value vectors, therefore any sum, multiplication, or mean calculus has to follow the complex arithmetic (i.e., mean of a complex vector is $mean(I) + j \cdot mean(Q)$)

$$Var(Y) = \frac{1}{N_{inc}}\sum_{i=1}^{N_{Inc}} |Y_i\ - \mu|^2 \tag{5.3}$$

$$\mu = \frac{1}{N_{inc}}\sum_{i=1}^{N_{Inc}} Y_i \tag{5.4}$$

The difference of Eqns. 2.4 and 5.3 leads to the coherent component computed as the average of N_{inc} samples, as shown in Eq. (5.5).

$$|E[Y]|^2 = \frac{1}{N_{inc}}\sum_{i=1}^{N_{inc}} |Y_i\ |^2 - \frac{1}{N_{inc}}\sum_{i=1}^{N_{inc}} |Y_i\ - \mu|^2, \tag{5.5}$$

where the first term in the right side equation is the incoherently averaged DDM shown in Eq. 2.5.

The implementation of the coherent integration as in Eq. 5.5 opens many possibilities and analysis methods for signal processing. As an example, the ratio of both coherent component and total power waveform is defined as proposed in [139] as the degree of coherency (DOC), as in Eq. 5.6. This ratio represents how coherent the GNSS signal is, for instance, a direct GNSS signal has a DOC very close to 1. A reflected GNSS signal may have a large DOC in case of a quasi-specular reflection, but in general, over land, it does not.

$$DOC = \frac{|E[Y]|^2}{E[|Y|^2]} \tag{5.6}$$

5.2.2 Data processing

The GNSS-R processing chain described in Chapter 4 has been modified to include a new processing module to compute the coherent component of the GNSS-R signal.

Once each waveform Y_i has been retrieved for each of the N_{inc} integration periods, the algorithm in Figure 5.2 is applied to provide the four products: total power waveform; variance part (which is the incoherent part); its difference, which corresponds to the coherent component of the signal; and finally the phase evolution for each integration period.

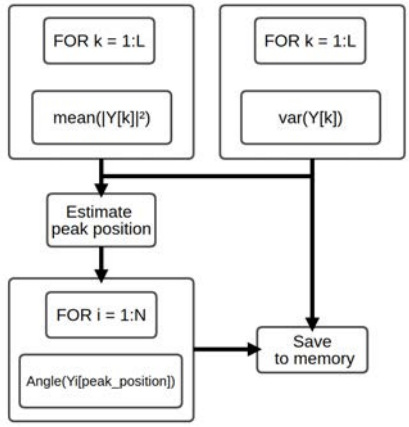

Figure 5.2: Total power waveform and coherent component processing algorithm of MIR data, including the phase retrieval of the peak.

Note that, mean() and var() functions are calculated over Y_i, where $i = 1$ to N, and N is the integration time.

5.2.3 Navigation bit transitions during the coherent integration

As described in [140], the bit transition in GNSS needs to be handled in case of large coherent integration periods. The variance method is also sensitive to the bit change, therefore a bit change in the middle of the integration process causes that the coherent term in Eq. 5.3 drops to zero. The bit transition effect can be compensated by retrieving the navigation bit sign and multiplying each of the resulting waveforms (Y_i), by the corresponding sign. The navigation bit sign is retrieved by looking at the phase evolution during the integration period.

The navigation bit transition can also affect the reflected GNSS signal in case the coherency is preserved in the reflection. However, this is not actually the case, and thus the navigation bit cannot be retrieved and compensated as easy as in the direct signal case. In such cases, the navigation bit can be compensated using the direct signal

information. The algorithm to retrieve the coherent part for both direct and reflected signals, compensating the navigation bit transition, is detailed in Fig. 5.3.

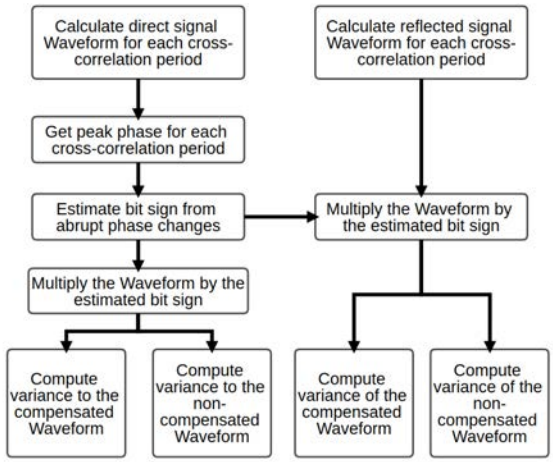

Figure 5.3: Variance calculus algorithm in the presence of bit transitions for both direct and reflected waveforms.

In order to estimate the bit sign ($\hat{x}$) in the direct signal, the discriminator in Eq. 5.7 is used.

$$\hat{x} = atan2\left(Q, I\right), \tag{5.7}$$

where Q is the imaginary component of the WAF (Y_i) at its peak (for both code and Doppler), I the real component, and *atan2* is the four quadrant arctangent function.

5.2.4 Open-Loop tracking of the coherent part of the reflected signal

The described algorithm allows for an open-loop tracking of the reflected signal with a variable coherent integration time compensating the bit transitions because of the information of the direct signal. In addition, this algorithm stores both the bit-compensated and the non-compensated coherent integrated waveforms, which are useful to evaluate the coherency characteristics of the signal (i.e., the reflected signal can contain a coherent part, but no bit information can be retrieved).

Figure 5.4 illustrates the bit change effect on the impact on the coherency part in a GPS L1 C/A GNSS signal captured by the MIR instrument and integrated during 40 ms. A data set containing two bit transitions (periods 12 and 32 as seen in the phase plot) in the middle of the integration has been selected. As it is seen, the coherent part in case the non-compensated case (dash-dot black line) for the direct signal goes down to zero, as the coherency is lost due to the navigation bit change. However, as the bit transition is detected and compensated, the coherent (dashed blue line) part goes almost as high as the total power waveform; therefore, the direct signal DOC for this example is $\sim$0.9.

The reflected case is quite different. First of all, as expected, the coherency of the

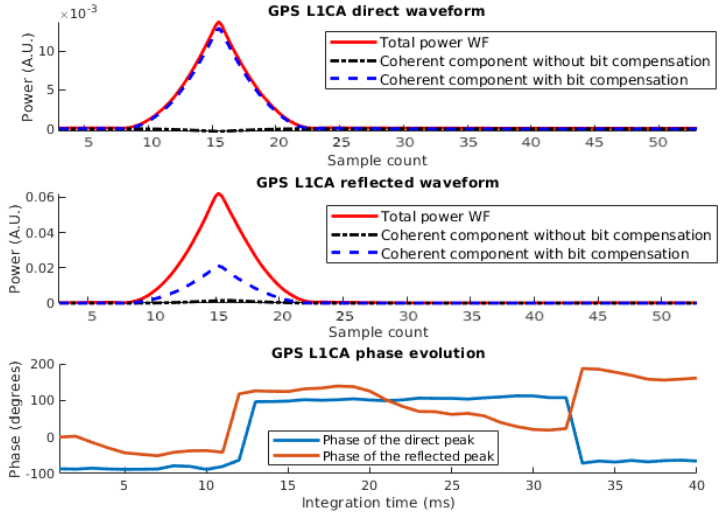

Figure 5.4: Coherency of a GPS L1 C/A direct signal (top figure) within 40 ms of integration with a two bit transitions, coherency of the same GPS signal once reflected over the sea (middle figure), and phase evolution of the peak for each integration sample (bottom figure). All figures with $f_s = 32.768$ MHz, 1 sample = 30 ns.

signal is much lower than for the direct one, but also the navigation bit compensation does not make any difference in terms of the coherency. Note that the phase evolution in the reflected peak presents the 180° jump at the 12th integration period, but after the 22nd period, it completely losses the phase and hence the coherency of the signal. Despite that, the signal presents a coherent component with a DOC ~ 0.2.

Note that in the case of reducing the integration time to 20 ms, to avoid the signal coherency degradation present at the 22nd period, the DOC of the reflected signal increases (as shown in Fig. 5.5) up to $\sim$0.8, as expected. Therefore, this increase on the DOC for 20 ms of integration that the reflection is almost coherent in this period.

5.2.5 Coherency in the presence of secondary codes

The secondary codes present in GPS L5 signal produce a similar behavior on the coherent part than the navigation bit. As the navigation information, the secondary code is a pseudorandom sequence of $+/-1$, thus multiple sign changes occur in a 1 ms integration period. As the repetition period of the secondary code for GPS L5 is 20 ms, performing the coherent integration as in GPS L1 C/A without the secondary code produces a degradation on both direct and reflected signals, as shown in Fig. 5.6, with a DOC for both direct and reflected <0.05. Note that the integration has been performed over the pilot component, as in that way we are able to remove the entropy of the navigation bit sign change.

However, performing the cross-correlation, but now including the secondary code, and preserving the integration time (40 ms) has a direct impact on the DOC. As seen in Fig.

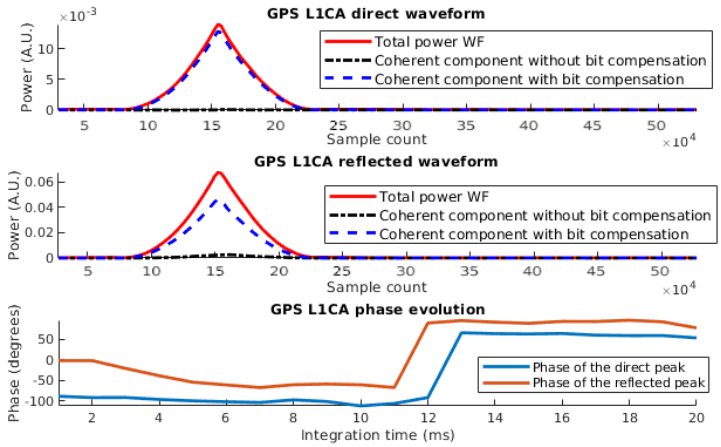

Figure 5.5: Coherency of a GPS L1 C/A direct signal (top figure) within 20 ms of integration with a bit transition in the middle, coherency of the same GPS signal once reflected over the sea (middle figure), and phase evolution of the peak for each integration sample (bottom figure). All figures with $f_s = 32.768$ MHz, 1 sample = 30 ns.

5.7, the DOC of both direct and reflected signal goes up to ~ 1, which means that, for the selected waveform, the coherency of the sea spectrum at L5 is preserved within 40 ms. Note as well the typical elongation of the trailing edge of the waveform (Fig. 5.6, central panel), and that, in the reflected signal case, two coherent peaks can be identified. In addition, the phase evolution of the L5Q signal with secondary codes included can only be represented once every 20 ms, as the cross-correlation process and waveform retrieval is taken in multiples of the code length.

The second reflection peak seen in this figure is placed seven samples away from the first peak. Converting the sample distance to meters (as in Eq. 5.8), we clearly see that this second peak is out of the first Fresnel zone (27 m for L5); therefore, it came from the glistening zone, but it presents a coherent component.

$$\Delta_m = c \cdot \frac{\Delta_{samples}}{f_s} \qquad \Delta_m = 64m \tag{5.8}$$

where c is the light speed, $f_s = 32.768$ MHz is the sampling rate, and $\Delta_{samples}$ corresponds to the peak-to-peak distance in samples.

5.2.6 Reflected signal coherency analysis

As seen in Eq. 5.8 in [54] the coherence time of a given surface for this flight is for both L1 and L5, and assuming an incidence angle of 0° and 45°.

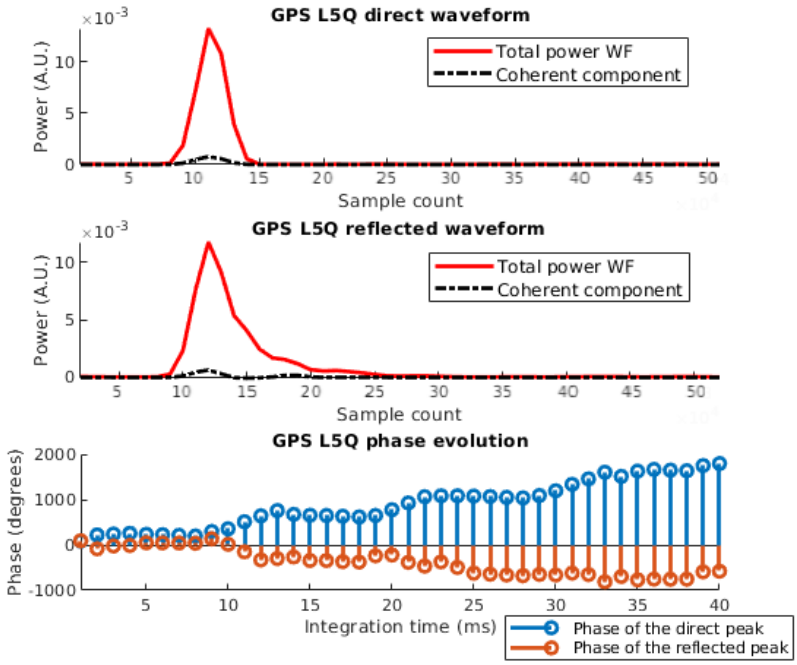

Figure 5.6: Coherency of a GPS L5Q without secondary codes direct signal (top figure) within 40 ms of integration with a two bit transitions, coherency of the same GPS signal once reflected over the sea (middle figure), and phase evolution of the peak for each integration sample (bottom figure). All figures with $f_s = 32.768$ MHz, 1 sample = 30 ns.

$$\begin{aligned} \tau_s &= \frac{\lambda}{2 \cdot v} \sqrt{\frac{h}{2 \cdot c \cdot \tau_c \cdot \cos(\theta_i)}}, \\ \tau_{s_{L1}}(\theta_{inc} = 0^\circ) &= 2\, ms, \tau_{s_{L1}}(\theta_{inc} = 45^\circ) = 2.8\, ms, \\ \tau_{s_{L5}}(\theta_{inc} = 0^\circ) &= 7.7\, ms, \tau_{s_{L5}}(\theta_{inc} = 45^\circ) = 10\, ms \end{aligned} \tag{5.9}$$

This section analyzes a set of different waveforms for GPS L1 C/A and GPS L5Q with secondary codes. Those waveforms have been selected and reproduced for a set of integration times, which are multiples (up to 10 times) of the sea coherence time. In addition, the analysis does not only cover the waveform shape, but the phase of the signal at all the integration steps, which helps to understand why the signal has a given coherency or not.

5.2.6.1 GPS L1 C/A reflected signal signatures

The GNSS reflected signal contains a portion of coherency, which is easily untangled from the incoherent one thanks to the proposed algorithm. A first example for GPS L1 C/A is provided in Fig. 5.8 showing four different integration times: 5 ms, 10 ms, 20 ms, and

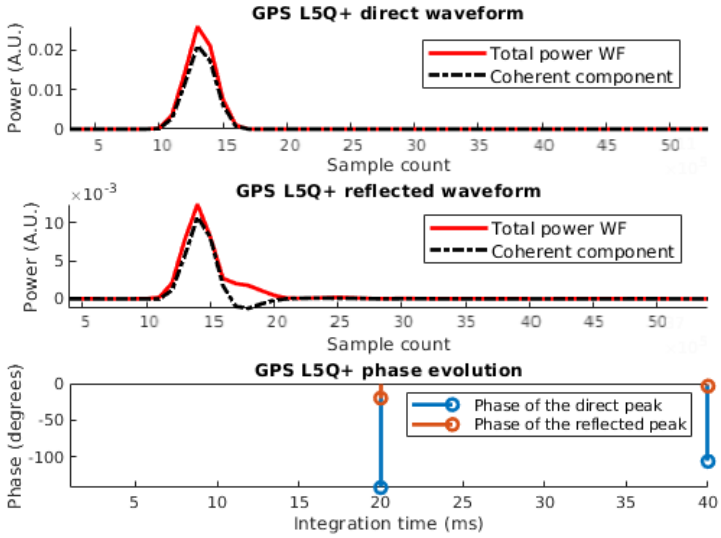

Figure 5.7: L5Q Coherency of a GPS L5Q with secondary codes direct signal (top figure) within 40 ms of integration with a two bit transitions, coherency of the same GNSS signal once reflected over the sea (middle figure), and phase evolution of the peak for each integration sample (bottom figure). All figures with $f_s = 32.768$ MHz, 1 sample = 30 ns.

40 ms. As it can be seen, the DOC of the reflected waveform decreases as the coherent integration time increases. In addition, the phase of the peak is detailed for each 1 ms cross-correlation interval. Note that, the scale of the phase evolution has been set the same for the four measurements to ease its visualization.

Note that, the phase for the direct signal is flat and does not present 180º jumps, as the navigation bit has the same sign for the 40 ms. Note also that the phase unwrapping function has been used to ease the visualization of the phase evolution.

Analyzing the DOC for the four cases, the DOC decreases as the integration time increases, which is logical due to the coherence time of the sea as shown in Eq. 5.9.

In addition, analyzing the phase variation for the four cases (and in particular the 20 and 40 ms cases), the coherency loss is coming from a change of the reflected surface, as, for instance, the reflection has disappeared from the wave crest to the wave valley. As seen, the peak phase is very smooth and follows a shape which can be identified as the wave evolution with time. This was first observed in 2010 in the GriPAU field campaign in Gran Canaria (Fig. 16 of [111]), and then verified in a controlled experiment in a water tank (Figs. 7 and 10 of [141]). This phase precision can be actually used to perform phase altimetry measurements as in [142, 143].

The second example (see Fig. 5.9) shows a *noisier* environment, where the coherency of the signal is almost lost after 10 ms of integration. As seen in the 10 ms and 20 ms examples, the phase evolution of the reflected signal is very noisy, which causes a coherence loss. However, despite the phase is not constant in this case, the coherent component can be still untangled from the incoherent one, allowing for that a better estimation of the

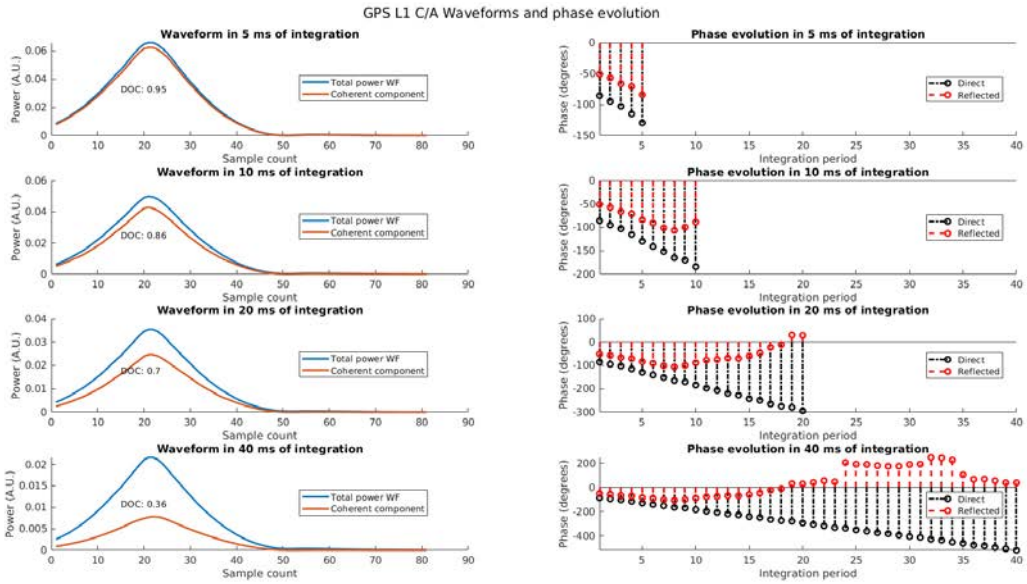

Figure 5.8: Left column: Total power waveform and coherent component for different integration times (from 5 to 40 ms). Right column: phase evolution of GPS L1 direct (black) and reflected (red) signals for the 1 ms coherently integrated waveforms used for different integration times (from 5 to 40 ms).

first Fresnel zone characteristics and the surface roughness associated to the illuminated area.

5.2.6.2 GPS L5Q reflected signal signatures

As presented in Section 5.2.5, the coherency of the L5 signal (either I or Q components) is lost if the secondary codes are not taken into account. Two examples for GPS L5Q with secondary codes are provided for five different integration time: 40, 80, 120, 160, and 200 ms.

The first example is shown in Fig. 5.10. In the 40 ms case of this figure, it is seen that the coherent component presents a positive and a negative part, as it is a real correlation and the coherent integration is not based on the absolute value operation. This negative part can be identified as an out-of-phase addition of the reflected signal paths. Despite that, the signal presents a high coherency, with a DOC ~ 0.22 for 40 ms of integration. In addition, the coherent peak due to the incoherent integration is not located in exactly the same chip delay than the incoherent one. The position of this coherent peak is also very useful for altimetry applications, as, from one side, the coherent reflection is linked only to the first Fresnel zone (i.e., better spatial resolution), and from the other side, the peak position estimation is better than in the incoherent case.

As seen in the 80, 120, 160, and 200 ms cases, increasing the integration time also increases the blurring of the total power waveform (no retracking applied [144]), also providing evidence that the peak position for the total power case is changing. Despite that, the coherent peak is not moving from its original position, as it is only identifying the

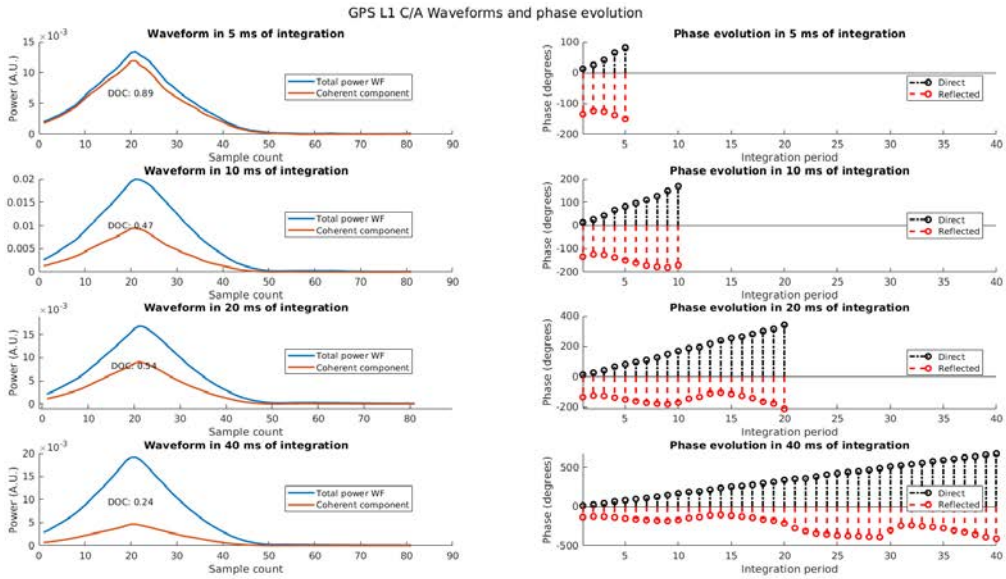

Figure 5.9: Left column: Total power waveform and coherent component for different integration times (from 5 to 40 ms). Right column: phase evolution of GPS L1 direct (black) and reflected (red) signals for the 1-ms coherently integrated waveforms used for different integration times (from 5 to 40 ms).

coherent reflection, and not all the contributions from the glistening zone. Even though the coherent component is still, its amplitude decreases as the integration time increases due to the surface changes over time. Take into account that after 200 ms, the plane has been moved $\sim$ 15 m, which is about half of the the first Fresnel zone size at L5.

In addition to the waveform analysis, the phase evolution and its difference with respect to the direct signal one gives very useful information. The difference between both is changing as the integration time increases. In this case, the direct phase is still, and the reflected phase changes within $\pm 100°$. The abrupt changes in phase are indicating two different phenomena: on one hand, the signal coherency is not 100% preserved between one integration step and the next one, which is also reflected in the DOC parameter. On the other hand, the phase evolution follows a *half-sine* slope, which may be linked to the sea surface shape at the specular point. Therefore, further processing of this phase evolution, taking into account the peak position enhancement thanks to the coherent integration, will help to enhance phase altimetry precision [54, 143].

Finally, the second example for L5Q shows a very different shape as the previous example. As seen in Fig. 5.11, the larger the integration time, the larger the change of the shape of the coherent component. First of all, the DOC for the 5 cases is very similar, on the order of $\sim$ 0.1, which means that even a small coherency is preserved even for large integration times.

The first case (40 ms of integration) shows a first negative peak on the coherent part, followed by a positive peak. Comparing it to the total power waveform, which uses the modulus operator, the presence of this negative peak tells us that the specular reflection

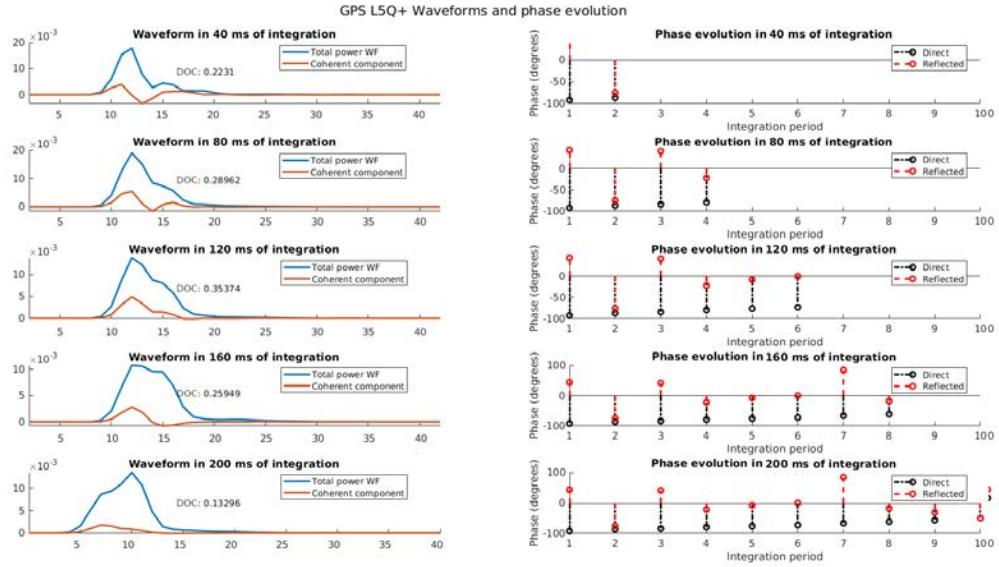

Figure 5.10: Left column: Total power waveform and coherent component for different integration times (from 5 to 40 ms). Right column: phase evolution of GPS L5Q direct (black) and reflected (red) signals for the 20 ms coherently integrated waveforms used for different integration times (from 40 to 200 ms).

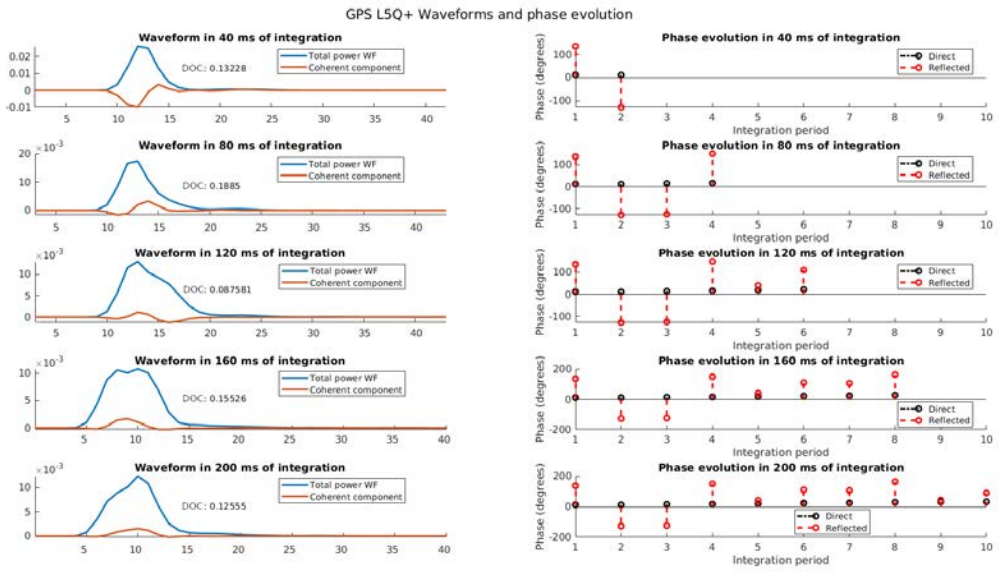

Figure 5.11: Left column: Total power waveform and coherent component for different integration times (from 5 to 40 ms). Right column: phase evolution of GPS L5Q direct (black) and reflected (red) signals for the 20 ms coherently integrated waveforms used for different integration times (from 40 to 200 ms).

(and hence the coherent one) is coming from the positive coherent component, which is two lags away from the peak estimation of the total one.

Looking at the evolution of both the coherent and total power peak positions with respect to the integration time, it is clear that as the total one gets blurred and its maximum moves within 20 samples, the coherent one is almost frozen at the same sample, and starts blurring when the integration time is too large. Looking at the phase evolution for this example, it is clear that the coherency of the signal is not high, as the phase performs $\sim 180^{o}$ jumps from one integration period to the next one, while the direct phase is the same. In this case, a *half-sine* shape can be identified for large integration times, which can be linked to the sea slope, and hence indicating that phase altimetry may be feasible and will be enhanced thanks to the coherent component peak position determination.

5.2.7 Potential applications using the GNSS-R coherent component

The previous sections have shown that the coherent component of the GPS L1 C/A and GPS L5, including secondary codes, is not negligible. This component decreases as the integration time increases, and its decreasing ratio depends on the roughness of the reflected surface, as it is linked to the surface coherence time. The application of the coherent component untangling technique opens a number of potential applications from its use, which are highlighted below.

5.2.7.1 Scatterometry using the coherent component

As seen from the GPS L1 C/A case, the coherent component is very strong for short integration times. In addition, knowing that the coherent component reflection comes from the specular point, scatterometry measurements are much easier to compute and also with a better spatial resolution.

From now, the scattering model used to compute scatterometry measurements assumes a normalized bi-static scattering cross section (σ_0) over the full glistening zone of the reflected surface [51]. In this case, the reflected area is very large, therefore having a poor spatial resolution. However, as the coherent component contains the reflection from the specular point, and hence the first Fresnel zone, the spatial resolution of the reflected signal is improved. At this point, scatterometry measurements are as easy to compute as the power ratio between the direct and the reflected signal coherent components, as in Eq. 5.10:

$$\Gamma = \frac{P_{ref}}{P_{dir}} = \left(\frac{R_{T-SP} + R_{SP-R}}{R_{T-R}} \right)^2 \cdot \frac{G_{zenith}(\theta_{dir}, \phi_{dir})}{G_{nadir}(\theta_{ref}, \phi_{ref})} \cdot \frac{G_T(\theta_1, \phi_1)}{G_T(\theta_2, \phi_2)}, \tag{5.10}$$

where R_{T-SP}, R_{SP-R}, and R_{T-R} are the distances from the transmitter to the specular reflection point, from the specular reflection point to the receiver, and from the transmitter to the receiver, respectively; G_{zenith} and G_{nadir} are the gain of the receiver antennas; and G_T is the gain of the transmitter antenna in the direction of the specular point and the receiver position. Note that the G_T term can be neglected for receivers and specular

points that are very close (i.e., the specular point is almost at nadir), or for low altitude receivers (i.e., a plane flying at 1500 meters height). In addition, the range correction term is $\simeq 1$ and can be neglected for low altitude platforms, but it can be a fraction of a dB for LEO satellites.

5.2.7.2 Precise altimetry from precise peak position estimation in L5Q+ waveforms

From the examples provided in Section 5.2.6.2, it is clear that the coherent part of the GNSS L5Q signal with secondary codes provides additional information of the peak position, which can be useful to estimate the lag corresponding to the maximum position of the waveform. The better the estimation of this peak, the better the altimetry resolution. The example shown in Fig. 5.12 is a zoom of a L5Q+ reflected waveform. Both total power and coherent parts of the reflected signal have been interpolated by 8 (i.e., $f_s = 262.144$ MHz) using the optimum FFT interpolation method. In addition, the derivative of the total power part is calculated. Note that all three signals have been normalized with respect to their maxima in order to ease its visualization.

For the four cases, 40, 60, 80, and 100 ms of integration time, the coherent component peak position is found in five samples for the 40 ms case, and seven samples for the next three cases before the peak of the total power averaged.

In addition, the peak of the coherent component is placed between 9 and 13 samples after the maximum of the derivative of the total power waveform, which means that the actual specular point (in terms of lag delay) is placed between the point of maximum slope of the total power waveform and the actual maximum of the waveform. This behavior was studied in [145], which for an ideal conditions of a rough surface, and a theoretically infinite incoherent integration time, the delay corresponding to the specular point was placed right on the maximum of the derivative of the total power waveform. In the example shown in this study, the delay corresponding to the specular point is identified as the coherent component peak.

A proper estimation of the specular reflection point gives an improved accuracy of the altimetry measurement, as seven samples of difference in the estimation of this peak leads to an error up to 3 m (i.e., for an incidence angle of 45°, from Eq. 34 in [17][2]).

5.2.7.3 Secondary peaks in L5Q+ waveforms

As seen in Fig. 5.12, apart from the waveform peak, there are several secondary peaks, mainly in the 40 ms of integration case, whose second reflection is identified in both the coherent component and the total power processed reflected waveforms. The 60, 80, and 100 ms cases present a secondary peak in the coherent component, but not in the total one. Despite the incoherent integration has blurred up the waveform for relative large integration times, the coherent component presents the same *secondary peak*, indicating that the incoherent integration is preventing other applications of the GNSS-R. Note that the secondary peaks that are always positive in the total power waveform, are negative in the coherent one, but still it represents a coherent reflection with negative sign (i.e., 180º rotation with respect to the specular peak).

[2]Eq. 34 in [17] is the Flat-Earth Approximation Altimetric Inversion

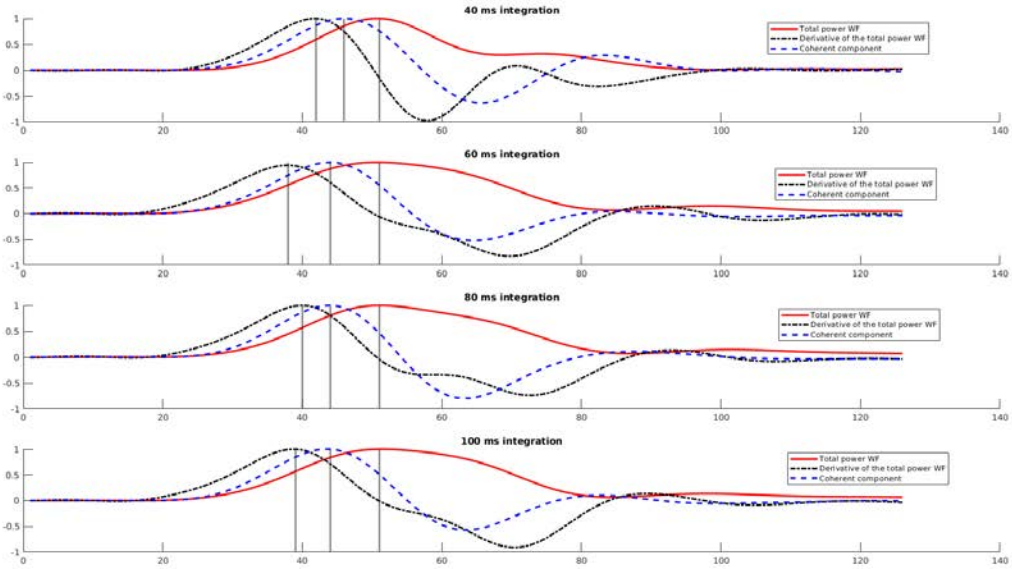

Figure 5.12: Peak position estimation depending on the integration time (40 to 100 ms) from the coherent component at L5Q with secondary codes, $f_s = 262.144$ MHz, 1 sample = 3.81 ns. Note all functions are normalized for the sake of clarity.

5.3 Swell Estimation using Airborne GNSS-R at L5

Thanks to the high spatial resolution of the L5 signal, several reflections coming from nearby wave crests can be collected within a single waveform. This section assess the feasibility of L5 waveforms to estimate wind and swell waves using GNSS-R.

5.3.1 Swell and wind-driven wavelength background

Wind-driven and swell period or wavelengths have both been measured using other remote sensing techniques such as High Frequency (HF) radar [146], where the HF signal is back Bragg scattered over multiple swell crests, and the signal retrieved contains a modulation in frequency based on the scattered signal. Swell retrieval has been also conducted using microwaves signals, as the approach using a Doppler radar at S-Band [147], where both wind sea and swell components can be measured through spectral analysis. Moreover, Synthetic Aperture Radar (SAR) instruments have also retrieved swell parameters from space based on spectral estimation, as in Sentinel-1 [148]. As seen, most of those measurements are based on a back Bragg scattering mechanism in consecutive wave crests (Chapter 10 of [149]).

The same physical principle is presented in this study, but using GNSS-R signals in a forward scattering configuration. As stated in [150], swell components can only be seen using large bandwidth signals with narrow auto-correlation functions. Examples are given for resolutions up to 30 m. However, this is not the case for current GNSS-R instruments, which are nearly all designed to work with GPS L1 C/A signals, with 300 m spatial resolution (width of the auto-correlation function). However, the use of a higher

Table 5.1: Track, beam, PRN, and mean incidence angle of the measurement.

Track ID	Beam ID	Constellation and PRN	Incidence Angle (º)
1	1	GPS #1	40
1	2	GPS #32	52
2	1	Galileo #3	20
2	2	GPS #3	42

spatial resolution signal, such as the GNSS L5 (with a spatial resolution of 30 m), opens the possibility to measure the swell spectra, as the spatial resolution provided by these signals is comparable to the swell wavelength, as will be covered in the next section.

5.3.2 Data set description and validation data

The data set used to perform this analysis are a subset of the Bass Strait flight presented in Section 5.1. Figures 5.13 and 5.14 show the selected fragments of the flight used to perform this study. Each track has two beams directly pointing to a GNSS satellite reflection, as detailed in Table 5.1, which summarizes the metadata information of the reflection, including the satellite PRN, constellation, and the reflection incidence angle to each of the tracks shown in Figure 5.14. The incidence angle is defined as the angle between transmitter-to-specular point ray and the zenith vector perpendicular to the reflection surface, which is assumed flat for the sake of simplicity.

To perform this study, the outputs from the waveform table from the MIR processor are used. In order to ease the data processing scheme, a single 300 ms packet is used to retrieve a single waveform, but using a shorter incoherent integration time of 40 ms is used to avoid blurring of the waveform due to the plane movement. Taking into account the plane speed (74 m/s), and the incoherent integration time (40 ms), the blurring corresponds to an integration over ∼3 m. In addition, the generation rate of the waveform (i.e. the final observable) is at 3.33 Hz, or one every 300 ms, hence each waveform is separated ∼22 m.

In order to understand the origin of all the secondary peaks observed in the waveforms (see Section 5.3.3), the sea state conditions during the flight are studied. As there is a lack of in situ buoy information in the area, the ICON model [151] wind wave period [s], swell wave period [s], and wind speed over the sea at 10 m altitude (U_{10}) [m/s] are shown in Fig. 5.13. The waves shown in Figure 5.13a have a period of $T_{wind} \approx 5$ s, and they are moving with a look angle with respect to the plane trajectory of ∼50º. The swell waves (Figure 5.13b) have a period of $T_{swell} \approx 9$ s, and the look angle with respect to the plane trajectory is ∼120º. Both wind-driven and swell wave period are related to the wave speed, and therefore to the waves wavelength (Λ_{waves}) [152] (i.e., distance between the crests of the wave) by means of Eq. 5.11.

$$\begin{aligned} C_{waves} &= 1.56 \cdot T_{waves}, \\ \Lambda_{waves} &= C_{waves} \cdot T_{waves}, \end{aligned} \tag{5.11}$$

where C_{waves} is the sea wave celerity (or speed (m/s)), and T_{waves} is either the swell period T_{swell} or the wind-driven period T_{wind} as defined in the previous section. In deep

water conditions, the relationship between them is the above closed formula.

Note that the nomenclature used in this study is X_{waves} (X stands for any parameter as C, T, or Λ) for any measurement that is not directly related to either wind-driven or swell waves, and X_{wind} or X_{swell} for any measurement directly related to the wind or the swell respectively, retrieved from the ICON model.

In the case under study, the wavelengths of the wind and swell waves are between 39 m and 126 m. Note that, the aggregation of the different waves may cause a different set of wavelengths or periods right with a minimum wavelength of 39 m and a maximum wavelength of 126 m. The following sections show a complete analysis of this second peak and its relations to the sea state conditions. As stated in [153,154], wind-driven and swell waves are combined forming different waves with different periods and heights. The wind and swell components (or even multiple swell components) can be separated by means of spectral analysis [155].

5.3.3 Sea wavelength retrieval

As in most GNSS scenarios, and due to the sea surface roughness, the combination of both swell waves and wind-driven waves cause multiple reflections, which are then captured by the down-looking antenna of the GNSS-R instrument. Despite that, and as covered in Section 5.2, the reflection over the sea surface presents a notable coherent component, which depends on the geometry of the reflection and the wind speed. Most of the waveforms retrieved in this Section present a significant coherent component, the same data set used in Section 5.2 is now used to analyze the presence of secondary peaks in the retrieved waveforms, which turns to be linked to two strong reflections over nearby wave crests.

The reflection scenario is illustrated in Fig. 5.15. Note that, the size of the first Fresnel zone has been already shown in the previous section, but reformulated here for the readers' convenience. At $\theta_{inc} = 45^{o}$, $l_{Fr_{\angle_{45}}} = 33$ m, whereas for an almost-nadir reflection as Beam 1 of Track 2, $l_{Fr_{\angle_{20}}} = 21$ m.

In this case, second and third reflections occurring in consecutive wave crests in the first Fresnel zone produce different signal wave fronts that are added constructively or destructively in the receiver antenna. However, thanks to the large bandwidth, and hence the very narrow auto-correlation [157] function of the L5/E5a GNSS signal (i.e., 30 m in space), reflections from nearby crests with a distance between them larger than 30 m can produce secondary peaks in the retrieved waveform.

As an example, two wavefronts are reflected over two successive wave crests, and hence two different specular points, resulting in the addition of the two signals in the receiver antenna, which is detected as a second peak in the processed waveform, as detailed in Fig. 5.16. Sometimes even a third peak appears.

Due to the variability and the surface roughness of the ocean, the distance between two crests varies. In this case, where wind wave and swell wave components are both strong and also with different directions of propagation, the peak-to-peak distance is not preserved from one realization to the next one.

As explained in [158], wind-driven or swell wave period is not a fixed magnitude, but the average of the swell waves component period for the swell waves, and the average

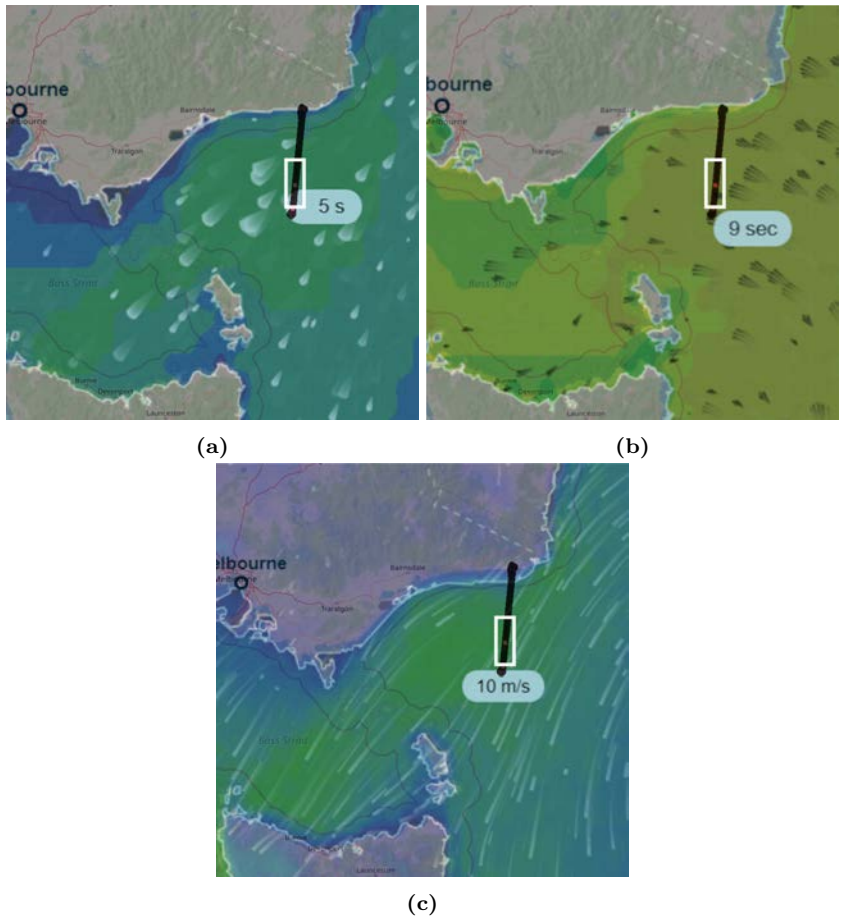

Figure 5.13: Position of the plane superposed to (**a**) wind-driven wave period, (**b**) swell wave period, and (**c**) wind speed over sea of the data used for the secondary specular reflection analysis. The plane trajectories framed in white box is zoomed in Fig. 5.14. The wind-driven period, the swell period, and the wind speed are provided below the white box [156]

of the wind-driven period for the wind-driven waves. As an example, a swell period of 9–10 s generates a larger span of waves, which have a period between them from 8 s to 11 s. Therefore, a relative large data set analysis is required to correctly retrieve the swell waves period or wind-driven waves period.

Finally, the peak-to-peak distance does not reproduce only the crest-to-crest between two consecutive waves, but also a modulation associated to the distance between the two waves where the reflection has occurred.

5.3.3.1 Waveform simulation

As opposed to reflections in L1 C/A, where the spatial resolution is mostly limited by the chip length (i.e., 300 m), the new GPS L5 or Galileo E5a signals have 10 times higher spatial resolution, as the auto-correlation function is 10 times narrower

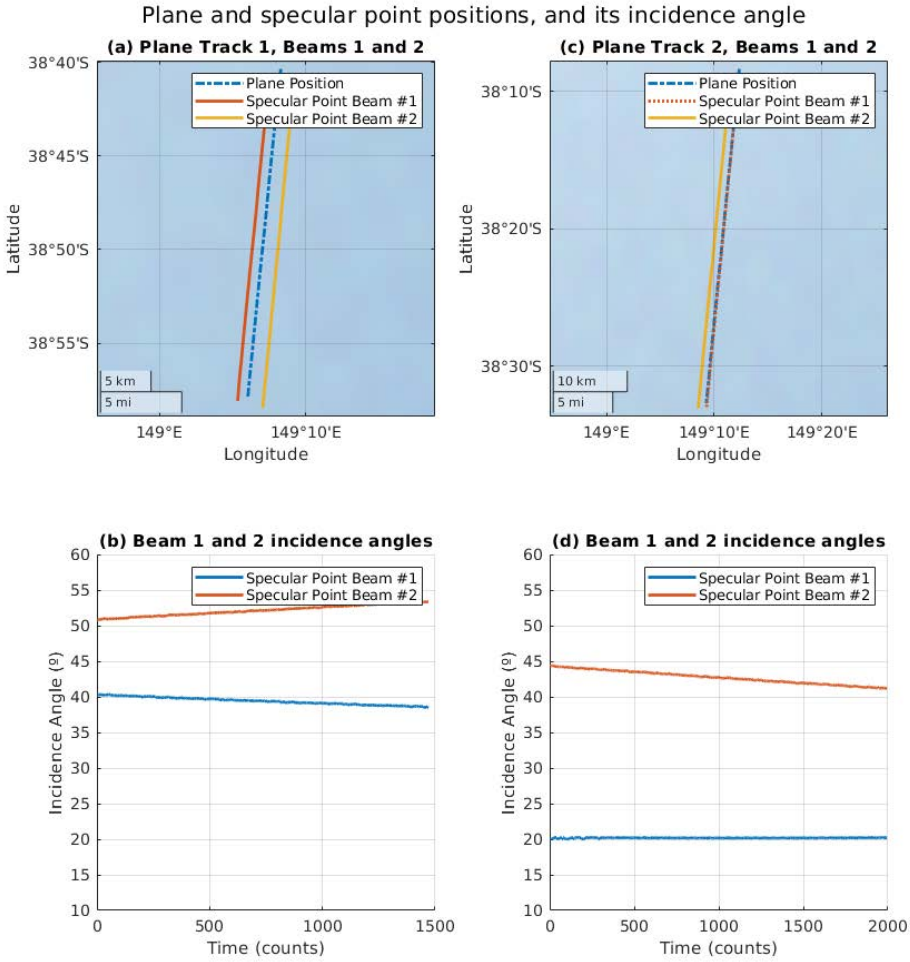

Figure 5.14: Top frame—plane position and specular point position of Track 1 (**a**) and Track 2 (**c**). Bottom frame—incidence angle to the specular point of Track 1 (**b**) and Track 2 (**d**). The plane positions correspond to the white frame box in Fig. 5.13. Note that, the plane position and specular point of Beam 1 of Track 2 are superposed due to the very low incidence angle (i.e., almost nadir).

(i.e., 30 m in space), allowing de reception of multiple specular points with a distance larger than 30 m. In this case, any reflection from any point separated by more than 30 m produces a secondary peak on the retrieved waveform instead of a blurring on the retrieved wavelength.

This section shows different simulation scenarios of the retrieved waveforms modulated by a forward scattering occurring at the crests of the waves, belonging to different Fresnel

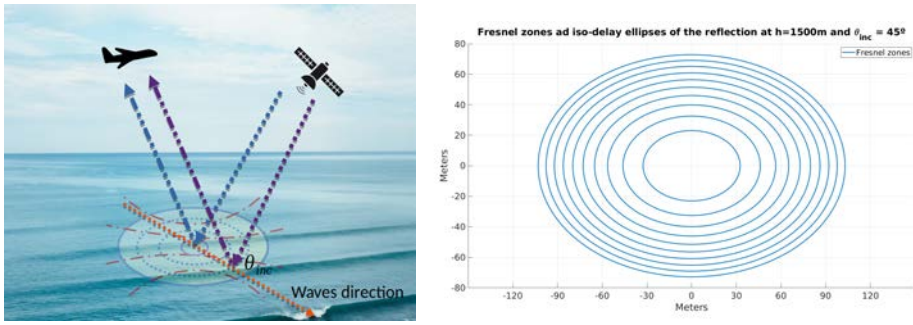

(a) **(b)**

Figure 5.15: (**a**) An example of the reflection scenario, where two wavefronts are reflected over two consecutive wave crests, where θ_{inc} is the incidence angle of the reflected signal. (**b**) The first 10 Fresnel zones associated to the reflection scenario described in (a), computed at $\theta_{inc} = 45^{o}$. Note that each Fresnel zone corresponds to a 180^{o} phase rotation.

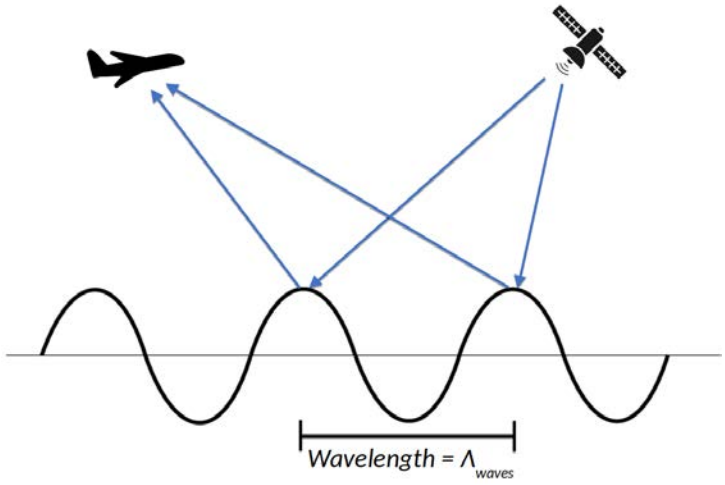

Figure 5.16: Forward scattering over two wave crests.

zones (Fig. 5.15). To do so, a given PRN of a GPS signal at L5 ($\tau_{coh} = \tau_{inc} = 1ms$) is sampled at 32.768 MHz (to have better granularity and mimic the MIR sampling ratio) which is then delayed and added as in Eq. 5.12. Note that, due to the sampling used, the distance from the peak to the zero of the auto-correlation (i.e., half the width of the whole auto-correlation function) is ∼3.2 samples.

$$S'[k] = \sum_{i=0}^{N-1} \Phi[i] \cdot S[k-i] \tag{5.12}$$

where $S'[k]$ is the resulting PRN sequence at the kth sample, sampled at 32.768 MHz, Φ is the amplitude coefficient applied to each sample of the clean PRN sequence, S, and N

is the length of the Φ vector, which represents the reflection scenario, where for this example is set to 10, causing a delay up to three L5 chips.

In order to illustrate this concept, three simulated waveforms are computed with different c coefficients. In the first example, using Φ = [1, 0.5, 0.5, 0.4, 0.4, 0.3, 0.3, 0.3, 0.2, 0.1] a reflection scenario is computed with lots of small contributions from all the Fresnel zones near the specular point. This produces a waveform as in Fig. 5.17a, where the power decreases, and no secondary peaks are found. However, using Φ = [0.1, 1.0, 0.1, 0.1, 0.1, 0.1, 0.1, 0.1, 1.0, 0.1] produces two identical peaks which are easily distinguished. Note that, the separation between the peaks in samples is seven samples. In order to convert the sample distance into a tangible magnitude, Eq. 5.13 is used.

$$\Delta_m = \Delta_{samples} \cdot \frac{c}{f_s}, \tag{5.13}$$

where c is the speed of light, $\sim 3 \cdot 10^8$ [m/s], and f_s is the receiver sampling rate, $32.768 \cdot 10^6$ [S/s].

Applying it to Fig. 5.17b, the distance between the two specular reflections (identified as $\Phi[1]$ and $\Phi[8]$ in previous example), a distance of 64 meters is retrieved.

However, reflections are not always as perfect as in Fig. 5.17b. A third simulation (Fig. 5.17c) is generated using a more realistic case, with Φ = [0.1, 0.1, 0.4, 1.0, 0.6, 0.1, 0.1, 0.2, 0.8, 0.4, 0.1, 0.1, 0.1], trying to reproduce two crests separated by five samples or 45 meters. Note that, the amplitudes of the neighbor areas have been also included, but they do not affect the high amplitude specular reflection contribution.

5.3.3.2 Evolution of complex waveforms in a single beam

The previous section has shown three different simulated waveforms synthetically generated to illustrate the concept of a second specular reflection in a consecutive wave crest around the second to sixth Fresnel zones.

In this section, three consecutive measured waveforms (see Fig. 5.18) have been selected to illustrate these effects. The separation in time between each waveform is 600 ms, and they have been selected because of their similitude to the ones simulated in the previous section. Note that, the three selected waveforms are from Track 1 Beam 1, and both the amplitude, and the phase evolution of the waveform are shown.

The first waveform (Fig. 5.18a) shows an example similar to the one in Fig. 5.17a, where very small contributions from all nearby Fresnel zones causes a blurring of the tail of the waveform.

The main peak is around sample count 17, with a phase approximately constant around $+100^{\text{o}}$. Furthermore, there is a second small peak (in sample 25) around eight samples (i.e., 73 m in space) after the main one (in sample 17). The distance between the peaks indicates that small reflections are coming from the sixth to eighth Fresnel zones.

The second waveform (Fig. 5.18b) shows a example similar to the one in Fig. 5.17b, but with the reflection occurring in a closer Fresnel zone. In this case, the distance between these two peaks is three samples or $\sim$30 m, which corresponds to a reflection in the second Fresnel zone. As compared to the first waveform, the reflections occurred within the first Fresnel zone causing a blurring and a widening of the L5 auto-correlation function are now split in two different peaks.

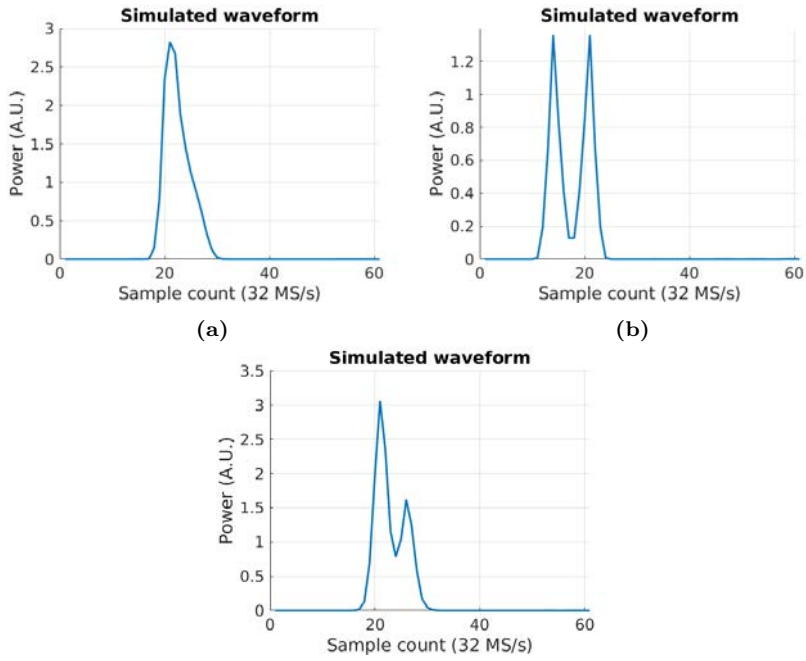

Figure 5.17: Three simulated waveforms different contributions from nearby Fresnel zones, producing secondary peaks driven by strong specular and coherent reflections over two hypothetical consecutive wave crest. (**a**) Simulated waveform with small contributions from all the nearby Fresnel zones, (**b**) simulated waveform with two ideal peak reflections separated by seven samples, and (**c**) simulated waveform with realistic contributions from a secondary strong reflection separated by five samples.

As seen, the first peak (in sample 17) has a phase of $\sim -110^{o}$, and the second peak (in sample 20) has a phase of $\sim 110^{o}$ (i.e., close to the phase of the peak in Fig. 5.18b), with a relative phase difference $\sim 220^{o}$, corresponding to reflection in the second Fresnel zone, as both are separated more than 180^{o}. Note that, there is a strong phase jump between the two peaks, indicating that both reflections are coherent (i.e., the phase information is preserved in both cases). As in the previous case, this third peak (in sample count 26) has an approximately constant phase around -50^{o}. In addition and similar to the first waveform, a third small peak is also present nine samples (i.e., 82 m in space) away from the very first one. In this case, the reflection is taking place between the eight and the tenth Fresnel zones.

Finally, the third waveform (Fig. 5.18c) shows a similar shape as the simulation in Fig. 5.17c, with a relative high second peak (in sample 22) in the reflected waveform which in this case is five samples from the main one (in sample 17). In this last case, the phase evolution is approximately constant in both peaks with a strong jump in the transition between them (i.e., very small incoherent reflection from other Fresnel zones). Note that in this case the relative phase difference is $\sim 50^{o}$, but as the delay in time is $\sim$45 m, the reflection takes place further away than the second Fresnel zone, the phase

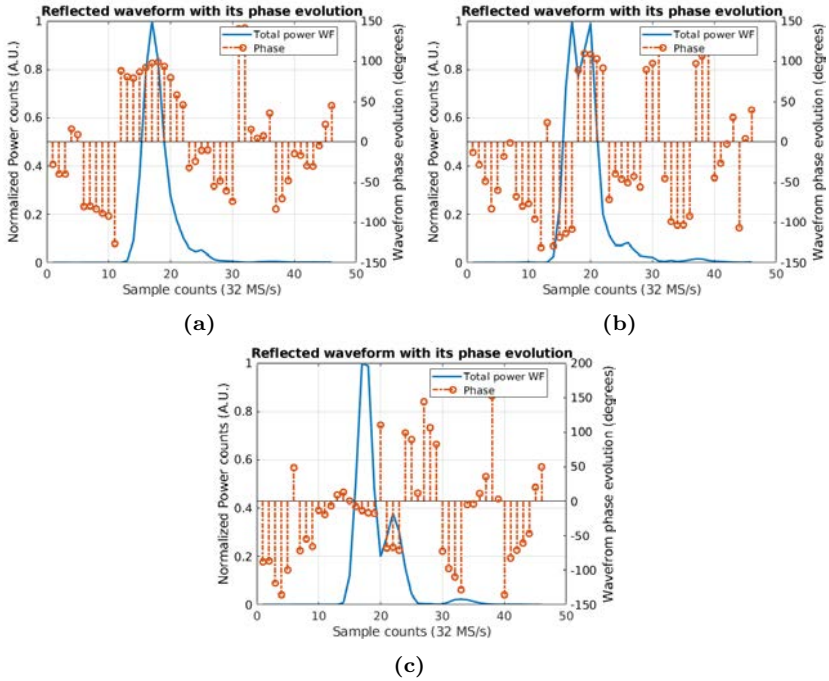

Figure 5.18: Three sample waveforms containing different contributions from different Fresnel zones, producing secondary peaks with different shapes. (**a**) Retrieved waveform with small contributions from all the nearby Fresnel zones, (**b**) retrieved waveform with two big peaks of the same amplitude separated three samples one from other, and (**c**) retrieved waveform with two peaks with different amplitudes and separated by five samples.

with respect to the first peak has advanced at least 180º. Therefore, the absolute phase shift between the two peaks is ∼315º.

5.3.3.3 First waveform analysis: determination of the crest-to-crest distance from peak-to-peak distance

The last section showed three examples of three different waveforms retrieved from Track 1 Beam 1, where the location of the second peak varies with time. Furthermore, it has been shown that this second reflection comes from a different Fresnel zone, and in some cases present a coherent component (i.e., a single specular reflection over a wave crest). Figure 5.19 illustrates the example of different consecutive peaks present in the GNSS waveforms originated by the forward scattering on two consecutive wave crests, but now in the two beams for the two tracks of the flight.

Note that, the two waveforms for each track (i.e., beams 1 and 2 for Track 1 and beams 1 and 2 for Track 2) are taken at the same moment. As seen, the four waveforms present, at least, one second reflection.

Analyzing each of the tracks, Fig. 5.19a,c present a single second reflection at six samples from the specular one. For the beam 2 case, Fig. 5.19b presents a very large second reflection at six samples from the specular one. In addition, two small reflections

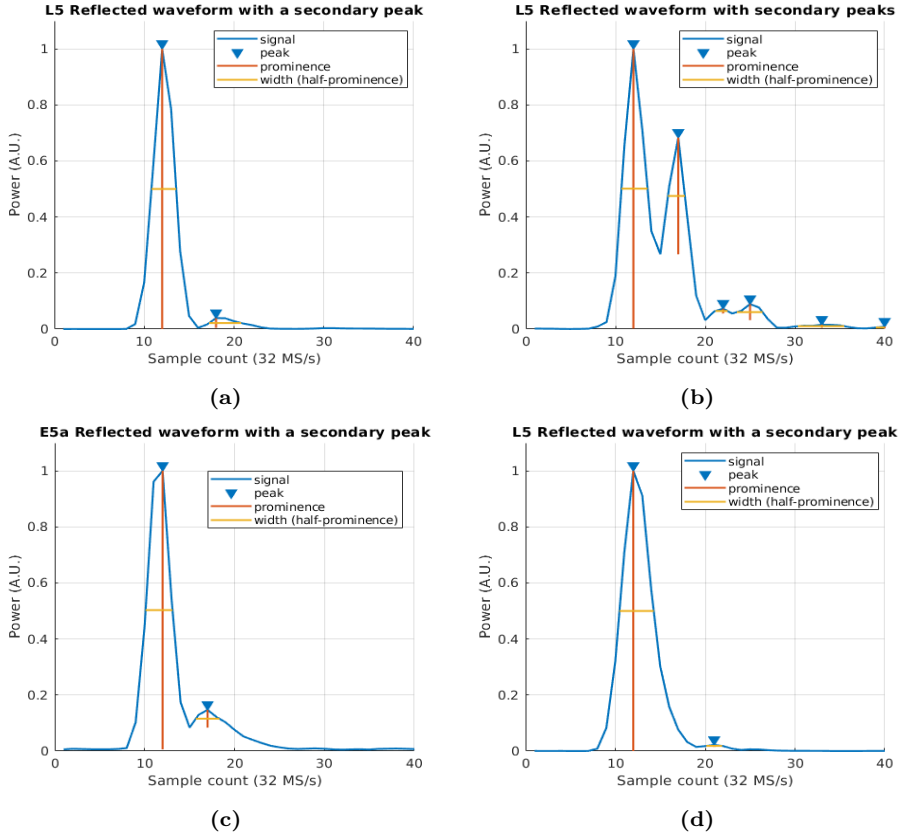

Figure 5.19: Reflected waveform for (a) Track 1, Beam 1; (b) Track 1, Beam 2; (c) Track 2, Beam 1; and (d) Track 2, Beam 2 of GPS L5 and Galileo E5a signals over the sea surface with an incoherent integration time of 40 ms.

are taking place 10 and 13 samples from the specular one. Finally, Fig. 5.19d shows a very low secondary reflection point at nine samples from the main peak.

Applying Eq. 5.13 to the waveform shown in Fig. 5.19, the distance between the peaks in meters are: 54.9 m for both Fig. 5.19a and 5.19c, 54.9 m for the first peak of 5.19b, and 91.5 m for the third peak. Finally for Fig. 5.19d, the distance between the peaks is 82.4 m.

Comparing the retrieved waveforms to the simulated waveforms from Fig. 5.17, it is possible to identify a clear similitude between them, where the second peak (i.e., the one in Fig. 5.19b) reminds the simulated in Fig. 5.17c, due to a specular reflection over a wave crest.

In order to improve the estimations of the separation between peaks in the waveform, since raw data was acquired satisfying the Nyquist criteria at baseband for L5/E5a signals (i.e., $f_s > 10$ MHz), therefore the signal can be re-sampled without loss of information. Therefore, waveforms are re-sampled using the Fourier interpolation method (i.e., by inverse FFT of the zero-padded FFT of the waveform), and the local maxima

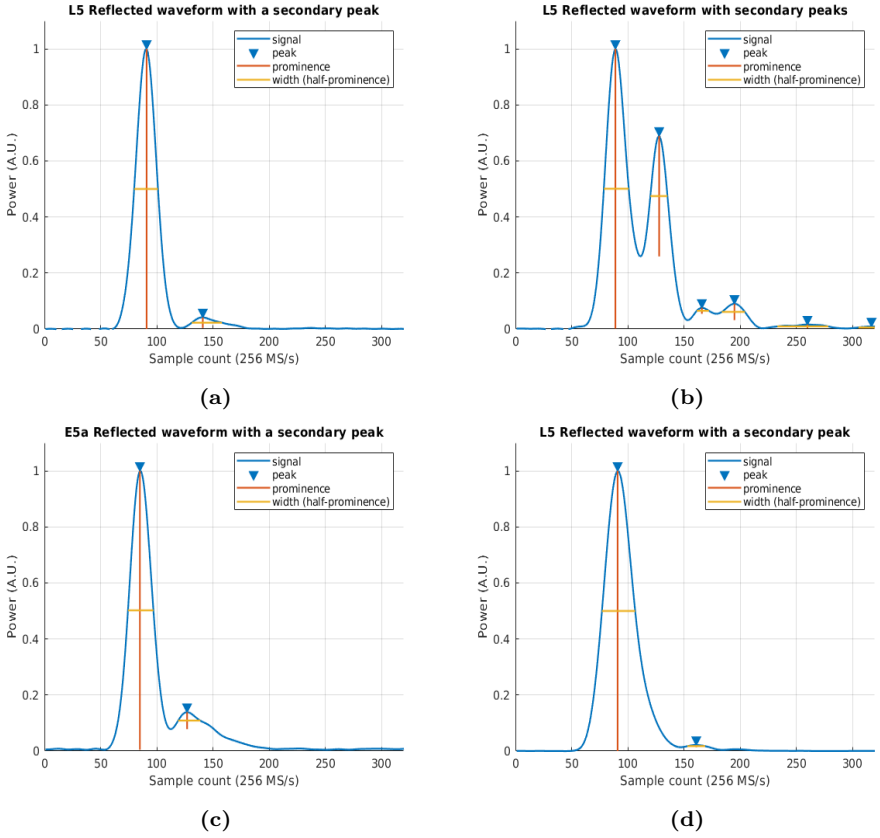

Figure 5.20: Reflected waveforms for (a) Track 1, Beam 1; (b) Track 1, Beam 2; (c) Track 2, Beam 1; and (d) Track 2, Beam 2 from Fig. 5.19 now sampled at 256 MHz. Note that, thanks to the re-sampling the determination of the peak position is enhanced.

of the interpolated waveform is located. The first two maxima of the waveform are the ones used to retrieve the distance between two consecutive wave crests. The difference in samples between the two peaks position is then converted into meters following the same approach as in the previous section, but with a sampling rate f_s scaled by the interpolation rate K.

The selection of this parameter is a trade-off between computational requirements and accuracy when selecting the final position of the multiple peaks. In order to efficiently apply the Fourier interpolation using the Fast Fourier Transform, the signal shall be a multiple of 2, and hence the interpolation rate K, shall be a multiple of 2 as well. In addition, the larger the K parameter is, the lower is the error determination of the peak position of the reflected waveform. For this case an interpolation rate of $K = 2$ has a peak position uncertainty of 4.5 meters, and a $K = 8$ has a peak position uncertainty of $\sim$1 m.

In this case, an interpolation rate of $K = 8$ has been selected (i.e., now $f_s = 256$ MHz). Furthermore, Fig. 5.20 shows the re-sampled version of the waveforms in Fig. 5.19 following the Fourier interpolation method.

Table 5.2: Track, beam, crest-to-crest estimated distance using the original waveform, and the crest-to-crest distance after re-sampling the original waveform using the FFT interpolation.

Track ID	Beam ID	Original Crest-to-Crest Distance [m]	Re-Sampled Crest-to-Crest Distance [m]
1	1	54.5	57.2
1	2	54.5	44.6
2	1	54.5	48.0
2	2	82.4	80.1

The re-sampled versions of the waveforms show a better spatial resolution when estimating the peak-to-peak distance. In this case the distance in samples is: 50, 39, 42, and 70 respectively form (a) to (d). Moreover, the third peak of Fig. 5.20b is located at 77 samples from the specular one.

Applying Eq. 5.13 to the above sample distances, the retrieved crest-to-crest distance (Λ_{waves}) in meters is: 57.2, 44.6, 48, and 80.1 m respectively for (a) to (d), and 88.1 m for the third peak of (b). Table 5.2 compares the values prior to the re-sampling with the re-sampled values. Note that, the estimation of both the first peak position is enhanced thanks to the FFT interpolation [159]. In addition, the estimation of the position of the second peaks is also enhanced. A proper estimation of the position of both peaks is crucial to better determine the distance between the two reflections (i.e., the two wave crests). Note the difference in Beam 2 of Track 1 and Beam 1 of Track 2, where the first approach does not show the proper crest-to-crest distance, introducing an error of almost 10 m in the measurement.

This section has covered the simulation and its comparison with real data of different scenarios where different specular reflections are generating second and even third peaks on the reflected waveform. The study on the phase evolution in this secondary peaks shows that the second reflection is coherent, and hence is coming from a different specular point, as was detailed in Fig. 5.16. Finally, the use of FFT interpolation enhances the determination of the peak-to-peak distance, showing a better granularity when determining this magnitude.

5.3.4 Results applied to the entire data set

The study of a larger data set is required to validate the relationship between sea waves wavelength Λ_{waves} or wave period T_{waves} to the distance between the peaks in the waveforms. Tracks identified in Table 5.1 of Section 5.3.2 are composed by 1470 waveforms, and 1994 waveforms respectively, generated once per 30 ms (i.e., 3.33 Hz), which corresponds to ∼8 min of data for each of the two beams for the first track, and 11 minutes of data for the second track. In order to analyze the data set, three different approaches are considered:

- Statistical analysis: statistics of the retrieved crest-to-crest distance and presence or not of third peaks.
- Time-series analysis: analysis in the time domain of the retrieved crest-to-crest distance.

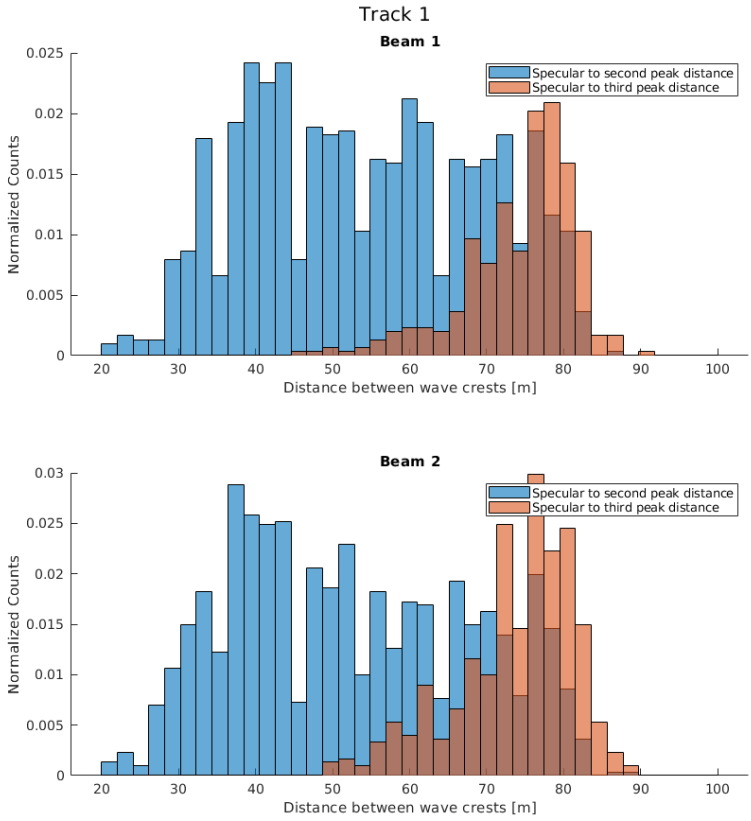

Figure 5.21: Histogram of the peak-to-peak distances for Track 1. Top figure corresponds to Beam 1 (GPS L5) and bottom figure to Beam 2 (GPS L5).

- Spectral analysis: analysis in the frequency domain of the time-series data.

5.3.4.1 Statistical analysis

Reviewing the histogram of all the 1470 measurements for Track 1 (see Fig. 5.21), most of the results are condensed between 30 m (the wind-driven wavelength from the model is 39 m) and 80 m (the swell wavelength from the model is 126 m).

In addition, the distance to a third peak (if is exists) is condensed just at the end of the histogram, at the end of the histogram of the distance to the second peak. As seen, the measurements are condensed mostly between 40 and 90 m for both beams.

Both beams are following similar statistics for the second peak distance, with an average value of 54.3 m for Beam 1, and an average value of 52.6 m for Beam 2. The third peak has an average value of 74.5 m for Beam 1, and 73.5 m for Beam 2. Note that, the average of the measurements is a mixture of all possible wave crests distance

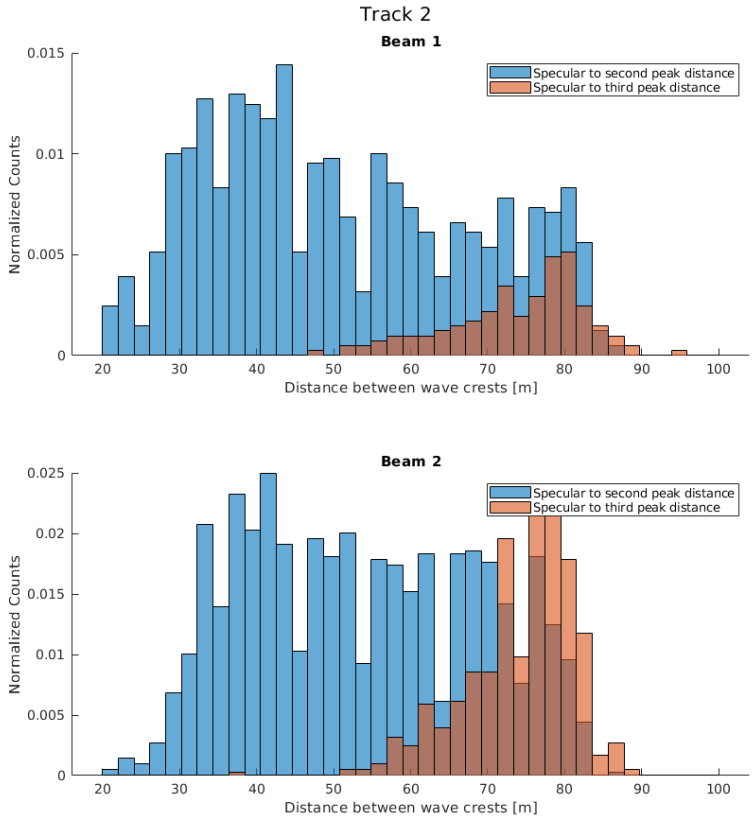

Figure 5.22: Histogram of the peak-to-peak distances for Track 2. Top figure corresponds to Beam 1 (Galileo E5a) and bottom figure to Beam 2 (GPS L5).

contributions. Note that, the least wave crest distance is $\sim$ 30 m, which coincides with the spatial resolution due to the chip bandwidth of the L5/E5a signal, 30 m.

In addition, the same histogram of the second-track is shown in Fig. 5.22. The first beam corresponds to a Galileo E5a signal, which has an incidence angle of $\sim 20^{\text{o}}$. The mean peak-to-peak distance in this case is 50.8 m. The second beam has an incidence angle of 42^{o}, with an average value of 53.5 m.

In case of this first beam, as the incidence angle is lower, the semi-radius of the first Fresnel zone is smaller (from 33 m with $\theta_{inc} = 45^{\text{o}}$ to 21 m with $\theta_{inc} = 20^{\text{o}}$). As the overall sizes of the Fresnel zones are smaller, the area where the possible strong reflection occurs over a wave crest is also smaller, hence some waves with a large distance between them cannot be captured.

Note that, in this case, the third peak position for Beam 1 is poorly determined because of the small incidence angle, and the size of the Fresnel zones for that case. As seen in the histogram, the amount of third peak reflections in Beam 1 with respect

to Beam 2 is in the order of 0.25.

As seen in the two tracks, the histogram analysis shows that multiple reflections are present in most of the waveforms, with an average value ∼50 m for the distance between the first two peaks. From this first analysis, the wind-driven waves wavelength can be estimated (i.e., the model set this distance to 40 m), and from it the wind-driven wave period.

5.3.4.2 Time-series analysis

The statistical analysis through the histogram visualization shows that the crest-to-crest distances are in the same range than in the ICON model (Section 5.3.2), the analysis of the time evolution of the peak-to-peak distances shows a wavy behavior.

In order to reduce the noise of the measurement, four different averaging windows have been applied to the peak-to-peak distance. In this case, the averaging selected is 5, 10, 15, and 30 samples. As seen in Fig. 5.23, this wavy behavior is clearly identified in the measurement, which is present even with large averaging windows. As seen with the highest averaging time, the mean of the crest-to-crest distance is ∼55 m for Beam 1, and ∼52.5 m for Beam 2. As seen in [155, 158], the average wave period, or the average wavelength, Λ_{waves}, tends to the combination of all the different wave contributions.

A similar behavior is also found in Track 2, as shown in Fig. 5.24. The Galileo signal (i.e., Beam 1), has a mean value ∼50 m, and Beam 2 a mean value on the order of ∼ 52.5 m, as in Track 1. Note that, a large portion (∼ 40%) of the Beam 1 reflections does not have a secondary peak because of the reflection geometry. As the incidence angle is very close to 0^{o} (i.e., very close to nadir), possible reflections are coming from closer wave crests, therefore the receiver is only able to infer consecutive crests which are closer one to each other.

5.3.4.3 Spectral analysis

The time-series analysis together with the statistical one show that there is a vast range of retrieved sea wave wavelengths Λ_{waves}, with some apparent periodicity. As detailed in [153, 155], a spectral analysis over the magnitude under study helps to separate the different swell or wind-driven wave contributions.

In order to do that, the power spectral density of the time-series data from previous section is computed. Figure 5.25 shows the power spectral density of the distance to the second peak (or the first encountered crest in the sea wave surface). In all four figures, there are some common frequencies at ∼0.06 Hz, 0.1 Hz, 0.15 Hz, and also a 0.2 Hz component in Beam 1 of both Tracks 1 and 2.

Converting those frequencies to seconds, the wave periods of each of the wavelengths are $T_1 = 16.6$ s, $T_2 = 10$ s, and $T_3 = 6.66$ s. Comparing the three periods to the swell and wind-driven wave periods to the ones of the ICON model in Fig. 5.13, $T_2 \simeq T_{swell}$ and $T_3 \simeq T_{wind}$.

In addition, the 0.2 Hz component, corresponding to a period of $T_4 = 5$ s, which is only present in Beam 1 of both Track 1 and Track 2, exactly matches the wind-driven prediction by the model, where $T_{wind} = 5$ s.

As already stated, the lower the incidence angle of the beam, the shorter waves can be retrieved (i.e., waves with shorter period), which is mostly the case for Fig. 5.25c,

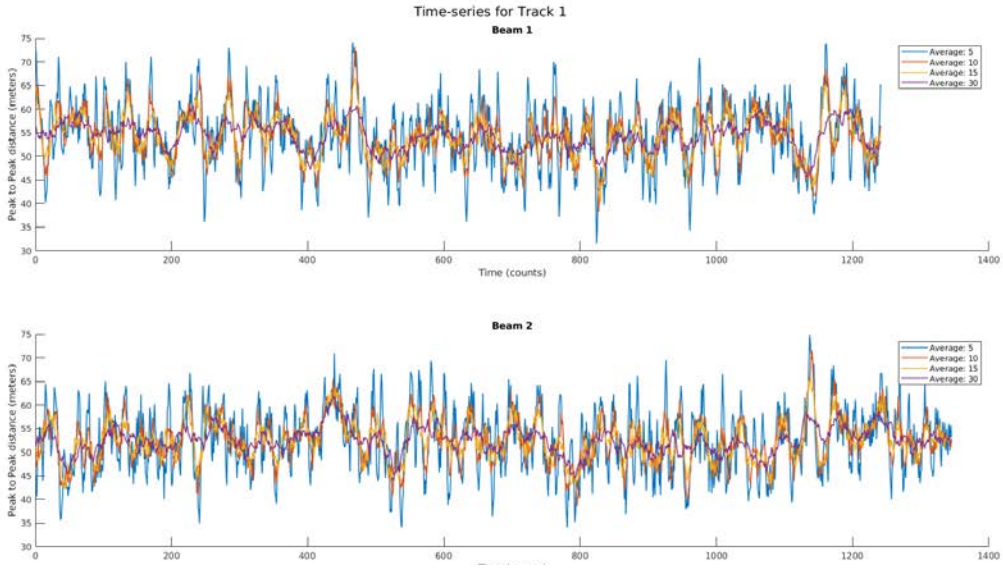

Figure 5.23: Time-series evolution of the Track 1 peak-to-peak calibrated distance with different moving average windows. Top figure corresponds to Beam 1, and bottom figure to Beam 2.

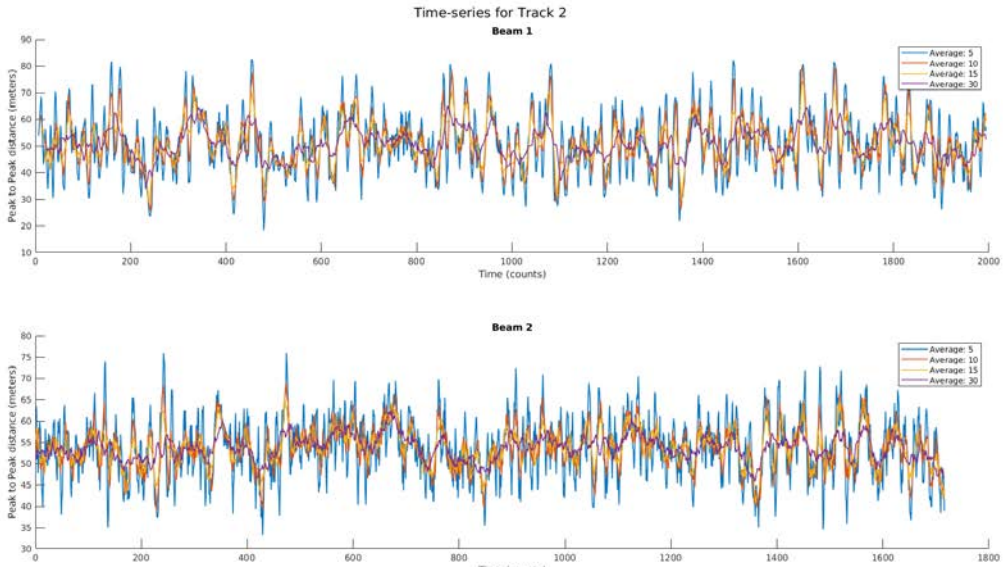

Figure 5.24: Time-series evolution of the Track 2 peak-to-peak calibrated distance with different moving average windows. Top figure corresponds to Beam 1, and bottom figure to Beam 2.

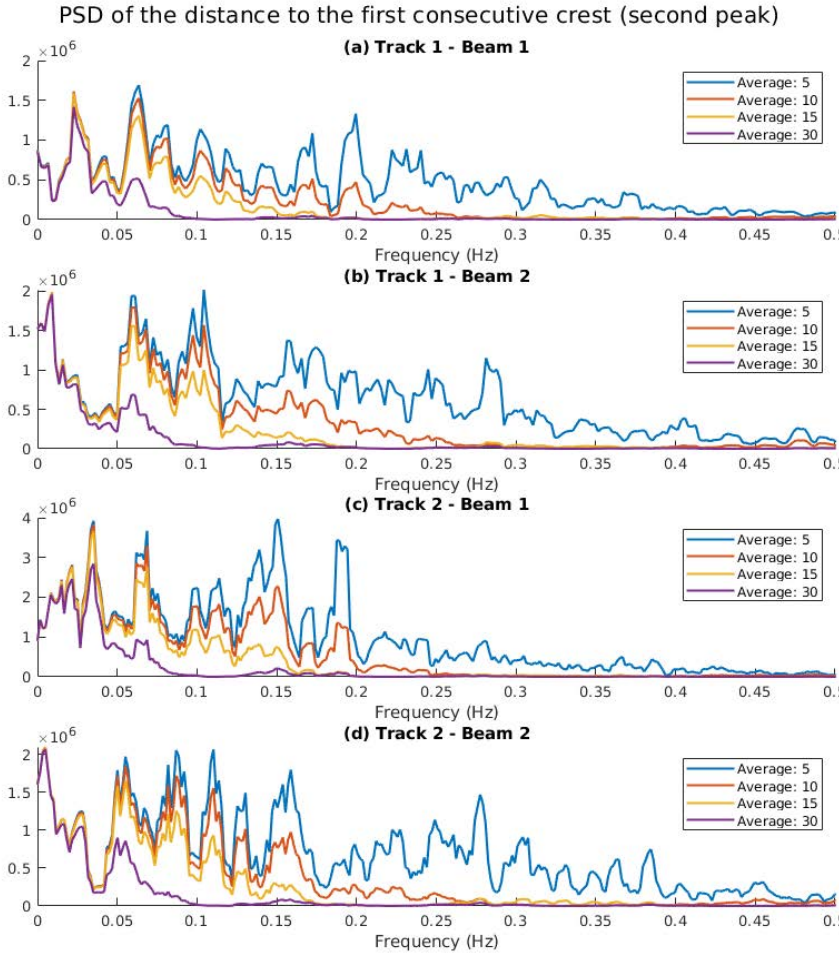

Figure 5.25: Fourier Transform of the time series evolution of (Figs. 5.23 and 5.24), for the second peak distances.

where the incidence angle is closer to 0^o (i.e., nadir), and hence wind-wave periods can be retrieved rather than swell-driven wave periods.

Furthermore, analyzing the power spectral density (Fig. 5.26) for the distance to the third peak, the fundamental frequencies are below the previous case, with a first fundamental frequency consistent in (a), (c), and (d) around ~ 0.03 Hz, 33 s of period.

The spectrum shape of this third peak indicates a long period sea wavelength which is not contemplated in the model. As stated in [158], this high order period is present on swell waves, and also modulates the amplitude of the swell waves, it is known as second swell.

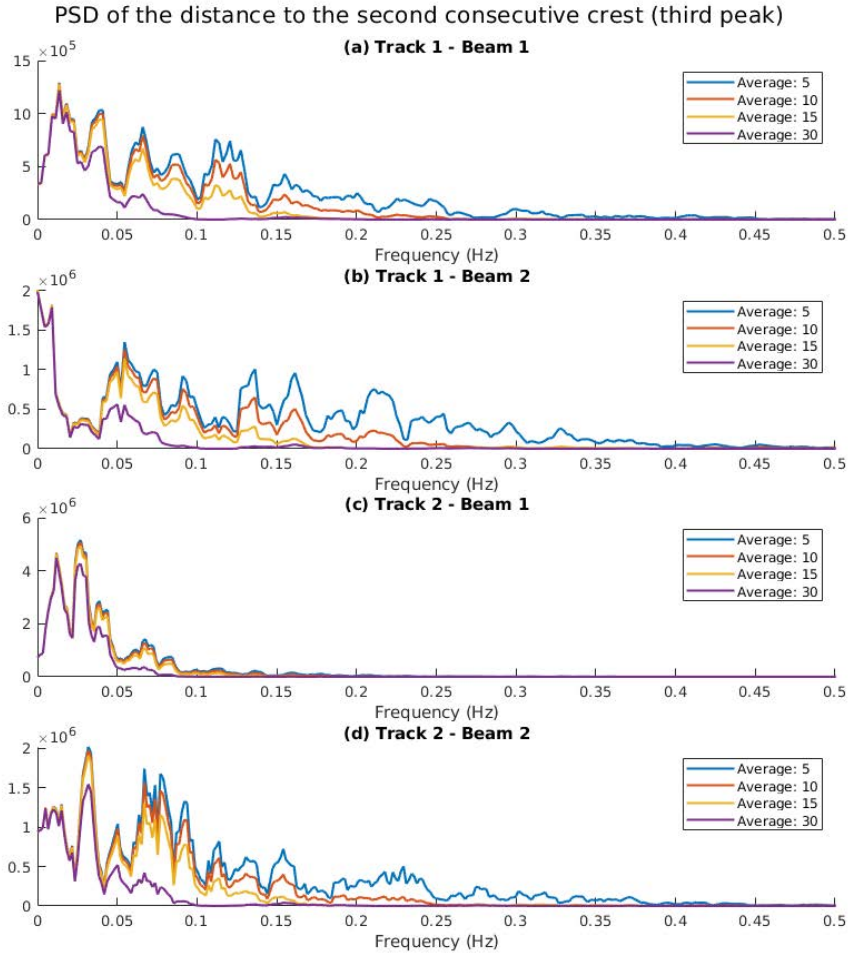

Figure 5.26: Fourier Transform of the time series evolution of (Figs. 5.23 and 5.24), for the third peak distances.

In this case, the third peak spectrum does not give as much information as the second peak, from where it is possible to infer the wave period for different wave sources, as swell, wind-driven wind, or secondary swell waves.

5.3.5 Discussion

Each analysis provides a different perspective and hence a different parameter of the ocean can be estimated, and they are all summarized and compared to the values predicted by the ICON model in Table 5.3. Note that, the wave periods in the statistical

Table 5.3: Estimated wave period from the three different analysis applied and its comparison ot the ICON model prediction.

Measurement	Estimated Wave Period	ICON Model Estimation
Statistical analysis	5.8 s	Wind-driven = 5 s Swell = 9 s
Time-series analysis	5.6 s	Wind-driven = 5 s Swell = 9 s
Spectral analysis	Four components: 5 s, 6.3 s, 10 s, 16.6 s	Wind-driven = 5 s Swell = 9 s

and time-series approaches have been determined from the average crest-to-crest distance and assuming $\Lambda_{waves} = 1.56 \cdot T^2_{waves}$, as in (5.11).

In this case, both the statistical and the time-series analysis are providing a good estimation of the wind-driven wavelength, as the period of the wind-driven waves is smaller, the amount of wave crests per unit of area is larger, and hence the mean value of the waves is biased towards the wind-driven waves.

It is also important to remark that the time analysis serves to illustrate the wavy behavior of the crest-to-crest distance with respect to time. In this case, this analysis shows in a qualitative way, how crest-to-crest distance is a mixture of different components, as explained in [153, 155].

Last, but not least, the spectral analysis clearly shows the different periods that can be identified in the time analysis. Multiple periods can be identified, among them τ_{swell} and τ_{wind} are identified as the main components of the spectrum of the crest-to-crest distance.

Furthermore, the results from the spectral analysis and the statistical analysis confirm that due to the geometry of the reflection, the lower the incidence angle is, the closer the reflection of the second crest occurs.

Finally, the spectral analysis also shows very low frequency components due to secondary swell or high period gravitational waves, which are interesting for other oceanographic studies, but still need further investigation.

5.4 Conclusions

MIR has shown great potential over the Ocean. The first part of this Chapter has presented an exhaustive study of the degree of coherency of both the L1 and the L5 waveforms, showing that the coherency of the reflection decreases as the integration time increases. Thanks to the large directivity of the MIR instrument, the presence of a non-negligible coherent component in a reflection over the sea surface has been confirmed. Furthermore, in the frame of this first section, a waveform and phase evolution analysis have been presented, allowing the processing of the coherent and total power components separately. The application of this technique to any GNSS-R signal opens new possible applications. Including a better resolution for altimetry products thanks to a better estimation of the peak position, the estimation of the wave period thanks to the identification of the secondary peaks present on the coherent component, and other

derived products such as the sea state (U_{10}), and the sea surface height with improved resolution. Moreover, the use of the coherent component enhances the determination of the specular reflection point, with can be used to provide precise altimetry measurements. One important finding to remark is that the total power waveform for short integration times mostly includes a very large coherent component. Thus, if the link budget is high enough, short integration times shall be used, as the reflected power will mostly come from the first Fresnel zone, providing the better spatial resolution, and simplifying the reflectivity calibration process.

In the second Section, a complete analysis of the secondary peaks detected in L5 waveforms has been presented. The presence of multiple peaks in the L5 GNSS-R reflected waveform has been correlated to the first experimental evidence of wind and swell waves signatures. An algorithm has been presented to retrieve the peak-to-peak distance. Evidence for both the first and the second peaks are presented, and a detailed analysis from a large data set $N > 1000$ waveforms has been presented. The analysis in three domains (statistical, time, and frequency) shows that additional ocean parameters can be retrieved from GNSS-R measurements, e.g., wind driven waves period and swell period, which have not been measured yet using GNSS-R technique. This application still requires further refinements, and a more exhaustive analysis with in-situ data. However, this study shows the promising results for the use of L5/E5a GNSS-R signals to infer new geophysical parameters as the wave period or wavelength of the sea thanks to the sharper shape of the auto-correlation function.

6

Chapter 6

Microwave Interferometric Reflectometer: Land experiments

This Chapter presents the results of the MIR campaign over land. Two main geophysical parameters can be retrieved over land using GNSS-R, SM and vegetation information. In here, data from three flights have been selected to study the retrieval of both parameters using MIR data at L1 and L5. Section 6.1 introduces the Chapter providing some literature review on the retrieval of SM and vegetation information using GNSS-R. Section 6.2 covers the retrieval of soil moisture using GNSS-R data collected by the MIR. The results presented in this Section have been adapted from a peer-reviewed journal entitled "Single-Pass Soil Moisture Retrieval using GNSS-R at L1 and L5 bands: Results from Airborne Experiment" [JP6], and are presented in the international conference [CP6]. Section 6.3 covers the impact that dense and tall vegetation (i.e., rainforest) has into GNSS-R L1 and L5 signals, proposing a methodology to retrieve canopy height information using GNSS-R measurements. The results presented in this Section have been submitted to a peer-reviewed journal, under the title "Vegetation Canopy Height Retrieval using L1 and L5 Airborne GNSS-R" [JP7], which at the time of writing this report is under review. Finally, Section 6.4 presents the conclusions of the Chapter.

6.1 Introduction

GNSS-R using L1 C/A signals has been widely studied from both low-altitude (i.e., airplane or balloon) or high-altitude (i.e., satellite) platforms to retrieve land-related parameters. In the past years, L1 GNSS-R data has been analyzed to retrieve Above-Ground Biomass (AGB) [63, 64], Canopy Height (CH) [63], and SM [74, 79, 80], showing promising results in all three cases.

6.1.1 Background: surface soil moisture content estimation using GNSS-R

Soil is a natural reservoir of water, being the main supply store for plants to live. The surface water storage is mainly depleted by the natural process of evaporation, percolation to lower layers in the soil, water uptake by plants, etc. Low SM values causes water stress, low crop yield, reduces tree senescence, etc. Conversely, moderate-to-high surface SM values increase flood risks [27], and affect soil erosion [160] by wind and rain. Consequently, monitoring the soil moisture content of this near-surface layer of soil is crucial for sustainable irrigation of crop fields (smart irrigation), forest fire risk prediction, assessment of vegetation senescence, and to have a better knowledge of the water cycle, which plays a key role in the climate feedback loops [2].

Soil moisture can be measured using in-situ probes, or by means of remote sensing techniques, for which several approaches have been shown to have the ability to retrieve surface soil moisture states at different spatio-temporal scales. Using L-band microwave radiometry, the ESA SMOS mission [28] and the NASA SMAP mission [161] are providing soil moisture maps at a native resolution of $\sim$55 km [162], and 36 km [163], respectively.

GNSS-R offers the promise of an enhanced spatial resolution when compared to microwave radiometers. The spatial resolution of GNSS-R receivers is mostly linked to the size of the first Fresnel zone, as covered in Chapter 3 for coherent reflections. However, current methods to retrieve SM from GNSS-R space-borne data are not providing such resolution. As discussed in [164], few reflections (less than 16%) contain a noticeable coherent component, thus showing that incoherent scattering is dominant over land. Under these conditions, the spatial resolution is degraded, as many contributions coming from the entire glistening zone are collected by the receiving antenna (i.e., 25-37 km as shown in [117]). Because of that, many algorithms to retrieve SM using GNSS-R data require averaging the GNSS-R observables over large grid cells, such as the SMAP native resolution of 36 km [73, 79], or by applying spatial and temporal averaging (i.e., 22 km resolution in [81]). Other works have shown an enhanced spatial resolution as compared to the previous ones. As CyGNSS data is now tagging reflections containing a large coherent component [165], new algorithms are being developed providing large spatial resolutions up to 2 km [89] or 3 km [80] just including coherent reflections retrieved by CyGNSS.

6.1.2 Background: vegetation height estimation using GNSS-R

As it is shown in [70], the presence of dense vegetation is linked to an increased attenuation and a decrease of the GNSS-R SNR, showing that the reflectivity can be linked to vegetation information. The same correlation is studied in [166], where the GNSS-R

reflectivity and SNR have a certain degree of correlation with the leaf index and the canopy height. GNSS-R using L1 C/A signals has been widely studied from both low-altitude (i.e., airplane or balloon) or high-altitude (i.e., satellite) platforms to retrieve vegetation-related parameters.

Other studies have shown that polarimetric GNSS-R from a high-altitude balloon could be used to infer AGB [106]. Moreover, in [63] it is shown that GNSS-R data collected by the UK TDS-1 mission and the CyGNSS mission have a certain degree of correlation to the SMAP vegetation optical depth (VOD). This last work proposes an ANN algorithm to retrieve both AGB and CH using CyGNSS reflectivity measurements, showing a root-mean-square error (RMSE) of 6.5 m at a spatial resolution of 5 km. In [64] it is shown that, with a large spatial averaging ($\sim$20 km), the trailing edge of the GNSS-R L1 C/A waveform over land collected by CyGNSS has a strong correlation with both SMAP VOD.

6.2 Single-pass Soil Moisture Retrieval using GNSS-R

Machine learning algorithms, and in particular ANNs, are now the latest approach to retrieve soil moisture from a wide range of remote sensing techniques. For instance, the SMOS soil moisture product assimilated by the European Centre for Medium-range Forecast (ECMWF) is obtained using an ANN [85]. However, ANNs' challenge is to correctly train the algorithm: in this process, the key is not only to select the correct target, but also the amount of ancillary data inputs used for the algorithm. Known ANN implementations are summarized in Table 1 from [79], which is reproduced in Table 6.1. They require a large spatial and temporal averagings, and the use of ancillary data to reduce the RMSE with respect to the SM "ground-truth" used for validation. In most of the cases discussed in [79], the ancillary data used is either NDVI, SMAP VOD, or a combination of the soil texture and topography data, and the SM "ground-truth comes from SMAP.

Current reflectivity models (Eq. 6.1 [168]) used to estimate SM from GNSS-R data compensate vegetation attenuation, and surface roughness effects according to:

$$\Gamma(\theta) = R^2(\theta, \epsilon_r(f, SM, Soil\,type, ...))\gamma^2 exp(-4k^2\sigma_h^2 cos^2(\theta)), \tag{6.1}$$

where Γ is the reflectivity, θ stands for the local incidence angle, R corresponds to the amplitude of the Fresnel reflection coefficient, which depends on the SM content, frequency, and several other parameters such as the soil type, composition, density, porosity... [169], γ is the transmissivity – which accounts for the vegetation attenuation – , and it is modeled by the VOD or the NDVI as a proxy, k is the wavenumber (i.e. $\frac{2\pi}{\lambda}$), and σ_h is the effective surface root-mean square (RMS) height. Note that, Eq. 6.1 neglects scattering within the vegetation layer, and cross-polarization effects due to surface roughness.

If any of the terms included in Eq. 6.1 is not estimated accurately, the soil moisture cannot be properly retrieved. This is shown experimentally in [69] and in [124]: at L-band, soil moisture produces a change in the retrieved reflectivity of up to 17 dB for a range between 0-0.45 m^3/m^3, while under coherent scattering conditions, the surface roughness effect by itself may reduce the reflectivity up to 18 dB for a local RMS surface height

Table 6.1: Applications of SM sensing using CyGNSS data. Reproduced from Table 1 from [79].

Source	Time span	Spatial coverage	Reference SM	Require ongoing SM	No. of ancillary data	RMSE (m^3/m^3)	R
Chew and Small (2018) [35]	1 year	Pan-tropical	SMAP	No	2	0.045	/
Kim and Lakshmi (2018) [167]	1 year	Regional	SMAP	Yes	1	/	0.68/ 0.77
Al-Khaldi et al. (2019) [81]	6 months	Pan-tropical	SMAP	Yes	1	0.04	0.82
Eroglu et al. (2019) [88]	2 years	Regional	In situ	No	5	0.054	0.90
Clarizia et al. (2019) [73]	5 months	Pan-tropical	SMAP	No	2	0.07	/
Yan et al. (2020) [79]	1 year	Pan-tropical	SMAP	No	1	0.07	0.80

variation of 0-4 cm [124], or up to 11 dB when a Kirchhoff Approximation simulator is applied to the multi-elevation surface [170]. Furthermore, vegetation may reduce the reflectivity by up to 11 dB for a VOD variation from 0 to 0.6. Therefore, it is critical to adequately estimate and include both parameters in the retrieval algorithm. While the vegetation impact can be, in principle, more easily corrected by means of the NDVI or the VOD, this is not the case for the surface roughness, as the effective surface RMS height is extremely complicated to be accurately modeled or retrieved. Previous studies from an airborne platform [69] showed that, even when estimating the surface roughness using laser profilers on ground, the reflectivity could not be properly corrected for, as the reflection of the GNSS signal actually takes place underneath the surface, at a depth depending on the soil moisture content itself of the reflecting area, and the signal wavelength [171]: the higher the soil moisture content, the lower the depth where the reflection takes place, and the closer the effective surface roughness to the surface roughness that can be measured with a laser profiler. The lower the soil moisture content, the more the wave penetrates in the soil, and the higher the volume scattering in the soil, and lower the value of the effective soil moisture surface roughness. Therefore, the effective RMS height also depends on the soil moisture content ($\sigma(\theta_i, SM)$) [172,173]. Note that, latest algorithms to estimate SM using L-band MWR measurements from SMOS (described in [173]) model the surface roughness by means of Eq. 6.2.

$$h = h_1 - h_2 \cdot SM, \tag{6.2}$$

(a) **(b)**

Figure 6.1: (a) Highlighted in black the NSW area of Australia where the flight was conducted, and (b) definition of the Yanco areas A (34º 43' S, 146º 05' E) and B (34º 59' S, 146º 18' E).

where h is the effective soil roughness, and h_1 values are 0.5–2.3, and h_2 values range from $2 \cdot h_1$ to $3 \cdot h_1$, depending on the incidence angle, as shown in Table 2 from [173].

Focusing on GNSS-R, the surface roughness is still the unresolved uncertainty to estimate SM from reflectivity measurements. In this regard, a detailed discussion of surface roughness modeling from GNSS-R measurements is provided in Section 6.2.4.1.

6.2.1 Data description

MIR flew over the Yanco-designated portion covered by OzNet [122], New South Wales, Australia, on 1 May, 2018, and on 18 June, 2018 (see Fig. 6.1). The two flights covered the same area, but the first flight was conducted after a long period without rain, under very dry soil conditions, while the second flight was conducted the day after a rainy day, in which the water content of the soil was substantially higher. These two flights are called herein as "Dry", and "Wet" flights, respectively.

6.2.1.1 Ground-truth and ancillary data

Areas covered by MIR in the two flights are highlighted in Fig. 6.1. As shown in Fig. 6.2, the OzNet soil moisture of both days is significantly different. In the area covered by the plane track, the ground stations showed an average SM of ~ 0.05 m^3/m^3, and $\sim$0.27 m^3/m^3, for the dry and wet flights, respectively. However, considering only a limited set of in situ measurements is not enough to compare it with the GNSS-R measurements. For that reason, other remote sensing products have been used as reference data.

Two ancillary SM products are key for the correct interpretation of the data in this section. The first ones are the SMOS and SMAP soil moisture products. However, as the resolution is too large for our data set ($\sim$55 and 36 km), a pixel down-scaling [174,175] of

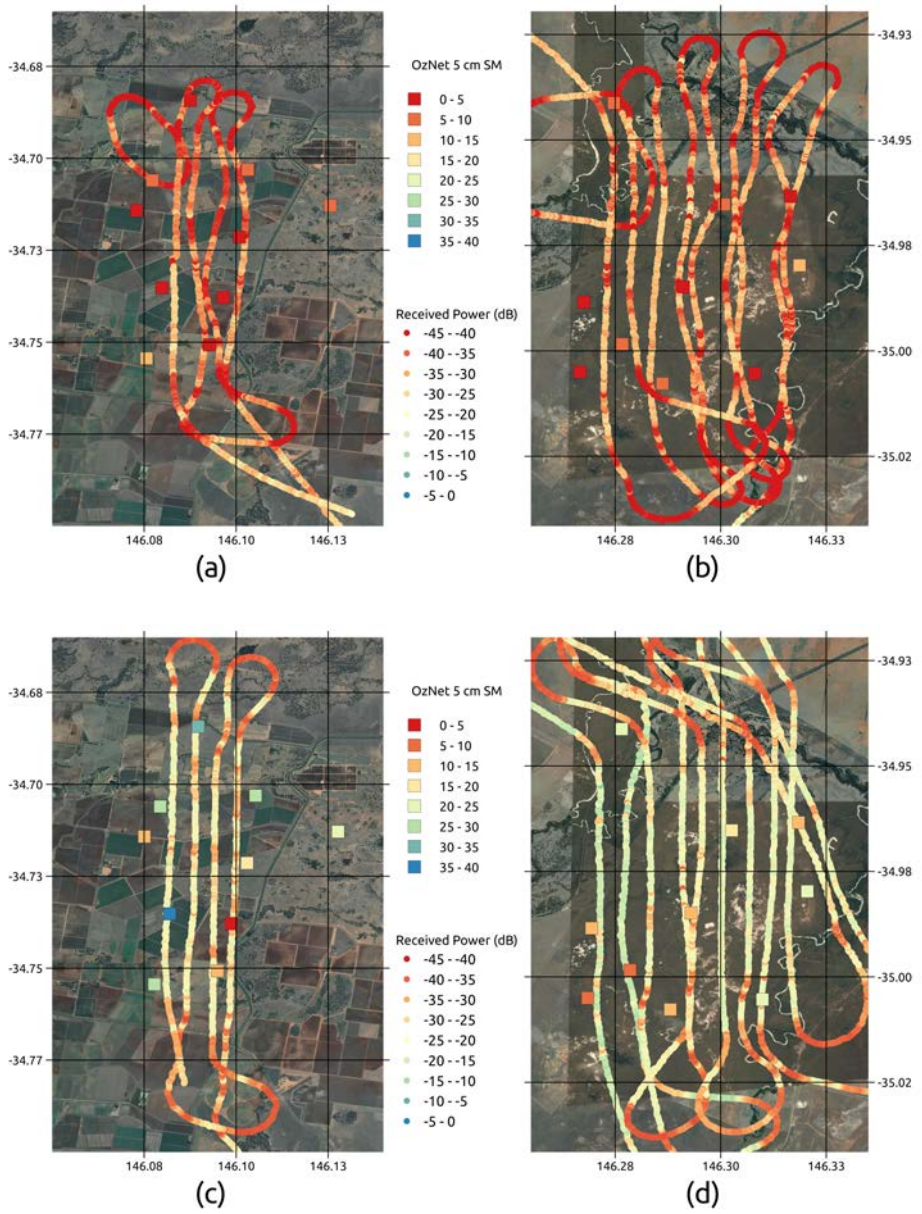

Figure 6.2: The tracks denoted by the *Received Power* color scale represent the uncalibrated received power (in arbitrary units) by the MIR instrument, and the coloured squares are the in-situ OzNet soil moisture (m^3/m^3) sensors at 5 cm depth. The received power and the in-situ SM measurement during the "Dry" flight is shown for (a) Site A, and (b) Site B; and during "Wet" flight for (c) Site A, and (d) Site B. Note: anomalous low reflectivity values for large banking angles during the turns are not used in the study.

the coarse resolution SMOS L3 soil moisture product has been enhanced down to 20 m, using SMOS brightness temperatures, ECMWF land surface temperature, and visible and near infra-red data from Sentinel-2. This technique has been validated with different soil moisture networks [176]. Moreover, the down-scaled data have been validated against the OzNet SM network data during both "Dry" and "Wet" flights, showing a bias of 0.01 m^3/m^3, with an RMSD of 0.032 m^3/m^3 for the "Dry" flight, and a bias of 0.02 m^3/m^3, with an RMSD of 0.038 m^3/m^3 for the "Wet" flight. The RMSD for both maps is lower than the SMOS accuracy at native resolution (0.04 m^3/m^3), and it is lower than the RMSD presented in other studies [177].

As it can be seen in Figs. 6.3 and 6.4, the NDVI from Sentinel-2 presents some differences between the "Dry" and "Wet" flights, and the down-scaled SMOS soil moisture product as well. However, the important values for this study are the ones collocated with the GNSS specular reflection points. For that reason, both the NDVI and the SM maps are interpolated to each of the specular points of the MIR instrument (tracks in Fig. 6.2), and the histograms of both measurements for the two flights are shown in Fig. 6.5.

6.2.1.2 GNSS-R data

The plane flew at an altitude of h ∼500 m, at an average speed of v ≃75 m/s for both flights. From this altitude, the size of the Fresnel zone l_{Fz} is (from Chapter 3, Eq. 3.3[1]) is $l_{Fz_{L1}} = 9.75$ m at L1/E1, and $l_{Fz_{L5}} = 10.75$ m at L5/E5a for an incidence angle θ_{inc} =0º.

Based on the flight characteristics, the maximum integration time to prevent blurring of the first Fresnel zone is bounded to $T_{int} < \frac{l_{Fz_{L1}}}{v} \simeq 130$ ms, as shown in Chapter 3. However, in order to have some oversampling over the same Fresnel zone, a smaller value has been selected: $T_{int} = 20$ ms. In that case, and depending on the local incidence angle, the number of samples overlapped in the same Fresnel zone varies from 6 to 11 samples, which corresponds to θ_{inc} =0º and to θ_{inc} =45º, respectively.

Because of the flight height and speed, the delay and Doppler spreads are negligible, and therefore the selected GNSS-R observable is the reflectivity as shown in Eq. 6.1. Applying the Pseudo-Random Noise injection technique conceived in [180], the MIR instrument is calibrated as described in [181], including the antenna pattern compensation as in [22]. Furthermore, the reflectivity is calculated assuming only the peak of the waveform minus the noise floor, according to Eq. 6.3:

$$\Gamma = \frac{P_{ref} - P_{N_{ref}}}{P_{dir} - P_{N_{dir}}} \cdot \frac{G_{up}(\theta_{dir}, \phi_{dir})}{G_{dn}(\theta_{ref}, \phi_{ref})}, \tag{6.3}$$

where P is the amplitude of the waveform at its maximum, P_N is the noise power of the waveform, computed as the average of the delay bins before the peak of the Delay-Doppler Map, G is the gain of either the up-looking or the down-looking antenna, θ and ϕ are the look angles to either the transmitting satellite (*dir*), and to the specular reflection point (*ref*). In this case, the GNSS satellite antenna pattern is not taken into account, neither the additional path losses, as the increased distance is negligible (500 m) with respect to the already traveled distance from the MEO GNSS satellite (> 20.000 km).

[1] $l_{Fz} = \frac{\sqrt{\lambda R_r}}{cos(\theta_{inc})}, R_r = \frac{h}{cos(\theta_{inc})}$

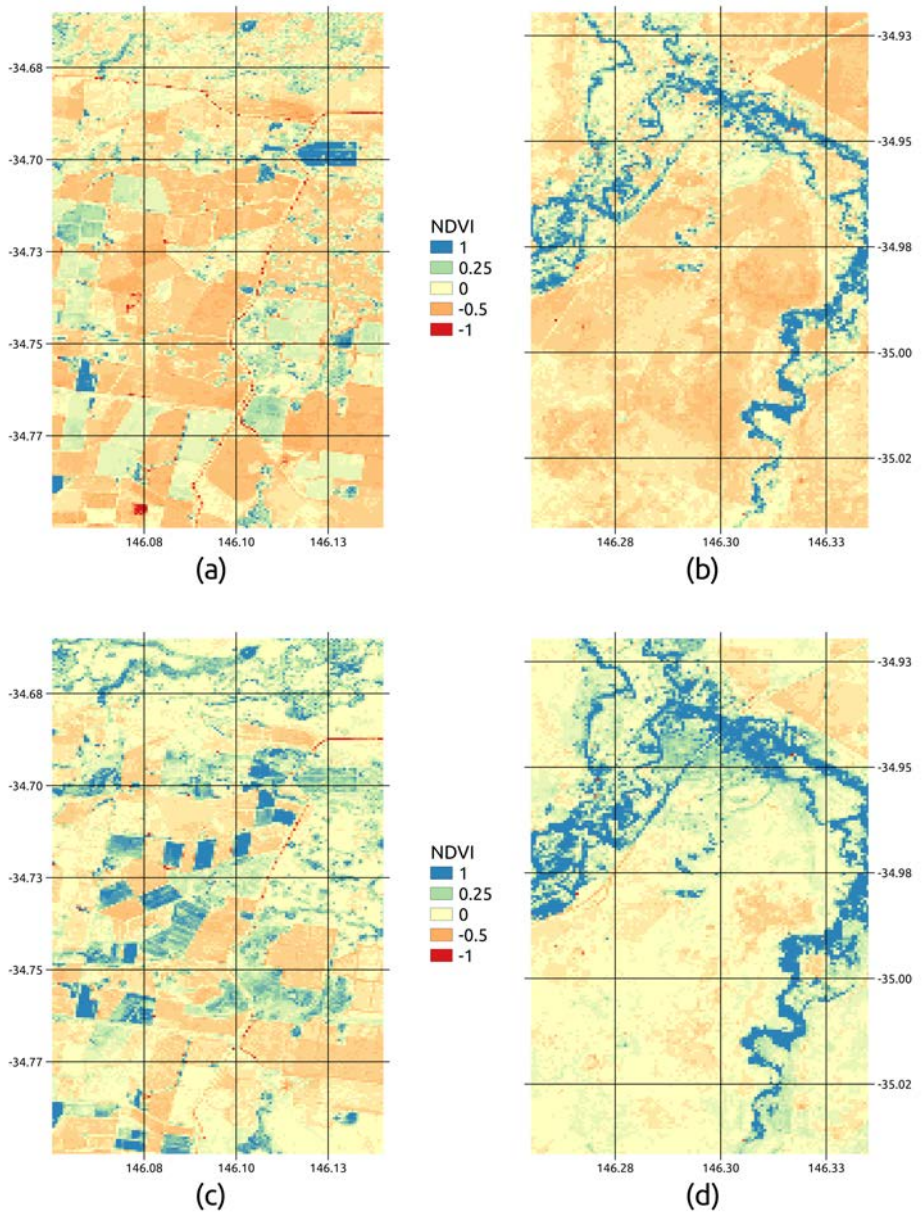

Figure 6.3: NDVI retrieved by Sentinel-2. The selected data sets contain Copernicus Sentinel data corresponding to 2018-05-01 (Dry) and 2018-06-16 (Wet) from the Sentinel Hub [178]. "Dry" flight at (a) Site A, and (b) Site B; and during "Wet" flight at (c) Site A, and (d) Site B. Note that negative NDVI values in (a) and (c) correspond to the Coleambally Canal.

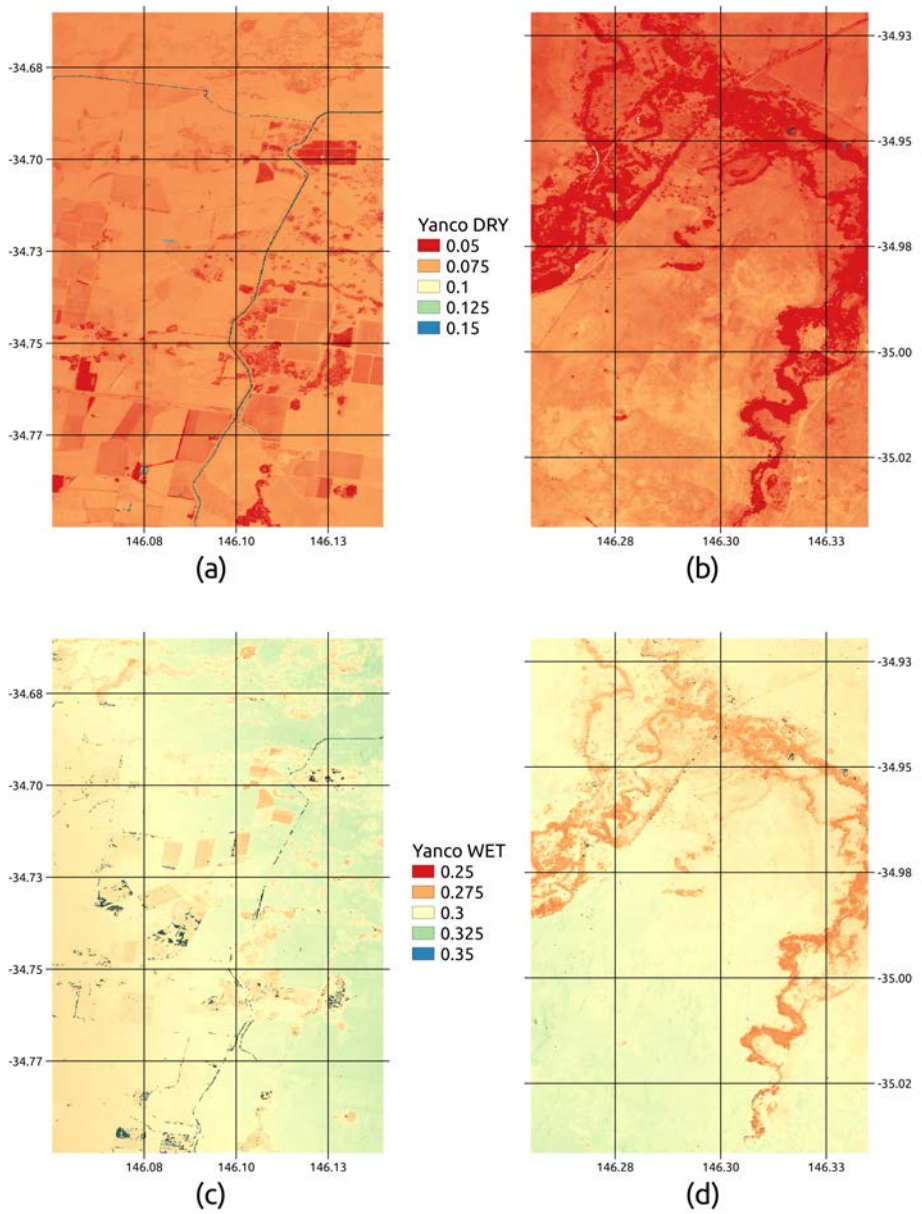

Figure 6.4: SM retrieved by the combination of SMOS SM and down-scaled using Sentinel-2 NDVI. "Dry" flight at (a) Site A, and (b) Site B; and during "Wet" flight at (c) Site A, and (d) Site B. Credits: Barcelona Expert Center [179]. Note that, the color scale is different in each plot to maximize the contrast and ease its visualization.

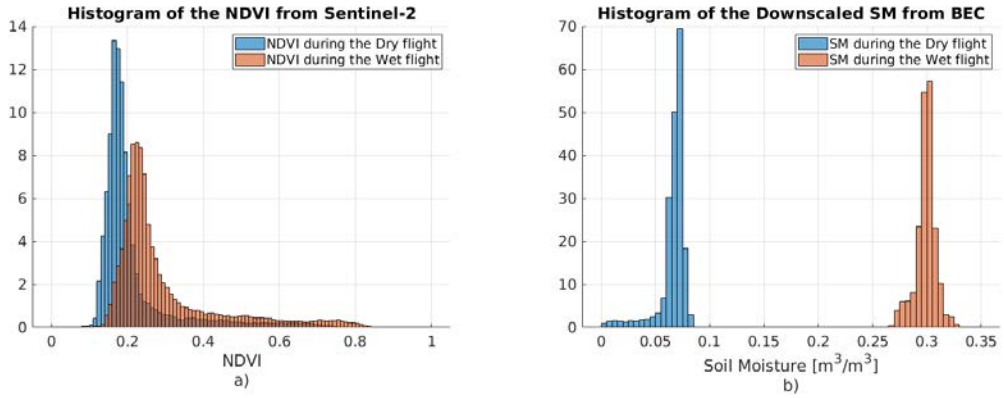

Figure 6.5: Histograms of the collocated Sentinel-2 NDVI (a) and downscaled SM (b) values over the MIR specular points for both the Dry and Wet flights.

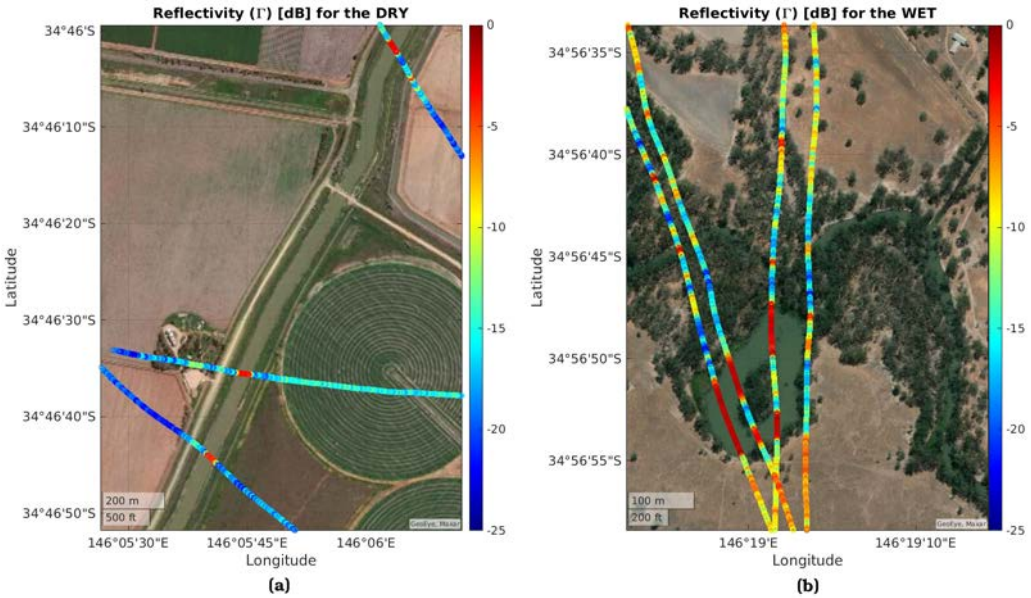

Figure 6.6: MIR reflectivity for both (a) Dry and (b) Wet flights (dB). Average Reflectivity over the selected water bodies is ∼-2.1 dB at an incidence angle ∼20º. The resulting reflectivity has been calibrated using a flat water surface model [182] with a dielectric constant of ∼80+9j, assuming a very low salinity (psu=1 ppm), and a temperature of 15 ºC.

The reflectivity is absolutely-calibrated using different water bodies that the MIR instrument crossed during both flights. As shown in Fig. 6.6, the reflectivity over the selected water bodies is ∼-2.1 dB at incidence angle ∼20º. Figure 6.7 shows the reflectivity histogram, normalized to have an area equal to 1 (i.e., Probability Density Function (PDF) estimate). As it can be seen, mean reflectivity values have a difference between "Dry"

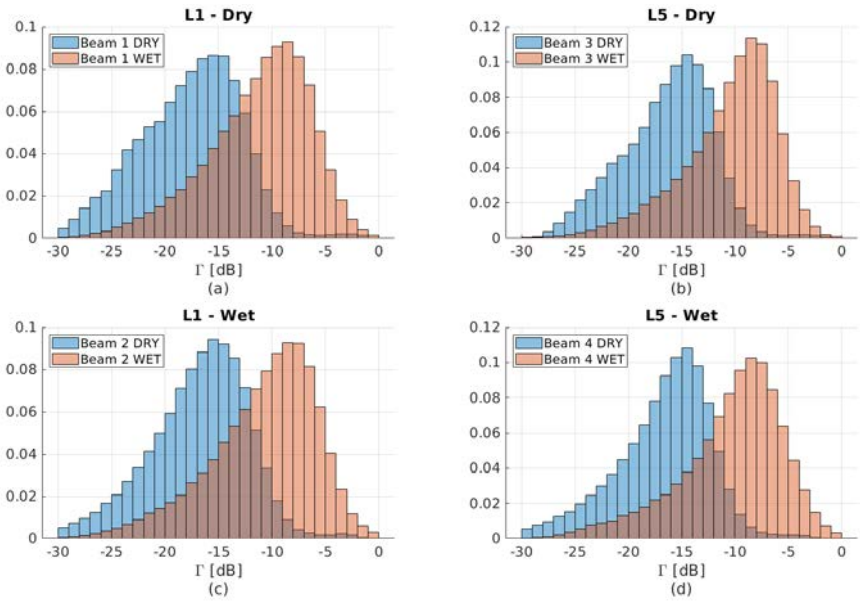

Figure 6.7: MIR reflectivity PDF for both (a)-(b) Dry and (c)-(d) Wet flights. The Y-axis is the normalized counts values of the PDF, and the average reflectivity for the four beams at the "Dry" flight are: -17.6 dB, -16.8 dB, -16.3 dB, and -16.7 dB, with a standard deviation of ∼4.7 dB; and for the "Wet" flight are: -11.2 dB, -10.8 dB, -10.5 dB, and -10.4 dB, with a standard deviation of ∼4.8 dB. Note that, the tracking algorithm selects those satellites whose reflection has a very small incidence, and the *average* incidence angle for the four beams is below ∼30º.

and "Wet" flights of ∼ 7 - 8 dB. Considering Fig. 21 from [124], the difference in the received power is expected to be ∼ 4 dB for a difference of ∼ 0.22 m^3/m^3. However, [124] does not take into account the effect of the penetration depth of the GNSS reflection signal in different soil moisture conditions. In this work, the surface roughness plays a significant role in this averaging operation, as the average of a magnitude affected by an attenuation is a biased estimator of the actual magnitude. Additionally, as previously discussed, this roughness also depends on the soil moisture content [171], and therefore an analytic solution to that problem is very complex.

6.2.2 Reflectivity statistics using different integration times

As shown in Fig. 23 from [124], and discussed in the introduction of this Section, herein a difference of just 4 cm in the local RMS height may produce a 18 dB drop in the power of the reflected GNSS signal. Furthermore, as the first Fresnel zone of the reflection is very small, the local surface roughness also has a high variability between overlapped nearby reflections.

Computing the average of the reflectivities (in linear units, and then taking its logarithm) of a certain area may reduce the effect of terrain inhomogeneity, also reducing the Speckle noise. In this section, the effect of increasing the integration time is addressed from a statistical point of view. In this case, consecutive incoherently-integrated

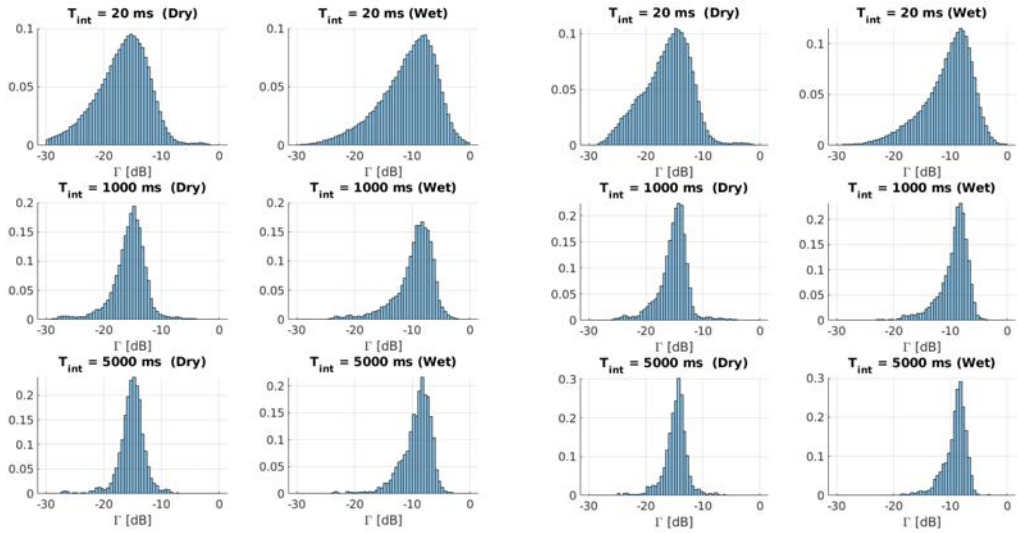

Figure 6.8: Normalized histogram PDFs of the MIR reflectivities retrieved at different effective integration times at (a) L1 and (b) L5.

reflectivity samples at T_{int} =20 ms are averaged (linearly, using a moving average filter, and then taking the logarithm of the resulting magnitude) up to 5 seconds. Different histograms for Beams 1 (L1) and 3 (L5) for both "Dry" and "Wet" flights are shown in Figs. 6.8a and 6.8b, respectively for L1 and L5 cases. As it can be seen, as the effective integration time increases, the average value remains constant, but the standard deviation of the reflectivity decreases.

In addition, Fig. 6.9 shows a selected track over a certain region where the local surface roughness of the crop field changes. As it can be seen, for shorter averaging times, a larger local variability of the signal is encountered, capturing small variations in the terrain, as in the middle of the image (outlined with a black box), where the signal crosses a small irrigation channel. However, as the effective integration time increases, small variabilities of the terrain (i.e., surface roughness) are averaged, and therefore the attenuation variability caused by the surface roughness is diluted, providing a negative bias in the reflectivity, which also varies as a function of the integration time.

6.2.3 Surface roughness effect in soil moisture retrievals

Since at high SM the reflectivity tends to saturate (Fig. 21 of [124]), its sensitivity to SM decreases. In this case, if the scattering occurs close to the surface, the roughness effects on reflectivity, and consequently SM, are more noticeable. This is observed in Fig. 6.9, in which the large variability in the reflectivity is mostly produced by local surface roughness variations. When the incoherent integration time is very short (i.e., 20 ms), the terrain contribution is not smoothed, and therefore the power changes caused by local roughness variations are highlighted.

In order to analyze in detail the effect of the surface roughness, the Wet flight over

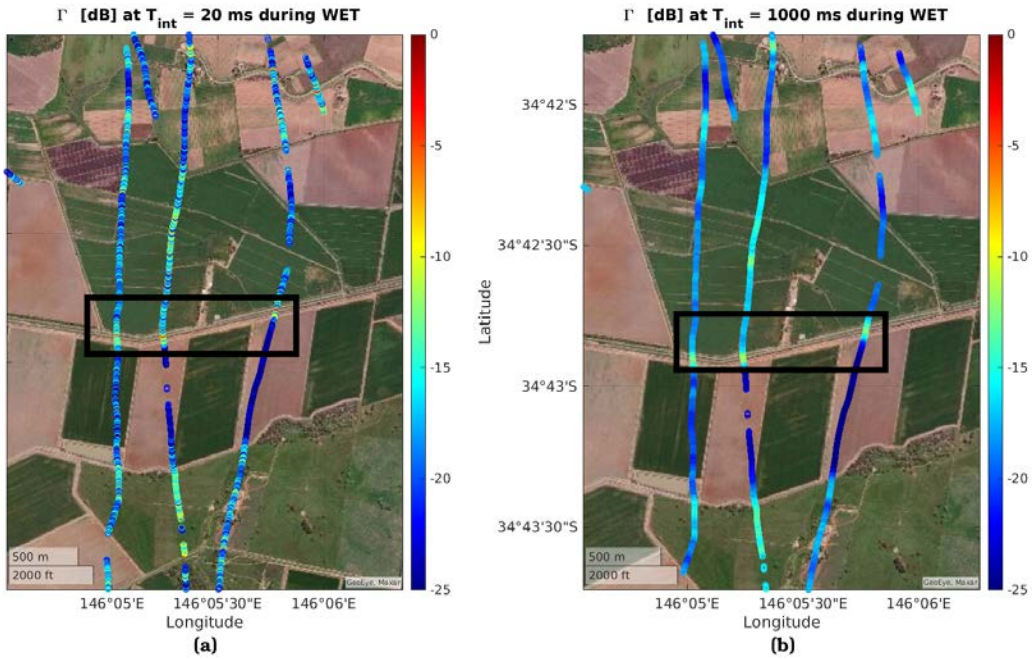

Figure 6.9: Geo-located MIR reflectivities in Yanco site A during "Wet" flight at different T_{int}: (a) 20 ms and (b) 1000 ms.

Yanco site B has been selected. The NDVI of the area is very low and almost constant, and the attenuation due to vegetation opacity can be neglected. The influence of the soil surface roughness on SM can be studied by isolating its corresponding term in Eq. 6.1, and assuming a saturated reflectivity due to very high soil moisture values. Therefore, the surface RMS roughness can be estimated from Eq. 6.4, as follows:

$$\sigma_h = \sqrt{\frac{(-ln(10^{\frac{\Gamma[dB]+5}{10}})}{(4k^2 \cdot \cos(\theta_{inc})^2))}}. \tag{6.4}$$

As it is seen in [124], the GNSS-R reflectivity saturates for SM values larger than ∼0.25-0.3 m^3/m^3. Moreover, as it can be seen in Fig. 7c from [71], these SM values produce a range of reflectivities from -6 to -4 dB. Thus, for the sake of simplicity, a reflectivity value of -5 dB has been selected for this study. Note that, this range of reflectivities is assuming a VOD < 0.2. As it is shown in Fig. 2a [183], an L-band VOD < 0.2 is provided for NDVI values < 0.4.

Figure 6.10a shows the results of applying Eq. 6.4 to the Yanco site B during the "Wet" flight, after removing all reflectivities from water bodies or with an NDVI > 0.4, so that the vegetation attenuation can be neglected. To perform this study, the selected beams at L1 and L5 are from the same GNSS spacecraft so that the specular reflection point is exactly the same and the only difference is the small difference in the size of the first Fresnel zone due to the different wavelength. In this case, for moist soils the penetration

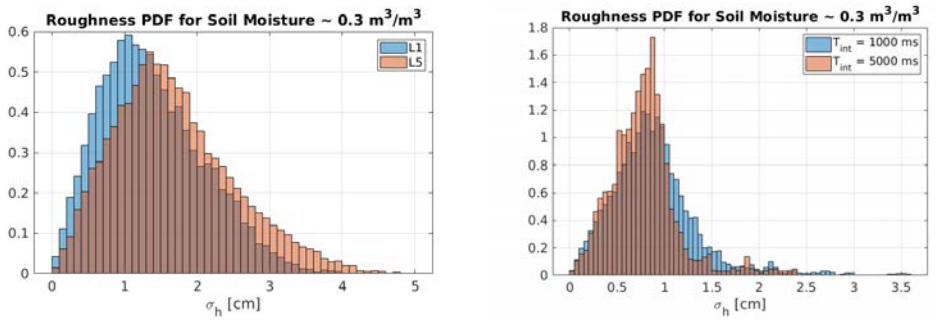

(a) **(b)**

Figure 6.10: Estimated Surface Roughness normalized PDF in Site B during "Wet" flight seen by L1 and L5 signals, assuming a flat reflectivity $\Gamma = -5$ dB, and using (a) $T_{int} = 20$ ms, and (b) at $T_{int} = 1000$ ms and 5000 ms only for the L1 case. The X and Y axes have been adjusted to ease its visualization.

depth at both bands is limited to ∼2 cm [171]. As it can be seen, the estimated roughness at both bands is very similar, with an average value of ∼1.23 m, and a standard deviation of ∼0.68 cm at L1/E1, and an average value of ∼1.37 cm, and a standard deviation of ∼0.59 cm at L5/E5a, which is consistent with a slightly larger penetration depth at L5/E5a, and a reflection accuracy over a slightly flatter interface. In this case, the impact of an average roughness of 1.3 cm produces a degradation in the reflectivity of ∼1.4 dB, while a surface roughness of 2 cm produces a degradation up to 4 dB.

Finally, the roughness at L1 as a function of the integration time is displayed in Fig. 6.10b. As the effective integration time increases, the estimated surface roughness decreases to values lower than 1 cm. Averaging up to 1000 ms produces a mean roughness of 0.88 cm, with a standard deviation of 0.45 cm, and averaging up to 5000 ms produces a mean roughness of 0.78 cm, and a standard deviation of 0.35 cm. Increasing the effective integration time reduces the surface roughness variability, but this introduces a bias in the estimation of the reflectivity. This qualitative analysis points out that the use of spatial averaging "averages" the surface roughness effect, providing a biased estimator of the reflectivity, which depends on the actual surface roughness.

6.2.4 Soil moisture retrieval algorithm

Surface roughness is the variable limiting the accuracy of SM retrievals using GNSS-R data [69]. As introduced in Section 2.4 from Chapter 2 and in the introduction of this Section, algorithms based on ANNs have proven to be very powerful tools to detect and solve non-linear problems by minimizing the error of the algorithm output with respect to a known target. Despite that, up to now, most of the algorithms to retrieve SM using GNSS-R data have shown a dependence on the ancillary data (e.g [79]). In our proposed approach, the use of ancillary data has been reduced by adding as algorithm inputs statistical metrics computed from the reflectivity itself, such as the standard deviation of the reflectivity over a set of consecutive samples. The hypothesis to study here is: is there a relationship between the standard deviation of the reflectivity and the surface roughness?

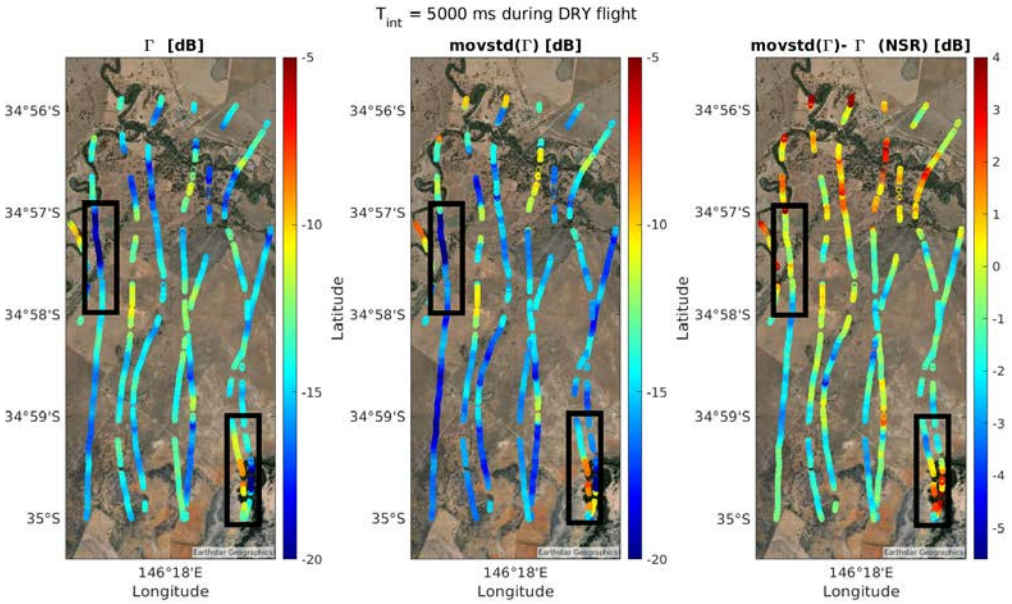

Figure 6.11: Geo-located Γ, movstd(Γ), and NSR, defined as movstd(Γ) - Γ, at T_{int} = 5000 ms or N = 250 at L1 C/A for the "Dry" flight. Black boxes identify areas with reflectivity drops due to vegetated areas and an increase of the surface roughness

6.2.4.1 Surface roughness and reflectivity standard deviation

To address this question, some examples are provided in both "Dry" and "Wet" flights over Yanco site B. The geo-located averaged Γ, and the moving standard deviation (movstd) of Γ are compute and presented in Figs. 6.11 and 6.12.

Both figures present the Γ, averaged to 5000 ms, the movstd(Γ) for the same integration interval. The movstd is calculated in linear units over N reflectivity measurements integrated at 20 ms of incoherent integration time (i.e., for a T_{int} = 5000 ms, N = 250), and then converted into dB units. Finally, the Noise-to-Signal Ratio (NSR), computed as movstd(Γ) minus Γ in dB, is presented in the third column. The color axis is evenly defined for the two flights and each of the three parameters.

As it can be seen in Fig. 6.11, the two highlighted areas present a large decrease of the average reflectivity down to ∼-20 dB. The moving standard deviation is also affected, and the computed NSR in both areas increases. In this case, the increase in this NSR term can be linked to a rougher area, as in the bottom one. In this case, the reflectivity drop is linked to the loss of coherency caused by a vegetated area. However, it is important to remark that the *average* NSR is large: -0.78 dB. As it can be seen, lower NSR values correspond to areas with a larger reflectivity, and a lower reflectivity variation, which can be linked to smoother surfaces.

Moving to the "Wet" flight (Fig. 6.12), the two previously highlighted areas are also shown, plus a third one in the middle of the map. First of all, it is important to remark that the average reflectivity is larger due to the higher soil moisture content of

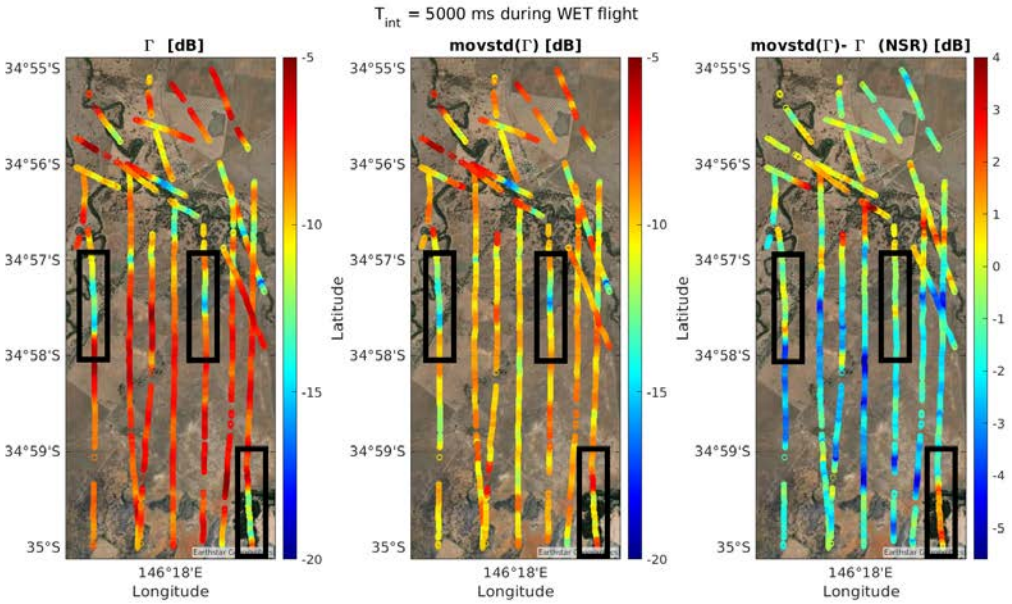

Figure 6.12: Same as in the Fig. 6.11, but for the "Wet" flight.

the flight. Moreover, the NSR is slightly lower than the "Dry" flight: -1.13 dB, and they are converging to the Speckle Noise NSR limit: -5.6 dB (p. 608 from [37]). This noise is the effect of the environmental conditions of the reflection scenario (i.e. surface facets, geometry, etc), and it is a multiplicative noise that can be reduced by low-pass filtering, averaging, or using neural networks [184]. The two selected sites of the "Dry" and "Wet" flights present a similar NSR, ∼1 dB for the top left one, and ∼2-3 dB for the one at the bottom right. Therefore, even though the soil moisture content is different, and the reflectivity value of the "Dry" flight is ∼7 dB lower than the "Wet" flight, the NSR is on the same order, therefore the terrain inhomogeneity is similar in both cases.

Finally, Fig. 6.13 presents a scatter density plot of the reflectivity computed at 20 ms, compared to the NSR computed at 5000 ms, for "Dry" and "Wet" cases, and at L1 and L5 bands. It is important to remark in the regime where the Speckle Noise is dominant (i.e. NSR close to -5.6 dB), the reflectivity tends to its average value, whilst for larger NSR values, the reflectivity displays a much larger variability due to terrain inhomogeneity and surface roughness.

The differences between the "Dry" and "Wet" flights are noticeable. In the "Dry" flight, the contribution from the surface roughness is dominant, and the NSR does not reach the -5.6 dB Speckle Noise NSR limit. On the contrary, for the "Wet" flight, and especially at L5, the NSR presents a larger number of points with NSR lower than -4 dB, with some of the realizations in the -5.6 dB of the Speckle Noise NSR limit. The differences in NSR in both flights are linked to the surface roughness variation depending on the moisture content, and therefore the penetration depth of the incidence wave. The higher NSR of the "Dry" flight indicates a rougher terrain than the "Wet" flight.

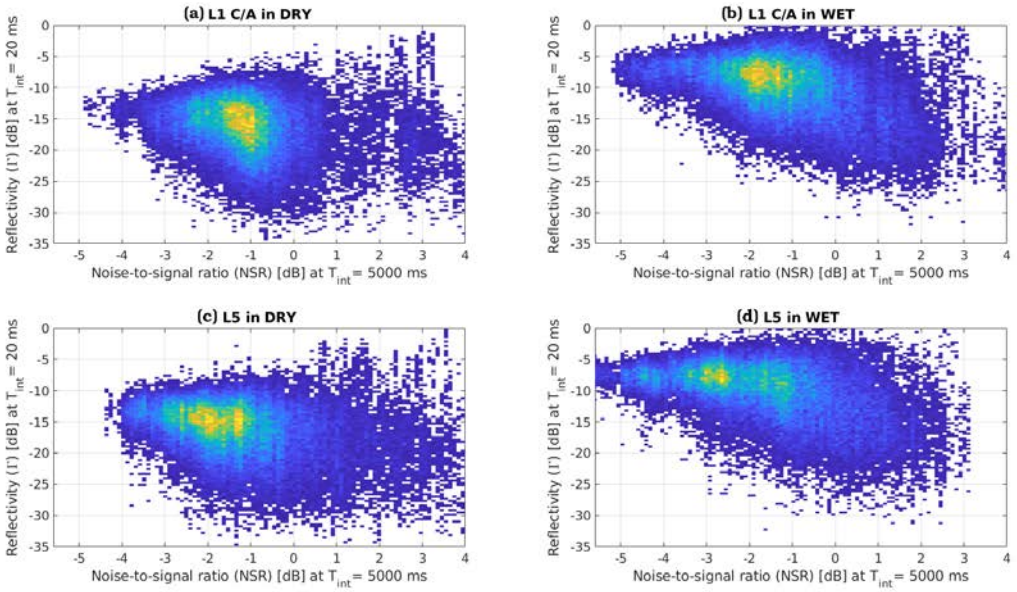

Figure 6.13: Scatter density plot of the NSR computed at T_{int} = 5000 ms with respect to the reflectivity values at T_{int} = 20 ms at L1 for (a) "Dry" and (b) "Wet" flights, and at L5 for (c) "Dry" and (d) "Wet" flights.

Furthermore, the flights at L5 also present a lower NSR than the ones at L1, due to the change in the penetration depth of the L5 signal, and the difference in the auto-correlation function width.

6.2.4.2 Artificial neural networks for SM retrieval

Due to the non-linear behavior of Γ and σ_h in relation to SM, the soil moisture retrieval process does not have an analytical closed-form solution. However, the use of machine learning algorithms, and neural networks in particular, is a growing technique broadly used to solve non-linear problems. In this case, selecting the proper inputs is crucial to accurately retrieve soil moisture. In the previous section it has been shown that the NSR is related to the surface roughness, but as this parameter is computed from the subtraction of movstd(Γ) and Γ, both parameters have been used separately in an ANN algorithm, therefore letting the network to use both parameters independently. To do that, the following ANNs are proposed using the following four cases:

1. Γ, movstd(Γ) as a proxy for σ_h, NDVI, and θ_{inc},
2. Γ, NDVI, and θ_{inc},
3. Γ, movstd(Γ) as a proxy for σ_h, and θ_{inc},
4. Γ, and θ_{inc}.

Furthermore, different integration times (T_{int} = 0.1, 1, 2, and 5 s) are used, and the target output for all cases is the collocated and down-scaled to 20 m SM data from

SMOS/Sentinel-2 described in Section 6.2.1. Finally, the input data is split in two: one network is deployed for L1 data and another for L5 one. Both networks are based on a three hidden-layer feed-forward network with 6 neurons each, and each data set (L1 and L5) is randomly divided into two parts: training and test. The training set is 20% of all the data available for both "Dry" and "Wet" flights, for the two Yanco A and B locations. The test set is the resulting 80%. This training set is the one used to train the network, randomly divided again in 70%,15%,15%, for training, validation, and testing of the network, respectively. In order to avoid neural network overfitting, early stopping and pruning techniques are applied to the trained network [94]. Finally, the results are applied to the overall data set. Note that the entire data set (i.e. both Yanco A and B areas, and all the possible NDVI values) are used in the algorithm to cover a wider reflectivity and terrain variability.

6.2.5 SM retrieval algorithm results

Due to the environmental constraints of the two flights, the SM values of the "Dry" flight and the SM values of the "Wet" flight are quite distant. It is important to remark that the "Dry" flight was conducted after ∼1 month without rain and most of the area is not irrigated. Moreover, during the "Dry" flight SM values from 0.05 m^3/m^3 up to 0.1 m^3/m^3 are found. In contrast, the "Wet" flight was conducted after a strong rain event, and therefore most of the soil is very moist, in this case, values from ∼ 0.26 m^3/m^3 up to 0.33 m^3/m^3 are found.

Figures 6.14 and 6.15 show the scatter density plot of the GNSS-R L1 SM output from the ANN, with respect to the SMOS/Sentinel-2 down-scaled SM. The color axis is the density of points in logarithmic units. Analyzing Fig. 6.14, it can be seen that the information provided by the NDVI increases the R parameter in any case. Moreover, the standard deviation of the error decreases, even without using the movstd(Γ), but the best case is when this parameter is used. For short effective integration times, the R and the standard deviation of the error are slightly worse than the case for longer integration times. As the averaging increases, the estimation of the attenuation due to both the surface roughness and the vegetation are averaged, and the use of the movstd(Γ) increases the correlation between the target and the ANN output. Furthermore, by looking at the shape of the output of the ANN, it can be seen the algorithm fails to recover the SM value, and points falling into the "Wet" area, are "classified" as low soil moisture. This is mostly due to the effect of the reflectivity reduction due to surface roughness. In this case, by increasing the effective integration time (Fig. 6.14 right, $T_{int} = 5$ s), the attenuation is "smoothed" and the algorithm shows a better behavior, showing the lowest error. Finally, it is important to remark that, in the case where the reflectivity is used alone, the ANN output is the least accurate one, clearly indicating that additional information is required to retrieve soil moisture.

Moving to the L5 case (displayed in Fig. 6.15), it can be seen that both the R and the standard deviation of the error are clearly better than in the L1 case. In any of the selected cases, the standard deviation of the error is ∼2-3 times lower than in the L1 case. Furthermore, even with a small averaging (i.e., T_{int} =0.1 s), the dispersion is smaller than at L1. Note that, these results are consistent with Fig. 6.13, where the NSR at L5 was very close to the Speckle Noise limit, indicating that the L5 signal is less affected by surface roughness variations, especially during the "Wet" flight.

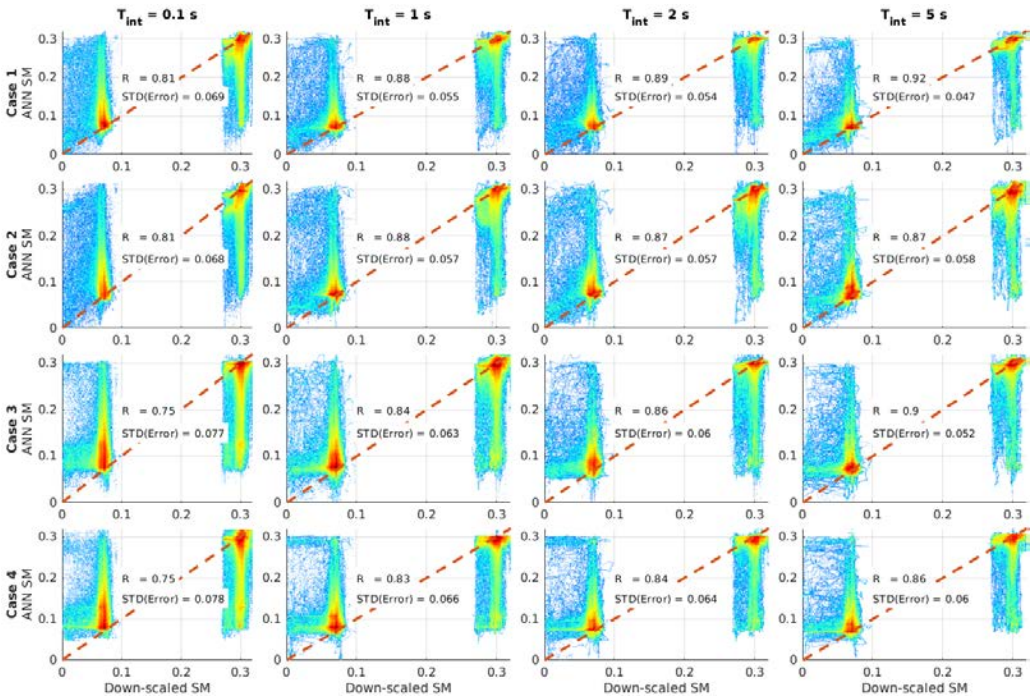

Figure 6.14: ANN estimated SM vs. SMOS/Sentinel-2 down-scaled SM at L1. Columns from left to right increasing T_{int} for 0.1, 1, 2, and 5 s. Row from top to bottom, ANN cases 1 to 4.

As the effective integration time increases, the ANN output shows lower error and a higher correlation coefficient with respect to the SMOS/Sentinel-2 down-scaled soil moisture. Note that errors are drastically reduced for the case with larger averaging, where the standard deviation of the error is very small (e.g., 0.016 m^3/m^3), showing a very low dispersion in both "Dry" and "Wet" flights.

6.2.6 Results discussion

The results presented in this Section show a significant difference between L1 and L5 bands, with a standard deviation of the error at L1 being three times larger than at L5, despite the higher antenna directivity (D_{L_1} = 21 dB, D_{L_5} = 18 dB). This is probably due to the longer wavelength and penetration depth at L5, and by waveform design, a much narrower auto-correlation function (30 m in space) at L5, which translates into a higher spatial resolution. In this case, the peak of the L5 waveform contains contributions from a smaller glistening zone, increasing the coherency of the received signal. On the contrary, the L1 signal has a much larger auto-correlation function (300 m in space), and therefore contributions from a larger glistening zone are added in the L1 waveform, producing larger fluctuations than at L5.

Aside from the difference in frequency bands, there is also a large variability depending on the selected integration time. In order to illustrate it, the same neural network is now

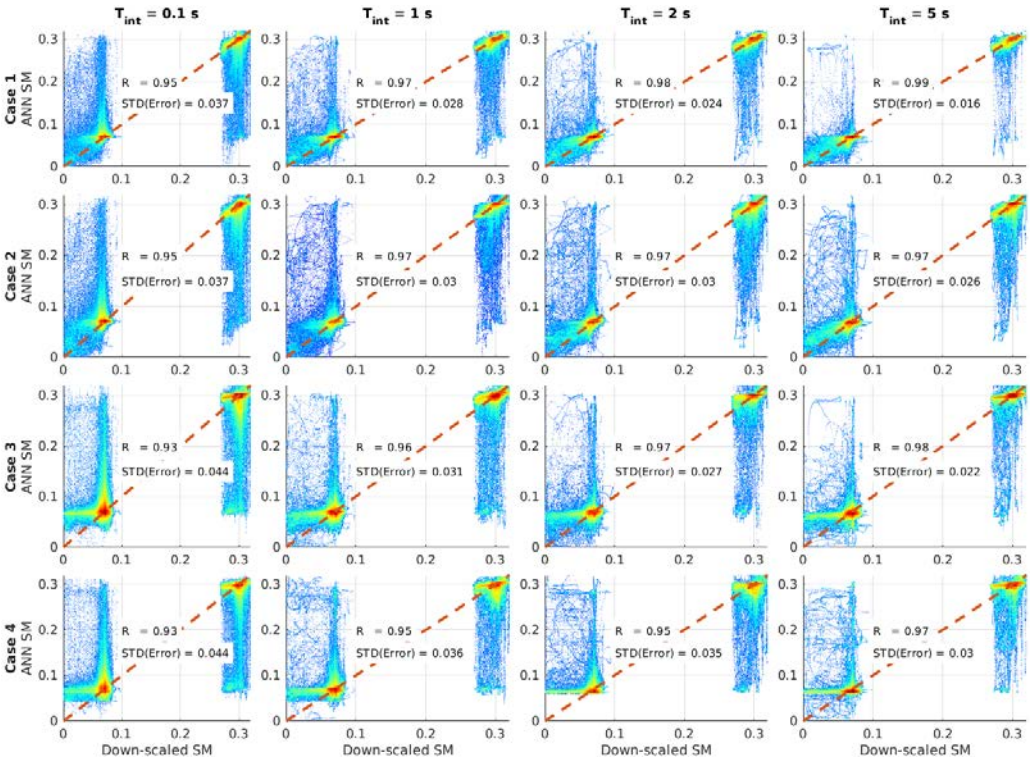

Figure 6.15: Same as in Fig. 6.14, but for L5.

deployed for T_{int} =0.1, 0.5, 1, 2, 3, 4, and 5 s. Results are shown in Fig. 6.16.

Comparing cases 2 and 3 for large integration times, case 3 (i.e., using movstd(Γ)) introduces larger errors than case 2 (i.e., using NDVI), which is not happening for lower integration times (i.e., 2000 ms at L1 and 1000 ms at L5). However, the combined use of the movstd(Γ) parameter together with the NDVI provides the lowest error for all integration times. In this case, as the vegetated areas are quite small (see Fig. 6.3), a very large integration time produces errors, as a T_{int} = 5000 ms is equal to a specular point movement of ∼375 m. However, the lower the integration time, the larger the surface roughness effect. On the contrary, for the smallest integration time, 100 ms, where the plane movement is equal to the size of the first Fresnel zone, case 3 provides the same error as case 1, and a much smaller error than cases 3 and 4. Thanks to the over-sampling in the along-track direction, several measurements of speckle noise and surface roughness are included in the recovery algorithm by means of the movstd(Γ) term. However, for longer integration periods, e.g. T_{int} =2000 ms, the signal covers up to ∼15 Fresnel zones (i.e., v_{plane}=75 m/s, and l_{Fz} ∼10 m). The terrain inhomogeneity while crossing these areas together with the presence of different vegetated areas induces errors in the retrieval algorithm, which can only be corrected using the NDVI.

By looking to the evolution of the log-log plots in Figs. 6.16c and d, a linear trend is easily identified. For the L1 case, the slope of the log-log curves is -0.04 and -0.06 for cases 2 and 4 (without NDVI), and -0.1 for cases 1 and 3 (using NDIV). For the L5 case, the

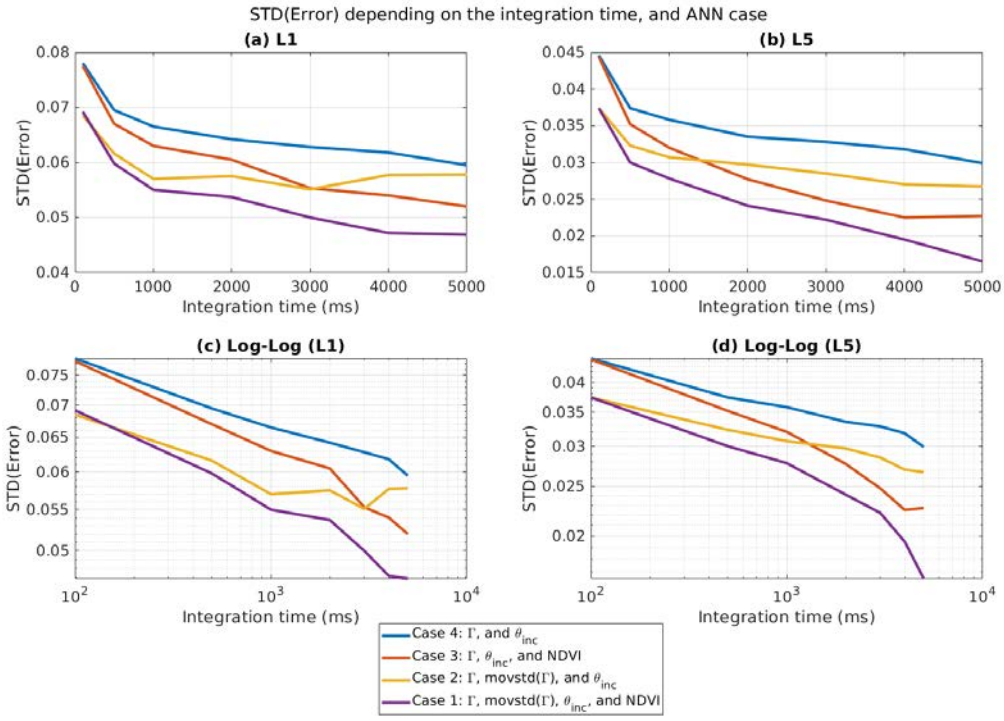

Figure 6.16: Standard deviation of the error of the ANN with respect to Sentinel-2/SMOS downscaled soil moisture for the four different cases for different integration times, at (a) L1, (b) L5, (c) L1 using a log-log plot, and (d) L5 using a log-log plot.

slope of the curves is -0.08 and -0.09 for for cases 2 and 4 (without NDVI), and -0.19 and -0.18 for cases 1 and 3 (using NDVI). The use of NDVI in combination with reflectivity measurements allows to produce a more precise SM product when increasing the N value (i.e., the integration time for the reflectivity values) to compensate the surface roughness estimations.

It is clear that there is a trade-off between spatial and radiometric resolution, where it is not possible to achieve a good radiometric resolution and low root-mean-square error of the retrieved parameter, and good spatial resolution at the same time. As shown in Fig. 13 from [79], the standard deviation of their spaceborne GNSS-R SM retrieval algorithm is decreased to $\pm 0.1 \mathrm{m}^3/\mathrm{m}^3$ when more than 25 averages are performed, and the smaller the number of averages, the larger the error, and hence the worse the radiometric resolution.

As shown in this study, when increasing the integration time, and therefore lowering the spatial resolution, the standard deviation of the error decreases, but effects due to terrain changes in the along-track direction of the GNSS-R measurement induce errors that need to be corrected for using NDVI measurements. On the contrary, reducing the averaging leads to a much higher resolution, and the NDVI term is not providing additional information to the ANN algorithm. However, the standard deviation of the error at such low integration times is larger.

Just to remark that the radiometric and the spatial resolutions cannot be optimized at the same time, and there will always be a trade-off (if no ancillary data is used) between the *required* SM error, and the spatial resolution of the GNSS-R-derived SM product.

6.3 Vegetation Canopy Height Retrieval using GNSS-R

In the previous section, the movstd(Γ) has been used to estimate and compensate the surface roughness effect. This is valid for those places with low vegetated areas (i.e., areas with low CH). As highlighted in Fig. 6.11, dense vegetated areas produce an additional attenuation on the GNSS-R signal, as modeled in Eq. 6.1 through the γ parameters (i.e., vegetation transmissivity). This parameter is usually modeled through the VOD or indirectly through the NDVI [163]. However, different studies have pointed out the relationship between GNSS-R measurements and AGB or CH [63,64,70,166], which is the last unknown to be solved for Eq. 6.1 without making use of ancillary data from other sensors.

6.3.1 Waveform widening due to canopy height

The widening of the trailing edge shown in [64] is a direct consequence of multiple wavefronts being scattered and then incoherently averaged in the receiver. As it is explained in [106], and then used in [64], this trailing edge widening is due to the reflection over two nearby surfaces, as it is detailed in Fig. 6.17. Applying the analysis of the simulation presented Section 5.3, if CH is larger than half the width of the ACF (i.e., CH larger than 150 m for GPS L1 C/A and larger than 15 m for GPS L5), the two reflections would cause two "peaks" in the retrieved waveform. For the GPS L1 C/A case, the two reflections are incoherently averaged into a single peak, as CH is normally below $\sim$40 m. However, higher bandwidth GNSS signals, such as the GPS L5 or the Galileo E5a/E5b signals, have a much narrower ACF, around $\sim$30 m in space, 10 times smaller than the GPS L1 C/A signal. Thus, thanks to the narrower ACF, multiple reflections coming from the glistening zone can be eventually captured, and the waveform may exhibit in some cases multiple peaks.

6.3.2 Data Description and study region

The vegetation effect is almost negligible in Yanco areas, as seen in Fig. 6.5, there is only a small amount of specular points falling into vegetated areas. In addition, those areas are not very dense, and with a small CH. For that reason, a few transects of the MIR flight over the Bass Strait have been selected. Although the objective of the flight was to cover the ocean, as seen in Chapter 5, it also entered the main land. In particular, the airplane flew over the "Croajingolong National Park", which is entirely covered by rainforest. Figure 6.18 presents two selected GNSS-R tracks at L1 and L5 over the rainforest area.

The characteristics of this flight are detailed in Section 5.1 of Chapter 5. In this case, the incoherent integration time has been tuned to enhance the SNR received just in the re-tracking limit discussed in Chapter 3. Thus, the GNSS-R data is processed with an incoherent integration time of 100 ms. Recall that, for this flight, the size of the first Fresnel zone is $\sim$30 m, and the incoherent integration time has been limited to prevent any waveform blurring.

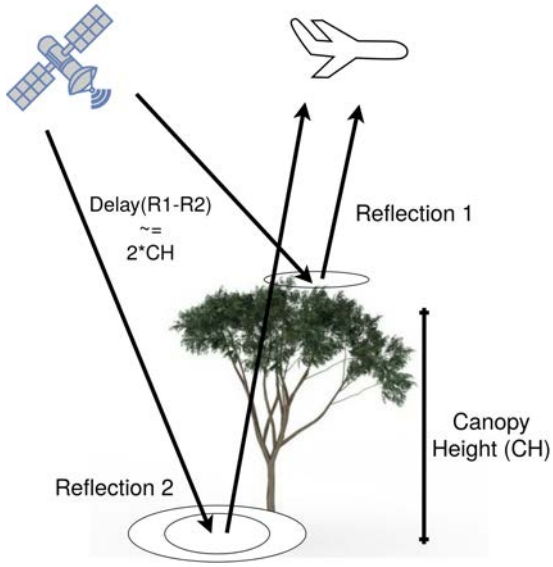

Figure 6.17: Scheme of a GNSS-R reflection over rain-forest vegetation.

The vegetation information used to compare the GNSS-R retrieved by MIR is detailed in Fig. 6.18. The product is the the Global Forest Canopy Height (GFCH) from the Global Land Analysis and Discovery [185]. This product provides a very fine spatial resolution of 30 m, and it is generated from the combination of LIDAR and multi-spectral data. Note that, the CH information is linked to both VOD and AGB products, as it is shown in [186]. Thus, this high-resolution product has been selected to demonstrate the capabilities of GNSS-R to retrieve a high-resolution vegetation product. The GFCH product is 2D linearly interpolated into the specular point positions, providing a total amount of 981 points for the L1 case, and 1655 for the L5 case.

6.3.3 Waveform analysis

The reflection in different layers of the canopy produces two phenomena. First, the dispersion produced by the scattering in different vegetation layers, which causes depolarization. Second, the attenuation of the reflected signal caused by the VOD. As it has been shown in Figs. 3 and 22 from [124], the AGB and the VOD are highly correlated. In the GNSS-R case, it has been shown in previous studies that the trailing edge of the L1 GNSS-R waveform is also correlated to the AGB [64]. Thus, this metric can be used to estimate the AGB rather than using the VOD.

Figure 6.19 presents two examples of GPS L1 C/A waveforms retrieved by MIR over the rainforest. As it can be seen, the width of the two waveforms (WF) varies. In Fig. 6.19a, the CH in the surrounding area is ∼13.2 m, and the WF width is ∼280 m, while for Fig. 6.19b, the CH is ∼30.8 m, and the WF width is ∼397 m. In this case, the WF width threshold is set at $1/e$ [187], assuming the waveform is re-scaled between 0 and 1. To have a better precision estimating the actual width, the WFs are re-sampled at 128 MS/s (2.3 m delay-bin size) from the initial 32 MS/s (9.4 m delay-bin size) value using a Fourier

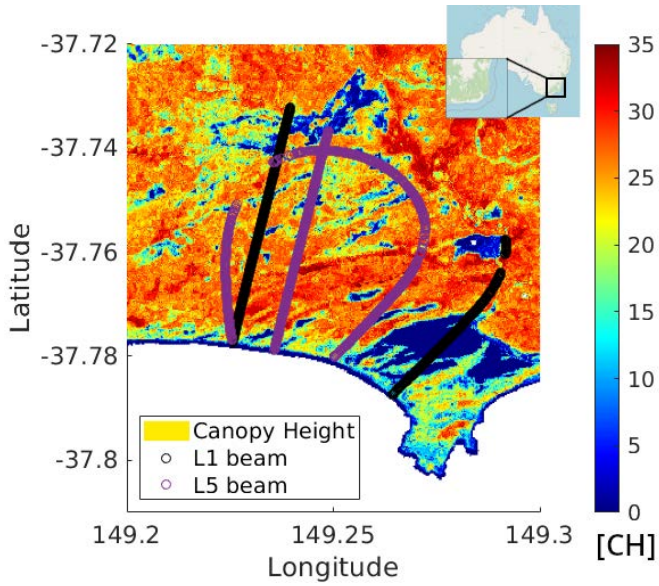

Figure 6.18: L1 and L5 MIR specular reflection point location overlaid by the CH map retrieved from GFCH [185].

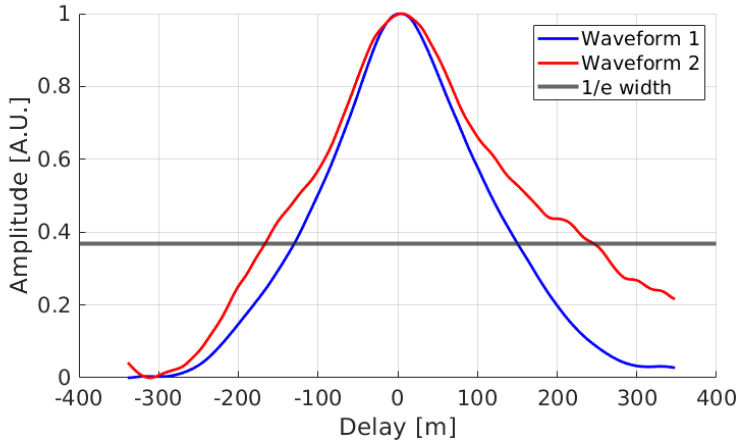

Figure 6.19: GPS L1 C/A waveform examples. The waveform 1 (in blue) with a ground-truth CH of ∼13.2 m, producing a WF width of 280 m, and the waveform 2 (in red) with a ground-truth CH of ∼30.8 m, producing a WF width of ∼397 m.

optimum interpolation method [159].

For the GPS L5 case, two situations may occur. In the first case, due to the reflection geometry, the delay between the two reflections might be lower than 30 m (i.e., a CH lower than 15 m), thus two "reflections" are merged in a single peak, as shown in Fig. 6.20a. On the contrary, if delay between the two reflections is larger than 30 m (i.e.,

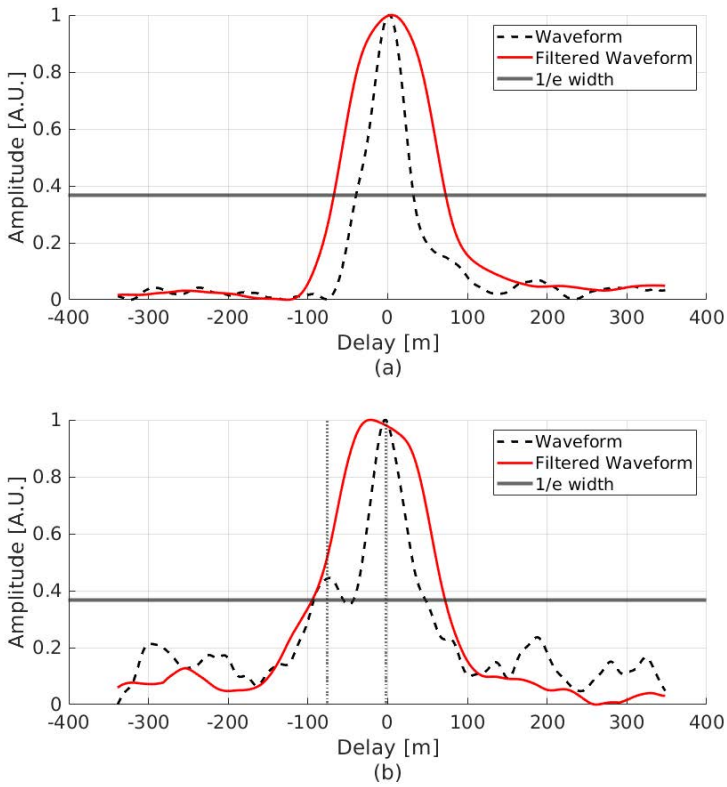

Figure 6.20: GPS L5 waveform example before (dashed in black) and after (line in red) low-pass filtering, (a) with a ground-truth CH of ∼14.1 m, and a WF width of ∼70.9 m before filtering, and ∼116.3 m after filtering; and (b) with a ground-truth CH of ∼31.0 m and a peak-to-peak WF distance of ∼73 m before filtering, and a WF width of ∼173.9 m after low-pass filtering.

CH larger than 15 m), two peaks will show up in the retrieved waveform, as shown in Fig. 6.20b. In the first case, the WF width is ∼70.9 m for CH ground-truth of ∼14.1 m. In the second case, two peaks can be easily identified, showing a distance ∼73 m, for a CH ∼31.0 m. If the peak-to-peak distance is directly translated to infer the CH (i.e., by dividing it by two), the estimated CH is ∼36.5 m. Upon initial inspection, the GPS L5 waveform looks limited by CH lower than 15 m. However, this secondary peak effect may also appear from other reflections coming from other areas of the glistening zone, and not necessarily from just the canopy and the soil, as it occurs in the ocean case (Section 5.3).

The first case (i.e., the waveform is blurred due to multiple reflections) occurs more than 50% of the measurements while having two differentiated peaks occurs in less than 20% of the waveforms. The remaining 30% of points present an almost negligible secondary peak, with a very small "bump". Hence, in order to use the same criterion to compare the L5 waveforms with the CH, all waveforms are low-pass filtered along the X-axis to blur it and combine the two peaks that may appear. The filter used is a 51-sample moving average over the re-sampled WF, which corresponds to 0.4 us at 128 MS/s. The

number of samples of the filter is heuristically selected to provide the larger correlation coefficient with respect to the CH, as detailed in the next section. In this way, nearby reflections are "integrated" into the main lobe. As seen in Fig. 6.20 (in red), the L5 waveform looks now similar to the L1 waveform, but with a narrower width.

Thanks to the waveform filtering applied, all GPS L5 reflections will now contain valuable information to estimate the CH. Note that, in the methodology proposed in this work, both the leading and the trailing edges are taken into account by looking at the waveform width when it has decayed to $1/e$ [187]. As it is seen, even though the waveform has been blurred, the peak width is 3-5 times smaller than the GPS L1 C/A.

6.3.4 Estimated waveform width and canopy height

For GPS L1 C/A, the waveform width at $1/e$ has been retrieved for all points presented in Fig. 6.18, the CH information is 2D linearly interpolated to the specular point location, and then compared as shown in Fig. 6.21a. The Pearson correlation coefficient (R) is computed to compare both magnitudes. Moreover, a regression fit is also computed and overlaid in all figures. As it is shown, the correlation between both variables is very low $R \sim 0.39$.

The results for GPS L5 are presented in Fig. 6.21b, and the same robust least square regression fit is applied. In this case, the correlation coefficient between both variables is $R \sim 0.43$, slightly larger than the GPS L1 C/A case, but still low.

6.3.5 Reflectivity and canopy height

The reflectivity of the GNSS-R signal collected by MIR is retrieved as explained in Section 6.2.1. Aside from its correlation with the SM and the surface roughness, this magnitude has also been proven to have a correlation with the VOD, the AGB, and the CH [63, 70, 166]. Note that, for this study the SM content and the surface roughness are assumed invariant within the region under study. In Fig. 6.22, the relationship between the CH and the reflectivity value is presented. In this case, the correlation coefficients are $R \sim -0.29$ and $R \sim -0.49$, for GPS L1 and GPS L5 cases, respectively. This result is consistent with the results presented in [63], where a negative correlation between both magnitudes is shown. However, the reflectivity correlation at L5 is significantly larger than L1. Note that, reflections at L1 range an incidence angle ∼14-28º, and L5 reflections range an incidence angle ∼36-48º.

6.3.6 Canopy height retrieval algorithm

Data-driven algorithms such as ANNs have been broadly used in GNSS-R to relate several magnitudes with a moderate correlation to provide a meaningful product. In our case, the WF width and the reflectivity are correlated with the CH magnitude, especially at L5. To address this problem, three ANNs are proposed per band (three for L1, and three for L5). The network topology is the same for all four cases, a 3-layer hidden network with 6, 9, and 6 neurons. All neurons use the *sigmoid* transfer function. The data set is split in 40% for training, 15% for validation, and finally 45% for testing. In all cases, the early stopping (30 epochs), and the network pruning processes are used to avoid ANN over-fitting [94]. For both bands, the three different networks are implemented.

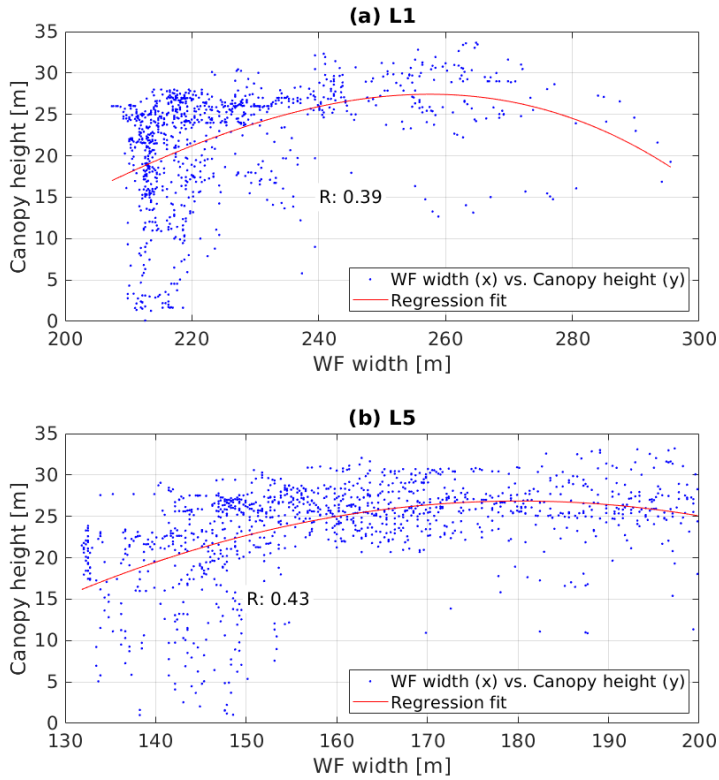

Figure 6.21: Scatter plot and robust least squares fit between the WF width and the CH for (a) L1, and (b) L5.

The first network uses the WF width as the single input. The second network uses the reflectivity and the reflection incidence angle as inputs, and the third network uses all three magnitudes.

Figure 6.23 presents the results of the ANN, and the data retrieved is compared to the CH ground truth from GFCH. In the left column, the network results at L1 are presented, and in the right column those at L5. As it can be seen in the first row of Fig 6.23, the network can "fit" the WF width data to the ground truth. However, the R and the RMSE show that the network is failing at some point. In particular, all those points where the CH is smaller than $\sim$ 16 m are not correctly fitted. In the L1 case, the R is 0.48, and the RMSE is 5.9 m, while for the L5 case the R is 0.51, and the RMSE 5.1 m. However, the data points with a lower CH are those providing larger reflectivity values, which indicates that the reflection is taking place on the ground (bare soil).

In the second row, the reflectivity and the incidence angle, θ_{inc} are introduced to the network and compared to the CH ground truth. In both L1 and L5 cases, the ANN performs well, showing a good correlation to the CH product. In the L1 case, R is 0.75 with an RMSE of 4.4 m, while in the L5 case, R is 0.76 with an RMSE of 3.9 m. Similarly to the WF width case, the L5 signal presents a lower RMSE than the L1 signal.

The third row presents the results of merging both data sets. In both cases, the R has

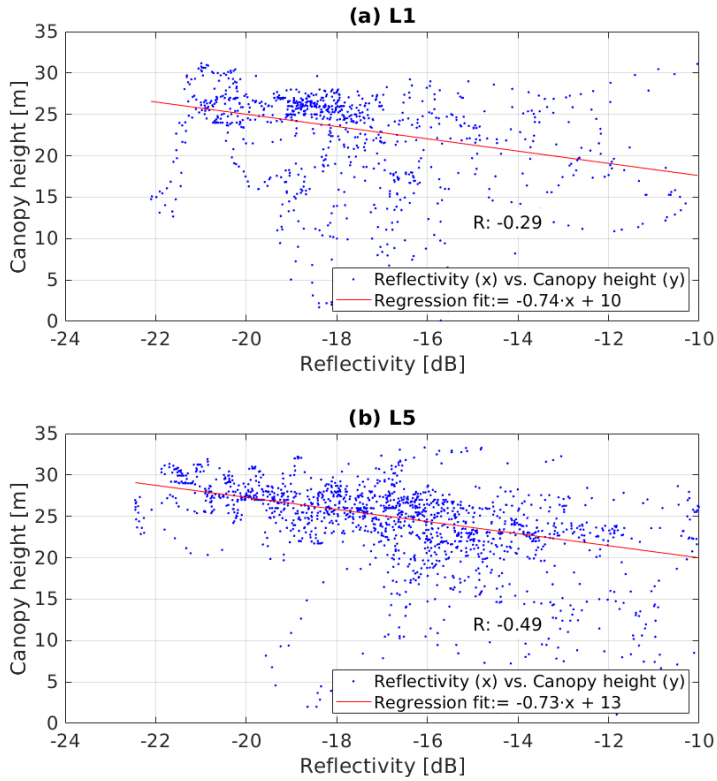

Figure 6.22: Scatter plots and robust least squares fit between the reflectivity (Γ) and the CH for (a) L1, and (b) L5.

significantly improved to 0.84, with an RMSE of 3.6 m and 3.2 m, respectively for the L1 and the L5 cases. The use of the WF width data combined with the reflectivity allows recovering CH at both L1 and L5 bands. In this case, the results are slightly better using L5 data, which is capable to retrieve CH down to zero, while at L1, the minimum CH is ∼8-10 m due to the longer C/A signal chip.

Finally, Fig. 6.24 presents the time evolution of both the GFCH ground-truth and the ANN estimation of the CH. As it can be seen, the algorithm using L1 data performs slightly worse for lower CH values, showing a RMSE of ∼6.27 m for CH lower than 15 m. In the L5 case, the RMSE for CH values lower than 15 m is ∼6 m. Analogously, for CH values larger than 15 m, the RMSE is 3 m and 2.65 m, respectively for L1 and L5 bands, and for CH values larger than 10 m the RMSE is 3 m and 2.85 m, respectively for L1 and L5 bands. Thus, GNSS-R is able to estimate CH with a good agreement with the GFCH product for CH values larger than 10 m. It is worth to mention that other approaches to retrieve CH, such as the Polarimetric SAR that will be used in ESA's BIOMASS mission [188], are targeting accuracies on the order of 30% of the CH for CH values CH larger than 10 m (i.e., 9 m for a CH of 30 m, 3 m for a CH of 10 m).

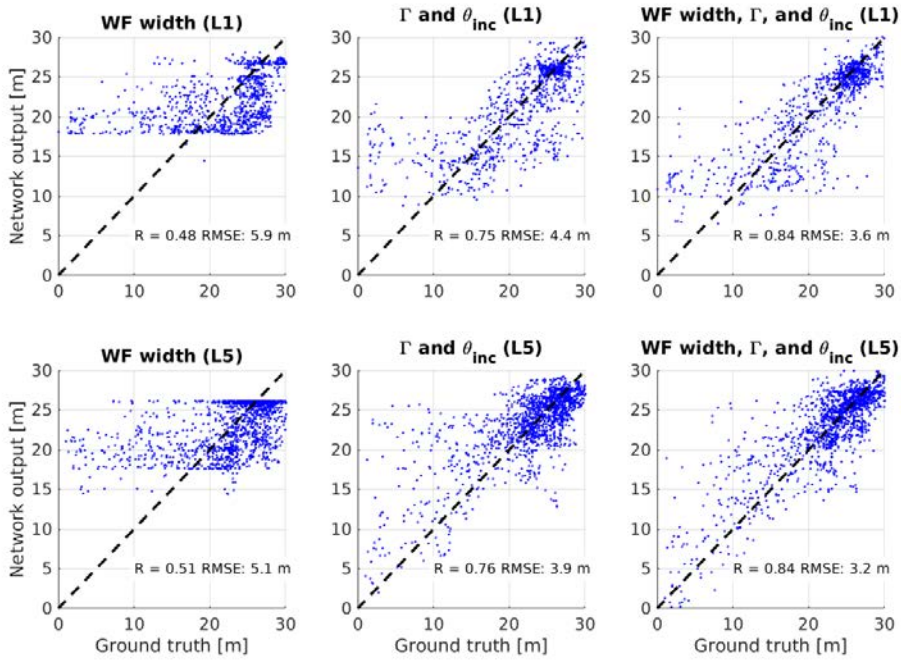

Figure 6.23: Scatter plots showing the relationship between the network output and the CH ground-truth for the three cases at L1 and L5.

6.4 Conclusions

In this Chapter, two algorithms to retrieve SM and CH using GNSS-R data have been proposed.

In the first case, data collected by the MIR instrument during two flights ("Dry" and "Wet") over the OzNet Yanco sites in New South Wales, Australia, during May-June 2018 have been analyzed. The effect of increasing the averaging and its impact on the surface roughness estimation are addressed, showing that the effective integration time has to be increased up to 5 s (up to 250 reflectivity measurements incoherently integrated during 20 ms) to neglect surface roughness effects. A statistical parameter based on the moving standard deviation over N samples of the reflectivity (movstd(Γ)) has been presented as a proxy of the surface roughness effects when the averaging (N) is large enough. Finally, an ANN-based algorithm has been presented for different combinations of auxiliary data and reflectivity averages, for L1 and L5 cases. In both cases, the use of the movstd(Γ) parameter reduces the error of the retrieved SM to 0.047 m^3/m^3 and 0.016 m^3/m^3 at L1 and L5 respectively, for a $T_{int} = 5000$ ms. Furthermore, the L5 signal shows a larger correlation coefficient with the expected SM output than the L1 signal because of the higher penetration depth, and the narrower auto-correlation function.

In the second case, the correlation between CH and MIR L1 and L5 GNSS-R WF width and reflectivity is analyzed. It is presented that some L5 waveforms exhibit multiple peaks. However, this is not always the case, as it depends on the geometry and the CH

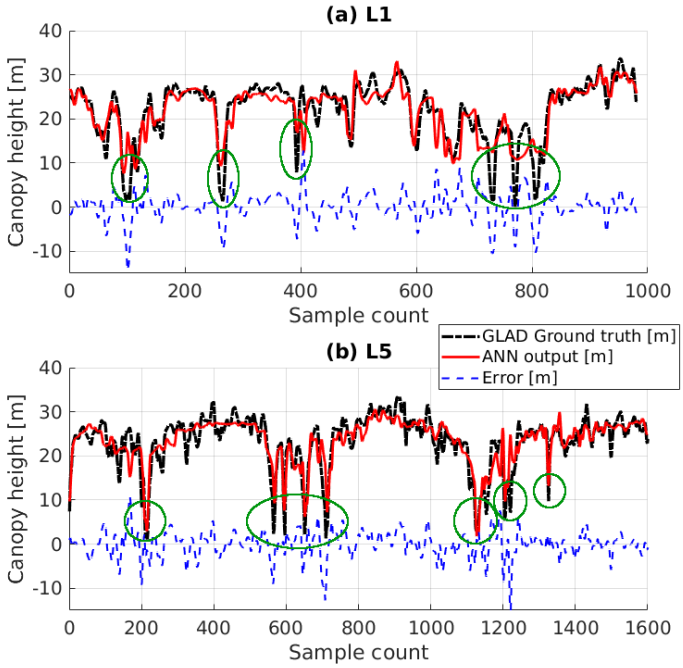

Figure 6.24: Time evolution of the canopy height, comparison between the GFCH ground-truth and the ANN estimation for (a) L1 with a bias of 0.16 m and an RMSE of 3.6 m, and (b) L5 with a bias of -0.06 m and an RMSE of 3.2 m.

itself. A moving-average low-pass filter is proposed to "join" both peaks, resulting in a waveform similar to those retrieved at GPS L1 C/A. It has been shown that both the WF width data and the reflectivity data are correlated to the CH data, and an ANN algorithm is proposed to "merge" the data sets to retrieve CH, showing a RMSE with respect ot the CH ground truth of 3.6 m at L1 and 3.2 m at L5. This improvement comes from two factors, first and most important one the ACF width at L5 is ten times narrower than the one at L1. Second, the difference in the wavelength at L5 allows the signal to penetrate slightly more into the dense canopy, thus being less affected by the vegetation attenuation. In this case, the accuracy of the CH product that is retrieved by the combination of WF widths and reflectivity measurements can be comparable to the expected accuracy of ESA's BIOMASS mission, but at a reduced cost using GNSS-R data.

In both studies, it is clear that the enhanced spatial resolution and slightly higher penetration depth allows for better recovery of either SM or CH. This clearly points out that the use of higher bandwidth and the use of GNSS signals located at the lowest part of the spectrum is the future of GNSS-R instruments.

7

Chapter 7

Ground-based GNSS-R in the Arctic Ocean: the MOSAiC field experiment

This Chapter explains part of the GNSS-R field experiment conducted in the Arctic Ocean as part of the MOSAiC expedition [189]. The development of this experiment has been performed in collaboration with the Institut d'Estudis Espacials de Catalunya (IEEC), the Institute of Space Sciences (ICE/CSIC), and the UPC NanoSat-Lab. The contents presented in this Chapter have been adapted from the peer-reviewed journal entitled "Snow and ice thickness retrievals using GNSS-R: Preliminary Results of the MOSAiC experiment" [JP1]. Moreover, this work has also been presented at an international conference [CP7].

The Chapter is organized as follows: Section 7.1 makes a short introduction of the MOSAiC campaign. Section 7.2 describes the PYCARO-2, the GNSS-R instrument developed and operated to conduct this campaign, the setup in the ice floe, and the ground-truth data used to analyze and validate the instrument measurements. Section 7.3 describes the theoretical background of the Interference Pattern captured by the instrument, which is modeled using a four-dielectric layer model composed by air, snow, sea-ice, and saline water. Section 7.4 describes the data collected during January 2020 and its comparison with the presented model. Section 7.5 presents the results of the algorithm applied for the entire data set. Finally, Section 7.6 concludes the chapter highlighting the main results of PYCARO-2.

7.1 Introduction

The GNSS signals produce a coherent reflection over the ice [32], that allows to precisely determine the ice edge [120]. Other studies have shown the potential of GNSS-R measurements to infer sea ice thickness, when the scattering is coherent and the complex reflected signals are downloaded to ground [190, 191], based on the reflection between the sea ice and the sea water underneath. However, this hypothesis has not been confirmed by in-situ measurements, as sea ice thickness has been only retrieved at L-band by radiometers [29, 31].

To further validate these hypothesis, the PYCARO-2 instrument (presented in Fig. 7.1), an evolved version of PYCARO [105], has been designed to take part on the MOSAiC expedition [189, 192], the largest campaign ever aiming to study the Arctic Ocean.

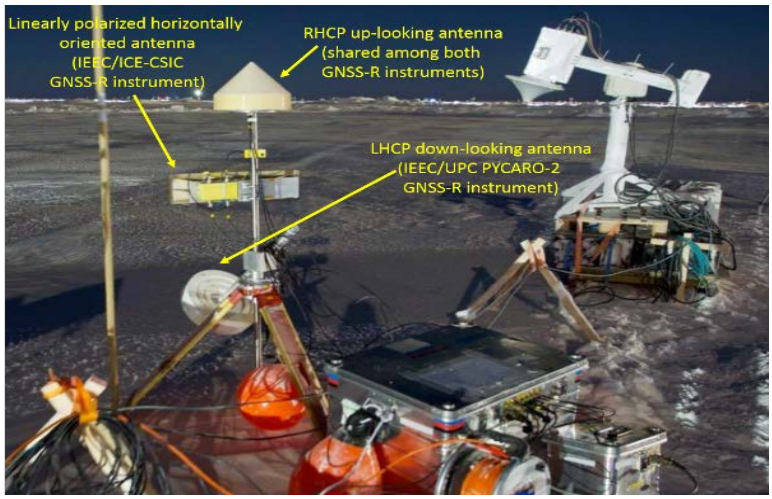

Figure 7.1: IEEC's GNSS-R instruments: IEEC-ICE/CSIC GNSS-R instrument is formed by the zenith antenna and by the 5x1 patch array pointing to the horizon. IEEC/CTE-UPC GNSS-R instrument is formed by the zenith antenna and the 45º incidence angle LHCP antenna. Credits: Gunnar Spreen.

The objective of MOSAiC was to understand the evolving Arctic climate system and the role it plays in changing the global climate. MOSAiC was a multidisciplinary campaign to study the Arctic Ocean from different points of view, and involving different teams: Ice, Ocean, Atmosphere, Ecology, Bio-geochemical systems, Satellite Remote Sensing, Modeling, and Aircraft teams. Most of them deployed a large suite of sensors to measure different parameters, such as ice thickness evolution, snow properties, the topography beneath the ice floe, etc. Most of the instruments run for over a year on top of a drifting ice floe. The diversity of simultaneous measurements and the extension of the campaign in time makes it an exceptional opportunity to cross-check and use the data retrieved as model validation for other sensors such as scatterometers, GNSS-R or radiometer sensors on satellites. Here, we will focus on the MOSAiC remote sensing site and its ancillary measurements, which include:

- Three Remote Sensing Sites (alternating measurements every 2-3 weeks), with the

following instruments: L-, C-, X-, Ka-, and Ku-band microwave scatterometers, P- to L-band, C-, X-, Ku-, K-, and W-band microwave radiometers, IR and hyperspectral cameras, and two multi-constellation and multiband GNSS-R instruments. The GNSS-R instruments (Fig. 7.1) are part of a joint effort from the IEEC, the ICE/CSIC, and UPC IEEC sections.

- Regular transects (1 km length over different sea ice types) to measure total sea ice thickness, snow depth and density, Ku- and Ka-band radar backscatter, L-band radiometry, and additionally surface albedo with the returning insolation from spring onwards.
- Other ice, snow, ocean, and atmospheric measurements.

7.2 Instrument Description and Experiment Setup

The GNSS-R instruments belonging to the Remote Sensing site are divided in two. One of them is the ICE/CSIC instrument, which is a GNSS-R instrument working at linear polarization to collect the reflected signals off the sea ice. Its aim is to provide sea ice properties from scattered GNSS signals. The other one is the IEEC/UPC instrument (named PYCARO-2), which operates at LHCP, and aims to support the reflectivity modeling activities in support for instruments embarking a LHCP antenna, as the MIR instrument, the SGR-ReSi on board TDS-1 or CyGNSS [193], or the FMPL-X instruments presented in Chapters 8, 9, and 10.

The ICE/CSIC instrument and the PYCARO-2 GNSS-R are sharing a common power and data interface, physical enclosure, and the RHCP antenna used to time tag and geo-reference the data collected by the instrument. The primary goal of both GNSS-R instruments is to provide ground-truth data for reflection modeling, and to validate the possibility of GNSS-R to retrieve sea ice thickness measurements. This Chapter is only focused on the data retrieved by the IEEC/UPC PYCARO-2 instrument [194].

7.2.1 Circular polarization GNSS-R instrument

PYCARO-2 is an evolved version of the PYCARO instrument, which was the first GNSS-R instrument collecting polarimetric reflected Galileo signals from a stratospheric balloon (Bexus 19 in 2014 [106]). PYCARO was also the payload of the UPC ^{3}Cat-2 CubeSat [99]. PYCARO-2 is enclosed into an aluminum case (Fig. 7.2). Moreover, as compared to the first version of PYCARO, PYCARO-2 includes the Beidou constellation. Together with the instrument, a control software has been developed to operate the PYCARO-2 instrument while deployed in the MOSAiC campaign. Further details of this software and the necessary operations to manage PYCARO-2 are detailed in Appendix A.

The down-looking antenna of the instrument is composed by a LHCP choke-ring antenna, tilted 45^o downwards to maximize the power of the reflected signals, as most GNSS satellites reach $\sim$50^o elevation angle in polar regions. The antennas have a very smooth radiation pattern (Fig. 7.3a), and their configuration (height and pointing) can be seen in Fig. 7.3b.

The instruments were shipped to Tromsø, Norway, on July 2019, from where the Polastern icebreaker carrying the MOSAiC expedition departed on 20 September, 2019.

Figure 7.2: PYCARO-2 instrument enclosed inside its aluminum box.

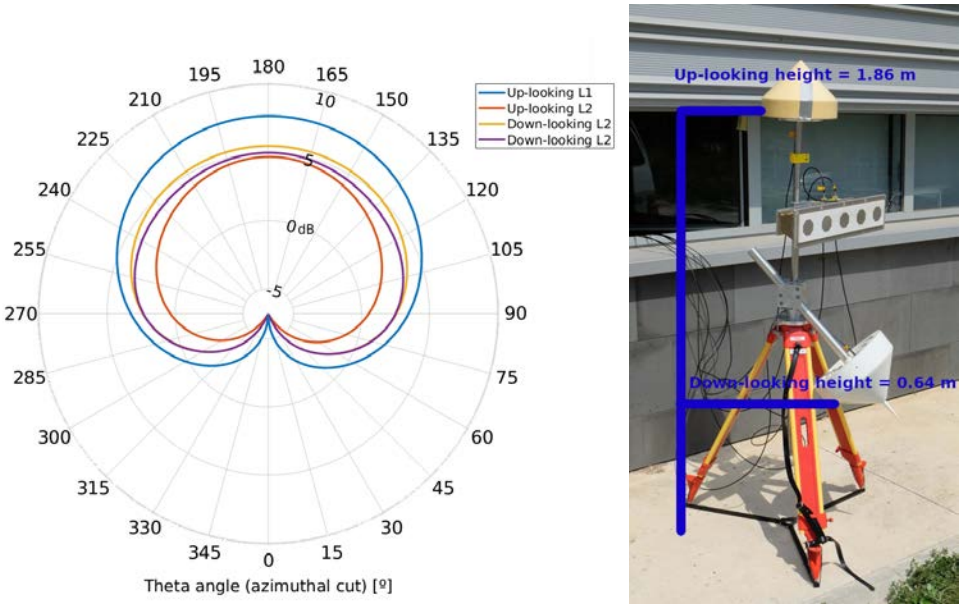

(a) **(b)**

Figure 7.3: (a) Up-looking and down-looking antenna pattern, and (b) antenna distribution and heights of each antenna.

The Remote Sensing site was set up during October 2019, and the instruments were successfully installed on 24 October, 2019 (Fig. 7.4a). Despite being installed on October, several ice cracks (Fig. 7.4b) during November and December forced a relocation of the Remote Sensing site, including the PYCARO-2 instrument. The final location of the

(a) **(b)**

Figure 7.4: (a) MOSAIC Remote Sensing site with GNSS-R instruments (yellow arrow), and (b) MOSAiC ice cracks during November-December 2019. Credits: Gunnar Spreen and Stefan Hendricks.

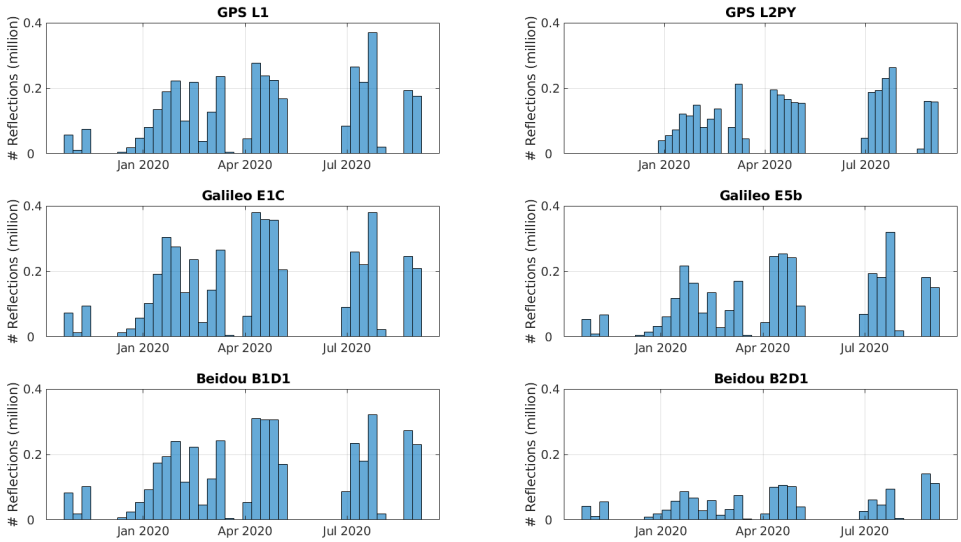

Figure 7.5: Histograms detailing the number of reflections collected for GPS (L1 and L2), Galileo (E1 and E5b), and Beidou (B1D1 and B2D1).

instrument for the winter season was set in late December 2019. This location was set from the 21 December 2019 to the 5 May 2020, where due to the 2020 COVID Pandemic the instrument was removed from the ice core to foresee a resupply operation to Norway. Then, the instrument was mounted again the 30 June 2020 to the 30 July 2020, and finally, the instrument was operated again from the 24 August 2020 to the 5 September 2020. The detailed dates of execution and the estimated amount of reflections collected are summarized in Fig. 7.5, and the position of the instrument in the different time instants is detailed in Fig. 7.6. Furthermore, the total amount of reflections captured during the entire campaign are summarized in Table 7.1.

Table 7.1: Amount of reflections captured by PYCARO-2 during the MOSAiC campaign.

Signal type	Number of reflections (millions)
GPS L1	3.85
GPS L2	3.32
Galileo E1C	4.76
Galileo E5b	3.22
Beidou B1D1	4.22
Beidou B2D1	1.43

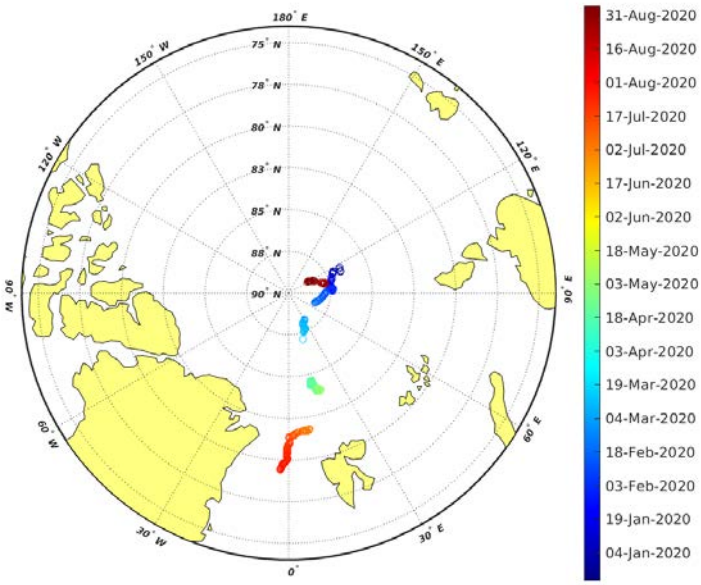

Figure 7.6: Time evolution of the MOSAiC Circular Polarization GNSS-R instrument in the Arctic Ocean during the expedition.

7.2.2 Ground-truth data

In the vicinity of the GNSS instrument, different types of measurements were collected of both snow depth, and sea ice thickness. Measurements were repeated every few weeks using the combination of a Magnaprobe snow probe and a broadband electromagnetic induction sensors (Geophex GEM-2). The Magnaprobe was used to retrieve snow thickness, with a precision better than 1 cm [195]. The GEM-2 was used to measure the combined thickness of the snow and the sea ice, as described by [196]. Finally, both measurements are combined to retrieve snow and sea ice thickness separately. In this study, we use the quick-view GEM-2 thicknesses based on the 18 kHz in-phase channel and processed directly on-board, and quality controlled against manual drill-hole observations.

We chose this channel out of the available frequency set of the GEM-2 for optimal retrieval of sea ice thickness with an accuracy better than 10 cm. In addition to the Magnaprobe measurements, a Distributed Thermistor Chain (DTC) sensor was also present near the instrument, providing an estimate of snow and ice thicknesses. The RMSD between the avalanche probe and the DTC sensor for the snow thickness is ∼2.3 cm.

The snow depth was also measured using an avalanche probe in the area surrounding the GNSS-R instrument mast. Figure 7.7a shows the evolution of the mean and standard deviation of the snow thickness in the area surrounding the GNSS instrument. Fig. 7.7b shows a broad distribution of snow depths as a PDF and points to a highly inhomogeneous snow surface, with developed snow dunes in two different time instants (blue, 12 January, 2020, and green, 7 February, 2020). Finally, Fig. 7.7c shows the PDF of the sea ice thickness measurements. Note that, the agreement between the GEM-2 ice thickness and the DTC sensor is around ∼ 3 cm for the two selected dates (2020/01/12 and 2020/02/07), and lower than the meter for December 2019.

At the time of writing this dissertation, there is still a lack of well-collocated data for the rest of the campaign (April-August). For this reason, to provide an estimate of the snow and ice thickness data to compare the PYCARO-2 measurements, IceSat-2 snow and ice thickness data has been selected. IceSat-2 is a satellite LiDAR, and its data has been used to estimate snow depth and sea ice thickness [197–199]. The methodology to retrieve snow depth and sea ice thickness from [199] is used here as a basis to compare PYCARO-2 measurements. The snow depth is retrieved from the subtraction between the total freeboard and the sea ice freeboard measured by IceSat-2 (see Eq. 7.1). For sea ice thickness, the methodology described in [200] is applied, as detailed in Eq. 7.2.

$$h_s = h_f - h_{f_{ice}}, \tag{7.1}$$

$$h_i = \frac{\rho_w}{\rho_w - \rho_i} h_f + \frac{\rho_s - \rho_w}{\rho_w - \rho_i} h_s, \tag{7.2}$$

where h_s is the snow thickness estimated from the total freeboard (h_f) and the ice freeboard ($h_{f_{ice}}$); and h_i is the sea ice thickness, where $\rho_w = 1025$ kg·m^{-3} accounts for the sea water density of, $\rho_i = 882$ kg·m^{-3} for the sea ice density of, and $\rho_s = 296$ kg·m^{-3} for the snow density.

IceSat-2 data has been retrieved for different tracks that are close to the MOSAiC position. Based on IceSat-2 availability, three data periods have been identified, between the 10 January 2020 and the 25 January 2020, between 26 January 2020 to 10 February 2020, between the 15 April 2020 and the 30 April 2020, and between the 10 July 2020 and the 30 July 2020. Figures 7.8 and 7.9 present the selected tracks from IceSat-2, and the snow and ice thickness estimated from the methodology described above.

As it can be seen, due to the large variability of the IceSat-2, and the few co-located points, MOSAiC and IceSat-2 measurements cannot be easily mapped. However, in average trends, the snow thickness estimation from IceSat-2 agrees the snow found in MOSAiC. As it can be seen, the ice thickness estimation in the second part of January and February –in average– is not consistent with the ground measurements. For the last selected period, it is important to remark that the ice freeboard in July is very thin, providing large inaccuracies in the estimated ice thickness, as already pointed out in [200].

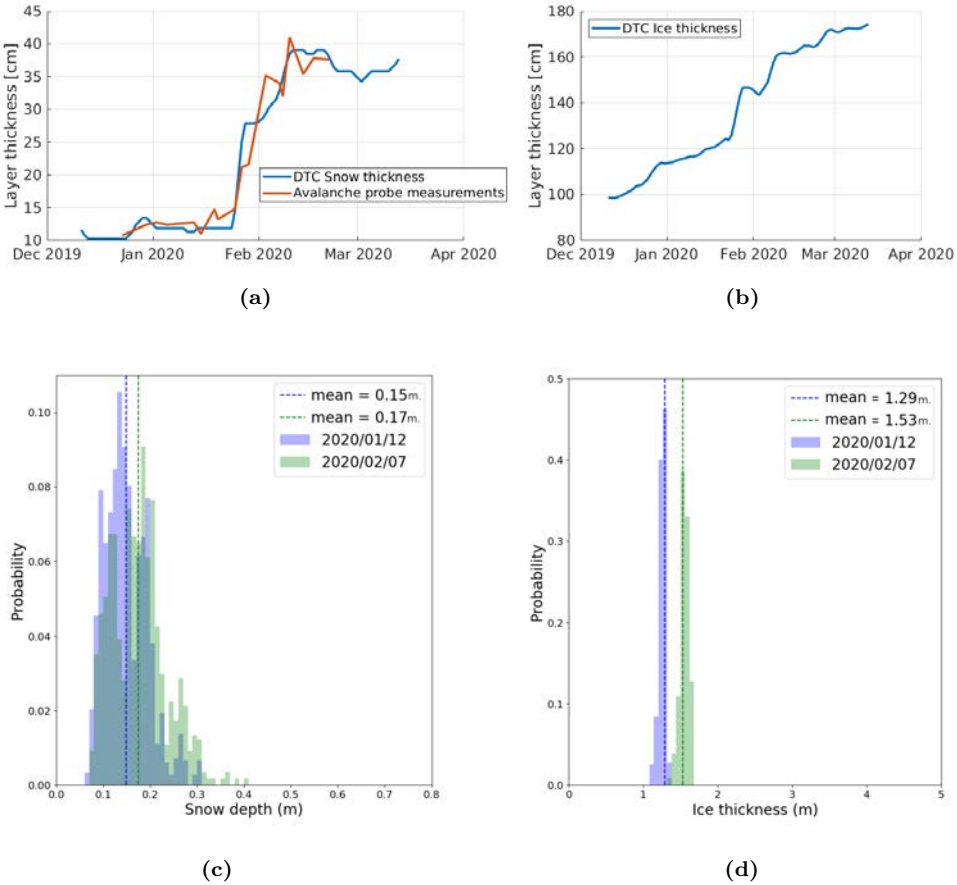

Figure 7.7: (a) Avalanche probe and DTC snow depth measurements in the vicinity of the GNSS-R instrument, (b) DTC ice thickness measurements, (c) snow depth and (d) sea ice thickness PDF for different dates in the level ice area adjacent to Remote Sensing site measured by Magnaprobe and GEM-2.

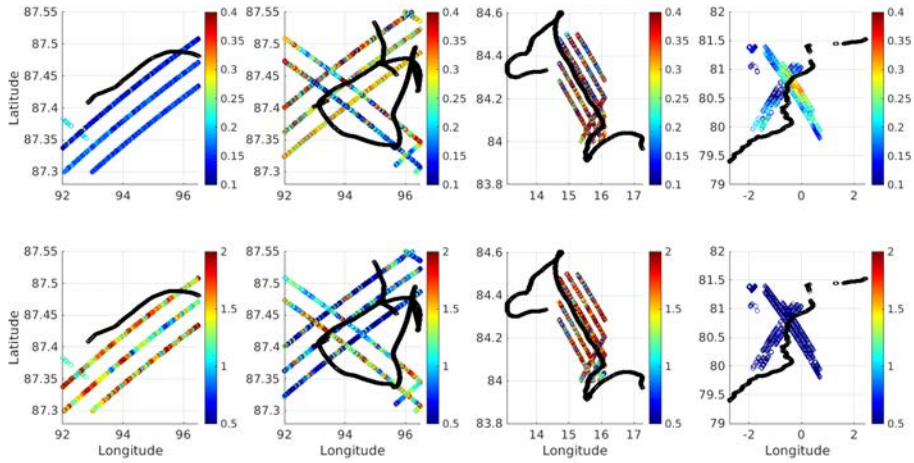

Figure 7.8: Co-located PYCARO-2 and IceSat-2 measurements. (Top row) Snow depth, and (bottom row) ice thickness. Highlighted in black the PYCARO-2 position for the four selected time periods (from left to right: 10-25 Jan, 26 Jan - 10 Feb, 15-30 Apr, 10-30 Jul, 2020).

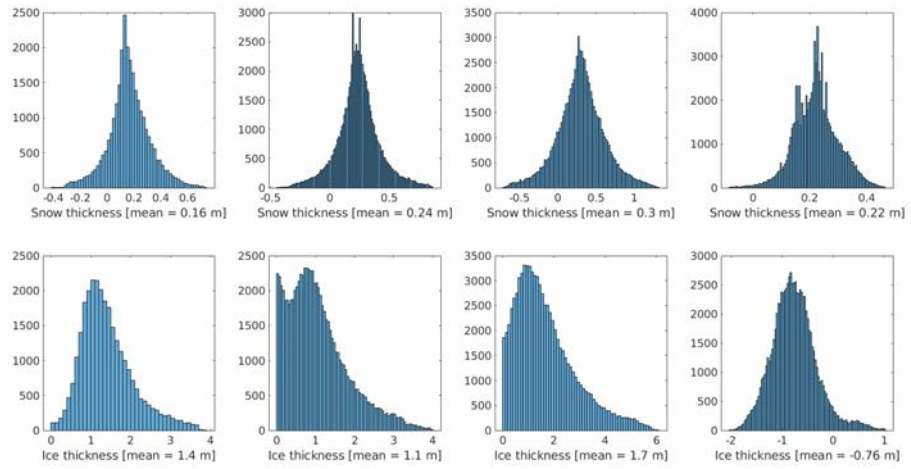

Figure 7.9: PDF of the IceSat-2 transects presented in Fig. 7.8.

7.3 Theoretical Background: IPT Applied to the Ice Floe

In navigation receivers, multipath is avoided as much as possible as it degrades positioning accuracy. For ground-based GNSS-R instruments, the signal collected by a GNSS antenna is a combination of the incident wave, i.e. the one coming directly from the GNSS satellite at RHCP, and the signal reflected over a certain surface. The combination of the direct and reflected signals creates strong reflectivity fluctuations or fringes, called an "Interference Pattern". In the PYCARO-2 case, the reflection of the GNSS signal on the sea ice floe produced the same type of fluctuations.

The Interference Pattern Technique (IPT) was conceived in 2009 [201] to extract a number of geophysical parameters from the Earth by means of ground-based instruments. Most of its applications are soil moisture [135], vegetation height [65], water level [202] monitoring, sea state [134], or snow depth [203] estimation. However, most of those works are based on a three-layer model, with the first layer being air, a second thin layer of substrate (i.e. snow, crop field), and finally, a third layer which is a semi-infinite reflective surface (i.e. land). Moreover, according to the author's knowledge, the IPT has never been applied over an ice floe, which contains four dielectric layers: air, a snow layer on top of the sea ice, the sea ice itself, and the sea water underneath.

To study the Interference Pattern (IP) fringes created by the multiple reflections in the floe, the instrument retrieves the signal-to-noise ratio (or peak of the Delay-Doppler Map minus noise background measured a few lags before the correlation peak [17]) once every 10 seconds, collecting thousands of reflections from different bands and constellations. The data used to perform this first study was collected from December 20, 2019, to January 27, 2020. However, due to several operational procedures of the instrument, most of the data was obtained between January 15 and 27, 2020. This study is focused on the analysis of this period of data, from which results and methodology will then be applied to the rest of the campaign.

7.3.1 Four-layer IPT model: theoretical formulation

The scattering geometry is modeled as shown in Fig. 7.10, where the dielectric constant of each media as in Section 6.2 of [204], and in particular, the sea ice dielectric constant model is based in [205], but for the direct model. This study is performed assuming the dielectric constant of the substrate is not varying. Furthermore, simulations have been performed to prove that the effect of varying the dielectric constant of the substrate produced a negligible effected as compared to the variation of either the snow or the ice thickness. In addition, the properties selected (i.e. snow density, ice type, and ice temperature) used to compute the dielectric constants shown in Fig. 7.10 are the average values of what MOSAiC researchers' measured. Therefore, following the procedures described in [206], the power received by either the zenith-looking or the 45º-looking antenna is proportional to (see Fig. 7.3a).

$$P(\theta) \propto |E_i(\theta_i) + E_r(\theta_i)|^2 = |E_0|^2 \cdot \left|F_n(\theta_{dir}) + F_n(\theta_{ref}) \cdot R(\epsilon_r, \theta_i) \cdot e^{j\Delta\phi}\right|^2, \tag{7.3}$$

where E_i is the incident electric field, E_r is the reflected electric field, $F_n(\theta)$ is the

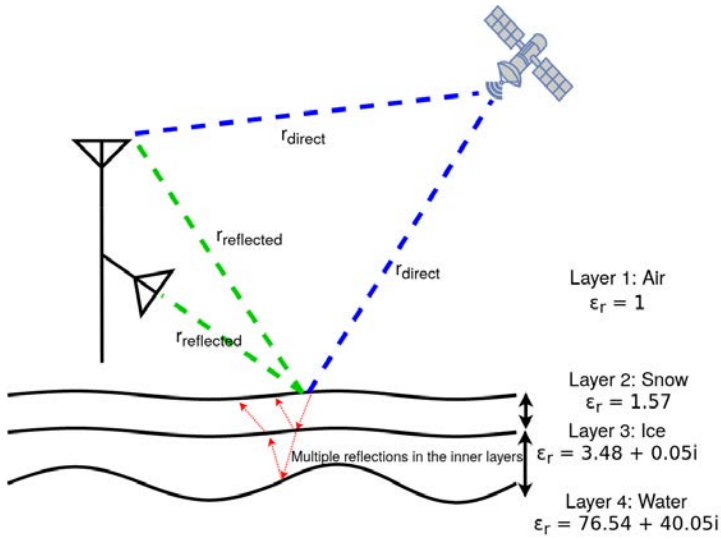

Figure 7.10: Four-model layer applied to PYCARO-2 instrument in MOSAiC campaign.

antenna voltage pattern (amplitude and phase) for the up-looking and down-looking signals arriving to either the up-looking or down-looking antennas, with different patterns for each one (see Fig 7.3a), θ_{dir}, and θ_{ref} are the off-boresight arriving angles of the direct and reflected signals, θ_i is the incidence angle of the signal arriving from a particular GNSS spacecraft, E_{0_i} is the direct signal, the one that would be received if there were no interferences, $R(\epsilon_r, \theta)$ is the reflection coefficient as defined in (7.5), and $\Delta\phi$ is the phase associated to the geometry. $\Delta\phi$ is given by

$$\Delta\phi = \frac{4\pi}{\lambda} \cdot h \cdot sin(\theta), \tag{7.4}$$

where λ is the electromagnetic wavelength, depending on the frequency band (L1 or L2), h is the antenna height, and θ is the satellite elevation angle. The reflectivity on top of the snow layer is computed iteratively as

$$R_i = e^{-(\frac{4\pi\sigma}{\lambda})^2} \frac{r_{i,i+1} + r_{i+1,i+2} \cdot e^S \cdot e^{j2\Psi}}{1 + r_{i+1,i+2} \cdot r_{i+1,i+2} \cdot e^S \cdot e^{j2\Psi}}, \tag{7.5}$$

where $r_{i,i+1}$ is the Fresnel coefficients between layers i and $i+1$, for the four-layer model being 1 = air, 2 = snow, 3 = ice, and 4 = saline water; S (see (7.6)) accounts for the reflectivity decrease due to the roughness at the interface [201], and Ψ is the phase produced by the reflection between the different layers, as detailed in (7.7)

$$S = -8 \cdot \left(\frac{\pi\sigma}{\lambda}\sqrt{\varepsilon_{r_{i+1}} - \varepsilon_{r_i} \cdot \cos^2(\theta)}\right)^2 \tag{7.6}$$

$$\Psi = \frac{2\pi}{\lambda} t_{i+1} \cdot \sqrt{\varepsilon_{r_{i+1}} - \varepsilon_{r_i} \cdot \cos^2(\theta)} \tag{7.7}$$

where t_{i+1} is the thickness of the $i+1$ layer, and ϵ_{r_i} is the permittivity of the i layer, and σ the surface roughness of the interface.

Each of the different surface permittivity values (ϵ_{r_i}) for this study have been modeled. The snow has been modeled as dry snow, as per in-situ measurements during the expedition, with a density of 296 kg/m^3, and -25 ^{o}C [207]. The ice has been modeled as a multi-year ice, with an average temperature of -25 ^{o}C. Note that simulations have been carried out at different temperatures, and the impact of varying the mean temperature was found negligible in front of the interference pattern produced by variations on the layer thickness. Finally, the water layer has been modeled as saline water (32 psu) at a temperature of -1.7 ^{o}C [207].

7.3.2 Interference pattern in the RHCP zenith-looking antenna

This study is focused on two frequencies: 1575.42 MHz, used by GPS L1 C/A code and Galileo E1C; and 1207.14 MHz, used by Galileo E5b and Beidou B2D1 signals. As a first example, the four-layer IP model simulation results are shown in Fig. 7.11a for the up-looking RHCP antenna at 1575.42 MHz for different values of snow, ice thickness and surface roughness. Note that the antenna heights used to simulate the model are the ones indicated in Fig. 7.3b. Moreover, the contribution to the interference pattern from the reflected path to the up-looking antenna starts to vanish at elevation angles larger than 25^o due to the antenna pattern itself (see Fig. 7.3a). Therefore, the model is only presented up to 30^o. Note that, the presented IPT is the normalized version of $P(\theta)$ from Eq. 7.3 (i.e. normalized by $|E_0|^2$).

As it can be seen, the position of the different peaks, as well as their shape, depend on the thickness of the snow layer. The position of both peaks and notches depends mainly on the snow thickness: from 10 to 15 cm thickness, the position of the notches shifts towards the left (lower elevation angles), but for a thicker snow layer (20 cm) the notch position moves towards higher elevation angles (e.g. the notch at 15^o of elevation in Fig. 7.11a). In addition, there is also a small dependence on the ice thickness. Comparing the top (ice thickness = 1.2 m) and bottom (ice thickness = 1.6 m) plots in Fig. 7.11a, the notch position is shifted slightly towards lower elevation angles, where thickness variation has less impact in the notch position.

A similar phenomenon happens at 1207.14 MHz (i.e. Galileo E5b and Beidou B2D1) where, depending on both the snow and the ice thickness in the four-layer model, the position where the minima occur fluctuates. As shown in Fig. 7.11b, the four-layer model is also affected by the snow thickness in both the peaks' shape and the notch position. However, the ice thickness has a larger impact on the notch position as compared to the 1575.42 MHz case as, due to the longer wavelength, the penetration depth into the ice is larger.

Finally, Fig. 7.12 presents a set of curves representing different values of both ice and snow thickness at 1575.42 MHz and 1207.14 MHz. The 1207.14 MHz signal is more sensitive to variations in the ice thickness than to snow thickness (10 to 15 cm), in terms of the positions of peaks and notches. In the 1575.42 MHz case, the nulls' position in the IP move $\sim$0.5^o ($\sim$0.1 ^{o}/cm) in elevation, while in the 1207.14MHz case they move $\sim$1.5^o ($\sim$0.3 ^{o}/cm).

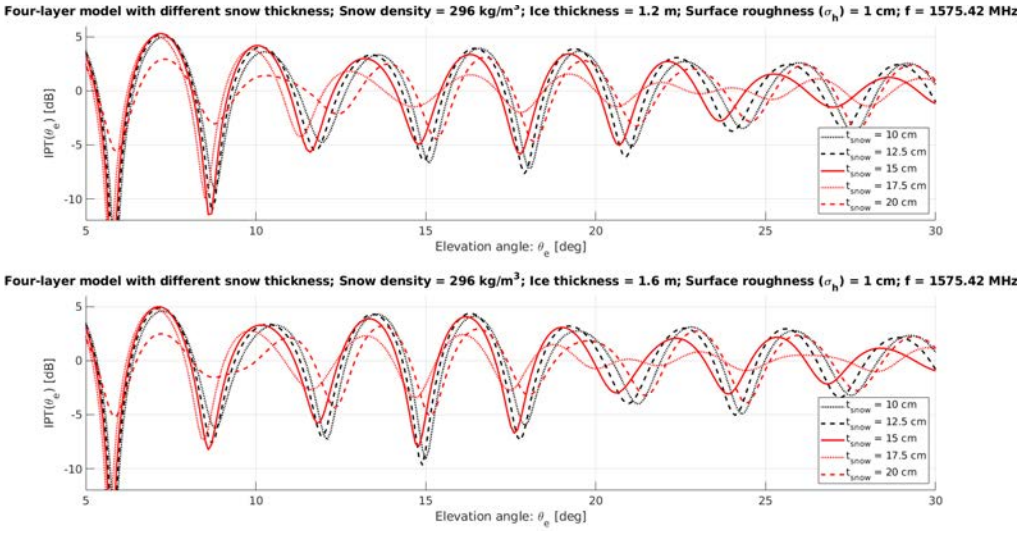

(a)

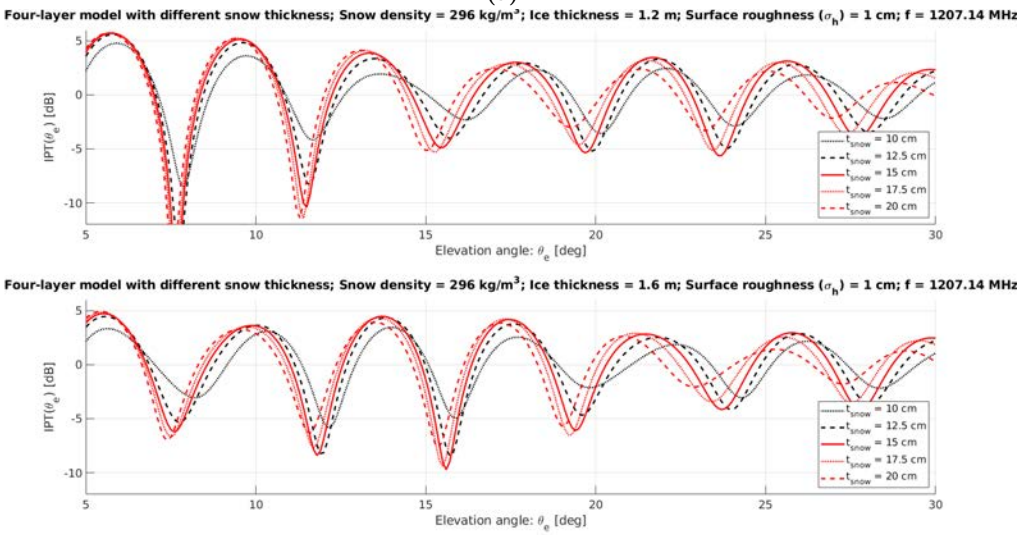

(b)

Figure 7.11: Four-layer model at RHCP for five different snow layer thickness, at two predefined ice thickness, (top) 1.2 m, and (bottom) 1.6 m. Simulation at 1575.42 MHz (a) and 1207.14 MHz (b). Assuming a surface roughness between layers of 1 cm.

7.3.3 Interference pattern in the LHCP down-looking antenna

As the LHCP signal is received by the 45º-tilted down-looking antenna, its reception is not limited by the lower back lobes of the radiation pattern of the RHCP antenna. For this reason, model predictions are presented for elevations from 5º to 60º. Figure 7.13a presents the IP at LHCP and 1575.42 MHz. Using the same parameters as for the RHCP signal case, the sensitivity to snow thickness is even larger than for the RHCP case (Fig.

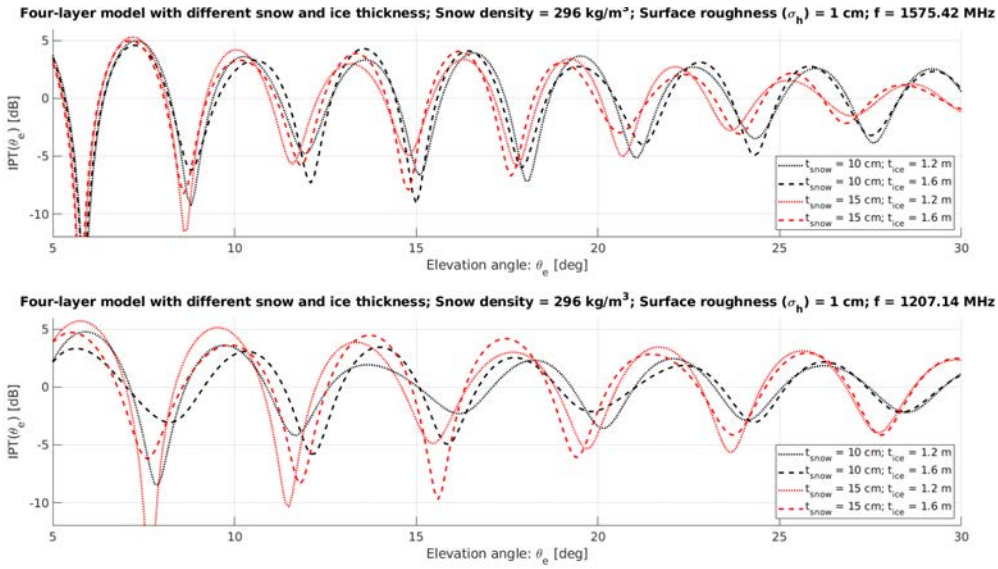

Figure 7.12: Comparison of the RHCP four-layer model at 1575.42 MHz (top) and 1207.14 MHz (bottom), using four different combinations of snow and ice thickness.

7.11a). Note that around 30º and 45º elevation, the ripples produced by the IP have the same shape for different snow thickness, i.e. the curve for 10 cm has the same shape as that for 20 cm, both for an ice thickness of 1.2 m and 1.6 m.

Figure 7.13b presents the IP at LHCP and 1207.14 MHz. As compared to Fig. 7.11b, the simulated IPs are now sensitive to both ice and snow thickness variations. Comparing both IPs (Fig. 7.13b top and 7.13b bottom) around 20º of elevation, it can be appreciated that the valleys are modulated by the snow thickness, and their depth (amplitude) and shape depend on the ice thickness.

The curves for different ice thicknesses (Figs. 7.13a and 7.13b bottom) are compared in Fig. 7.14, where it can be clearly seen that the ice thickness variation does not affect the interference pattern produced between 30º and 42.5º (R2 in Fig. 7.14) of elevation, although at low elevation angles, between 10º and 30º, the IP is sensitive to both snow and ice thickness. Note that, for the sake of simplicity, two ice thickness are shown, but simulations have been carried out for the complete range between 0.6 m. and 1.8 m. in steps of 0.1 m., showing that ice thickness variations do not affect the interference pattern produced between 30º and 42.5º. To summarize, the IPT with the four-layer model is sensitive to changes in the snow and ice thickness in both RHCP and LHCP signals. However, at 1575.42 MHz, the RHCP has a lower sensitivity to ice thickness. In the 1207.14 MHz case, as the wavelength is longer, and thus able to penetrate more into the ice, it shows a larger sensitivity to ice thickness variations. The LHCP case shows a mixture of both phenomena depending on the elevation angle: for low elevation angles, the IPT is affected by both snow and ice thickness, but for angles between 30º and 42.5º, the IPT mainly depends on the snow thickness. Note that this model does not take into account any antenna orientation, as antenna pattern of the received signal is compensated for.

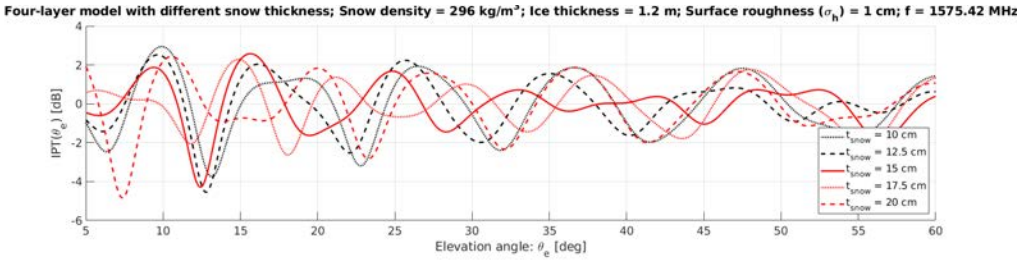

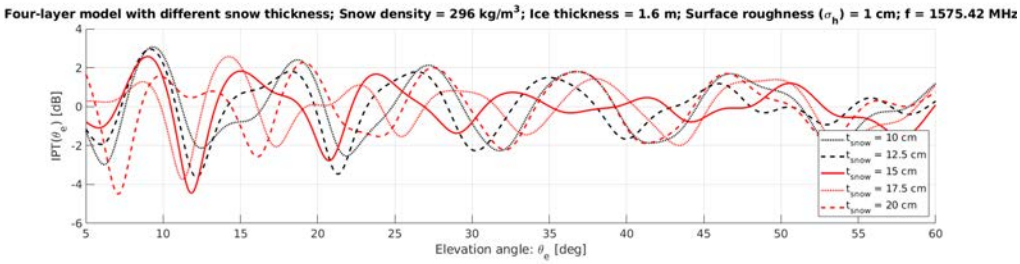

(a)

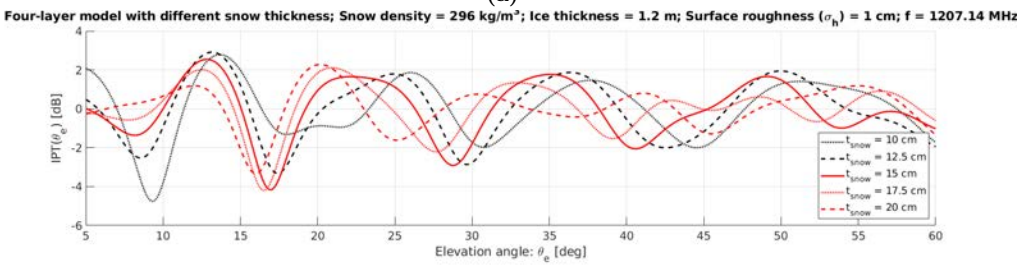

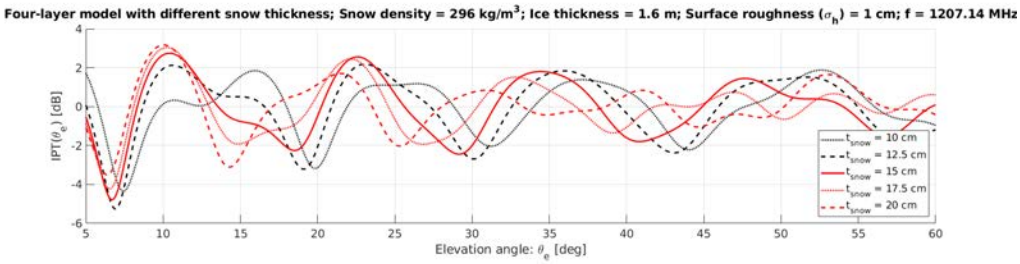

(b)

Figure 7.13: Four-layer model at LHCP for five different snow thickness, at two pre-defined ice thickness, 1.2 m (top), and 1.6 m (bottom). Simulation at 1575.42 MHz (a) and 1207.14 MHz (b). Assuming a surface roughness of 1 cm.

7.4 Data Analysis

The PYCARO-2 instrument receives the direct and reflected GNSS signals. In this section, the waveforms' SNR are presented as radar plots for the different frequencies and constellations. The fringes produced by the reflection geometry can be easily detected by the angle of arrival of the signal (i.e. azimuth and elevation angles).

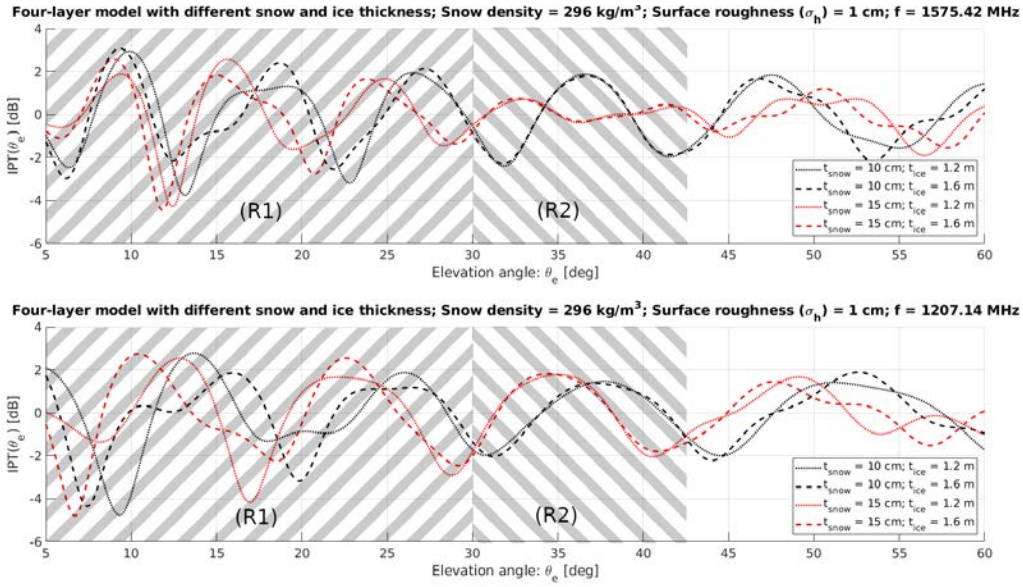

Figure 7.14: Comparison of the LHCP four-layer model at 1575.42 MHz and 1207.14 MHz, using four different combinations of snow and ice thickness. IPT in region 1 (R1) is affected by ice and snow thickness, while IPT in region 2 (R2) is unaffected by ice-thickness variations.

Figure 7.15a shows the IPT corresponding to Galileo E1C code, and Fig. 7.15b to the GPS L1 C/A code. The direction of arrival of the reflections is clearly identified in the GPS and Galileo RHCP plots, located in the azimuth range from ∼180º to ∼300º. However, in the LHCP signal collected by the down-looking antenna, other interference patterns can be identified in both GPS and Galileo, most of them grouped around 220º and 250º. Moreover, at 1207.14 MHz (Figs. 7.15c and 7.15d) Galileo E5B and Beidou B2D1 signals are also exhibiting an IP. As it can be seen, the pattern can be appreciated around 210º and 260º of azimuth, whereas for other angles the fringes are slightly changed or even lost. Because of the antenna pattern of the 45º down-looking antenna, most of the IPs are detected around 220º and 250º, where the fringes are stable at both frequencies. In order to compare the measurements from PYCARO-2 and the four-layer model described in Section 3, the signals have been filtered, and only those received in the 220º-250º of azimuth are used.

In order to ease the visualization of the signal in a 2D form, each SNR measurement retrieved by the instrument has been binned depending on the elevation angle of the transmitting satellite. Each measurement has been divided depending on the receiving antenna (i.e. RHCP or LHCP) and band (1575.42 MHz or 1207.14 MHz). Figure 7.16 shows, after calibration and azimuth filtering, a 2D histogram of the PYCARO-2 measurements overlaid with the RHCP (a) and the LHCP (b) four-layer model for different snow and ice thicknesses. In order to ease the representation and comparison of the interference pattern, the model curve has been re-scaled to have its range in the same span as the PYCARO-2 measurement.

Note that, as seen in the previous section, both snow and ice thickness have an impact

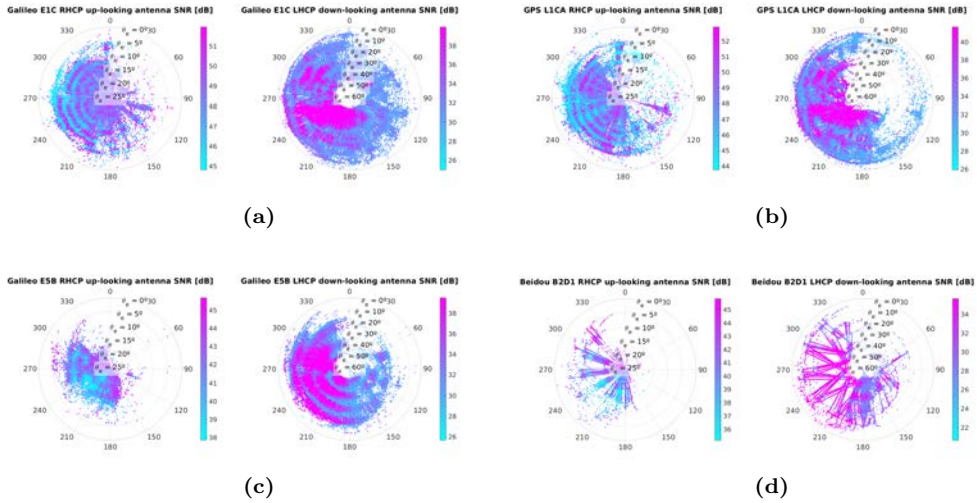

Figure 7.15: Radar plot of the SNR for (a) Galileo E1C, (b) GPS L1 C/A, (c) Galileo E5b signal, and (d) Beidou B2D1 during January 2020.

on the 1575.42 MHz band. However, it is not large enough to clearly distinguish which model parametrization is closer to the observed pattern. For the 1207.14 MHz case, the number of reflections received for low elevation angles is very small, and therefore, the ripples caused by the interference pattern cannot be clearly identified.

When moving to the LHCP case, as seen in Fig. 7.16b, the retrieved signal is noisier at 1575.42 MHz, where there is only a small range of elevation angles (20º to 35º) with ripples present. However, at 1207.14 MHz, the signal presents notches that can be easily identified as the ones described by the red curve in Fig. 7.16b. In this case, the signal at 1207.14 MHz is able to penetrate deeper into the substrate (i.e. the snow), and therefore it is slightly less sensitive to snow variations. As shown in Figs. 7.7b and 7.7c, the snow depth has a larger dispersion than the sea ice thickness.

In order to compare the model and the 2D histogram, the median curve shown in Fig. 7.17 has been computed on a running window with a width of 0.5º in elevation angle. In order to compare those curves and the model, a non-linear least square (NLS) minimization is performed in different steps, using the mean-squared error (MSE) of the SNR (dB) as the error function.

In order to properly retrieve snow and ice thickness, a first NLS minimization is performed for the LHCP signal at elevation angles between 30º and 42.5º, where the minimization parameter is the snow thickness. As seen in the previous section, the LHCP signal around 30º and 42.5º elevation angle is insensitive to ice thickness variations, but not to snow thickness variations. In this case, the notch position of the different ripples can be used to estimate the snow thickness.

When the snow thickness is retrieved, a second NLS minimization is performed for the RHCP up-looking signal, between 5º and 25º of elevation. In this second case, the variable used for the second minimization is the ice thickness, using the snow thickness

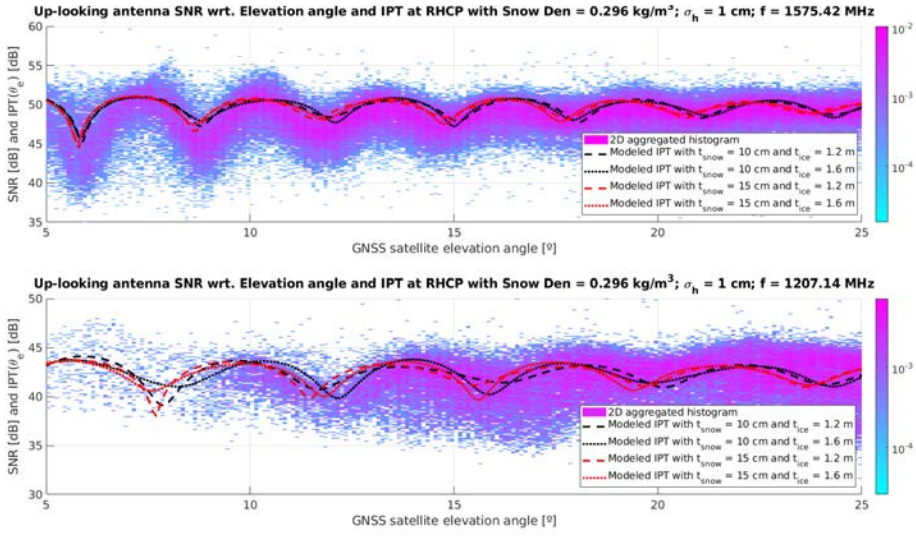

(a)

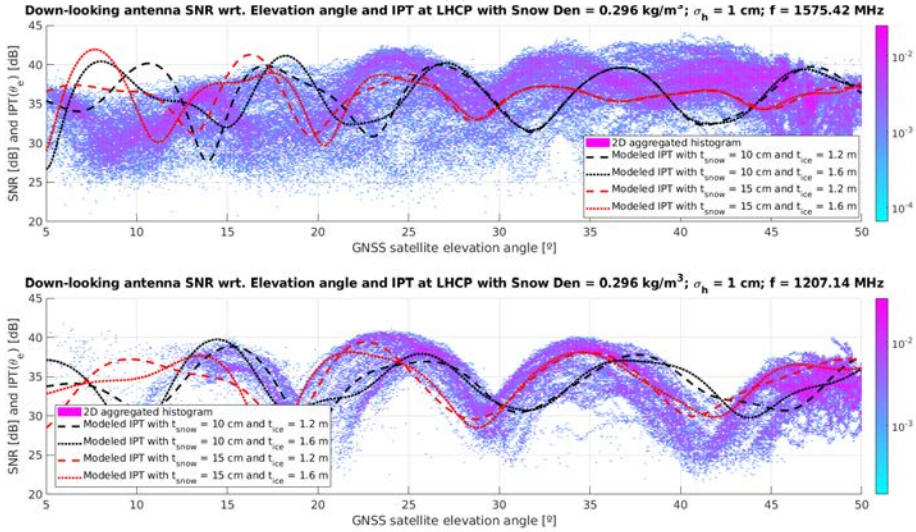

(b)

Figure 7.16: Aggregated 2D histogram (density plot) for the up-looking RHCP signal SNR for both 1575.42 MHZ and 1207.14 MHz; and IPT for RHCP (a) and LCHP (b) signal for different snow and ice thickness.

retrieved by the first NLS minimization. Note that in the RHCP case, both snow and ice thickness have an impact on the notch position, and therefore it is very advisable to first retrieve the snow thickness, as in the LHCP case the signal is mainly sensitive to the snow. Moreover, as the RHCP signal is coming from the up-looking antenna, the IPT can only be applied at very low elevation angles, where the antenna pattern has similar values for both the direct and the reflected signal. In this case the reflected signal is also

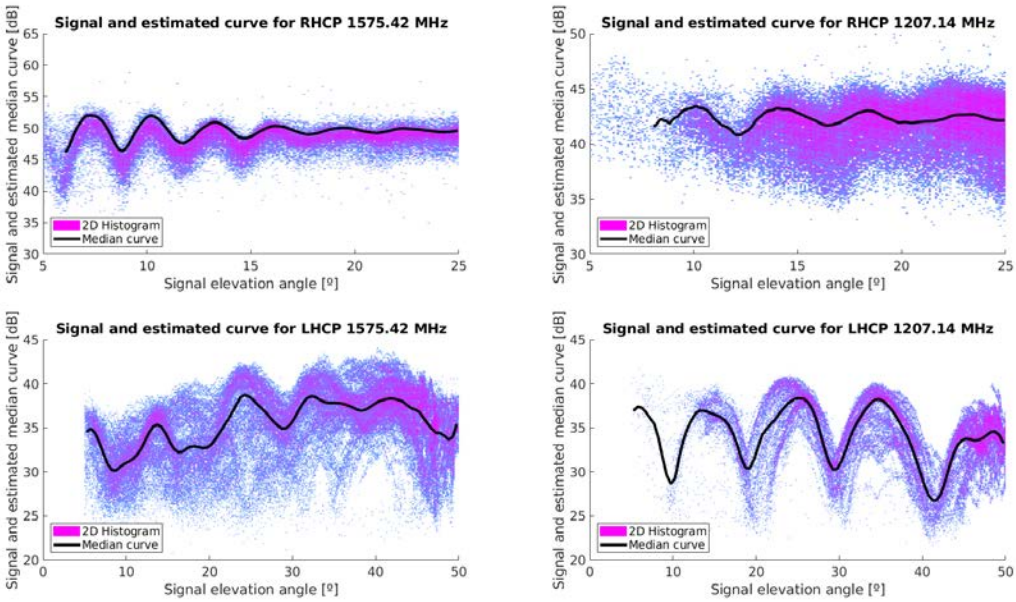

Figure 7.17: 2D histograms (density plot) and median curve (in black) for the received signals in GPS L1 C/A, Galileo E1C, Galileo E5b, and Beidou B2D1.

RHCP, as the incidence angle is smaller than the Brewster angle.

7.4.1 Error function analysis and ambiguity removal

Both the snow and ice thickness IP produce periodic notches. Therefore, almost equal interference patterns are generated by different combinations of snow and ice thickness. To resolve this uncertainty, data from the two frequency bands (1575.42 MHz and 1207.14 MHz) can be used. The error function with respect to snow and ice thickness is shown in Fig. 7.18. It can be clearly seen that the periodicity of the error function at 1575.42 MHz and 1207.14 MHz are different. In our case, there is a point where both error functions exhibit a minimum at the same time (blue dashed line). This point is the actual snow and ice thickness. The final algorithm implemented to estimate both snow and ice thicknesses is detailed in Fig. 7.19.

In the case of snow thickness (Fig. 7.18, top), the signal presents a periodicity every 10 cm, and therefore both signals will not present a minimum at the same time in the observation range (i.e. 5 to 35 cm). Therefore, the actual snow thickness can be estimated by overlapping the two normalized error functions. By looking to the sum of both normalized curves, the minimum value is the actual thickness (14.4 cm), which is very close to the measurements by the MOSAiC Remote Sensing team, which were 14.5±0.2 cm.

As for the ice thickness case, as shown in Fig. 7.18 (bottom), a minimum in the MSE function is present every ∼20 cm. Similar to the snow thickness case, the periods are not

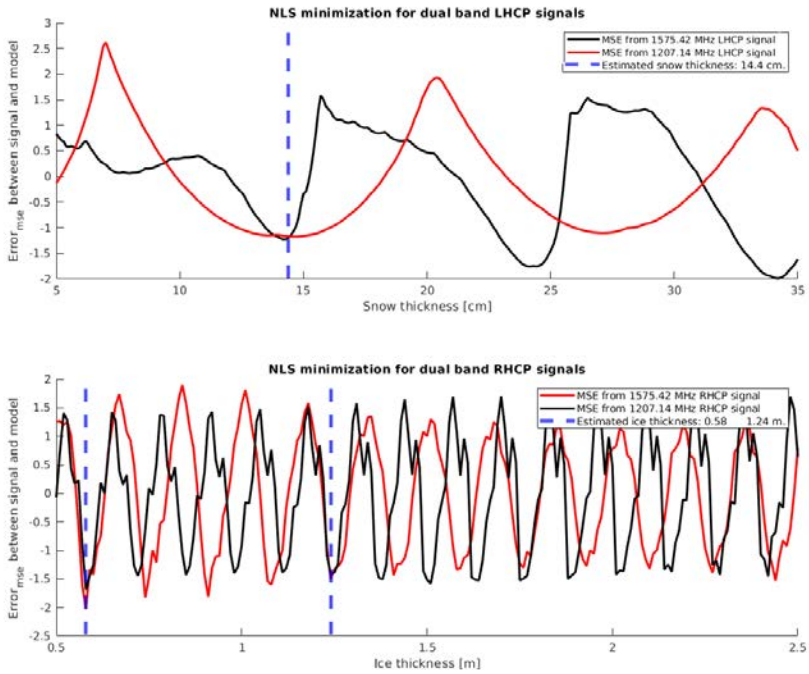

Figure 7.18: NLS minimization output for the data set between the 15^{th} and the 27^{th} of January, 2020. MSE is represented for both snow and ice thickness, for different signal frequencies and polarization, and it has been normalized (z-score normalization) to ease its visualization. Note that, the exact place where both signals present a minimum at the same thickness is represented by the blue dashed line thickness and the ice thickness have an impact on the notch positions, therefore it is very advisable to first retrieve the snow thickness, as in the LHCP case, the signal is mainly sensitive to the snow.

the same for each band. However in this case, as the observation range (i.e., 0.5 to 2.5 m) is larger, there are different combinations of thickness values producing a minimum at the same time: 0.58 m. and 1.24 m. Since some a priori knowledge of the ice is required to resolve the ambiguity, we rely on the measured value of 1.21 m on 15 January, 2020. Therefore, from both possible solutions, the correct value is likely 1.24 m. In the absence of a priori information, a third frequency band (or more) would be required.

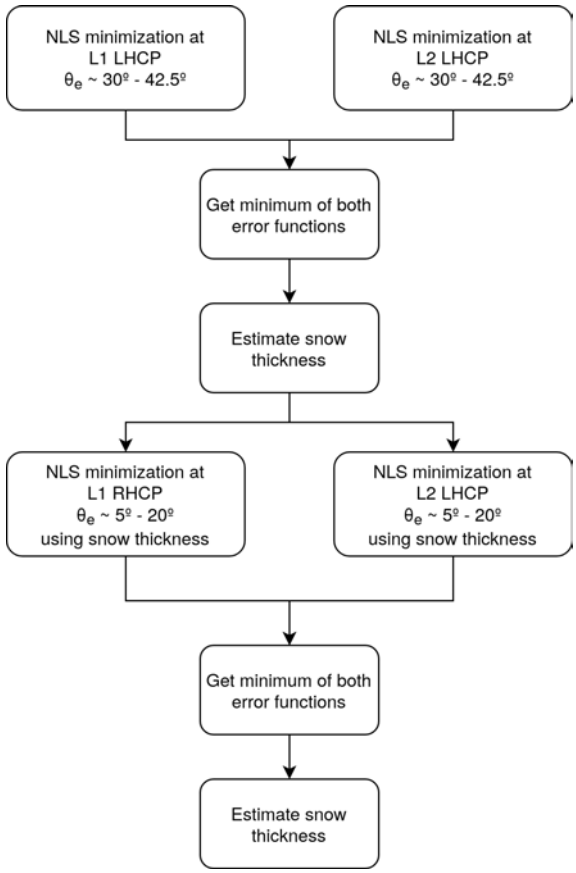

Figure 7.19: Algorithm to estimate both snow and ice thicknesses using PYCARO-2 dual-polarization IPT data.

7.4.2 Model and measured signal overlay

Once the thickness parameters have been retrieved, they can be used as input for the four-layer IPT model. The modelled IPT is then overlaid on top of the PYCARO-2 data, as shown in Fig. 7.20. Note that the IPT model has been normalized in range (i.e. added a bias and multiplied by a scale factor) in order to better compare it with the SNR values of PYCARO-2.

It can be noticed that the IPT curves are not 100% coincident with PYCARO-2 data in all elevation angles. Despite that, the estimated thickness values are extracted from an MSE minimization process, therefore giving a minimum error for all elevation angles with respect to the median curve used.

Note that in the 1575.42 MHz RHCP signal the notches are also very clear, and therefore we can check that the IPT model and the median curve present the same notches at 6º, 8º, 12º, 14.5º, and 17.5º elevation angles. In the same way, the median curve and the IPT model for the 1207.14 MHz RHCP signal is presenting two notches at the same position, around 12º and 15.5º elevation angles.

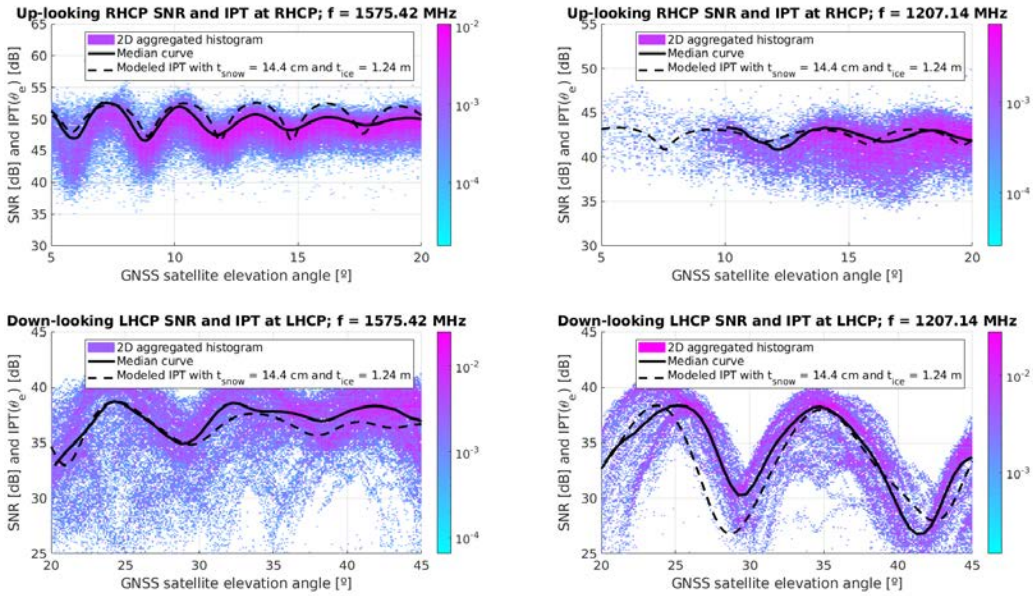

Figure 7.20: Modeled IPT using the retrieved snow and ice thickness overlaid on top of the signal retrieved by the PYCARO-2 instrument in the MOSAiC campaign during January 2020. Both the median curves and the modeled interference patterns are represented in black.

In order to validate the model for other data sets, another period of data has been used, between 23 and 27 December, 2019. In this case, the snow thickness measured in-situ by MOSAiC researchers was 11-13 cm, and the estimated ice thickness by means of ice core drilling performed some days before, on 20 December, 2019, was around 90 cm. Figure 7.21 shows the error functions for both ice and snow thickness. In this case, for the minimization process at LHCP, both curves exhibit a minimum at 12 cm of snow thickness, being consistent with the measurements carried out during the campaign. Furthermore, the error curves for RHCP present once more a combination of two values with a minimum, 0.79 m, and 1.68 m. In this case, thanks to the knowledge of the actual ice floe thickness, the selected solution is 0.79 m.

The overlaid version is presented in Fig. 7.22. In this case, the notches at 1207.14 MHz, both RHCP and LHCP, are well-matched, as well as the minima and maxima at 1575.42 MHz, LHCP. Despite that, the modelled IPT for the RHCP signal at 1575.42 MHz, and the actual measured data by PYCARO-2 present a slight mismatch. Even then, the snow and ice thicknesses selected are the ones presenting a minimum MSE between the median curve and the IPT curve.

Even though the estimated ice thickness in this second case differs by 10 cm from the actual measured value, the accuracy of the GEM-2 instrument is 10 cm as well. In addition, as pointed out by the MOSAiC researchers, the ice floe is not evenly growing. To prove that, underwater pictures were taken by a remotely operated vehicle (ROV) during the MOSAiC expedition (see Fig. 7.23). Furthermore, it is known that small (e.g. 10 cm) and local (meter-scale) undulations are present during the sea ice freeze up [208], and therefore a single GEM-2 measurement cross-validated using an ice drilling may not

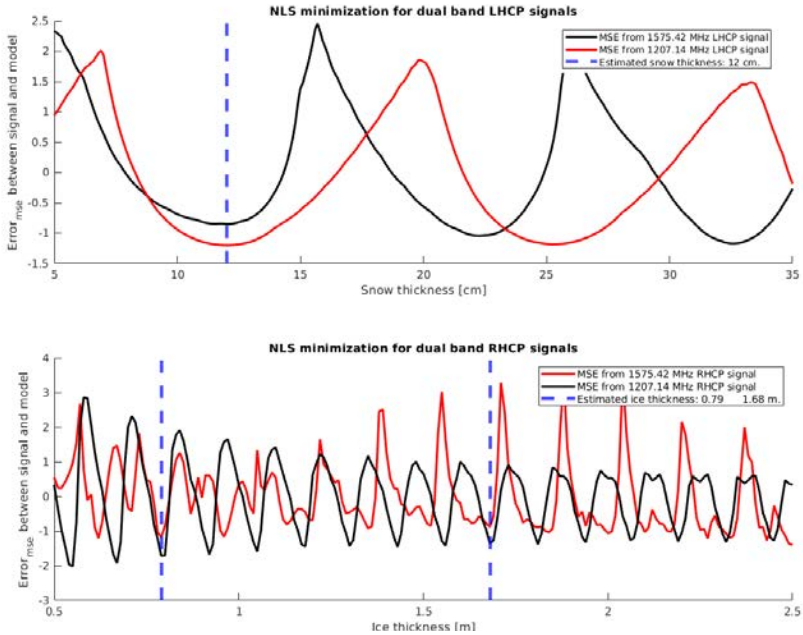

Figure 7.21: NLS minimization output for the data set between 23 and the 27 December, 2019. MSE is represented for both snow and ice thickness, for different frequencies and signal polarization, and it has been normalized (z-score normalization) to ease its visualization. Note that the blue-dashed line shows the exact thickness at which both signals present a minimum.

be representative of the overall sea ice thickness. It is important to note that this second example of measurements was conducted during December, which is the time period when the ice floe is packed together to form new ice. In this case, some regions may present thinner or thicker spots of ice, which can affect the GNSS-R data measured by PYCARO-2. This phenomena may not be present in the data presented for January, as the different ice sheets have been already merged together.

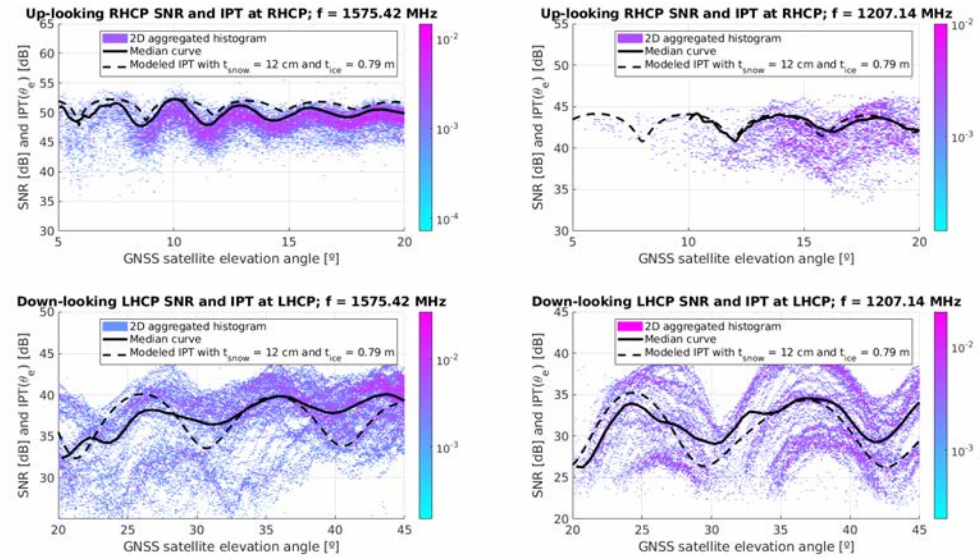

Figure 7.22: Modeled IPT using the retrieved snow and ice thickness overlaid on top of the signals retrieved by the PYCARO-2 instrument in the MOSAiC campaign during December 2019. Both the median curves and the modeled interference patterns are represented in black.

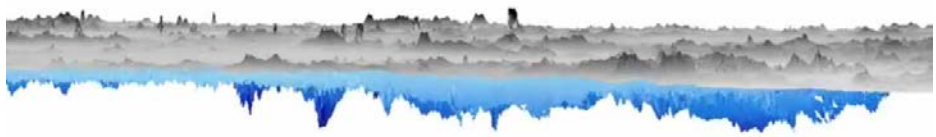

Figure 7.23: Ice topography over the water interface (gray) and underneath the water interface (light blue) captured by a ROV during the MOSAiC expedition.

7.5 Snow and Ice Retrieval Algorithm for the Entire PYCARO-2 Data Set

The data presented in the previous section has shown that the L2 LHCP signal collected by the 45º-tilted down-looking antenna contains lots of information to retrieve both the sea ice thickness and the snow thickness, being most sensitive to the snow variations rather than to the sea ice thickness. However, it is seen that, for larger thickness (i.e., in the ice case), there is a potential error when estimating either the snow or the ice thickness if no a priori information is used. In order to implement the algorithm described in the previous section for the entire data set, some a priori information shall be used. In this case, the available ground truth data is only for the first observation period, from December, 2019, to end of March 2020. In addition, measurements in August, 2020, were provided by the MOSAiC research team, with a measured snow thickness around 5-15 cm for the entire summer, and ice thicknesses between several centimeters up to 0.9 m (thinner than in

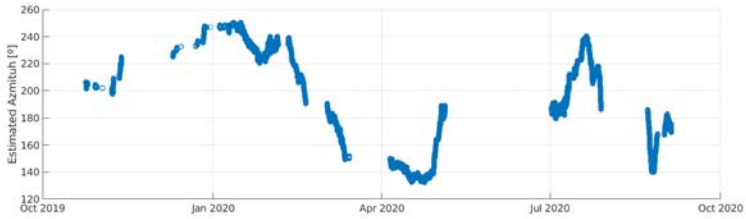

Figure 7.25: Estimated azmith pointing of the 45º-tilted antenna.

December). Thus, this a priori data has considered to implement the NSL minimization process, and an lower and upper bounds are used for the NSL minimization process. The bounds are 20-30 cm thick for the snow case, and 60 cm thick for the ice case. The bounds are detailed in Fig. 7.24.

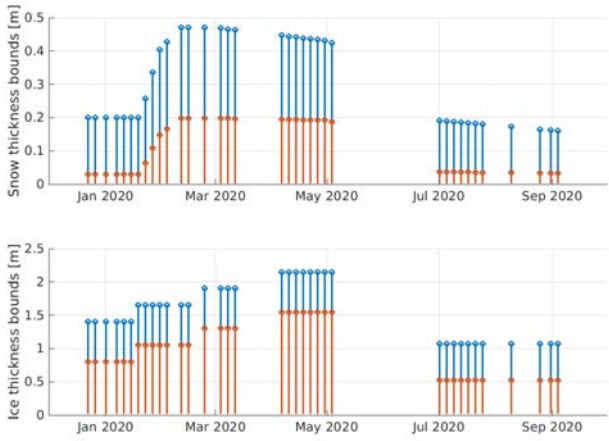

Figure 7.24: Snow and Ice thickness bounds used for the NSL minimization process.

7.5.1 Azimuth pointing estimation and 2D histogram generation

In order to easily handle the large amount of data collected, different averages are considered, similar to the methodology explained in Section 7.4. First, all reflections having an azimuth angle of arrival out of a cone of $\pm 30^{o}$ from the estimated azimuth pointing are filtered out. Second, all reflections captured within a time span of 4 days are kept in separate vectors. This filtered data is then used to compute the 2D histograms presented in Section 7.4. In total, 36 histograms are computed for the entire campaign for L1 (using combined data from GPS L1 and Galileo E1C) and L2 (using combined data from Galileo E5b and Beidou B2D1). Note that, the estimated azimuth pointing is determined from the direction of arrival of the GNSS-R reflections at all bands. The data is temporary filtered with a moving window to finally provide the azimuth pointing of the 45º-tilted antenna at any time instant (Fig. 7.25).

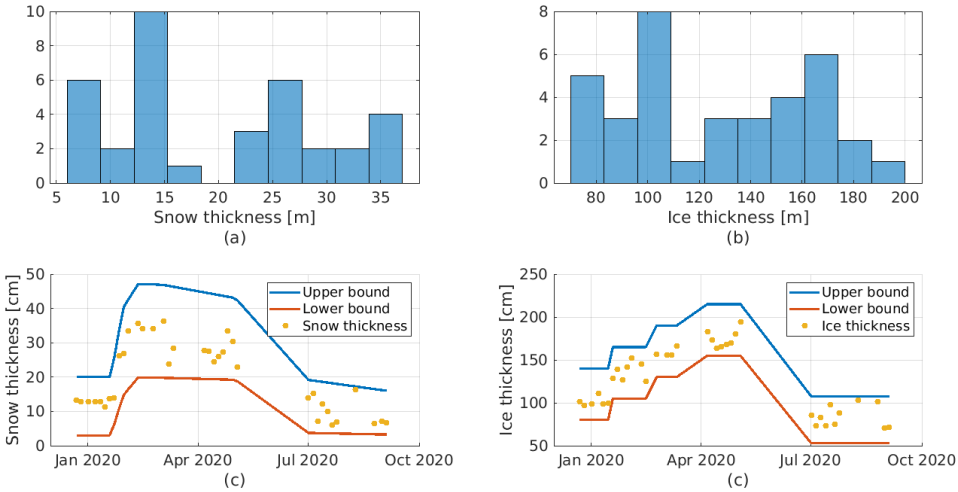

Figure 7.26: (a) Snow and (b) ice thickness histograms for the entire data set, and (c) and (d) time evolution of the snow and ice thickness retrieved by the algorithm, and in blue and orange the upper and lower bounds used as a prior data by the algorithm

7.5.2 Results for the entire data set

The median curve to estimate the IPT from the 2D histogram is computed for all the available histograms. The NSL minimization process is performed for both RHCP and LHCP signals, according to Fig. 7.19. The snow and the ice thickness data estimated by the algorithm is presented in Fig 7.26.

The results are compared to the DTC measurements presented in Section 7.2.2. As it is shown in Fig. 7.27, the RMSE between the GNSS-R method and the DTC is 6.6 cm for the snow thickness, and 12 cm for the ice thickness. The snow thickness rapidly increases from 10 cm at January to 25-35 cm, and it remains consistent during the entire period (from February to April, 2020). It is also noticeable that the ice thickness retrieved in April is ∼1.7 m, consistent with IceSat-2 measurements for this period. Finally, measurements taken in July/August show a decrease on the estimated snow thickness down to 5-10 cm, similar to the ones provided in January, which ware taken before the first "hard" snows of the year. The ice thickness for this period is ∼75 cm, which is well below the meter, as expected from MOSAiC staff measurements provided in this period.

7.6 Conclusions

This chapter has presented the GNSS-R theory and techniques required to estimate the snow and ice thickness of the sea ice. Multi-frequency and dual-polarization GNSS-R can be used to determine both snow and ice thickness by means of the IPT. A peculiarity is that the error functions of the non-linear least-square minimization of the RHCP and LHCP signals at different bands, exhibits a periodicity, leading to multiple solutions. These uncertainties can be solved by comparing the error functions and looking for the

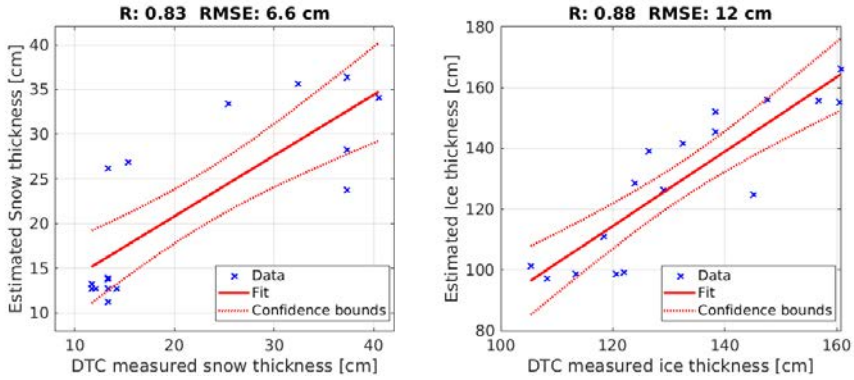

Figure 7.27: Scatter plot for the snow and the ice thicknesses retrieved by the proposed algorithm compared to the DTC measurements used as ground truth.

portions where the minimum error are coincident. Snow thickness can be easily estimated from this process, as the periodicity of the error with the snow thickness has the same order than the observation range (i.e. a period every 10 cm, observation range ∼40 cm). However, for the ice thickness case, the periodicity of the error with the ice thickness is one order of magnitude smaller than the observation range (i.e. a period every 20 cm, observation range ∼2 meters), which leads to multiple solutions for ice thickness that, from the data available for PYCARO-2, cannot be resolved without a priori information.

The interference pattern produced by the four-layer model exhibits some sensitivity to ice thickness variations, especially at the lower frequency band. This means that signals do reflect off the bottom of the ice and reach the air media with still enough power to induce an interference with the direct signal, supporting the hypothesis from [190], where measurements of the sea ice draft could be possible using GNSS-R data. However, there is a wide range of elevation angles where the snow thickness is dominant in the reflection (i.e., 30^{o} and 42.5^{o} elevation angles). In this range of angles, the reflection takes place mostly in the snow-ice interface, while for other elevation angles, the interference pattern is produced in the air-snow, snow-ice, and ice-water interfaces.

The algorithm presented has been applied to the entire data set using a priori information to minimize the observation range, and thus to avoid having multiple coincident minimums in the error function. The results for the entire data set have been compared to the DTC ground truth data, showing a very good agreement for the period where DTC data is available (December, 2019 to March, 2020), with a RMSE of 6.6 cm for the snow thickness, and 12 cm for the ice thickness.

Part III

Development of Space-borne Instrumentation

8

Chapter 8

The Flexible Microwave Payload -1

This Chapter has two main goals. First, to give an overview of the most common architecture of a CubeSat-based spacecraft, and the ^{3}Cat-4 mission is presented as an example of a CubeSat-based Earth Observation mission. Concepts and definitions introduced in this Chapter are part of the basic contents that will serve as a baseline to design more advanced microwave payloads (FMPL-2 in Chapter 9 and FMPL-3 in Chapter 10). Second, this Chapter presents the design of the FMPL-1 payload, the first version of the "Flexible Microwave Payloads" family of passive microwave instruments developed within the frame of this Ph.D. thesis. Note that, as part of an educational program, the entire satellite has been designed and developed by more than 20 UPC NanoSat-Lab students.

The ^{3}Cat-4 mission was selected in the second edition of the ESA Fly Your Satellite! (FYS) program. ^{3}Cat-4 is an educational mission to educate new students in space engineering. Due to its educational purpose, the project timeline is more "relaxed" than the other instruments presented in the following Chapters, and the tentative launch date of the satellite is foreseen in Q1/Q2 2022.

The Chapter is organized as follows: Section 8.1 introduces the ^{3}Cat-4 mission. Section 8.2 presents the design of ^{3}Cat-4 subsystems, such as the Communication system, the Attitude system, and the On board Computer system. Section 8.3 presents the design of the FMPL-1 instrument. Section 8.4 presents the implementation details of FMPL-1. Finally, Section 8.5 concludes the Chapter. Note that, part of this Chapter has been adapted from International conference publications available in IEEE ©Proceedings entitled "^{3}Cat-4: Combined GNSS-R, L-Band Radiometer with RFI Mitigation, and AIS Receiver for a 1-Unit Cubesat Based on Software Defined Radio" [CP1] and "^{3}Cat-4 Mission: A 1-Unit CubeSat for Earth Observation with a L-band Radiometer and a GNSS-Reflectometer Using Software Defined Radio" [CP3].

8.1 Introduction

The ^{3}Cat-4 mission is the evolution of UPC ^{3}Cat-2 [99] mission, which aimed to provide a proof of concept on GNSS-R receivers for nano-satellites. ^{3}Cat-4 aims at addressing this technology challenge by integrating a payload that combines a dual-band (L1 & L2) GNSS-R and an L-band TPR in a 1-Unit CubeSat. This resulting payload, called the FMPL-1, uses the RTL2823u, a low-power COTS Software Defined Radio (SDR) module to combine both technologies in a single subsystem. Finally, to demonstrate the power of this architecture, the FMPL-1 also includes an Automatic Identification System (AIS) receiver. This mission was selected for the FYS II program of the ESA academy in May 2017.

The ESA-FYS program gives the possibility to follow an educational experience on space engineering for students to design, build, and verify a CubeSat. Moreover, the resulting spacecraft will be launched into a LEO orbit. Aside from the educational point of view, one of the goals is to demonstrate the capabilities of nano-satellites, and in particular those based in the 1-unit CubeSat standard, for a challenging Earth Observation mission. The ^{3}Cat-4 mission is being conducted at the UPC NanoSat-Lab by a team entirely composed of students and led by Dr. Joan Adrià Ruiz-de-Azúa during his Ph.D., and now by Ms. Lara Fernández.

8.2 ^{3}Cat-4: Mission and Subsystems Description

The ^{3}Cat-4 satellite is a 1-Unit CubeSat (detailed in Fig. 8.1) composed of different subsystems to provide the required power, processing capacity, and communications capability to accomplish the mission. In particular, these are the Electrical and Power Subsystem (EPS), the On-Board Computer (OBC), and the Communications Subsystem (COMMS). One additional subsystem is included in this group, called Zenith Antenna and Deployment Subsystem (ZADS), which contains the communications antenna. The payload-oriented subsystems aim at providing the different functions to achieve the scientific mission. It is mainly composed of the FMPL-1 and the Nadir Antenna and Deployment Subsystem (NADS), which includes a deployable helix antenna for the payload. Finally, the Attitude and Determination Control Subsystem (ADCS) ensures a nadir pointing to observe the Earth's surface.

An additional board has been conceived to interface the platform subsystems with the payload. Specifically, this Interface Board contains a PC104 connector that unifies the pinout of the entire spacecraft. It also contains an umbilical port that allows external operators to connect to the spacecraft. All these subsystems are integrated in a 1-Unit structure, covered by five solar panels. This is the default stowed configuration (Fig. 8.2, left), but after satellite ejection the helix payload antenna will be deployed reaching the nominal configuration (Fig. 8.2, right).

8.2.1 Electrical Power System

The EPS of the ^{3}Cat-4 CubeSat is the Nanopower P31u, a COTS product from Gomspace [209], which interfaces with ten photo-voltaic cells (two per face), and uses a highly efficient boost-converter to adapt their output voltages. It provides a 3.3 V and a 5 V

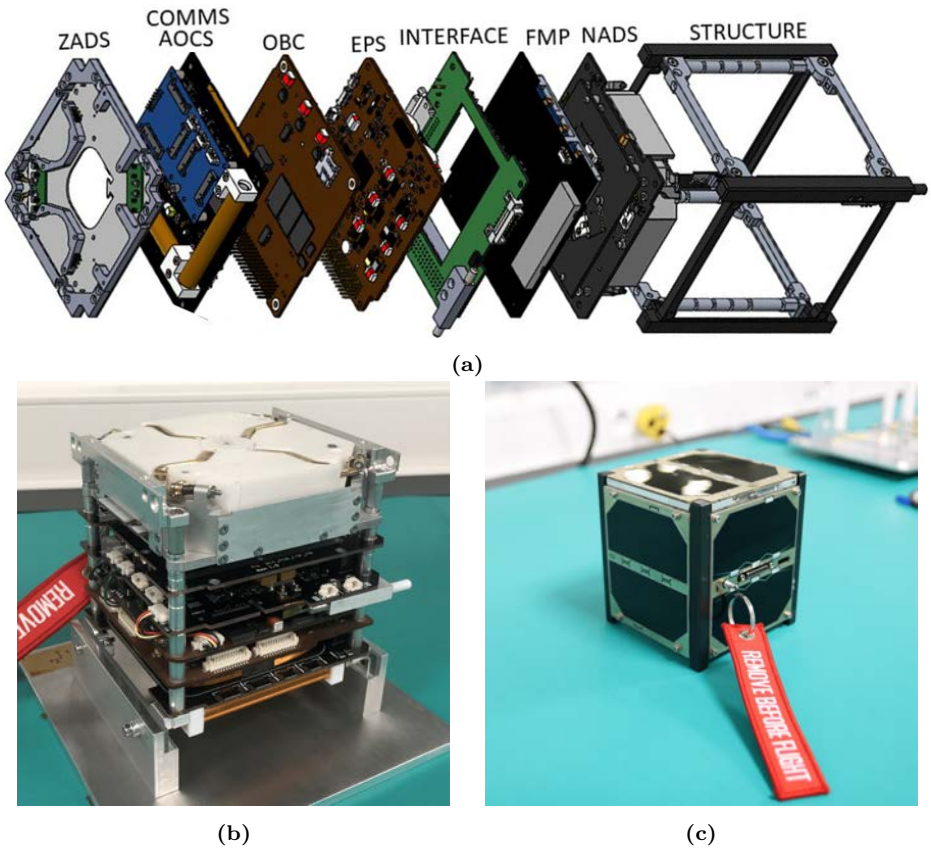

(a) **(b)** **(c)**

Figure 8.1: (a) [3]Cat-4 spacecraft internal distribution, (b) [3]Cat-4 integrated during satellite fit-check test without solar panels, (c) spacecraft fit-check including solar panels.

channels to supply the entire spacecraft. This subsystem also includes a pair of lithium-ion battery cells with 18650 form factor. The batteries are mounted in series, giving up to ∼7.4 V with a capacity of 2600 mAh. This configuration is one of the most commonly used in 1 to 3-unit CubeSats. For larger formats (i.e. 6U), from four to six batteries are normally used in a series/parallel approach (i.e., up to 7.4 V and 5200 mAh when mounted two series and two in parallel, or up to 7800 mAh when mounted two in series and three in parallel).

In the [3]Cat-4 case, with the simplest configuration of two battery cells, the power budget becomes positive in all the operating modes of the spacecraft. However, the most critical feature of this subsystem is the temperature during charge and discharge states. Therefore, a heater is installed around the battery cells to ensure a minimum temperature during cold scenarios. The thermal analysis with the worst hot and cold cases (pessimistic scenarios) has been performed. Table 8.1 presents the temperature range the EPS and the battery cells, which confirms that the current satellite configuration ensures the correct operation of this subsystem in all conditions.

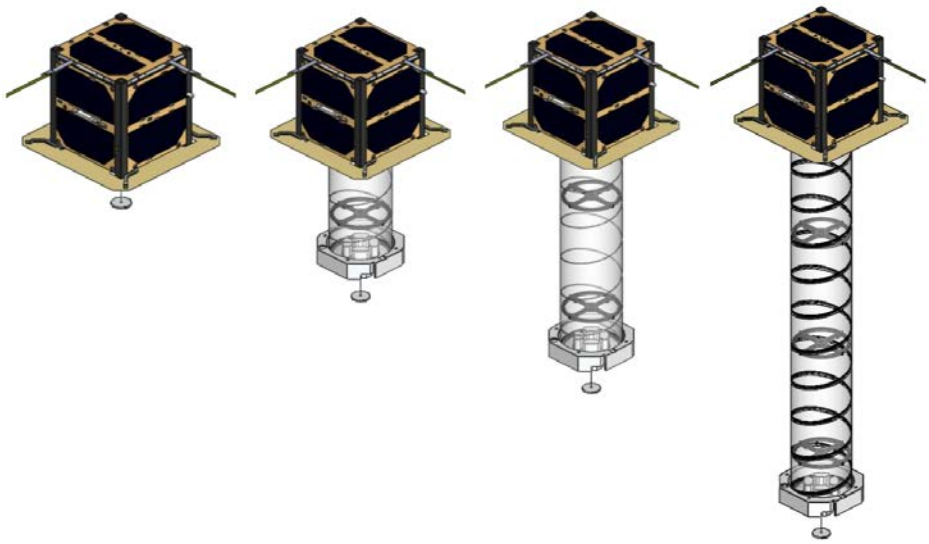

Figure 8.2: ^{3}Cat-4 in different configurations, from stowed (left) to the nominal configuration with the L-band antenna deployed (right).

Table 8.1: Temperature ranges (in ºC) of the EPS and battery

	Hot case		Cold case		Design range	
	Min	Max	Min	Max	Min	Max
EPS	22.77	34.86	-6.75	20.79	-30	+75
Battery	25.04	37.13	5.13	27.64	5	+40

8.2.2 On Board Computer

The OBC subsystem of the ^{3}Cat-4 is the NanoMind A3200 module from Gomspace [209], which has all the required interfaces (e.g. UART, I2C, etc.) to interconnect with the other subsystems. At software level, the OBC uses the Free Real-Time Operative System (FreeRTOS) that provides a means to schedule tasks with their own context, which are pre-empted by external notifications/events. This priority-based task scheduler allows the execution of a task depending on its priority level.

The software architecture is based on a star framework, in which a central task manages the other ones that communicate with the external subsystems. This central task is also responsible to execute the different spacecraft modes: launch early operations mode, nominal mode, Sun-safe mode, and survival mode. This architecture enables to monitor the battery status, the transition from the different spacecraft modes, the execution of the payload, the attitude control, and the communications with the ground station. The generated data is stored in the internal OBC memory, which is robust against radiation effects, e.g. total ionizing dose (TID) and single events upsets (SEU).

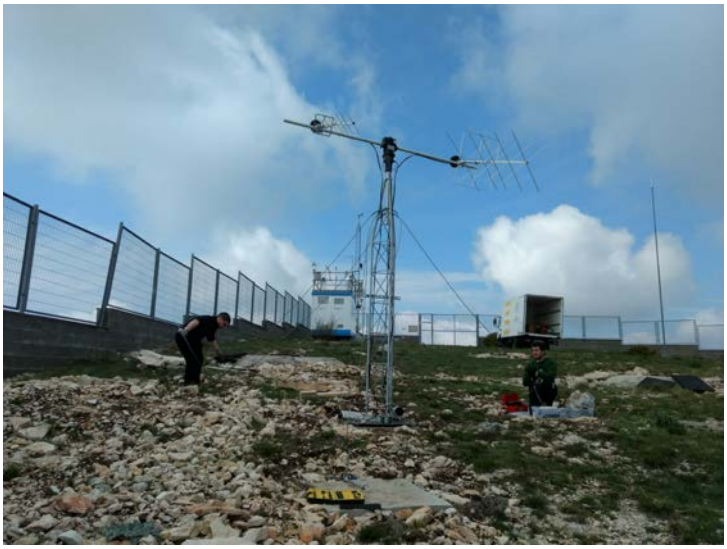

Figure 8.3: VHF/UHF antenna at the UPC/IEEC Montsec Ground Station while it was being installed in 2018.

8.2.3 Communication System

The COMMS provides a direct downlink and uplink between the CubeSat and the ground station. The exchanged messages are commands, payload data, and spacecraft telemetry. Nowadays, CubeSats use the Ultra High Frequency (UHF) band (400-438 MHz) to retrieve the basic spacecraft telemetry, and to command the satellite. In case that the satellite is follows an educational mission, or deploys an amateur radio service, the amateur band (435-438 MHz) can be used. For commercial purposes the UHF band (400-402 MHz) should be used. Moreover, CubeSats that require a larger data bandwidth to download their scientific data are using higher frequencies, as the commercial S- (2.2-2.29 GHz), or X-bands (7.75-8.5 GHz).

The communications link in [3]Cat-4 is allocated in the radio amateur UHF band. Packets are fragmented in blocks of 255 bytes and protected using a convolution code ($\frac{r=1}{2}$) to overcome channel errors [210]. Moreover, an Erasure Reed-Solomon code generates four redundant packets per each transmitted to avoid slow fadings [211]. This probabilistic communications mechanism downloads without using an Automatic Repeat-Request algorithm. At hardware level, the COMMS has a half-duplex transceiver that modulates the incoming messages using a Gaussian Minimum Shift-Keying (GMSK) modulation. Its reception and transmission chains are composed of a set of amplifiers, which provides up to 15 dB of reception gain, 30 dBm transmitted power, respectively. The antenna used to communicate with ground is a monopole antenna placed in the ISISpace antenna subsystem [212], called ZADS. The signals collected by the COMMS subsystem are transmitted/received from/at the UPC/IEEC Montsec VHF/UHF Ground Station, in Sant Esteve de la Sarga, Catalonia, Spain. The station is located on a secure place as part the IEEC Montsec astronomic observatory premises (Fig. 8.3) [213].

8.2.4 Attitude Determination and Control System

The ADCS ensures that the NADS antenna is always pointing to nadir after its deployment. For that reason, the subsystem performs first a B-dot detumbling algorithm to stabilize the spacecraft rotation speed below 2^o/s. Then, it changes to nadir-pointing mode in which the spacecraft attitude is determined using Optimal REQUEST algorithm, and a Proportional-Derivative controller.

The Optimal REQUEST algorithm provides the quaternion from the spacecraft coordinate reference to the Earth-Centered Inertial reference. The determination is possible because it uses the measurements from the magnetometers, Sun sensors, and gyroscopes to determine the attitude of the spacecraft. Following the REQUEST nomenclature, the two former sensor types help to determine the state of the spacecraft attitude, while the gyroscope input helps to define the state prediction. Current analyses indicate that this algorithm is able to determine the attitude with less than 3% of error. The PD control uses the attitude determination to compare it with a reference to actuate. The corresponding actuator used consists of three independents magnetorquers placed in each body axis. In addition, the gravity boom of the NADS works in the actuation, because it generates a non-negligible gravity gradient towards the nadir.

8.3 FMPL-1 Hardware and Software Design

The FMPL-1 is the platform that integrates the three experiments of the ^{3}Cat-4 mission. The FMPL-1 is composed of four different modules:

- Payload Antennas: Different antennas are used depending on the experiment (i.e. frequency band, polarization...), therefore they are connected to the corresponding RF chain input.
- Radio Frequency module: includes a low noise amplification chain for each experiment in order to filter and amplify the received signals.
- SDR platform: It is the digital unit of a RF receiver which performs RF amplification, filtering, demodulation, and analog-to-digital conversion.
- Computer On-Module: it is the microcontroller which executes the FMPL-1 control software and performs the different experiment algorithms.

The AIS receiver uses a VHF antenna which is directly connected to the receiving chain; the GNSS-R experiment uses an zenith-looking antenna for the GNSS direct signal path (i.e., reference signal). Finally, a nadir-looking antenna is used to receive both GNSS-R signals and to measure the antenna temperature at L-band. The nadir-looking antenna has been designed to receive from L2 to L1 bands for GNSS signals, including the radiometry L-band from 1400 to 1427 MHz. In addition, this antenna includes an RF circuit that contains an internal hot load (matched load), and an active cold load to calibrate the microwave radiometer as close as possible to the antenna plane. As detailed in Fig. 8.4, the different FMPL-1 antennas are connected to the RF module to condition the signal. Finally, a receiver selector chooses the desired path, and the signal is sampled by the SDR.

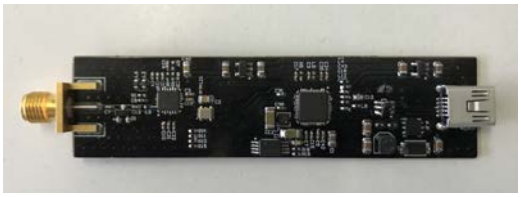

Figure 8.5: In-house developed RTL-SDR used as a prototype of the FMPL-1.

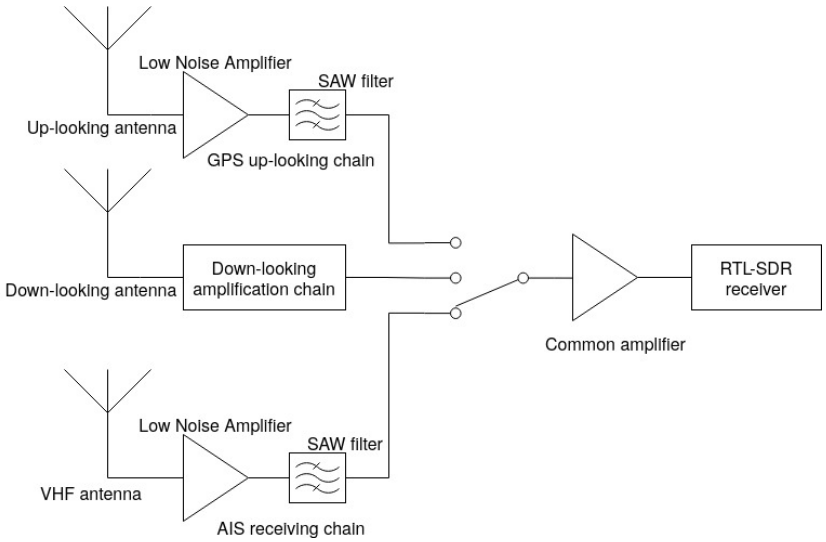

Figure 8.4: FMPL-1 block diagram. Schematic details provided in Appendix B.3.

The SDR used in the mission is an in-house development based on the well-known RTL-2823u chip (Fig. 8.5) [214]. The version used in this mission contains a temperature controlled crystal oscillator and a low-dropout Regulator (LDO). The SDR and the whole receiving chain (i.e., switch selector, receiver selector, etc.) are controlled by the P/L-OBC, the payload computer, which is based on a Gumstix Overo Ironstorm computer [215].

Further details of the FMPL-1 payload are described in the following sections. Moreover, additional details on the design of the FMPL-1 instrument, such as board schematics, are provided in Appendix B.

8.3.1 Antenna design

Three different antennas are used in FMPL-1: the VHF AIS monopole antenna, part of the ZADS subsystem; a zenith-looking RHCP antenna; and the nadir-looking LHCP antenna.

The ZADS VHF antenna is part of a commercial antenna product from ISISpace [212]. The antennas are kept in a stowed configuration and released once in orbit. The zenith-looking antenna is the combination of two linear ceramic loop Surface Mount Device

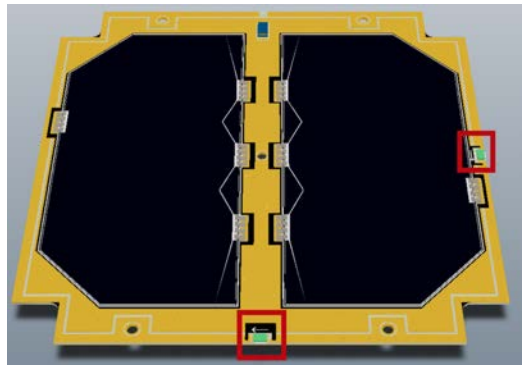

Figure 8.6: zenith-looking antennas (inside the red box) mounted at ^{3}Cat-4 solar panels

(SMD) antennas. To preserve space, those antennas are mounted near the CubeSat solar panels thanks to their reduced dimensions, taking profit of the PCB used by the solar panels as a ground plane (Fig. 8.6).

Finally, the nadir-looking antenna is mounted on the NADS subsystem (detailed in [SJP1]). The antenna design is based on an helix antenna (see Fig. 8.7a), and it works in axial mode to have enough bandwidth and directivity to satisfy the system requirements. The antenna is composed of 11 turns equally distributed in a total axial length of 50.6 cm. The antenna is stored in a stowed configuration (i.e., folded), and once in orbit it is deployed, as presented in Fig. 8.7b. Moreover, at the end of the antenna a gravity boom helps to point the antenna to nadir.

8.3.2 Radio-Frequency module

The main objective of the RF module is to give high performance capabilities to a COTS SDR to receive AIS signals, and to perform GNSS-R, and to retrieve high-precision radiometric measurements at L-band.

8.3.2.1 GNSS-R/Radiometry receiving chain

The L-band receiving stage comprises both the GNSS-R and L-band radiometry signals. Note that for this case different signal sources are required:

- Nadir-looking antenna signal is used for both GNSS-R and radiometry.
- Hot/cold loads for the calibration of the microwave radiometer.

The three sources are combined into a single circuit (Fig. 8.8), where a controllable input switch selects between the nadir-looking signal or the different calibration loads for the radiometer.

The input signal is amplified by a high-IP3 Low Noise Amplifier (LNA) followed by a second stage amplification, which is split for each band, GPS-L2, GPS-L1, and radiometry, which allows the use of a very-narrow band pass filter at each band by using a Surface Acoustic Wave (SAW) filter. For each of the three bands, the SAW filter gives more than

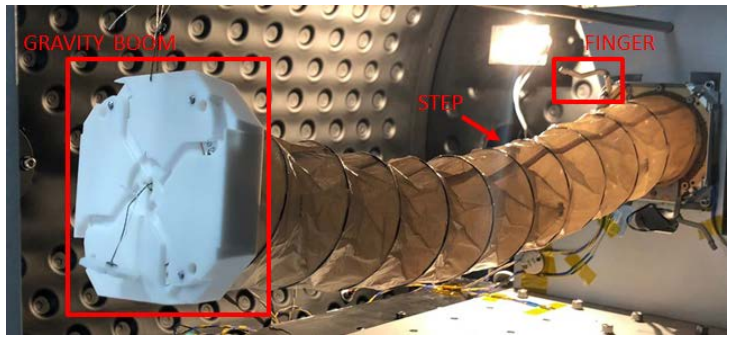

(a)

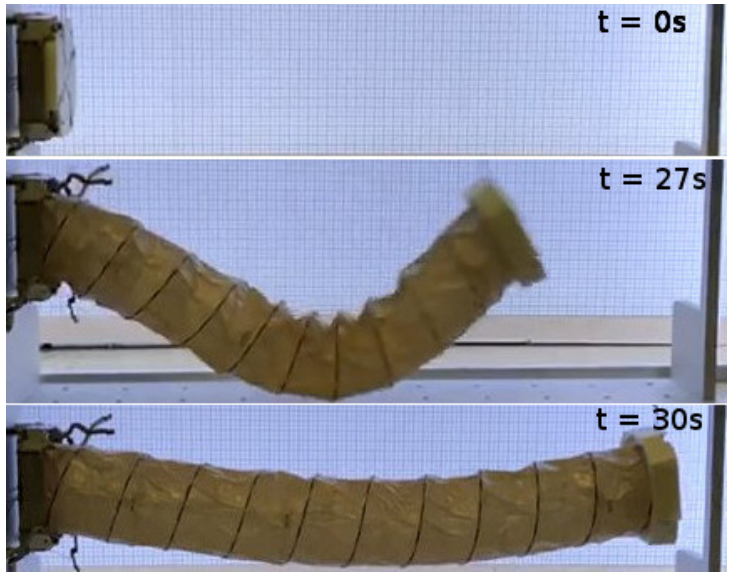

(b)

Figure 8.7: (a) FMPL-1 NADS antenna prototype during a deployment inside a Thermal Vacuum Chamber (TVAC) at ESA Redu premises, and (b) Deployment sequence of the NADS antenna, from stowed (top) to deployed (bottom)

30 dB of attenuation at 50 MHz from the central frequency of each band. The gain and noise figures of the GNSS-R and radiometry chains are summarized in Table 8.2.

At the end, a separate stage is connected to the zenith-looking antenna in order to collect the GNSS direct signal. This stage comprises a two-stage amplifier with a SAW filter, only at L1 band, configured to provide the same gain as the nadir-looking L1 GNSS-R channel. Finally, the receiver is connected to each of the stages through the switch.

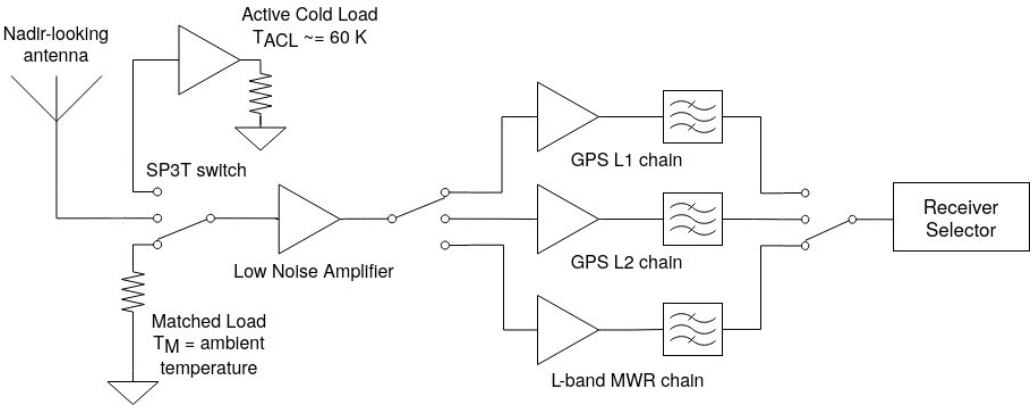

Figure 8.8: Nadir-looking antenna receiving chain (see Fig. 8.4). Detailed in Appendix B.3.1.

Table 8.2: RF-FE gain and noise figure reference for the L-band receiving chain

RF path	Gain [dB]	NF [dB]
Radiometry channel	44.05	0.63
Nadir-looking L1 GNSS-R channel	45.45	0.65
Nadir-looking L2 GNSS-R channel	42.35	0.68

8.3.2.2 AIS receiving chain

The AIS receiving architecture is based on two filtering and two amplifying stages. The very first stage is a low-losses low-pass filter plus a high-IP3 low noise amplifier in order to avoid intermodulation products from undesired sources, which can be found at VHF. Then, a very narrow band-pass filter (with higher losses than the first one) filters again the signal and, a second amplifier increases once more the signal level to compensate previous components insertion losses. The presented architecture has a total gain of 42 dB with noise figure of 2 dB. Achieving enough SNR so that the AIS signals can be decoded from a LEO orbit. The receiver details to deal with the different Doppler shifts are provided later. The block diagram of the AIS receiver is very simple and it is skipped in this section, but it is presented in Appendix B.3.2.

8.3.3 Software architecture overview

The FMPL-1 processing software runs in a dual-core ARM7 working at 1 GHz clock and 1 GB RAM carrying a Linux-based distribution as operative system. The module is turned on by the spacecraft main computer when passing over an area of interest and is turned off again when the experiment execution is finished. Depending on the desired experiment, the computer selects which antennas and receiving chain is used. Once selected, it starts recording raw data for the IQ signals using the SDR. As soon as it has been recorded, both the SDR and the hardware receiver are turned off to save power. The raw data is passed to different processing blocks, depending on the desired experiment. Note that,

the instrument cannot perform different experiments at the same time, as it only has a single receiving channel.

8.3.3.1 GNSS-R experiment

In the GNSS-R experiment, different integration times for different L1 and L2 signals will be tested. For data budget limitations of the platform, and considering the maximum integration time limitations in Chapter 3, L1 and L2 signals will be recorded with a configurable integration time between 40 ms and 80 ms. Note that, the maximum theoretical integration time to prevent waveform blurring due to the code length for a GPS L1 C/A signal is 40 ms.

In this case, the SDR collects from 10 ms of raw data for the zenith-looking antenna (which is enough to have the reference signal), and from 40 to 80 ms for the nadir-looking antenna at both L1 and L2 bands. The signals are stored at 1 bit precision, and time-tagged using the OBC clock. Later, the retrieved data is downloaded using the UHF communication channel of the spacecraft.

Once the data is downloaded to Earth, an orbit propagator is executed with all the available GNSS satellites to retrieve its position based on the time and position telemetry. All estimated GNSS satellite positions and the spacecraft telemetry information are introduced to the GNSS-R processing framework developed for MIR and described in Chapter 4, but now using FMPL-1 data.

8.3.3.2 Radiometer experiment

The radiometer on board ^{3}Cat-4 is a real aperture nadir-looking TPR radiometer with frequent internal calibration, and includes an RFI detection and mitigation technique. The SDR is required to acquire data in the whole 27 MHz radiometry band. Due to its hardware limitations, the whole band is divided into 27 bins of 1 MHz each. The SDR is tuned to acquire 660 ms of I/Q data at a 1 MHz sampling rate for each bin, providing an accuracy of:

$$\Delta T = \frac{T_{sys}}{\sqrt{B \cdot \tau}}, \tag{8.1}$$

where $T_{sys} = T_A + T_R = 380$, with $T_R = 80$ K, and $T_A^{max} = 300$ K (pointing towards dry soil), $B = 1$ MHz and $\tau = 660$ ms, $\Delta T = 0.46$ K.

The experiment, for each frequency bin, sequentially performs a hot and cold calibration by measuring, for each bin, the total noise power when connected to each of the loads. After calibration, the radiometer retrieves the nadir-looking signal and measure the antenna received power measurements two times for each bin of the whole band. Once measures are done, the calibration is performed again.

The processing algorithm integrates the measured power for each realization (660 ms of raw I/Q data at 1 MHz sampling rate, a total of 27 realizations to cover the whole band, as detailed in Fig. 8.9), and applies a RFI mitigation technique based on a statistical complex Kurtosis normality test and performing a pulse blanking to the potential interfered samples [216]. As a final product, the radiometer experiment generates the power data corresponding to the signal before and after the RFI mitigation technique, as well as the

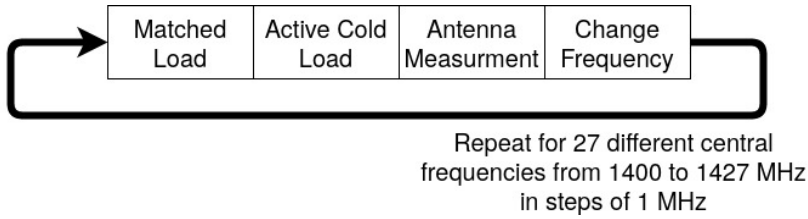

Figure 8.9: FMPL-1 MWR acquisition diagram to cover the entire protected L-band MWR band in steps of 1 MHz.

statistical values from the Kurtosis estimation, the noise power received when switched to the calibration loads, and the physical temperature of the antenna, the amplifier, and the calibration loads. Note that, the calibration process of a TPR radiometer using frequent internal calibration is presented in Chapter 9 (Section 9.4). Finally, the radiometer output is stored in a comma-separated value (CSV) file, which is then compressed and downloaded through the spacecraft UHF link.

8.3.3.3 AIS experiment

The third experiment combined in the FMPL-1 is a message demodulator and decoder that receives telemetry signals emitted by ships and vessel traffic services, AIS base stations, and other satellites. All those signals follow a specific protocol, use a GMSK modulation, and access the channel using Time Division Multiple Access (TDMA) with pre-defined slots managed by a central AIS coordinator. However, as in the GNSS-R experiment, the satellite velocity produces an important Doppler shift in the received signal. The AIS signals are split in two channels centered at 162 MHz, the two channels are separated 25 kHz. In order properly receive all the possible messages coming from any AIS source, a filter bank is used for each band, and an automatic gain control is followed by a frequency locked loop [217] to compensate the Doppler shift induced by the relative speed of the spacecraft. Note that, at VHF the maximum expected Doppler shift is $\sim \pm 5$ kHz. Then, this output is routed to a GMSK demodulator, one per channel, that gets the raw bits of the received signal. The binary stream is then passed to a High-Level Data Link Control (HDLC) packet decoder, which saves the messages with a correct checksum, and stores them in a binary ASCII format, ready to be downloaded as a final product of the experiment.

The receiving flowgraph is generated using an open-source software called GNURadio [218]. The software is installed as a Linux package and a Python program is generated and executed. Fig. 8.10 details the GNURadio scheme developed to demodulate the AIS signals.

8.4 FMPL-1 Implementation and Testing Phase

The FMPL-1 has been manufactured following the Engineering Model (EM), Qualification Model (QM), and Flight Model (FM) philosophy. Three versions are built, the first one is used to prototype the payload (see Fig. 8.11). Then, the QM and FM models are built and validated. The QM is extensively in extreme conditions inside a thermal-vacuum

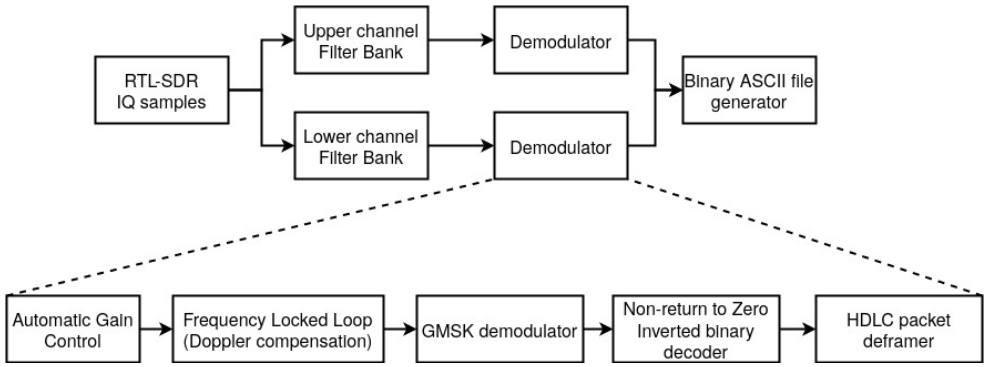

Figure 8.10: GNURadio flowgraph developed to demodulate and store AIS signals.

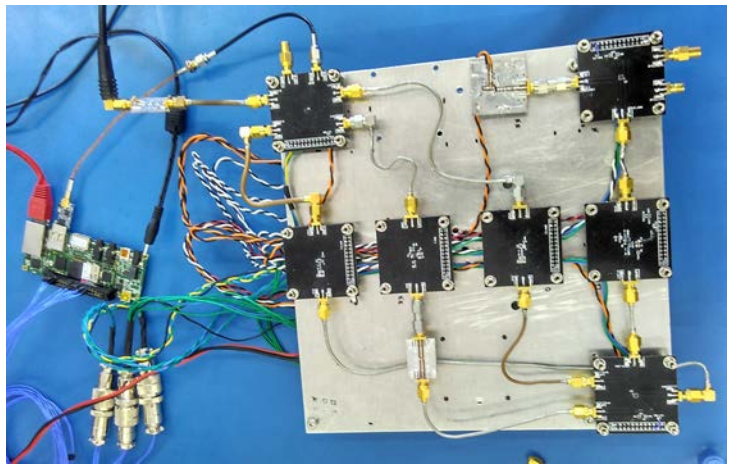

Figure 8.11: First Engineering Model prototype of the FMPL-1 electronics disposed in separate boards to ease the characterization of single components.

chamber (TVAC) (i.e., to validate the system can withstand vacuum conditions), and in a launcher simulator (i.e., shake table to simulate environmental conditions during launch). Finally, the FM environmental testing included TVAC and vibrations, but with attenuated profiles. This approach is typical in space, as the QM serves to qualify and stress the instrument (i.e., to know the limits), and the FM just undergoes the "minimum" amount of tests to ensure proper manufacturing procedures, but not to over-stress the instrument. The first procedure is known as Qualification Test (and the test levels are known as Qualification levels), and the second is known as Acceptance Test (and the test levels are known as Acceptance levels).

Both QM and FM models are first validated in ambient conditions to see that the main characteristics of the payload (Table 8.3) remain the same before and after the tests. Note that, for CubeSat systems, volume is specified in internal CubeSat Units, being a single unit 90x96x90 mm^3 (PC-104 standard), and not which is not 10x10x10 cm^3 presented in Chapter 1. Thus, the inner size is given instead of the outer size, the remaining cm is

Table 8.3: Main Characteristics of FMPL-1.

Parameter	Value
Volume (electronics)	0.15 Units: ∼9x9x1.5 cm^3
Volume (nadir-looking antenna)	0.2 Units: ∼9x9x2 cm^3 (stowed)
Mass (electronics)	115 g
Mass (nadir-looking antenna)	253 g
Power Consumption	435 mA at 5 V
Data rate (GNSS-R)	∼30 kB per execution
Data rate (Radiometer)	$<$ 100 Bytes/s
Data rate (AIS)	$<$ 100 Bytes/s

occupied by the CubeSat structure and the harnessing.

8.4.1 FMPL-1 electronics

The FMPL-1 has been implemented in two Printed-Circuit Boards (PCB). The first board is the "FMPL-1 motherboard", which carries all the power electronics (i.e. DC/DC converters), and also serves as interface board to the P/L OBC module (Fig. 8.12a). The second board is the "FMPL-1 daughterboard", and it carries all the RF equipment previously described. Moreover, an aluminum shield has been manufactured to mitigate any possible EMI in the RF circuitry. The three boards (motherboard, daughterboard, and COM) are stacked together with the aluminum shield as detailed in Fig. 8.12b-c.

Furthermore, aside from the RF daughterboard, some RF circuitry is also implemented in other boards to minimize the noise figure and the losses of the system. As highlighted in Fig. 8.13a, part of the nadir-looking RF chain is implemented in the NADS antenna system, in a small board called RF ring adapter, detailed in Fig. 8.13b. Moreover, as previously introduced, the GNSS zenith-looking receiving chain is also mounted in the backside of the Z solar panel presented in Fig. 8.6, as detailed in Fig. 8.13c.

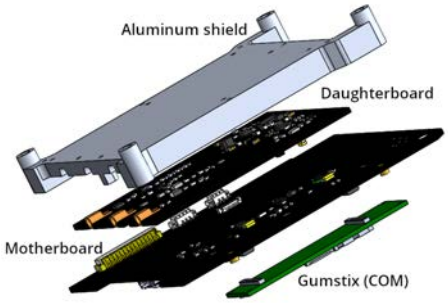

(a)

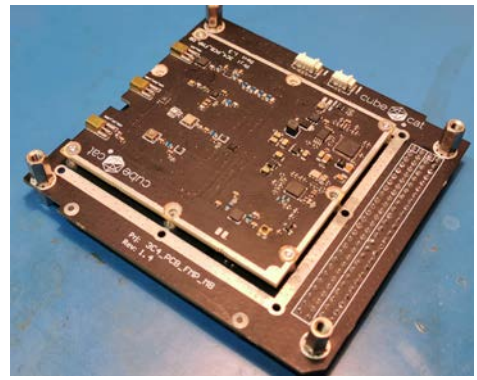

(b)

(c)

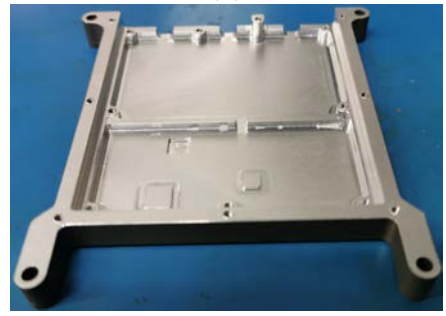

(d)

Figure 8.12: (a) Exploded view of the 3D model of FMPL-1, (b) FMPL-1 (top view) without the aluminum shield, (c) FMPL-1 (bottom view) including P/L OBC board inserted, and (d) FMPL-1 aluminum shield.

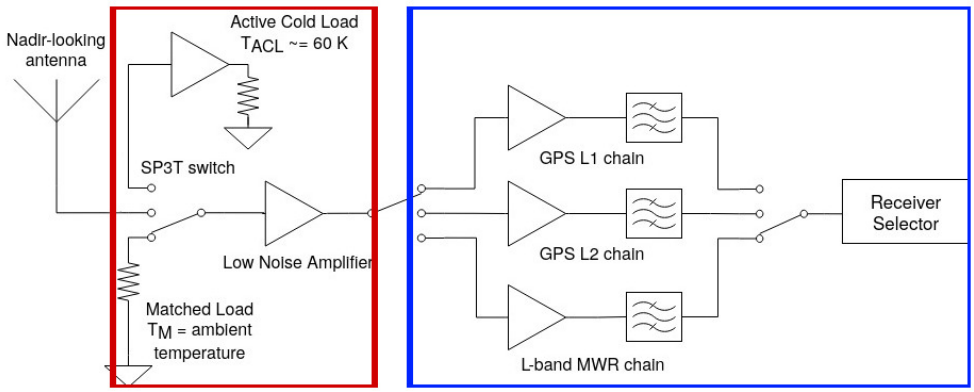

(a)

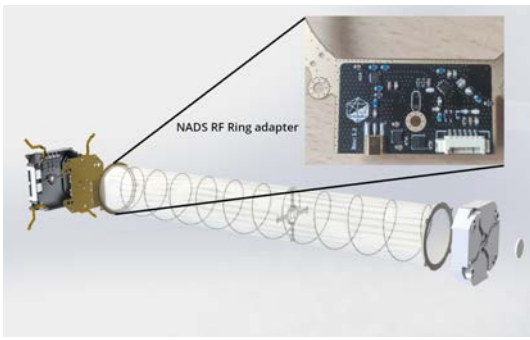

(b)

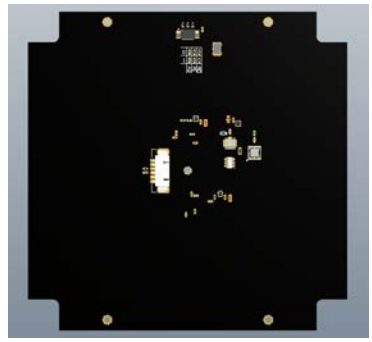

(c)

Figure 8.13: (a) Fig. 8.8 where the RF circuitry which is part of the NADS matching PCB is highlighted in red, and the RF circuitry part of the RF daugtherboard is in highlighted in blue, (b) RF ring adapter part of the nadir-looking amplification chain, and part of the NADS antenna system, and (c) zenith-looking GPS L1 antenna RF amplification circuit mounted on the backside of its solar panel.

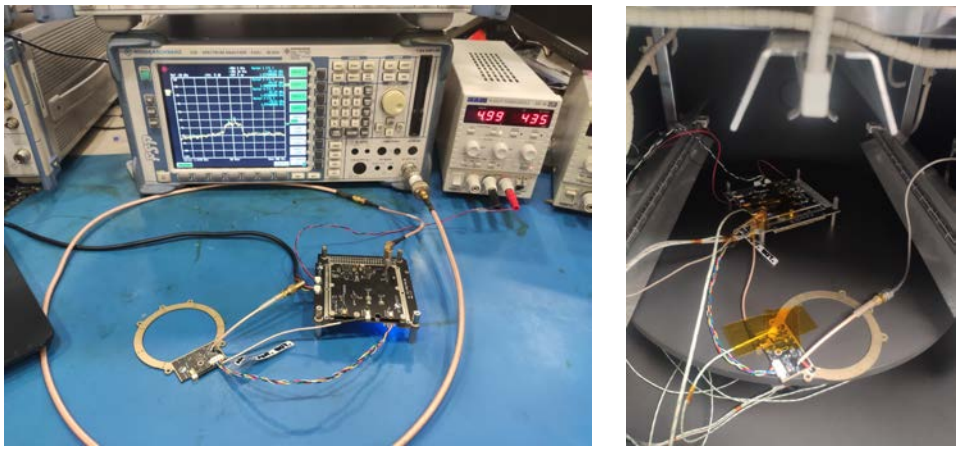

(a) **(b)**

Figure 8.14: FMPL-1 subsystem in (a) the standalone ambient test campaign to verify the MWR chain, and (b) the TVAC test to verify the thermal dissipation and the performance of the instrument in extreme temperatures.

Table 8.4: Measured directivity of the FMPL-1 helix antenna

Band	Directivity
L1	13.5 dB
L2	8.8 dB
L-band (1400-1427 MHz)	12.0 dB

Finally, the FMPL-1 electronics went under ambient and environmental testing in accordance to the ^{3}Cat-4 schedule. The testing will be carried out with the satellite integrated (Q3 2021). At the time of writing this dissertation, the FMPL-1 radiometry chain has already been tested both in ambient (8.14a) and thermal-vacuum conditions (Fig. 8.14b). The tests were conducted by UPC NanoSat-Lab members, validating the gains and noise figures presented in Section 8.3.2.1, verifying the dissipation capabilities of the aluminum shield (i.e., to prevent overheating), and the performance of the instrument at different temperatures.

8.4.2 FMPL-1 antenna

The FMPL-1 antenna has been characterized at the UPC CommSensLab anechoic chamber, as seen in Fig. 8.15, and the measured normalized antenna radiation patterns for each band are detailed in Fig. 8.16. Moreover, the computed directivities for each band are detailed in Table 8.4.

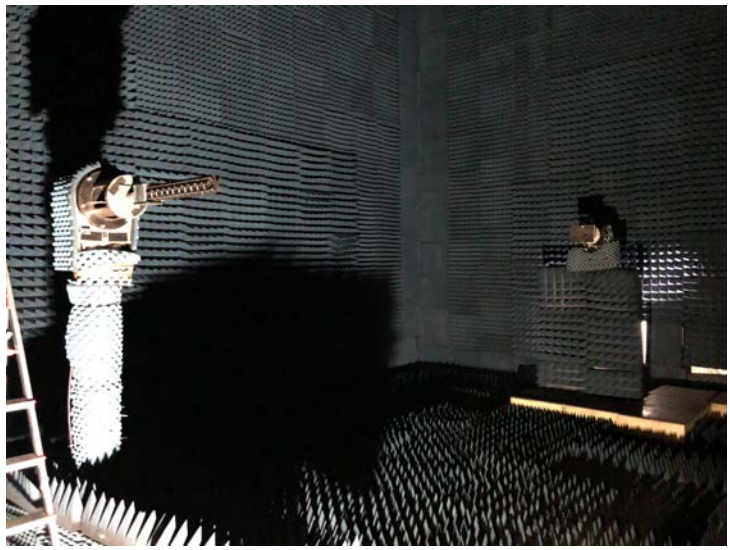

Figure 8.15: L-Band helix antenna prototype measured in the UPC CommSensLab anechoic chamber [http://www.tsc.upc.edu/es/instalaciones/camara-anecoica]

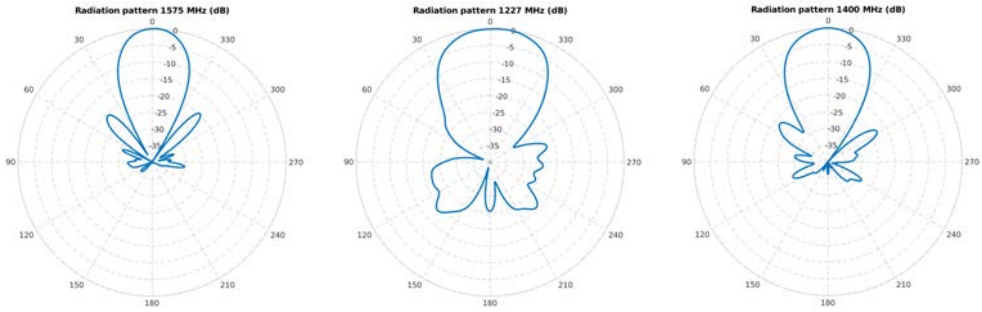

(a) **(b)** **(c)**

Figure 8.16: Normalized antenna radiation pattern for (a) L1, (b) L2, and (c) L-band radiometry (1400-1427 MHz) bands.

8.5 Conclusions

The ^{3}Cat-4 mission has been presented as an example of a 1U CubeSat EO mission. A high-level description of all its subsystems has been presented, focusing on its payload, the FMPL-1. This instrument comprises an in-house developed COTS RTL-SDR to demonstrate capabilities of a 1U CubeSat for EO. The system has been designed to fit in a 10x10x10 cm^3 structure, and a deployable helix antenna has been developed for such purpose.

The FMPL-1 comprises three different experiments: an L1/L2 GNSS-R receiver working as a data-logger, storing raw data at 1-bit precision, an L-band MWR with

RFI detection working as a TPR with frequent internal calibration, and an AIS receiver. This instrument is the first of the "FMPL" family, and serves as a baseline for the next EO instruments both for CubeSats and for other platforms. It is important to remark that, without the support of the ESA Fly Your Satellite! program, and to all previous UPC PSR instruments[1] FMPL-1 would not had been possible at all.

At the time of writing this dissertation, the mission is at the end of the hardware and software development stage, and it is foreseen that by Q4 2021 the spacecraft undergoes both ambient and environmental testing campaigns, which validate that the satellite withstands the launch conditions and the vacuum environment in space.

[1] Presented in Section 2.5.

9

Chapter 9

The Flexible Microwave Payload -2

From the knowledge acquired during the design and development of the FMPL-1, the FMPL-2 was conceived. This second iteration of the "FMPL" family comprises a GNSS-R receiver at L1 and an L-band MWR that are working in synchronous operation. Thanks to the enhanced processor used in this FMPL version, GNSS-R observables are computed in real-time during payload executions. In this case, the timeline of this mission was very tight, as one of the goals was to implement the mission (from the conception to the integration in the launcher) in one year and a half. For that reason, the spacecraft design and manufacturing process was outsourced to Tyvak International, based in Turin, Italy. The design of FMPL-2 was carried out in the UPC NanoSat-Lab, and the development of the RF hardware boards outsourced to a UPC spin-off company (Balamis S.L.), all in a record time of less than a year, from the first designs to the final environmental testing and instrument calibration, which have been also carried out at the UPC NanoSat-Lab.

This Chapter is organized as follows: Section 9.1 introduces the FSSCat mission and goals. Section 9.2 presents the design of FMPL-2, the instrument requirements, and the details in terms of hardware and software design. Section 9.3 presents the implementation details, the final hardware once integrated, and the ambient and environmental tests performed to validate the instrument for space conditions. Section 9.4 presents the required operations to calibrate both the GNSS-R and the L-band MWR instruments. Finally, Section 9.5 concludes the Section.

Note that, part of this Chapter has been adapted from a previously published manuscript in a peer-reviewed journal. The manuscript is entitled "The Flexible Microwave Payload-2: A SDR-Based GNSS-Reflectometer and L-Band Radiometer for CubeSats" [JP2]. Moreover, the work presented in this Chapter has also been presented in several international conferences [CP2, CP8, CP9, CP10].

9.1 Introduction

FSSCat was the winner of the ESA Sentinel Small Sat (S^3) Challenge of the Copernicus Masters Competition in 2017, and the mission is the first CubeSat-based third party ESA mission contributing to the Copernicus system [19]. The mission was proposed in June 2017, awarded in November 2017, and the design and manufacturing process started in March 2018. The FSSCat mission is composed by two 6-unit CubeSats: ^{3}Cat-5/A (NORAD id: 46292, Int'l Code: 2020-061W) and ^{3}Cat-5/B (NORAD id: 46293, Int'l Code: 2020-061X). The "A" spacecraft embarks the FMPL-2, a dual passive microwave remote sensing payload (GNSS-R and L-band MWR), developed by the UPC in Barcelona, Spain; and an RF/Optical Inter-satellite link payload, developed by the UPC (RF) and by Golbriak Space OÜ (Optical) in Estonia. ^{3}Cat-5/B is composed by the same RF/Optical Inter-satellite link payload, and the remote sensing payload is Cosine's Hyperscout-2 [219], an hyper-spectral and thermal infrared imager.

The platform provider, satellite integration, and mission planner is Tyvak International [220], based in Torino, Italy. Moreover, the mission has the support from Deimos Engenharia, who provides the data processing ground system, and the financial, technical and programmatic support, and laboratory facilities of ESA.

9.1.1 Mission goals

From now on, we will focus in ^{3}Cat-5/A, which is the one carrying the UPC NanoSat-Lab payload. The mission goal for this spacecraft is to provide almost full coverage (there is a $\sim 4^{\circ}$ latitude gap near the geographic poles due to the orbit inclination) of both the North and South poles providing Sea Ice Concentration (SIC) and Sea Ice Thickness (SIT) products from the data acquired from FMPL-2. SIC will be derived from combination of MWR and GNSS-R measurements, and SIT is derived from the L-band radiometry data [29], combined with SIC or sea-ice extent from other sensors (i.e., SAR, cGNSS-R, or Ku/Ka microwave radiometry).

Thanks to GNSS-R, the SIC product can be produced along the specular reflection points at a higher spatial resolution, as the reflections come from the first Fresnel zone (i.e., $\sim$500 m. from a spaceborne instrument [17]), and not from the glistening zone. This improved resolution allows a precise edge detection between sea-ice and ocean. Furthermore, the combination of SIC and SIT products from GNSS-R and L-band radiometry sensors in a CubeSat constellation would help to increase the amount of data collected, and reduce the revisit time, which is needed to monitor and understand the evolution of sea-ice [221].

As a third goal, ^{3}Cat-5/A will also provide low resolution soil moisture maps over selected targets (i.e. non-polar areas), which will be down-scaled using multi-spectral optical data. The pixel downscaling technique has been successfully applied to SMOS and SMAP data [174, 175].

9.1.2 ^{3}Cat-5/A design overview

The mission was designed to minimize both the mission risk and the delivery time of both spacecrafts, as one of the challenges was to finalize the production phase in less than a year. Thus, the two CubeSats are designed using the same avionics and a similar strategy

to fulfill the mission requirements.

In the case of ^{3}Cat-5/A, the spacecraft avionics (see Fig. 9.1) are entirely implemented by Tyvak International:

- The OBC is a Linux-based microprocessor board developed by Tyvak. The OBC connects the different subsystems, turning them ON/OFF, and controlling the entire spacecraft.
- The ADCS system is based on two star-trackers for attitude determination, providing a fine pointing accuracy, and a set of reaction wheels and magnetorquers for attitude control.
- The EPS is one of the parts which is typically re-designed entirely for each mission. The EPS used in the ^{3}Cat-5/A spacecraft comprises twelve lithium-ion batteries connected to a backplane, which include the required voltage regulators to power the entire satellite. In this case, one of the 6U faces is entirely covered by solar panels. This face is pointed towards the Sun while the spacecraft is not acquiring payload data.
- The COMMS is based on two approaches, a commercial UHF communication system for basic telemetry and commanding, and an S-band link used to download the scientific data and the high-resolution telemetry information. In ^{3}Cat-5/A the UHF link is entirely manged by Tyvak International in one of their ground stations, and the S-band link is downloaded through the S-band antenna of the UPC/IEEC Montsec Ground Station (see Fig. 9.2).

9.2 FMPL-2 Hardware and Software Design

The FMPL-2 performs cGNSS-R [17] by means of the direct correlation of the GNSS signals collected by the nadir-looking antenna, with all the available codes transmitted by the satellites in view and for a reduced set of Doppler bins, for both GPS L1 C/A, and Galileo E1 signals. The cGNSS-R processor is highly configurable in terms of incoherent integration, Doppler cuts, and maximum number of satellites to be observed. However, changing those parameters out of the default ones impacts on the amount of DDMs per second that this processor can generate.

For the radiometric measurements, the payload follows a TPR architecture with frequent internal calibrations using: an Active Cold Load (ACL), and a matched load (ML) at known physical temperatures. Moreover, the signal collected by the antenna is evaluated using a normality test to check the presence of interference [216].

As detailed in Fig. 9.3, the FMPL-2 is composed by four modules:

- The Payload Antennas (#1 in Fig. 9.3) are composed by two antennas: a zenith-looking L1-band right-hand circular polarization patch antenna for the direct GNSS signal, and a nadir-looking dual-band (1400-1427 MHz for the radiometer, and L1 for GNSS-R) left-hand circular polarization 6-element patch antenna for the reflected GNSS signal and for the L-band microwave radiometer.

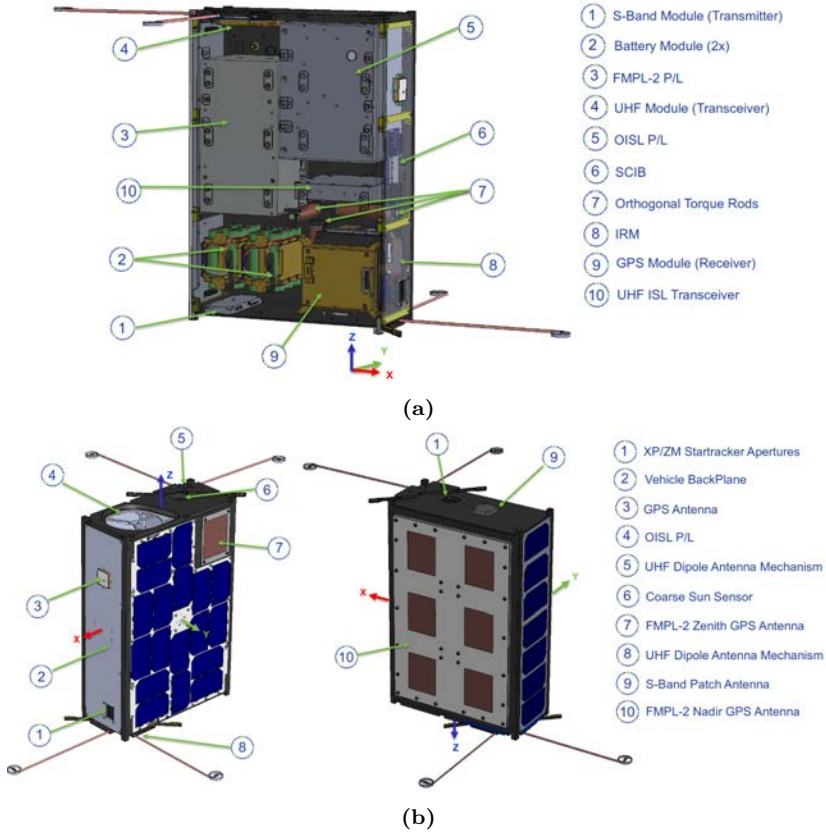

Figure 9.1: (a) ^{3}Cat-5/A spacecraft 3D CAD representation highlighting its main internal parts, and (b) detailed diagram showing the ^{3}Cat-5/A external panels, including FMPL-2 antennas used to perform GNSS-R and L-band MWR. Credit: Tyvak International.

- The Radio Frequency - Front End board (RF-FE) (#2 in Fig. 9.3) amplifies and conditions the signals. It is composed by different LNAs, filters, and a set of power splitters/switches to perform signal amplification and selection to the different SDR input channels.

- The Interface board (IB) (#3 in Fig. 9.3) is a simple board used to interconnect the data processing unit, the RF-FE board, and the Novatel OEM719B GNSS receiver, used to geo-reference and time-tag the observables. This board also includes a circuit that acquires the temperature readings from the other payload modules, and serves as a mechanical interface for the GPS receiver.

- The Data Processing Unit (DPU) (#4 in Fig. 9.3) is implemented through the NanoSDR module from GomSpace [222], hence is both the SDR front-end and the microprocessor unit. This unit is in charge of the data collection (Analog-to-Digital conversion), the execution of the FMPL-2 control software, and the execution of the processing software for both GNSS-R and L-band radiometry. The DPU is in charge

Figure 9.2: S-band antenna used to download FMPL-2 scientific data, located at the UPC/IEEC Montsec Ground Station.

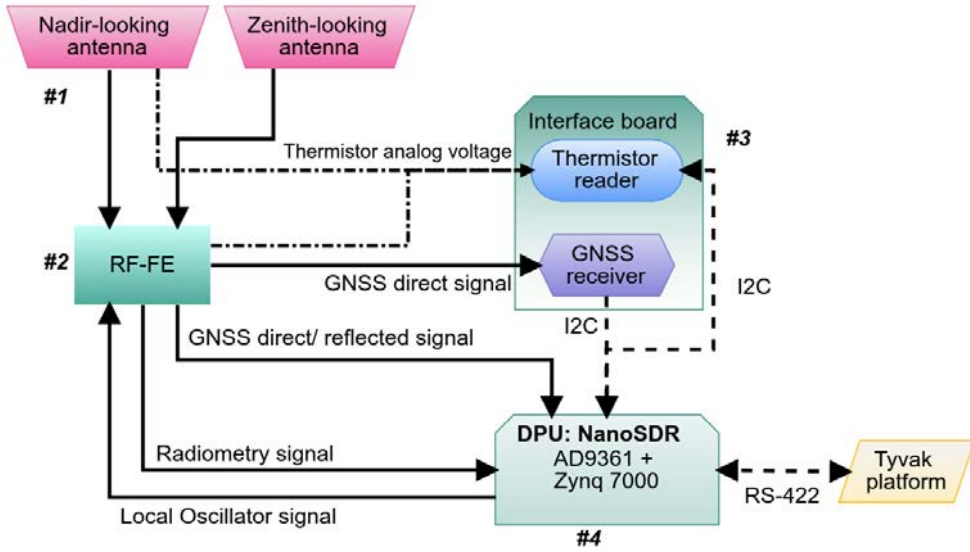

Figure 9.3: Flexible Microwave Payload 2 block diagram.

of the communication with the platform OBC through a RS-422 link. This module is a mixture of a SDR, based on the AD9361 chip from Analog Devices, which is a RF front end broadly used for SDR, and it has two RX channels, sharing the Local Oscillator (LO), and two TX channels, also sharing the LO. The microprocessor unit of the DPU is based on a dual core ARM microprocessor, which is part of the based

on the Zynq7045 Field Programmable Gate Array (FPGA) from Xilinx [223].

Further details of the FMPL-2 payload are described in the following sections. Moreover, additional details on the design of the FMPL-2 instrument, such as board schematics, or additional tests are provided in the Appendix C.

9.2.1 Antenna design

The FMPL-2 payload is designed to work with two antennas: a nadir-looking dual-band passive antenna for both GNSS-R and L-band radiometry measurements, and a zenith-looking antenna for the GNSS direct signal acquisition, both designed by Ms. Lara Fernández.

On one hand, the zenith-looking antenna is based on a passive RHCP micro-strip patch antenna centered at GPS L1 band, 1575.42 MHz. The zenith-looking antennas has a 3 dB beam-width of 87º and a directivity of 6.9 dBi.

On the other hand, the nadir-looking antenna design is based on a 6-element passive patch array (Fig. 9.4). Furthermore, the antenna does not contain any resistor that may generate additional thermal noise. Hence, the combiner used to merge the signals coming from the 6 elements is made of transmission lines only.

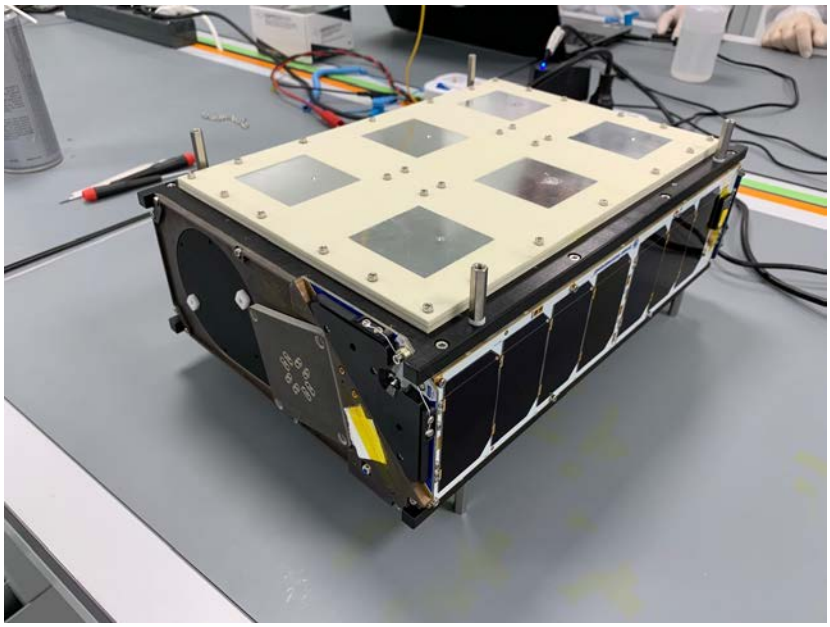

Figure 9.4: UPC FMPL-2 six-element patch antenna array integrated into Tyvak's 6U CubeSat platform (credit: Tyvak International [220]).

As detailed in Fig. 9.5 the antenna is designed in different layers. The first two layers contain the resonator patches, which have been designed to resonate at both 1413 MHz and 1575.42 MHz. Those layers are then followed by a ground plane, and finally by the combiner layer, which takes the signal coming from the 6 patches, and combines them using a stripline-based combiner, which is afterwards routed to a single SMA connector.

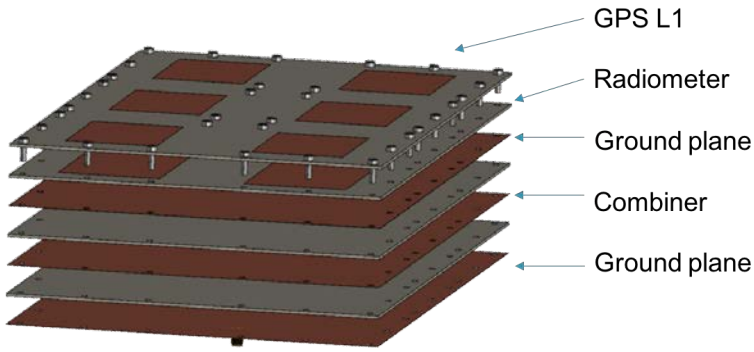

Figure 9.5: FMPL-2 Nadir antenna design including its patches and combiner in the internal layers

9.2.2 Radio-Frequency Front-End

Figure 9.6 shows, the signal routing from the nadir-looking antenna to a 3-channel switch, which selects between the antenna input or any of the calibration loads (either the ACL or the matched load).

This input signal passes through a 20 dB isolator to improve the antenna return loss, and a high-IP3 LNA (19 dB of gain, 36 dBm of OIP3, and 0.37 dB of noise figure) that amplifies the signal before it is split in two channels: one for the Radiometer and the other one for the GNSS-R. Each of the channels is filtered using a Surface Acoustic Wave (SAW) filter (60 MHz bandwidth for the radiometry channel and 2.4 MHz bandwidth for the GNSS channel), and then amplified using the same LNA model so as to have the gain matched. After all, the radiometric signal is routed to its output connector, while the GNSS signal passes through a two-channel switch, which can select between the nadir-looking path or the zenith-looking path.

After the signal conditioning, the signal is routed to the DPU board, where the AD9361, the SDR chip (explained in detail in section 9.2.4), performs the analog-to-digital conversion. The AD9361 has two receiver inputs, but with the same Local Oscillator (LO). Thus, in order to sample both GNSS L1 and L-band radiometry signals at the same time and using the same AD9361 receiver, the L1 signal is down-converted to have the same central frequency. In this case, an active mixer is used to convert the GNSS signal to the same frequency of the radiometer channel. To perform the down-conversion, one of the transmission channels of the AD9361 is used as LO of the external mixer (Fig. 9.6).

The signal coming from the zenith-looking antenna undergoes also a two-stage amplification with a SAW filter in between, before it is connected to the GPS receiver, and to the switch of the GNSS channel from the AD9361 receiver [224]. Table 9.1 summarizes the different RF paths with their measured gains and noise figures.

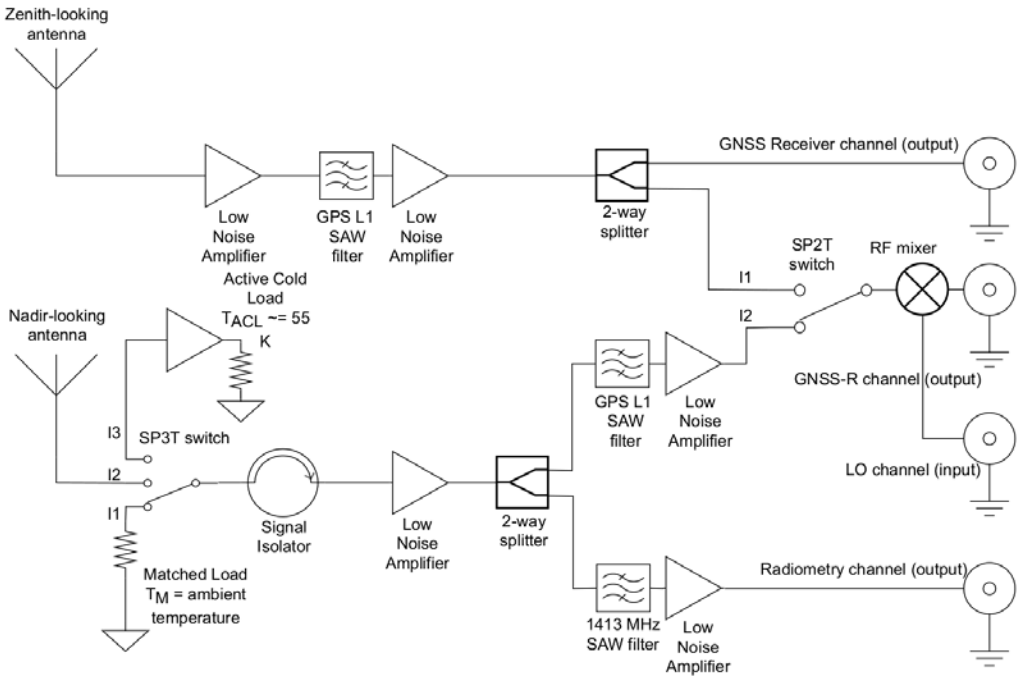

Figure 9.6: RF-FE receiving chain. Schematic detailed in Appendix C.

Table 9.1: RF-FE gain and noise figure (NF) reference.

RF path	Gain [dB]	NF [dB]
Radiometry channel	56.2	0.96
Nadir-looking antenna to GNSS-R channel	52.9	1.14
Zenith-looking antenna to GNSS-R channel	53.3	0.60
Zenith-looking antenna to GNSS receiver channel	31.7	0.60

9.2.3 Interface board

The interface board is a simple 2-layer board which main purpose is to provide a mechanical and data interface for the GNSS receiver, the Novatel OEM719B. The NanoSDR has a single I2C interface to connect any other peripheral, therefore this interface is used to interface an I2C to the Universal Asynchronous Receiver Transmitter (UART) device, which is connected to the GNSS receiver COM interface.

In addition, this board contains a six-channel 14-bit ADC, which is also controlled by I2C interface, that is connected to different thermistors distributed in the nadir-looking antenna and the RF-FE board. The thermistors are distributed in the RF-FE board critical components where noise is generated, as the isolator, the Single Pole Three Throw (SP3T) switch and the main LNA. Finally, two thermistors are placed in the inner face of the nadir-looking antenna, which is then used for calibration (see section 9.4.2).

9.2.4 Data processing unit

The DPU is the payload processing unit, and it is in charge of sampling the RF signal (i.e. RF down-conversion and IQ sampling), sending the IQ data to the ARM processor, applying the different processing algorithms (radiometry, GNSS-R), as well as the storage of the processor results. Moreover, this unit is in charge of the retrieval, storage, and forwarding of the payload housekeeping data (i.e., temperature measurements for both the signal conditioning board and the antennas), and the establishment of the communications with the platform OBC.

This board is based on the Nano-SDR from GomSpace, with flight heritage from the GOM-X4 mission. This module is composed by the TR-600 module [225], a two-channel 12-bit ADC, and two-channel Digital-to-Analog Converter (DAC) based on the AD9361 chip. The TR-600 is controlled by the Nanomind Z7000 from GomSpace [222].

As detailed in Fig. 9.7, the DPU with its two main components: the Zynq7045 FPGA and the AD9361 chip. The FPGA implements a dual core ARM, where all the code is implemented and executed. This module is interfaced to a eMMC memory, where the main code is stored, as well as the results of the FMPL-2 execution. In addition, the Zynq is connected to a RS-422 transceiver through UART, which is used to interface with the platform OBC. Moreover, the FPGA also implements a control module to acquire I/Q samples, and tune the AD9361. Finally, the FPGA implements the correlation module used by the cGNSS-R processor, which is connected to a DMA module to transfer the data from the ARM processor to the FPGA and viceversa.

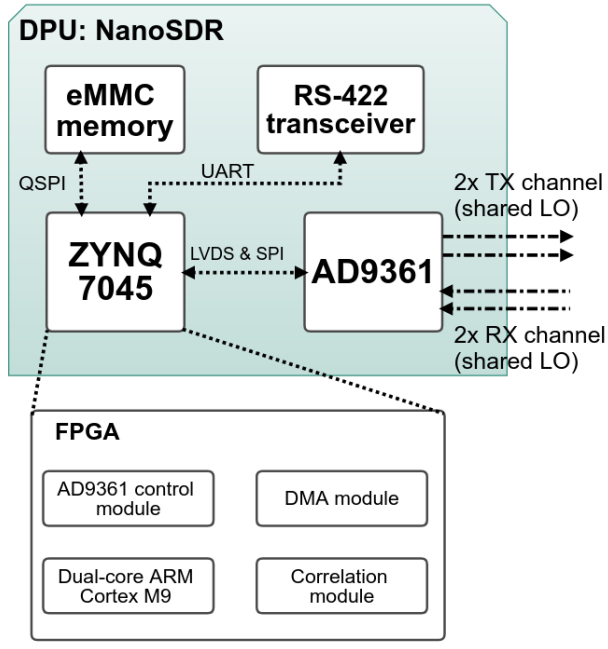

Figure 9.7: DPU detailed block diagram.

The microcontroller unit of the DPU is a System on Chip (SoC) based on an FPGA

running a 667 MHz dual-core ARM Cortex-A9 processor. The SoC runs a custom Linux Kernel from Analog Devices, which enables the DPU to easily configure, communicate, and stream I/Q data from the AD9361 chip to the user space, as the data interface between both modules is performed through a Linux standard library (LibIIO [226]), which is used to control industrial input/output peripherals, as the TR-600. The library uses a Direct Memory Access (DMA) peripheral installed in the FPGA to transfer directly from the ADC/DAC to the ARM processor RAM memory.

9.2.5 Software architecture overview

Moreover, the use of a Linux-based OS eases the communication between the platform computer, which is also running Linux, and the instrument computer. For the FSSCat mission, both computers are running a Point-to-Point Protocol (PPP) over RS-422, which at the end gives an IP address to the payload computer. Hence, the use of IP protocol gives the possibility to use a variety of already implemented network tools for communication such as: Secure Shell, File Transfer Protocol, TCP/IP stack, and the Linux socket API. The use of these validated tools reduces the overall mission risk, and speeds up the development time.

The DPU runs several Linux user-applications split in different processes, and also FPGA devices accessed through the Linux Kernel space in order to satisfy the payload requirements. As detailed in Fig. 9.8, the software developed is mostly running on top of the Linux user-space (rectangular diamond, in purple), which can be easily monitored and debugged. Other open source tools (circular shape, in blue) are used to communicate internally between the different process and towards the platform, and finally some kernel modules (rectangular, in green) are used to perform all the functions.

To speed up the computation of the Delay-Doppler Maps, the DDM calculator uses some modules of the FPGA to perform the cross-correlation of the GNSS. In order to transfer the data between the FPGA fabric and the microcontroller memory, the software uses a kernel-space driver to interface with the direct memory access (DMA) peripheral.

- The SDR reader and the radiometry processor are merged into a single process. On one hand, the process is in charge of the communications through LibIIO with the SDR ADC. In addition, this process controls the switching through the different calibration loads. On the other hand, it also performs the radiometric observables calculation by integrating the square of the I/Q samples acquired for both GNSS and L-band radiometry channels. LibIIO is configured with two buffers: when one is full, it swaps to the next buffer, so as the user space can retrieve the first buffer contents. For this instrument configuration, each buffer can keep up to 50 ms of raw data.

- The DDM calculator (or cGNSS-R processor) is in charge of performing the correlation of the GNSS (GPS and Galileo) signals. It is detailed in the next section.

- The GNSS reader process is in charge of the configuration and communication with the Novatel OEM719B [227], the payload on-board GNSS receiver. The receiver streams *NMEA* messages as: *RANGE, BESTPOS, and SATVIS2*, which are including position, velocity, time, and pseudorange measurements which are then used to time-tag and geo-locate the GNSS-R and Radiometry data.

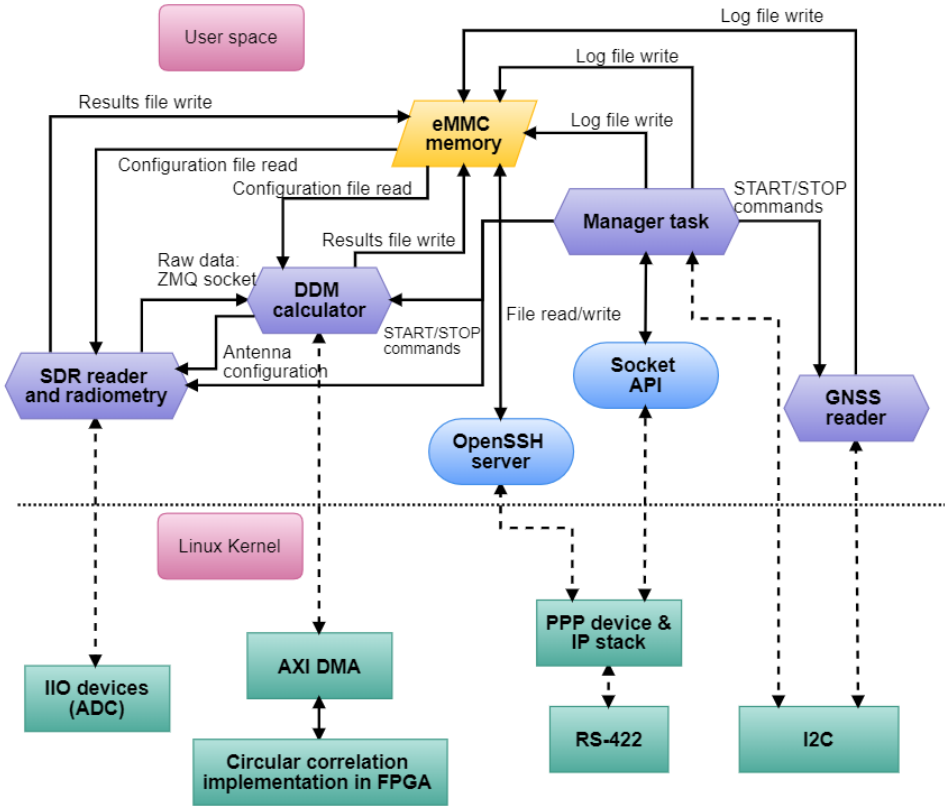

Figure 9.8: FMPL-2 software architecture is divided in two sections: User space (top part of the image), and Linux Kernel space (bottom of the image).

- The Manager Task is the single point of communication with the platform computer and also process the platform commands or messages.

9.2.5.1 Signal acquisition and software processing steps

Both NanoSDR channels are sampled at the same time, hence the cGNSS-R data and L-band radiometry data are exactly synchronized. Both channels need to be configured with the same parameters, which for the FMPL-2 case are set to 4.096 MSps and per channel.

The processing flowgraph is divided in blocks (Fig. 9.9), with a repetition period of 500 ms, splitting the measurements in three steps, as shown in Table 9.2.

In addition, each acquisition step has a guard period of the size of the acquisition buffer. Once a switch position is toggled, some samples of the current buffer being streamed may contain data from both switch positions, for that reason the system waits for a buffer duration.

Table 9.2: State of the RF-FE switches (Fig. 9.6) during the different acquisitions.

Switch state during acquisition	SP3T position	SP2T position
Antenna acquisition	I2	I1: zenith-antenna path I2: nadir-antenna path
Matched load	I1	I2: nadir-antenna path
Active cold load	I3	I2: nadir-antenna path

- Antenna measurement (100 ms): For the radiometer, 100 ms of raw data are copied to user-space floating point complex buffer using the DMA peripheral. For the cGNSS-R, 40 ms of raw data are copied to the user-space 16-bit complex buffer, which is passed to the cGNSS-R processor through a ZMQ socket [228]. In addition, the power of the 40 ms of cGNSS-R signal is computed for calibration purposes.
- Matched Load measurement (100 ms): as in the antenna measurement case, the power is retrieved for both cGNSS-R and radiometry signal when the nadir-antenna is short circuited to the matched load.
- Active Cold Load (ACL) measurement (100 ms): as in the antenna measurement case, the power is retrieved for both cGNSS-R and radiometry signal when the nadir-antenna is connected to the ACL.

In order to implement the 50 ms guard times, the LibIIO is configured two continuously stream the ADC IQ data to a 50 ms buffer, which is read by the SDR process (see section 9.2.5.2). The LibIIO uses up to four 50 ms buffers, thus the SDR process has enough margin to make the radiometric processing during the guard times. In addition, the remaining 200 ms are used as guard time between each acquisition block, with another 50 ms at the end of all the acquisitions to retrieve and store to the eMMC memory all the results generated by the radiometer.

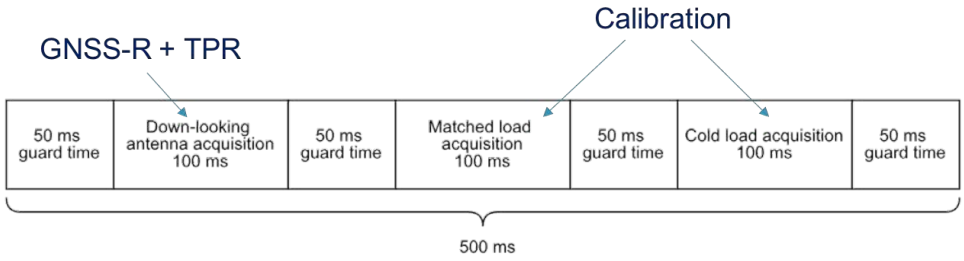

Figure 9.9: Signal acquisition and processing steps to provide cGNSS-R and L-band radiometry at the same time.

The purpose of retrieving a pair of calibration measurements (hot and cold loads) for each antenna measurement is fundamental for these small spacecrafts, as temperature stability is not as good as in larger spacecrafts.

9.2.5.2 SDR reader and radiometer processor

This process is in charge of both controlling the SDR through LibIIO and to compute the power averaging of the I/Q samples for the radiometer. As shown in Figure 9.10, this process is connected to the cGNSS-R processor through an Inter Process Communication (IPC) pipe, from which the cGNSS-R processor can request data from either zenith antenna (for the direct signal path) or nadir antenna (for the reflected signal path).

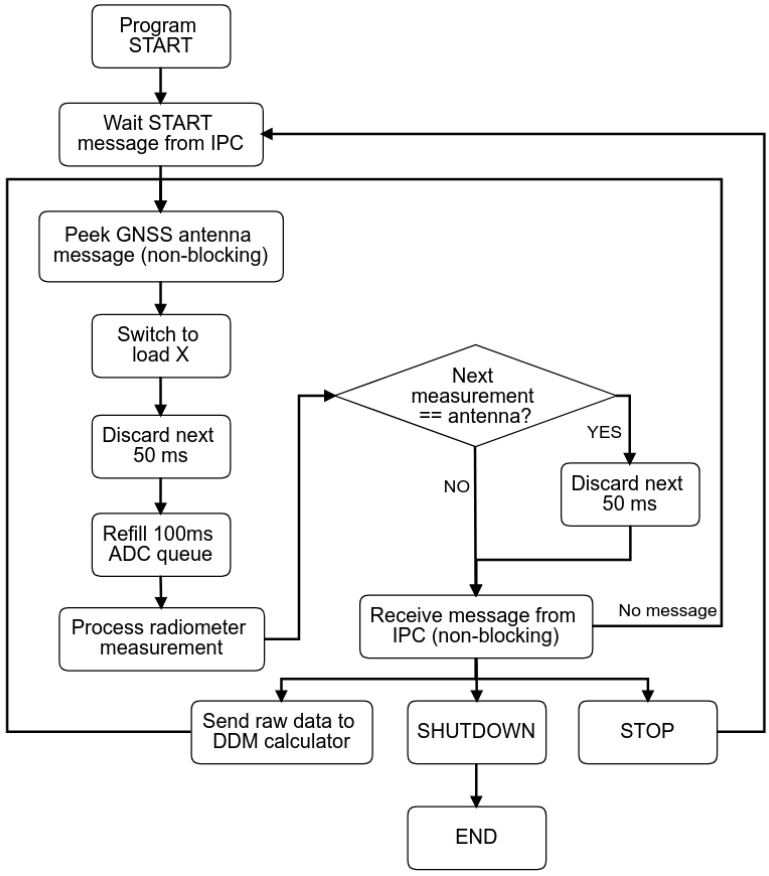

Figure 9.10: SDR reader and Radiometer processor block diagram.

The FMPL-2 radiometer covers the L-band radiometry (1400-1427 MHz) in 4 MHz wide sub-bands. The system is able to provide radiometric measurements at a rate of 2 Hz for its three sources: the nadir antenna, the ACL ($T_{cold} = 55$ K), and the matched load (T_{hot} = ambient temperature). Neglecting gain fluctuations, the theoretical radiometric sensitivity for a TPR was given in Eq. 8.1, and it is reproduced below for the readers' convenience.

$$\Delta T = \frac{T_{sys}}{\sqrt{B \cdot \tau}}, \tag{8.1}$$

where $T_{sys} = T_A + T_R = 322$, with $T_R = 72$ K, and $T_A^{max} = 250$ K (pointing to thick ice), $B = 4$ MHz and $\tau = 0.1$ seconds, $\Delta T = 0.5$ K.

Besides the measurement of each calibration source, all the antenna measurements are evaluated using an statistical complex Kurtosis test [216], to decide if the measurements contain any potential RFI. In case an interference is detected the block with RFI is flagged for post-processing on ground.

The Kurtosis values computed for each block are also downloaded as part of the instrument results data. The Complex Signal Kurtosis (CSK) is computed as in Eq. 9.1. A CSK equal to two means the I/Q samples received are Gaussian (i.e. thermal noise), therefore the received samples do not contain any interference.

$$CSK = \frac{E[X-\mu]^4}{(E[X-\mu]^2)^2} \tag{9.1}$$

For the FMPL-2 case, the CSK is computed in blocks of 1 ms, which means that each 100 ms of I/Q data is split in 100 blocks, and the CSK calculation is repeated for each of the 1 ms blocks. A CSK value is retrieved for each block and then averaged for all the blocks. The resulting CSK and the amount of blocks which contain a Kurtosis value out of 2 (± 0.2, which corresponds to a probability of false alarm of $6 \cdot 10^{-6}$ [229]) are tagged and downloaded for post-processing.

9.2.5.3 cGNSS-R processor

The cGNSS-R processor is divided in three different steps (Fig. 9.11), the first step is a direct signal acquisition of all the visible PRNs corresponding to the GPS/Galileo satellites in view. The cGNSS-R processor requests the SDR reader process to switch the GNSS ADC to the zenith-looking signal.

The received signal is correlated against all visible PRNs using the Parallel Code Phase Search (PCPS) [230] algorithm, with and all possible Doppler shifts for the direct signal one. After the correlation, the instrument selects the PRN signals with the highest SNR, and it passes them to the next processing block, including the absolute Doppler shift of the signal. The *reflected signal acquisition* block repeats the process with a longer incoherent integration time, but with a narrower Doppler span, as the direct and reflected signals have a similar Doppler shift. Finally, this last block is repeated, but now with a even shorter Doppler span, in that way the processor is able to generate a DDM for the selected satellites before a new segment of I/Q data is received by the SDR process.

Table 9.3 summarizes the different parameters chosen by default in the different steps for both GPS L1 C/A and Galileo E1 signals.

Each processing step of the cGNSS-R processor performs the GNSS signal acquisition by means of averaging incoherently the DDMs generated from a PCPS scheme [230].

In order to accelerate the GNSS signal acquisition, the PCPS implemented has been slightly modified from the original one [230]. Instead of performing the frequency shift of the acquired signal to perform the circular correlation, all code replicas are shifted. A total of 161 shifts per code are performed for all the available GPS and Galileo codes, which correspond to a total of ± 40 kHz Doppler span.

Furthermore, an FFT is performed to each frequency-shifted PRN and saved in the

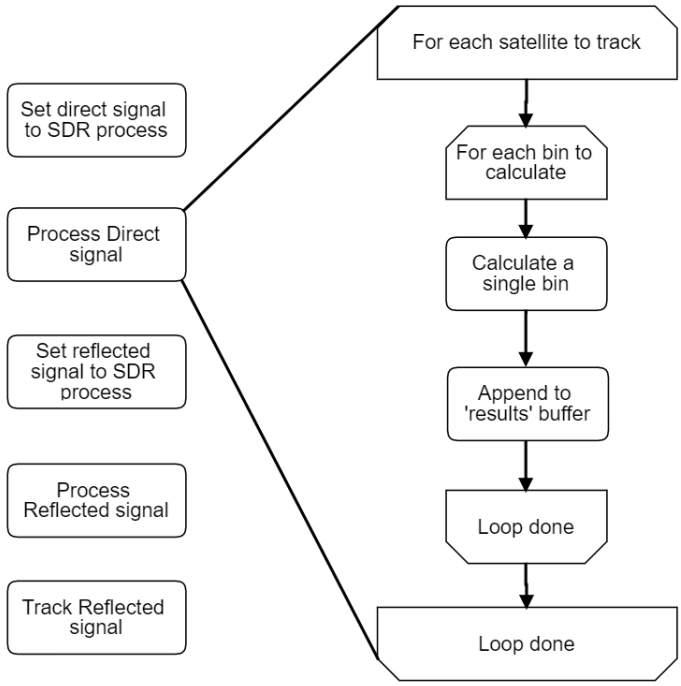

Figure 9.11: GNSS-R processor steps and flowgraph.

Table 9.3: cGNSS-R individual processing steps parameters

Step	Incoherent averaging	Doppler bin amount
Process Direct signal	10 ms	160 bins
Process Reflected signal	40 ms	20 bins
Track Reflected signal	40 ms	5 bins

processor memory. Therefore, all possible replicas are saved into the processor RAM memory as a 2D matrix, ready to be cross-correlated with the incoming signal.

Part of the PCPS algorithm is executed in the FPGA fabric and other part of the algorithm is performed by the ARM processor. Figure 9.12 details the implementation of the modified PCPS for FMPL-2. As it can be seen, both the pre-computed PRN and the incoming signal are copied into the FPGA fabric, and then the FPGA performs the circular cross-correlation. The data is then pulled out from the FPGA memory back to the ARM processor memory, the samples are modulus squared, and the ARM processor accumulates the circular cross-correlation result in a separate buffer. This process is repeated for each Doppler bin and for each satellite to be processed.

The communication between the FPGA fabric and the processor memory is implemented through DMA devices, once the data is received by both DMA in the FPGA, the correlation process starts (as detailed in Fig. 9.13) by performing the FFT of the incoming

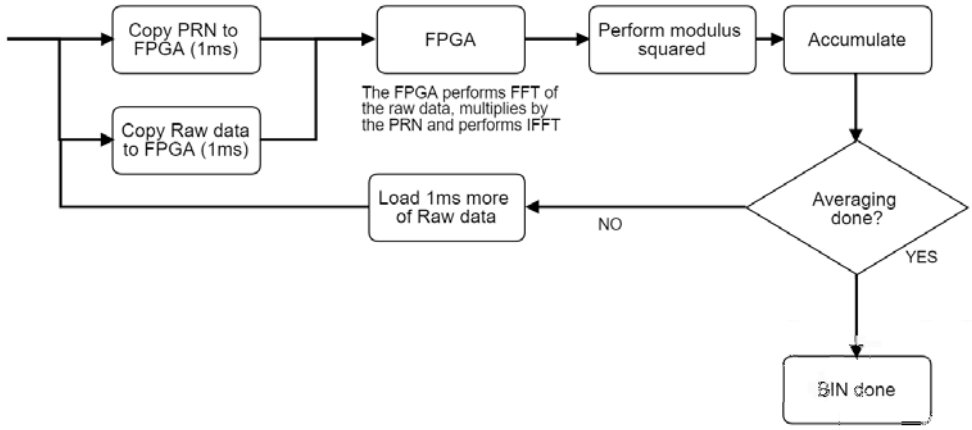

Figure 9.12: Delay-Doppler-Maps process design inside the ARM processor

I/Q data, performing the complex multiplication of both signals, and then calculating the inverse FFT. The data is transferred back to the ARM memory through another DMA device.

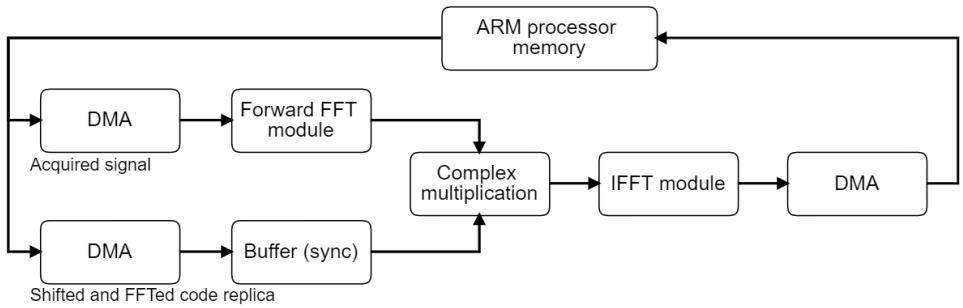

Figure 9.13: Circular correlation implemented in FPGA

Both complex number multiplication and FFT algorithm are given by Xilinx as an IP Core Block [223]. An specific circular correlation module is used for each GPS L1 and Galileo E1 signal, as the coherent integration time for GPS L1 is 1 ms and Galileo E1 is 4 ms (i.e. pre-programmed FFTs with different lengths for GPS L1, and Galileo E1).

The cGNSS-R processor takes packets of data from the SDR process once every 500 ms. From each packet, the processor is able to provide either 8 GPS-L1 DDM/s or 2 Galileo-E1 DDM/s with up to 40 ms incoherent integration time with a default resolution of 100 delay bins, and 5 Doppler bins (user selectable, 500 Hz Doppler spacing and 0.25 C/A chips for GPS-L1). Note that, changing those parameters (i.e. increase the Doppler bin resolution) impacts on the performance of the receiver. In addition, the chip resolution may be improved on ground by means of Fourier Interpolation, as the signal is sampled satisfying the Nyquist criterion[1].

[1]Following the same FFT optimum interpolation presented for the MIR field experiments in

Table 9.4: Main Characteristics of FMPL-2.

Parameter	Value
Volume (electronics)	1 Unit: ∼9x9x9 cm^3
Volume (aluminum box)	∼16.7x9.2x9 cm^3 (see Fig. 9.14)
Volume (zenith-looking antenna)	∼9x9x0.54 cm^3
Volume (nadir-looking antenna)	∼30x20x2.7 cm^3
Mass (electronics)	578 g
Mass (aluminum box)	850 g
Mass (zenith-looking antenna)	19 g
Mass (nadir-looking antenna)	730 g
Power Consumption	1500 mA at 5 V
Data rate (GNSS-R)	∼2.2 kB/s
Data rate (Radiometer)	< 100 Bytes/s

As discussed in Chapter 3, and in [121, 144], the maximum incoherent time selected is 40 ms so that the reflection does not get blurred in the delay axis.

9.3 FMPL-2 Implementation and Testing Phase

9.3.1 Implementation overview

The FMPL-2 was implemented with mechanical compatibility with the PC104 CubeSat standard following the Proto-Flight Model (PFM) philosophy. This philosophy is one of the most used in CubeSat-based equipments. As opposed to the QM/FM philosophy, where two units of the same hardware are built and tested, in the PFM approach there is just one unit being built. This PFM model is then tested at Qualification Levels (i.e., extreme conditions), but with a shorter test duration. This definition is called Qualification Levels, at Acceptance duration, as introduced in Chapter 8.

The instrument fits inside a single CubeSat unit, but to ease the integration with the platform, and provide an added robustness to the instrument, it was enclosed inside a larger anodized aluminum box (90x91.80x167 mm^3, as detailed in Fig. 9.14). The instrument main characteristics are summarized in Table 9.4. Furthermore, Figs. 9.16 and 9.15 present the three main boards of the instrument during different phases of the payload integration.

9.3.2 Ambient test campaign

FMPL-2 ambient test campaign was split in two different sets, a pre-integration test campaign and a post-integration test campaign. As the FMPL-2 implementation approach is a single PFM development, both the hardware and the software used need to

Chapters 5 and 6.

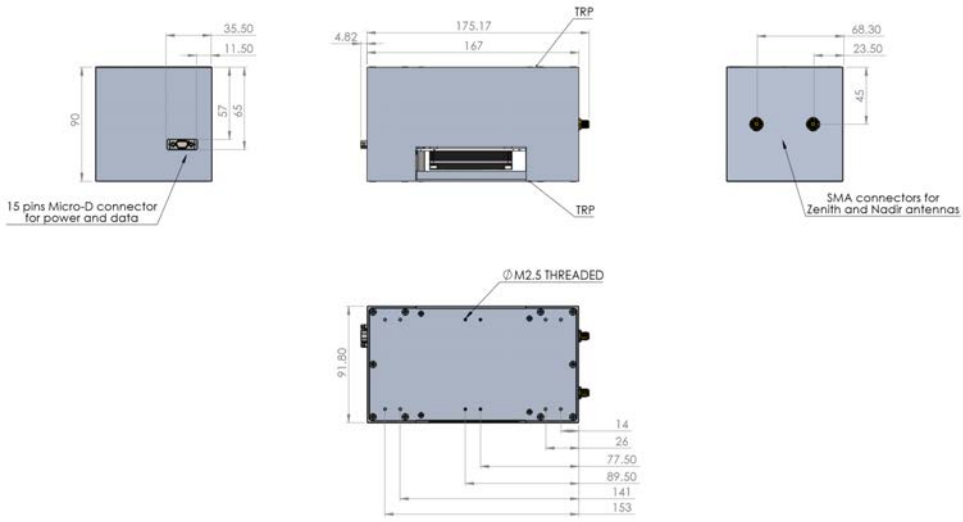

Figure 9.14: Aluminum box 3D CAD used to enclose FMPL-2 electronics.

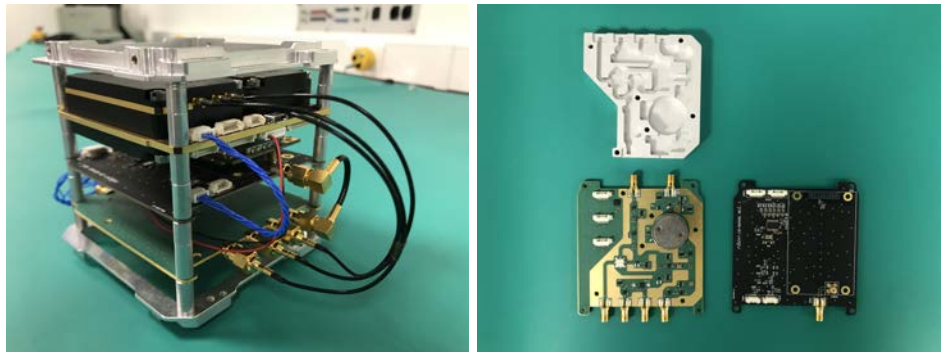

(a) **(b)**

Figure 9.15: (a) FMPL-2 avionics stack mounted in a 1U structure to verify its functionality before integration into the aluminum box, and (b) detailed view of the RF-FE shield, RF-FE board (left), and IB (right).

be tested before and after the integration inside its aluminum case. In this case, the pre-integration test campaign, even being part of the ambient test campaign, it was conducted during the implementation phase of the instrument development.

The anticipation of those tests before the final integration of the instrument was considered as a risk mitigation action, as in case of any failure (i.e. protocol mismatch, wrong voltage level on the power lines, etc.) a corrective action can be taken without a major impact on the overall system schedule.

The pre-integration campaign consisted of the validation of both the hardware and the software of the instrument with:

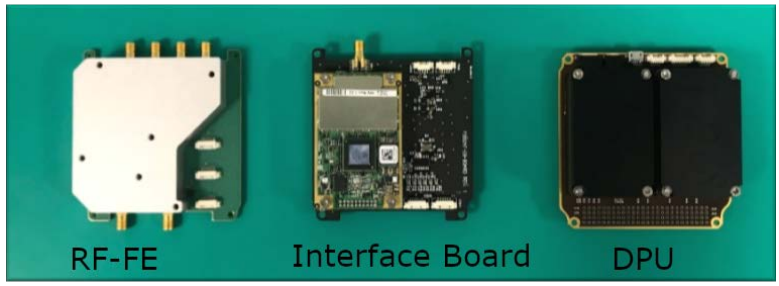

(a)

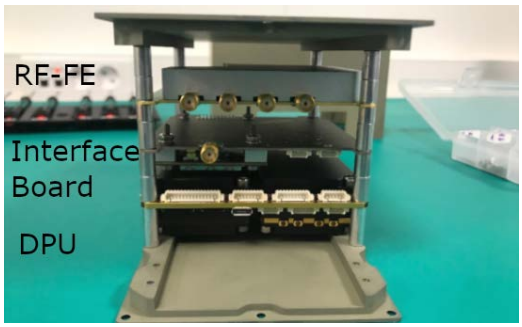

(b)

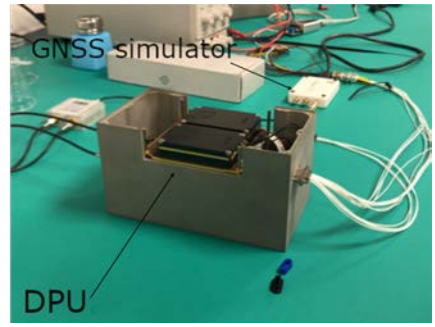

(c)

Figure 9.16: FMPL-2 boards (a), from left to right: (1) RF-FE board, (2) Interface board (including Novatel OEM719B), (3) GomSpace NanoSDR, (b) the boards already stacked in its final configuration during dry build fit-check, and (c) FMPL-2 already integrated in its aluminum box during the ambient test campaign

- A platform interface emulator test: the communication channel was simulated using a RS-422 to USB adapter, which turns a regular laptop into a simulator of the platform OBC.
- Platform interface test using an engineering model of the OBC: this test allows to validate the platform interface emulator. The purpose of this test is to check that the payload implementation that works with the platform interface emulator is valid also for the real platform. Note that, this test is not easily repeatable, as the platform OBC was at the platform integrator premises, in Torino, Italy, meanwhile the FMPL-2 was located at the UPC NanoSat Lab in Barcelona, Spain. The validation of the instrument performance relies on the platform emulator validation during the rest of the test campaign.
- High-dynamics GNSS reception test: the entire instrument and both GNSS receiver and GNSS-R chain were tested with a high-dynamics direct signal for both direct and reflected channel. In addition, the high-dynamics direct signal was obtained from a SPIRENT simulator at the GNSS laboratory in ESA/ESTEC. The high-dynamics signal used during the test was recorded using a SDR for later play back in order to reproduce the test outputs in house.

Right after the finalization of the pre-integration campaign, the payload enclosed in

its aluminum box, glued, and tested again following the post-integration or ambient test campaign. In this case, the instrument went over the following tests again:

- A platform interface emulator test: same as during pre-integration test campaign.
- High-dynamics GNSS reception test: using the recorded signal from the SPIRENT simulator at ESA/ESTEC Navigation Lab premises using a SDR.
- RFI detection test: by adding a spurious signal right on top the L-band radiometry band and checking that the CSK algorithm is able to detect and report the interference.
- Radiometer calibration load measurement: a set of measurements of both the matched load and the ACL to check the correct operation of the amplification and sampling chain.

Figure 9.17 shows a snap-shot of two waveforms from the injected PRN 16 and PRN 23 of the GPS constellation.

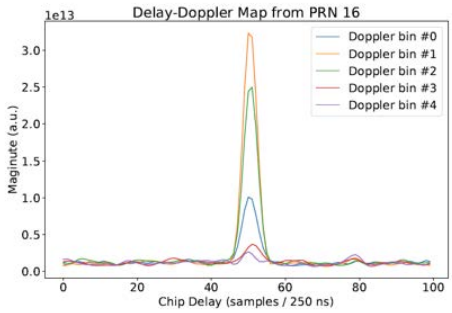

(a) PRN 16 waveform with different Doppler cuts

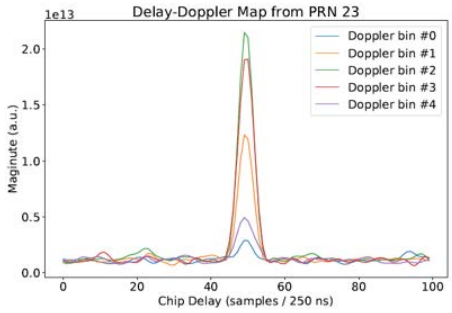

(b) PRN 23 waveform with different Doppler cuts

Figure 9.17: cGNSS-R processor output waveforms including 5 Doppler bins (frequency resolution = 500 Hz) of two of the in-view satellites during the ambient test campaign

The RFI detection test (Fig. 9.18) was based on the injection of a CW tone centered at 1413 MHz with a power of -100 dBm, which produces an increase on the received power, and also the Kurtosis indicator passes from 2, indicating the absence of interference, to almost zero, where the signal is totally contaminated by an interference.

To conclude the functional tests during the ambient test campaign, Fig. 9.19 shows the result of the radiometric calibration loads measurements over time and with respect to temperature variations, in both matched and ACL cases with a $R^2 = 0.95$ and a slope of -288 counts/ºC for the matched load and -136 counts/ºC for the ACL.

Aside the electronics functional tests, the FMPL-2 nadir antenna module has been measured for both S_{11} parameter (Fig. 9.20), and radiation pattern (Figures 9.21 and 9.22) at the UPC Antenna Lab anechoic chamber).

The nadir-looking antenna at the 1413 MHz has a directivity of 12.25 dB with a cross-track beam-width of 36º and an along-track beam-width of 58º.

The nadir-looking antenna at the 1575.42 MHz has a directivity of 12.22 dB with a cross-track 3 dB beam-width of 35º and an along-track 3 dB beam-width of 54º.

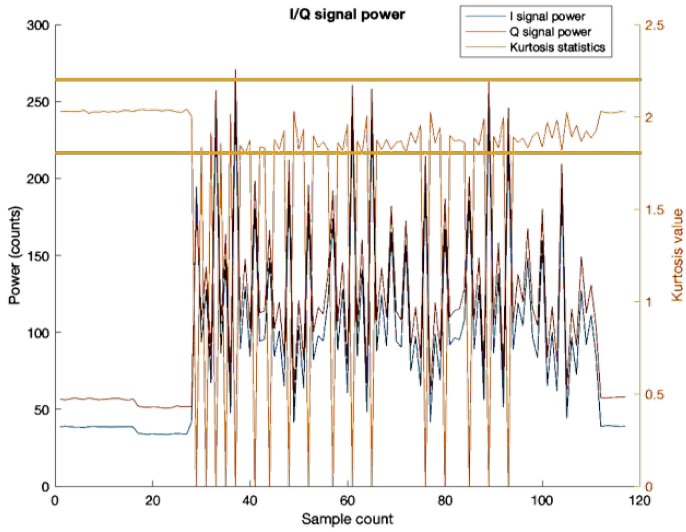

Figure 9.18: CW RFI detection test performed during the ambient test campaign, with the two horizontal lines in orange indicating the CSK limits for RFI detection (1.8 and 2.2)

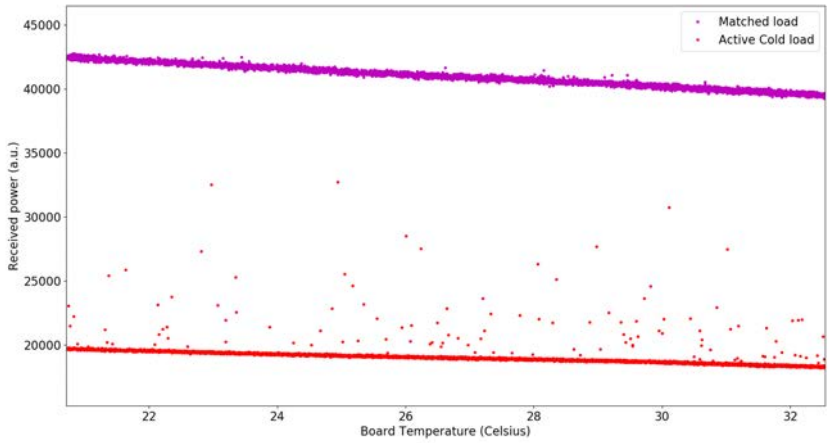

Figure 9.19: Radiometer calibration performed during the Ambient test campaign

9.3.3 Environmental test campaign

Once the payload has been functionally validated in ambient conditions, it shall be validated for the space environment, which includes:

- Thermal-vacuum cycling test in a TVAC: a total of four thermal cycles (Fig. 9.23a) are performed in vacuum in order to verify that the payload is able to operate and to dissipate through conduction and radiation the internally generated heat towards the

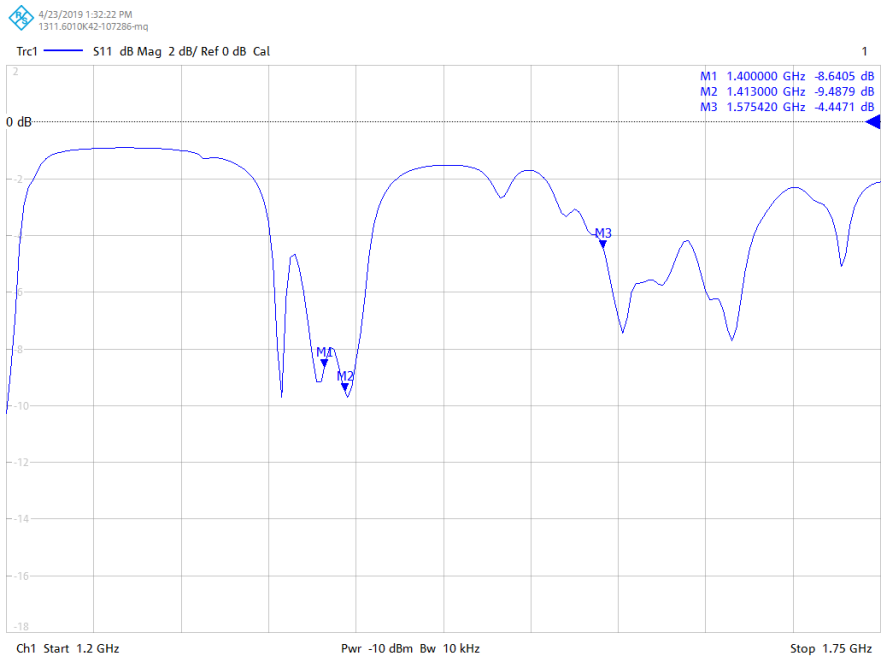

Figure 9.20: FMPL-2 nadir antenna mounted in a 6-unit CubeSat model for radiation pattern measurement in UPC Antenna Lab anechoic chamber [231]

platform. According to the platform simulations [232], the FMPL-2 will be from 0ºC to 30ºC, therefore the FMPL-2 has been tested with 10ºC of margin on both sides, -10ºC and +40ºC.

- Extended thermal-vacuum cycle calibration test: apart from the regular TVAC test, the FMPL-2 required a full temperature sweep to have a measurement of the radiometer output linearity with the temperature variation. As it can be seen in Fig. 9.24, the FMPL-2 shows a small non-linearity ($R^2 = 0.75$) at the ACL at low temperatures at the begging of the execution (at -10ºC). However, a linearity better than 2% is preserved ($R^2 > 0.95$) in the operational temperature range (from 0ºC to 40ºC), with a slope of -364 counts/ºC for the matched load. The non-linearity needs to be taken into account and a linear closed formula cannot be used to calibrate the radiometer, hence a look-up table (LUT) is required for temperatures out of the operational temperature range. Note that, some outlier measurements are present in both matched load and ACL, which correspond to less than 1% of the measurements, and they can be filtered by means fo a 3 or 5-element median filter.

- Vibration test: during the launch the spacecraft suffers from a intense random acceleration, which can damage any of the boards, components, or causing a harnessing release. FMPL-2 has been tested (Fig. 9.23b) with a shaking profile up to 12.4 g_{rms} in its the three axis. The results of this test are detailed in Appendix C.

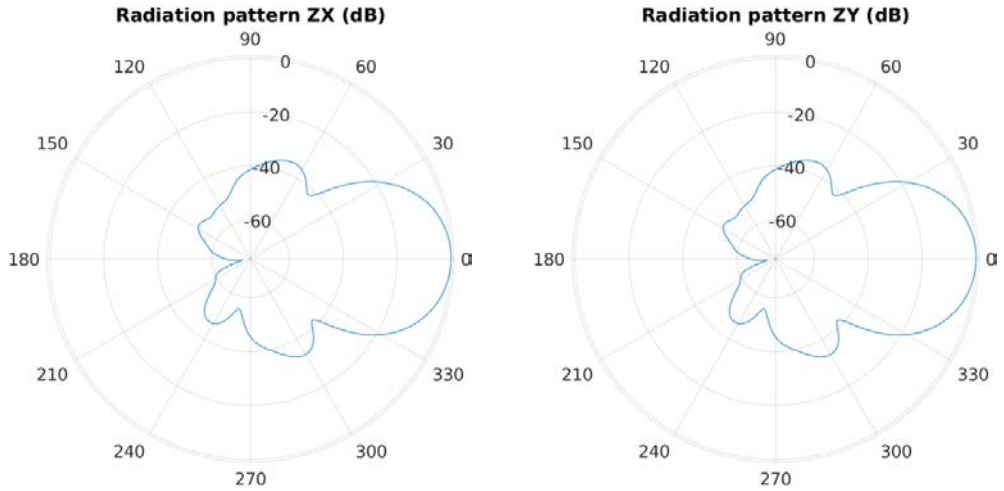

(a) ZX cut ($E_\phi = 0$ž) **(b)** ZY cut ($E_\phi = 90$ž)

Figure 9.21: Nadir antenna measured radiation pattern at 1413 MHz measurement in UPC Antenna Lab anechoic chamber [231]

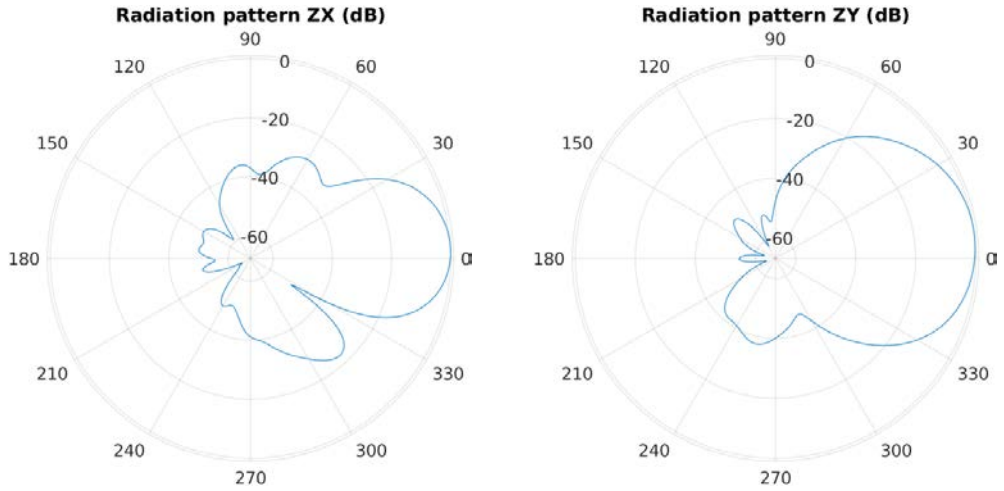

(a) ZX cut ($E_\phi = 0$ž) **(b)** ZX cut ($E_\phi = 90$ž)

Figure 9.22: Nadir antenna measured radiation pattern at 1575 MHz measurement in UPC Antenna Lab anechoic chamber [231]

9.4 FMPL-2 Instrument Calibration

Calibration of the raw data is extremely important for both GNSS-R and L-band radiometer. Both systems require a perfect knowledge of the instrument gain and noise temperature to retrieve absolute value of the observables (i.e. antenna temperature on the radiometer and power received on the GNSS-R).

(a) FMPL-2 preparation for thermal-vacuum cycling

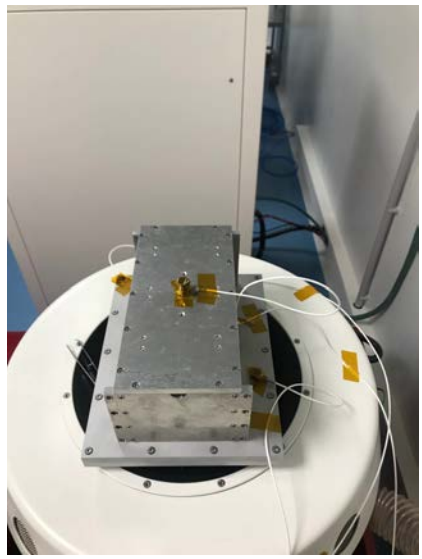

(b) FMPL-2 preparation for vibration test at Z axis

Figure 9.23: Environmental test at UPC NanoSat-Lab facilities [233]

9.4.1 Instrument two-point calibration

As detailed in section 9.2.5.1, the instrument performs the matched load and ACL measurements for calibration for both the GNSS-R and the L-band radiometer chains.

The simplified block diagram of a receiver for a single channel radiometer is shown in Fig. 9.25. In our case, both instruments are calibrated independently, thus the single channel scheme is applied to both the GNSS-R and L-band chains, but with some of the components shared between them.

Both gain and noise temperature are retrieved for both chains using the two-point calibration method. This method consists of using the internal matched load and the ACL as standards in order to measure the receiver gain (Eq. 9.2), and the receiver noise temperature (Eq. 9.3).

$$G = \frac{v_{hot} - v_{cold}}{T_{hot} - T_{cold}}, \tag{9.2}$$

$$T_R = \frac{T_{hot} v_{cold} - T_{cold} v_{hot}}{v_{hot} - v_{cold}}, \tag{9.3}$$

where $T_{hot} = T_M$ is the physical temperature of the matched load, and T_{cold} is the noise temperature of the ACL at the calibration plane, which can be estimated from Eq. 9.4.

$$T_{cold} = T_{ACL} \frac{1}{L_s} + T_M (1 - \frac{1}{L_s}), \tag{9.4}$$

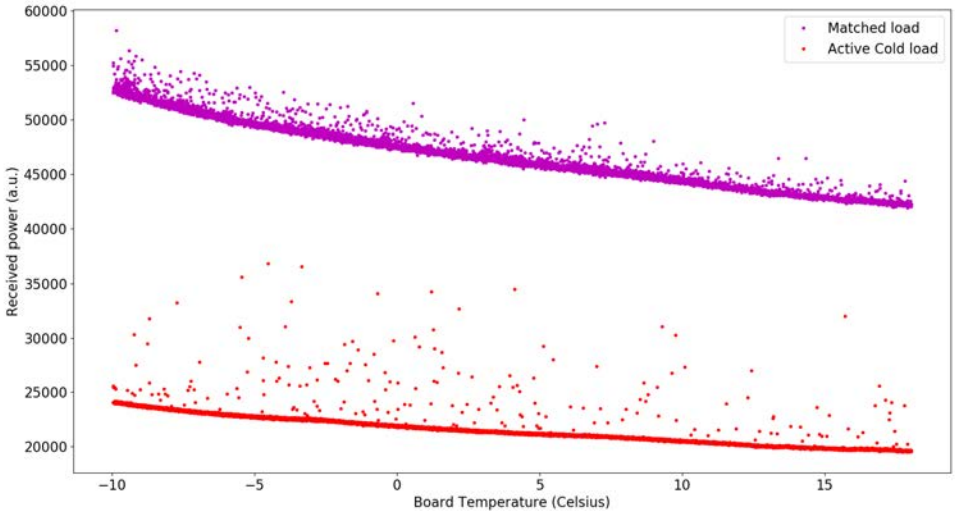

Figure 9.24: L-band radiometry results of the extended TVAC calibration test. With a slope of -364 counts/ºC and $R^2 = 0.95$ for the matched load and a slope of -154 counts/ºC and $R^2 = 0.75$ for ACL measurement

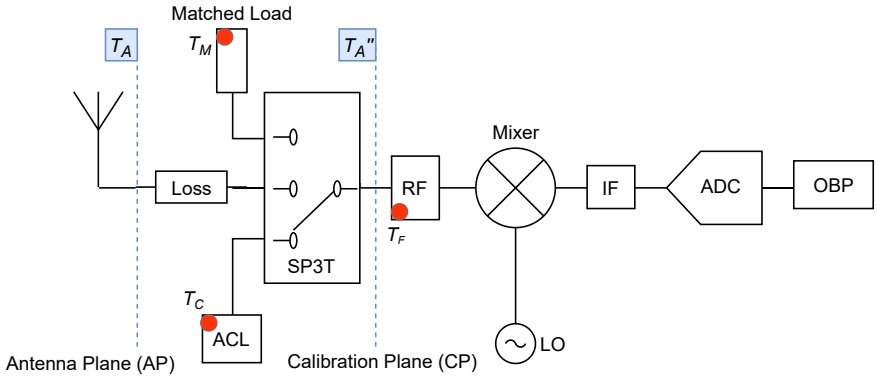

Figure 9.25: Simplified block diagram model of a single channel microwave radiometer

where T_{ACL} is the noise temperature of the ACL, measured on ground by the manufacturer at different ACL temperatures, as shown in Eq. 9.5.

$$T_{ACL} = 56K + 0.46K/^{\circ}C \cdot (T_c - 25^{\circ}C), \tag{9.5}$$

and $L_s = 0.24dB$ is the loss of the SP3T switch, measured on ground, and T_c is the physical temperature of the ACL.

9.4.2 Microwave radiometer calibration

The radiometer output power (9.6) is related to the antenna temperature at the calibration plane T_A'' by Eq. 9.6.

$$v = G(T_A'' + T_R), \tag{9.6}$$

where G is the transducer power gain (Eq. 9.2), and T_R is the receiver noise temperature calculated in the previous section (Eq. 9.3). The internal calibration estimates both parameters in order to solve this equation for T_A'' (Eq. 9.7).

$$T_A'' = \frac{v}{G} - T_R, \tag{9.7}$$

Finally, the retrieved antenna temperature at the calibration plane shall be compensated for connector losses between the instrument and the antenna, and for the ohmic losses of the antenna itself, as detailed in Eq. 9.8. Note that, the physical temperatures are retrieved from the thermal probes (PT-1000) readings installed in the nadir-looking antenna and in the RF-FE board near the SP3T switch. In addition, the estimates losses are given by design and also validated during the board implementation by the manufacturer.

$$T_A = (T_1 \cdot (1 - \frac{1}{L_{Ant}}) + T_2 \cdot (L_s - 1) - T_A'' \cdot L_s) \cdot L_{Ant}, \tag{9.8}$$

where T_1 is the physical temperature of the antenna, T_2 is the temperature of the SP3T switch at the input of the calibration plane, L_s are the SP3T switch losses, and L_{Ant} the antenna losses (taking into account the connection or cable losses).

9.4.3 GNSS-Reflectometer calibration

Depending on the final application or data product, the GNSS-R instrument has to provide the delay between direct and reflected signals (delay altimetry), the reflectivity, which ism proportional to the power ratio between the direct and the reflected signals (scatterometry), and those measurements retrieved from the shape of the DDM itself.

Each DDM cell output from the FMPL-2 is stored as normalized counts, which can be linked to the received signal power in Watts by Eq. 9.9.

$$C = G \cdot (P_a + P_r + P_{ref}), \tag{9.9}$$

where

- C is the DDM value at a particular delay and Doppler frequency in counts output from the instrument at each delay/Doppler bin (for both nadir and zenith-looking antennas),
- P_a is the thermal noise power generated by the antennas in [W],
- P_r is the thermal noise power generated by the instrument in [W],
- P_{ref} is the scattered signal power at the instrument in [W] at a particular delay and Doppler frequency, and

- G is the total instrument gain applied to the incoming signal in counts per [W].

The terms C and P_{ref} are functions of delay (τ) and Doppler frequency (f_d), while P_a and P_r are assumed to be independent of the delay-Doppler bin the DDM. Every DDM includes 30 delay bins before the DDM peak, where signal power is not present, and from which the noise floor level in counts can be estimated following:

$$C_N = \frac{1}{N_{dopplers} \cdot 30} \sum_{d=1}^{N_{dopplers}} \sum_{i=1}^{30} C[d][i] \tag{9.10}$$

9.4.3.1 Calibration of the signal power

The DDM received power can be calibrated by subtracting the noise power from the received signal as in Eqns. 9.11 and 9.12.

$$C_{ref} = C - C_N = G \cdot P_{ref}, \tag{9.11}$$

$$C_{dir} = C - C_N = G \cdot P_{dir} \tag{9.12}$$

where C_{ref} and C_{dir} are the peak power of the DDM, and G can be calculated as for the microwave radiometer (Eq. 9.2), as the matched and ACL measurements are also taken periodically for the GNSS receiving chain.

At the end, both powers are retrieved by isolating the power term (Eqns. 9.13 and 9.14).

$$P_{ref} = \frac{C_{ref} - C_N}{G}, \tag{9.13}$$

$$P_{dir} = \frac{C_{dir} - C_N}{G} \tag{9.14}$$

9.4.3.2 Reflectivity computation

FMPL-2 targets are ice and land, where the scattering has a coherent component larger than the incoherent (diffuse) one. Therefore, the DDM of the reflected signal looks like the direct one, with no tails (i.e. "boomerang" shape), but with a noisier background. In these conditions, a reflection coefficient can be computed for the coherent component at the specular reflection point. In addition, it is assumed that the transmitting antenna of the navigation satellite has a different directivity (G_T) for the transmitter-receiver path (θ_1, ϕ_1) and the transmitter-specular point path (θ_2, ϕ_2).

The next step is to compensate for the free-space propagation losses for both direct (Eq. 9.15) and reflected signals (Eq. 9.16):

$$P_{dir} = P_T \cdot G_T(\theta_1, \phi_1) \cdot \left(\frac{\lambda}{4\pi \cdot R_{T-R}} \right)^2 \cdot G_{zenith}(\theta_{dir}, \phi_{dir}) \tag{9.15}$$

$$P_{ref} = P_T \cdot G_T(\theta_2, \phi_2) \cdot G_{nadir}(\theta_{ref}, \phi_{ref}) \cdot \left(\frac{\lambda}{4\pi \cdot (R_{T-SP} + R_{SP-R})} \right)^2 \tag{9.16}$$

The reflection coefficient can now be estimated as follows[2]:

$$\Gamma = \frac{P_{ref}}{P_{dir}} = \left(\frac{R_{T-SP} + R_{SP-R}}{R_{T-R}} \right)^2 \cdot \frac{G_{zenith}(\theta_{dir}, \phi_{dir})}{G_{nadir}(\theta_{ref}, \phi_{ref})} \cdot \frac{G_T(\theta_1, \phi_1)}{G_T(\theta_2, \phi_2)} \tag{9.17}$$

All the unknowns, can be extracted from the satellite telemetry, and from the antenna radiation patterns measured in the anechoic chamber (Section 9.3.2).

9.5 Conclusions

This Chapter has presented the FMPL-2, a novel CubeSat-based instrument that provides two passive microwave remote sensing techniques combined: L-band microwave radiometry and cGNSS-R. In this Chapter, the science case of the FSSCat mission and the design, implementation, and test of the FMPL-2 has been presented. Furthermore, the calibration methods for both the microwave radiometer and the GNSS-R receiver have been presented as well as the calibration parameters and temperature sensitivities derived during the environmental tests, which are needed to provide antenna temperatures, and reflectivities.

The FMPL-2 was integrated in Tyvak's platform on February 2019, system-level environmental tests where conducted in April 2019, and the two CubeSats were ready for launch in July 2019. However, due to the failure of Vega VV15 first, and the 2020 COVID pandemic, the final launch date was delayed until 3 September 2020. In the last part of this Ph.D. thesis (Chapters 11 and 12), the results of FMPL-2 are presented, showing the capabilities of the instrument to perform scientific Earth Observation measurements from a CubeSat platform. The sensor miniaturization as the one presented in this Chapter may pave the path to large constellations of small passive microwave Earth Observation satellites.

[2]The reflectivity equation proposed in Eq. 5.10 from Chapter 5 does not include the difference in G_T for the GNSS transmitting antenna, and the path losses of the distance between the specular point to receiver. For an airplane-based platform, these terms are negligible, and therefore not considered to compute the reflectivity, but this is not the case in a spaceborne receiver.

10

Chapter 10

The Flexible Microwave Payload -3

This Chapter presents the last instrument developed within this Ph.D. thesis: the FMPL-3. The FMPL-3 is one of the secondary payloads composing the GNSSaS mission [24] from NSSTC[1], the instrument includes technology demonstrator for GNSS-R at L5 from a spaceborne platform. Moreover, aligned to NSSTC primary payload goals, the instrument includes a ionosphere characterization experiment at VHF, UHF, and L5 bands. The mission is entirely managed by NSSTC, and the launch date is not confirmed yet. Mission details aside from those related to FMPL-3 cannot be disclosed and therefore are not covered in this dissertation.

This Chapter is organized as follows: Section 10.1 introduces the FMPL-3 in the frame of the GNSSaS mission. Section 10.2 presents the software and hardware design of the instrument. Section 10.3 presents the implementation details of FMPL-3. Finally, Section 10.4 concludes the Chapter.

[1]The National Space Science and Technology Center (NSSTC) is a joint initiative of the United Arab Emirates University, and the United Arab Emirates (UAE) Space Agency and the Telecommunications Regulatory Authority.

10.1 Introduction

The GNSSaS mission is based on a 6-unit CubeSat to prove an RF signaling technology. The mission also aims to provide the UAE a unique opportunity to become an international actor promoting technology and education through this mission [24]. The spacecraft follows the standard 6U format including a UHF transceiver for basic telemetry and telecommand, and an S-band downlink to download scientific experiments. Moreover, the spacecraft includes deployable solar panels to generate more than 25 Wh per orbit.

The primary payload of the GNSSaS mission is a GNSS augmentation signal transmitter in both GNSS L and S bands, which is entirely managed by NSSTC. The secondary payload is the FMPL-3, a GNSS-R L5 technology demonstrator experiment, and a VHF/UHF/L5 ionosphere characterization experiment. Both FMPL-3 experiments are implemented following a similar approach than previous FMPL instruments, as it will be covered in the next sections.

The results presented in Chapters 5 and 6 showed the potential of L5 signals to perform GNSS-R. The L5 signals transmitted by the GPS constellation have an additional 3.6 dB link budget margin as compared to L1 C/A signals [157]. These signals also have a much narrower auto-correlation function than GPS L1 C/A signals, providing an improved resolution as compared to GPS L1 C/A ones. In addition, by design, a secondary code is also transmitted with a code length of 20 ms, which is not modulated by any data sequence and it is transmitted as a pilot signal, as detailed in Chapter 5. As presented in Chapter 6, the geophysical parameters retrieved using L5 signals present lower errors as compared to L1 signals.

Complementary to the GNSS-R experiment, and aligned with the primary goals of the GNSSaS mission, the FMPL-3 instrument also includes a multi-band ionosphere experiment. This experiment consists of a reception equipment to simultaneously track a CW tone at three frequencies: VHF, UHF, and L5 band. The differences in amplitude and phase produced by the ionosphere in different bands will help to understand the ionospheric scintillation. This characterization will allow to refine current ionospheric models to better understand the fadings introduced by the ionospheric scintillations. This characterization is critical for many systems, including GNSS positioning, UHF radars (e.g., ESA BIOMASS mission [188]), and also to calibrate GNSS-R observables. As discussed in [234], the fading introduced by the ionospheric scintillation is detected as a fluctuation in certain CyGNSS DDMs. Thus, showing that further ionospheric corrections are required to better calibrate both reflectivity and altimetry GNSS-R observables.

The FMPL-3 has the objective of retrieving for the first time from space GNSS reflected signals at L5, and to provide a characterization of the ionosphere scintillation in VHF, UHF, and L5 bands. Thus, a set of requirements are defined for the FMPL-3 platform:

- Capable of receiving GNSS direct and reflected signals at the GPS L5 band (1176.45 MHz), with the required bandwidth (10 MHz as presented in Table 2.1 from Chapter 2).
- For the GNSS-R reception, the antenna gain shall be larger than 10 dB to cope with the attenuation of the GNSS signal due to the reflection on the Earth's surface.

- The integration time of the GNSS-R receiver shall be configurable.
- Capable of receiving and monitoring synchronously the power and phase of a CW tone at VHF, UHF, and L5 bands.

10.2 FMPL-3 Hardware and Software Design

Despite the use of the L5 signal is promising, it is also a challenge. As it is presented in Chapter 3, the maximum integration time to prevent blurring of the GNSS waveform is driven by Eq. 3.5, which is reproduced below for convenience. For the GPS L5 signal it is limited by the chip length: 30 m. In this case, the maximum integration time assuming a platform moving at ∼7.5 km/s (i.e., LEO orbit) is $T_{int} = 4$ ms. This short integration time will require that the specular reflection point is re-tracked [144] to cover an entire Fresnel zone. The lack of knowledge on how GPS L5 reflection will be collected by a spaceborne receiver requires a highly flexible GNSS-R instrument. Nonetheless, the instrument design shall also include the ionosphere experiment previously presented.

$$T_{int_{max}} = \frac{min|L_{chip}, L_{Fz}|}{v_{platform}}. \tag{3.5}$$

As presented in Fig. 10.1, FMPL-3 is composed by the following elements:

- Four different antennas are used in the FMPL-3: a Tallyman active RHCP dual band L1/L5 GNSS patch antenna to receive the direct GNSS signal, a 4-element array of active LHCP (L5) patch antennas to collect the GNSS reflected signals for the GNSS-R experiment. For the ionospheric experiment, the same nadir-looking patch antenna is used to collect the L5 CW tone, and to receive the VHF and UHF tones, a 6U VHF/UHF antenna system from GomSpace [235] is used.
- The Radio-Frequency conditioning board or RF-FE module is composed of a set of amplifiers and filters, as in the previous FMPL models. In this case, this module is also in charge of powering the L5 antennas by means of a bias tee circuit. Moreover, the instrument includes a switch to select whether the GNSS-R mode or the ionospheric mode is executed.
- The DPU selected for FMPL-3 is the same as FMPL-2: the GomSpace NanoSDR [222]. In this case, the two RX channels will be used to retrieve both zenith-looking and nadir-looking signal during the GNSS-R mode. While performing the ionospheric experiment, one channel will collect both VHF/UHF tones, previously conditioned in the RF-FE board on one channel, and the L5 tone in the other channel. Analogously to FMPL-2, the TX channel will be used as a LO reference for the RF-FE up-convert the VHF/UHF frequencies to L5. Recall that, despite the AD9361 transceiver used in the NanoSDR has two channels, the central frequency of both RX channels is fixed by a single LO.

Further details of the FMPL-3 payload are described in the following sections. Moreover, additional details on the design of the FMPL-3 instrument, such as board schematics, are provided in the Appendix D.

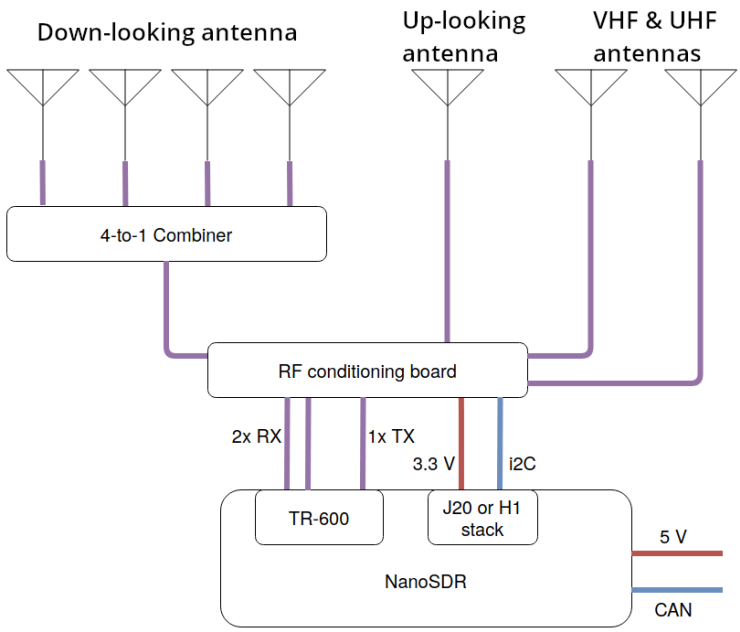

Figure 10.1: FMPL-3 block diagram.

10.2.1 Antenna design

The FMPL-3 is composed by four different antennas. For the GNSS-R experiment, the RHCP zenith-looking antenna and the LHCP nadir-looking antenna are used to receive the direct (zenith) and reflected (nadir) GNSS signals at L5.

The zenith-looking antenna (Fig. 10.3a) is a commercial Tallysman dual-band (L1 and L5) patch antenna (model TW1825 [236]). The antenna has a built-in LNA providing a gain up to 26 dB with a NF<2 dB. The signal collected by this antenna is used for both the FMPL-3, and the GNSSaS navigation receiver to geo-locate the spacecraft. Thus, a power splitter is needed to split the signal.

The elementary antenna (Fig. 10.3b) of the nadir-looking patch array is a custom product from MatterWaves [237] manufactured according to UPC design and specifications. It is a dual polarization (RHCP and LHCP) L5 patch antenna which specifications are given in Fig. 10.2. The LHCP port includes a LNA and it is used by the FMPL-3 instrument, and the RHCP port is passive and it is part of the GNSSaS L5 augmentation transmitter, not covered in this Ph.D. dissertation. The antenna LNA included in the LHCP path has a built-in gain of 35 dB with a NF<2.8 dB. Finally, the signals from the four antennas are combined using a 4:1 power splitter. The combiner is design to allow the DC signal to pass through. Thus, a single DC power supply is needed for the four antennas.

For the ionosphere characterization experiment, the same nadir-looking antenna is used to collect the L5 signal. The VHF and UHF tones are received by a pair of VHF monopoles and UHF monopoles, each of them receiving at RHCP polarization. The VHF/UHF antenna system is the GomSpace VHF/UHF deployable antenna system

SPECIFICATIONS

ELECTRICAL:

	L5 GPS	L5 GPS
FREQUENCY:	(1176 +/- 24) MHz	(1176 +/- 24) MHz
RADIATION PATTERN:	HEMISPHERICAL	
POLARIZATION:	LHCP	RHCP
VSWR:	< 2.0:1	< 2.0:1
IMPEDANCE:	50 ohms	50 ohms
ANTENNA GAIN (dBic):		
90° Elevation (Zenith)	+4 dBic	
BEAM WIDTH (3dB):	90° (FS) / 140° (GP)	
AXIAL RATIO:	3 dB	
LIGHTNING PROTECTION:	DC GROUNDING	

LNA OPTION (Rx Only):	35 dB Gain	Passive
LNA NOISE FIGURE:	2.8 dB (Include Filter Loss)	
LNA P1dB Out:	+20 dBm	
LNA DC POWER:	(2.5 to 22)V @ < 30mA	
FILTER:	YES	

MECHANICAL:

SIZE:	2.290 in [58.17 mm] SQ. HEIGHT: 0.387 in [9.82 mm]
WEIGHT:	2.8 oz. (79 g)
FINISH:	SKYDROL RESISTANT POLYURETHANE ENAMEL BASE IRIDITE PER MIL-C-5541F
MATERIAL:	6061-T6 ALUMINUM ALLOY BASE COMPOSITE RADOME, IMPACT, ABRASION, UV, SOLVENT AND SKYDROL RESISTANCE, FIRE RETARDANT
CONNECTOR:	2 X SMA FEMALE (OPTION: TNC, N, N-BH, MCX, MMCX, SMB, SSMB)
MOUNTING:	FLAT TOP, BOTTOM, BULK-HEAD, OR BRACKET/PIPE MOUNT

ENVIRONMENTAL:

TEMPERATURE:	-71 °F TO +203 °F [-57 °C TO +95 °C]
ALTITUDE:	70,000 ft.
VIBRATION:	> 30 G's
LEAKAGE / IP RATING:	HERMETICALLY SEAL / IP69K

FEDERAL & MILITARY SPECIFICATIONS DESIGNED TO:

TSO-C129/C139/C144, MIL-C-5541F(Finish), MIL-DTL-14072(Finish), DO-160D/228(Test)
MIL-STD-810G(Test), MIL-STD-461E/F(Elec Interfer), MIL-STD-464C(ELEC MAG), SAE J1455(Env)
MIL-STD-202(Elec Comp), MIL-HDBK-5400/454(Elec Eq), MIL-PRF-39012(Con), MIL-STD-889B(Metal)
EN 55155(Terminals), RCC-319-14 (Termination), MIL-STD-129/1285(Marking), MIL-STD-130N-1(ID)
MIL-C-85704B(Solvent), MIL-G-81827(Grease), RCC-324-01(Safety), MIL-I-45208A/NAS411-1(HAZ)

Figure 10.2: FMPL-3 nadir-looking antenna element specification document from MatterWaves (internal communication).

(a) **(b)**

Figure 10.3: (a) Tallysman TW1825 [236] zenith-looking antenna, and (b) elementary antenna used in the nadir-looking 4-element patch antenna array.

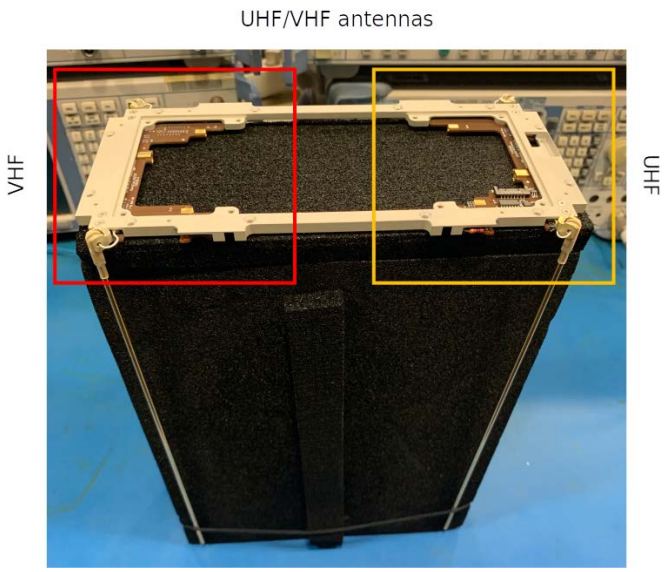

Figure 10.4: VHF/UHF GomSpace antenna system in folded configuration (i.e., not deployed), mounted in a 6U dummy structure used to characterize the system.

adapted for a 6U CubeSat [235], as detailed in Fig. 10.4. The VHF antennas are two short monopoles tuned at 144 MHz, and the UHF antennas are also two short monopoles tuned at its 3^{rd} harmonic.

10.2.2 Radio-Frequency Front-End

The signals coming from the four antennas are collected by the RF-FE. In this case, the zenith-looking and the nadir-looking L5 antennas are active, and they include a LNA, which set the noise floor of the receiving chain. Then, a second amplification stage is implemented in the RF-FE to boost the signal before filtering it with a SAW filter.

As it can be seen in Table 10.1, the NF of the four RF paths is lower than 2 dB. The zenith-looking path has third amplifier to provide a larger gain to compensate with the lower amplification of the active antenna, and to compensate the losses of the SP2T switch used to select between the different modes. Moreover, the VHF channel has 12 dB less gain than the UHF channel, to compensate the different free-space propagation losses (FSPL):

$$FSPL(dB) = 20\log_{10}(d) + 20\log_{10}(f) + 20\log_{10}(\frac{4\pi}{c}), \tag{10.1}$$

where d is the distance in m, f is the frequency in Hz, and c is the speed of light. Thus, for a given d, $\Delta FSPL = FSPL_{VHF} - FSPL_{UHF} = 20\log_{10}(144 \cdot 10^6)$ - $20\log_{10}(435 \cdot 10^6) =$ -9.6 dB. The remaining 2.4 dB compensate the difference of the antenna gains: 0.6-0.8 dB for the VHF antenna, and 2.8-3 dB for the UHF antenna [235].

The high-level block diagram schematic of the RF-FE board is detailed in Fig. 10.5, showing all amplifiers and filters used. Note that, a detailed schematic of the RF-FE can

Table 10.1: RF-FE gain and noise figure reference

RF path	Gain [dB]	NF [dB]
Nadir-looking antenna to SDR channel 1	13	0.67
Zenith-looking antenna to SDR channel 2	33	0.70
VHF antenna to SDR channel 2	13	1.2
UHF antenna to SDR channel 2	25	0.9

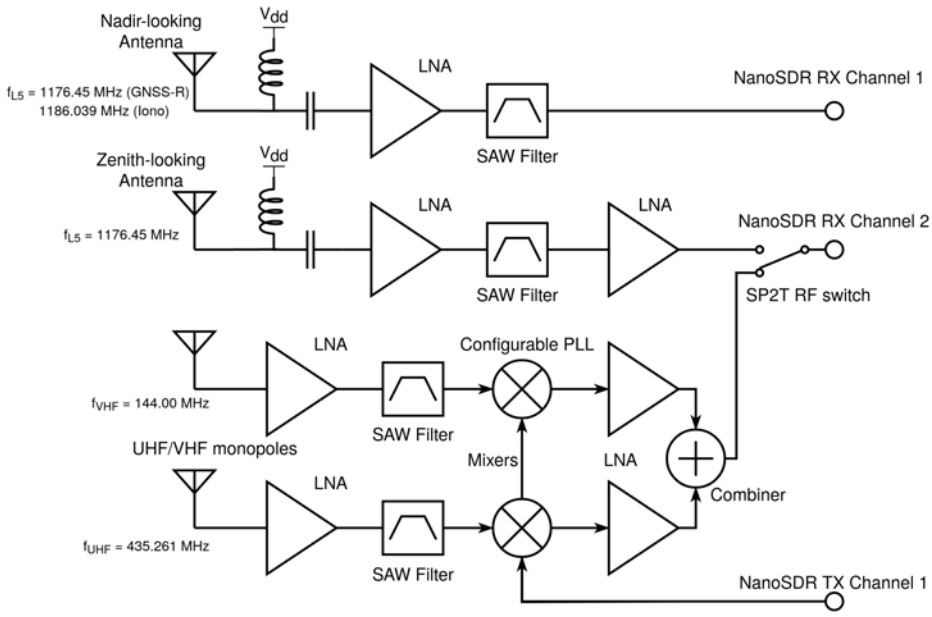

Figure 10.5: FMPL-3 RF-FE schematic.

be found in Appendix D.

Finally, a 3D CAD model of the RF-FE board is detailed in Fig. 10.6, showing an exploded view of the board and the connectors enclosed inside its aluminum box.

10.2.3 Data processing unit

The DPU of FMPL-3 is based on the GomSpace NanoSDR [222], the same commercial product used in the FMPL-2 (explained in detail in Section 9.2.4). This board is a state-of-the-art SDR for CubeSats, and thanks to the knowledge from FMPL-2, adapting it to the FMPL-3 needs decreased significantly the development time of the instrument, and should increase the chances of mission success.

As introduced in Section 10.2.2, the TR-600 [225] transceiver receives through its two receiving channels either the direct GNSS and the reflected GNSS signal in the GNSS-R mode; or the VHF/UHF CW signal in one channel, and the L5 CW signal in the second channel in the ionospheric scintillation experiment. In this last case, due to the limitation

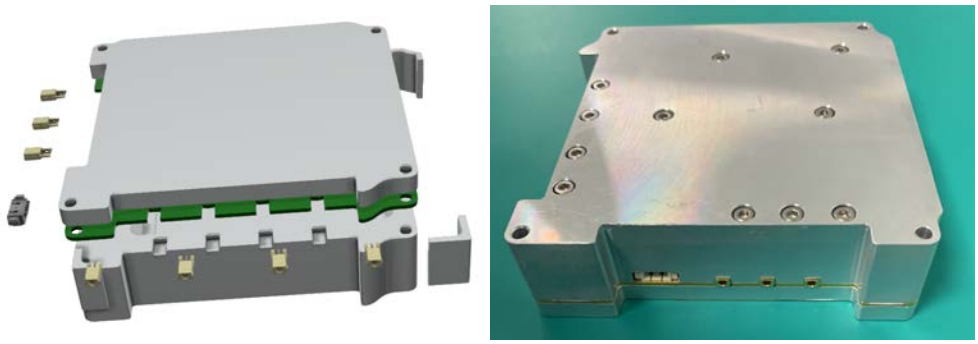

(a) **(b)**

Figure 10.6: (a) 3D CAD file corresponding to the FMPL-3 RF-FE board enclosed inside a aluminum box, with the four RF antenna connectors (front), and the three RF connecters for the DPU (left), and (b) FMPL-3 RF-FE board integrated in its aluminum box. Credit: Balamis S.L.

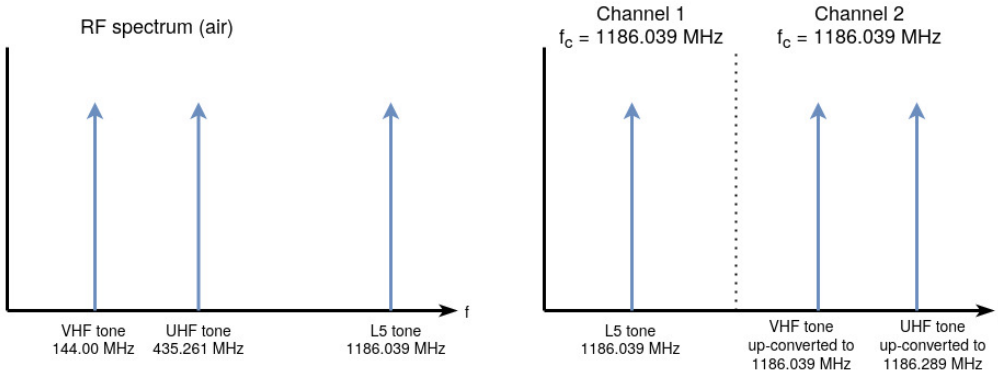

Figure 10.7: VHF, UHF, and L5 CW tones up-conversion performed by the RF-FE, and detailed central frequencies where the tones are received.

that the AD9361 [224] transceiver can only tune the receiver to a single frequency for both channels (as it also happened in the FMPL-2, Section 9.2.4), one of the TX channels is used as a reference signal for two Phase Locked Loops (PLL) used to generate the LO for the mixers that up-convert the VHF and UHF tones to the same frequency band of the L5 tone (Fig. 10.7).

The central frequency of the receiver in ionospheric mode is 1186.039 MHz[2]. Thus, the VHF tone, transmitted at 144.00 MHz[1] is up-converted to 1186.039 MHz, and the UHF tone, transmitted at 435.261 MHz[1] is up-converted 250 kHz apart from the VHF tone to 1186.289 MHz, as detailed in Fig. 10.7. Thus, the receiver bandwidth is configured to receive both tones (i.e., receiver bandwidth larger than 250 kHz).

Finally, the communication channel between the DPU and the platform OBC is the

[2]The tone frequencies have been selected in accordance to the PLL dividers used to up-convert the VHF and UHF tones into the L5 frequency.

Table 10.2: Queues used by FMPL-3 to exchange information between threads

Queue direction (from $->$ to)	Contents
CCT to GT	Events (1 byte)
CCT to GT	Configuration structure (40 bytes)
GT to CCT	Thread status (1 byte)
CCT to IT	Events (1 byte)
CCT to IT	Configuration structure (84 bytes)
IT to CCT	Thread status (1 byte)
CCT to HK	Events (1 byte)

GomSpace CubeSat Space Protocol (CSP) [238] using the Controller Area Network (CAN) bus.

10.2.4 Software architecture overview

Because of the uncertainties of the processing of L5 signals with high dynamics, the FMPL-3 has been simplified with respect to FMPL-2, and it only as a data logger in GNSS-R mode. Moreover, instead of having different processes and binary files executed, a single binary file is built, but with four threads running in parallel, as detailed in Fig. 10.8. In this case, the threads are synchronized by using the POSIX API, and set of mutex-protected circular queues are used to share data among the different threads, as detailed in Table 10.2. Note that, all queues are designed to allow data from a unique type of data structure, and there is only one structure allowed inside the queue (i.e., the queue size is 1).

The tasks performed by each of the four threads are the following ones:

- The Communication and Control Thread (CCT) is in charge of receiving and processing any message coming from the platform. This thread initializes the other three threads and sends events to them. The events are sent by the event queues detailed in Table 10.2, and the events are to START or to STOP a given execution, and to LOAD a new configuration file.

- The Housekeeping Thread (HT) is in charge of monitoring the basic telemetry of the RF-FE board, which carries a set of voltage, current, and temperature sensors to monitor the status of the board.

- The GNSS-R Thread (GT) is in charge of executing the GNSS-R experiment, and detailed in Section 10.2.4.1.

- The Ionosphere Thread (IT) is in charge of executing the GNSS-R experiment, and detailed in Section 10.2.4.2. Note that, the CCT ensures that both threads cannot be executed at the same time, and in case the GT thread is started, the IT cannot be triggered on too.

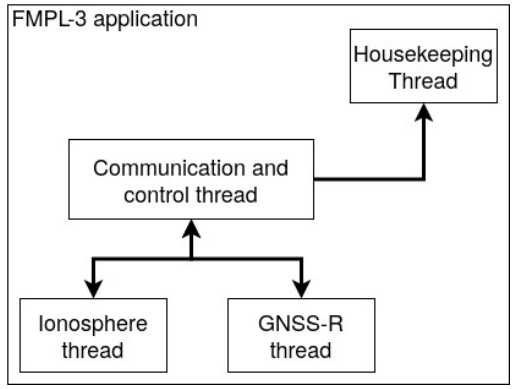

Figure 10.8: Thread distribution of FMPL-3 application.

Figure 10.9 presents the flowchart of the FMPL-3 application. Once a "START" message is received from the platform OBC, the requested configuration is loaded, and either the GNSS-R or the ionosphere experiments are executed. Note that, in both modes the TR-600 radio is controlled using the LibIIO interface also used in FMPL-2.

In the ionosphere experiment, a Frequency Locked Loop (FLL) aided PLL is used to track the different CW tones, while for the GNSS-R experiment, the IQ data is stored at 1-bit following the same scheme as in the MIR instrument (Chapter 4). In both cases, results are saved to the DPU eMMC memory, which will be later downloaded through the S-band link to ground.

As the instrument's goal is to have enough flexibility to be as versatile as possible to execute and validate the performance of GNSS-R at L5, a set of pre-defined configuration files are pre-loaded before launch into the memory, and up to 255 new configurations can be uploaded using the spacecraft communication link provided by NSSTC. To select the different configurations, the "START" command contains a 1-byte flag used to identify the configuration file identifier, as it is shown in Fig. 10.10. In this case, the same configuration strategy has been selected for the ionosphere experiment to take profit from the already-developed structure used by the GNSS-R experiment.

10.2.4.1 GNSS-R experiment thread

The GNSS-R experiment goal is to act as a "data logger". In this case, IQ data sampled at 10.230 MS/s will be recorded at 1 bit precision. As the amount of data generated is quite large (i.e. ∼2.56 MBytes/second per channel), the data recorder selects the number of samples per second based on the content of the GNSS-R configuration file following three parameters:

- Continuous segment size (in ms): the number of milliseconds (integer, non-negative, minimum of 1 ms, maximum of 100 ms) that comprise a single acquisition or data segment, e.g. a "20" means that 20 ms will be recorded.
- Segment drop ratio: the amount of segments dropped with respect to the stored ones (integer, non-negative, minimum of 0, no maximum), e.g. a "0" means that no data

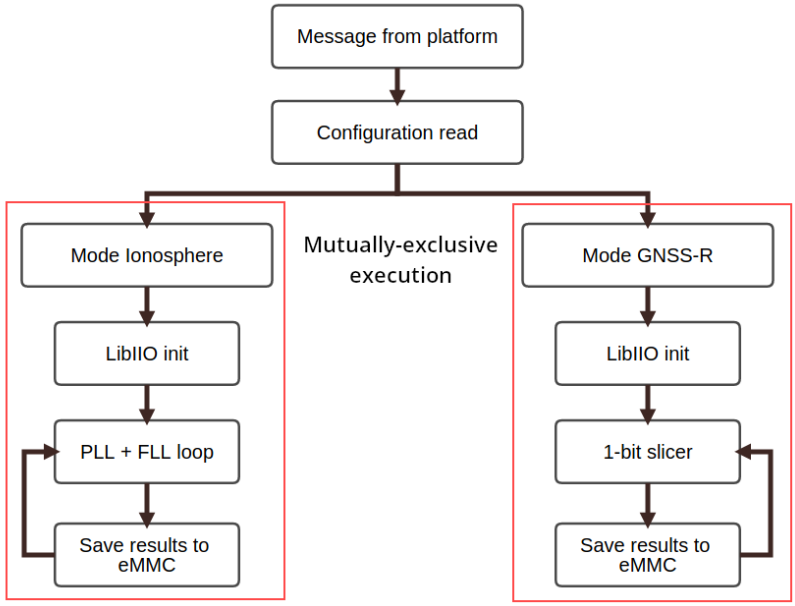

Figure 10.9: High-level flowchart for presenting the FMPL-3 application logic controlled by the CCT. Note that, both ionosphere or GNSS-R modes are mutually-exclusive.

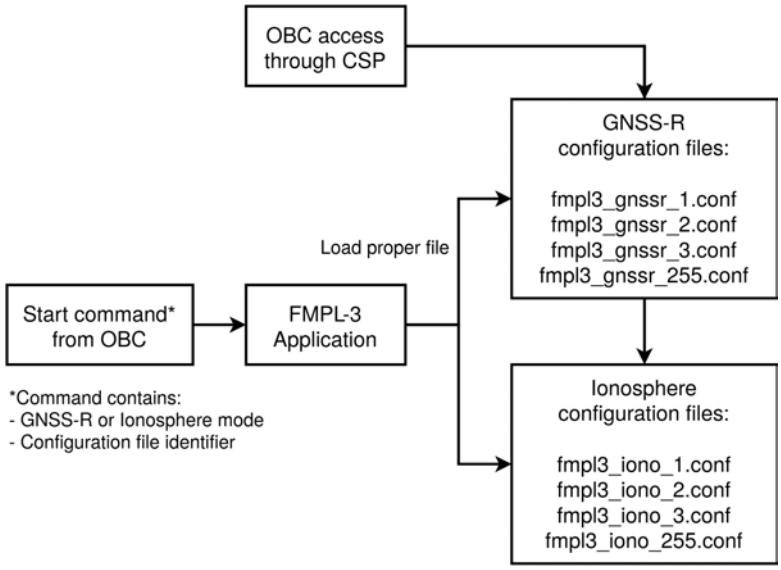

Figure 10.10: Configuration file structure used in FMPL-3.

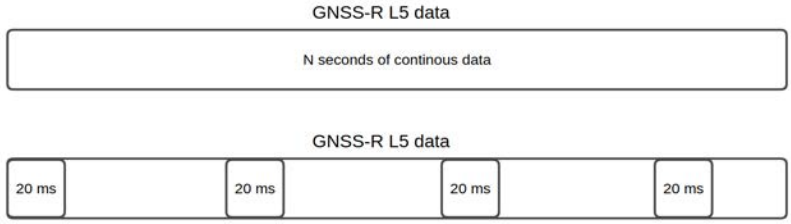

Figure 10.11: Example of two different configurations used to stream and store the GNSS-R data collected following a continuous acquisition (top), or a 20 ms acquisition every 100 ms (i.e. 1 packet is stored and four are dropped).

segments are dropped (i.e., Fig. 10.11 top); and a "4" means that for each segment stored, 4 segments are dropped (i.e., Fig. 10.11 bottom).

- Direct-to-Reflected signal ratio: the amount of data segments stored for the zenith-looking antenna with respect to the ones stored for the nadir-looking antenna (integer, non-negative, minimum of 1, no maximum), e.g. a "1" means that for every recorded nadir-looking signal, a zenith-looking signal is also recorded; a "5" means that for every 5 records on the nadir-looking signal, a single zenith-looking signal is recorded.

10.2.4.2 Ionosphere experiment thread

The ionosphere experiment goal is to continuously and synchronously track the three CW tones transmitted to the satellite from ground. As detailed in Fig. 10.7, the L5 tone is collected by one of the SDR channels, and the VHF and UHF tones are collected by the other channel. Both channels are IQ sampled at 2.4 MS/s, and as shown in Fig. 10.12, the L5 tone is down-sampled to 48 kS/s by means of a decimating Flat Impulse Response (FIR) filter with decimation ratio of 50. The filter response is presented in Fig. 10.13. The filter has been designed with 19 coefficients, which gives the optimum trade off between frequency selectivity and computation load for the ARM processor. In the VHF/UHF case, the signal is filtered by the same FIR filter, which has more than 40 dB of attenuation at $f = 250$ kHz. Finally, the entire channel two is multiplied by a the complex exponential $e^{j2\pi f_c t}$, where f_c 250 kHz, and then filtered by the same FIR filter as in the previous cases. This strategy ensures that both tones are can be introduced in separated processing chains.

Once all tones are filtered and the input signal is decimated, a FLL-aided PLL block is used to track the phase and frequency of the signal. This block has been adapted based on the FLL-aided PLL used in the GNSS-SDR project [239] (function name: *dll_pll_veml_tracking*), and based on the FLL-aided PLL filter proposed in [240]. Note that, the maximum Doppler shift for a spaceborne receiver at v_{sat} =7.5 km/s at L5 (f_c = 1186.039 MHz) is 29.650 kHz[3].

[3] $\Delta f = \frac{v_{sat}}{c} f_c$, where c is the speed of light, $3 \cdot 10^8$ m/s

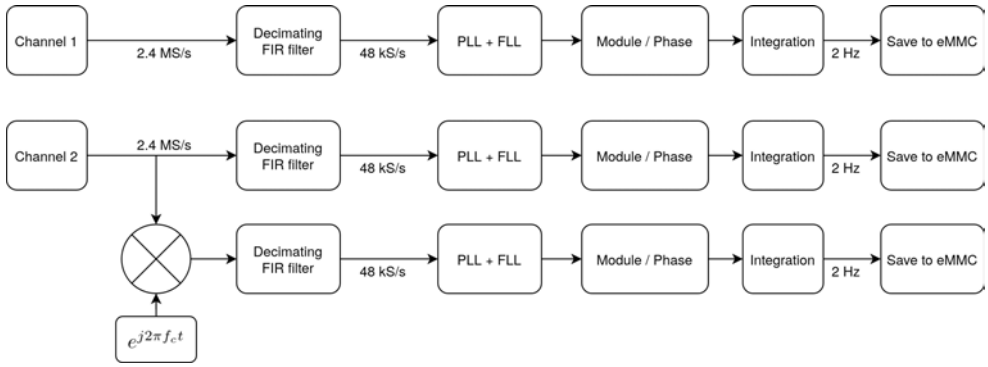

Figure 10.12: FMPL-3 Ionosphere experiment processing chain. At the top, the single-tone L5 processing chain is detailed, at the bottom, the dual-tone VHF+UHF receiver is detailed. The f_c used to performed the frequency shift of the UHF signal on channel 2 is 250 kHz.

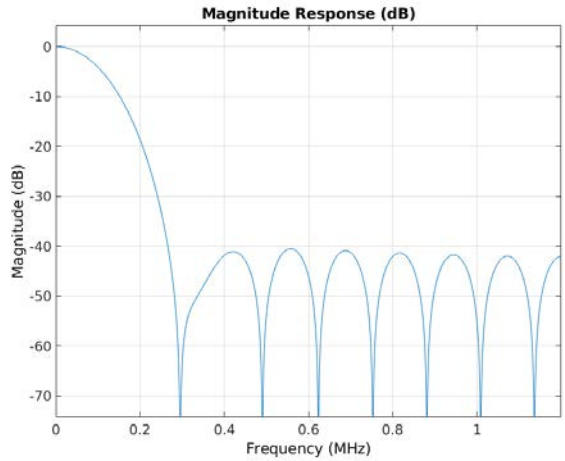

Figure 10.13: Frequency Response of the FIR filter used to filter the different CW tones used to conduct the ionosphere experiment. The filter is composed of 19 coefficients, and from that constrain and using a Blackman-Harris window the 3 dB cut-off frequency is at 80 kHz, and the stop frequency (40 dB attenuation) at 250 kHz.

10.3 FMPL-3 Implementation and Testing Phase

Because of the short development time (10 months), as for the FMPL-2, a PFM approach has been followed to shorten the development time and cost of the instrument, and the volume and integration requirements of the GNSSaS platform have been taken into account, i.e., the system has not been enclosed into an aluminum box.

The main characteristics of the instrument are summarized in Table 10.3.

Table 10.3: Main Characteristics of FMPL-3.

Parameter	Value
Volume (electronics)	∼0.85 Units: ∼9x9x7.6 cm^3
Volume (zenith-looking antenna)	∼4.8x4.8x1.3 cm^3
Volume (nadir-looking antenna)	∼32x21x1.3 cm^3
Mass (electronics)	657 g
Mass (zenith-looking antenna)	37 g
Mass (nadir-looking antenna, including ground plane)	751 g
Power Consumption	1060 mA at 5 V
Data rate (GNSS-R continuous data in 1 channel)	∼2.5 MB/s
Data rate (Ionosphere experiment)	< 100 Bytes/s

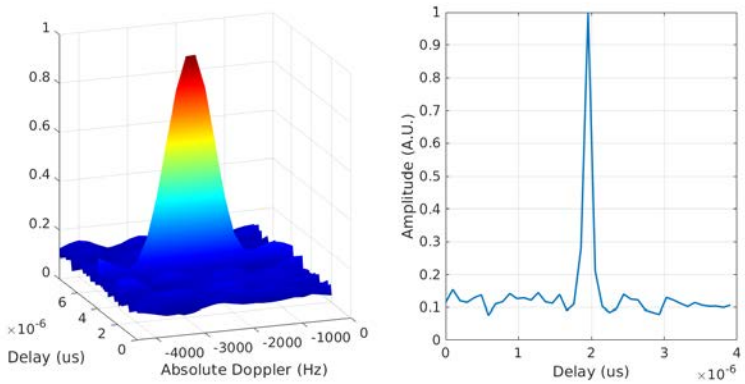

Figure 10.14: (a) DDM and (b) Waveform cut at the maximum Doppler of the GPS L5 signal transmitted by the satellite vehicle carrying the PRN #3.

10.3.1 Functional test campaign

The ambient test campaign comprises two tests. The first test aims to prove the capabilities of FMPL-3 to receive GPS L5 signal, which can be then processed to retrieve the ACF. As it can be seen in Fig. 10.14, the GPS L5 signal is correctly received, and both the DDM and the waveform can be later retrieved using the GNSS-R processor. In this case, MATLAB® is used to read and process the signal.

The second test aims to demonstrate the capabilities of the instrument to receive the three different tones of the ionosphere experiment. The test has been conducted at the UPC NanoSat-Lab premises (see Fig. 10.15), using a Rohede&Schwarz signal generator and varying the amplitude of the transmitter signal. In this case, the signal generator is directly connected to the RF-FE. The goal of this test is to set a link budget margin to dimension to ground equipment that will be required to transmit the VHF/UHF/L5 CW tones.

According to the measurements performed in the laboratory, a received power larger

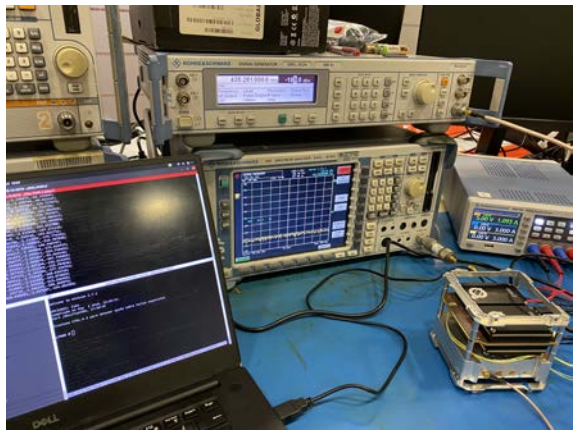

Figure 10.15: Functional test campaign to characterize the link budget of the ionosphere experiment, conducted at the UPC NanoSat-Lab.

Table 10.4: VHF, UHF, and L5 link budget.

	VHF	**UHF**	**L5**
FSPL at 5º elevation angle (d =2000 km)	141.6 dB	151.3 dB	163.9 dB
RX antenna gain	0.6 dB	2.8 dB	10.1 dB
Desired received power	>-105 dBm	>-105 dBm	>-105 dBm
Required EIRP[5]	36 dBm	43.5 dBm	48.8 dBm

than -105 dBm is required to ensure a SNR of 20 dB, which is large enough to compensate the potential attenuation due to the atmospheric scintillation. In this case, as the PLL/FLL block works with a bandwidth of 48 kHz[4], this is the receiver bandwidth used to compute the signal link budget, according to Table 10.4.

The antenna array and the UHF monopoles have been characterized in the UPC Antenna Lab anechoic chamber[6]. A 6U CubeSat with flight configuration (i.e., deployable solar panels, VHF/UHF monopoles, ground plane) has been designed to mimic the final flight configuration, as it can be seen in Fig. 10.16. The measured antenna pattern is shown in Fig. 10.17. Note that, the cross-polar component has been also measured to ensure there is no coupling between the RHCP antenna and the LHCP antenna, showing more than 20 dB of isolation between the two components. The antenna directivity is 10.1 dB, satisfying the requirements to receive L5 GNSS-R signals from space.

[4] $10 \cdot \log_{10}(K_B \cdot T_{Ref} \cdot B_f)$ = -124.8 dBm, being K_B the Boltzmann constant, and T_{Ref} = 500 K, and B_f = 48 kHz.

[6] The UPC Antenna Lab anechoic chamber does not support the VHF band, but as the monopole disposition is the same as for the UHF antennas, it is assumed they have equivalent diagrams.

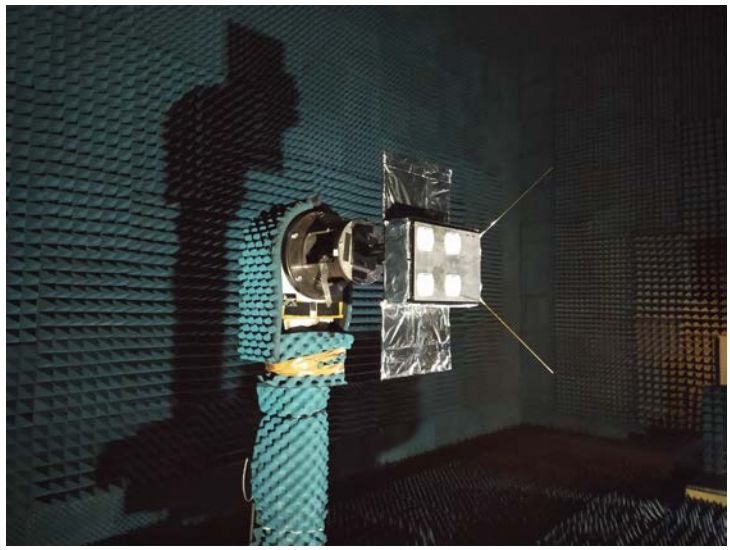

Figure 10.16: Representative 6U CubeSat model with the final flight configuration used to measure the antenna pattern in the UPC Antenna Lab anechoic chamber [231].

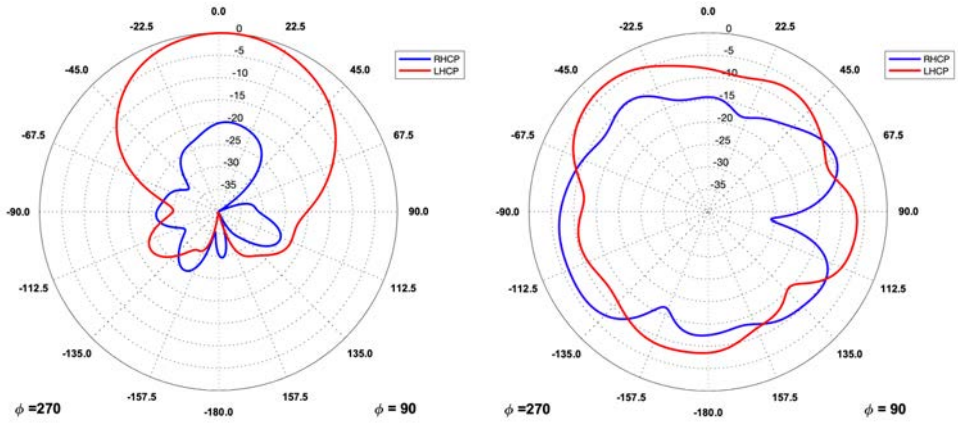

Figure 10.17: Antenna radiation patterns at (a) L5 and (b) UHF bands measured at the UPC Antenna Lab anechoic chamber [231].

10.3.2 Environmental test campaign

The FMPL-3 will be tested with the overall satellite, once integrated. Despite that, the RF-FE board, which is a new manufactured board, has undergone an acceptance vibration test to validate that it can withstand the launch dynamics without compromising the entire spacecraft. This subsystem has been tested in the UPC NanoSat-Lab shake table (see Fig. 10.18) at qualification levels, with a shaking profile of 8.2 g_{rms} in the three axis. Test details are provided in Appendix D.

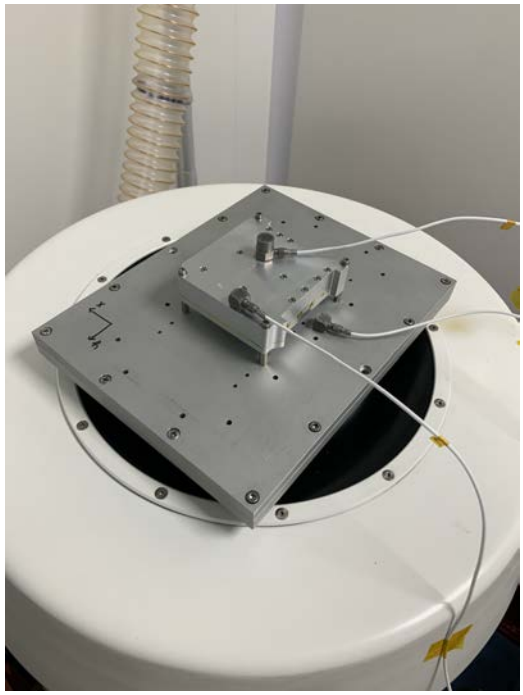

Figure 10.18: RF-FE subsystem tested in the UPC NanoSat-Lab shake table (Z-axis direction).

10.4 Conclusions

In this Chapter, the third generation of the FMPL family instruments has been presented. The instrument comprises a dual experiment in a SDR platform. The first experiment is a technology demonstrator for spaceborne L5 GNSS-R. Because of its novelty and unknowns, the GNSS-R data is recorded at 1 bit and it will be downloaded to ground to assess different processing techniques and specular point re-tracking strategies. The second experiment comprises a ionospheric scintillation study to assess the correlation of intensity and phase scintillations over frequency at VHF, UHF, and L5 bands simultaneously.

The instrument has been designed, implemented, and tested and it is now at NSSTC premises in the UAE to be integrated into the 6U CubeSat. The launch date is not confirmed yet.

Part IV

FMPL-2 Results

11

Chapter 11

In-orbit Validation of the FMPL-2 Instrument

This Chapter presents the results of the first weeks of operation of FMPL-2 onboard ^{3}Cat-5/A after platform commissioning. This Chapter has been adapted from the peer-reviewed journal publication entitled "In-Orbit Validation of the FMPL-2 Instrument—The GNSS-R and L-Band Microwave Radiometer Payload of the FSSCat Mission" [JP8], and the work has been presented in international conferences [CP11, CP12]. The Chapter is organized as follows: Section 11.1 briefly introduces the Vega VV16 flight which launched the FSSCat mission with ^{3}Cat-5/A carrying FMPL-2 to space, and the key dates in the instrument commissioning. Section 11.2 presents an overview of the main telemetry parameters of FMPL-2. Section 11.3 presents the first results of the FMPL-2 MWR from space. Section 11.4 presents the capabilties of FMPL-2 to perform GNSS-R from space. Finally, Section 11.5 presents the conclusions of the Chapter.

11.1 Introduction

The first European ride share was the Vega Small Satellite Mission Service (SSMS) flight or VV16, launched from Kourou spaceport on 3 September 2020. Vega SSMS is a European initiative to provide low-cost launch opportunities for small satellites, from 1U to 6U CubeSats, and satellites up to 400 kg [241]. On this flight, Vega carried 7 micro-satellites and 46 nano-satellites, two of them were ^{3}Cat-5/A and /B, forming the FSSCat mission. The satellites were deployed in a Sun-synchronous LEO orbit, at ∼530 km height.

FMPL-2 was executed in orbit for the very first time on 14 September 2020, and the commissioning of the instrument last 10 days, formally ending on 25 September 2020. During these first days, the instrument was successfully executed 8 times over the North Pole, providing quality radiometric measurements at L-band, and GNSS-R measurements that were used to calibrate and tune the configuration of the instrument. Since then, the instrument entered into nominal operations, being executed over both poles in a 5-day basis (i.e., five days over the North Pole, and five days over the South Pole).

11.2 FMPL-2 Telemetry Review

As explained in detail in Chapter 9, FMPL-2 operates both as a GNSS-Reflectometer, and as a microwave radiometer simultaneously, and using the same antenna. To operate as a radiometer, frequent calibration is required, and therefore internal hot and cold loads are sampled at 2 Hz. This acquisition strategy allows to calibrate the noise temperature, and the system gain for both the radiometer, and the GNSS reflectometer. This allows to calibrate not only the antenna temperature, but also the DDM noise floor, and assign an absolute power unit to each GNSS-R measurement. As both radiometric and reflectometric measurements depend on noise temperature calibration measurements, a high thermal stability, and an accurate knowledge of the instrument temperature and their calibration loads are required. In the case of FMPL-2, the instrument was designed and validated to work with a temperature stability of 1 °C/min.

Figure 11.1 shows four different histograms corresponding to the measured temperatures by the FMPL-2 payload, normalized as a PDF. Note that Figs. 11.1a,c correspond to the measured temperatures in 128 different executions, while Figs. 11.1b,d correspond to the 1-minute temperature gradient (i.e., $\Delta T/\Delta t$ with $\Delta t = 1$ min). Note that, the temperature gradient of both the instrument board and the antenna are always below 0.6ºC/minute, and therefore meet the instrument requirements. In addition, the temperature range of the instrument is also within specifications, between 10ºC and 25ºC for both the instrument and the nadir-looking antenna.

Finally, Fig. 11.2 shows the different ^{3}Cat-5/A tracks (in red) projected using the Lamber-Azimuthal-Equal-Area (LAEA) projection, including the ice extent map (i.e., SIE product from the Satellite Application Facility on Ocean and Sea-Ice (OSI SAF) [242]) on 13 October 2020. The OSI SAF SIE product identifies three types of ice depending on the concentration. In Fig. 11.2, the blue color shows areas without ice concentration (lower than 30%), the light-green area corresponds to open ice (ice concentration between 30% and 70%), and the yellow color identifies closed-ice areas (more than 70% of ice concentration).

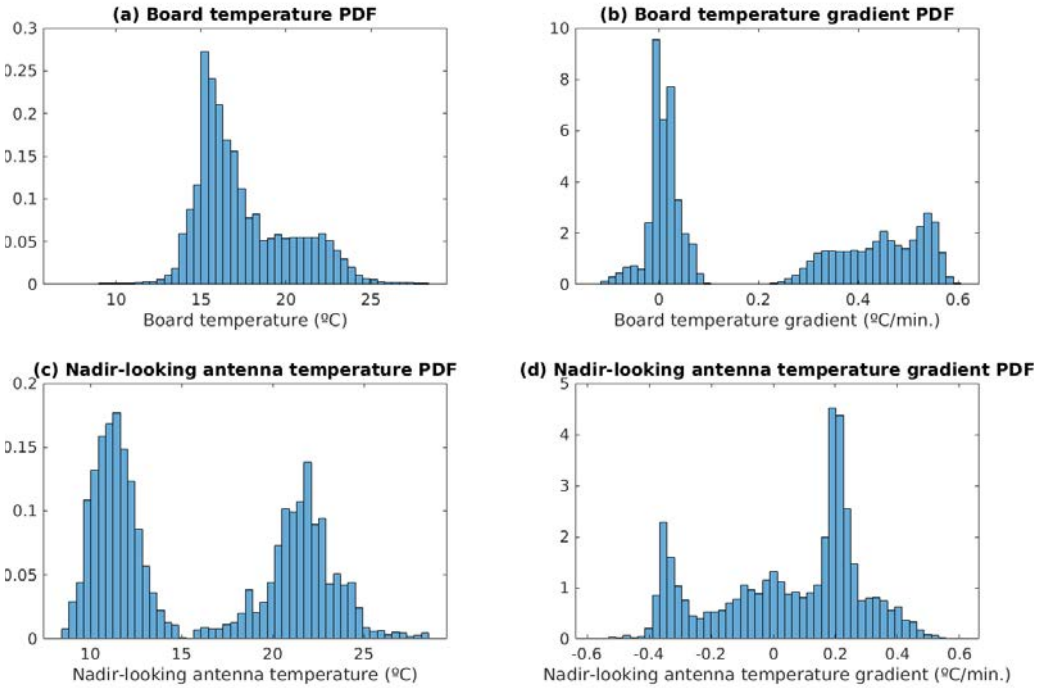

Figure 11.1: (**a**) Temperature probability density function (PDF) of the instrument board during executions, (**b**) 1-minute integrated temperature gradient of the instrument board, (**c**) Temperature PDF of the nadir-looking antenna during executions (**d**) 1-minute integrated temperature gradient of the nadir—looking antenna

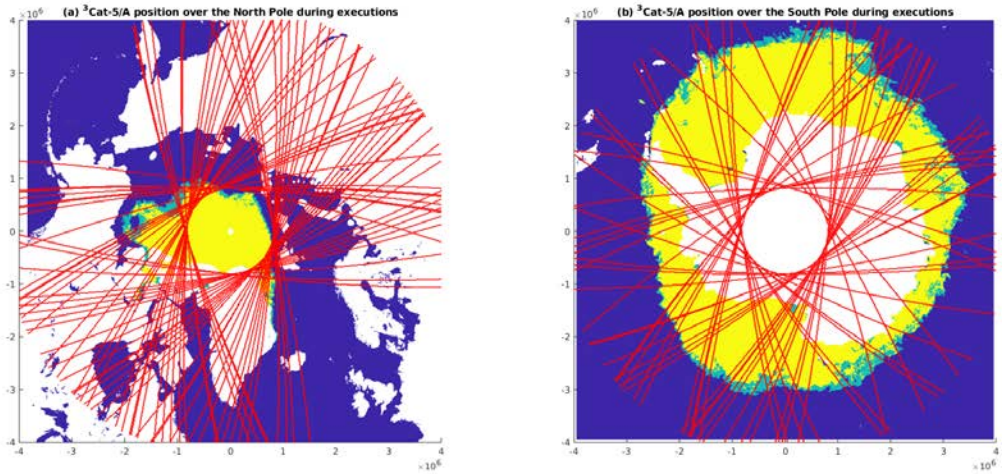

Figure 11.2: (**a**) North Pole tracks of FMPL-2 executions in LAEA coordinates, and (**b**) South Pole tracks of FMPL-2 executions in LAEA coordinates. Both figures with OSI SAF Sea-ice edge product (in blue-green-yellow) overlaid.

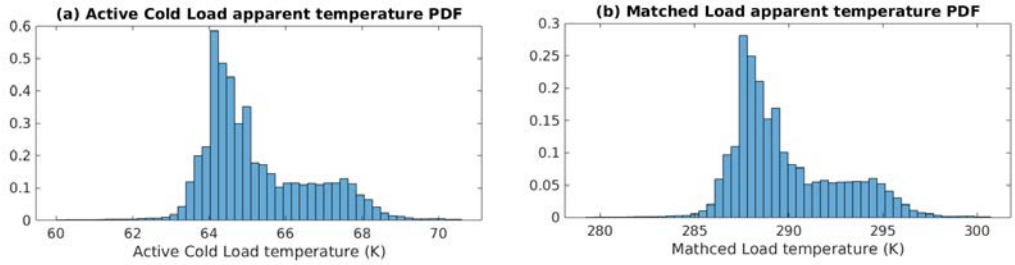

Figure 11.3: (**a**) Active Cold Load apparent temperature (Kelvin), and (**b**) Matched Load apparent temperature (Kelvin).

11.3 FMPL-2 L-Band Radiometer Review

As introduced in the last section, the temperature knowledge and its stability are crucial for the correct operation of the radiometer. The two main requirements of the instrument are the sensitivity (i.e., radiometric resolution), which shall be lower than 1 K, and the accuracy, which shall be lower than 2 K [243]. This section presents a summary of the hot and cold load measurements, and the very first geo-located microwave radiometer data for both the North and South poles. Finally, a study of selected stable regions (i.e., middle of the ocean) is presented, which are used to validate both the radiometric sensitivity, and the accuracy of the instrument.

The PDF of the temperature for both internal calibration loads is shown in Fig. 11.3. As it can be seen, the ML (a 50 Ohm resistor) temperature matches the board temperature (i.e., its noise temperature corresponds to the physical temperature of the component), and the ACL noise measurement has been calibrated for the thermal drifts and switch losses, taking into account the contribution from the ML, as shown in Eq. 9.4 from Chapter 9.

11.3.1 Measured antenna temperature

Once the ancillary data is used to calibrate the radiometer, the final antenna temperature (T_A) measurement is computed using the instrument gain and bias estimated during the calibration, and finally compensating for the antenna losses, as shown in Chapter 9.

Figure 11.4 presents 13 days of geo-located FMPL-2 L-band radiometer measurements over the North Pole, for all latitudes above 55º. The geo-located T_A clearly shows the difference between Land, with a T_A larger than 180 K; ocean, with an average $T_A \sim$ 90–95 K; and ice, with a T_A larger than 150 K. It is also remarkable how Greenland and Iceland are identified at the bottom the image. Even though the instrument has a very wide footprint in the cross-track direction (∼500 km), the oversampling (2 Hz) in the along-track direction, and a later co-location of consecutive passes allows to reconstruct a 2D image from a number of 1D tracks. Note that, geo-located images are not projected over a grid yet, and the pixels are not at antenna footprint scale. The ground-truth ice edge data is overlaid below the T_A track, as it can be seen for latitudes above 86º (dark-yellow), where the S/C cannot measure using the radiometer due to the orbit inclination.

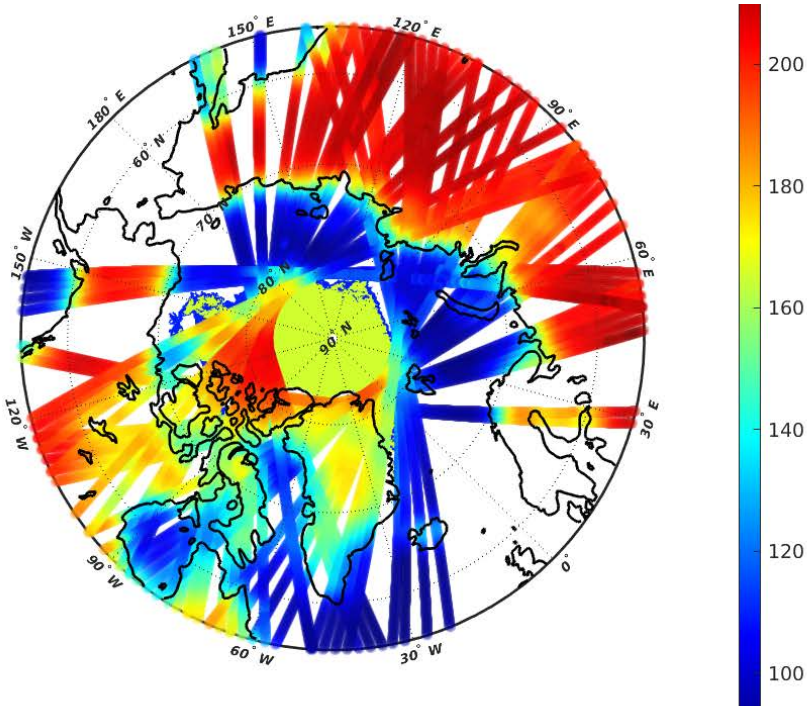

Figure 11.4: FMPL-2 calibrated antenna temperature (T_A) (K) over the North Pole overlaid with OSI SAF SIE product (in yellow at the background).

Moreover, Fig. 11.5 shows the corresponding data for the South Pole, for all latitudes below -55º. Note that, some of the passes of the South Pole show a degraded value of the calibrated antenna temperature, which was identified as an attitude loss for a given set of orbits due to Sun glint entering into the field of view of the start trackers. Despite that, it is clearly seen the T_A gradient in the along-track direction when the S/C enters into the ice, going from 90 K up to ∼180–200 K in a few samples. Thanks to the very high along-track overlapping (∼99%), the sea-ice edge can be accurately estimated by analyzing the gradient of the T_A evolution, which can then be compared to the tracks of the OSI SAF SIE product (in yellow). Note that, the Copernicus Imaging Microwave Radiometer (CIMR) will also include a similar oversampling technique to provide a better resolution product. In this case, CIMR will perform a footprint overlapping of 20%, reducing the spatial resolution from 60 km to 40 km [244].

As it can be seen in different regions of the image, as in the top right corner or in the bottom left corner, by overlapping different consecutive passes, and assuming the sea-ice edge has not significantly changed between consecutive passes (i.e., separated less than a few days), a 2D reconstructed image of the sea-ice surrounding the Antarctica could be retrieved.

Finally, the PDF of the T_A for both poles is presented in Fig. 11.6. As it can be seen in (a), the distribution of antenna temperatures is more evenly distributed than in the South Pole, because in the North Pole images there is a combination of land, water, and

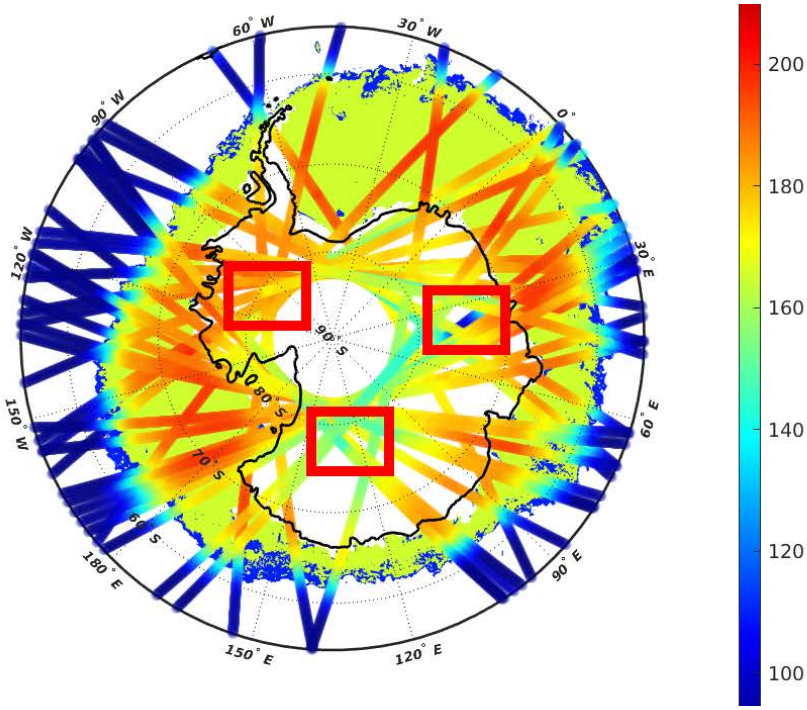

Figure 11.5: FMPL-2 calibrated antenna temperature (T_A) (K) over the South Pole overlaid with OSI SAF SIE product (in yellow at the background). Highlighted in red some tracks that contain attitude losses, and therefore erroneous T_A values.

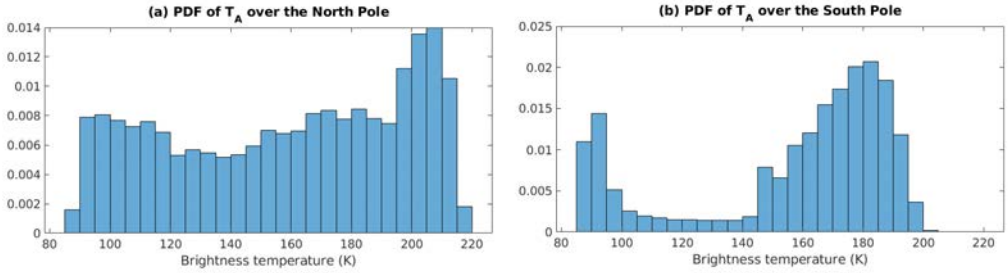

Figure 11.6: FMPL-2 calibrated brightness temperature (T_A) PDF for (**a**) the North Pole, and (**b**) the South Pole.

notably different types of ice with different thickness, with some regions with multiple contributions in the antenna footprint (i.e., Greenland), while in the South Pole there is only ice, land completely covered by ice/snow, and water, with well defined boundaries in the along-track direction of the measurements.

11.3.2 Radiometric accuracy

As introduced at the beginning of this section, the L-band radiometer has been designed to provide an absolute accuracy better than 2 K. To validate this requirement, the following scenarios are selected:

- A track in the Arctic Ocean over water, with enough separation from any land body, or sea-ice, on the 4th of October at 20 UTC, and
- A track in the Antarctic ocean before entering into the Antarctica on 1 October 2020 at 18 UTC.

The two selected tracks are shown in Fig. 11.7. Note that both the geo-located version, and the time-series evolution of the T_A are presented. Furthermore, a 5-second window (10 samples) standard deviation is shown, together with the time series evolution. The following list summarizes the ground-truth data generated by the ICON model [151], and downloaded through [156] for the regions under study:

- Arctic track: Ocean salinity ∼35.5 psu, temperature ∼4–6ºC, wind speed almost calm ∼2–3 m/s (Fig. 11.7), and different wind speeds varying as detailed in Fig. 11.8a,
- Antarctic track: Ocean salinity ∼34 psu, temperature ∼2–6ºC, wind speed varying as detailed in Fig. 11.8b.

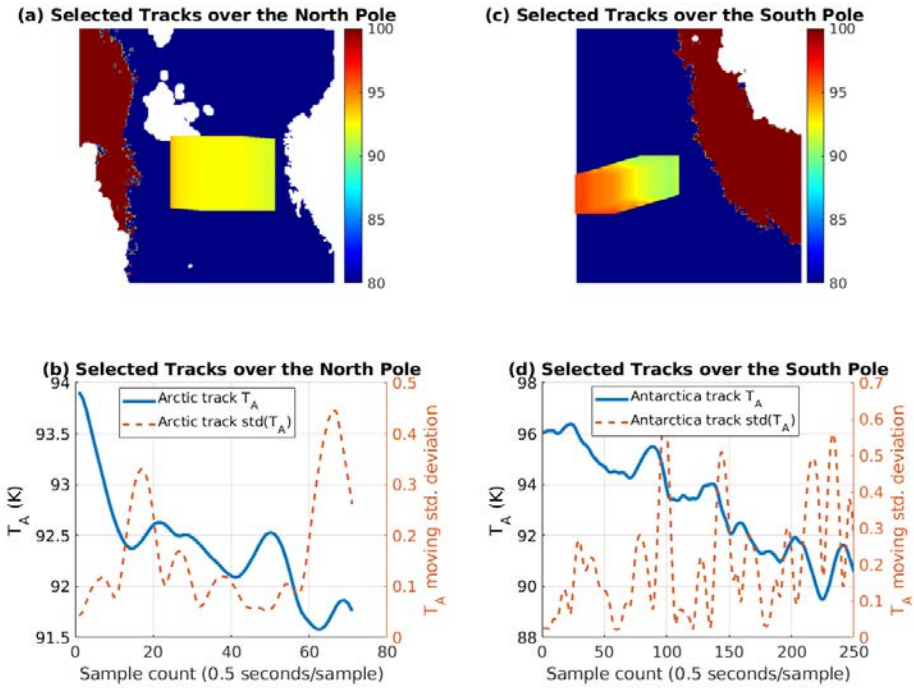

Figure 11.7: (**a**,**c**) are the Geo-located selected tracks for both North and South poles used to compute sensitivity and accuracy analysis, and (**b**,**d**) are the time evolution of the brightness temperature and a 5-second window standard deviation of the T_A.

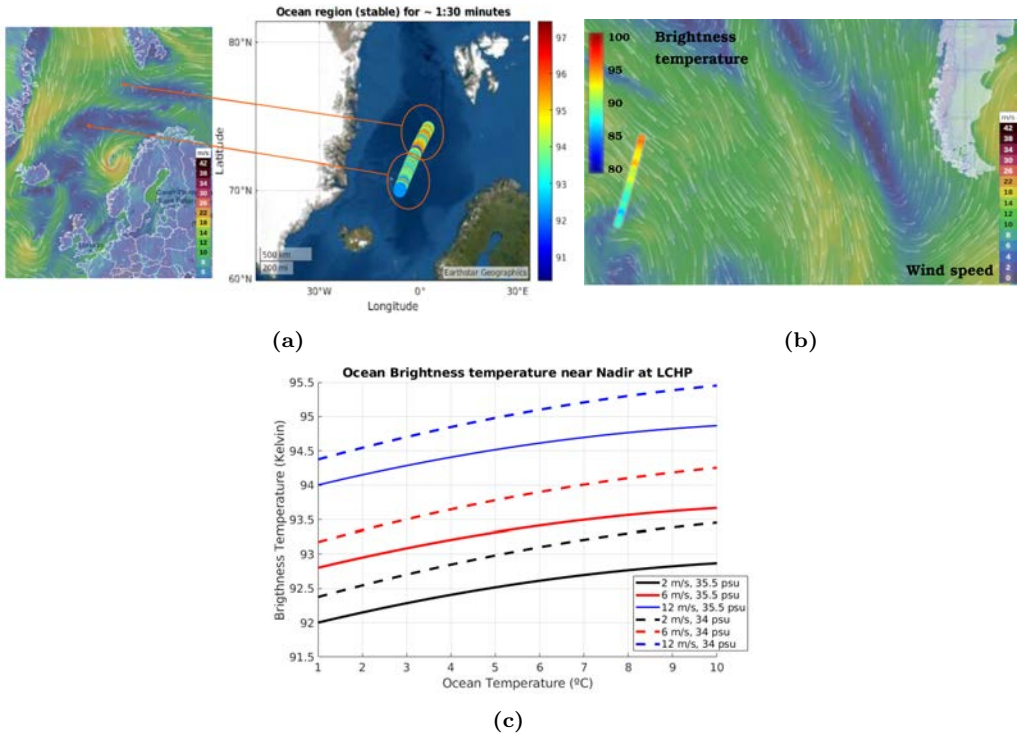

Figure 11.8: (a) North Pole and (b) South Pole tracks overlaid with the wind speed over the ocean, retrieved from ICON model [151], and (c) brightness temperature for different psu (34 and 35.5 psu), temperatures (1ºC to 10ºC), and wind speeds (from 2 m/s to 12 m/s).

The Arctic track (Figs. 11.7a,b) is a descending orbit pass, and T_A is initially decreasing from ∼94 K rapidly to ∼92.5 K, because the antenna footprint is still collecting some portion of Svalbard. From this point, around sample count 15, the measurements are less noisy, maintaining the measurement ∼92–92.5 K during ∼30 s. Comparing it to Fig. 11.8c, the actual measurement corresponds to the blue curve (∼2 m/s wind) at ∼4ºC, therefore the absolute accuracy of this measurement is estimated to be better than ∼0.5 K.

Moreover, the same curve is presented for the Antarctica track (Figs. 11.7c,d). In this case, and as shown in Fig. 11.8, the measurement starts in a very windy area, with winds going from 15 m/s down to 12 m/s. The brightness temperature out of this area is high ∼96 K, which corresponds to high winds (>12 m/s). Despite that, as the satellite moves towards the Antarctica, it enters into a very calm area, with wind speeds ranging from 2–4 m/s, and therefore the received T_A significantly drops from 96 K down to 92 K, providing in this case an accuracy better than 2 K along the overall time series.

Finally, the instrument shall be stable among consecutive measurements. To validate this stability, five consecutive tracks over the same regions have been selected over Alaska. Four consecutive tracks have been selected, with a separation of one day between them. In addition, a fifth acquisition one week apart has been selected. Figure 11.9 shows the evolution of those tracks. As it can be seen, blue (1 October 2020) and green (12 October

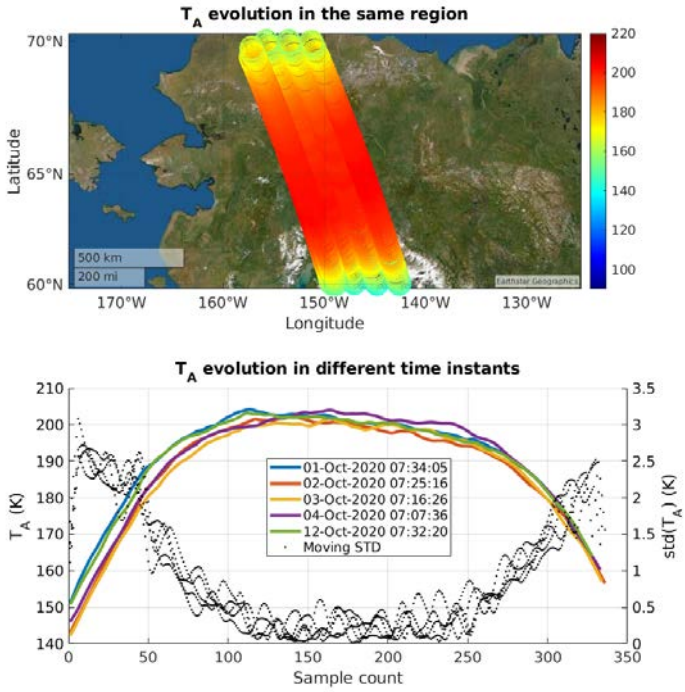

Figure 11.9: Five FMPL-2 tracks used to validate the antenna temperature (K) drift of a given region in consecutive orbits. Selected region is Alaska in four consecutive days plus a fifth day with a separation of one week.

2020) tracks are coincident (i.e., the footprint over the same exact region), and both are showing the same evolution, with a mean square error between both at the central part (i.e., between samples count 100 and 250) of 0.34 K. The central point of each of the four consecutive tracks is separated a longitude of $\sim 2.2^{o}$ or $\sim$100 km, which corresponds to an 82% of overlapping in the cross-track direction.

11.3.3 Radiometric sensitivity

In order to check the radiometric sensitivity, the same scenarios as in the previous section are used. In this case, the radiometer has been designed to provide a sensitivity better than 1 K. The moving standard deviation of T_A is computed over stable regions, as in the middle of the image of Fig. 11.7c (from samples 20 to 60), and in the land part (from samples 150 to 250) of Fig. 11.9. In both images, the moving standard deviation of T_A is below 1 K. In the first case, this magnitude is below 0.2 K, as the ocean is pretty stable with very low speed winds. However, for the land case, the sensitivity in the center of the figure goes up to $\sim$0.5 K. This behavior is the expected, as on one hand, land is less homogeneous. The antenna footprint collects multiple contributions from different sources (i.e., different soil moisture values or vegetation changes), as compared to a calm and open sea. On the other hand, the sensitivity of a TPR depends on the measured T_A, as shown

in Eq. 8.1 from Chapter 9, and therefore the higher the measured T_A, the higher the sensitivity value. In our case, comparing the theoretical radiometric sensitivity presented in Chapter 9, but assuming a T_A of 100 K instead of 250 K, the expected radiometric sensitivity of FMPL-2 shall be on the order of 0.27 K, as detailed below (reproduced from Eq. 8.1 and from Section 9.2.5.2):

$$\Delta T = \frac{T_{sys}}{\sqrt{B \cdot \tau}}, \tag{8.1}$$

where $T_{sys} = T_A + T_R = 172$ K, with $T_R = 72$ K, and $T_A^{max} = 100$ K (pointing to open water), $B = 4$ MHz and $\tau = 0.1$ seconds, $\Delta T = 0.27$ K.

11.3.4 2D image reconstruction

The overlapping in the cross-track direction (i.e., after 13 days of measurements), allows to compose 2D images, such as the Arctic Ocean one shown in Fig. 11.10. As it can be seen, two weeks of data allows not only to fill all data gaps over the pole, but also to have enough overlapping in the cross-track direction to reconstruct a 2D image. To reconstruct the image, each measurement is aggregated into a 3 km grid taking into account the antenna footprint (i.e., 500 km in the cross-track and 350 km in the along track) following a Nearest Neighbor Interpolation (NNI) algorithm. Finally, measurements laying in the same pixel after multiple orbits are averaged. Thanks to the overlap in the cross-track direction, most of the pixels composing a single 1D track are averaged with other 1D tracks, and therefore forming the 2D image with a higher resolution.

11.3.5 Radio-Frequency interference detection using FMPL-2 MWR data

The FMPL-2 L-band MWR also includes a Radio-Frequency Interference (RFI) detector. The RFI detector was explained in Section 9.2, and an RFI detection test was presented in Fig. 9.18. During the first weeks of operations, two main sources of interference were encountered. First, RFIs that can be detected through the Kurtosis flag were encountered in few number of samples, as in the example shown in Fig. 11.11a. As it can be seen, strong RFI events that can be identified by a sudden increase of the received power (up to ∼2500 K) are correlated with a variation of the complex Kurtosis flag, from 2 (which means that Gaussian noise is being received) to ±0.05 from this value, showing that potential RFI is being received. Second, two RFI events were also detected by visual inspection of the received power evolution of the FMPL-2 antenna temperature. As it is presented in Figs. 11.11b and c, a sinusoidal signal with a very low intensity can be identified in two acquisitions. Note that, the sampling rate is 2 Hz, thus, the period of the sinusoidal signal is ∼14-15 s. This type of RFIs are not detected by the complex Kurtosis test, showing a complex Kurtosis value always around 2±0.01 (5 to 10 times lower than in the detected RFI case). For such low-intensity events, the RFI cannot be tagged through the Kurtosis flag. Different hypothesis are being studied to identify the source of the RFI, from any platform jitter (i.e., EMI), or interference from long-range radars operating at L-band. For this last case, the sinusoidal period might be linked to the rotation speed of the radar (i.e., ∼4-5 revolutions per minute, as the Air Route Surveillance Radars -4, working at 5 rpm). Note that, similar RFI events have been detected in different time

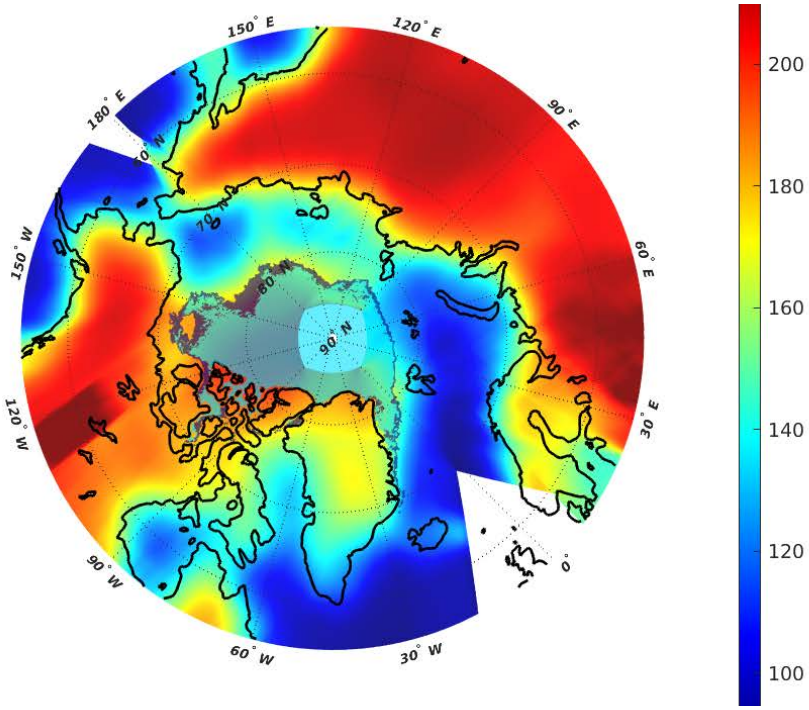

Figure 11.10: Reconstructed 2D antenna temperature (T_A) (K) image over the North Pole by aggregation of multiple scattered FMPL-2 executions over an EASE Grid of 3 km. Note that, transparency is added to show land boundaries, and OSI SAF SIE product is also overlaid.

instants, and always with similar periods.

To conclude the L-band radiometry review section, it is important to remark that the requirements of the instrument have been successfully achieved, providing an accuracy below 2 K, and a sensitivity lower than 1 K. In addition, the measurement drift between consecutive orbits has been quantified, showing negligible drift between consecutive tracks (<0.34 K in 12 days) with a footprint overlap of 82%. It has been presented that the instrument is able to detect strong RFI events using the complex Kurtosis, but it fails to detect periodic signals that might be transmitted by long-range radars. Finally, the instrument along-track axis oversampling allows to detect the ice edge as it will be shown in Chapter 12, and to compose 2D images over a 3 km grid.

11.4 FMPL-2 GNSS-R Review

The second part of the instrument is a GNSS-R receiver. The presented data is for the same period of the radiometer, and some selected tracks are presented for GPS L1 C/A case. This part of the instrument measures the GNSS reflections that are produced in either the ocean, the land, or the sea-ice. On contrary to other GNSS-R instruments [137, 138], the instrument was designed with a maximum incoherent integration time of $T_{int} = 40$ ms to avoid the need to retrack in orbit [54, 144, 245] and avoid the blurring of

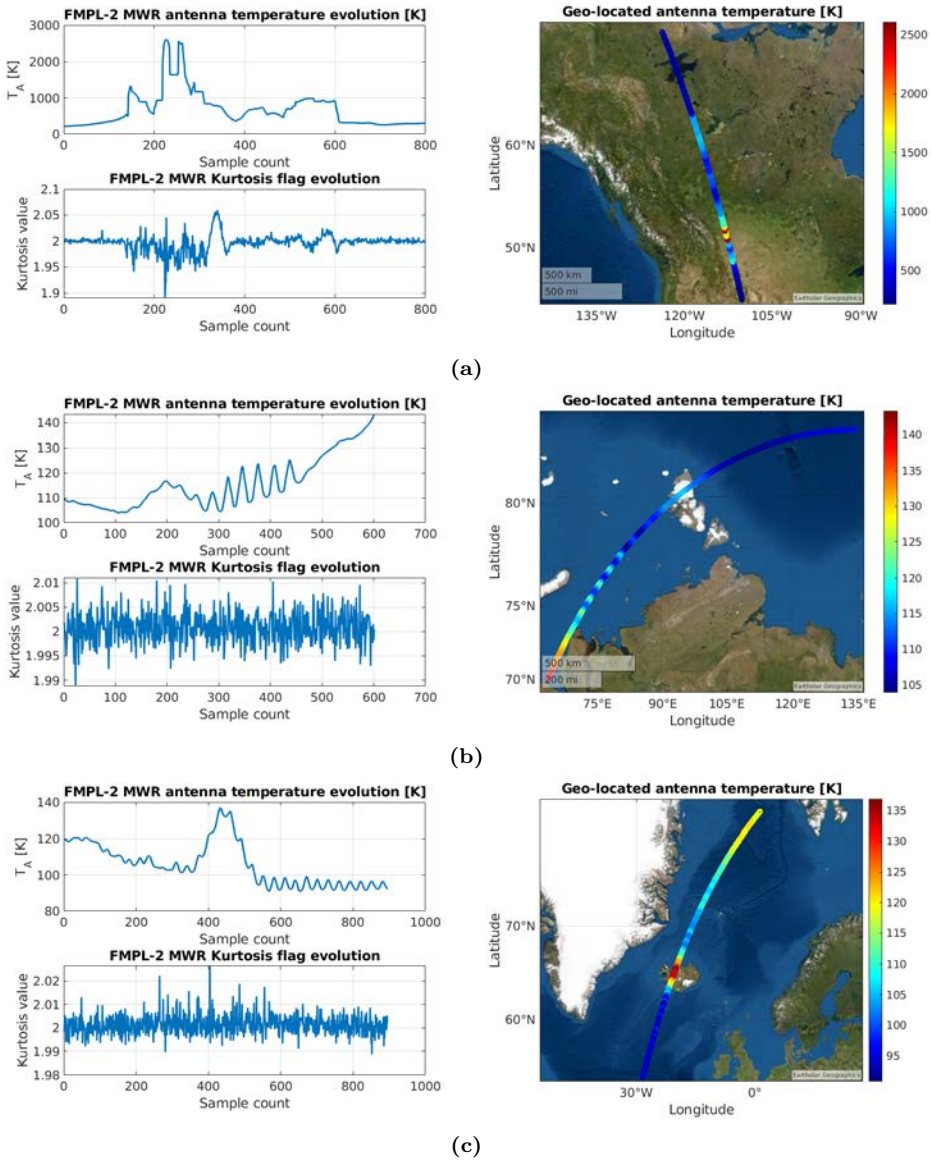

Figure 11.11: (a) Strong RFI event identified using the complex Kurtosis flag, and (b) and (c) two RFI events that are not noticeable through the complex Kurtosis flag, produced by a low-intensity periodic signal.

the DDMs [17], so as to increase the spatial resolution. In this case, the spacecraft ground-track velocity is equal to the size of the 1st Fresnel zone (i.e., ∼6.5 km/s ground-track at 40 ms = 250 m), and therefore the spatial resolution of the measurement is the one of the GPS L1 C/A chip (∼300 m). Currently, the SGR-ReSi [246] GNSS-R spaceborne instrument on board CyGNSS are working with an integration time of 0.5 s, providing a

lower spatial resolution of ∼3.25 km.

In order to review the capabilities of FMPL-2 to receive GNSS reflected signals with such high spatial resolution, several examples are provided over ice, ocean, and land. It is important to mention that all tracks presented have been processed to check that the absolute Doppler of the reflected signal is consistent with the expected one [121], and that the on-board processor is correctly tracking a GNSS reflection, and not a peak induced by speckle noise or the direct signal. This pre-processing takes the direct signal Doppler frequency, which is received by the instrument and downloaded as telemetry information, and based on the reflection geometry the estimated Doppler frequency for the reflected signal is computed. All reflected tracks with a Doppler window ±4 kHz around this last estimated Doppler frequency are tagged as valid reflections. Finally, all presented tracks show the geo-located SNR, the evolution of the received power, and a DDM time series evolution. The received power is computed previously introduced in Chapter 9, and all DDMs are normalized to have the peak equal to 1, and the estimated noise power is subtracted from them to ease its visualization.

11.4.1 Limitations of the short integration time

While the very short incoherent integration time avoids tracking of the DDM peak on board, it limits our capability to collect reflections that are almost specular, and with moderate-high SNR. As opposed to typically-seen DDMs [247], which are based on 0.5 or 1-s integration, FMPL-2 DDMs cannot reproduce the "famous" horseshoe-shaped DDMs, because the tails are blurred into the noise.

However, as it will be presented in the next section, sea-ice to ocean transitions will be easily identified because of the signal tracking loss. Because of this very short integration time, as the signal reflects over the oceans it gets blurred under the noise floor. Despite that, as detailed in Fig. 11.12, the distribution of SNRs is consistent to what is shown in [248], where the distribution of SNRs behaves as a Rice distribution, and therefore the retrieved data is consistent with the expected behavior for the selected integration time.

11.4.2 Sea-Ice/Ocean transition

Figure 11.13 shows the geo-located SNR of a single track collected 6 October 2020, as in other figures, OSI SAF SIE is overlaid. Furthermore, Fig. 11.14 shows a zoom of the boxed data in the top, where the estimated received power P_R after radiometric calibration is shown. In addition, in the bottom part of the image, a set of DDMs is presented, where the X-axis is a combined Doppler-Time axis, composed by 5 Doppler bins (500 Hz) per DDM, and 30 DDMs in total (i.e., X axis goes from 1 to 151), and the Y-axis is the DDM code-delay axis. The incidence angle of this track is ∼33º.

Due to the very short integration time, as the system goes off the sea-ice and enters into the rough ocean, the coherency of the reflected signal decreases, and thus the reflection gets less specular, and the SNR decreases. This can be also identified in the shape of the DDMs, going from a very clear peak (left part of the DDM strip) without Doppler extension, to a noisier observable (in the right part of the DDM strip). As it was introduced in the previous section, this is not a limitation of the instrument, but a design choice to increase the resolution of the SIE products.

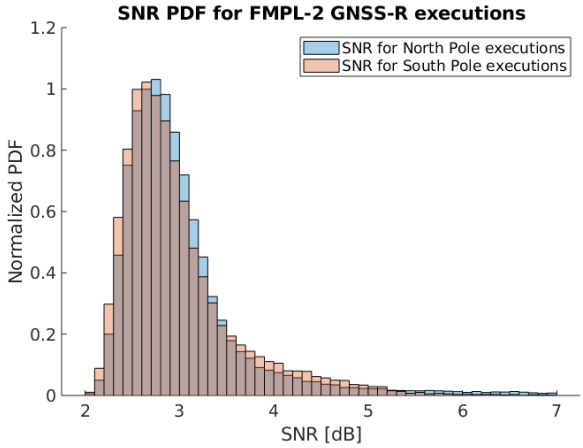

Figure 11.12: SNR histogram for both North and South poles for all GNSS-R tracks collected from the 1st to the 13th of October 2020.

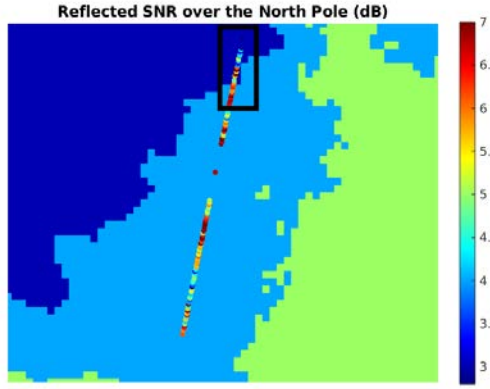

Figure 11.13: Geo-referenced SNR (dB) for a single FMPL-2 GNSS-R track, overlaid with OSI SAF SIE product. Dark-blue is open water, light blue is open ice (concentration between 30% and 70%), and green is closed ice. Note that, the color contrast has been adjusted to ease its visualization.

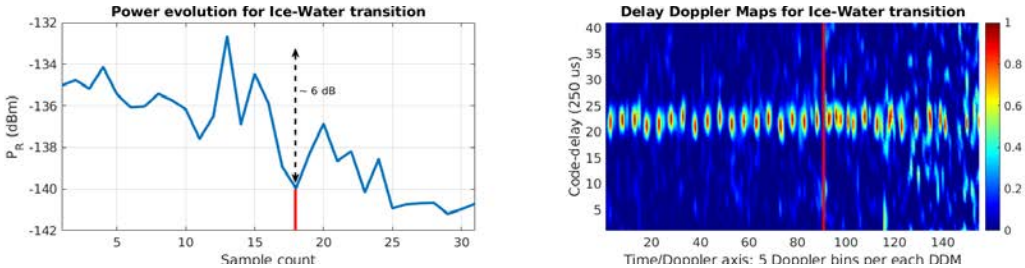

Figure 11.14: (**Left**) P_R by FMPL-2 for the area highlighted in Fig. 11.13, (**Right**) Normalized Delay-Doppler Maps (Doppler-Time and Code-Delay axis) for the highlighted area.

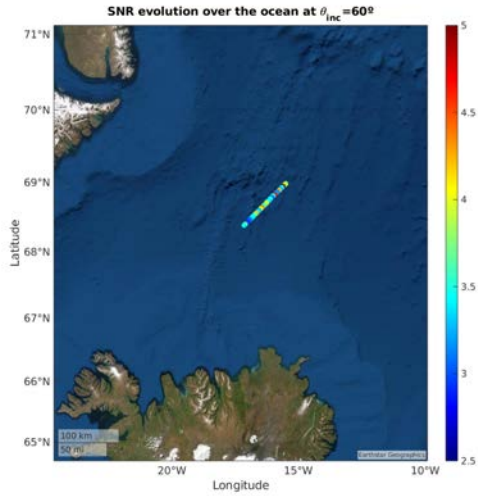

Figure 11.15: SNR evolution (dB) for a selected track near Iceland, collected on 10 October 2020.

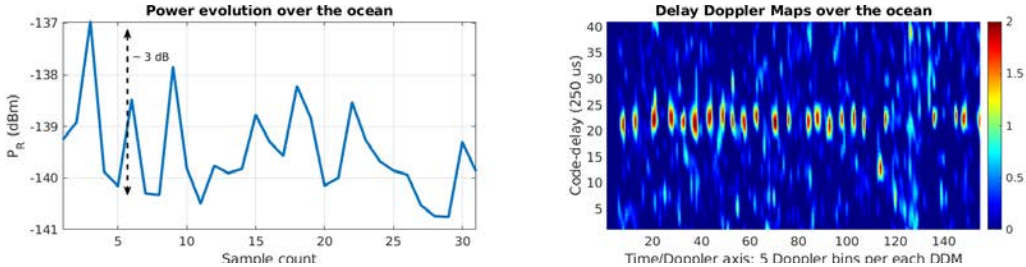

Figure 11.16: (Left) Received power and **(right)** DDM track for the selected track near Iceland, collected on 10 October 2020.

11.4.3 Reflections over the ocean

Despite the fact that specular reflections are not likely to occur, under certain conditions [249], such as low elevation angles, receiving a high coherent component is possible. Figure 11.15 shows a GNSS-R track acquired by FMPL-2 on 10 October 2020, at 16 UTC, containing several consecutive reflections over the ocean, on the area comprised between Iceland and Greenland. The incidence angle of the reflection is ∼60º, and the wind speed data [156] of the selected region is under 3–4 m/s, and thus it is likely to encounter strong coherent reflections [134]. As in Fig. 11.14, Fig. 11.16 shows both the received power P_R and the DDM time series evolution with the same Doppler bin space. In this case, the shape of the DDMs is noisier, despite the SNR being larger than 4 dB. However, there is not a notable difference in the DDM shape, mostly because the received reflections are specular.

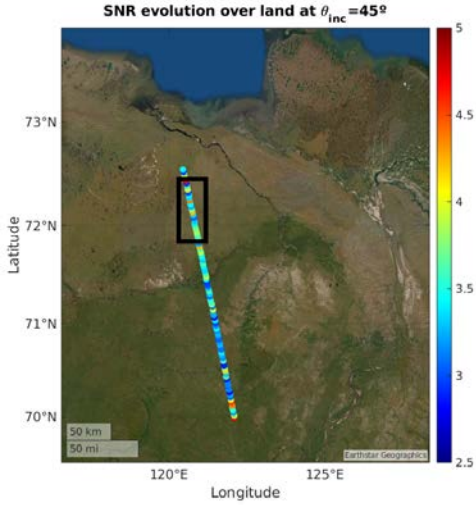

Figure 11.17: SNR evolution (dB) for a selected track at the North of Russia, collected on the 12 October 2020.

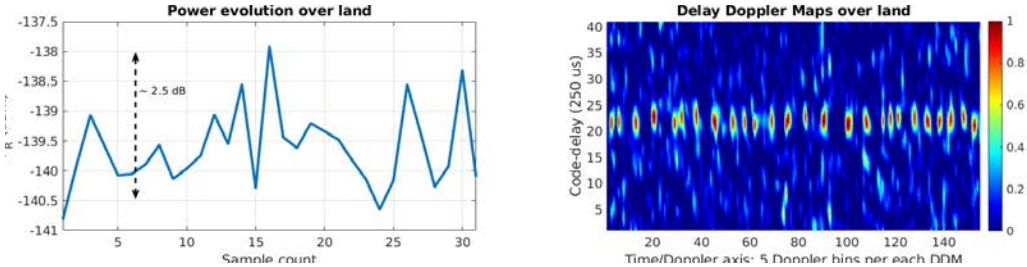

Figure 11.18: (Left) Received power and **(right)** DDM track for the selected track at the North of Russia, collected on the 12 October 2020. The black box in Fig. 11.17 indicates the selected region shown in this figure.

11.4.4 Reflections over land

To finalize this section, a track has been selected to show the capabilities of FMPL-2 over land, where specular reflections are also more likely to occur [120]. As in the other examples, Figures 11.17 and 11.18 show the geo-located SNR over the area of interest, the estimated received power P_R, and the retrived DDMs in the time series format.

In this last case, it can be identified that the overall SNR increases as the track goes towards the North. An increase in the received power that can be linked to either a decrease of the local surface roughness, a decrease of the local vegetation, and/or an increase of the SM of the measured area. In that case, the area with lower reflectivity is populated with trees, which causes additional attenuation to the reflected signal [69].

To summarize, this section has presented the capabilities of FMPL-2 to receive GNSS-R data over ice, land, and ocean even using short incoherent integration times. The shorter integration times allows to have an enhanced spatial resolution of ∼300 m, and it

has been presented that the sea-ice and ocean transition can be detected as a change in the GNSS-R reflectivity. Moreover, thanks to the selected incoherent integration time, it is easier to calibrate the reflectivity measurements, as most reflections just have contributions from the first Fresnel zone (i.e., ∼300 m), and thanks to the internal radiometric calibration used for the L-band radiometer, the noise power of the instrument can be calibrated. Therefore, the DDM noise power can be calibrated and an absolute radiometric measurement can be provided for each GNSS reflection.

11.5 Conclusions

This Chapter has presented the validation of the FMPL-2, a dual microwave (GNSS-R and MWR) instrument on board the FSSCat mission. After the commissioning of the instrument, the measurements provided in the first weeks of October 2020 have been used to validate the mission requirements. The radiometric sensitivity of the FMPL-2 L-band MWR was found to be better than 0.2 K for the selected target areas, and the accuracy was found on the order of ∼0.5 K, being able to detect wind speed changes of 2 m/s, providing a initial spatial resolution of ∼350x500 km^2 per acquisition. However, thanks to the large oversampling of the radiometer footprint in the along-track direction, the resolution can be improved. Preliminary brightness temperature maps were presented showing the agreement with respect to the OSI SAF SIE product. In terms of the RFI detection capabilities of the instrument, it has been shown that strong RFI events can be identified thanks to the onboard complex Kurtosis module, described in Chapter 9. However, some low-intensity RFI events causing a sinusoidal component are not detected through the complex Kurtosis, and would require additional processing. Finally, for the GNSS-R part, different tracks have been presented over ice, ocean, and land, showing the performance of GNSS-R even using short (40 ms) incoherent integration times. In this regard, the reflections' spatial resolution is increased up to the size of the first Fresnel zone (∼310 m at $\theta_{inc} = 0^o$, ∼430 m at $\theta_{inc} = 45^o$).

12

Chapter 12

Geophysical Data Processing Algorithms using FMPL-2 In-Orbit Data

This Chapter describes the methodology and results to estimate four geophysical parameters using FMPL-2 data, in particular, the Sea-Ice Concentration (SIC), the Sea-Ice Extent (SIE), the Sea-Ice Thickness (SIT), and the Soil Moisture (SM) over land, with some materials and contents reproduced from [JP2]. Section 12.1 introduces SIC, SIE, SIT, and SM monitoring using L-band MWR and/or GNSS-R measurements. Section 12.2 is adapted from the peer-reviewed journal publication entitled "Sea Ice Concentration and Sea Ice Extent Mapping with L-band Microwave Radiometry and GNSS-R data from the FFSCat Mission using Neural Networks" [JP9], co-authored by the Ph.D. candidate, and led by Mr. David Llavería. Section 12.3 is adapted from the peer-reviewed journal publication entitled "Arctic and Antarctic Sea Ice Thickness Estimations based on Regression Neural Networks using L-band Microwave Radiometry Data from the FSSCat mission" [JP10], co-authored by the Ph.D. candidate, and led by Mr. Christoph Herbert. Section 12.4 is adapted from the peer-reviewed journal publication entitled "Soil Moisture estimation synergy using GNSS-R and L-band microwave radiometry data from FSSCat/FMPL-2" [JP11], and also presented in the international conference [CP13]. Finally, Section 12.5 presents the conclusions of the Chapter.

Sections 12.2 and 12.3 are developed jointly within the frame of other two Ph.D. theses. For that reason, the results presented in these two sections are just an overview of the final sea ice products retrieved using FMPL-2 data.

12.1 Introduction

The ECVs established by the UN are key geophysical variables to understand climate change and its impact on the planet. L-band radiometers are sensitive to water, and they have been used to monitor sea-ice extension and thickness [29], and soil moisture [36], among other applications. SIC, SIT, and SM play a crucial role in regulating the temperature of the planet. Thermohaline circulation (Fig. 12.1) regulates the Earth's climate by transporting warm water from Equatorial latitudes into polar regions and viceversa, and from the surface to the bottom of the ocean. The heat released at the poles is captured by the atmosphere, which is then regulated by the land-atmosphere feedback loop, mainly driven by the soil water content (or soil moisture) [2]. A constant monitoring of these variables is required to understand the impact of the water cycle in our planet.

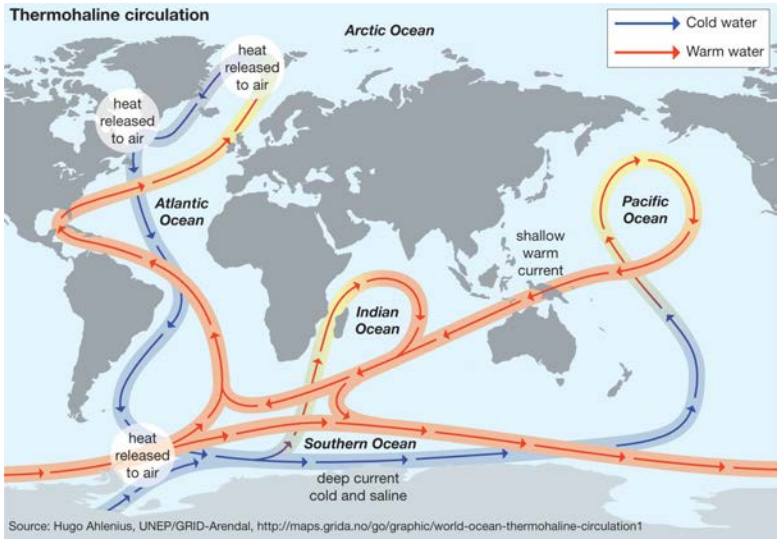

Figure 12.1: Thermoaline circulation. Reproduced from `https://www.britannica.com/science/thermohaline-circulation`.

L-band measurements have been used in the last decades to monitor the SIT and the SM. Moreover, L-band measurements can also be suitable to retrieve SIC or SIE. The ESA SMOS mission is the only one currently providing SIT and SM measurements. The mission is currently at its 10^{th} year of operation, and the follow-up mission, the CIMR mission from ESA is planned not earlier than 2025 [250]. To cover the gap between SMOS and CIMR, one could envisage a Constellation of ^{3}Cat-5/A's embarking FMPL-2 to monitor SIC, SIE, SIT, and SM.

12.2 SIC/SIE Retrieval using FMPL-2 Data

As described in [29] and introduced in Section 2.2, the sea-ice emission at L-band varies from ∼120 K for very thin ice (i.e., ∼10 cm), to ∼220-240 K for a thicker ice (i.e., >60-70 cm), as shown in Fig. 12.2. As the apparent brightness temperature emitted by the sea-ice is larger than the one emitted by the ocean (i.e., 0 cm in Fig. 12.2), the SIC and the SIT can be derived from FMPL-2 L-band MWR measurements. In this section, a SIC/SIE retrieval algorithm is proposed using FMPL-2 L-band MWR data.

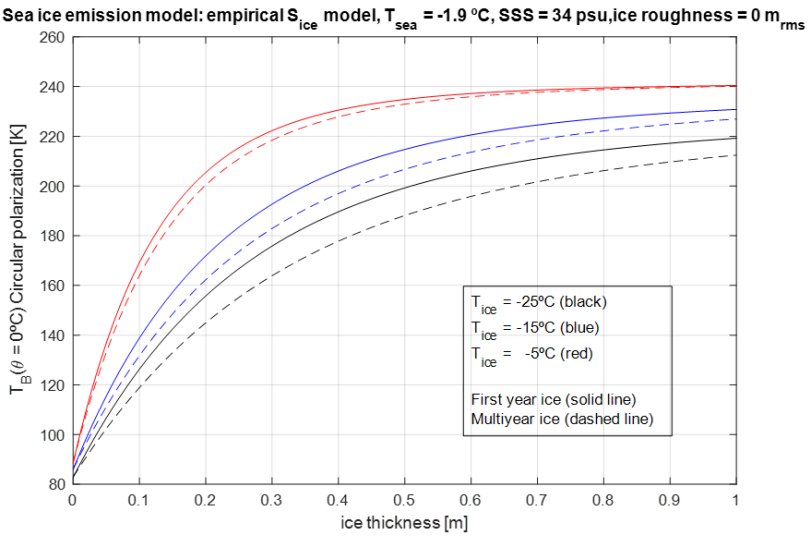

Figure 12.2: Sea-ice thickness as a function of the measured brightness temperature by a circular polarized antenna at L-band according to the model used in [29].

As introduced in Chapter 2 (Fig. 2.5, and Section 2.3.2), and notably described in [32], GNSS-R data has proven to estimate SIC and SIE. However, current implementations using TDS-1 data require DDMs to be produced with a large incoherent integration time (∼1 s), which degrades the spatial resolution. In the FMPL-2 case, the spatial resolution is maximized by using shorter integration times, and despite the DDMs retrieved by the instrument (Chapter 11) are almost the same for sea-ice and ocean, the GNSS-R reflectivity suffers a detectable variation when the reflection goes from the ocean to the sea-ice or vice-versa.

In this section, GNSS-R and L-band MWR data collected by FMPL-2 are used to generate a SIC/SIE product. To generate the SIC/SIE product, two approaches are followed. First, an ANN-based algorithm is proposed using only FMPL-2 L-band MWR data. This first algorithm produces "coarse" measurements gridded into a 12.5 km map, and compared to the OSI SAF SIC/SIE product [242]. Then, a second ANN is proposed by combining both FMPL-2 MWR and GNSS-R data to retrieve a higher resolution product, which is approximately the size of the first Fresnel zone from space ∼300 m.

It is important to remark the OSI SAF SIE product is produced out of a 3-level classification of the SIC product: "open water" corresponds to areas with 0% of ice,

"open ice" corresponds to areas with a SIC from 30% to 70%, and "closed ice" corresponds to those areas with more than 70% of SIC. For that reason, the results presented in this Section correspond to the SIC algorithm. Then, a SIE classification based on the previous definition is computed and compared to the OSI SAF SIE to estimate the evolution of the total sea-ice extent during the presented period.

12.2.1 SIC/SIE using L-band MWR data: Methodology

The algorithm selected to estimate SIC using FMPL-2 L-band MWR data is based on an ANN. In this case, as the native pixel of FMPL-2 has a low resolution of ∼350x500 km^2, daily skin temperature data gridded at 12.5 km is used as ancillary data. This skin temperature is coming from the European Centre for Medium-Range Weather Forecasts (ECMWF) [251]. In addition, a land cover product from MODIS is used [252] to correct for the effect of land when trying estimating the ice border. The chosen network topology is the following:

- Input layer: 5 neurons for both poles, as explained below.
- 3 hidden layers: consisting of 5, 10 and 5 neurons, respectively, using the sigmoid activation function.
- Output layer: a single neuron with a linear output function.

Each of the input neurons corresponds to one variable of the same point of the EASE grid, and is composed by the following 5 input variables:

- FMPL-2 antenna temperature,
- Temporal standard deviation of the antenna temperature,
- Bi-dimensional gradient of the antenna temperature,
- Land cover fraction from MODIS [252], and
- Skin surface temperature (SKT) from ECMWF [251].

The FMPL-2 MWR data is gridded into a 12.5 km grid following a nearest neighbor interpolation (NNI), as described in Chapter 11, for both the North and the South poles projections. The algorithm geo-locates each MWR antenna temperature measurement into a single 12.5 km cell of an EASE Grid 2.0 [253] using the NNI algorithm. Then, measurements with a time-span of 5 days are averaged into a single map, followed by a triangulation-based natural neighbor interpolation. Finally, an antenna pattern compensation is performed based on a 2D moving window filter[1]. In this way, an entire map out of 5 days of measurements can be generated.

This process generates a large set of points, time-tagged and geo-located. The data used used, comprised from October to December, 2020, contains more than one million points. Therefore, a small subset of points is used to train and validate the network. In this case, ∼200.000 random samples are used for such purpose. The training algorithm

[1] A circular window equivalent to the antenna pattern area has been used.

Table 12.1: SIC algorithm MAE for the Arctic Ocean using different combinations of input parameters and for two SIC ranges. MWR data includes the FMPL-2 antenna temperature, the temporal standard deviation, and the bi-dimensional gradient as presented in Section 12.2.1.

ANN inputs	MAE for full SIC range	MAE for 0<SIC<90
SKT	3.18%	14.04%
SKT + Land Cover	2.89%	13.03%
MWR	12.08%	25.06%
MWR + Land Cover	7.15%	19.86%
MWR + SKT	2.80%	13.10%
MWR + SKT + Land Cover	2.37%	11.27%

used is the Levenberg-Marquardt method [254], and the selected ground-truth is the daily OSI SAF SIE product, originally with a spatial resolution of 10 km, but re-gridded into a 12.5 km EASE grid.

12.2.2 SIC/SIE using L-band MWR data: Results

12.2.2.1 Arctic Ocean

To show the impact of the ancillary data used, the training process is evaluated using different combinations of the five input variables previously presented. The mean absolute error (MAE) is used to compare the performance of each algorithm, and the results are presented in Tables 12.1 for the Arctic Ocean. Note that the MAE is presented for two SIC ranges, for the full range (0 to 100), and for all SIC values between 0 and 90 (limits not included). As it can be seen, the use of the SKT already provides a very accurate estimation of the SIC, which is then enhanced ∼0.8% when MWR and Land cover is combined to . In this case, the Arctic is in the freeze-up period, with very low temperatures on top of the ice floes while it is freezing.

Four SIC maps are presented in Fig. 12.3 for different dates using the MWR+SKT+Land Cover inputs. The differences with respect to OSI SAF SIC product are presented in Fig. 12.4. As it is seen, most errors are concentrated in transition regions, where the FMPL-2 footprint covers both land and ice, and regions with low ice concentration, being difficult for the algorithm to differentiate due to the large antenna footprint. Even though, the proposed algorithm is able to enhance the spatial resolution by a factor of 40 in the along-track direction.

Binarizing[2] the SIC as explained in Section 12.1, the SIE can be retrieved. This product can be then used to compute the total area of the pole covered by ice, which is a crucial product to understand the ice dynamics over time. This product is called total sea-ice extent, and thanks to the mesh used (Equal-Area), it can be computed by adding all 12.5 km cells that contain ice, and then multiplying the resulting number by the cell extension, 12.5x12.5 km^2. Figure 12.5 presents the time evolution if this magnitude in the

[2]All SIC larger than 15% is tagged as ice, otherwise is tagged as open ocean.

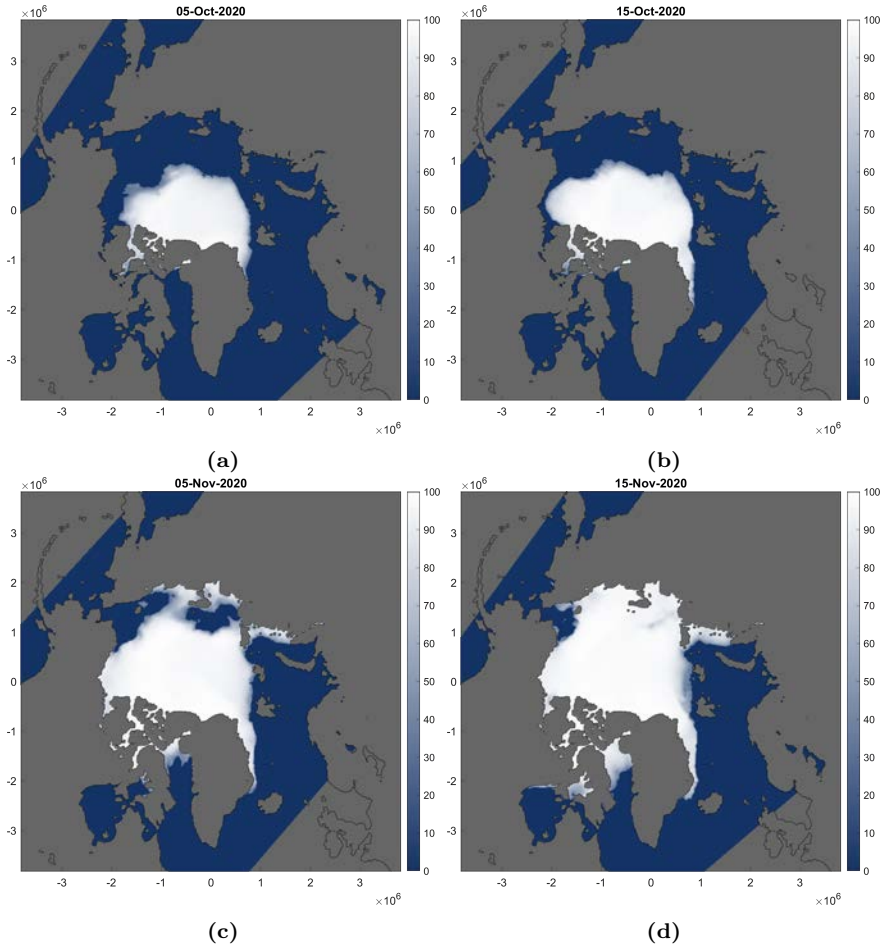

Figure 12.3: Arctic SIC composites using FMPL-2 MWR data for (a) October the 5^{th}, (b) October the 15^{th}, (c) November the 5^{th}, and (d) November the 15^{th}, 2020.

Arctic Ocean, and the comparison with respect to the SIE product from OSI SAF [242]. As it can be seen, the mean absolute difference is $\sim$0.15 million km^2, which is lower than the actual difference between OSI SAF SIE product and other SIE products [255].

12.2.2.2 Antarctic Ocean

Table 12.2 presents the output of the ANN for the same combination of inputs, but for the Antarctic Ocean. In this case, the use of SKT does not significantly contribute to estimate the SIC. As studied in [256], the sea-ice temperature observations during melting periods present a positive bias (i.e., larger temperature than the real one) with respect to areas that are not melting, which is the case of the Antarctic Ocean during the observed period. As described in [257], this bias is caused when the radiative-transfer model for sea-ice is applied to estimate the temperature emission from the snow-ice interface, but the snow layer is too thin or it has already melt. For this reason, the use of SKT by itself

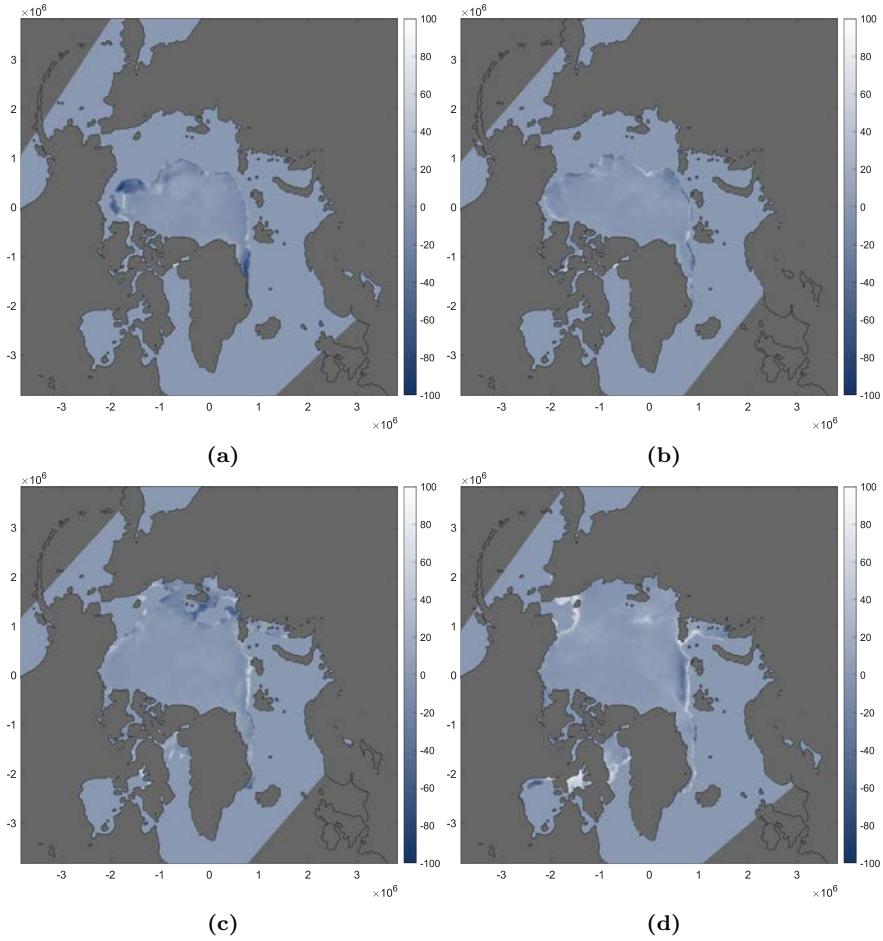

Figure 12.4: Arctic SIC errors with respect to OSI SAF SIC product for (a) October the 5^{th}, (b) October the 15^{th}, (c) November the 5^{th}, and (d) November the 15^{th}, 2020.

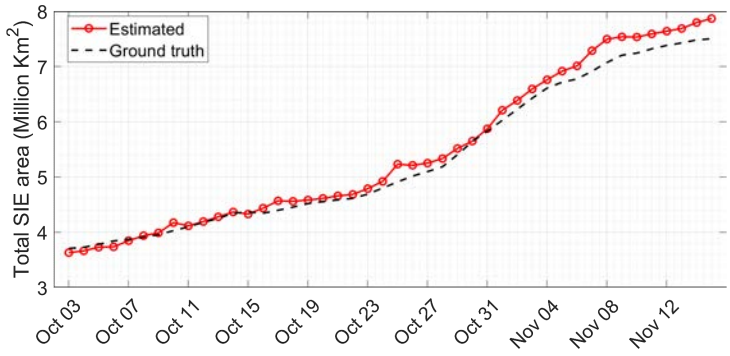

Figure 12.5: Total SIE time evolution comparison between FMPL-2 estimated SIE and OSI SAF ground-truth in the Arctic Ocean.

Table 12.2: Same as Table 12.1 but for the Antarctic Ocean.

ANN inputs	**MAE for full SIC range**	**MAE for 0<SIC<90**
SKT	17.02%	25.19%
SKT + Land Cover	15.78%	24.13%
MWR	6.90%	13.02%
MWR + Land Cover	6.37%	12.46%
MWR + SKT	5.89%	11.64%
MWR + SKT + Land Cover	5.55%	11.30%

does not provide enough information to estimate the SIC during the melting periods.

Figures 12.6 and 12.7 present the same composite and error maps as in the previous section but for the Antarctic Ocean. In this case, most errors are concentrated in the ice borders.

Finally, Fig. 12.8 presents the time evolution of the total SIE in the Antarctic Ocean, computed in the same way as in the Arctic Ocean, binarizing the SIC product at 15%. In this case, the mean absolute difference is larger, $\sim$0.7 million km^2, however the total ice extension measured in the Antarctic Ocean is $\sim$4 times the one at the Arctic Ocean. Thus, the ratio between both differences is also similar to this ratio, $\sim$4.6. In any case, both metrics fall within the expected range SIE differences observed by other SIE products, which is $\sim$1 million km^2 [255].

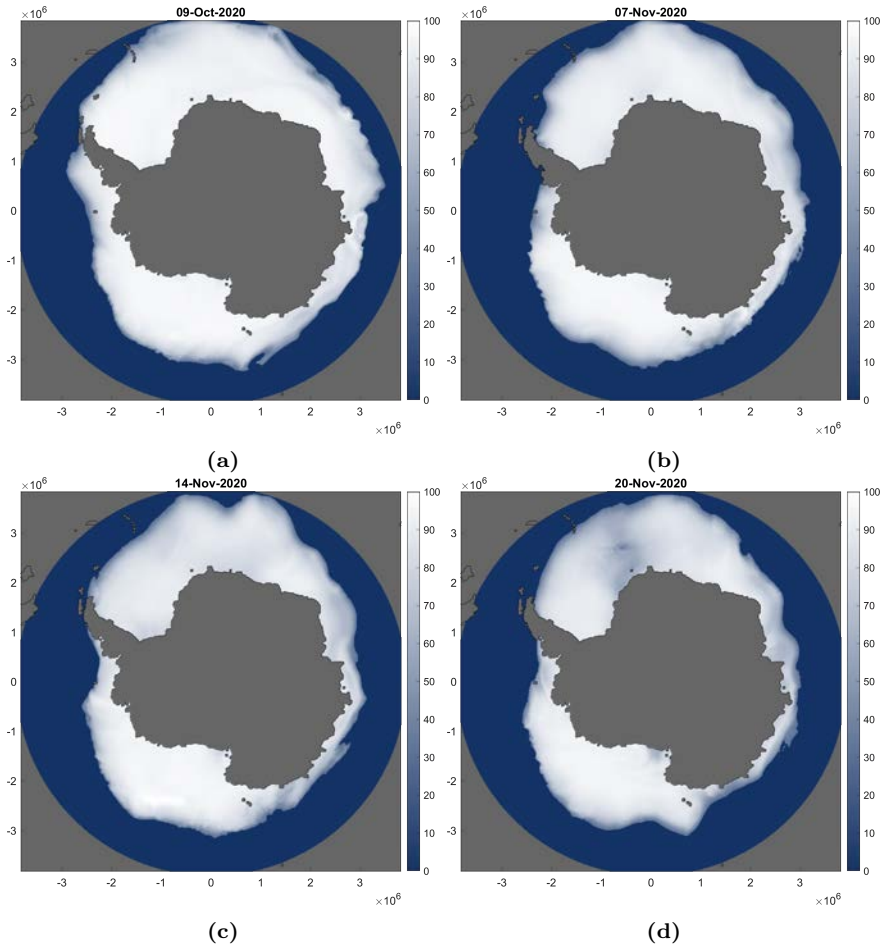

Figure 12.6: Antarctic SIC composites using FMPL-2 MWR data for (a) October the 9^{th}, (b) November the 7^{th}, (c) November the 14^{th}, and (d) November the 20^{th}, 2020.

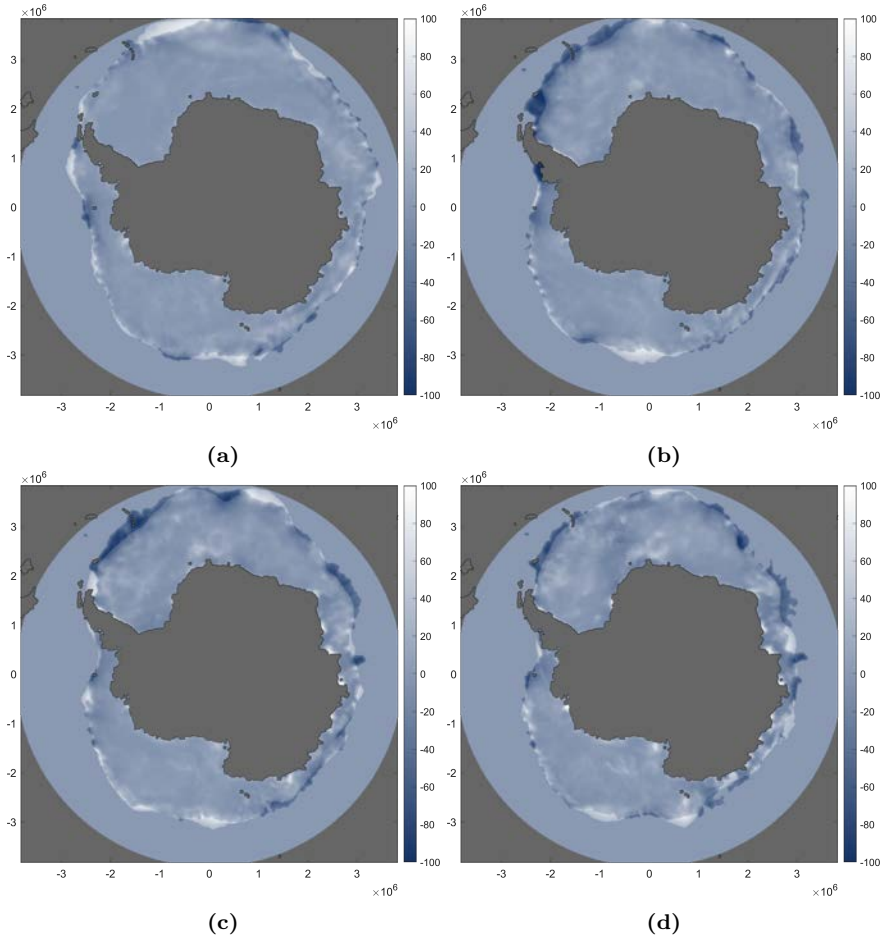

Figure 12.7: Antarctic SIC errors with respect to OSI SAF SIC for (a) October the 9^{th}, (b) November the 7^{th}, (c) November the 14^{th}, and (d) November the 20^{th}, 2020.

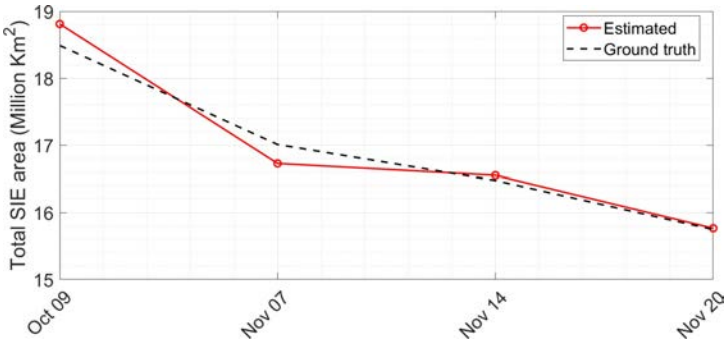

Figure 12.8: Total SIE time evolution comparison between FMPL-2 estimated SIE and OSI SAF ground-truth in the Antarctic Ocean.

12.2.3 SIC/SIE using combined L-band MWR and GNSS-R data: Methodology

In order to improve the resolution of the SIC maps presented in Section 12.2.2, GNSS-R data is used. As opposed to other methods to detect the sea-ice border using GNSS-R [32], the horseshoe shape cannot be retrieved due to the short incoherent integration time used to enhance the spatial resolution. Thus, the Doppler-integrated waveform methodology described in [32] cannot be applied here. However, as it is shown in Fig. 11.14, and reproduced here in Fig. 12.9 for the readers' convenience, the DDM exhibits a Doppler enlargement when reflections are occurring over the ocean.

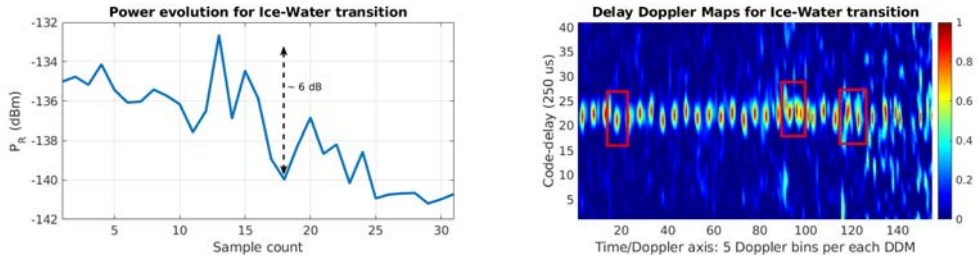

Figure 12.9: Reproduction of Fig. 11.14, but highlighting in red the Doppler enlargement when the GNSS-R signal transits from the sea-ice to the ocean.

As it can be seen, the power in the left side of the image is concentrated in a single region, while during the transition and in the middle of the ocean, the power is spread in nearby delays and Dopplers. In addition, the reduction of receiver power is also providing important information of whether the reflection is occurring on top of the sea-ice or over the ocean. However, it is important to remark that the reflection the sea-ice is largely affected by the incidence angle, as shown in Chapter 7.

The algorithm used here to estimate the sea-ice border is the same ANN as proposed for the MWR case, but now using the following inputs:

- Delay-integrated DDM: DDM integrated along the "delay" dimension, producing 5 inputs which corresponds to the 5 Doppler bins.
- Reflectivity,
- Moving standard deviation of the reflectivity,
- SNR of the reflection,
- Elevation angle,
- 2D linearly interpolated FMPL-2 antenna temperature to the specular reflection point.

To train and validate the model, the OSI SAF SIC is also 2D linearly interpolated to the specular reflection location.

12.2.4 SIC/SIE using combined L-band MWR and GNSS-R data: Results

In order to compare the performance achieved when GNSS-R data is added to the model, the outputs of the models presented in Section 12.2.2 are 2D linearly interpolated to the location of the specular reflection point.

12.2.4.1 Arctic Ocean

The results for the Arctic Ocean are presented in Table 12.3. In this case, the use of the SKT provides a lot of information to estimate the SIC. However, when adding GNSS-R data the MAE slightly decreases 0.4% with respect to the case without GNSS-R.

Table 12.3: SIC algorithm MAE comparison in the Arctic Ocean over specular reflection points using different inputs.

ANN inputs	MAE for full SIC range
SKT	5.4%
SKT + MWR + Land Cover	3.4%
GNSS-R + MWR + Land Cover	6.9%
GNSS-R + SKT + MWR + Land Cover	3.0%

Although the error improvement is not significant, one potential error source is the difference in spatial resolution between the training/validation product (OSI SAF SIC resolution is ∼10 km) and the resolution of the GNSS-R data (∼300-500 m). Figure 12.10 presents some examples of the GNSS-R + SKT + MWR + Land Cover product on top of the OSI SAF SIC product. As it can be seen, areas closer to open water regions present a larger variability in the estimated SIC product, showing "jumps" of SIC up to ∼20% between consecutive pixels. Abrupt changes in SIC cannot be discerned with the 10 km resolution OSI SAF SIC product, but thanks to the enhanced spatial resolution of the GNSS-R, these changes are more noticeable.

12.2.4.2 Antarctic Ocean

The results for the Antarctic Ocean are presented in Table 12.4. Similar to what has been discussed in Section 12.2.2, the use of the SKT produces a very large MAE, and when MWR data is added, the error is drastically decreased. Furthermore, the use of combined GNSS-R and MWR data provides a decrease of the MAE of ∼1.1%.

As it is seen in both Arctic and Antarctic oceans the use of GNSS-R data allows, in general, to lower the error with respect to OSI SAF. However, as the spatial resolution of the GNSS-R product is much finer than the OSI SAF one, some errors may be induced from the difference in resolution of both products, and the error introduced by the 2D linear interpolation.

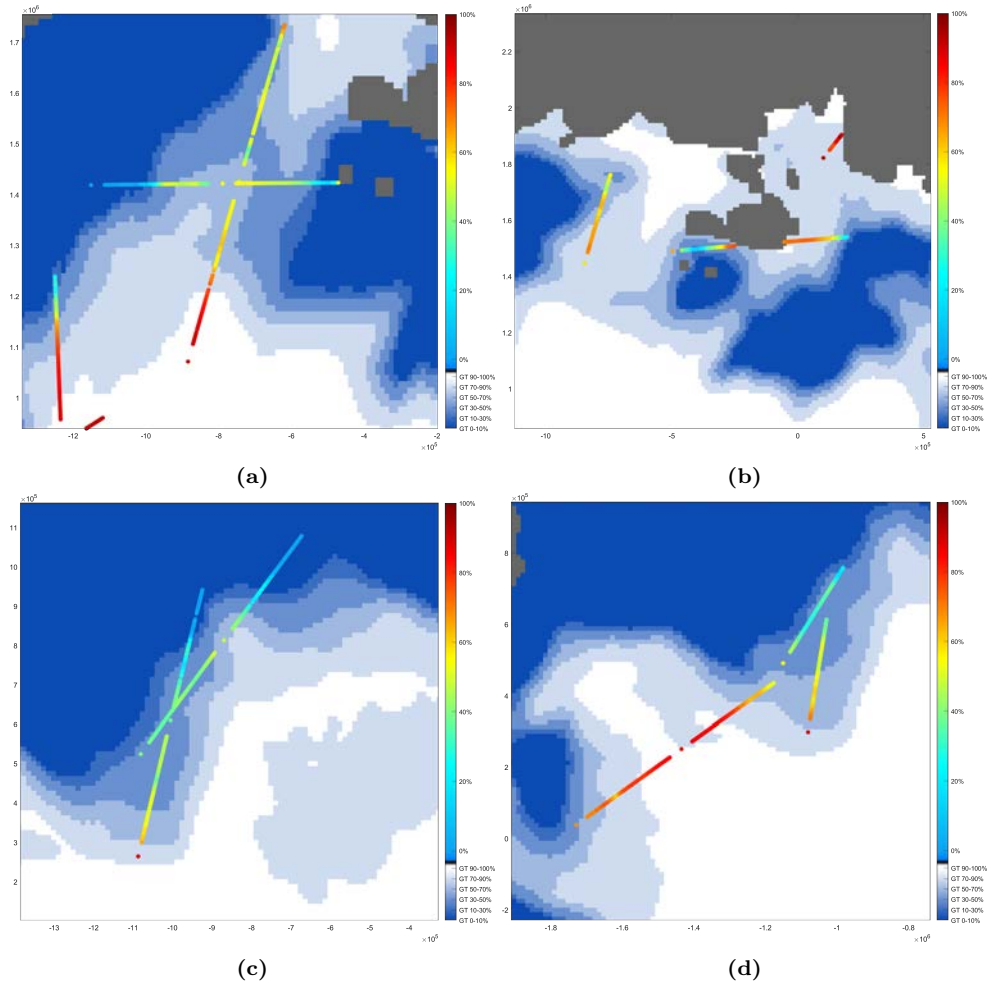

Figure 12.10: Four examples of the combined GNSS-R + SKT + MWR + Land Cover tracks product on top of the OSI SAF SIC product binarized at 6 different levels

Table 12.4: SIC algorithm MAE comparison in the Antarctic Ocean over specular reflection points using different inputs.

ANN inputs	**MAE for full SIC range**
SKT	38.1%
SKT + MWR + Land Cover	3.6%
GNSS-R + MWR + Land Cover	3.4%
GNSS-R + SKT + MWR + Land Cover	2.7%

12.3 SIT Retrieval using FMPL-2 Data

As shown in Fig. 12.2, L-band MWR measurements are also sensitive to SIT. In this Section, the L-band MWR data collected by FMPL-2 is used to implement an ANN-based retrieval algorithm to estimate thin SIT in the Arctic Ocean. In this case, the Antarctic Ocean lacks SIT ground-truth to train and validate the algorithms, and it is not presented here. Thin SIT and full-range SIT algorithms have been developed for the Antarctic Ocean and are further detailed in [JP10].

12.3.1 SIT using FMPL-2 MWR data: Methodology

The FMPL-2 antenna temperature maps are gridded in the same way as in the previous Section for the Arctic Ocean. In this case, additionally to the ECMWF skin temperature data [251], the sea-ice concentration (SIC) product from OSISAF [242] is used as ancillary data to define more precisely the ice border. The ANN is trained using SMOS SIT data, and the topology of the network consist of the following layers:

- Input layer: three neurons are used, one for the FMPL-2 antenna temperature, one for the SIC data, and one for the ECWMF skin temperature;
- Hidden layers: two hidden layers with 64 neurons each are used. The transfer function used is the Rectified Linear Unit or ReLU [258];
- Output layer: a single neuron layer to provide a continuous output.

The data is split in 65% for training, 15% for validation, and 20% for testing, and the training algorithm used is the Adaptive Moment estimation [259].

12.3.2 SIT using FMPL-2 MWR data: Results

Figure 12.11 presents the scatter plot of the SMOS-retrieved SIT and the estimation using the ANN over the Arctic Ocean. The RMSD between the SMOS ground-truth and the FMPL-2 estimation is 9.3 cm, with a bias of 6.5 cm. As it can be seen, the ANN algorithm gets saturated for values larger than 0.5 m. For values larger than 0.4 m the neural network is underestimating the SIT.

As it can be seen in Fig. 12.12a, the error is slightly biased, and the error histogram seems to underestimate many SIT values (i.e., the estimated SIT for larger values of SIT should be larger). Moreover, as it can be seen in Fig. 12.12b, the MAE for predictions larger than 0.5 m are again lower. This could be explained because the model contains a small bias towards higher values and ground truth values beyond 0.6 m were filtered beforehand.

Finally, Fig. 12.13 presents two weekly composite maps of SIT, comparing the ANN estimation with the SMOS ground-truth. As it is seen, under-estimated values are located around the 0.6 m threshold, at the model range of validity.

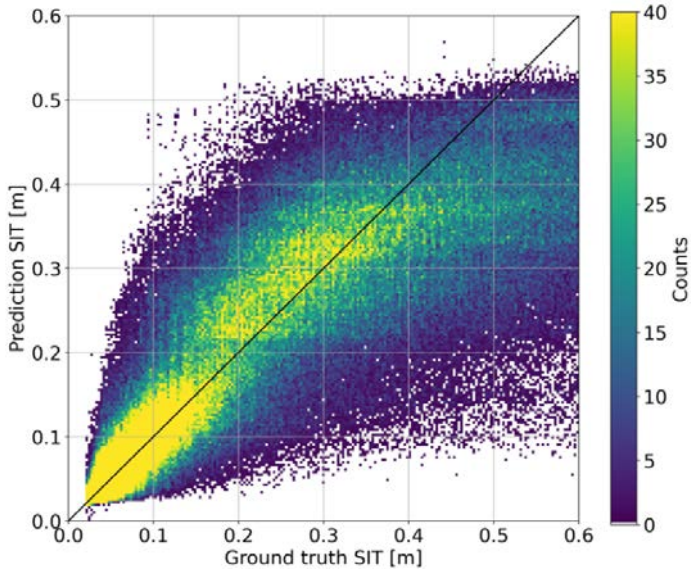

Figure 12.11: Scatter plot and comparing SMOS SIT product with the predicted SIT by the ANN using FMPL-2 MWR data.

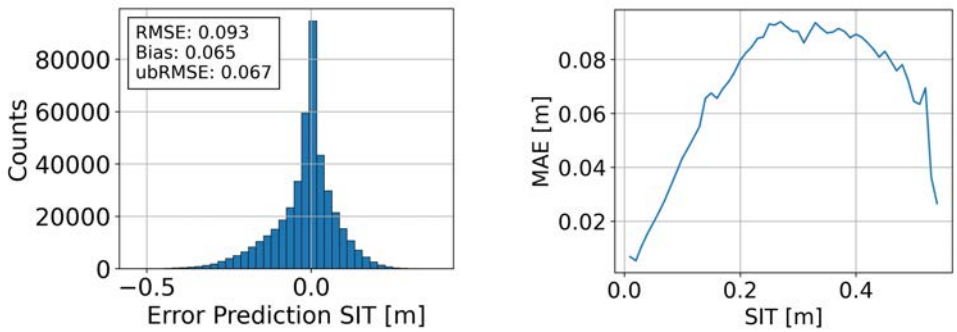

(a) **(b)**

Figure 12.12: (a) Error histogram and (b) mean absolute error evolution with respect to the SMOS SIT.

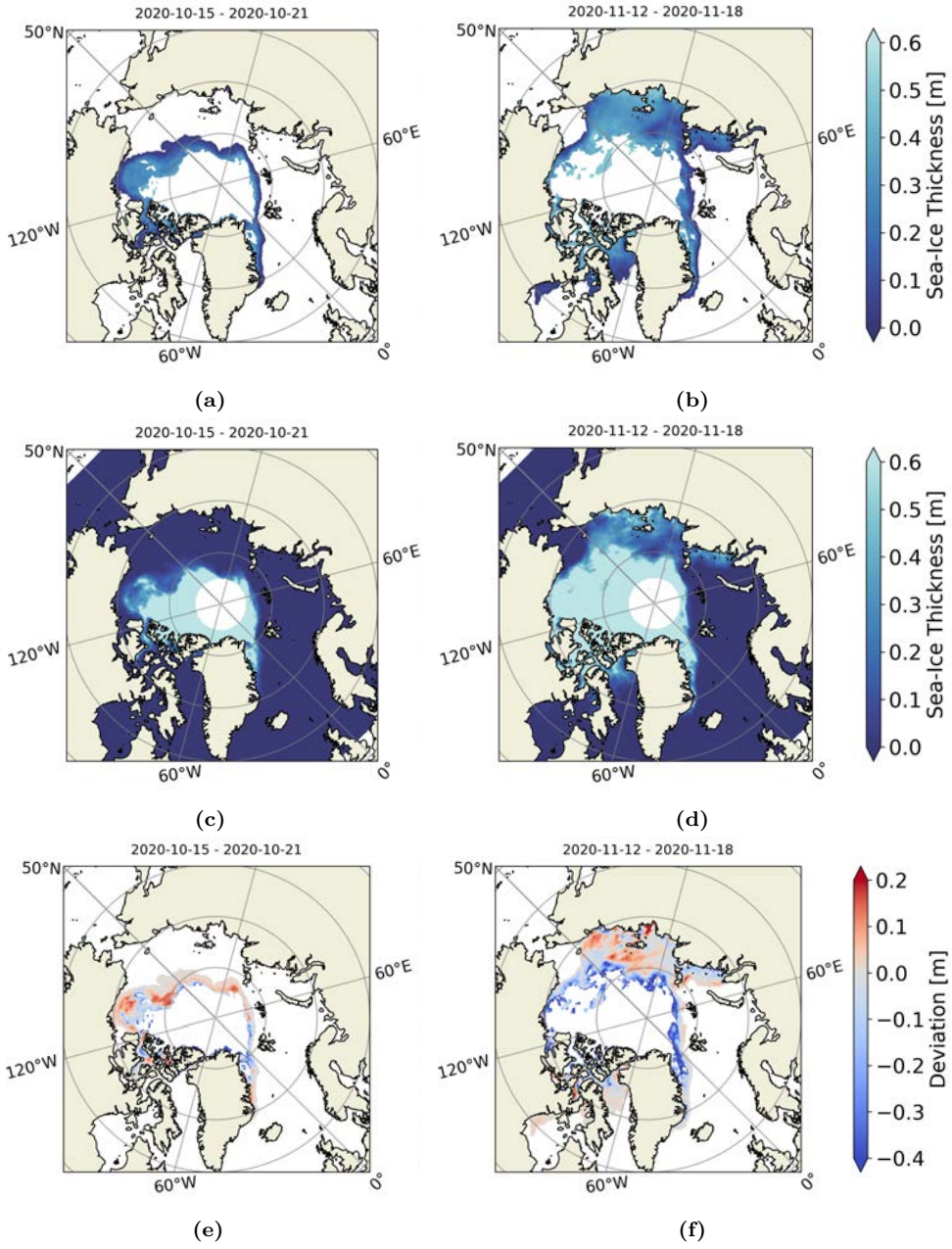

Figure 12.13: (a) and (b) are the FMPL-2-derived SIT using ANN for to selected dates, (c) and (d) the SMOS SIT for the same time period as in (a) and (b), and (e) and (f) are the error maps by subtracting (a) to (c) and (b) to (d).

12.4 SM Retrieval using FMPL-2 Data

Optical-based sensors, as those acquiring reflectances or thermal infrared data [260–262], have been used to retrieve SM due to their high spatial resolution, but they are limited by the vegetation cover, the cloud conditions, and they cannot acquire during night time, providing a low effective temporal resolution. Passive microwave-based sensors are neither affected by clouds, nor Sun illumination. In this regard, L-band radiometers as the MIRAS instrument onboard the ESA SMOS mission [28], and the SMAP mission from NASA [161] are currently providing near-surface soil moisture (i.e., up to 5 to 20 cm depth) measurements, at a global coverage with a revisit of ∼3 days, and a spatial resolution of ∼ 55 km for SMOS [162], and ∼ 36 km for SMAP [163]. Moreover, radar-based approaches such as scatterometers (e.g. [263]), or SAR (e.g. [264–268]) have also been used to retrieve near-surface soil moisture indices from space. As it is seen in Fig. 12.14, L-band MWR antenna temperature measurements as the ones retrieved by FMPL-2 are sensitive to SM variations. In this case, the water content in the soil is linked to the variation of the antenna temperature. Thus, the larger the water content, the lower the apparent brightness temperature.

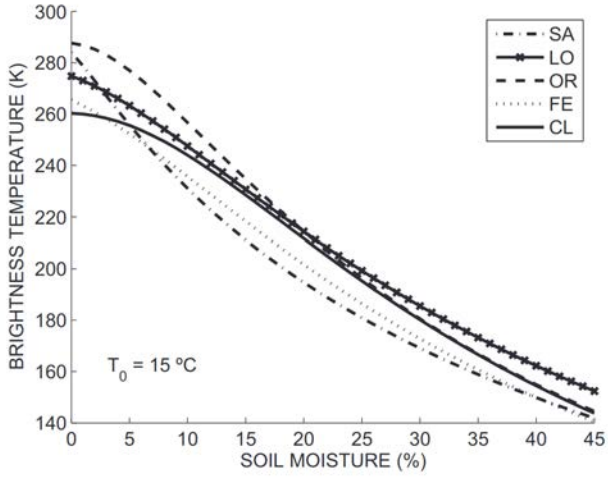

Figure 12.14: Soil brightness temperature dependence on soil type and moisture at nadir, $T_0 = 15$ ºC . Reproduced from [269].

Furthermore, GNSS-R measurements are also sensitive to SM if proper processing is applied. In this case, the larger the water content, the higher the GNSS-R reflectivity, but the reflectivity is highly attenuated by surface roughness effects, and needs to be corrected by either using statistical properties of the reflectivity, or combining data from other sensors. Different studies have proven the capabilities of GNSS-R to retrieve SM, as presented in Chapter 6 from an airborne platform. From space, TDS-1 [33, 34, 70] and CyGNSS [35, 74, 79] have also proven to estimate SM. However, a large dispersion in the reflectivity was produced due to the surface roughness [34, 124], making a single-pass retrieval a titanic task [69].

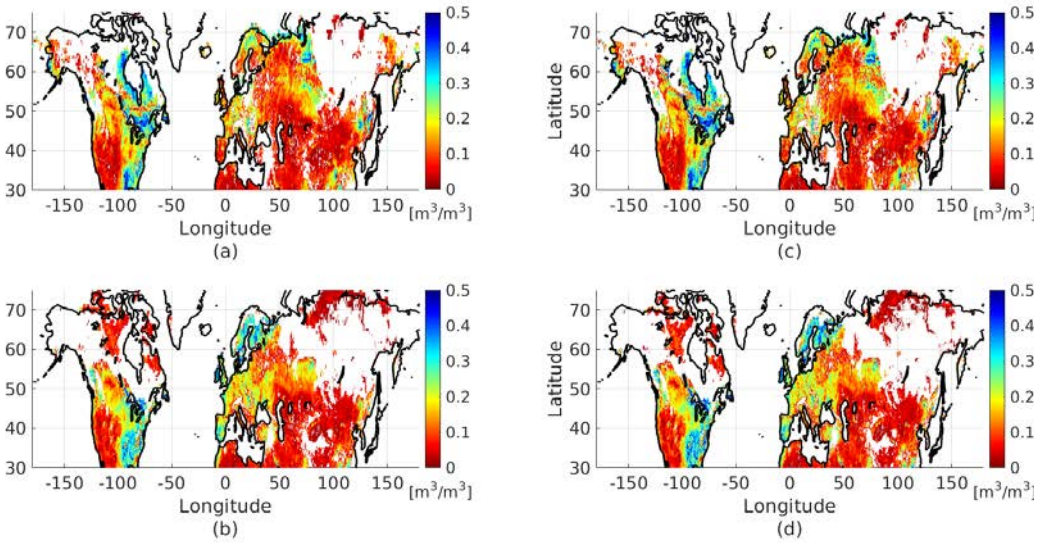

Figure 12.15: SMOS-derived soil moisture from [179] for (a) and (b) at 36 km grid on the 15 October 2020, and the 5 November 2020, respectively, and (c) and (d) at 9 km grid on the 15 October 2020, and the 5 November 2020, respectively.

12.4.1 Data description

12.4.1.1 Ancillary data

A global SM dataset was needed as a reference for training the ANNs. In this regard, two SMOS products were selected. The nominal accuracy of SMOS SM is 0.04 m^3/m^3. The error standard deviation (std) obtained when validating the ESA SMOS Level 2 SM against in-situ SM observations ranged between 0.04 and 0.07 m^3/m^3 [270]. In this study, the Barcelona Expert Center on Remote Sensing (BEC) [179] provided two dedicated SMOS SM data on a daily basis at two different spatial resolutions: 36 km and 9 km [175]. The accuracy of the products has been assessed in previous studies over areas with different environmental characteristics. It is important to remark that the product used here shows a dry bias with respect to in-situ SM data,. Finding in many sites an unbiased root mean square error around ∼0.04–0.08 m^3/m^3 [176, 271, 272].

The SMOS SM at 36 km is used to train and validate a data-driven algorithm implemented using FMPL-2 radiometry measurements, and the one at 9 km is used for the FMPL-2 GNSS-R measurements. The 9 km product is used to validate the combined MWR/GNSS-R SM product. The ground-truth product is shown in Fig. 12.15. Note that, the projection of all maps presented in this manuscript is the global Equal-Area Scalable Earth EASE Grid 2.0 [253].

As the FMPL-2 pixel is ∼ 10 times larger than the SMOS one, other data sources are used to down-scale the original FMPL-2 pixel down to 36 km. The ancillary data used to down-scale those measurements are a re-gridded version of the 16-day average Normalized Difference Vegetation Index (NDVI) from MODIS [252], and the daily skin temperature

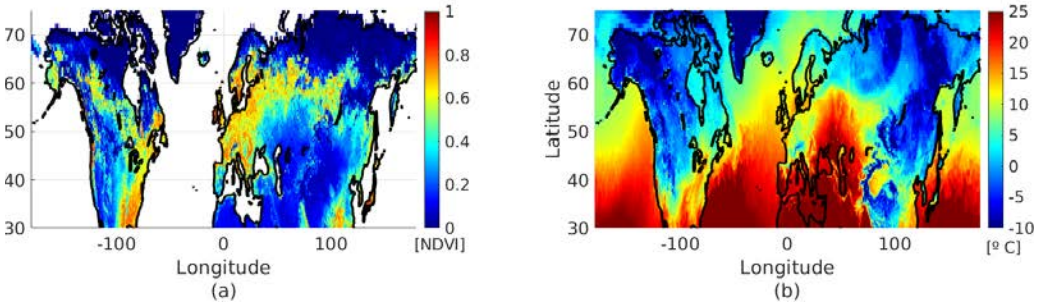

Figure 12.16: (a) 16-day averaged NDVI from MODIS [252] on the 22 October 2020, and (b) Skin temperature from [251] on the 15 October 2020.

from ECMWF [251], also gridded at 36 km. In addition, a land cover mask derived from MODIS is also used, gridded at 36 km. The two products are shown in Fig. 12.16.

12.4.1.2 FMPL-2 data

The calibration procedures and the validation of FMPL-2 were explained in Chapters 9 and 11, respectively. The geo-location process followed to retrieve SM maps is similar to the NNI in Chapter 11, but using a global EASE Grid 2.0 projection at 36 km, instead of a polar EASE2 grid. The algorithm geo-locates each MWR antenna temperature (T_A) measurement into a single 36 km. Then, all T_A measurements within a time-span of five days are averaged into a single map, followed by a triangulation-based natural neighbor interpolation (NNI). Finally, an antenna pattern compensation was performed based on a 2D moving window filtering, using a circular window representing the same area of the antenna footprint. In this way, an entire map out of five days of measurements was generated. Thanks to this technique, there are no gaps in the antenna temperature data, which will help to lately collocate GNSS-R and MWR measurements to provide the combined MWR/GNSS-R SM estimation. Figure 12.17 illustrates the results of the NNI algorithm. This method allows to detect the coastline borders with a finer resolution than the one given by the antenna footprint (350x500 km^2), as it can be seen over Greenland. Just to remark, the ocean area on top of Canada, where it seems there is no land-water transition, is completely covered by sea-ice, thus there is a "jump" in the measured antenna temperature values, as the entire region is covered by sea-ice, which has a larger apparent brightness temperature than the ocean [31].

Finally, Fig. 12.18 shows the reflectivity of the collected (a) GNSS reflections over land, (b) the associated incidence angles, and (c) the estimated SM values interpolated from the SMOS SM product. The reflectivity is calculated as shown in Section 9.4, and as explained in Section 11.4, all the GNSS-R tracks have been pre-processed to filter out reflections with poor SNR, or with inconsistent absolute Doppler frequencies. Just to remark, the displayed reflection points are the ones that have a time-collocated measurement in the SMOS SM product shown in Fig. 12.15. After filtering, the resulting amount of specular reflections was 12.585. The collocation of the SMOS SM product was performed by interpolating the SMOS SM values to the reflection points' location using a nearest neighbor 2D interpolation (NNI), producing scattered SM values over the

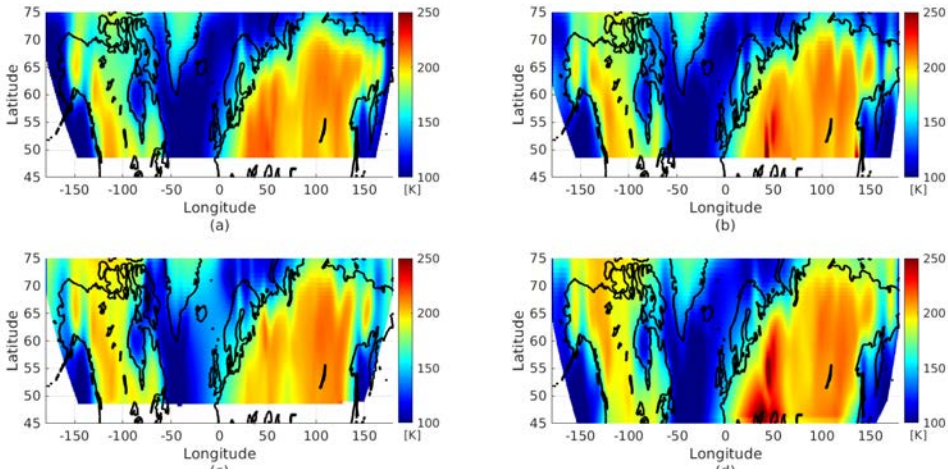

Figure 12.17: FMPL-2 MWR measurements geo-located using NNI algorithm comprising 5 days of measurements with and centered in the (a) 7 October 2020, (b) 21 October 2020, (c) 3 November 2020, and (d) 10 November 2020.

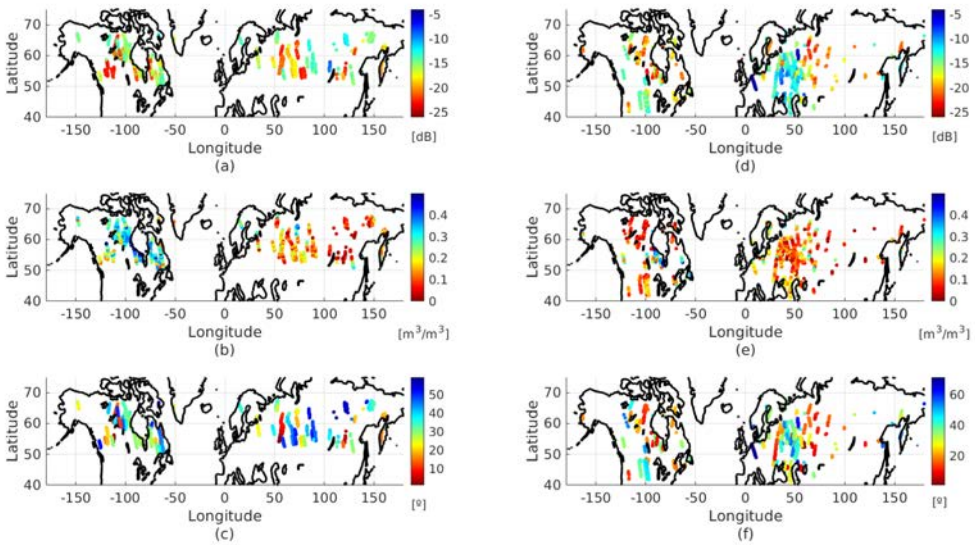

Figure 12.18: (a) GNSS-R reflectivity calibrated as shown in Chapter 9, (b) the incidence angle of the reflection, and (c) the SMOS SM (9 km) estimation interpolated over the GNSS-R specular reflection position.

specular points.

12.4.2 Soil Moisture retrieval using ANN

As ANNs show a great potential to solve non-linear problems, these algorithms have been applied to soil moisture retrieval. ECMWF is assimilating real-time Level 2 SM derived from SMOS using ANN [85], and several other SM retrieval algorithms using CyGNSS GNSS-R data are also using ANNs [79, 88]. However, ANNs have several challenges: to select the *correct* ground truth (known as algorithm "target") to train the algorithm, to correctly pre-filter and collocate the input data set, and to avoid network over-fitting [94].

All previous ANN algorithms using GNSS-R to retrieve SM use either SMAP or in-situ probes as ground-truth. However, there is a large collocation error when the CyGNSS observable, with a native resolution ∼0.5x6.5 km^2 [75], is collocated with a SMAP cell of 36 km. In all previous cases, multiple averages are used to finally provide a good agreement between the resulting network and the target values (see Table 1 and Fig. 13 from [79]). Moreover, algorithms using in-situ probes as ground-truth (e.g. [80, 89]) compare the CyGNSS reflectivity with a single point measurement. Thus, it is necessary to apply either an averaging of different in-situ probes or a statistical estimation of the SM of the equivalent GNSS-R pixel under study. In this case, using erroneous targets may introduce a bias in the algorithm, and network over-fitting (i.e. the ANN does not perform well out of the training set).

The aim of this work is to investigate different ANN algorithms to retrieve SM using FMPL-2 MWR and GNSS-R data. For that reason, different ANNs are proposed to validate the performance of the MWR, and the GNSS-R data separately. Each of the ANNs used in this study has been dimensioned to avoid network over-fitting [94]. The amount of neurons in each of the layers is always less than two times the number of inputs. Each neuron uses the *sigmoid* function as the transfer function, and the training process is stopped at an early stage to prevent noise over-fitting, as suggested in [94]. Finally, the trained networks are always pruned [95] after training.

Table 12.5 details the different data-driven algorithms studied in this section, indicating the input data for each algorithm and the "ground-truth" used for training each ANN.

12.4.2.1 Using optical data

L-band MWR data has been used to recover SM, but several algorithms have also been proposed using optical data only, as NDVI and Land Surface Temperature (LST) measurements (e.g [261]). In [262] (p. 47-72) other methods based on optical data are summarized. Although it is possible to retrieve SM from optical data, errors are larger than if L-band MWR is incorporated into the model. The two following main objectives are pursued in this section. First, to show the capabilities of an ANN-based algorithm to provide SM estimates just using optical data, and second, is to serve as a validation base of the down-scaling algorithm from FMPL-2 MWR data provided in Section 12.4.2.2.

The first approach is based on the aforementioned skin temperatures and NDVI datasets. The ANN used here is a 3-hidden layer network with 6 neurons per layer. The data are divided into 15% for training, 5% for validation, and 80% for testing, and the network "ground-truth" is the SMOS-derived SM product gridded at 36 km. The input data is the following:

Table 12.5: Summary of the ANN-based models implemented to estimate SM.

Model	Input data	Ground-truth
Optical	• NDVI from MODIS, • Skin temperature from ECMWF.	SMOS SM product at 36 km
Optical + MWR	• NDVI from MODIS, • Skin temperature from ECMWF, • FMPL-2 L-band MWR T_A.	SMOS SM product at 36 km
GNSS-R	• FMPL-2 reflectivity data.	SMOS SM product at 9 km
GNSS-R + MWR	• FMPL-2 reflectivity data, • FMPL-2 L-band MWR T_A.	SMOS SM product at 9 km

- NDVI from MODIS [252],
- Skin temperature from ECMWF [251], and
- Land Cover mask from MODIS [252].

Results are shown in Fig. 12.19. As it can be seen, the $R^2 = 0.56$, and the standard deviation of the error (STD(Err)) is 0.084 m^3/m^3. Note that, the scatter-density plot shows many pixels with a SM value of $\sim$ 0.2 m^3/m^3 in order to minimize the error. The shortcoming of this method becomes clear as the network is missing the valuable information coming from the L-band MWR.

12.4.2.2 Using L-band microwave radiometry data

In this second approach, the FMPL-2 MWR data are added to the skin temperature, and to the NDVI data sets to improve the SM estimation. The 5-day averaged FMPL-2 MWR data presented in Fig. 12.17 is combined with the daily skin temperature and the 16-day averaged NDVI data. This will produce a daily product which can be compared to the daily SMOS SM product gridded at 36 km.

The same network topology using 3 hidden layers is used here, but with 10 neurons per layer. In this case, the number of neurons has been increased as more inputs are used in the model. Then, the data is divided again into 15% for training, 5% for validation, and 80% for testing. In this case, additional low-resolution data inputs are used (see Fig. 12.20) in addition to the FMPL-2 MWR data. The inputs of the network are:

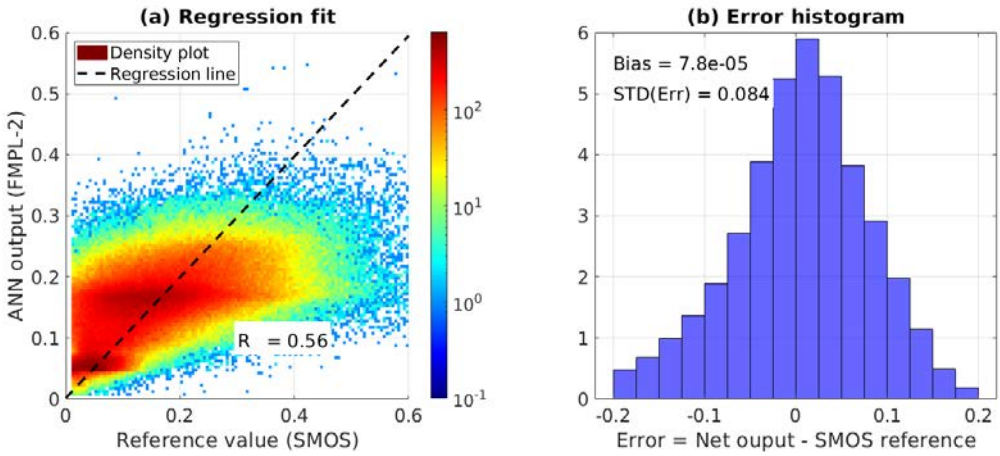

Figure 12.19: (a) Scatter-density plot between the ANN output using NDVI and Skin temperature as input data, and the SMOS SM product as the network reference value, and (b) error histogram between the ANN output and the SMOS reference.

- FMPL-2 antenna temperature,
- FMPL-2 standard deviation of the antenna temperature in the along-track measurement,
- NDVI from MODIS [252],
- Low-resolution NDVI from MODIS [252],
- Skin temperature from ECMWF [251],
- Low-resolution Skin temperature from ECMWF [251],
- Land Cover mask from MODIS [252], and
- Low-resolution Land Cover mask from MODIS [252].

The objective of this second approach is to down-scale the coarse footprint measurement of the FMPL-2 radiometer to a "higher-resolution" pixel by using the NDVI and the skin temperature gridded at 36 km. Pixel down-scaling with L-band MWR data is a known technique [174, 175], where optical datasets are usually complemented to coarse-scale radiometry observations to achieve higher resolved images. However, to authors' knowledge, this is the first implementation of a down-scaling algorithm using ANNs. The idea behind the network architecture is similar to the one conceived in [175], but here the ANN algorithm takes the NDVI, the skin temperature, the land cover mask, and the antenna temperature at a coarse resolution, and then with the help of higher resolution NDVI, skin temperature, and land cover maps, it down-scales the original antenna temperature to provide a down-scaled SM product. An example of the skin temperature after "blurring" is provided in Fig. 12.20a for illustration purposes.

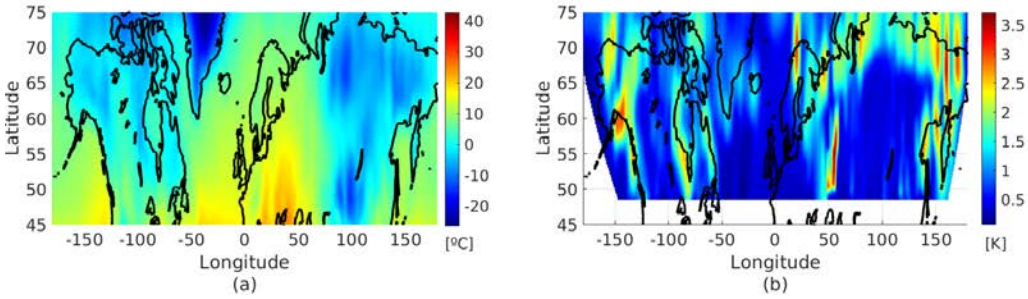

Figure 12.20: (a) Low-resolution skin temperature [ºC], and (b) sample FMPL-2 standard deviation [K] in the along-track direction after applying the NNI algorithm. Note that, land-water transitions in the Northern part of Siberia are highlighted in red.

Moreover, the standard deviation of the antenna temperature measured in the along-track direction is also used as a proxy to correct the edge transitions (i.e., land-water transitions, as highlighted in Fig. 12.20b).

Figure 12.21 shows the scatter-density plot and the error histogram of the ANN used to provide the down-scaled FMPL-2 soil moisture at 36 km. As compared to the previous case, adding the FMPL-2 MWR data results in more accurate ()SM estimations. The R has been increased from $R = 0.56$ to $R = 0.69$, and the STD(Err) has decreased from 0.084 to 0.074 m^3/m^3, showing a negligible bias in both cases. This result validates that the 5-day averaged FMPL-2 antenna temperature data enhances the SM retrieval algorithm. Therefore, even at a coarse resolution, the FMPL-2 MWR data can be used to estimate SM. It is important to remark that studies comparing different remote sensing SM products (i.e., from the Advanced Microwave Scanning Radiometer, SMAP, or SMOS) to ground-truth sensor networks [177] showed similar errors to the ones presented in this section (i.e., root-mean-square differences of ~ 0.076 m^3/m^3, and unbiased root-mean-square difference of ~ 0.056 m^3/m^3).

Figure 12.22 shows the estimated SM maps using the FMPL-2 MWR data, and the errors with respect to the SMOS SM estimations. In this case, high resolution ancillary data contains the relevant information to obtain SM maps at full coverage. The first remarkable aspect is that the map corresponding to the latest period (Fig. 12.22d) includes lower latitudes due to a change in the spacecraft execution scheduling, which started acquiring data above 45º latitude North, as explained in Section 12.4.1.1. The error maps present many areas with errors lower than 0.1 m^3/m^3 (i.e., color scale around yellow, green, and light-blue). Note that, as the FMPL-2 antenna temperature measurements used in this algorithm are built from the average of 5 days in order to provide a full-coverage map, SM estimations on areas with strong rain events occurred after FMPL-2 measurement will exhibit a larger errors. To solve this problem, additional data sets could be used in the algorithm: for example, a constellation of multiple satellites including FMPL-2 sensors would provide a finer temporal resolution. Thus, if 5-8 satellites are used in different orbital planes, the required amount of time-averages would decrease from 5 days to just one day, making it possible to provide a daily full coverage SM map above 45 ºN.

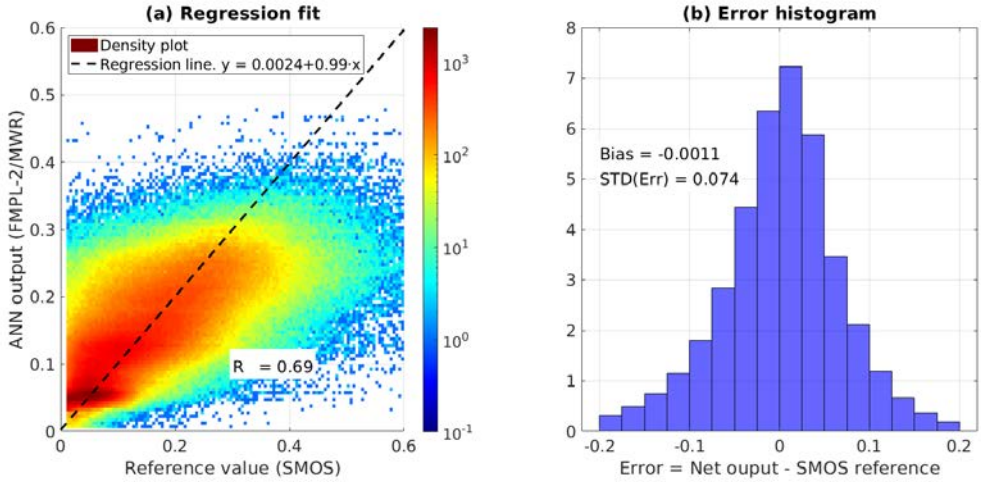

Figure 12.21: (a) Scatter-density plot between the ANN output using FMPL-2 data, and the SMOS reference value, and (b) error histogram between the ANN output and the SMOS reference.

12.4.2.3 Using GNSS-R data

Since the launch of CyGNSS, several data-driven algorithms have shown its potential to estimate SM from their measurements [72]. However, the GNSS-R data retrieved by the SGR-ReSi receiver [246] used in TDS-1 and CyGNSS missions is configured with long integration times (i.e., 0.5 or 1 s incoherent integration time), as the main objective of these missions is to study the ocean.

In the FMPL-2, the integration time of the GNSS-R processor is set to 40 ms in order to enhance the spatial resolution, and to avoid waveform blurring. As seen in [121], the ground-track displacement in 40 ms from a spacecraft orbiting at ∼550 km is equivalent to the size of the first Fresnel zone (i.e. 7.5 km/s · 40 ms = 300 m) of the GNSS signal reflection.

In this section, an ANN approach based on the methodology presented in Section 6.2.4 from Chapter 6 is proposed to retrieve SM from GNSS-R measurements. The method uses the moving average (*movmean*) and the moving standard deviation (*movstd*) of the reflectivity (computed in linear units and then converted to dB) to infer the SM values. As discussed in Section 6.2.4, the *movmean* and the *movstd* parameters are used by the ANN as a proxy to correct for the surface roughness effects.

In this case, a very simple network is proposed, using just 2-hidden layers, with 6 neurons per layer. The ANN target is the SMOS 9 km SM product. However, as introduced in Section 12.4.1.2, instead of gridding the GNSS-R data into the 9 km SMOS grid, the SMOS SM product is interpolated over the specular point location using a 2D linear interpolation algorithm. As the data set (Fig. 12.18) contains less number of points as compared to the MWR case, enough data should be used to train the algorithm to prevent over-fitting. Thus, the data is randomly divided into 60% for training, 10% for validation, and 30% for testing. The input data of this network are the following:

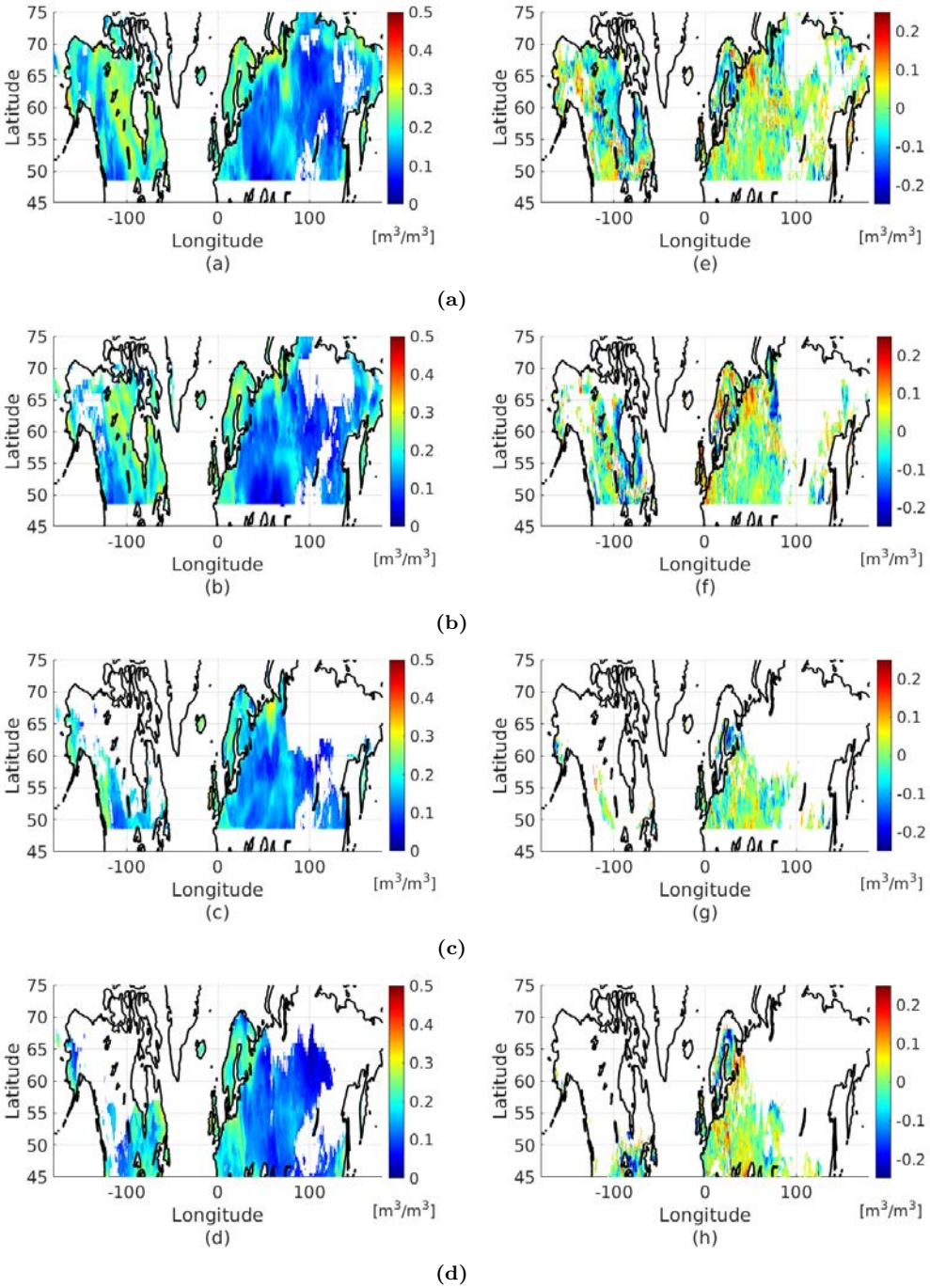

Figure 12.22: (a) to (d) FMPL-2/MWR down-scaled SM estimations corresponding to (a) 1-5 October 2020, (b) 10-15 October 2020, (c) 25-30 October 2020, and (d) 9-14 November 2020. (e) to (h) Errors with respect to the SMOS SM product, for the same date periods specified in (a) to (d). Note that, SMOS GT data is not available in regions in blank (e.g. northern part of Russia).

- Incidence angle θ_{inc},
- Moving average of the reflectivity (movmean(Γ)) over N samples,
- Moving standard deviation of the reflectivity (movstd(Γ)) over N samples, as a proxy to correct the surface roughness and speckle noise effects, and
- Moving average of the SNR (movmean(SNR)) over N samples.

where N is the number of samples used in the *movmean* and *movstd* operations. Note that, four different N values are proposed: 3, 5, 10, and 20. By instrument design, the length of a GNSS track produced by FMPL-2 is up to 90 samples successively (i.e., 45 seconds of data sampled at 2 Hz).

Figure 12.23 presents the density-scatter plot and the error histogram of the ANN output developed to estimate SM using GNSS-R data from FMPL-2 with respect to the collocated SMOS SM from BEC [179]. By looking at the shape of the density-scatter plot and the error histograms, in general, the ANN algorithm is not providing accurate results for low SM values (<0.15 m^3/m^3), showing a large dispersion in this range. Similar results were discussed in [273], as due to the very low reflectivity of dry soils, GNSS-R losses sensitivity, thus, causing the ANN algorithm to over-estimate low SM values, and to under-estimate larger SM values.

As it can be seen, when using small averages (i.e. $N = 3$, $N = 5$), the R^2 and the STD(Err) are very poor, showing a correlation coefficient $R^2 = 0.48$ and 0.51, and a STD(Err) = 0.097 and 0.095 m^3/m^3 for $N = 3$ and $N = 5$, respectively. This is similar to the error graph shown in Fig. 13 from [79], where the larger error was linked to areas where fewer samples where used to average the GNSS-R reflectivities. As important as the decrease of the STD(Err) is the decrease in the bias of the estimator: from -0.015 m^3/m^3 ($N = 3$) to 0.00011 m^3/m^3 ($N = 20$). As discussed in Chapter 6, the effect of these "moving" operations is to smooth the surface roughness, and to reduce speckle noise effects. When the averaging is large enough (i.e., $N = 10$, $N = 20$), the R^2 is increased up to 0.61, and 0.66, and the STD(Err) is also reduced to 0.087 m^3/m^3, and 0.082 m^3/m^3, respectively for $N = 10$, and $N = 20$. Moreover, it is important to remark that the algorithm bias is negligible in these last two cases.

The increased average (i.e., larger N) produces a degradation of the spatial resolution, as more samples are required to derive a single measurement. In this case, taking into account the sampling rate (2 Hz), and the ground-track velocity ($v_{track} \sim 6.5$ km/s), a $N = 3$ means that the S/C has moved ~ 9.75 km during moving window computation, thus the equivalent spatial resolution following this technique would be ~ 9.75 km for $N = 3$, 16.25 km for $N = 10$, 32.5 km for $N = 10$, and 65 km for $N = 20$. This phenomenon illustrates the remote sensing trade-off, where maximizing the spatial and the radiometric resolution at the same time is not possible, and one must be sacrificed for the benefit of the other.

Finally, Figs. 12.24 present the geo-located specular points with the estimated SM values, and their computed errors with respect to the SMOS SM estimates, for two time periods, from October the 1^{st} to October the 31^{st}, 2020, and from November the 1^{st} to December the 4^{th}, 2020.

The error maps are defined as the network output minus the ground-truth. Thus, a negative error means that the ANN algorithm estimates a lower SM than the actual

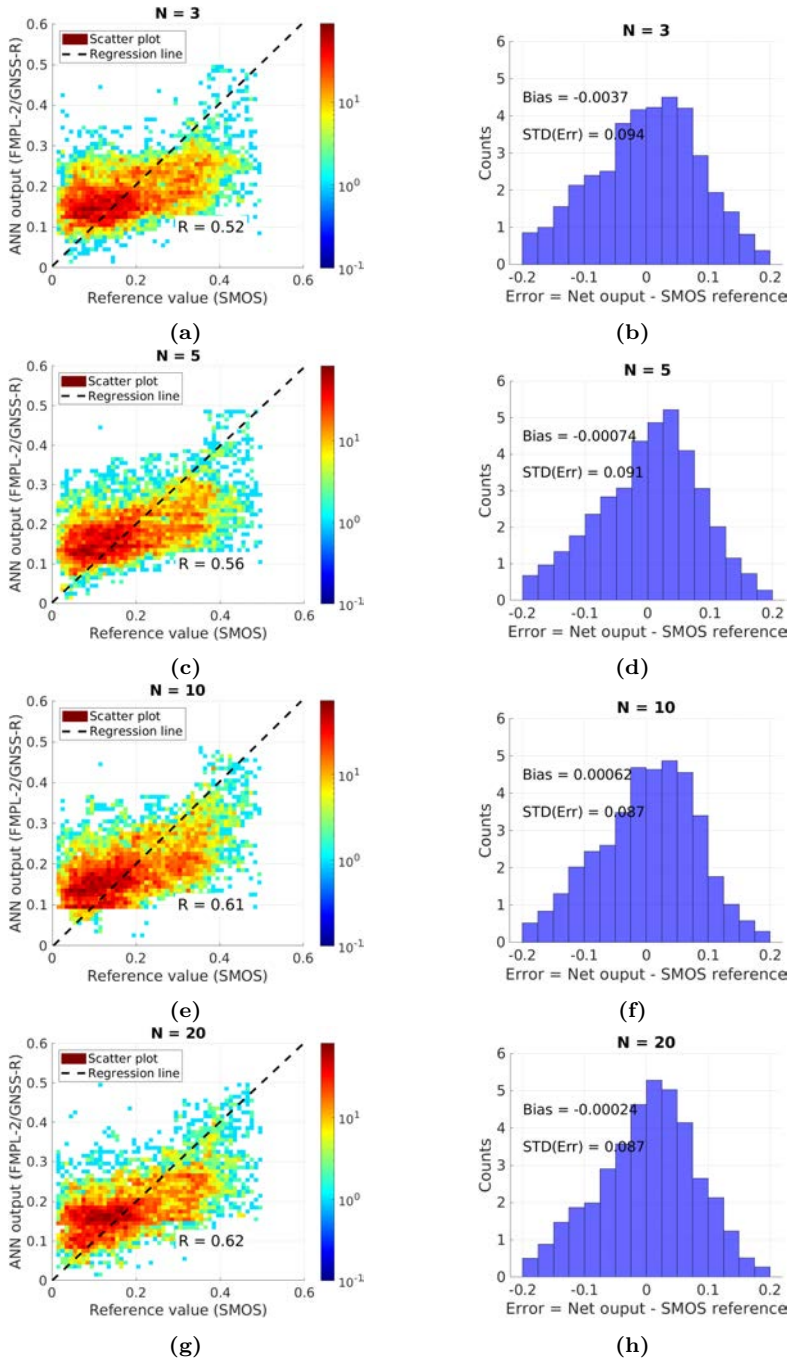

Figure 12.23: (left) Scatter-density plot, and (right) error histogram of the GNSS-R-based ANN output with respect to the collocated SMOS SM product from BEC [179], showing the four different values of N used to compute the *movmean* and *movstd* inputs for the network.

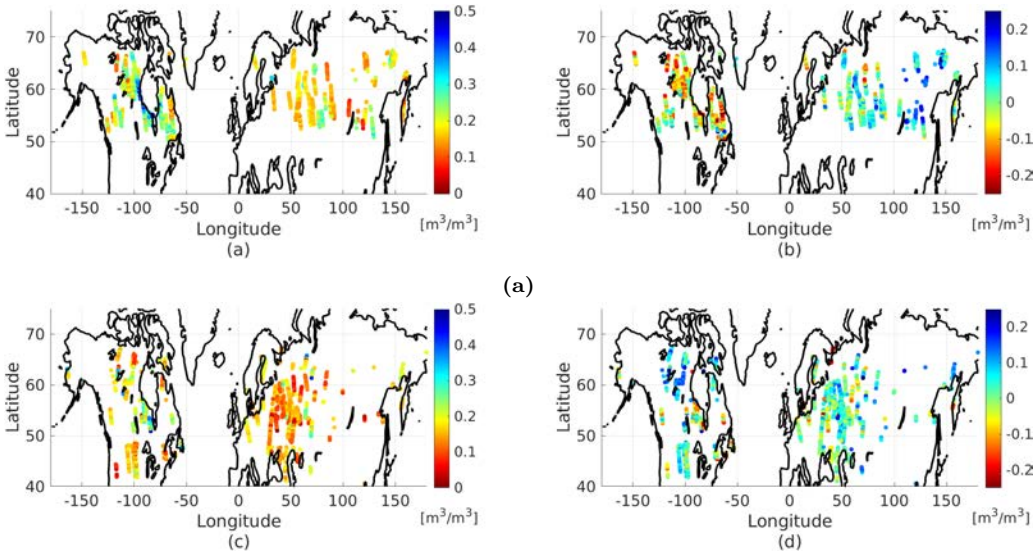

Figure 12.24: (a) and (c) GNSS-R-derived SM estimations corresponding to $N = 20$. (b) to (d) Error with respect to the collocated SMOS SM product. The map presents the measurements collected by the FMPL-2 from (a-b) October the 1^{st} to October the 31^{st}, 2020, and from November the 1^{st} to December the 4^{th}, 2020. Only reflections collocated with SMOS SM data are presented.

ground-truth (under-estimation), and a positive error means that the algorithm estimates a larger SM value than the actual ground-truth (over-estimation). By looking at the first data period, it can be seen that larger errors are found in the area on top of Canada (65º N, 100º W). In this case, most errors are under-estimations of SM for areas with moderate-low moisture content, as also identified in the scatter plots in Fig. 12.23. In this case, the SM monitored area in Russia shows, in general, a good accuracy, with some SM over-estimations on low-moderate SM values ($\sim$0.1 0.2 m^3/m^3).

For the second period, focusing on the area on top of Canada, the algorithm now presents SM over-estimations. In this case, the area contains several points over very dry areas (see Fig. 12.18), and some others that are very wet, at the southern side of the Hudson Bay. As expected from the scatter-density plots, dry areas are over-estimated, and wet areas are under-estimated.

Retrieving soil moisture using single-pass GNSS-R is a complex task [69]. In many cases, the surface roughness, and its dependence on SM, difficult the SM recovery. In our case, the training process of the ANN algorithm gets biased because of the large dispersion of the GNSS-R reflectivity values due to this effect. For this reason, additional data must be used to develop a more accurate model, even using the movstd(Γ) as a proxy to correct the surface roughness effects.

12.4.2.4 Using combined GNSS-R and radiometry data

Although using GNSS-R data provides good results with respect to the SMOS SM product at 9 km, the algorithm can be improved by adding the appropriate ancillary data. In order to correct the fitting errors produced by lower SM values, which then causes this "bias" for larger SM values, the L-band MWR data by FMPL-2 is used. Brightness temperature data is the complementary magnitude of the reflectivity [3]. Thus, even at a very low resolution, FMPL-2 data may contain meaningful and valid information to enhance the SM recovery when combined with GNSS-R.

The algorithm proposed in this Section combines both measurements to provide a more accurate SM estimation. As it is seen in Eq. 12 from [274], the reflectivity of a given area is linked to its brightness temperature. In our example, the coarse resolution MWR data is used as ancillary data to improve the SM retrieval algorithm using the high-resolution GNSS-R data. The network proposed here is the same as in the GNSS-R example: 2-hidden layers with 6 neurons per layer, using the same train/validation/test division. The target output is the same as in the previous case, and the input set now includes the MWR radiometry data as follows:

- FMPL-2 antenna temperature,
- FMPL-2 standard deviation of the antenna temperature in the along-track measurement,
- Incidence angle θ_{inc},
- Moving average of the reflectivity (movmean(Γ)) over N samples,
- Moving standard deviation of the reflectivity (movstd(Γ)) over N samples, and
- Moving average of the SNR (movmean(SNR)) over N samples.

In this case, the same approach to collocate the target output is used to collocate the FMPL-2 measurements. Therefore, a 2D linear interpolation is used to generate the scattered data from the 36 km FMPL-2 gridded data. In this case, the standard deviation of the antenna temperature is also used as a proxy to correct the edge transitions (i.e., land-water transitions).

Figure 12.25 shows the scatter-density plot and error histogram of the new ANN algorithm to derive SM from the combined MWR and GNSS-R data, as compared to the SMOS SM. In this last case, the resulting network shows a significant improvement with respect to the GNSS-R-only case. For lower SM values, the algorithm is more accurate, presenting, in general, a lower dispersion.

This is also reflected in the Pearson correlation coefficient and in the STD(Err). The R has improved from 0.52 to 0.79 for $N = 3$, from 0.56 to 0.80 for $N = 5$, from 0.61 to 0.81 for $N = 10$, and from 0.62 to 0.82 for $N = 20$. In the four cases, the bias is also negligible, and the STD(Err) has also decreased from 0.094 m^3/m^3 to 0.067 m^3/m^3, from 0.091 m^3/m^3 to 0.066 m^3/m^3, from 0.087 m^3/m^3 to 0.064 m^3/m^3, and from 0.087 m^3/m^3 to 0.063 m^3/m^3, for the four N cases: 3, 5, 10, and 20, respectively. The use of the FMPL-2 MWR data contributes to decrease the overall error with respect to SMOS SM

at 9 km, even for small values of N. The error difference between the shortest integration time and the longest integration times is 0.04 m^3/m^3.

Finally, Fig. 12.26 presents the geo-located specular points as in the previous section, but with this new ANN algorithm that uses the MWR and GNSS-R data. As compared to the previous case, most of the errors previously analyzed in Fig. 12.24 are now lower than 0.1 m^3/m^3. As compared to the previous case (using only GNSS-R data), the errors produced in the northern part of Canada are now drastically reduced. Drier areas are better-detected thanks to the use of the MWR data, which is the complementary magnitude of the reflectivity. Thus, when the GNSS-R reflectivity is low, the antenna temperature retrieved by the FMPL-2 MWR is high, and vice versa. This synergy allows to solve the uncertainty for the surface roughness attenuation, which produces low reflectivity values for high SM values. Thanks to the MWR data, low reflectivity values that are collocated with a low antenna temperature correspond to wet soils, but the reflection is largely affected by the surface roughness causing a low reflectivity value. Analogously, low reflectivity values collocated with a high antenna temperature corresponds to drier soils.

Finally, Fig. 12.26 presents the geo-located specular points as in the previous section, but with this new ANN algorithm that uses the MWR and GNSS-R data. As compared to the previous case, most of the errors in previously analyzed regions (65º N, 100º W), are now showing a lower error with respect to the SMOS SM values. Moreover, as the N value of *movmean* and *movstd* increases, the error map shows even fewer number of points out of the ± 0.1 m^3/m^3 range.

12.4.3 Discussion

Machine learning works as a data-driven approach, and data from different sources must be introduced as input data to deliver quality results. Different space-borne approaches have presented in the last years using ANN to estimate SM from GNSS-R measurements, as seen in Table 1 from [79]. As summarized in Table 12.6, four ANN-based models have been implemented to infer SM from a different combination of input features.

Table 12.6: Main performance parameters of the ANN-based models implemented to infer SM from optical, MWR, and GNSS-R data.

Model	**R**	**Std(Err) [m^3/m^3]**	**Bias [m^3/m^3]**
Optical	0.56	0.084	$< 10^{-4}$
Optical + MWR	0.69	0.074	$\sim 10^{-3}$
GNSS-R ($N = 20$)	0.62	0.087	$\sim 10^{-4}$
GNSS-R ($N = 20$) + MWR	0.82	0.063	$\sim 10^{-3}$

As it is presented, the use of FMPL-2 combined GNSS-R and MWR data improves the accuracy of the SM retrieval algorithm. Thus, showing the potential of GNSS-R sensors to estimate SM. However, GNSS-R data by itself is also showing promising results in terms of SM retrieval. **The algorithm proposed in Section 6.2.4 from Chapter 6, where the *movstd* of consecutive samples is used to correct the speckle noise**

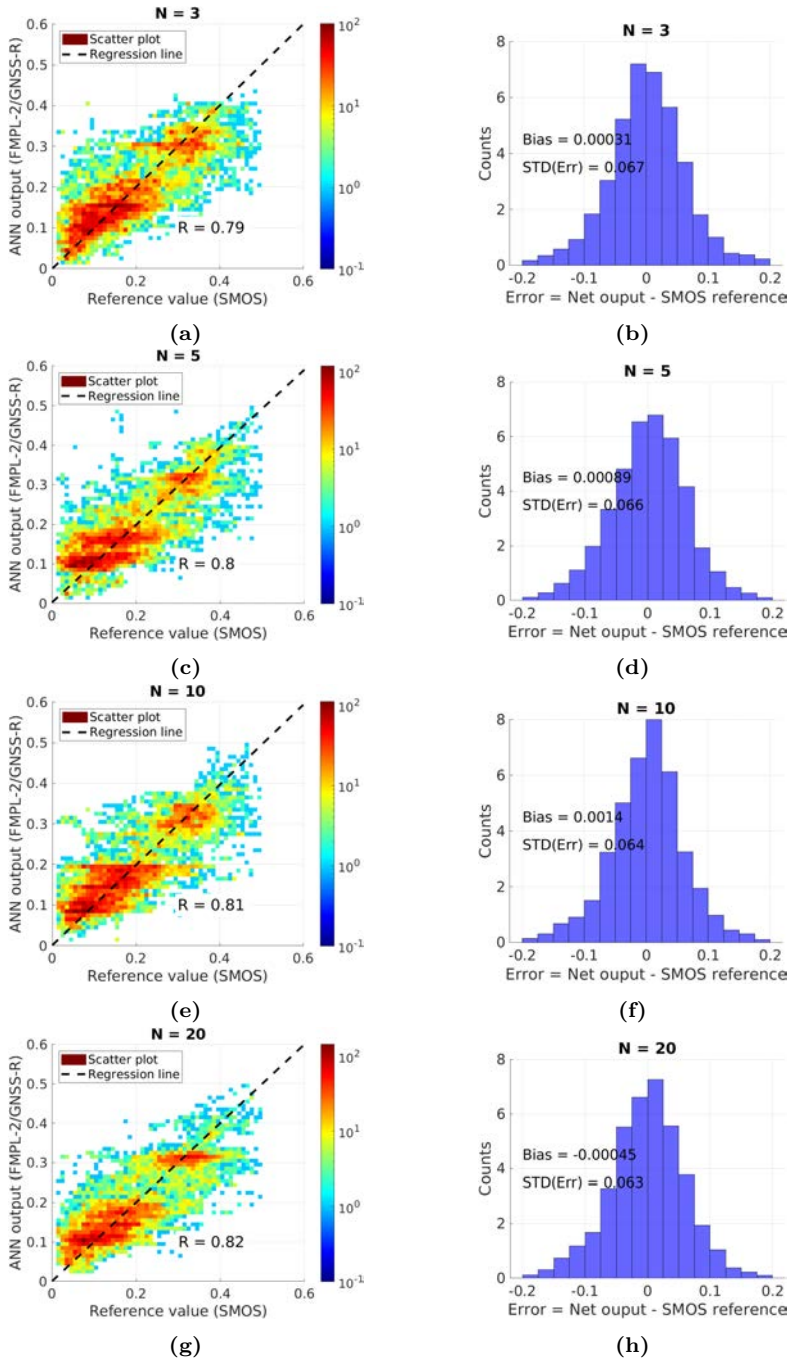

Figure 12.25: (left) Scatter-density plot, and (right) error histogram of the combined MWR and GNSS-R ANN output with respect to the collocated SMOS SM product from BEC [179], for the four different values of N used to compute the *movmean* and *movstd*, used as inputs for the ANN.

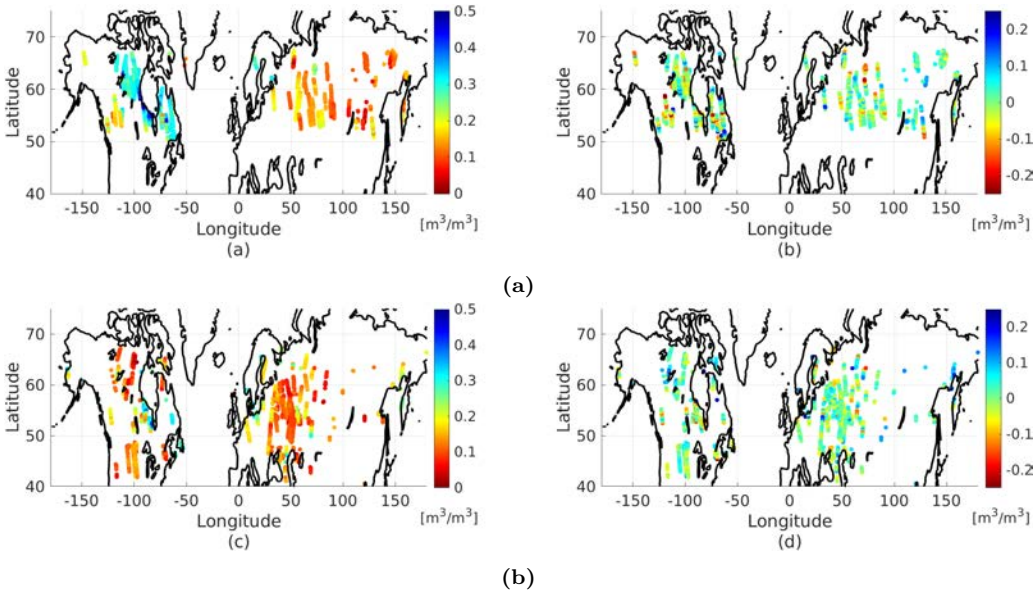

Figure 12.26: (a) and (c) Combined MWR and GNSS-R SM estimations corresponding to $N = 20$. (b) to (d) Error with respect to the collocated SMOS SM product. The map presents the measurements collected by the FMPL-2 from (a-b) October the 1^{st} to October the 31^{st}, 2020, and from November the 1^{st} to December the 4^{th}, 2020. Only reflections collocated with SMOS SM data are presented.

and surface roughness effects, has been proven to work for SM retrieval using spaceborne GNSS-R data. In Fig. 12.27, the error of the airborne algorithm presented in Section 6.2.5 is compared to the error achieved using FMPL-2 GNSS-R data. As it can be seen, both error curves follow the same trend, where a large number of measurements or Fresnel zones are required to provide a lower error. Note that, this effect was also studied in Fig. 13 of [79], where a large number of samples within a grid where required to achieve a lower error. Moreover, there is an almost constant "gap" between both curves of $\sim$0.03 m^3/m^3, which in this case might be due to the difference in directivity between the airborne GNSS-R instrument (i.e., $\sim$21 dB [97]) and the FMPL-2 (i.e., $\sim$12 dB, as shown in Chapter 9).

In both the MIR case (Section 6.2), and in the methodology described in Section 12.4.2.4, the use of combined data decreases the SM error with respect to a given target. However, this is not the case for other algorithms (e.g., Table 1 from [79]), where the efforts are focused to decrease the amount of ancillary data used to retrieve SM from GNSS-R data, at the expense of using larger spatial and temporal averages. However, this is not how a data-driven (and machine learning) algorithms work. Proper inputs shall be strategically selected to retrieve SM at larger spatial and radiometric resolutions. Thus, to combine data from different sensors is key to retrieve a higher quality product.

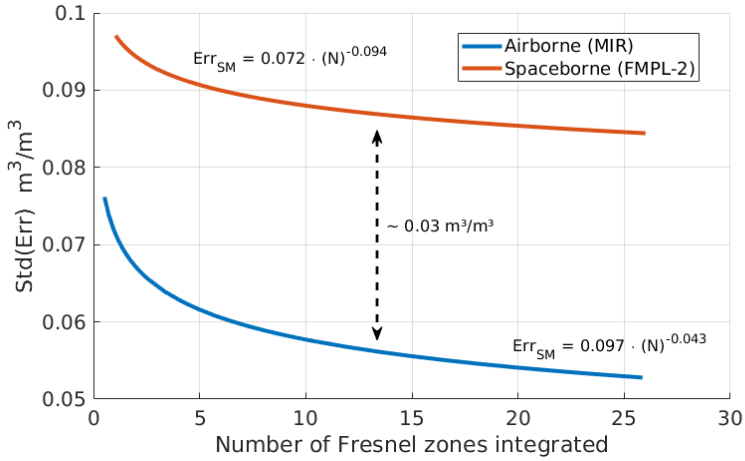

Figure 12.27: Std(Err) evolution as a function of the number of consecutive Fresnel zones used to derive the SM estimation. Comparison between airborne case (MIR instrument in Section 6.2.5), and spaceborne case (FMPL-2). Note that, the X-axis has been normalized by the number of Fresnel zones used to derive the SM estimation (i.e., the N parameter used in Section 12.4.2.3). A regression curve is fitted to the Std(Err) of both error curves to ease the comparison.

12.5 Conclusions

This Chapter has presented the first SIC/SIE, SIT, and SM retrievals using FMPL-2 data, showing the potential of CubeSats to produce quality science products for sea-ice and land monitoring applications.

For the SIC/SIE algorithm, FSSCat MWR maps generated with the algorithm presented in this Chapter are resampled at a resolution of 12.5 km. The use of the SST enhances the recovery of the SIC, and once combined with FMPL-2 MWR data, the SIC MAE with respect to OSI SAF SIC product is minimized for both Arctic and Antarctic Oceans. Furthermore, the combination of MWR and GNSS-R data shows an improved SIC/SIE estimation with a better spatial resolution. In this Section, SIC maps were presented, showing an MAE with respect to the OSI SAF SIC product of 2.37% for the Arctic Ocean and 5.55% for the Antarctic Ocean. It has been found that the use of the SST during the melting period in Antarctica leads to larger errors, due to the warm bias of the skin temperature during the melting period, mostly due to the model applied to solve the radiate-transfer equation. It has been seen that the use of GNSS-R data allows to improve the spatial resolution of the model over specular reflection points. In this case, the use of GNSS-R in future polar mission would allow to retrieve a SIC/SIE product with a much finer resolution and less sensitivity to errors induced by the the skin temperature warm bias.

Regarding the SIT algorithm, a thin SIT model was implemented using ANN using the SMOS SIT product as ground truth data, targeting SIT values up to 0.6 m, which is limited by the sensitivity of L-band T_B observations. The input features were trained on Arctic data during early Arctic freeze up from 15 October to 4 December, 2020. The

thin ice model shows good performance with an overall MAE of 0.065 m and generalizes well up to a SIT of 0.5 m, while underestimating for higher SIT values.

For the SM retrieval part, four different algorithms based on ANNs have been presented. The first algorithms serves as validation of the initial ECMWF skin temperature, and MODIS NDVI data to retrieve SM. The second algorithm presents an ANN-based pixel down-scaling technique, which takes the FMPL-2 MWR data along with MODIS NDVI data, and ECMWF skin temperature to produce down-scaled SM measurements at 36 km resolution from an initial MWR pixel of 350x500 km^2. The effect of adding FMPL-2 data to the ANN has been validated, showing a performance improvement when the FMPL-2 antenna temperature is used.

The third algorithm presents an ANN using GNSS-R data from FMPL-2 to estimate SM content, without using any ancillary data. The proposed ANN takes the "movmean" and the "movstd" of N consecutive samples together with the incidence angle, and compares it to a down-scaled SMOS SM product at 9 km resolution. As it is expected from other SM studies using GNSS-R, the larger the N samples used to produce a measurement, the smaller the error. In this case, by just utilizing GNSS-R data, the algorithm shows an standard deviation of the error of 0.079 m^3/m^3 at $N = 20$ samples.

To finalize the SM part, a fourth algorithm that combines FMPL-2 MWR and GNSS-R data is presented. It is shown that the combination of L-band antenna temperature measurements with GNSS-R reflectivity data significantly enhances the retrieval algorithm performance. In this case, the error is decreased by $\sim 27.5\%$, with a standard deviation of the error of 0.067-0.063 m^3/m^3, for $N = 3$ to $N = 20$, respectively. In concludes that the combination of collocated MWR and GNSS-R data from FMPL-2 produces a higher accuracy in the soil moisture estimation.

This Chapter has presented the capabilities of small satellites to retrieve different ECV. Current missions, as the ESA SMOS mission, currently retrieving these ECVs might be replaced by nano-satellites embarking FMPL-2. As an example, a constellation of CubeSats comprising at least 8 nano-satellites embarking FMPL-2 as the main payload would allow covering all latitudes above +45 ºN every single day[3]. Providing low-resolution L-band MWR that could be down-scaled to 36 km using optical measurements. Those measurements could also come from other CubeSat-based imagery constellations, or using data from traditional satellites. In addition, thanks to the synergy of L-band MWR and GNSS-R data covered in this dissertation, FMPL-2 measurements could be totally independent of data from other sensors. Thus, providing a closed solution to sense SIC, SIT, and SM through a CubeSat-based platform.

[3]The FMPL-2 MWR on board [3]Cat-5/A requires up to 3-5 days, depending on the downlink scheduling, to cover all latitudes above 45º N, and 5-8 days to cover all latitudes above 35º N.

Part V

Conclusions and Future Research Lines

13

Chapter 13

Conclusions and Future missions

This Chapter presents the main conclusions and original contributions of this Ph.D. thesis. Then, ideas for future research lines are proposed and discussed.

13.1 Conclusions

This Ph.D. dissertation has contributed to passive microwave remote sensing from different points of view. The two techniques covered in this Ph.D. dissertation are the L-band radiometry and the GNSS-Reflectometry. L-band radiometry is a very well known technique. However, GNSS-R is a quite novel and still growing technique. In the first part of this dissertation, a review of the theory was conducted. The second part was committed to the analysis of different field experiments to develop new algorithms to retrieve ECV using GNSS-R data. The third part was dedicated to the design of three CubeSat-based passive microwave remote sensing instruments, providing a new family of passive remote sensing instruments based on the Software Defined Radio concept. The last part was dedicated to the study of the results retrieved by one of these instruments: the FMPL-2, which was launched into space on 3 September, 2020 using the Vega VV16 SSMS PoC Maiden Flight.

In the first part, the achievable spatial of GNSS-R systems were addressed. Different waveforms and GNSS-R tracks retrieved from the airborne GNSS-R instrument MIR were analyzed. The statistics of different L1 and L5 waveforms were presented, showing that the achievable spatial resolution of GNSS-R systems is limited by the size of the first Fresnel zone, which is on the order of $\sim$500 m from a satellite platform. However, this can be only achieved if the maximum integration time is not exceeded. Otherwise, the GNSS-R observable would be blurred, and will include reflections from different Fresnel zones, which difficult the task of retrieving geophysical parameters.

In the second part of the thesis, different field experiments were conducted to develop new algorithms to retrieve several ECV using GNSS-R, including sea state monitoring (i.e., swell), soil moisture content over land, vegetation canopy height, and sea-ice thickness and snow content. The methodology and algorithms used have been implemented and validated using data from other sensors as ground-truth. First, a processing framework to process GNSS-R data (e.g. MIR data) was presented. The advantages of using GIS-enabled systems were presented, pointing out future guidelines for new GNSS-R instruments. Second, the field experiment conducted by MIR over the Bass Strait, in Australia, was analyzed. A new processing scheme is proposed, and the coherent and incoherent parts of a GNSS-R waveform are untangled and analyzed. The results showed that, for longer integration times, the specular reflection point, identified by the coherent component, is placed between the total power waveform and its derivative. Thus, providing important findings for altimetry applications. In this part, the appearance of multiple peaks in high-bandwidth GNSS signals was also noticed. The analysis conducted showed that the distance between those peaks could be related to wind-driven and swell signatures over the ocean. The third field experiment conducted was analyzing the potential of MIR data to retrieve geophysical parameters from the land. Data from two flights over different crop fields were used to develop a methodology to estimate soil moisture content using GNSS-R L1 and L5 data for the first time. The use of statistical properties of the reflectivity allowed to correct the surface roughness effect, delivering a quality soil moisture product. Then, data over a rainforest area was also analyzed to derive a methodology to estimate canopy height from both L1 and L5 GNSS-R measurements. In this case, reflectivity and waveform width measurements are used to estimate the vegetation height. Finally, the last field experiment conducted within this dissertation is a ground-based GNSS-R instrument to monitor sea-ice parameters,

as sea-ice thickness and snow depth on top of the sea-ice, of an ice floe. In this last experiment, an IPT was proposed to simultaneously retrieve snow and ice thickness from dual-band dual-polarization GNSS-R measurements, providing different realization of a four-layer interference pattern formed by the air, the snow, the sea-ice, and the water underneath. Then, the technique is applied to estimate the snow and sea-ice thickness for the entire campaign.

The third part presents the family of CubeSat-based passive microwave instruments called "Flexible Microwave Payload". First, the ^{3}Cat-4 mission was presented as an example of an Earth Observation mission composed of a 1-unit CubeSat. The FMPL-1 was presented, focusing on the design and implementation of the instrument. The instrument is a proof-of-concept of a low-cost commercial SDR technology to provide remote sensing measurements from a 1-unit CubeSat platform. The instrument integrated an L-band radiometer, a GNSS reflectometer, and an AIS receiver. Second, the FSSCat mission and the FMPL-2 instrument were presented. This second instrument of the FMPL family is the evolution of the FMPL-1, where the L-band radiometer and GNSS-R chains are designed to provide synchronous operation, thus retrieving both measurements at the same time. It is detailed the design, implementation, testing, and calibration of this advanced passive remote sensing instrument for CubeSats, detailing the procedures required to operate and calibrate the instrument. Finally, the design, implementation, and testing of FMPL-3 were presented. This last instrument takes the knowledge acquired during the processing of MIR L5 GNSS-R signals to develop the first-ever L5 GNSS-R space-borne instrument.

Concerning the last part, the calibration and the validation of the FMPL-2 instrument were presented, showing the potential of CubeSat-based instruments to perform passive remote sensing at L-band. Finally, different algorithms were proposed to retrieve ECV from FMPL-2 measurements: SIC/SIE, SIT, and SM. In this part, different algorithms based on neural networks were presented, showing the potential of FMPL-2 to retrieve ECV at a low-moderate spatial resolution –using L-band MWR data–, or moderate resolution –when used GNSS-R data in combination to L-band MWR data–. The synergy of L-band MWR and GNSS-R data was addressed, showing the enhancement of SIC or SM retrieval algorithms potential by merging L-band MWR and GNSS-R data. Furthermore, two ANN-based algorithms were presented to estimate SM using optical data, and to perform pixel down-scaling of the FMPL-2 MWR data using neural networks.

13.2 Original contributions

This Ph.D. thesis contributes directly to the development of novel passive microwave remote sensing instruments specifically designed for CubeSats. The algorithms and instruments presented set up an inflection point for CubeSat for passive microwave remote sensing specially at low frequencies. The capabilities of such systems have been presented, showing the potential these very small spacecraft have in front of the traditional satellite approach.

The following list contains the main original contributions of this Ph.D. thesis. Moreover, Table 13.1 includes the performance of the different algorithms implemented in Chapters 6, 7, and 12.

- The **analysis** of different GNSS-R waveforms and GNSS-R data segments to provide

a **new formulation** for the computation of the GNSS-R **achievable spatial resolution** based on the size of the first Fresnel zone. Moreover, considerations on the **optimum incoherent integration time** are presented to prevent waveform blurring and Fresnel zone overlapping due to the platform velocity.

- The **development** of a GNSS-R processing framework with system interoperability. The use of SQL and GIS-enabled systems allowed for easier data manipulation, visualization, and storage. Thus, taking profit from new geospatial systems to analyze GNSS-R data. The processing framework is also scalable and new modules can be easily added thanks to the designed software architecture.
- The **analysis** of the coherent and the incoherent components of GNSS-R reflections over the ocean at L1 and L5. For that, a new GNSS-R processing algorithm has been **developed**, allowing to untangle the coherent and the incoherent components.
- The **analysis** of multiple peaks in GNSS-R L5 waveforms to infer sea-state information. An algorithm has been **developed** using large-bandwidth signals (L5) collected by MIR. In this algorithm, the separation between multiple peaks in the received waveform is linked to wind-driven and swell wave periods.
- The analysis of GNSS-R L1 and L5 reflectivities retrieved by MIR over land to estimate soil moisture. In this case, the analysis showed that the use of the "movstd" operation along consecutive GNSS-R reflectivity samples allows to correct for the surface roughness effects, by using artificial neural networks as retrieval algorithm. The first results of soil moisture retrieval using L5 GNSS-R signals have been presented. This type of signal has shown a lower error with respect to the algorithm presented using L1 data (Table X), due to the larger penetration depth and larger spatial resolution.
- The analysis of GNSS-R L1 and L5 peak width and reflectivities to estimate vegetation canopy height. A correlation analysis has been conducted, following the development of an artificial neural network retrieval algorithm to estimate vegetation canopy height using only GNSS-R measurements, both at L1 and L5, for the first time. The first results of canopy height retrieval using L5 GNSS-R signals have been presented.
- The **development** of a four-layer interference pattern model to estimate sea-ice thickness and snow depth using multi-band circular polarization GNSS-R measurements of an ice floe. The algorithm developed follows a two-step process to estimate the snow depth from a given range of elevation angles (LHCP, 30^{o} to 42.5^{o}), and the estimate snow depth is then used to estimate the sea-ice thickness looking at a different range of elevation angles (RHCP, 5^{o} to 20^{o}).
- The **development** of an ANN-based snow depth retrieval algorithm using 2D IPT data collected by PYCARO-2.
- The **design and implementation** of FMPL-1, FMPL-2, and FMPL-3, three novel instruments specifically designed for CubeSat missions to perform Earth Observation. Moreover, the testing, calibration, and in-flight operations of FMPL-2 were conducted within this Ph.D. thesis. Providing for the **first time L-band MWR measurements from a CubeSat,** demonstrating the potential of CubeSats to perform radiometry. Moreover, FMPL-3 will be the **first-ever** L5 GNSS-R spaceborne receiver.

- The **development** of ANN-based SIC/SIE and SIT retrieval algorithms using FMPL-2 L-band MWR data, providing a product gridded at 12.5 km.
- The **development** of ANN-based SM retrieval algorithm only using optical and skin temperature data at a resolution, providing a product gridded at 36 km.
- The **development** of ANN-based SM retrieval algorithm that performs pixel down-scaling of the FMPL-2 L-band MWR pixel (350x500 km^2) to a pixel of 36 km.
- The **development** of ANN-based SM retrieval algorithm using GNSS-R data, following the methodology acquired during the MIR field experiment over land.
- To **study the synergy** between L-band MWR and GNSS-R measurements using an ANN algorithm to provide an finer resolution SIC and SM product.

13.3 Future research lines

This Section provides a few ideas to follow-up on the work presented in this thesis. The first ideas presented here are referred to data processing of MIR, PYCARO-2, and FMPL-2. Those are:

- Develop a new module to perform iGNSS-R for MIR data using the processing framework in Chapter 4.
- Explore the retrieval of altimetry measurements using L1 and/or L5 MIR data over the ocean, and possibly over land as well.
- Analyze the coherency of the L1 and L5 GNSS-R signal over the ocean and over land, using MIR data from the Bass Strait flight.
- Analyze the WF width and its correlation to the surface roughness or to the movstd(Γ) metrics in both Yanco flights.
- Analyze the evolution of the code-phase delay between the direct and the reflected signal of PYCARO-2 to perform altimetry measurements of the ice floe.
- Develop an algorithm to retrieve ocean salinity using FMPL-2 MWR data.
- Further explore the combination of GNSS-R and L-band MWR data to estimate SM using data from other missions, such as CyGNSS and SMOS or SMAP.
- Combined SM and CH/VOD recovery using L1/L5 GNSS-R data using iterative or neural network algorithms.

13.4 Future of CubeSats for Earth Observation

We are now living in the *big data* era, new algorithms are being developed, and neural networks are a good example of simple algorithms with multiple inputs being able to construct valuable outputs. Future Earth Observation missions should aim at reducing cost and increase the revisit time. One efficient way to do that may be by means of

Table 13.1: Summary of the different algorithms implemented within this Ph.D. thesis.

Algorithm target	Description	R	Error
Soil Moisture (L1/L5)	Airborne GNSS-R data retrieved by MIR over Yanco (Section 6.2)	0.86/ 0.97	0.06/0.03 m^3/m^3
Vegetation canopy height (L1/L5)	Airborne GNSS-R data retrieved by MIR over Australian rainforest (Section 6.3)	0.84/ 0.84	3.6/3.2 m
Snow thickness	Ground-based GNSS-R instrument part of the MOSAiC expedition (Section 7.5)	0.83	6.6 cm
Sea-ice thickness	Ground-based GNSS-R instrument part of the MOSAiC expedition (Section 7.5)	0.88	12 cm
Sea-ice Concentration (Arctic/Antarctic)	FMPL-2 MWR measurements over the poles combined with SKT (Section 12.2)	/	2.37%/5.55%
Sea-ice Concentration (Arctic/Antarctic)	Combined FMPL-2 GNSS-R and MWR measurements over the poles combined with SKT, only over selected target areas (Section 12.2)	/	3.0%/2.7%
Sea-ice Thickness	FMPL-2 measurements over the poles combined with SKT (Section 12.3)	/	6.7 cm (unbiased)
Soil Moisture	FMPL-2 MWR measurements over latitudes above 35 ^{o}N combined with SKT and NDVI (Section 12.4)	0.69	0.074 m^3/m^3
Soil Moisture	Combined FMPL-2 GNSS-R and MWR measurements over latitudes above 35 ^{o}N (Section 12.4)	0.82	0.063 m^3/m^3

CubeSat-based missions. From the results presented in this dissertation, it is clear that CubeSat-based remote sensing instruments can contribute to Earth Observation at a fraction of the cost of the "traditional" satellite approach. CubeSats have a great potential for Earth Observation. As it has been presented here, a CubeSat-based instrument as FMPL-2 can be used to retrieve SIC, SIT, and SM measurements with good accuracy. Although not as good as with traditional larger satellites, FMPL-2 has shown its potential to infer an enhanced resolution SIC and SM products by means of combined MWR and GNSS-R measurements.

One of the goodness of CubeSats, is their ability to deploy large constellations, as

Spire Global, Inc. or Planet Labs is nowadays doing. Taking advantage of "big-data" developments, such as artificial neural networks, the more sensors in orbit, the more data will be available to implement those data-driven algorithms like the ones used in this dissertation. The use of multiple distributed satellite sensors, such as a CubeSat constellation based on FMPL-2 instruments, will be able to bring this large amount of points, providing lots of measurements both in space and time at a reduced cost, as compared to a *big* satellite approach.

These potential CubeSat constellations embarking passive microwave remote sensing sensors would allow high-quality Earth Observation products, with improved revisit times, radiometric accuracy, and spatial resolution. The combination of such nano-satellite constellations and data-driven algorithms seems to be the natural path to beat the trade-off between spatial and radiometric resolutions, having large amounts of data and benefiting from artificial intelligence algorithms.

Evolved versions of ^{3}Cat-5/A could be conceived, using deployable solar panels and using X-band to transmit the scientific data, allowing the execution of FMPL-2 for the entire globe. Assuming the flight direction is swapped so that the cross-track direction is the narrower lobe of the antenna footprint (i.e., half power bandwidth of $\sim 40^{\text{o}}$, providing a cross-track footprint of 350 km), a constellation comprising 3 CubeSats would cover the planet, including the poles, with a revisit time of 3 days[1].

[1]Based on internal analysis performed by Deimos and UPC.

Part VI

Appendices

A

Appendix A

PYCARO-2 Operations Manual

This Appendix describes the instrument setup in the frame of the MOSAiC project. The appendix presented here is reproduced from Reproduce from [275] with permission from the author. The documentation presented here comprises both IEEC-ICE/CSIC and IEEC/CTE-UPC instruments, which both share the zenith-looking antenna and the isolating case. The design and integration of the antennas, isolating boxes, etc. has been carried out by the IEEC-ICE/CSIC staff. The integration of the 45º-looking antenna, the PYCARO-2 instrument, and the software developed to operate the instrument has been developed in the frame of this Ph.D. thesis.

A.1 Instrument setup

The experiment set-up is composed by the antenna tripod, the receiver box, the battery box, and the operations laptop. All the equipment is shared by both circular (IEEC/CTE-UPC) and linear polarization (IEEC-ICE/CSIC) experiments. Figure A.1 shows a general description of the different parts of the experiment and its connection between them.

A set of GNSS antennas are mounted on top of a tripod in the following configuration: a RHCP zenith-looking antenna collects direct GNSS signals, and a LHCP down-looking antenna (45° of tilt with respect to Nadir) collects the GNSS signals that are being reflected over the sea ice floe. The RF signals of all antennas are delivered to the receiver box, where different GNSS receivers receive and process them. The GNSS observables are stored at the receivers themselves and the data is periodically downloaded to a laptop computer placed at the icebreaker ship by means of an Ethernet connection.

The instrument box is supplied by 220 VAC voltage and an external 12 V battery, both simultaneously.

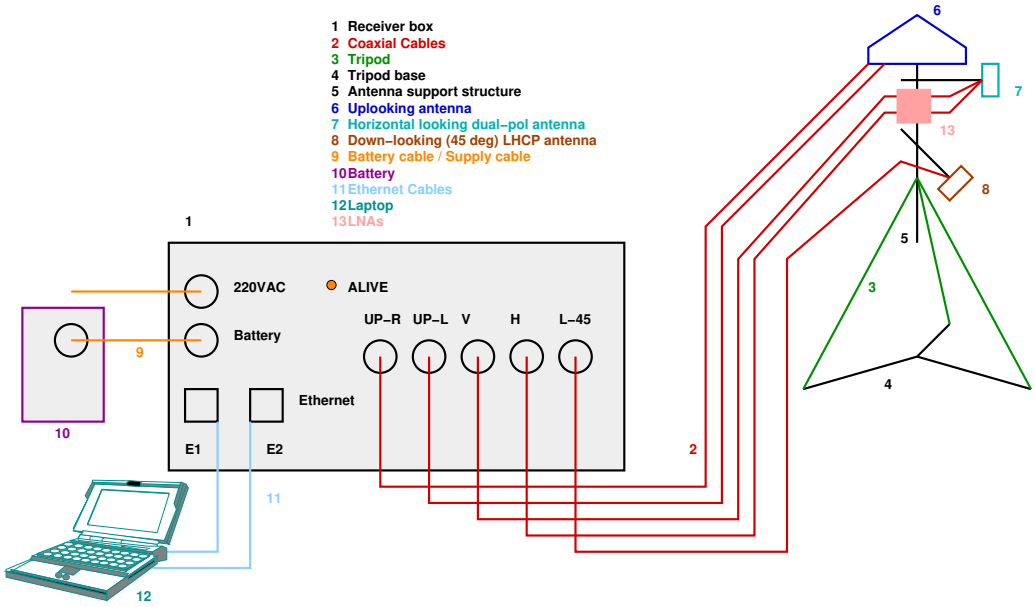

Figure A.1: General Experiment Setup.

A.1.1 Mechanical Set-up

A.1.1.1 Tripod

The tripod used as mechanical support for the circular GNSS-R experiment is also shared with the linear GNSS-R experiment from ICE, thus there are more than two antennas in the setup.

The tripod is deployed at its minimum height. As it is seen in Fig. A.2, the tripod legs are attached to the base using rubber rings.

Figure A.2: Mounted tripod, and tripod legs inserted into the tripod base.

A.1.1.2 Tripod baseplates

Figure A.3 presents the baseplates that are used to attach the antenna pole to the tripod.

Figure A.3: Top baseplate (left), and bottom baseplate (right), and baseplate screws. In the picture they are shown in the correct mounting orientation. The right image shows the baseplates attached to the top of the tripod.

A.1.2 Antenna set-up

A.1.2.1 Up-looking antenna

The up-looking antenna is the one with the conical radome and with two connectors at the base of the antenna. This antenna is screwed at the top of the pole, as presented in Fig. A.4.

Figure A.4: Up-looking antenna mounted at the top of the pole.

A.1.2.2 45-deg downlooking antenna

Finally, the 45º down-looking antenna is screwed to a pole, as shown in Fig. A.5.

Figure A.5: 45 degrees down-looking antenna shall be screwed to its pole.

Finally, the pole is inserted into its mechanical support. As highlighted in Fig. A.6, the distance at which the mechanical support must be screwed and tightened is highlighted in blue.

A.1.2.3 Stability ropes

In order to provide the setup more stability to the setup, stability ropes are provided. As shown in Fig. A.7 the pink ropes are attached to the yellow piece at the top of the antenna pole, and they are ice-screwed to fix the instrument to ground. The ropes must be attached to the ground in such a way that they do not obstruct the field of view of the antennas.

Figure A.6: The blue line at the 45 degrees down-looking pole shall be as in the picture.

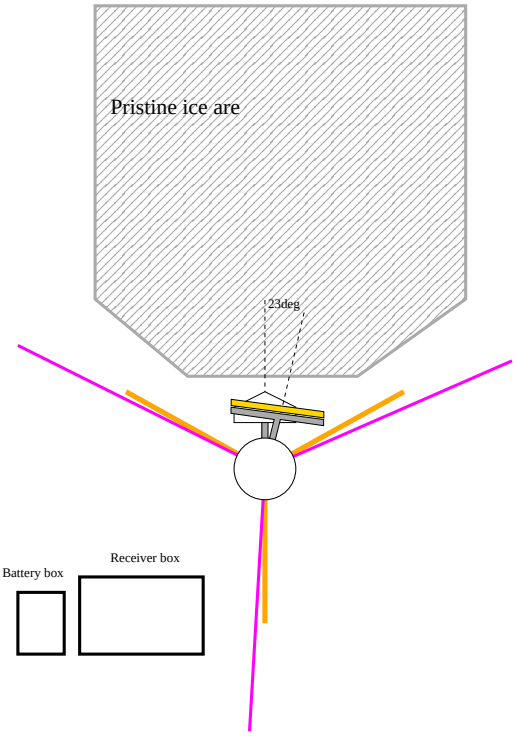

Figure A.7: Top view diagram of the setup. Stability ropes attached to the pole are attached to the ground so that the view of the antennas towards the pristine ice are is clear. The receiver box and the battery box are outside the field of view of the antennas.

A.1.2.4 Instrument and battery boxes

Figure A.8 presents the battery box, that provides energy support during the campaign, and the receiver box. This second box encloses both IEEC/CTE-UPC and IEEC/ICE-CSIC instruments, providing them a thermal and tightness support.

Figure A.8: Battery Box and Receiver Box.

A.2 Test operations and data retrieving

The equipment described above must stay on the RS site, except for the laptop used for data downloading and data transfer to mainland at the end of the legs. The laptop is pre-configured with all the required programs and drivers required by the different instruments. The laptop is also pre-configured with an static IP address as requested by MOSAiC team. The address is within the same range that the instrument addresses. Furthermore, the logging info for this laptop is user: `ieec`, and password: `mosaic`.

A.2.1 Starting the PYCARO-2 control program

Go to *the instrument laptop* Desktop and click on a shell-like icon named: Anaconda Shell for mo-GNSS-R-circ. A shell is open in an already pre-defined directory:

```
C:\Users\ieec\Desktop\mo GNSS R circ
```

And execute the following .bat file:

```
.\gnssr circ.bat
```

This will show up a GUI as in Fig A.9.

A.2.2 GUI commands

The GUI is already configured with the instrument IP address and contains only 4 buttons and 1 label:

- Disconnected - Connected label: This label changes its content and color depending if the program has an established TCP connection with the instrument (**Connected**) or not (**Disconnected**).
- Connect to instrument: creates a TCP Socket connection with the instrument. Once the connection is established, the ''Disconnect' label in red turns to 'Connected', in green.

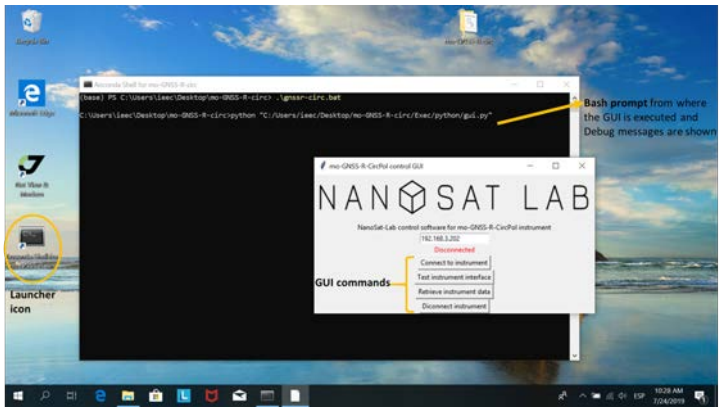

Figure A.9: Graphical User Interface for the PYCARO-2 instrument

- Test connection: performs a ping and sends a debug message towards the instrument, which will be replied after 1-5 seconds, and the output of the Test will be shown in the screen.
- Retrieve instrument data: opens a folder selector dialog where all the data stored in the instrument internal memory will be dumped to.
- Disconnect instrument: closes the TCP Socket connection with the instrument. Once disconnected the GUI can be closed.

A.2.3 Data downloading operation

In order to download the instrument the steps are:

- Click on the **Connect to instrument** button
- Wait for the *Disconnected to Connected* label to change
- Click on the **Retrieve instrument data** button and click OK in the dialog that informs that a folder shall be selected.
- Select a folder inside the 'Data' sub-folder (i.e. create a folder with the current date inside Data folder).
- After a some time (depending on the amount of data to be downloaded) the program will show up a dialog informing that a number of files have been correctly downloaded. Close the dialog. Note that the download process can be also checked in the *bash* prompt form where the program has been launched.
- Click on the **Disconnect instrument** and close the GUI and the *bash* prompt

After all the data retrieved can be checked by browsing to the selected folder (nominally placed in Desktop\mo-GNSS-R-circ\Data\...) and viewing the downloaded files, which have the format "mo-GNSS-R-CircPol˙YYYY-MM-DD˙HH-MM-SS.log"

A.3 Pictures of GNSS-R instrument during MOSAiC campaign

Lately, Fig. A.10 presents two pictures of the Remote Sensing site including the GNSS-R experiment and the Polastern icebreaker.

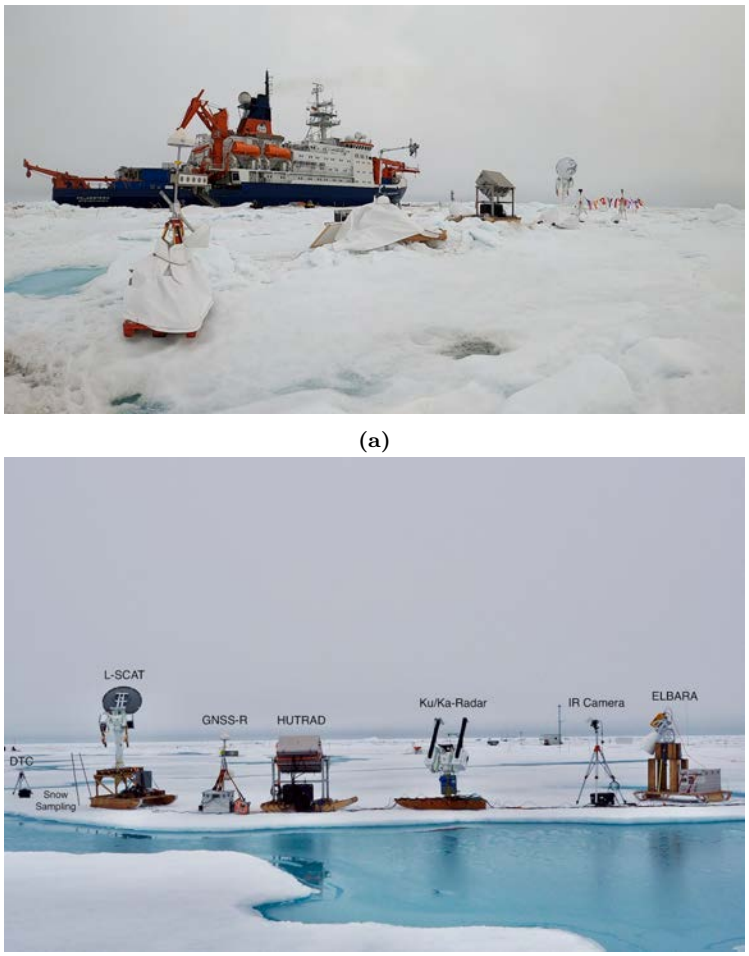

(a)

(b)

Figure A.10: Pictures of the Remote Sensing site during the MOSAiC expedition, (a) 23 July 2020, and (b) 28 August 2020.

B

Appendix B

FMPL-1 Detailed Design

This Appendix presents the hardware design, board schematics, and board layout files of the FMPL-1 payload. The work presented in this appendix is reproduced from internal documentation developed by the ^{3}Cat-4 hardware team and revised by ESA Fly Your Satellite! staff.

B.1 NADS Ring Adapter Schematics

Figure B.1 presents the schematic of the NADS first stage amplifying board of the down-looking L-band antenna of FMPL-1. Note that, this board also includes the necessary calibration loads (i.e., matched load and ACL) and the SP3T switch to commute between them. This board is powered and controlled by the FMPL-1 motherboard.

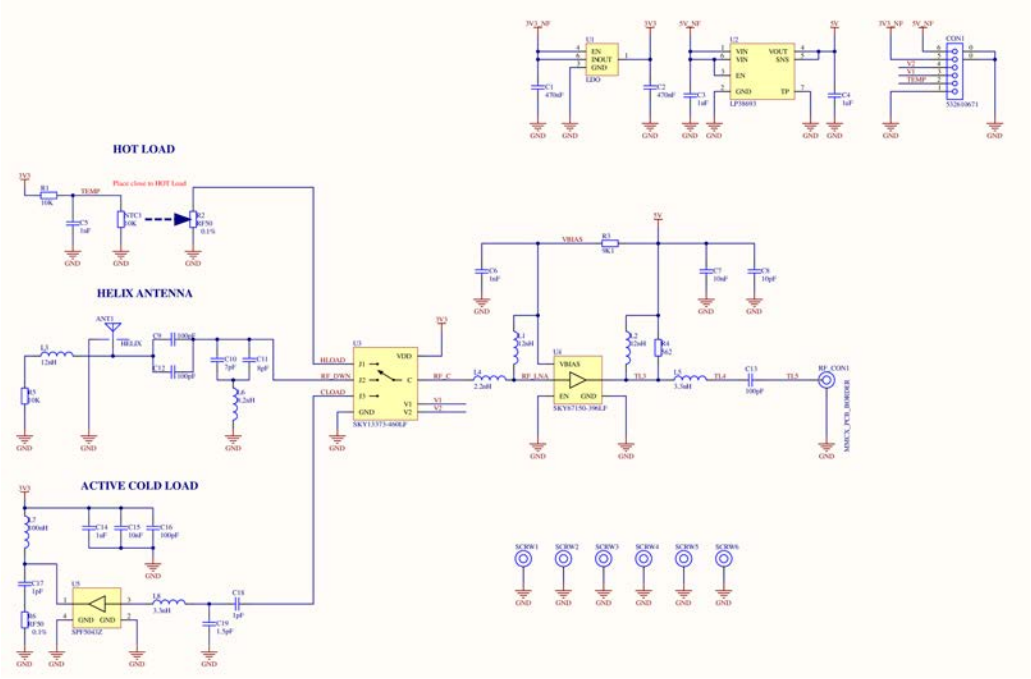

Figure B.1

B.2 FMPL-1 Motherboard Schematics

The FMPL-1 motherboard includes the Gumstix Overo computer and all the necessary connectors to interface with the NADS board and with the FMPL-1 daughterboard. Figure B.2 details all connections between this board and the other two boards.

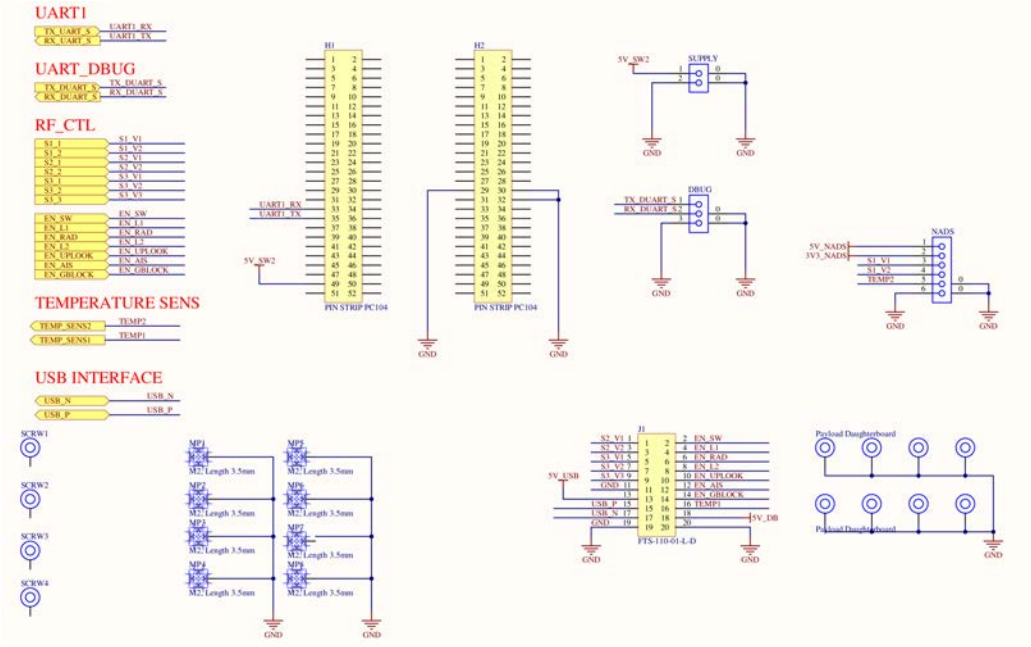

Figure B.2

Figure B.3 presents the schematic that interfaces the FMPL-1 Gumstix computer to the USB bus used to control the FMPL-1 SDR. Finally, Fig. B.4 presents the electrical supply converters, including several DC/DC converters for the different subsystems powered by the FMPL-1 motherboard.

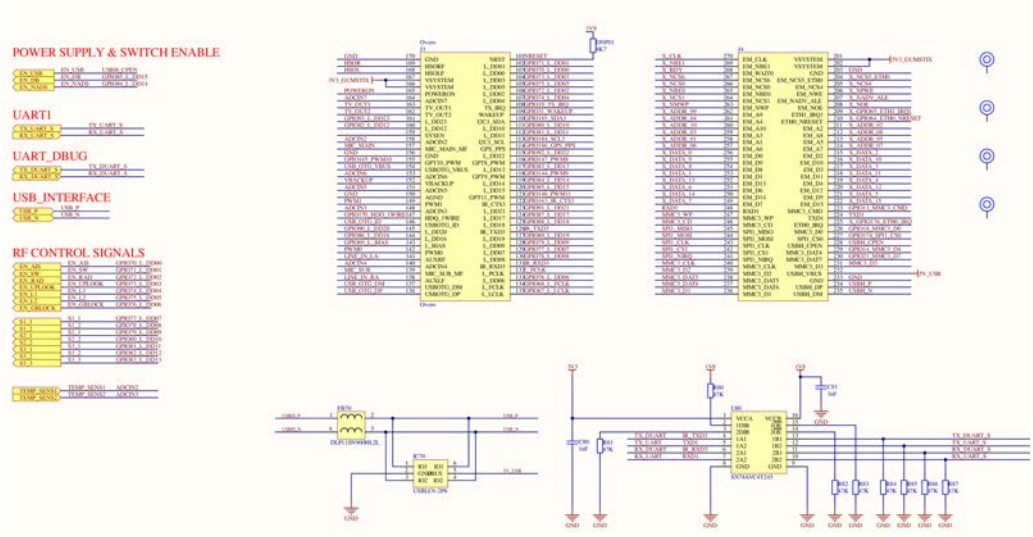

Figure B.3: Detailed schematic of the Gumstix pinout of the FMPL-1 motherboard.

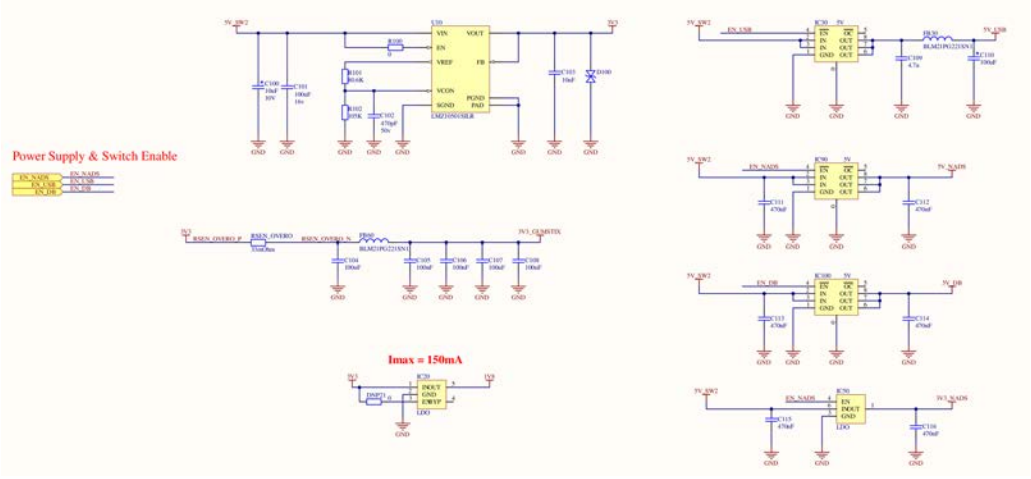

Figure B.4: Detailed schematic of the FMPL-1 motherboard electrical power system.

B.3 FMPL-1 Daughterboard Schematics

The FMPL-1 daughterboard is in charge of providing the proper amplification and filtering to each of the signals collected by the instrument. Moreover, as presented in Chapter 8, different switches are used to commute between the different modes (i.e., GNSS-R at L1 and L2, L-band radiometry, and AIS). Finally, this board also includes a low-cost SDR based on the RTL-SDR receiver [214], also detailed in this section.

Figure B.5 presents a high-level schematic of the interfaces of this board. Different input signals are filtered out in the RF-FE part, and then digitalized in the SDR. The final outcome is delivered through the J1 connector to the FMPL-1 daughterboard through USB.

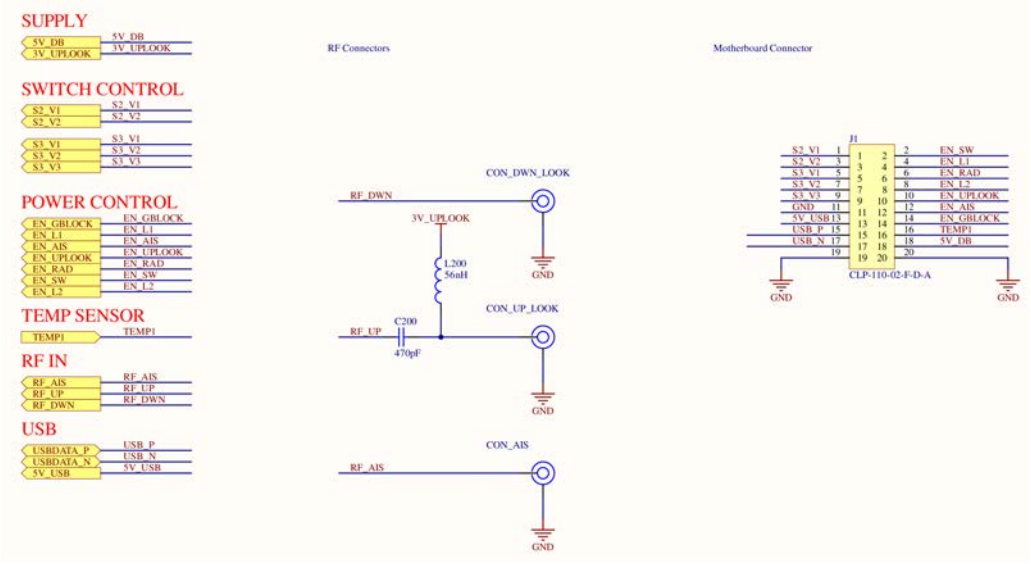

Figure B.5: Schematic representing the main interfaces of the FMPL-1 daughterboard.

B.3.1 Down-looking antenna path

The down-looking antenna reception chain schematic is detailed in Fig. B.6.

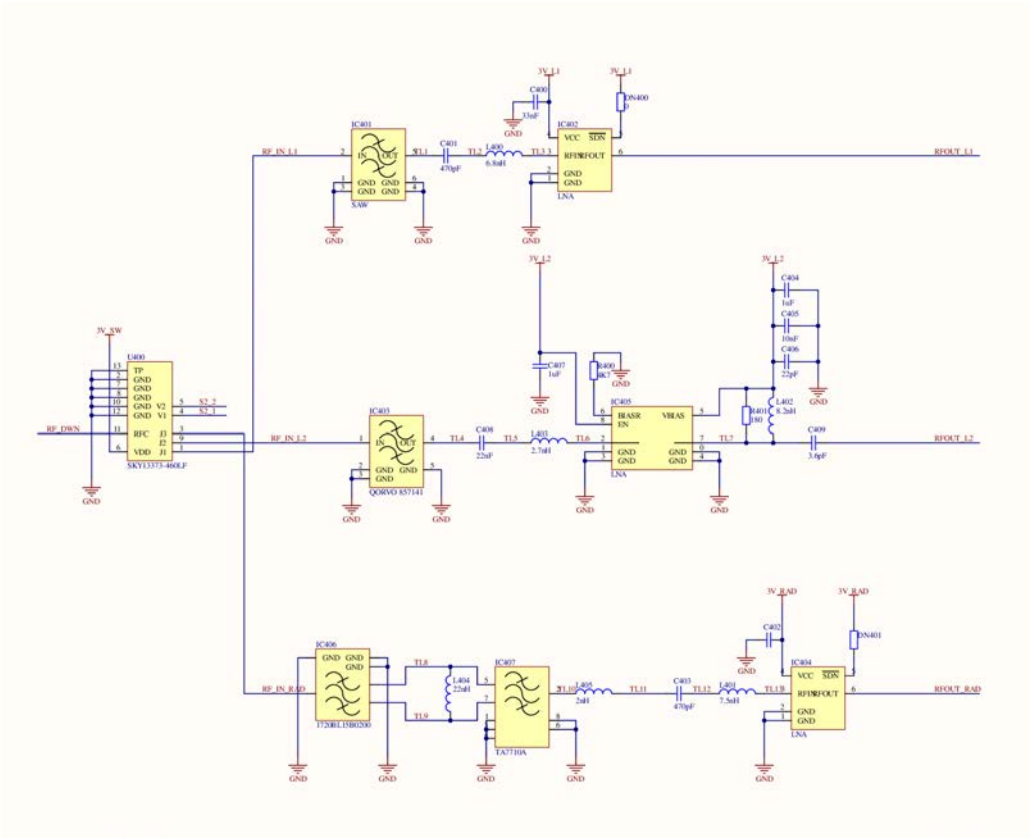

Figure B.6: Down-looking antenna filtering and amplification chains for the GPS L1 (top), GPS L2 (mid), and L-band radiometry (bottom) channels.

B.3.2 AIS antenna path

The AIS reception chain schematic is detailed in Fig. B.7.

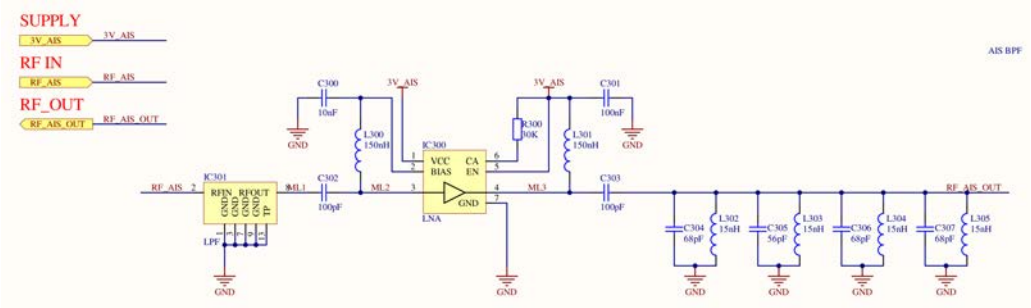

Figure B.7: AIS reception chain, including filtering and amplification chains.

B.3.3 Broadband amplifier

Finally, all signals are combined using a SP5T switch, the resulting signal is amplified by a broad-band amplifier, and then introduced into the SDR, as detailed in Fig. B.8.

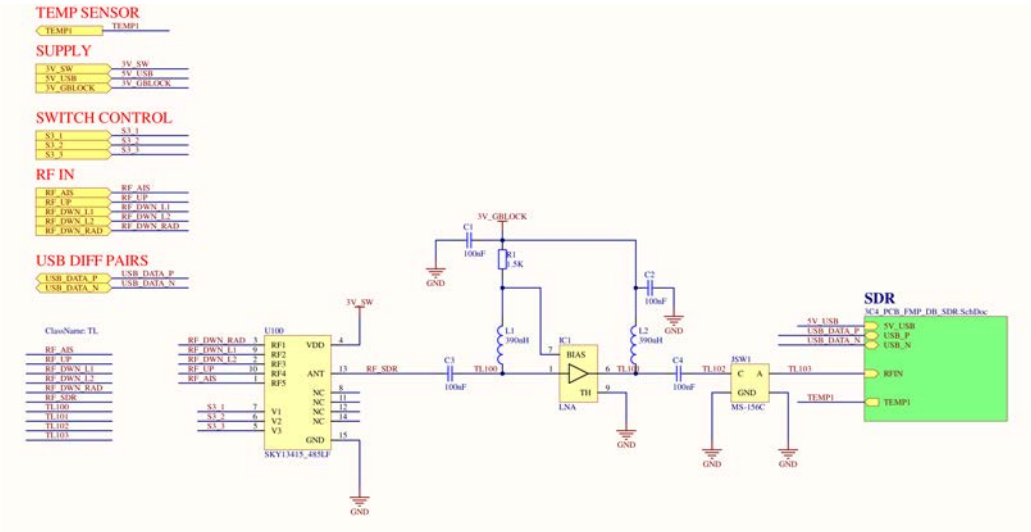

Figure B.8: SP5T switch to select the daughterboard mode, and a broadband amplifier used to compensate the switch losses.

B.3.4 Software Defined Radio

The schematic of the SDR is detailed in Fig B.9, and the electrical power system of the FMPL-1 daughterboard is presented in Fig. B.10.

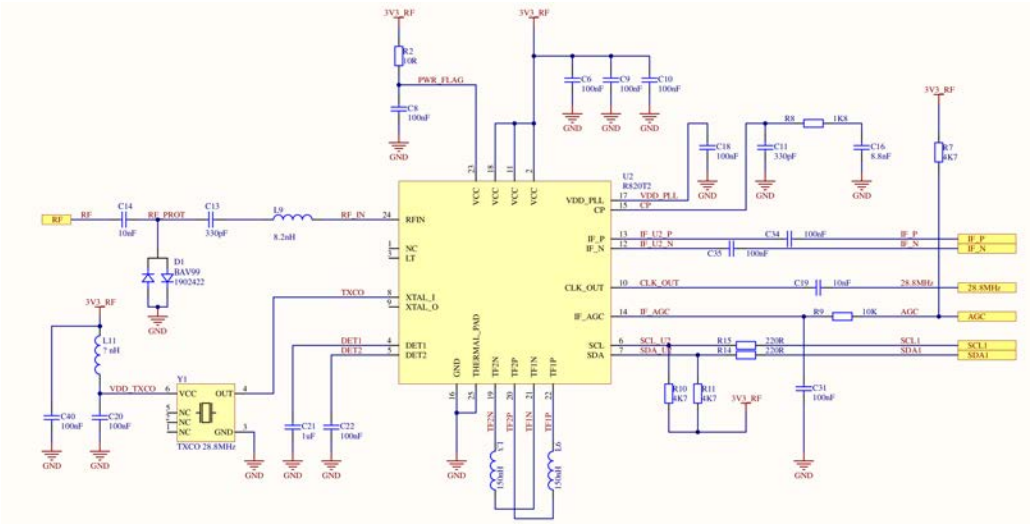

(a)

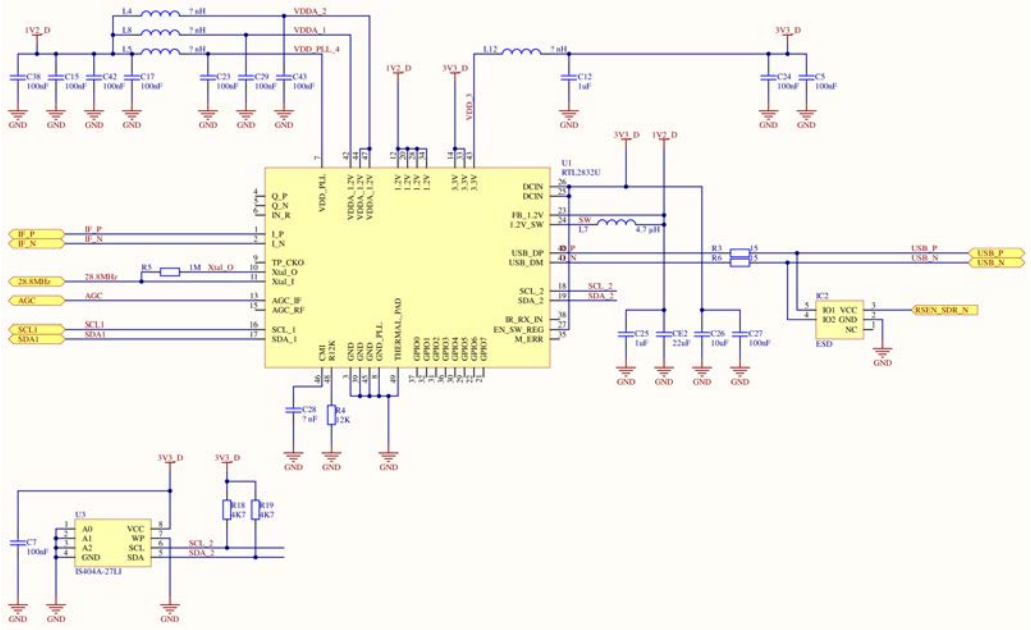

(b)

Figure B.9: (a) schematic of the R820T2 ADC and down-converter, and (b) schematic of the RTL2832U used to transfer the IF samples to the computer using USB protocol.

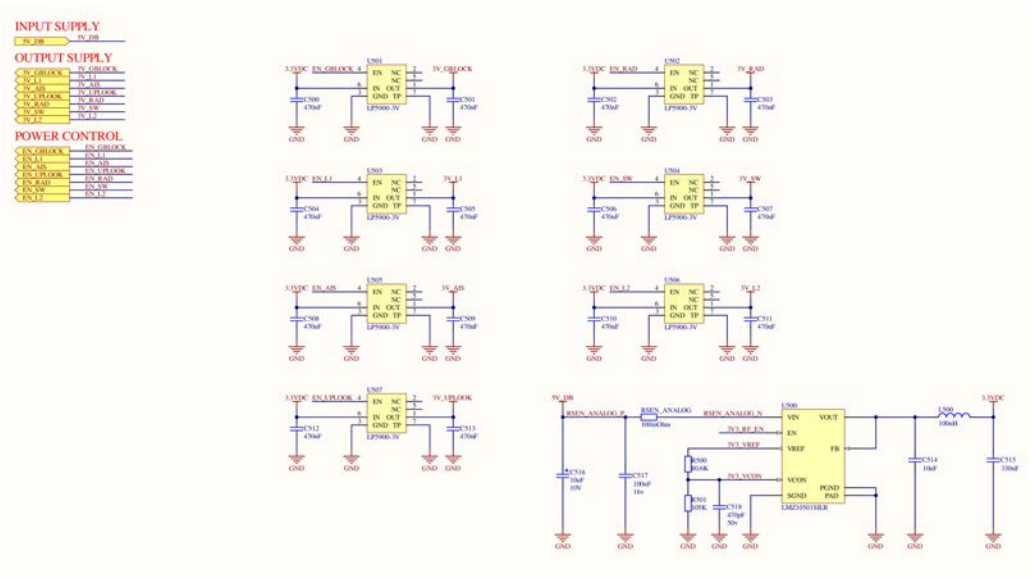

Figure B.10: Electrical power system of the FMPL-1 daughterboard, including all necessary Low-dropout voltage regulators to filter and isolate the power signal.

C

Appendix C

FMPL-2 Detailed Design, Integration, and Tests

This Appendix presents the hardware design, board schematics, and board layout files of the FMPL-2 payload. The work presented in this appendix is reproduced from internal documentation developed by Balamis S.L., the company that designed and manufactured the board. In addition, integration details of FMPL-2 are presented in this appendix, including thermal interfaces, center-of-mass analysis, and preliminary fit-checks. Finally, the results of the vibration test are presented in this appendix, detailing the resonances of the instrument and the vibration levels that the payload has withstood during the test.

C.1 Schematics

In this section, the schematics of the two RF-FE and interface boards designed and developed for the FMPL-2 payload are presented.

C.1.1 FMPL-2 RF-FE schematics

Figure C.1 presents the general schematic of the FMPL-2 RF-FE board.

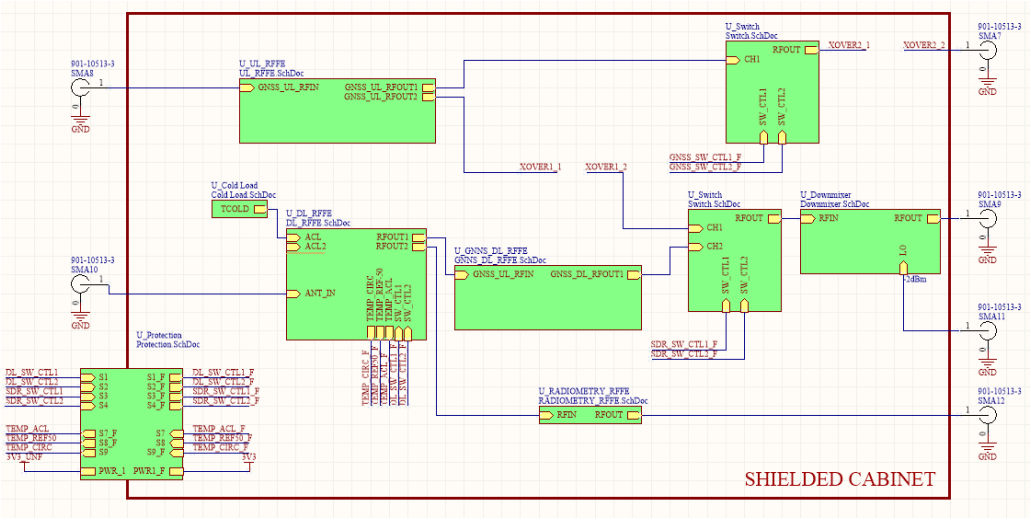

Figure C.1: General schematic of the RF-FE board.

Figure C.2 presents the schematic and the circuitry related to the isolator and the SP3T switch used to commute between the antenna and the different calibration loads. The last part of the schematic shows the first amplifier, covering both the L-band radiometry channel (1400-1427 MHz) to the GPS L1 channel (1575.42 MHz), and Fig. C.3 presents the schematic and circuitry of the radiometry chain, which is composed by a SAW filter and two LNAs.

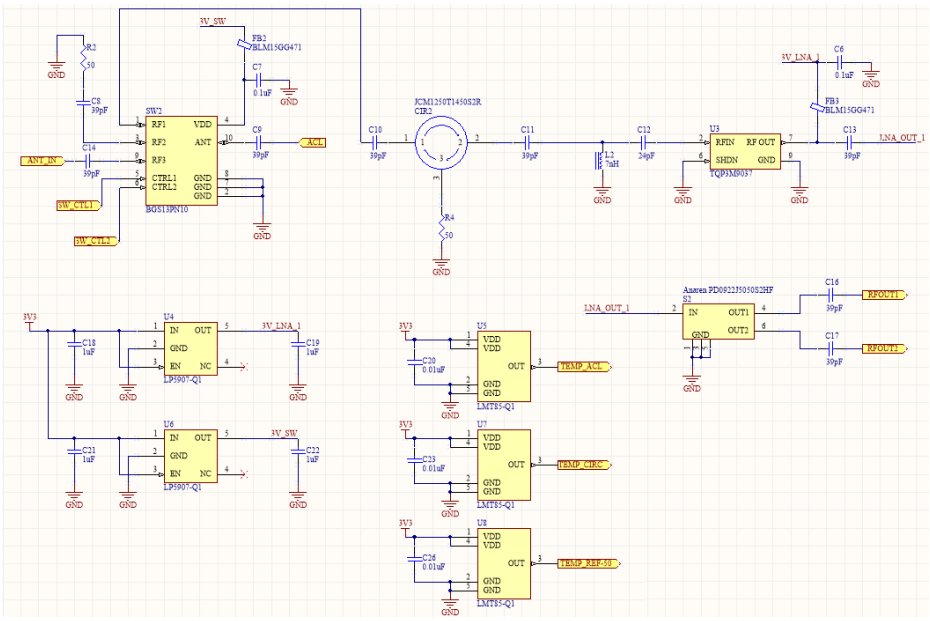

Figure C.2: Detailed schematic of the isolator, the SP3T switch used to calibrate the radiometer, and the first stage amplifier.

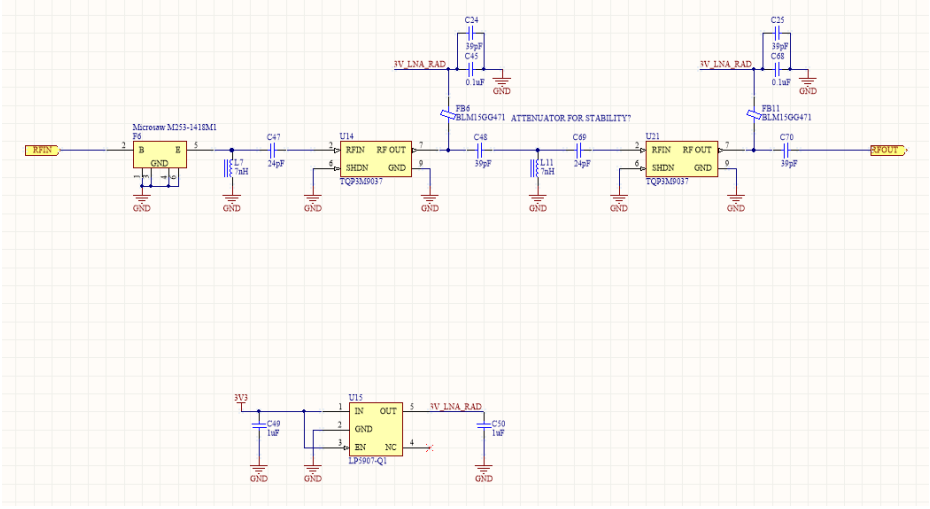

Figure C.3: Detailed schematic of the L-band radiometry amplification chain.

Figure C.4 presents the GNSS-R chain for both channels. Note that, the up-looking channel does not has the first stage amplifier presented in Fig. C.2, thus two LNAs are used.

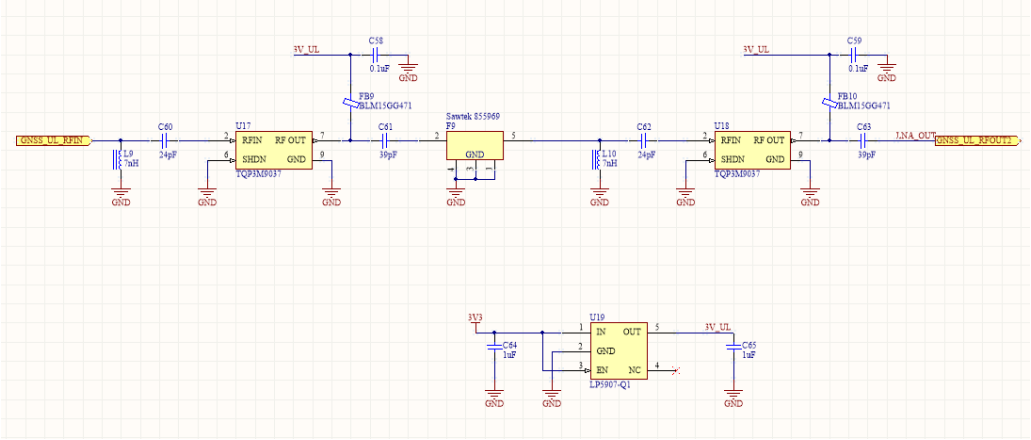

(a)

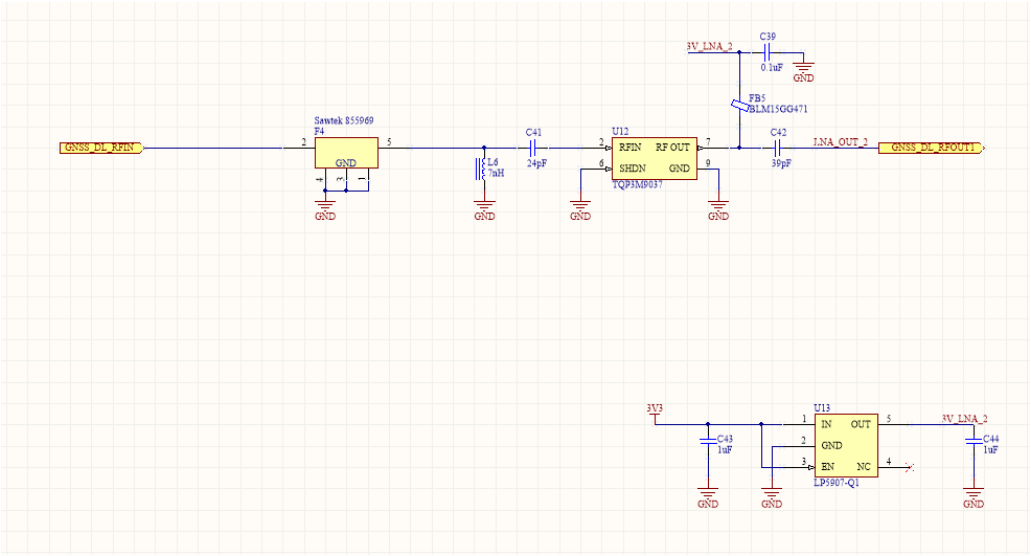

(b)

Figure C.4: Detailed schematic of the GNSS-R amplification chain for (a) the up-looking channel and (b) the down-looking channel.

Figure C.5 presents the schematic of the mixer circuitry used to down-convert the GNSS-R signal to the L-band radiometry frequency.

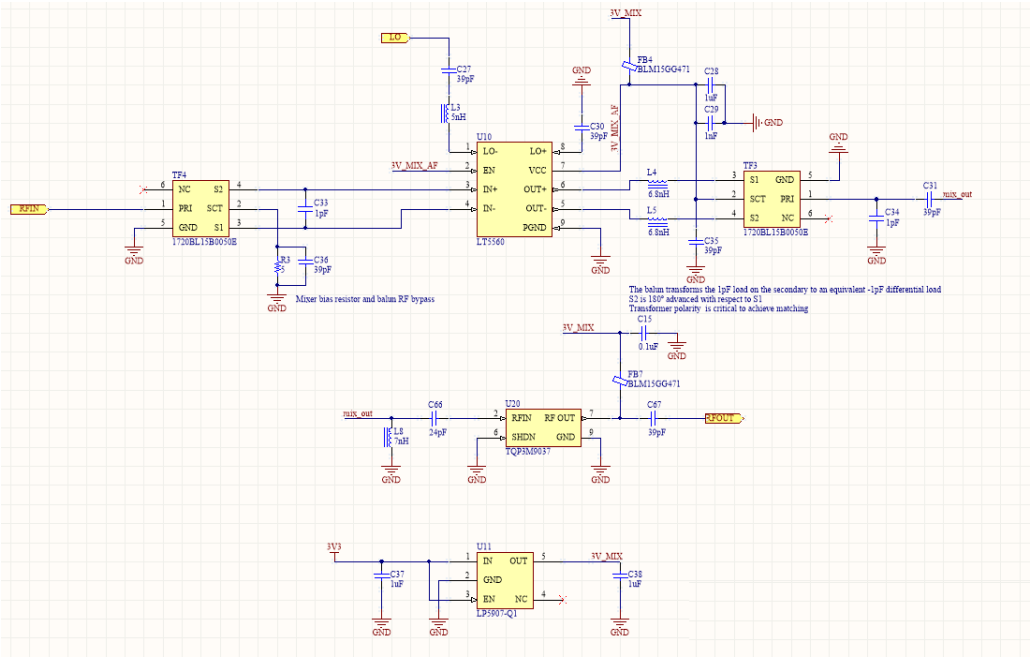

Figure C.5: Schematic of the GNSS-R down-conversion stage to 1413 MHz.

C.1.2 FMPL-2 Interface board schematics

Figure C.6 presents the schematic of the IB board, detailing the pinout of the thermistor reader and the Novatel OEM719.

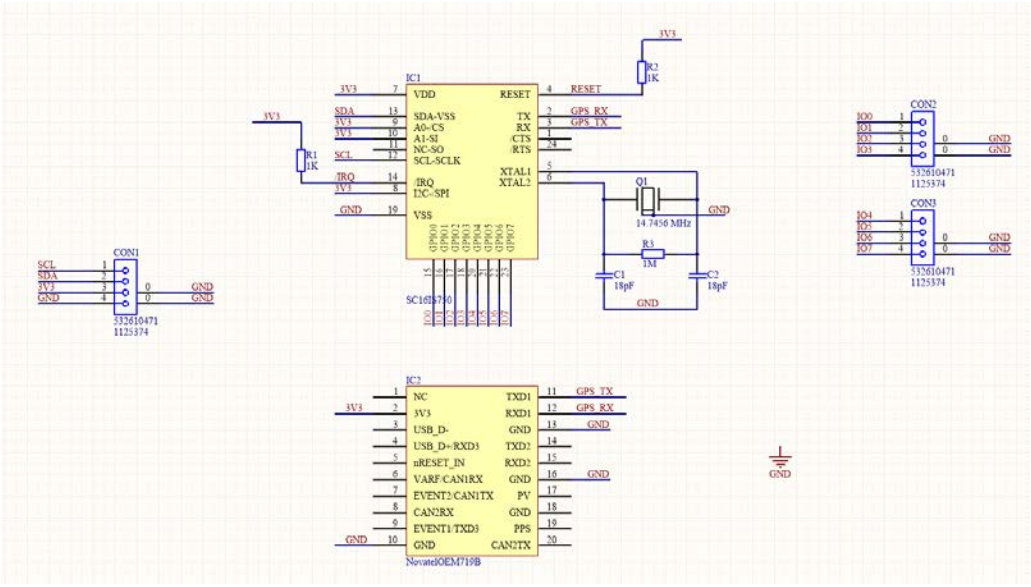

Figure C.6: Interface board schematic.

C.2 Board Layouts

In this section, the 3D board layout of both the RF-FE and the IB are presented in Figures C.7 and C.8, respectively.

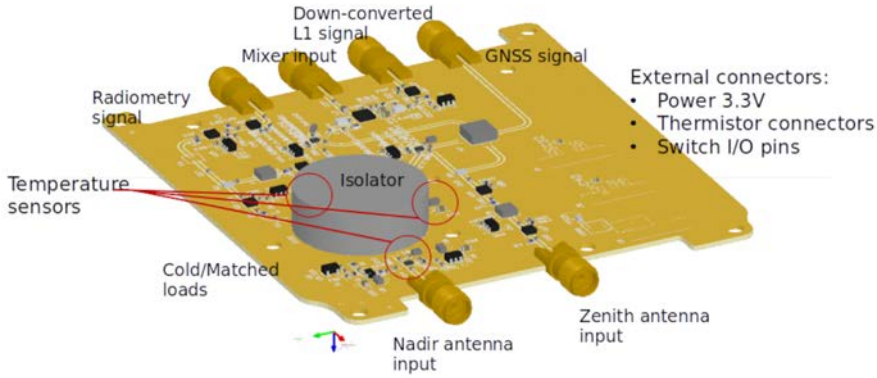

Figure C.7: Representative 3D CAD model of the FMPL-2 RF-FE board.

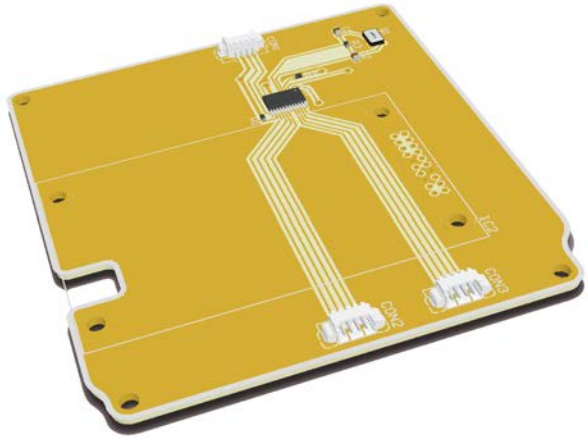

Figure C.8: Representative 3D CAD model of the FMPL-2 Interface Board.

C.3 Ambient Test Campaign

Figure C.9 present the result of the Electromagnetic Interference Test conducted in the UPC NanoSat-Lab facilities to ensure no harmful emissions are produced by the FMPL-2 instrument.

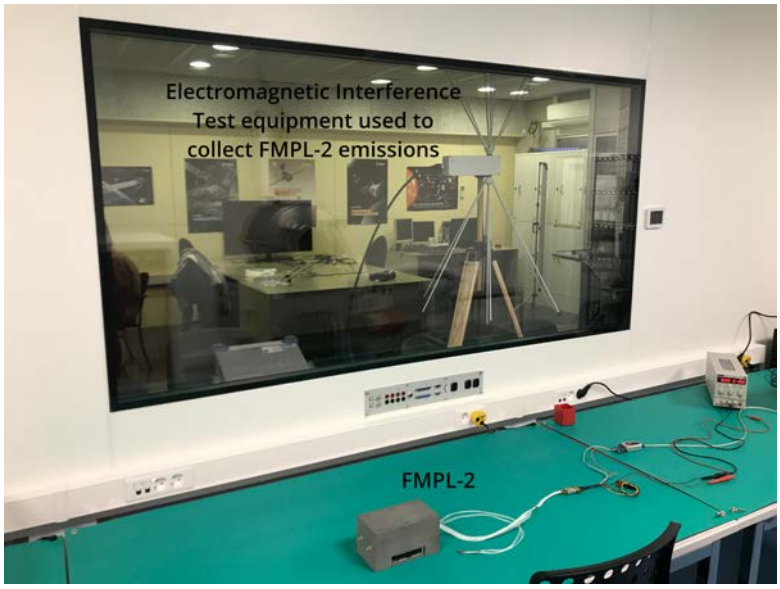

(a)

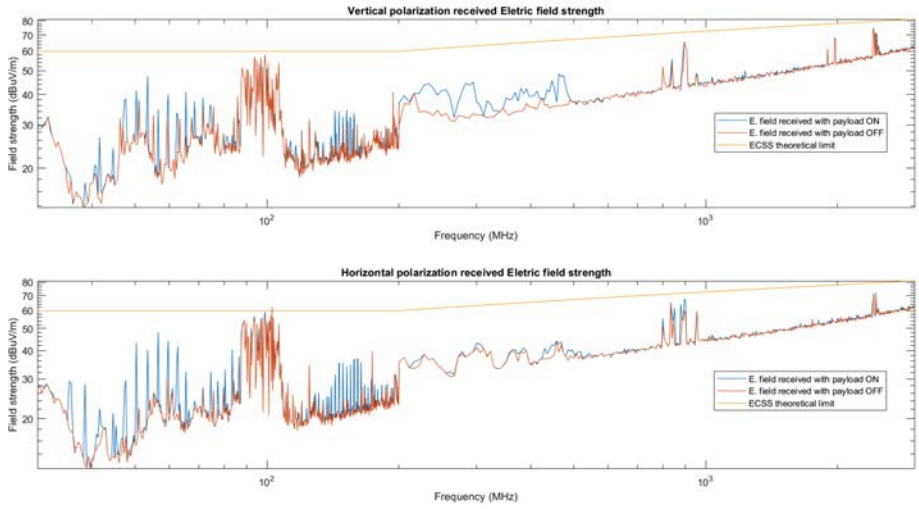

(b)

Figure C.9: (a) Electromagnetic Interference test conducted inside the UPC NanoSat-Lab clean room, and (b) the emissions collected by the test equipment while the payload was turned ON (blue) and OFF (orange).

C.4 Environmental Test Campaign

The environmental test campaign of FMPL-2 for TVAC conditions has been already presented in Chapter 9. In this case, the instrument is able to withstand the vacuum conditions under thermal stress. The second environmental test carried out to the FMPL-2 is the vibration or shake test. This test aims to demonstrate that the instrument can withstand the launch conditions without compromising the entire mission or the launch vehicle. For that reason, launch authorities issue different recommendations and vibration levels that the satellites shall withstand. In this case, one of the requirements is that the first mode (i.e., the first resonance) is always above 150 Hz.

C.4.1 Modal simulation

For new design, it is recommended, but not mandatory, a modal analysis to estimate the resonance frequencies from a simulation. For the FMPL-2 case, both the avionics stack and the aluminum box are simulated using ANSYS®. Figure C.10 shows the results of the modal analysis used to estimate the first resonance of both the FMPL-2 avionics stack and the FMPL-2 aluminum box.

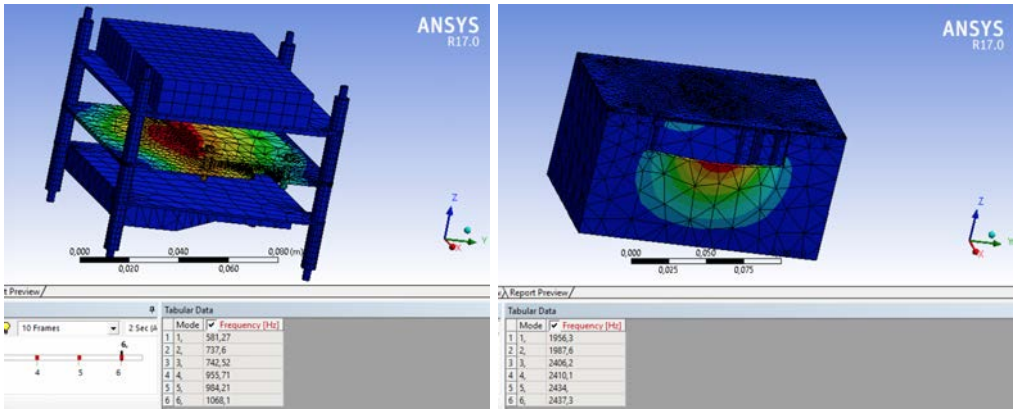

(a) **(b)**

Figure C.10: Modal simulation of (a) the FMPL-2 stack and (b) its aluminum box, showing the first resonance around ∼600 Hz.

C.4.2 Vibration test outcome

The vibration test aims to validate the previous modal analysis to validate that the resonance frequency is above 150 Hz. Moreover, the test aims to verify that the instrument is able to withstand the vibrations during launch. The vibration test is composed by three steps. First, a resonance search is performed, then a random vibration at levels specified by the launch authority, and finally a second resonance search is performed to check no resonances have been changed after the random vibration test.

Figures C.11, C.12, and C.13 present, for the X-, Y-, and Z-axis respectively, the random vibration test report, and the resonance survey before and after the random vibration test, respectively for each of the axis.

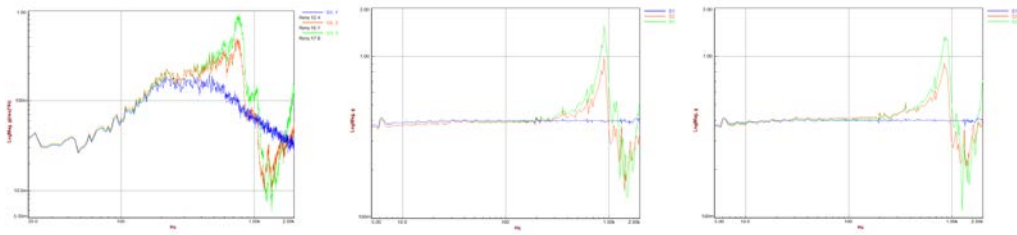

(a) **(b)** **(c)**

Figure C.11: (a) Random vibration profile used to test the FMPL-2 paylaod (X-axis - 12.4 g_{rms}), and (b) and (c) resonance surveys of the FMPL-2 payload conducted at 0.4 g along the X-axis (b) before the random vibration test, and (c) after the random vibration test. Measured in the UPC NanoSat-Lab shake table facility [233].

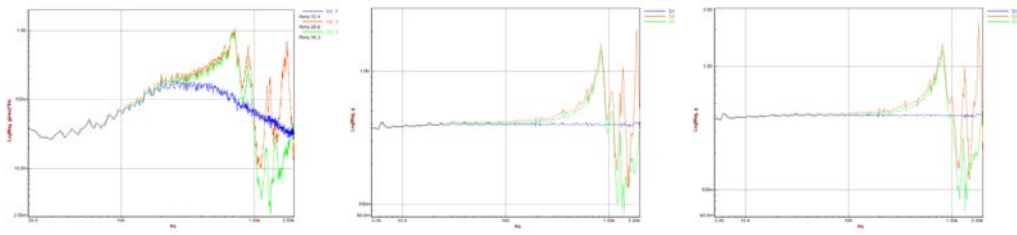

(a) **(b)** **(c)**

Figure C.12: Same as in Fig. C.11 but for the Y-axis.

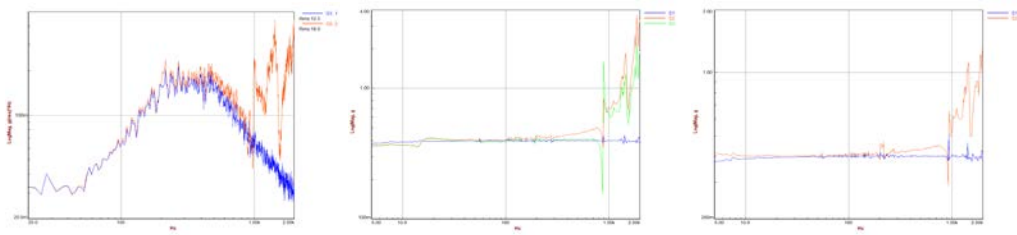

(a) **(b)** **(c)**

Figure C.13: Same as in Fig. C.11 but for the Z-axis.

D

Appendix D

FMPL-3 Detailed Design and Tests

This Appendix presents the hardware design, board schematics, and board layout files of the FMPL-3 payload. The work presented in this appendix is reproduced from internal documentation developed by Balamis S.L., the company that designed and manufactured the board. In addition, the results of environmental campaign shake test are presented in this appendix, detailing the resonances of the instrument and the vibration levels that the payload has withstood during the test.

D.1 Schematics

In this section, the schematics of the RF-FE board developed for the FMPL-3 payload are presented.

Figure D.1 presents the general schematic of the FMPL-3 RF-FE board. All modules are detailed, including the L5 chain, the VHF and UHF chains, the channel selector for the ionosphere and GNSS-R experiment, and the analog and digital interfaces of the board.

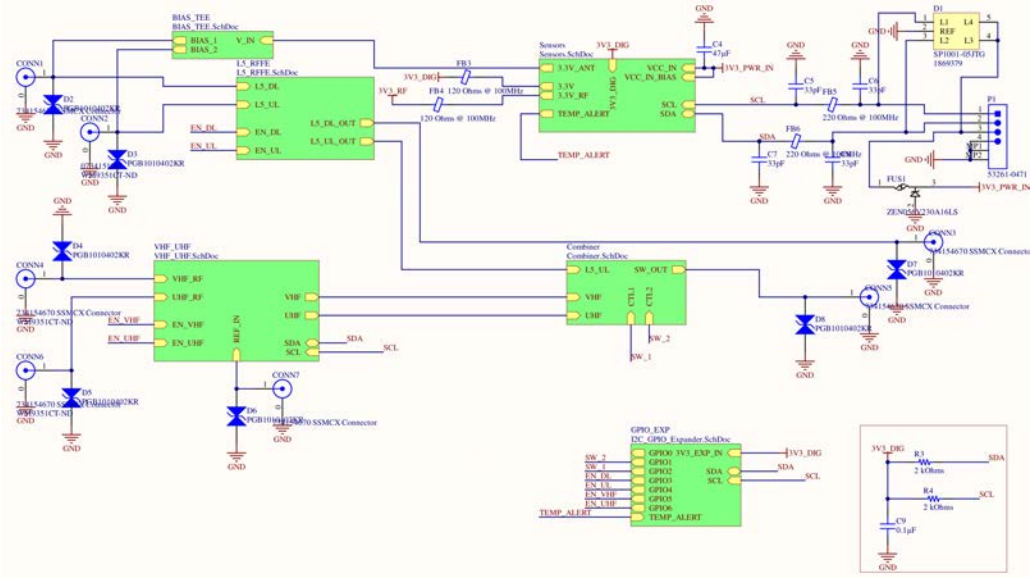

Figure D.1: High-level schematic of FMPL-3 RF-FE board.

Figure D.2 presents the both nadir and zenith-looking L5 chains. As it is seen, both chains are composed by the same amplifier and SAW filter. But in the zenith-looking chain an additional amplifier is used, as explained in Chapter 10.

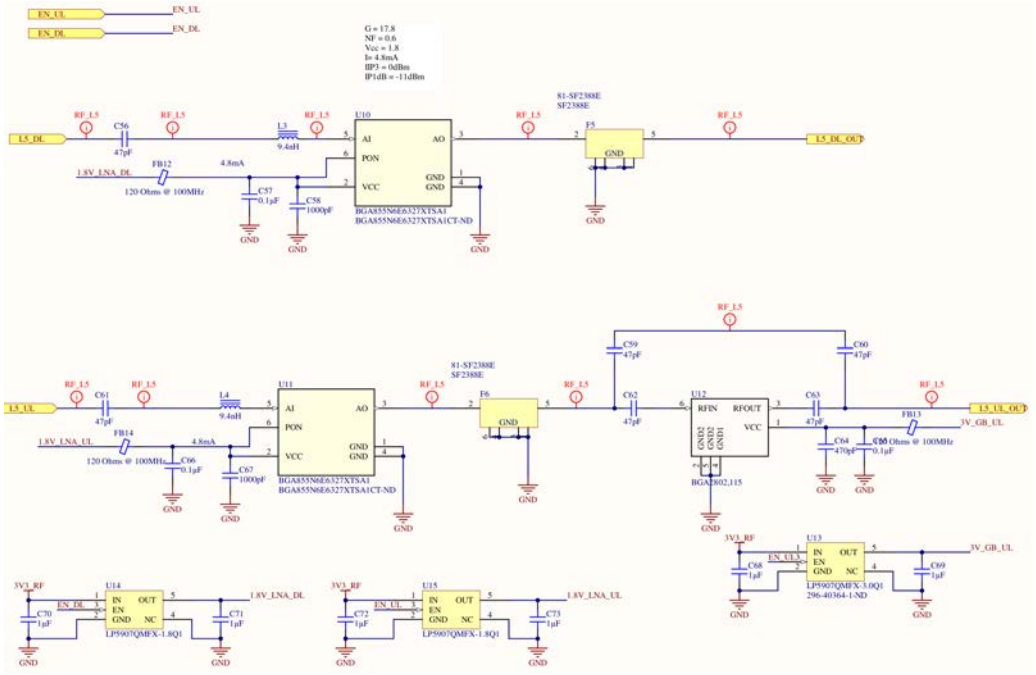

Figure D.2: L5 zenith and nadir-looking amplification and filtering RF chains. Including voltage regulation scheme.

Figure D.3 presents the high-level block diagram of both the VHF and the UHF amplification chains of the ionosphere experiment.

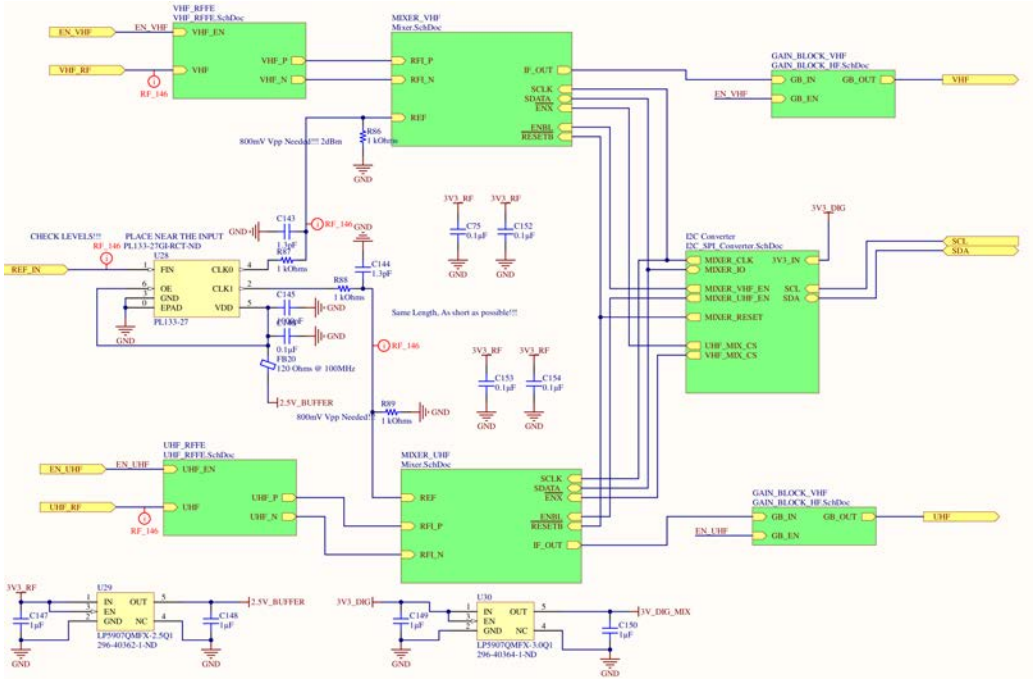

Figure D.3: High-level schematic of the VHF and the UHF amplification chains, including control signal for the mixers and voltage regulation scheme.

Figure D.4 presents the schematic of both VHF and UHF amplification and filtering chains.

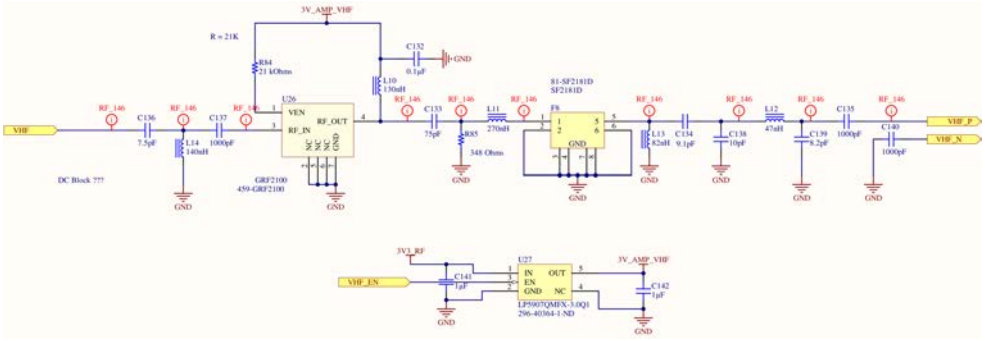

(a)

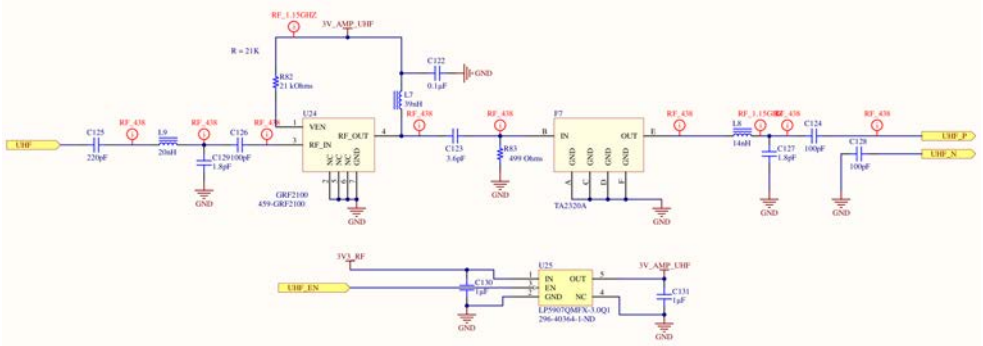

(b)

Figure D.4: (a) VHF and (b) amplification chains, including voltage regulation scheme.

Figure D.5 presents the schematic of the mixer circuit used in to up-convert the VHF and UHF signals to the L5 band. Note that, two mixers are used, one for the VHF and one for the UHF channel, but the circuit is the same. Thus, only one of the two mixers is presented.

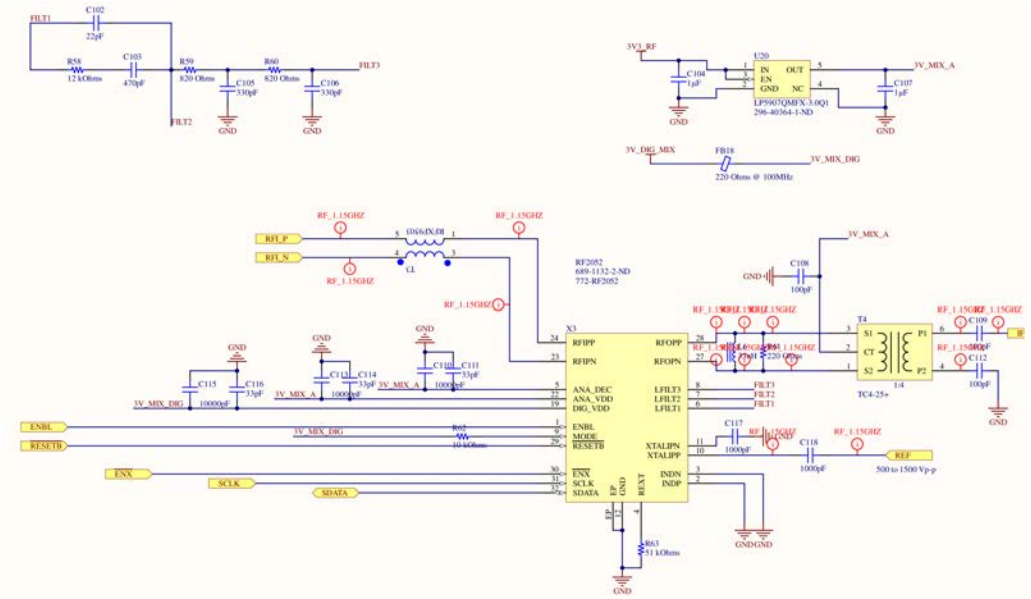

Figure D.5: Schematic of the mixer circuitry used to up-convert the VHF and the UHF signal to L5.

Figure D.6a presents the gain block amplification chain presented in Fig. D.4 (right side of the figure). Figure D.6b presents the combiner and SP3T circuit to select between GNSS-R (L5 zenith-looking signal) and ionosphere mode (VHF/UHF signal).

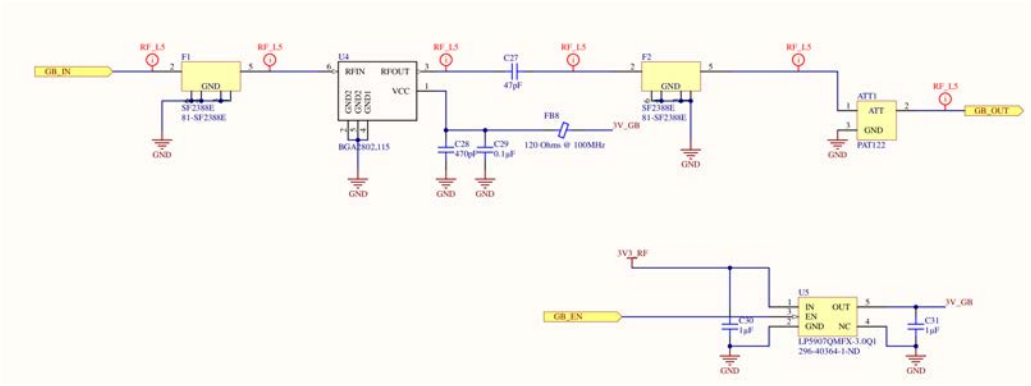

(a)

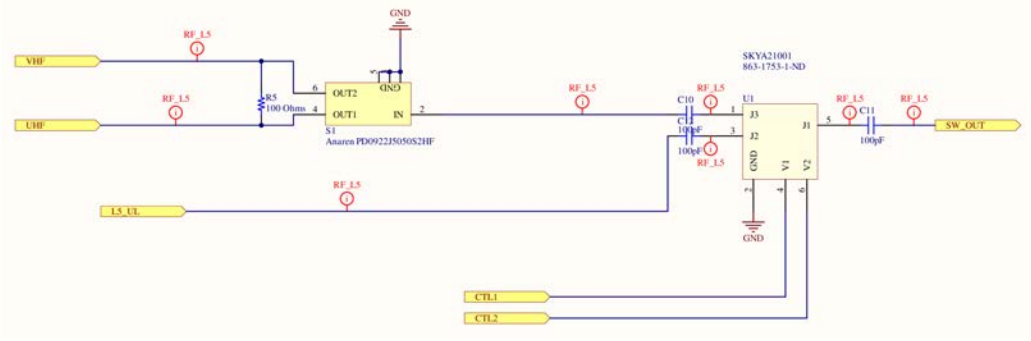

(b)

Figure D.6: (a) Gain block amplification chain used after the L5 up-conversion for both VHF and UHF bands, (b) combiner and channel selector between the VHF/UHF signal and the L5 zenith-looking signal.

D.2 Environmental Test Campaign: Vibration Test

The FMPL-3 is a particular instrument. The NanoSDR platform is shared with NSSTC to perform other experiments. Because of that, it was been decided to just conduct the environmental vibration campaign to the RF-FE module. Analogously to the FMPL-2 case, this board has undergone a random vibration test (8.2 g_{rms}) with to resonance surveys (at 0.4 g) to find its resonances, before and after the random test.

Figures D.7, D.8, and D.9 present, for the X-, Y-, and Z-axis respectively, the random

vibration test report, and the resonance survey before and after the random vibration test, respectively for each of the axis.

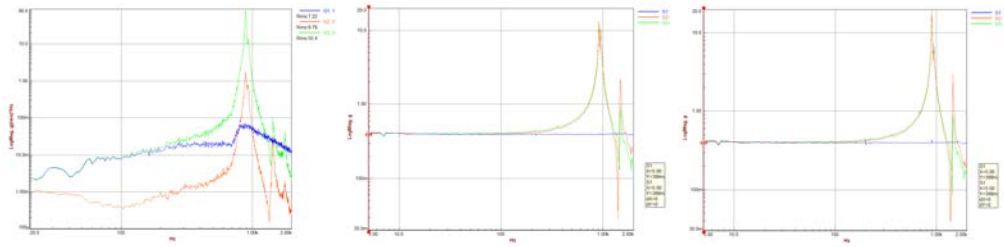

(a) **(b)** **(c)**

Figure D.7: (a) Random vibration profile used to test the FMPL-3 RF-FE module (X-axis - 12.4 g_{rms}), and (b) and (c) resonance surveys of the FMPL-2 payload conducted at 0.4 g along the X-axis (b) before the random vibration test, and (c) after the random vibration test. Measured in the UPC NanoSat-Lab shake table facility [233].

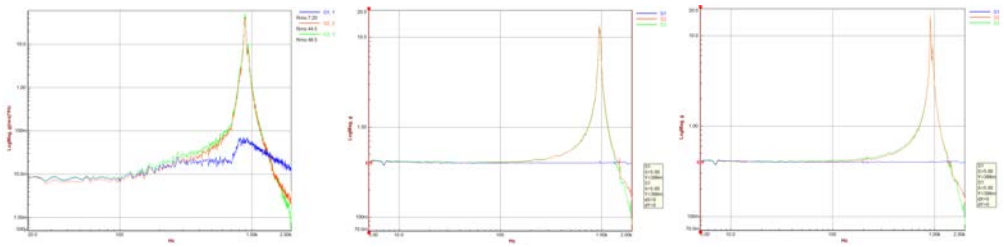

(a) **(b)** **(c)**

Figure D.8: Same as in Fig. D.7 but for the Z-axis.

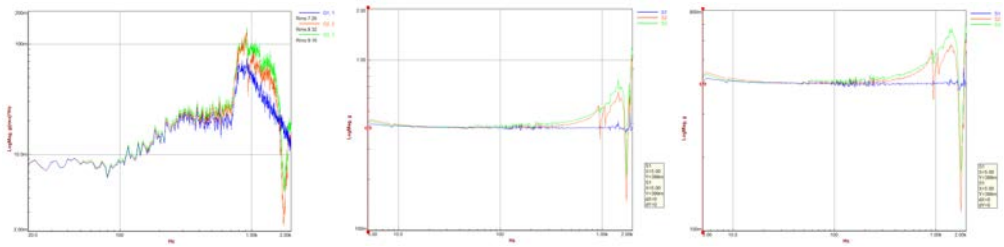

(a) **(b)** **(c)**

Figure D.9: Same as in Fig. D.7 but for the Z-axis.

Part VII

Bibliography and List of Publications

Bibliography

[1] GCOS, "What are essential climate variables?" Available at: https://gcos.wmo.int/en/essential-climate-variables/abouth. Last visited: 18 Jan 2021. (Cited on pages 4, 16, and 20.)

[2] D. G. Miralles, P. Gentine, S. I. Seneviratne, and A. J. Teuling, "Land-atmospheric feedbacks during droughts and heatwaves: state of the science and current challenges," *Annals of the New York Academy of Sciences*, vol. 1436, no. 1, pp. 19–35, Jun. 2018. (Cited on pages 4, 16, 110, and 256.)

[3] W. Emery and A. Camps, "The history of satellite remote sensing," in *Introduction to Satellite Remote Sensing*. Elsevier, 2017, pp. 1–42. [Online]. Available: https://doi.org/10.1016/b978-0-12-809254-5.00001-4 (Cited on pages xvii, 4, 10, 16, 17, 18, 19, 26, and 284.)

[4] A. Witze, "A timeline of Earth observation," *Nature*, Dec. 2007. (Cited on page 4.)

[5] The CubeSat Program - California Polytechnic State University, "Cubesat design specification rev. 13," Available: http://www.cubesat.org/resources. Last visited: Oct 07. 2019. (Cited on page 6.)

[6] NASA, "What are SmallSats and CubeSats?" Available: https://www.nasa.gov/content/what-are-smallsats-and-cubesats. Last visited: Jan 2021. (Cited on pages xvii and 7.)

[7] A. Camps, "Nanosatellites and applications to commercial and scientific missions," in *Satellites Missions and Technologies for Geosciences*. IntechOpen, Jul. 2020. [Online]. Available: https://doi.org/10.5772/intechopen.90039 (Cited on page 7.)

[8] SpaceWorks Enterprises, Inc., "Nano/microsatellite market forecast, 10th edition," Available at: https://www.spaceworks.aero/wp-content/uploads/Nano-Microsatellite-Market-Forecast-10th-Edition-2020.pdf. Last visited: 9 Dic. 2020. (Cited on page 7.)

[9] O. A. Weaver and J. P. Kerekes, "The role of large constellations of small satellites in emergency response situations," in *2015 IEEE International Geoscience and Remote Sensing Symposium (IGARSS)*, July 2015, pp. 4200–4203. (Cited on page 7.)

[10] Lemur-2, "Gunter's Space Page," Available at: https://space.skyrocket.de/doc_sdat/lemur-2.htm. Last visited: 3-Nov-2020. (Cited on pages 7 and 8.)

[11] "Nanosats database," Available: www.nanosats.eu. Last visited: Jan 2021. (Cited on pages xvii and 7.)

[12] E. Peral, S. Tanelli, S. Statham, S. Joshi, T. Imken, D. Price, J. Sauder, N. Chahat, and A. Williams, "RainCube: the first ever radar measurements from a CubeSat in space," *Journal of Applied Remote Sensing*, vol. 13, no. 3, pp. 1 – 13, 2019. (Cited on page 8.)

[13] W. J. Blackwell, "Radiometer development for small satellite microwave atmospheric remote sensing," in *2017 IEEE International Geoscience and Remote Sensing Symposium (IGARSS)*, 2017, pp. 267–270. (Cited on page 8.)

[14] S. Misra, S. Brown, R. Jarnot, C. Felten, R. Bendig, J. Kocz, C. McKelvey, C. Ball, C. Chen, A. O'Brien, G. Smith, M. Andrews, J. L. Garry, J. Johnson, P. Mohammed, J. Lucey, K. Horgan, Q. Bonds, C. Duran-Aviles, M. Solly, J. Peng, J. Piepmeier, D. Laczkowski, M. Pallas, and E. Krauss, "CubeSat Radiometer Radio Frequency Interference Technology (CubeRRT) Validation Mission: Enabling Future Resource-Constrained Science Missions," in *IGARSS 2018 - 2018 IEEE International Geoscience and Remote Sensing Symposium*, 2018, pp. 6308–6311. (Cited on page 8.)

[15] S. C. Reising, T. C. Gaier, C. D. Kummerow, S. Padmanabhan, B. H. Lim, S. T. Brown, C. Heneghan, C. V. Chandra, J. Olson, and W. Berg, "Temporal Experiment for Storms and Tropical Systems Technology Demonstration (TEMPEST-D): Reducing risk for 6U-Class nanosatellite constellations," in *2016 IEEE International Geoscience and Remote Sensing Symposium (IGARSS)*, 2016, pp. 5559–5560. (Cited on page 8.)

[16] W. J. Blackwell, S. Braun, R. Bennartz, C. Velden, M. DeMaria, R. Atlas, J. Dunion, F. Marks, R. Rogers, B. Annane, and R. V. Leslie, "An overview of the TROPICS NASA Earth Venture Mission," *Quarterly Journal of the Royal Meteorological Society*, vol. 144, no. S1, pp. 16–26, 2018. (Cited on page 8.)

[17] V. U. Zavorotny, S. Gleason, E. Cardellach, and A. Camps, "Tutorial on remote sensing using GNSS bistatic radar of opportunity," *IEEE Geoscience and Remote Sensing Magazine*, vol. 2, no. 4, pp. 8–45, Dec 2014. (Cited on pages 8, 10, 87, 148, 190, 191, and 248.)

[18] P. Jales, S. Esterhuizen, D. Masters, V. Nguyen, O. N. Correig, T. Yuasa, and J. Cartwright, "The new Spire GNSS-R satellite missions and products," in *Image and Signal Processing for Remote Sensing XXVI*, L. Bruzzone, F. Bovolo, and E. Santi, Eds., vol. 11533, International Society for Optics and Photonics. SPIE, 2020. (Cited on pages 8 and 28.)

[19] European Space Agency, "Introducing the newest ESA third party missions," Available at: https://earth.esa.int/eogateway/news/introducing-the-newest-esa-third-party-missions Last visited: 8-ene-2020. (Cited on pages 8 and 190.)

[20] M. E. Gorbunov and B. G. Kutuza, "Cosmos-243 as the starting point for the development of microwave radiometry methods of the earth's atmosphere and surface," *Izvestiya, Atmospheric and Oceanic Physics*, vol. 54, no. 3, pp. 275–281, May 2018. (Cited on page 10.)

[21] S. Bojinski, M. Verstraete, T. C. Peterson, C. Richter, A. Simmons, and M. Zemp, "The concept of essential climate variables in support of climate research, applications, and policy," *Bulletin of the American Meteorological Society*, vol. 95, no. 9, pp. 1431–1443, Sep. 2014. (Cited on page 10.)

[22] R. Onrubia, "Advanced GNSS-R Instruments for Altimetry and Scatterometry," Ph.D. dissertation, Universitat Politècnica de Catalunya, 2020. [Online]. Available: https://upcommons.upc.edu/handle/2117/328191 (Cited on pages 10, 34, 62, and 115.)

[23] D. Pascual, "Design and Performance Analysis of Advanced GNSS-R Instruments Back-end," Ph.D. dissertation, Universitat Politècnica de Catalunya, 2020. [Online]. Available: https://www.tdx.cat/handle/10803/670632 (Cited on pages xvii, 10, 24, 25, and 62.)

[24] K. Alhashmi, O. Al-Emam, and A. Hasbi, "NSSTC capabilities and the GNSSaS satellite project," in *Aeronautics and Aerospace Open Access Journal*, vol. 4, 2020, pp. 156–159. (Cited on pages 11, 35, 217, and 218.)

[25] A. Lang, S. Yang, and E. Kaas, "Sea ice thickness and recent Arctic warming," *Geophysical Research Letters*, vol. 44, 12 2016. (Cited on page 16.)

[26] E. Lancheros, A. Camps, H. Park, P. Sicard, A. Mangin, H. Matevosyan, and I. Lluch, "Gaps Analysis and Requirements Specification for the Evolution of Copernicus System for Polar Regions Monitoring: Addressing the Challenges in the Horizon 2020–2030," *Remote Sensing*, vol. 10, no. 7, 2018. (Cited on page 16.)

[27] C. Wasko and R. Nathan, "Influence of changes in rainfall and soil moisture on trends in flooding," *Journal of Hydrology*, vol. 575, pp. 432–441, Aug. 2019. (Cited on pages 16 and 110.)

[28] Y. H. Kerr, P. Waldteufel, J.-P. Wigneron, S. Delwart, F. Cabot, J. Boutin, M.-J. Escorihuela, J. Font, N. Reul, C. Gruhier, S. E. Juglea, M. R. Drinkwater, A. Hahne, M. Martín-Neira, and S. Mecklenburg, "The SMOS mission: New tool for monitoring key elements of the global water cycle," *Proceedings of the IEEE*, vol. 98, no. 5, pp. 666–687, May 2010. (Cited on pages 16, 110, and 271.)

[29] L. Kaleschke, X. Tian-Kunze, N. Maaß, M. Mäkynen, and M. Drusch, "Sea ice thickness retrieval from smos brightness temperatures during the arctic freeze-up period," *Geophysical Research Letters*, vol. 39, no. 5, 2012. (Cited on pages xxix, 16, 20, 140, 190, 256, and 257.)

[30] Z. Yongchao, K. Yu, J. Zou, and J. Wickert, "Sea Ice Detection Based on Differential Delay-Doppler Maps from UK TechDemoSat-1," *Sensors*, vol. 17, p. 1614, 07 2017. (Cited on pages 16 and 27.)

[31] European Space Agency, "Eight years of SMOS Arctic sea ice thickness level now available from SMOS Data dissemination portal," Available: https://earth.esa.int/web/guest/missions/esa-operational-eo-missions/smos/news/-/article/ eight-years-data-of-smos-arctic-sea-ice-thickness-level-now-available-from-smos-data-dissemination-portal. Last visited: Nov 11. 2019. (Cited on pages 16, 140, and 273.)

[32] A. Alonso-Arroyo, V. Zavorotny, and A. Camps, "Sea Ice Detection Using U.K. TDS-1 GNSS-R Data," *IEEE Transactions on Geoscience and Remote Sensing*, vol. PP, pp. 1–13, 06 2017. (Cited on pages 16, 27, 140, 257, and 265.)

[33] C. Chew, R. Shah, C. Zuffada, G. Hajj, D. Masters, and A. J. Mannucci, "Demonstrating soil moisture remote sensing with observations from the UK TechDemoSat-1 satellite mission," *Geophysical Research Letters*, vol. 43, no. 7, pp. 3317–3324, Apr. 2016. (Cited on pages 16 and 271.)

[34] A. Camps, M. Vall · llossera, H. Park, G. Portal, and L. Rossato, "Sensitivity of TDS-1 GNSS-R Reflectivity to Soil Moisture: Global and Regional Differences and Impact of Different Spatial Scales," *Remote Sensing*, vol. 10, no. 11, 2018. (Cited on pages 16, 27, and 271.)

[35] C. C. Chew and E. E. Small, "Soil moisture sensing using spaceborne GNSS reflections: Comparison of CyGNSS reflectivity to SMAP soil moisture," *Geophysical Research Letters*, vol. 45, no. 9, pp. 4049–4057, May 2018. (Cited on pages 16, 27, 28, 112, and 271.)

[36] Y. H. Kerr, P. Waldteufel, P. Richaume, J. P. Wigneron, P. Ferrazzoli, A. Mahmoodi, A. Al Bitar, F. Cabot, C. Gruhier, S. E. Juglea, D. Leroux, A. Mialon, and S. Delwart, "The SMOS soil moisture retrieval algorithm," *IEEE Transactions on Geoscience and Remote Sensing*, vol. 50, no. 5, pp. 1384–1403, 2012. (Cited on pages 16, 20, and 256.)

[37] F. Ulaby, R. Moore, and A. Fung, *Microwave Remote Sensing: Active and Passive*, ser. Artech House remote sensing library. Addison-Wesley Publishing Company, Advanced Book Program/World Science Division, 1981, no. v. 3. (Cited on pages 17 and 124.)

[38] R. H. Dicke, "The measurement of thermal radiation at microwave frequencies," *Review of Scientific Instruments*, vol. 17, no. 7, pp. 268–275, 1946. (Cited on page 17.)

[39] A. Camps, J. Font, M. Vall-llossera, C. Gabarro, I. Corbella, N. Duffo, F. Torres, S. Blanch, A. Aguasca, R. Villarino, L. Enrique, J. J. Miranda, J. J. Arenas, A. Julia, J. Etcheto, V. Caselles, A. Weill, J. Boutin, S. Contardo, R. Niclos, R. Rivas, S. C. Reising, P. Wursteisen, M. Berger, and M. Martin-Neira, "The WISE 2000 and 2001 field experiments in support of the SMOS mission: sea surface L-band brightness temperature observations and their application to sea surface salinity retrieval," *IEEE Transactions on Geoscience and Remote Sensing*, vol. 42, no. 4, pp. 804–823, 2004. (Cited on pages 20 and 35.)

[40] J. Font, A. Camps, A. Borges, M. Martín-Neira, J. Boutin, N. Reul, Y. H. Kerr, A. Hahne, and S. Mecklenburg, "SMOS: The challenging sea surface salinity measurement from space," *Proceedings of the IEEE*, vol. 98, no. 5, pp. 649–665, 2010. (Cited on page 20.)

[41] Y. Kerr, "L-band radiometry from space: SMOS, SMAP, AQUARIUS," 2017 2017. (Cited on page 20.)

[42] M. Spencer, Y. Kim, and S. Chan, "The soil moisture active/passive (SMAP) radar," in *2008 IEEE Radar Conference*. IEEE, May 2008. (Cited on pages xvii and 20.)

[43] H.-G. Kahle, M. Cocard, Y. Peter, A. Geiger, R. Reilinger, A. Barka, and G. Veis, "GPS-derived strain rate field within the boundary zones of the Eurasian, African, and Arabian Plates," *Journal of Geophysical Research: Solid Earth*, vol. 105, no. B10, pp. 23 353–23 370, oct 2000. (Cited on page 21.)

[44] V. Janssen, "Indirect Tracking of Drop Bears Using GNSS Technology," *Australian Geographer*, vol. 43, no. 4, pp. 445–452, dec 2012. (Cited on page 21.)

[45] R. Manson, R. Coleman, P. Morgan, and M. King, "Ice velocities of the Lambert Glacier from static GPS observations," *Earth, Planets and Space*, vol. 52, no. 11, pp. 1031–1036, jun 2014. (Cited on page 21.)

[46] G. A. Hajj, R. Ibañez-Meier, E. R. Kursinski, and L. J. Romans, "Imaging the ionosphere with the global positioning system," *International Journal of Imaging Systems and Technology*, vol. 5, no. 2, pp. 174–187, 1994. (Cited on page 21.)

[47] C. Rocken, Y.-H. Kuo, W. Schreiner, D. Hunt, S. Sokolovsky, and C. McCormick, "COSMIC System Description," *Terrestrial, Atmospheric and Oceanic Sciences*, vol. 11, no. 1, pp. 21–52, 2000. (Cited on page 21.)

[48] C. Hall and R. Cordey, "Multistatic Scatterometry," in *International Geoscience and Remote Sensing Symposium, 'Remote Sensing: Moving Toward the 21st Century'.*, vol. 1. IEEE, 1988, pp. 561–562. (Cited on page 21.)

[49] M. Martin-Neira, "A Passive Reflectometry and Interferometry System (PARIS): Application to Ocean Altimetry," *ESA Journal*, vol. 17, pp. 331–355, 1993. (Cited on page 21.)

[50] S. Katzberg and J. Garrison, "Utilizing GPS To Determine Ionospheric Delay Over the Ocean," *NASA Technical Memorandum 4750*, 1996. (Cited on page 21.)

[51] V. U. Zavorotny and A. G. Voronovich, "Scattering of GPS signals from the ocean with wind remote sensing application," *IEEE Transactions on Geoscience and Remote Sensing*, vol. 38, no. 2, pp. 951–964, March 2000. (Cited on pages 21, 22, and 86.)

[52] A. Perez, J. F. Munoz-Martin, J. Querol, H. Park, and A. Camps, "Implementation of a testbed for GNSS-R payload performance evaluation," *IEEE Journal of Selected Topics in Applied Earth Observations and Remote Sensing*, vol. 13, pp. 2708–2715, 2020. (Cited on pages xvii and 22.)

[53] A. Camps, G. Forte, I. Ramos, A. Alonso, P. Martinez, L. Crespo, and A. Alcayde, "Recent advances in land monitoring using GNSS-R techniques," in *2012 Workshop on Reflectometry Using GNSS and Other Signals of Opportunity (GNSS+R)*. IEEE, oct 2012, pp. 1–4. (Cited on pages xvii, 23, and 33.)

[54] A. Camps, H. Park, E. Valencia i Domenech, D. Pascual, F. Martin, A. Rius, S. Ribo, J. Benito, A. Andres-Beivide, P. Saameno, G. Staton, M. Martin-Neira, S. DAddio, and P. Willemsen, "Optimization and Performance Analysis of Interferometric GNSS-R Altimeters: Application to the PARIS IoD Mission," *IEEE Journal of Selected Topics in Applied Earth Observations and Remote Sensing*, vol. 7, no. 5, pp. 1436–1451, may 2014. (Cited on pages 23, 32, 41, 45, 80, 84, and 247.)

[55] J. W. Betz, "Binary Offset Carrier Modulations for Radionavigation," *Journal Of The Institute Of Navigation*, vol. 48, no. 4, pp. 227–246, dec 2002. (Cited on page 24.)

[56] D. Pascual, A. Camps, F. Martin, H. Park, A. A. Arroyo, and R. Onrubia, "Precision Bounds in GNSS-R Ocean Altimetry," *IEEE Journal of Selected Topics in Applied Earth Observations and Remote Sensing*, vol. 7, no. 5, pp. 1416–1423, may 2014. (Cited on page 24.)

[57] D. Pascual, H. Park, A. Camps, A. A. Arroyo, and R. Onrubia, "Simulation and analysis of GNSS-R composite waveforms using GPS and galileo signals," *IEEE Journal of Selected Topics in Applied Earth Observations and Remote Sensing*, vol. 7, no. 5, pp. 1461–1468, may 2014. (Cited on page 24.)

[58] M. Unwin, S. Gleason, and M. Brennan, "The Space GPS Reflectometry Experiment on the UK Disaster Monitoring Constellation Satellite," in *Proceedings of the 16th International Technical Meeting of the Satellite Division of The Institute of Navigation (ION GPS/GNSS 2003)*, Portland, OR, 2003, p. 2656. (Cited on page 27.)

[59] S. Gleason, S. Hodgart, Y. Sun, C. Gommenginger, S. Mackin, M. Adjrad, and M. Unwin, "Detection and processing of bistatically reflected GPS signals from low earth orbit for the purpose of ocean remote sensing," *IEEE Transactions on Geoscience and Remote Sensing*, vol. 43, no. 6, pp. 1229–1241, jun 2005. (Cited on page 27.)

[60] M. Unwin, R. d. V. Van Steenwijk, C. Gommenginger, C. Mitchell, and S. Gao, "The SGR-ReSI - A New Generation of Space GNSS Receiver for Remote Sensing," in *Proceedings of the 23rd International Technical Meeting of The Satellite Division of the Institute of Navigation (ION GNSS 2010)*, sep 2010, pp. 1061–1067. (Cited on page 27.)

[61] N. Rodriguez-Alvarez, B. Holt, S. Jaruwatanadilok, E. Podest, and K. C. Cavanaugh, "An Arctic sea ice multi-step classification based on GNSS-R data from the TDS-1 mission," *Remote Sensing of Environment*, vol. 230, p. 111202, 2019. (Cited on page 27.)

[62] M. P. Clarizia, C. S. Ruf, P. Jales, and C. Gommenginger, "Spaceborne GNSS-R Minimum Variance Wind Speed Estimator," *IEEE Transactions on Geoscience and Remote Sensing*, vol. 52, no. 11, pp. 6829–6843, nov 2014. (Cited on page 27.)

[63] E. Santi, S. Paloscia, S. Pettinato, G. Fontanelli, M. P. Clarizia, D. Comite, L. Dente, L. Guerriero, N. Pierdicca, and N. Floury, "Remote sensing of forest biomass using

gnss reflectometry," *IEEE Journal of Selected Topics in Applied Earth Observations and Remote Sensing*, vol. 13, pp. 2351–2368, 2020. (Cited on pages 27, 110, 111, 130, and 134.)

[64] H. Carreno-Luengo, G. Luzi, and M. Crosetto, "Above-Ground Biomass Retrieval over Tropical Forests: A Novel GNSS-R Approach with CyGNSS," *Remote Sensing*, vol. 12, no. 9, p. 1368, Apr. 2020. (Cited on pages 27, 43, 110, 111, 130, and 131.)

[65] N. Rodriguez-Alvarez, X. Bosch-Lluis, A. Camps, A. Aguasca, M. Vall-llossera, E. Valencia, I. Ramos-Perez, and H. Park, "Review of crop growth and soil moisture monitoring from a ground-based instrument implementing the interference pattern GNSS-R technique," *Radio Science*, vol. 46, no. 6, 2011. (Cited on pages 27 and 148.)

[66] C. Yin, E. Lopez-Baeza, M. Martin-Neira, R. Fernandez-Moran, L. Yang, E. A. Navarro-Camba, A. Egido, A. Mollfulleda, W. Li, Y. Cao, B. Zhu, and D. Yang, "Intercomparison of soil moisture retrieved from GNSS-R and from passive L-band radiometry at the Valencia Anchor Station," *Sensors*, vol. 19, no. 8, p. 1900, Apr. 2019. (Cited on page 27.)

[67] A. Alonso-Arroyo, A. Camps, A. Monerris, C. Rudiger, J. P. Walker, G. Forte, D. Pascual, H. Park, and R. Onrubia, "The light airborne reflectometer for GNSS-R observations (LARGO) instrument: Initial results from airborne and Rover field campaigns," in *2014 IEEE Geoscience and Remote Sensing Symposium*. IEEE, jul 2014, pp. 4054–4057. (Cited on pages 27 and 33.)

[68] A. Egido, S. Paloscia, E. Motte, L. Guerriero, N. Pierdicca, M. Caparrini, E. Santi, G. Fontanelli, and N. Floury, "Airborne GNSS-R Polarimetric Measurements for Soil Moisture and Above-Ground Biomass Estimation," *IEEE Journal of Selected Topics in Applied Earth Observations and Remote Sensing*, vol. 7, no. 5, pp. 1522–1532, may 2014. (Cited on page 27.)

[69] A. Camps, H. Park, J. Castellví, J. Corbera, and E. Ascaso, "Single-pass soil moisture retrievals using GNSS-R: Lessons learned," *Remote Sensing*, vol. 12, no. 12, p. 2064, Jun. 2020. (Cited on pages 27, 33, 111, 112, 122, 252, 271, and 283.)

[70] A. Camps, H. Park, M. Pablos, G. Foti, C. P. Gommenginger, P. Liu, and J. Judge, "Sensitivity of GNSS-R Spaceborne Observations to Soil Moisture and Vegetation," *IEEE Journal of Selected Topics in Applied Earth Observations and Remote Sensing*, vol. 9, no. 10, pp. 4730–4742, 2016. (Cited on pages 27, 110, 130, 134, and 271.)

[71] A. Calabia, I. Molina, and S. Jin, "Soil moisture content from GNSS reflectometry using dielectric permittivity from Fresnel reflection coefficients," *Remote Sensing*, vol. 12, no. 1, p. 122, Jan. 2020. (Cited on pages 27 and 121.)

[72] K. Edokossi, A. Calabia, S. Jin, and I. Molina, "GNSS-Reflectometry and remote sensing of soil moisture: A review of measurement techniques, methods, and applications," *Remote Sensing*, vol. 12, no. 4, p. 614, Feb. 2020. (Cited on pages 27 and 279.)

[73] M. P. Clarizia, N. Pierdicca, F. Costantini, and N. Floury, "Analysis of CyGNSS Data for Soil Moisture Retrieval," *IEEE Journal of Selected Topics in Applied Earth*

Observations and Remote Sensing, vol. 12, no. 7, pp. 2227–2235, 2019. (Cited on pages 27, 28, 110, and 112.)

[74] C. Chew and E. Small, "Description of the UCAR/CU soil moisture product," *Remote Sensing*, vol. 12, no. 10, p. 1558, May 2020. (Cited on pages 27, 110, and 271.)

[75] M. Unwin, P. Jales, P. Blunt, S. Duncan, M. Brummitt, and C. Ruf, "The SGR-ReSI and its application for GNSS reflectometry on the NASA EV-2 CyGNSS mission," in *2013 IEEE Aerospace Conference*. IEEE, mar 2013, pp. 1–6. (Cited on pages 27 and 275.)

[76] C. S. Ruf, S. Gleason, Z. Jelenak, S. Katzberg, A. Ridley, R. Rose, J. Scherrer, and V. Zavorotny, "The CyGNSS nanosatellite constellation hurricane mission," in *International Geoscience and Remote Sensing Symposium (IGARSS)*. IEEE, jul 2012, pp. 214–216. (Cited on page 27.)

[77] C. Ruf, M. Unwin, J. Dickinson, R. Rose, D. Rose, M. Vincent, and A. Lyons, "CyGNSS: Enabling the Future of Hurricane Prediction [Remote Sensing Satellites]," *IEEE Geoscience and Remote Sensing Magazine*, vol. 1, no. 2, pp. 52–67, jun 2013. (Cited on page 27.)

[78] C. S. Ruf, S. Gleason, and D. S. McKague, "Assessment of CyGNSS wind speed retrieval uncertainty," *IEEE Journal of Selected Topics in Applied Earth Observations and Remote Sensing*, vol. 12, no. 1, pp. 87–97, 2019. (Cited on page 27.)

[79] Q. Yan, W. Huang, S. Jin, and Y. Jia, "Pan-tropical soil moisture mapping based on a three-layer model from CyGNSS GNSS-R data," *Remote Sensing of Environment*, vol. 247, p. 111944, Sep. 2020. (Cited on pages xv, 27, 28, 110, 111, 112, 122, 129, 271, 275, 281, 285, and 287.)

[80] V. Senyurek, F. Lei, D. Boyd, M. Kurum, A. C. Gurbuz, and R. Moorhead, "Machine learning-based CyGNSS soil moisture estimates over ISMN sites in CONUS," *Remote Sensing*, vol. 12, no. 7, p. 1168, Apr. 2020. (Cited on pages 27, 28, 110, and 275.)

[81] M. M. Al-Khaldi, J. T. Johnson, A. J. O'Brien, A. Balenzano, and F. Mattia, "Time-Series Retrieval of Soil Moisture Using CyGNSS," *IEEE Transactions on Geoscience and Remote Sensing*, vol. 57, no. 7, pp. 4322–4331, 2019. (Cited on pages 28, 110, and 112.)

[82] C. Jing, X. Niu, C. Duan, F. Lu, G. Di, and X. Yang, "Sea surface wind speed retrieval from the first chinese GNSS-R mission: Technique and preliminary results," *Remote Sensing*, vol. 11, no. 24, p. 3013, Dec. 2019. (Cited on page 28.)

[83] D. M. Skapura, *Building Neural Networks*. USA: ACM Press/Addison-Wesley Publishing Co., 1995. (Cited on page 28.)

[84] D. J. Lary, G. K. Zewdie, X. Liu, D. Wu, E. Levetin, R. J. Allee, N. Malakar, A. Walker, H. Mussa, A. Mannino, and D. Aurin, *Machine Learning Applications for Earth Observation*. Cham: Springer International Publishing, 2018, pp. 165–218. (Cited on pages xviii, 28, and 29.)

[85] N. J. Rodriguez-Fernandez, F. Aires, P. Richaume, Y. H. Kerr, C. Prigent, J. Kolassa, F. Cabot, C. Jimenez, A. Mahmoodi, and M. Drusch, "Soil moisture retrieval using neural networks: Application to SMOS," *IEEE Transactions on Geoscience and Remote Sensing*, vol. 53, no. 11, pp. 5991–6007, Nov. 2015. (Cited on pages 28, 111, and 275.)

[86] E. Santi, S. Paloscia, S. Pettinato, and G. Fontanelli, "A prototype ANN based algorithm for the soil moisture retrieval from L-band in view of the incoming SMAP mission," in *2014 13th Specialist Meeting on Microwave Radiometry and Remote Sensing of the Environment (MicroRad)*, 2014, pp. 5–9. (Cited on page 28.)

[87] K. H. Breen, S. C. James, J. D. White, P. M. Allen, and J. G. Arnold, "A hybrid artificial neural network to estimate soil moisture using SWAT+ and SMAP data," *Machine Learning and Knowledge Extraction*, vol. 2, no. 3, pp. 283–306, Aug. 2020. (Cited on page 28.)

[88] O. Eroglu, M. Kurum, D. Boyd, and A. C. Gurbuz, "High spatio-temporal resolution CyGNSS soil moisture estimates using artificial neural networks," *Remote Sensing*, vol. 11, no. 19, p. 2272, Sep. 2019. (Cited on pages 28, 112, and 275.)

[89] Q. Yan, S. Gong, S. Jin, W. Huang, and C. Zhang, "Near real-time soil moisture in china retrieved from CyGNSS reflectivity," *IEEE Geoscience and Remote Sensing Letters*, pp. 1–5, 2020. (Cited on pages 28, 110, and 275.)

[90] Y. Liu, I. Collett, and Y. J. Morton, "Application of neural network to gnss-r wind speed retrieval," *IEEE Transactions on Geoscience and Remote Sensing*, vol. 57, no. 12, pp. 9756–9766, 2019. (Cited on page 28.)

[91] Q. Yan, W. Huang, and C. Moloney, "Neural networks based sea ice detection and concentration retrieval from GNSS-R delay-doppler maps," *IEEE Journal of Selected Topics in Applied Earth Observations and Remote Sensing*, vol. 10, no. 8, pp. 3789–3798, Aug. 2017. (Cited on page 28.)

[92] S.-C. Wang, "Artificial neural network," in *Interdisciplinary Computing in Java Programming*. Springer US, 2003, pp. 81–100. [Online]. Available: https://doi.org/10.1007/978-1-4615-0377-4_5 (Cited on page 29.)

[93] A. K. Jain, Jianchang Mao, and K. M. Mohiuddin, "Artificial neural networks: a tutorial," *Computer*, vol. 29, no. 3, pp. 31–44, 1996. (Cited on page 30.)

[94] X. Ying, "An overview of overfitting and its solutions," *Journal of Physics: Conference Series*, vol. 1168, p. 022022, Feb. 2019. (Cited on pages 32, 126, 134, and 275.)

[95] E. D. Karnin, "A simple procedure for pruning back-propagation trained neural networks," *IEEE Transactions on Neural Networks*, vol. 1, no. 2, pp. 239–242, 1990. (Cited on pages 32 and 275.)

[96] A. Camps, J. F. Marchan-Hernandez, X. Bosch-Lluis, N. Rodriguez-Alvarez, I. Ramos-Perez, E. Valencia, J. M. Tarongi, H. Park, H. Carreno-Luengo, A. Alonso-Arroyo, D. Pascual, R. Onrubia, G. Forte, and J. Querol, "Review of GNSS-R

instruments and tools developed at the Universitat Politecnica de Catalunya-Barcelonatech," in *2014 IEEE Geoscience and Remote Sensing Symposium*. IEEE, Jul. 2014. (Cited on page 32.)

[97] R. Onrubia, D. Pascual, J. Querol, H. Park, and A. Camps, "The global navigation satellite systems reflectometry (GNSS-R) microwave interferometric reflectometer: Hardware, calibration, and validation experiments," *Sensors*, vol. 19, no. 5, p. 1019, Feb. 2019. (Cited on pages 32, 34, 62, and 287.)

[98] H. Carreno-Luengo, A. Camps, I. Ramos-Perez, and A. Rius, "Experimental Evaluation of GNSS-Reflectometry Altimetric Precision Using the P(Y) and C/A Signals," *IEEE Journal of Selected Topics in Applied Earth Observations and Remote Sensing*, vol. 7, no. 5, pp. 1493–1500, may 2014. (Cited on pages 32 and 34.)

[99] H. Carreno-Luengo, A. Camps, P. Via, J. F. Munoz, A. Cortiella, D. Vidal, J. Jané, N. Catarino, M. Hagenfeldt, P. Palomo, and S. Cornara, "^{3}Cat-2 An Experimental Nanosatellite for GNSS-R Earth Observation: Mission Concept and Analysis," *IEEE Journal of Selected Topics in Applied Earth Observations and Remote Sensing*, vol. 9, no. 10, pp. 4540–4551, Oct 2016. (Cited on pages 32, 34, 141, and 170.)

[100] O. Nogues, A. Sumpsi, A. Camps, and A. Rius, "A 3 GPS-channels Doppler-delay receiver for remote sensing applications," in *IGARSS 2003. 2003 IEEE International Geoscience and Remote Sensing Symposium. Proceedings (IEEE Cat. No.03CH37477)*, vol. 7, 2003, pp. 4483–4485 vol.7. (Cited on page 33.)

[101] N. Rodriguez Alvarez, R. Acevo, A. Aguasca, E. Valencia, A. Camps, M. Vall-llossera, X. Bosch, and I. Ramos-Perez, "Altimetry study performed using an airborne gnss-reflectometer," 08 2010, pp. 3833 – 3836. (Cited on page 33.)

[102] A. Alonso-Arroyo, "Contributions to land, sea, and sea ice remote sensing using GNSS-Reflectometry," Ph.D. dissertation, Universitat Politècnica de Catalunya, 2016. [Online]. Available: https://www.tdx.cat/handle/10803/404062 (Cited on pages 33 and 34.)

[103] N. Rodríguez-Álvarez, "Contributions to Earth Observation using GNSS-R opportunity signals," Ph.D. dissertation, 2011. [Online]. Available: http://hdl.handle.net/2117/94511 (Cited on page 33.)

[104] R. Onrubia, D. Pascual, J. Querol, J. Castellvi-Esturi, J. Corbera, H. Park, and A. Camps, "Preliminary altimetry results of the malygnss instrument in the humit project," in *IGARSS 2018 - 2018 IEEE International Geoscience and Remote Sensing Symposium*, 2018, pp. 3331–3334. (Cited on page 34.)

[105] H. Carreno-Luengo and A. Camps, "First dual-band multiconstellation GNSS-R scatterometry experiment over boreal forests from a stratospheric balloon," vol. 9, no. 10, pp. 4743–4751, 10 2016. (Cited on pages 34 and 140.)

[106] H. Carreno-Luengo, A. Amézaga, D. Vidal, R. Olivé, J. M. Martin, and A. Camps, "First Polarimetric GNSS-R Measurements from a Stratospheric Flight over Boreal Forests," *Remote Sensing*, vol. 7, pp. 13 120–13 138, 10 2015. (Cited on pages 34, 75, 111, 130, and 141.)

[107] R. Acevo-Herrera, A. Aguasca, X. Bosch-Lluis, A. Camps, J. Martínez-Fernández, N. Sánchez-Martín, and C. Pérez-Gutiérrez, "Design and first results of an UAV-borne L-band radiometer for multiple monitoring purposes," *Remote Sensing*, vol. 2, no. 7, pp. 1662–1679, Jun. 2010. (Cited on page 35.)

[108] J. Querol, J. Tarongí, G. Forte, J. Gómez, and A. Camps, "MERITXELL: The multifrequency experimental radiometer with interference tracking for experiments over land and littoral—instrument description, calibration and performance," *Sensors*, vol. 17, no. 5, p. 1081, May 2017. (Cited on page 35.)

[109] A. Camps, X. Bosch-Lluis, I. Ramos-Perez, J. Marchán-Hernández, N. Rodríguez, E. Valencia, J. Tarongi, A. Aguasca, and R. Acevo, "New passive instruments developed for ocean monitoring at the Remote Sensing Lab—universitat politècnica de catalunya," *Sensors*, vol. 9, no. 12, pp. 10 171–10 189, Dec. 2009. (Cited on page 35.)

[110] J. Marchan, A. Camps, N. Rodriguez Alvarez, X. Bosch, I. Ramos-Perez, and E. Valencia, "PAU/GNSS-R: Implementation, performance and first results of a real-time delay-doppler map reflectometer using global navigation satellite system signals," *Sensors*, vol. 8, 05 2008. (Cited on page 36.)

[111] E. Valencia, a. Camps, J. F. Marchan-Hernandez, X. Bosch-Lluis, N. Rodriguez-Alvarez, and I. Ramos-Perez, "Advanced architectures for real-time Delay-Doppler Map GNSS-reflectometers: The GPS reflectometer instrument for PAU (griPAU)," *Advances in Space Research*, vol. 46, pp. 196–207, 2010. (Cited on pages 36 and 82.)

[112] X. Bosch, A. Camps, I. Ramos-Perez, J. Marchan, N. Rodriguez Alvarez, and E. Valencia, "PAU/RAD: Design and preliminary calibration results of a new l-band pseudo-correlation radiometer concept," *Sensors*, vol. 8, 07 2008. (Cited on page 36.)

[113] I. Ramos-Perez, A. Camps, X. Bosch-Lluis, N. Rodriguez-Alvarez, E. Valencia-Domènech, H. Park, G. Forte, and M. Vall-llosera, "PAU-SA: A synthetic aperture interferometric radiometer test bed for potential improvements in future missions," *Sensors*, vol. 12, no. 6, p. 7738–7777, Jun 2012. (Cited on page 36.)

[114] I. Ramos-Perez, G. F. Forte, A. Camps, X. Bosch-Lluis, E. Valencia, N. Rodriguez-Alvarez, H. Park, and M. Vall-llosera, "Calibration, Performance, and Imaging Tests of a Fully Digital Synthetic Aperture Interferometer Radiometer," *IEEE Journal of Selected Topics in Applied Earth Observations and Remote Sensing*, vol. 5, no. 3, pp. 723–734, jun 2012. (Cited on page 36.)

[115] A. Camps, J. Marchan, E. Valencia, I. Ramos, X. Bosch-Lluis, N. Rodriguez, H. Park, A. Alcayde, A. Mollfulleda, J. Galindo, P. Martinez, S. Chavero, M. Angulo, and A. Rius, "PAU instrument aboard INTA MicroSat-1: A GNSS-R demonstration mission for sea state correction in L-band radiometry," in *2011 IEEE International Geoscience and Remote Sensing Symposium*. IEEE, jul 2011, pp. 4126–4129. (Cited on page 37.)

[116] M. Martin-Neira, "A Passive Reflectometry and Interferometry System(PARIS)-Application to ocean altimetry," *ESA journal*, vol. 17, pp. 331–355, 1993. (Cited on page 40.)

[117] M. P. Clarizia and C. S. Ruf, "On the spatial resolution of GNSS reflectometry," *IEEE Geoscience and Remote Sensing Letters*, vol. 13, no. 8, pp. 1064–1068, Aug. 2016. (Cited on pages 40 and 110.)

[118] F. Martin, A. Camps, F. Fabra, A. Rius, M. Martin-Neira, S. D'Addio, and A. Alonso, "Mitigation of direct signal cross-talk and study of the coherent component in GNSS-R," *IEEE Geoscience and Remote Sensing Letters*, vol. 12, no. 2, pp. 279–283, feb 2015. (Cited on pages 40, 73, 75, and 76.)

[119] John S. Seybold, *Fading and Multipath Characterization*. John Wiley & Sons, Ltd, 2005, ch. 8, pp. 163–207. (Cited on pages 40 and 47.)

[120] A. Camps, "Spatial Resolution in GNSS-R Under Coherent Scattering," *IEEE Geoscience and Remote Sensing Letters*, 2019, doi: 10.1109/LGRS.2019.2916164. (Cited on pages 41, 56, 140, and 252.)

[121] H. Park, D. Pascual, A. Camps, F. Martin, A. Alonso-Arroyo, and H. Carreno-Luengo, "Analysis of Spaceborne GNSS-R Delay-Doppler Tracking," *IEEE Journal of Selected Topics in Applied Earth Observations and Remote Sensing*, vol. 7, no. 5, pp. 1481–1492, may 2014. (Cited on pages 41, 45, 205, 249, and 279.)

[122] A. B. Smith, J. P. Walker, A. W. Western, R. I. Young, K. M. Ellett, R. C. Pipunic, R. B. Grayson, L. Siriwardena, F. H. S. Chiew, and H. Richter, "The Murrumbidgee soil moisture monitoring network data set," *Water Resources Research*, vol. 48, no. 7, Jul. 2012. (Cited on pages 42 and 113.)

[123] F. Martin, "Interferometric GNSS-R processing: modeling and analysisof advanced processing conceptsfor altimetry," Ph.D. dissertation, Universitat Politècnica de Catalunya, 2020. [Online]. Available: https://www.tdx.cat/handle/10803/316583 (Cited on page 42.)

[124] H. Park, A. Camps, J. Castellvi, and J. Muro, "Generic Performance Simulator of Spaceborne GNSS-Reflectometer for Land Applications," *IEEE Journal of Selected Topics in Applied Earth Observations and Remote Sensing*, vol. 13, pp. 3179–3191, 2020. (Cited on pages 43, 111, 112, 119, 120, 121, 131, and 271.)

[125] J. Kong, *Electromagnetic Wave Theory*, ser. A Wiley-Interscience publication. Wiley, 1986. (Cited on page 46.)

[126] M. Born and E. Wolf, "Chapter iii - foundations of geometrical optics," in *Principles of Optics (Sixth Edition)*, sixth edition ed., M. Born and E. Wolf, Eds. Pergamon, 1980, pp. 109 – 132. [Online]. Available: http://www.sciencedirect.com/science/article/pii/B9780080264820500104 (Cited on page 48.)

[127] G. Kubicke, Y. A. Yahia, C. Bourlier, N. Pinel, and P. Pouliguen, "Bridging the gap between the babinet principle and the physical optics approximation: Scalar problem," *IEEE Transactions on Antennas and Propagation*, vol. 59, no. 12, pp. 4725–4732, Dec. 2011. (Cited on page 48.)

[128] R. Onrubia, D. Pascual, H. Park, A. Camps, C. Rüdiger, J. Walker, and A. Monerris, "Satellite Cross-Talk Impact Analysis in Airborne Interferometric Global Navigation

Satellite System-Reflectometry with the Microwave Interferometric Reflectometer," *Remote Sensing*, vol. 11, no. 9, p. 1120, may 2019. (Cited on pages xix and 62.)

[129] PostgreSQL, "PostgreSQL: The worlds' most advanced open source database," Available at: https://www.postgresql.org/ Last visited: 26 Jan 2021. (Cited on page 63.)

[130] PostGIS, "PostGIS: Spatial and Geographic Objects for PostgreSQL," Available at: https://postgis.net/ Last visited: 26 Jan 2021. (Cited on page 64.)

[131] QGIS, "A Free and Open Source Geographic Information System," Available at: https://www.qgis.org/ Last visited: 26 Jan 2021. (Cited on page 65.)

[132] Google, Inc., "The Go Programming Language," Available at: https://golang.org/ Last visited: 26 Jan 2021. (Cited on page 65.)

[133] S. G. Johnson and M. Frigo, "Implementing FFTs in practice," in *Fast Fourier Transforms*, C. S. Burrus, Ed. Rice University, Houston TX: Connexions, September 2008, ch. 11. [Online]. Available: http://cnx.org/content/m16336/ (Cited on page 67.)

[134] A. Alonso-Arroyo, A. Camps, H. Park, D. Pascual, R. Onrubia, and F. Martin, "Retrieval of Significant Wave Height and Mean Sea Surface Level Using the GNSS-R Interference Pattern Technique: Results From a Three-Month Field Campaign," *IEEE Transactions on Geoscience and Remote Sensing*, vol. 53, no. 6, pp. 3198–3209, jun 2015. (Cited on pages 75, 148, and 251.)

[135] N. Rodriguez-Alvarez, A. Camps, M. Vall-llossera, X. Bosch-Lluis, A. Monerris, I. Ramos-Perez, E. Valencia, J. F. Marchan-Hernandez, J. Martinez-Fernandez, G. Baroncini-Turricchia, C. Pérez-Gutiérrez, and N. Sánchez, "Land geophysical parameters retrieval using the interference pattern gnss-r technique," *IEEE Transactions on Geoscience and Remote Sensing*, vol. 49, no. 1, pp. 71–84, 2011. (Cited on pages 75 and 148.)

[136] C. Gerlein-Safdi and C. S. Ruf, "A CyGNSS-Based Algorithm for the Detection of Inland Waterbodies," *Geophysical Research Letters*, vol. 46, no. 21, pp. 12 065–12 072, 2019. (Cited on page 75.)

[137] P. Jales, "Spaceborne Receiver Design for Scatterometric GNSS Reflectometry," *PhD. thesis from University of Surrey*, 2012. (Cited on pages 75 and 247.)

[138] eoPortal Directory, "Cyclone GNSS mission description website," Available: https://directory.eoportal.org/web/eoportal/satellite-missions/c-missions/cygnss. Last visited: Jan. 2019. (Cited on pages 75 and 247.)

[139] J. A. Holzer and C. C. Sung, "Scattering of electromagnetic waves from a rough surface. II," *Journal of Applied Physics*, vol. 49, no. 3, pp. 1002–1011, Mar. 1978. (Cited on page 76.)

[140] M. Foucras, B. Ekambi, F. Bacard, O. Julien, and C. Macabiau, "Optimal GNSS acquisition parameters when considering bit transitions," in *2014 IEEE/ION Position, Location and Navigation Symposium - PLANS 2014*, May 2014, pp. 804–817. (Cited on page 77.)

[141] H. Carreno-Luengo and A. Camps, "Empirical results of a surface-level gnss-r experiment in a wave channel," *Remote Sensing*, vol. 7, no. 6, pp. 7471–7493, 2015. (Cited on page 82.)

[142] F. Fabra, E. Cardellach, A. Rius, S. Ribo, S. Oliveras, O. Nogues-Correig, M. Belmonte Rivas, M. Semmling, and S. D'Addio, "Phase Altimetry With Dual Polarization GNSS-R Over Sea Ice," *IEEE Transactions on Geoscience and Remote Sensing*, vol. 50, no. 6, pp. 2112–2121, jun 2012. (Cited on page 82.)

[143] F. Fabra, E. Cardellach, S. Ribo, W. Li, A. Rius, J. Arco-Fernández, O. Nogués-Correig, J. Praks, E. Rouhe, J. Seppänen, and M. Martin-Neira, "Is Accurate Synoptic Altimetry Achievable by Means of Interferometric GNSS-R?" *Remote Sensing*, vol. 11, 03 2019. (Cited on pages 82 and 84.)

[144] H. Park, A. Camps, E. Valencia, N. Rodriguez-Alvarez, X. Bosch-Lluis, I. Ramos-Perez, and H. Carreno-Luengo, "Retracking Considerations in Spaceborne GNSS-R Altimetry," *GPS Solutions*, vol. 16, pp. 507–518, 10 2012. (Cited on pages 83, 205, 219, and 247.)

[145] A. Rius, E. Cardellach, and M. Martin-Neira, "Altimetric analysis of the sea-surface GPS-reflected signals," *IEEE Transactions on Geoscience and Remote Sensing*, vol. 48, no. 4, pp. 2119–2127, apr 2010. (Cited on page 87.)

[146] J. S. Bathgate, M. L. Heron, and A. Prytz, "A method of swell-wave parameter extraction from hf ocean surface radar spectra," *IEEE Journal of Oceanic Engineering*, vol. 31, no. 4, pp. 812–818, 2006. (Cited on page 88.)

[147] Z. Chen, L. Zhang, C. Zhao, and X. Chen, "Wind sea and swell meansurements using S-band Doppler radar," in *OCEANS 2016 - Shanghai*, 2016, pp. 1–5. (Cited on page 88.)

[148] H. Johnsen, R. Husson, P. Vincent, and G. Hajduch, "Sentinel-1 ocean swell wave spectra (osw) algorithm definition," 02 2020. (Cited on page 88.)

[149] I. S. Robinson, "Measuring the oceans from space: The principles and methods of satellite oceanography," 2004. (Cited on page 88.)

[150] K. D. Ward, R. J. A. Tough, and S. Watts, "Sea clutter: Scattering, the k distribution and radar performance," *Waves in Random and Complex Media*, vol. 17, no. 2, pp. 233–234, 2007. (Cited on page 88.)

[151] Deutscher Wetterdienst (DWD), "ICON model description by DWD," Available at: https://www.dwd.de. Last visited: 07 Jan. 2021. (Cited on pages xxviii, 89, 243, and 244.)

[152] U. A. C. of Engineers, *Coastal Engineering Manual Part II: Coastal Hydrodynamics (EM 1110-2-1100)*. Books Express Publishing, 2012. (Cited on page 89.)

[153] D. W. Wang and P. A. Hwang, "An operational method for separating wind sea and swell from ocean wave spectra," *Journal of Atmospheric and Oceanic Technology*, vol. 18, no. 12, pp. 2052–2062, 2001. (Cited on pages 90, 102, and 106.)

[154] J. Portilla, F. J. Ocampo-Torres, and J. Monbaliu, "Spectral partitioning and identification of wind sea and swell," *Journal of Atmospheric and Oceanic Technology*, vol. 26, no. 1, pp. 107–122, 2009. (Cited on page 90.)

[155] P. A. Hwang, F. J. Ocampo-Torres, and H. García-Nava, "Wind sea and swell separation of 1d wave spectrum by a spectrum integration method," *Journal of Atmospheric and Oceanic Technology*, vol. 29, no. 1, pp. 116–128, 2012. (Cited on pages 90, 102, and 106.)

[156] InMeteo, "Ventusky," Available at: https://ventusky.com. Last visited: 07 Jan. 2021. (Cited on pages xxi, 91, 243, and 251.)

[157] T. Saleem, M. Usman, A. Elahi, and N. Gul, "Simulation and performance evaluations of the new GPS L5 and L1 signals," *Wireless Communications and Mobile Computing*, vol. 2017, pp. 1–4, 2017. (Cited on pages 90 and 218.)

[158] Australian Government, "Waves," Available at: http://www.bom.gov.au/marine/knowledge-centre/reference/waves.shtml. (Cited on pages 90, 102, and 104.)

[159] R. Bracewell, *The Fourier Transform and its Applications*, 2nd ed. Tokyo: McGraw-Hill Kogakusha, Ltd., 1978. (Cited on pages 99 and 132.)

[160] L. Wei, B. Zhang, and M. Wang, "Effects of antecedent soil moisture on runoff and soil erosion in alley cropping systems," *Agricultural Water Management*, vol. 94, no. 1-3, pp. 54–62, Dec. 2007. (Cited on page 110.)

[161] D. Entekhabi, E. G. Njoku, P. E. ONeill, K. H. Kellogg, W. T. Crow, W. N. Edelstein, J. K. Entin, S. D. Goodman, T. J. Jackson, J. Johnson, J. Kimball, J. R. Piepmeier, R. D. Koster, N. Martin, K. C. McDonald, M. Moghaddam, S. Moran, R. Reichle, J. C. Shi, M. W. Spencer, S. W. Thurman, L. Tsang, and J. V. Zyl, "The soil moisture active passive (SMAP) mission," *Proceedings of the IEEE*, vol. 98, no. 5, pp. 704–716, May 2010. (Cited on pages 110 and 271.)

[162] Array Systems Computing Inc, "ATBD for SMOS Level 2 Soil Moisture Processor Development Continuation Project," Available at: https://earth.esa.int/documents/10174/ 1854519/SMOS_L2_SM_ATBD. Last visited: 9 Nov. 2020. (Cited on pages 110 and 271.)

[163] P. O'Neill, R. Bindlish, S. Chan, J. Chaubell, E. Njoku, and T. Jackson, "ATBD for Level 2 & 3 Soil Moisture (Passive) Data Products," Available at: https://smap.jpl.nasa.gov/system/internal_resources/details/ original/484_L2_SM_P_ATBD_rev_F_final_Aug2020.pdf. Last visited: 9 Nov. 2020. (Cited on pages 110, 130, and 271.)

[164] Y. Wang and Y. J. Morton, "Coherent GNSS reflection signal processing for high-precision and high-resolution spaceborne applications," *IEEE Transactions on Geoscience and Remote Sensing*, pp. 1–12, 2020. (Cited on page 110.)

[165] M. M. Al-Khaldi, J. T. Johnson, S. Gleason, E. Loria, A. J. O'Brien, and Y. Yi, "An algorithm for detecting coherence in cyclone global navigation satellite system

mission level-1 delay-doppler maps," *IEEE Transactions on Geoscience and Remote Sensing*, pp. 1–10, 2020. (Cited on page 110.)

[166] M. Zribi, E. Motte, N. Baghdadi, F. Baup, S. Dayau, P. Fanise, D. Guyon, M. Huc, and J. Wigneron, "Potential applications of GNSS-R observations over agricultural areas: Results from the GLORI airborne campaign," *Remote Sensing*, vol. 10, no. 8, p. 1245, Aug. 2018. (Cited on pages 110, 130, and 134.)

[167] H. Kim and V. Lakshmi, "Use of cyclone global navigation satellite system (CyGNSS) observations for estimation of soil moisture," *Geophysical Research Letters*, vol. 45, no. 16, pp. 8272–8282, Aug. 2018. (Cited on page 112.)

[168] B. J. Choudhury, T. J. Schmugge, A. Chang, and R. W. Newton, "Effect of surface roughness on the microwave emission from soils," *Journal of Geophysical Research*, vol. 84, no. C9, p. 5699, 1979. (Cited on page 111.)

[169] V. L. Mironov, L. G. Kosolapova, and S. V. Fomin, "Physically and mineralogically based spectroscopic dielectric model for moist soils," *IEEE Transactions on Geoscience and Remote Sensing*, vol. 47, no. 7, pp. 2059–2070, 2009. (Cited on page 111.)

[170] J. Zhu, L. Tsang, H. Xu, and W. Gu, "A patch model based on numerical solutions of Maxwell equations for GNSS-R land applications," in *IGARSS 2019 - 2019 IEEE International Geoscience and Remote Sensing Symposium*. IEEE, Jul. 2019. (Cited on page 112.)

[171] F. Li, X. Peng, X. Chen, M. Liu, and L. Xu, "Analysis of Key Issues on GNSS-R Soil Moisture Retrieval Based on Different Antenna Patterns," *Sensors*, vol. 18, no. 8, p. 2498, Aug. 2018. (Cited on pages 112, 119, and 122.)

[172] M. Parrens, J.-P. Wigneron, P. Richaume, A. Mialon, A. A. Bitar, R. Fernandez-Moran, A. Al-Yaari, and Y. H. Kerr, "Global-scale surface roughness effects at l-band as estimated from SMOS observations," *Remote Sensing of Environment*, vol. 181, pp. 122–136, Aug. 2016. (Cited on page 112.)

[173] R. der Schalie, Y. Kerr, J. Wigneron, N. Rodríguez-Fernández, A. Al-Yaari, and R. Jeu, "Global SMOS soil moisture retrievals from the land parameter retrieval model," *International Journal of Applied Earth Observation and Geoinformation*, vol. 45, pp. 125–134, Mar. 2016. (Cited on pages 112 and 113.)

[174] M. Piles, A. Camps, M. Vall-llossera, I. Corbella, R. Panciera, C. Rüdiger, Y. H. Kerr, and J. Walker, "Downscaling SMOS-Derived Soil Moisture Using MODIS Visible/Infrared Data," *IEEE Transactions on Geoscience and Remote Sensing*, vol. 49, no. 9, pp. 3156–3166, Sep. 2011. (Cited on pages 113, 190, and 277.)

[175] G. Portal, M. Vall-llossera, M. Piles, A. Camps, D. Chaparro, M. Pablos, and L. Rossato, "A Spatially Consistent Downscaling Approach for SMOS Using an Adaptive Moving Window," *IEEE Journal of Selected Topics in Applied Earth Observations and Remote Sensing*, vol. 11, no. 6, pp. 1883–1894, June 2018. (Cited on pages 113, 190, 272, and 277.)

[176] M. Pablos, M. Piles, and C. Gonzalez-Haro, "BEC SMOS Land Products Description," Available at: http://bec.icm.csic.es/doc/BEC-SMOS-0003-PD-Land.pdf Last visited: 22 Dec 2020. (Cited on pages 115 and 272.)

[177] M. E. Hajj, N. Baghdadi, M. Zribi, N. Rodríguez-Fernández, J. Wigneron, A. Al-Yaari, A. A. Bitar, C. Albergel, and J.-C. Calvet, "Evaluation of SMOS, SMAP, ASCAT and sentinel-1 soil moisture products at sites in southwestern france," *Remote Sensing*, vol. 10, no. 4, p. 569, Apr. 2018. (Cited on pages 115 and 278.)

[178] Singergise Ltd., "Sentinel hub," Avilable: https://www.sentinel-hub.com/. Last visited: Nov 2020. (Cited on pages xxii and 116.)

[179] B. E. Center, "Barcelona expert center webpage," Available at: http://bec.icm.csic.es/ Last visited: 22 Dec 2020. (Cited on pages xxii, xxx, xxxi, 117, 272, 281, 282, and 286.)

[180] I. Ramos-Pérez, X. Bosch-Lluis, A. Camps, N. Rodriguez-Alvarez, J. F. Marchán-Hernandez, E. Valencia-Domènech, C. Vernich, S. de la Rosa, and S. Pantoja, "Correction: Ramos-Pérez, I. et al. Calibration of Correlation Radiometers Using Pseudo-Random Noise Signals. Sensors 2009, 9, 6131-6149," *Sensors*, vol. 9, no. 9, p. 7430, sep 2009. (Cited on page 115.)

[181] D. Pascual, R. Onrubia, J. Querol, H. Park, and A. Camps, "Calibration of GNSS-R receivers with PRN signal injection: Methodology and validation with the microwave interferometric reflectometer (MIR)," in *2017 IEEE International Geoscience and Remote Sensing Symposium (IGARSS)*, 2017, pp. 5022–5025. (Cited on page 115.)

[182] L. Klein and C. Swift, "An improved model for the dielectric constant of sea water at microwave frequencies," *IEEE Journal of Oceanic Engineering*, vol. 2, no. 1, pp. 104–111, Jan. 1977. (Cited on pages xxii and 118.)

[183] J. Grant, J.-P. Wigneron, R. D. Jeu, H. Lawrence, A. Mialon, P. Richaume, A. A. Bitar, M. Drusch, M. van Marle, and Y. Kerr, "Comparison of SMOS and AMSR-e vegetation optical depth to four MODIS-based vegetation indices," *Remote Sensing of Environment*, vol. 172, pp. 87–100, Jan. 2016. (Cited on page 121.)

[184] A. Maity, A. Pattanaik, S. Sagnika, and S. Pani, "A comparative study on approaches to speckle noise reduction in images," in *2015 International Conference on Computational Intelligence and Networks*, 2015, pp. 148–155. (Cited on page 124.)

[185] P. Potapov, X. Li, A. Hernandez-Serna, A. Tyukavina, M. C. Hansen, A. Kommareddy, A. Pickens, S. Turubanova, H. Tang, C. E. Silva, J. Armston, R. Dubayah, J. B. Blair, and M. Hofton, "Mapping global forest canopy height through integration of GEDI and landsat data," *Remote Sensing of Environment*, vol. 253, p. 112165, Feb. 2021. (Cited on pages xxiii, 131, and 132.)

[186] A. G. Konings, M. Piles, N. Das, and D. Entekhabi, "L-band vegetation optical depth and effective scattering albedo estimation from smap," *Remote Sensing of Environment*, vol. 198, pp. 460–470, 2017. (Cited on page 131.)

[187] E. Valencia, A. Camps, J. F. Marchan-Hernandez, N. Rodriguez-Alvarez, I. Ramos-Perez, and X. Bosch-Lluis, "Experimental determination of the sea correlation time using GNSS-R coherent data," *IEEE Geoscience and Remote Sensing Letters*, vol. 7, no. 4, pp. 675–679, oct 2010. (Cited on pages 131 and 134.)

[188] S. Quegan, T. L. Toan, J. Chave, J. Dall, J.-F. Exbrayat, D. H. T. Minh, M. Lomas, M. M. D'Alessandro, P. Paillou, K. Papathanassiou, F. Rocca, S. Saatchi, K. Scipal, H. Shugart, T. L. Smallman, M. J. Soja, S. Tebaldini, L. Ulander, L. Villard, and M. Williams, "The european space agency BIOMASS mission: Measuring forest above-ground biomass from space," *Remote Sensing of Environment*, vol. 227, pp. 44–60, Jun. 2019. (Cited on pages 136 and 218.)

[189] MOSAiC expedition, "MOSAiC expedition web page," 2020. [Online]. Available: https://mosaic-expedition.org/ (Cited on pages 139 and 140.)

[190] W. Li, E. Cardellach, F. Fabra, A. Rius, S. Ribó, and M. Martín-Neira, "First spaceborne phase altimetry over sea ice using TechDemoSat-1 GNSS-R signals," *Geophysical Research Letters*, vol. 44, no. 16, pp. 8369–8376, Aug. 2017. (Cited on pages 140 and 165.)

[191] E. Cardellach, J. Wickert, R. Baggen, J. Benito, A. Camps, N. Catarino, B. Chapron, A. Dielacher, F. Fabra, G. Flato, H. Fragner, C. Gabarró, C. Gommenginger, C. Haas, S. Healy, M. Hernandez-Pajares, P. Høeg, A. JäGgi, J. Kainulainen, S. A. Khan, N. M. K. Lemke, W. Li, S. V. Nghiem, N. Pierdicca, M. Portabella, K. Rautiainen, A. Rius, I. Sasgen, M. Semmling, C. K. Shum, F. Soulat, A. K. Steiner, S. Tailhades, M. Thomas, R. Vilaseca, and C. Zuffada, "GNSS transpolar earth reflectometry exploring system (g-tern): Mission concept," *IEEE Access*, vol. 6, pp. 13 980–14 018, 2018. (Cited on page 140.)

[192] R. Knust, "Polar research and supply vessel POLARSTERN operated by the alfred-wegener-institute," *Journal of large-scale research facilities JLSRF*, vol. 3, Oct. 2017. (Cited on page 140.)

[193] M. Unwin, R. De Vos Van Steenwijk, M. Brenchley, C. Gommenginger, C. Mitchell, and S. Gao, "Sensing the Earth with the SGR-ReSI multi-antenna space GPS / GNSS receiver," in *Advances in the Astronautical Sciences*, vol. 141, 2011, pp. 735–744. (Cited on page 141.)

[194] J. F. Munoz-Martin, A. Camps, E. Cardelach, and M. Pastena, "Circular polarization GNSS-R measurements of MOSAiC RS site during January 2020," PANGAEA, https://doi.org/10.1594/PANGAEA.924837. (Cited on page 141.)

[195] M. Sturm and J. Holmgren, "An automatic snow depth probe for field validation campaigns," *Water Resources Research*, vol. 54, no. 11, pp. 9695–9701, 2018. (Cited on page 144.)

[196] P. A. Hunkeler, S. Hendricks, M. Hoppmann, S. Paul, and R. Gerdes, "Towards an estimation of sub-sea-ice platelet-layer volume with multi-frequency electromagnetic induction sounding," *Annals of Glaciology*, vol. 56, no. 69, pp. 137–146, 2015. (Cited on page 144.)

[197] J. King, H. Skourup, S. M. Hvidegaard, A. Rösel, S. Gerland, G. Spreen, C. Polashenski, V. Helm, and G. E. Liston, "Comparison of freeboard retrieval and ice thickness calculation from ALS, ASIRAS, and CryoSat-2 in the norwegian arctic to field measurements made during the n-ICE2015 expedition," *Journal of Geophysical Research: Oceans*, vol. 123, no. 2, pp. 1123–1141, Feb. 2018. (Cited on page 145.)

[198] A. J. Martino, T. A. Neumann, N. T. Kurtz, and D. McLennan, "ICESat-2 mission overview and early performance," in *Sensors, Systems, and Next-Generation Satellites XXIII*, S. P. Neeck, T. Kimura, and P. Martimort, Eds. SPIE, Oct. 2019. (Cited on page 145.)

[199] R. Kwok, S. Kacimi, M. Webster, N. Kurtz, and A. Petty, "Arctic snow depth and sea ice thickness from ICESat-2 and CryoSat-2 freeboards: A first examination," *Journal of Geophysical Research: Oceans*, vol. 125, no. 3, Mar. 2020. (Cited on page 145.)

[200] A. A. Petty, N. T. Kurtz, R. Kwok, T. Markus, and T. A. Neumann, "Winter arctic sea ice thickness from ICESat-2 freeboards," *Journal of Geophysical Research: Oceans*, vol. 125, no. 5, May 2020. (Cited on page 145.)

[201] N. Rodriguez-Alvarez, X. Bosch-Lluis, A. Camps, M. Vall-llossera, E. Valencia, J. Marchan-Hernandez, and I. Ramos-Perez, "Soil Moisture Retrieval Using GNSS-R Techniques: Experimental Results Over a Bare Soil Field," *IEEE Transactions on Geoscience and Remote Sensing*, vol. 47, no. 11, pp. 3616–3624, nov 2009. (Cited on pages 148 and 149.)

[202] N. Rodriguez-Alvarez, X. Bosch-Lluis, A. Camps, I. Ramos-Perez, E. Valencia, H. Park, and M. Vall-llossera, "Water level monitoring using the interference pattern GNSS-R technique," in *2011 IEEE International Geoscience and Remote Sensing Symposium*. IEEE, jul 2011, pp. 2334–2337. (Cited on page 148.)

[203] N. Rodriguez-Alvarez, A. Aguasca, E. Valencia, X. Bosch-Lluis, I. Ramos-Perez, H. Park, A. Camps, and M. Vall-llossera, "Snow monitoring using GNSS-R techniques," in *2011 IEEE International Geoscience and Remote Sensing Symposium*. IEEE, jul 2011, pp. 4375–4378. (Cited on page 148.)

[204] L. Kaleschke, "SMOS Sea ice retrieval study (SMOSSIce) : Final report. ESA ESTEC Contract No: 4000202476/10/NL/CT," Dec. 2013. [Online]. Available: https://doi.org/10.5281/zenodo.3406130 (Cited on page 148.)

[205] M. R. Vant, R. O. Ramseier, and V. Makios, "The complex-dielectric constant of sea ice at frequencies in the range 0.1–40 GHz," *Journal of Applied Physics*, vol. 49, no. 3, pp. 1264–1280, Mar. 1978. (Cited on page 148.)

[206] G. Lérondel and R. Romestain, "Fresnel coefficients of a rough interface," vol. 74, no. 19, pp. 2740–2742, 5 1999. (Cited on page 148.)

[207] F. Ulaby and D. Long, *Microwave radar and radiometric remote sensing*. Norwood, MA: Artech House, 2015. (Cited on page 150.)

[208] D. K. Perovich, T. C. Grenfell, J. A. Richter-Menge, B. Light, W. B. Tucker III, and H. Eicken, "Thin and thinner: Sea ice mass balance measurements during sheba," *Journal of Geophysical Research: Oceans*, vol. 108, no. C3, 2003. (Cited on page 160.)

[209] GomSpace Group AB, "GomSpace Avionics product description website," Available at: https://gomspace.com/shop/subsystems/default.aspx. Last visited 24 Jan 2021. (Cited on pages 170 and 172.)

[210] A. Bensky, "Chapter 9 - introduction to information theory and coding," in *Short-range Wireless Communication (Third Edition)*, third edition ed., A. Bensky, Ed. Newnes, 2019, pp. 211–236. [Online]. Available: https://www.sciencedirect.com/science/article/pii/B9780128154052000099 (Cited on page 173.)

[211] J. Lacan, V. Roca, J. Peltotalo, and S. Peltotalo, "Reed-solomon forward error correction (FEC) schemes, RFC 5510," *https://tools.ietf.org/html/rfc5510*, 04 2009. (Cited on page 173.)

[212] ISISpace, "Antenna System Electrical Model Datasheet," Available at: https://www.isispace.nl/wp-content/uploads/2016/04/ISIS.ANTS-ELEC.DS˙.001˙v2.0-Antenna-System-Electrical-Model-Datasheet.pdf Last visited: 24 Ene 2020. (Cited on pages 173 and 175.)

[213] Institut d'Estudis Espaials de Catalunya, "OAdM - Montsec Observatory," Available at: http://www.ieec.cat/en/content/145/oadm-montsec-observatory Last visited 24 Jan 2021. (Cited on page 173.)

[214] RTL-SDR group, "RTL-SDR (RTL2832U) and software defined radio news and projects," Available at: https://www.rtl-sdr.com/ Last visisted: 24 Jan 2021. (Cited on pages 175 and 315.)

[215] Gumstix, Inc., "Gumstix main page," Available at: https://www.gumstix.com/ Last visited: 20 Jan 2021. (Cited on page 175.)

[216] J. Querol, R. Onrubia, A. Alonso-Arroyo, D. Pascual, H. Park, and A. Camps, "Performance Assessment of Time-Frequency RFI Mitigation Techniques in Microwave Radiometry," *IEEE Journal of Selected Topics in Applied Earth Observations and Remote Sensing*, vol. 10, no. 7, pp. 3096–3106, July 2017. (Cited on pages 179, 191, and 202.)

[217] F. Harris, *Let's Assume the System Is Synchronized*. Dordrecht: Springer Netherlands, 2011, pp. 311–325. (Cited on page 180.)

[218] GNURadio - The Free & Open Source Radio Ecosystem, "GNURadio, version 3.7.x," Avilable at https://www.gnuradio.org/ Last viisted: 24 Jan 2021. (Cited on page 180.)

[219] Cosine measurement systems, "Hyperscout from Cosine website," Available at: https://hyperscout.nl/. Last visited: Dec. 2018. (Cited on page 190.)

[220] Tyvak International, "Tyvak Internal: A Terran Orbital Corporation official website," Available: https://www.tyvak.eu. Last visited: Oct 21. 2019. (Cited on pages xxvi, 190, and 194.)

[221] R. Kwok, "Satellite remote sensing of sea-ice thickness and kinematics: a review," *Journal of Glaciology*, vol. 56, no. 200, p. 1129–1140, 2010. (Cited on page 190.)

[222] GomSpace Group AB, "GomSpace Software Defined Radio product description website," Available at: https://gomspace.com/shop/payloads/software-defined-radio.aspx. Last visited Oct 7. 2019. (Cited on pages 192, 197, 219, and 223.)

[223] Xilinx, "Fast Fourier Transform (FFT), available: https://www.xilinx.com/products/intellectual-property/fft.html," 2018. [Online]. Available: https://www.xilinx.com/products/intellectual-property/fft.html (Cited on pages 194 and 204.)

[224] Analog Devices, "Analog Devices AD9361 datasheet," Available: https://www.analog.com/media/en/technical-documentation/data-sheets/AD9361.pdf. Last visited Oct 7. 2019. (Cited on pages 195 and 224.)

[225] GomSpace Group AB, "TR-600: Radio daughterboard for use in SDR platforms," Available: https://gomspace.com/shop/subsystems/communication-systems/nanocom-tr-600.aspx. Last visited Oct 7. 2019. (Cited on pages 197 and 223.)

[226] Analog Devices, "Analog Devices LibIIO reference," Available: https://github.com/analogdevicesinc/libiio. Last visited Dec. 2018. (Cited on page 198.)

[227] Novatel, "OEM719 Multi-Frequency GNSS Receiver," Available: https://www.novatel.com/products/gnss-receivers/oem-receiver-boards/oem7-receivers/oem719/. Last visited Oct 7. 2019. (Cited on page 198.)

[228] S. McCoy and L. Naude, "ZMQ reference guide website," Available: http://zeromq.org/. Last visited Jun. 2019. (Cited on page 200.)

[229] J. Querol, "Radio frequency interference detection and mitigation techniques for navigation and Earth observation," PhD. thesis from Technical University of Catalonia. Available: https://upcommons.upc.edu/handle/2117/125028. Last visited: Oct 15. 2019, 2018. (Cited on page 202.)

[230] R. Khan, S. U. Khan, R. Zaheer, and S. Khan, "Acquisition strategies of GNSS receiver," in *International Conference on Computer Networks and Information Technology*, July 2011, pp. 119–124. (Cited on page 202.)

[231] "UPC AntennaLab anechoic chamber," Available: https://www.tsc.upc.edu/en/facilities/anechoic-chamber. Last visised Oct 21. 2019. (Cited on pages xxvii, xxviii, 210, 211, and 232.)

[232] Tyvak International, "Tyvak Internal Communication," 2018. (Cited on page 210.)

[233] "UPC NanoSat-Lab website," Available: https://nanosatlab.upc.edu. Last visited: Oct 7. 2019. (Cited on pages xxvii, xxxii, xxxiii, 212, 330, and 338.)

[234] C. Molina and A. Camps, "First evidences of ionospheric plasma depletions observations using GNSS-R data from CyGNSS," *Remote Sensing*, vol. 12, no. 22, p. 3782, Nov. 2020. (Cited on page 218.)

[235] GomSpace Group AB, "GomSpace 6U Antenna system," Available at: https://gomspace.com/shop/subsystems/communication-systems/nanocom-ant-6f.aspx. Last visited 2 Feb 2021. (Cited on pages 219 and 222.)

[236] Tallysman, "TW1825 Accutenna® Pre-Filtered Embedded Dual-Band GNSS Antenna," Available at: https://www.tallysman.com/product/tw1825-embedded-dual-band-gnss-antenna/ Last visited: 28 Jan 2021. (Cited on pages xxvii, 220, and 221.)

[237] Matterwaves, "CRPA Antenna Matterwaves Antenna Technology," Available at: http://matterwaves.com/ Last visited 28 Jan 2021. (Cited on page 220.)

[238] GomSpace Group AB, "GitHub - libcsp: CubeSat Space Protocol," Available at: https://github.com/libcsp/libcsp. Last visited 29 Jan 2021. (Cited on page 225.)

[239] C. Fernández-Prades, J. Arribas, P. Closas, C. Avilés, and L. Esteve, "GNSS-SDR: An open source tool for researchers and developers," *24th International Technical Meeting of the Satellite Division of the Institute of Navigation 2011, ION GNSS 2011*, vol. 2, 09 2011. (Cited on page 228.)

[240] *A Software-Defined GPS and Galileo Receiver*. Birkhäuser Boston, 2007. (Cited on page 228.)

[241] Arianespace, "Vega flight vv16 launch kit (pdf)," Avialable: https://www.arianespace.com/wp-content/uploads/2020/06/VV16-launchkit-EN3.pdf, Retrieved 3 September 2020. (Cited on page 238.)

[242] EUMETSAT, "Sea ice edge product of the EUMETSAT Ocean and Sea Ice Satellite Application Facility," Available at: OSI SAF, www.osi-saf.org. Last visited: 25 Oct 2020. (Cited on pages 238, 257, 260, and 268.)

[243] FSSCat consortia, "FSSCat Mission Requirement Document (MRD)." (Cited on page 240.)

[244] Shannon Brown et al., "Joint Cryopshere-Ocean-Land-Ecosystems Copernicus Imaging Microwave Radiometer (CIMR) Science Workshop," 2019. [Online]. Available: https://cimr.eu/sites/cimr.met.no/files/documents/CIMRScienceWorkshopFinalReport.pdf (Cited on page 241.)

[245] H. Park, E. Valencia, A. Camps, A. Rius, S. Ribó, and M. Martin-Neira, "Delay tracking in spaceborne GNSS-R ocean altimetry," *IEEE Geoscience and Remote Sensing Letters*, vol. 10, no. 1, pp. 57–61, jan 2013. (Cited on page 247.)

[246] M. Unwin, "The SGR-ReSI Experiment on the TechDemoSat-1 Mission," Surrey Satellite Technology LTD, Tech. Rep., 2015. [Online]. Available: http://www.merrbys.co.uk:8080/CatalogueData/Documents/TDS-1SGR-ReSIExperiment.pdf (Cited on pages 248 and 279.)

[247] G. Foti, C. Gommenginger, P. Jales, M. Unwin, A. Shaw, C. Robertson, and J. Roselló, "Spaceborne GNSS reflectometry for ocean winds: First results from the UK TechDemoSat-1 mission," *Geophysical Research Letters*, vol. 42, no. 13, pp. 5435–5441, jul 2015. (Cited on page 249.)

[248] P. Ferre-Lillo, N. Rodriguez-Alvarez, X. Bosch-Lluis, E. Valencia, J. Marchan-Hernandez, I. Ramos-Perez, and A. Camps, "Delay-doppler maps study over ocean, land and ice from space," in *2009 IEEE International Geoscience and Remote Sensing Symposium*. IEEE, 2009. (Cited on page 249.)

[249] A. M. Balakhder, M. M. Al-Khaldi, and J. T. Johnson, "On the coherency of ocean and land surface specular scattering for GNSS-R and signals of opportunity systems," *IEEE Transactions on Geoscience and Remote Sensing*, vol. 57, no. 12, pp. 10 426–10 436, 2019. (Cited on page 251.)

[250] L. Kilic, C. Prigent, F. Aires, J. Boutin, G. Heygster, R. T. Tonboe, H. Roquet, C. Jimenez, and C. Donlon, "Expecte´d Performances of the Copernicus Imaging Microwave Radiometer (CIMR) for an All-Weather and High Spatial Resolution Estimation of Ocean and Sea Ice Parameters," *Journal of Geophysical Research: Oceans*, vol. 123, no. 10, pp. 7564–7580, Oct. 2018. (Cited on page 256.)

[251] R. Owens and T. Hewson, "ECMWF Forecast User Guide," 2018. (Cited on pages xxx, 258, 268, 273, 276, and 277.)

[252] K. Didan, "MOD13Q1 MODIS/Terra Vegetation Indices 16-Day L3 Global 250m SIN Grid V006," 2015. [Online]. Available: https://lpdaac.usgs.gov/products/mod13q1v006/ (Cited on pages xxx, 258, 272, 273, 276, and 277.)

[253] M. J. Brodzik, B. Billingsley, T. Haran, B. Raup, and M. H. Savoie, "Ease-grid 2.0: Incremental but significant improvements for earth-gridded data sets," *ISPRS International Journal of Geo-Information*, vol. 1, no. 1, pp. 32–45, 2012. (Cited on pages 258 and 272.)

[254] H. Yu and B. M. Wilamowski, "Levenberg–Marquardt Training," in *Intelligent Systems*. CRC Press, Oct. 2018, pp. 12–1–12–16. [Online]. Available: https://doi.org/10.1201/9781315218427-12 (Cited on page 259.)

[255] W. N. Meier and J. S. Stewart, "Assessing uncertainties in sea ice extent climate indicators," *Environmental Research Letters*, vol. 14, no. 3, p. 035005, Mar. 2019. (Cited on pages 260 and 262.)

[256] T. A. S. Rasmussen, J. L. Høyer, D. Ghent, C. E. Bulgin, G. Dybkjaer, M. H. Ribergaard, P. Nielsen-Englyst, and K. S. Madsen, "Impact of assimilation of sea-ice surface temperatures on a coupled ocean and sea-ice model," *Journal of Geophysical Research: Oceans*, vol. 123, no. 4, pp. 2440–2460, Apr. 2018. (Cited on page 260.)

[257] Y. Batrak and M. Müller, "On the warm bias in atmospheric reanalyses induced by the missing snow over Arctic sea-ice," *Nature Communications*, vol. 10, no. 1, Sep. 2019. (Cited on page 260.)

[258] A. F. Agarap, "Deep learning using rectified linear units (relu)," 2018, cite arxiv:1803.08375Comment: 7 pages, 11 figures, 9 tables. [Online]. Available: http://arxiv.org/abs/1803.08375 (Cited on page 268.)

[259] D. P. Kingma and J. Ba, "ADAM: A Method for Stochastic Optimization," 2014. [Online]. Available: http://arxiv.org/abs/1412.6980 (Cited on page 268.)

[260] R. D. Jackson, "Soil moisture inferences from thermal-infrared measurements of vegetation temperatures," *IEEE Transactions on Geoscience and Remote Sensing*, vol. GE-20, no. 3, pp. 282–286, 1982. (Cited on page 271.)

[261] M. Moran, T. Clarke, Y. Inoue, and A. Vidal, "Estimating crop water deficit using the relation between surface-air temperature and spectral vegetation index," *Remote Sensing of Environment*, vol. 49, no. 3, pp. 246–263, Sep. 1994. (Cited on pages 271 and 275.)

[262] P. Rahimzadeh-Bajgiran and A. Berg, "Soil moisture retrievals using optical/TIR methods," in *Satellite Soil Moisture Retrieval*. Elsevier, 2016, pp. 47–72. [Online]. Available: https://doi.org/10.1016/b978-0-12-803388-3.00003-6 (Cited on pages 271 and 275.)

[263] V. Naeimi, K. Scipal, Z. Bartalis, S. Hasenauer, and W. Wagner, "An improved soil moisture retrieval algorithm for ERS and METOP scatterometer observations," *IEEE Transactions on Geoscience and Remote Sensing*, vol. 47, no. 7, pp. 1999–2013, Jul. 2009. (Cited on page 271.)

[264] S. L. Hegarat-Mascle, M. Zribi, F. Alem, A. Weisse, and C. Loumagne, "Soil moisture estimation from ERS/SAR data: toward an operational methodology," *IEEE Transactions on Geoscience and Remote Sensing*, vol. 40, no. 12, pp. 2647–2658, Dec. 2002. (Cited on page 271.)

[265] C. Pathe, W. Wagner, D. Sabel, M. Doubkova, and J. B. Basara, "Using ENVISAT ASAR global mode data for surface soil moisture retrieval over oklahoma, USA," *IEEE Transactions on Geoscience and Remote Sensing*, vol. 47, no. 2, pp. 468–480, Feb. 2009. (Cited on page 271.)

[266] H. Srivastava, P. Patel, Y. Sharma, and R. Navalgund, "Large-area soil moisture estimation using multi-incidence-angle RADARSAT-1 SAR data," *IEEE Transactions on Geoscience and Remote Sensing*, vol. 47, no. 8, pp. 2528–2535, Aug. 2009. (Cited on page 271.)

[267] S. Paloscia, S. Pettinato, E. Santi, C. Notarnicola, L. Pasolli, and A. Reppucci, "Soil moisture mapping using sentinel-1 images: Algorithm and preliminary validation," *Remote Sensing of Environment*, vol. 134, pp. 234–248, Jul. 2013. (Cited on page 271.)

[268] A. Gorrab, M. Zribi, N. Baghdadi, B. Mougenot, P. Fanise, and Z. Chabaane, "Retrieval of both soil moisture and texture using TerraSAR-X images," *Remote Sensing*, vol. 7, no. 8, pp. 10 098–10 116, Aug. 2015. (Cited on page 271.)

[269] A. Monerris, "Experimental estimation of soil emissivity and its application to soil moisture retrieval in the SMOS Mission," Ph.D. dissertation, Universitat Politècnica de Catalunya, 2009. [Online]. Available: https://www.tdx.cat/handle/10803/6940 (Cited on pages xxx and 271.)

[270] Y. Kerr, A. Al-Yaari, N. Rodriguez-Fernandez, M. Parrens, B. Molero, D. Leroux, S. Bircher, A. Mahmoodi, A. Mialon, P. Richaume, S. Delwart, A. A. Bitar, T. Pellarin, R. Bindlish, T. Jackson, C. Rüdiger, P. Waldteufel, S. Mecklenburg, and J.-P. Wigneron, "Overview of SMOS performance in terms of global soil moisture monitoring after six years in operation," *Remote Sensing of Environment*, vol. 180, pp. 40–63, Jul. 2016. (Cited on page 272.)

[271] M. Pablos, M. Vall-llossera, M. Piles, A. Camps, C. González-Haro, A. Turiel, C. J. Herbert, D. Chaparro, and G. Portal, "Influence of Quality Filtering Approaches in BEC SMOS L3 Soil Moisture Products," in *IGARSS 2019 - 2019 IEEE International Geoscience and Remote Sensing Symposium*, 2019, pp. 6941–6944. (Cited on page 272.)

[272] G. Portal, T. Jagdhuber, M. Vall-llossera, A. Camps, M. Pablos, D. Entekhabi, and M. Piles, "Assessment of multi-scale SMOS and SMAP soil moisture products across the iberian peninsula," *Remote Sensing*, vol. 12, no. 3, p. 570, Feb. 2020. (Cited on page 272.)

[273] E. Valencia, A. Camps, M. Vall-llossera, A. Monerris, X. Bosch-Lluis, N. Rodriguez-Alvarez, I. Ramos-Perez, J. F. Marchan-Hernandez, J. Martinez-Fernandez, N. Sanchez-Martin, and C. Perez-Gutierrez, "GNSS-R Delay-Doppler Maps over land: Preliminary results of the GRAJO field experiment," in *2010 IEEE International Geoscience and Remote Sensing Symposium.* IEEE, jul 2010, pp. 3805–3808. (Cited on page 281.)

[274] Jiancheng Shi, K. S. Chen, Qin Li, T. J. Jackson, P. E. O'Neill, and Leung Tsang, "A parameterized surface reflectivity model and estimation of bare-surface soil moisture with l-band radiometer," *IEEE Transactions on Geoscience and Remote Sensing*, vol. 40, no. 12, pp. 2674–2686, 2002. (Cited on page 284.)

[275] S. Ribó, E. Cardellach, J. F. Munoz-Martin, and A. Camps, "FSSCAT validation experiment in MOSAiC: Test specification and Test procedures version 1.0," 2019. (Cited on page 303.)

List of Publications

Relevant peer-reviewed journal publications associated to this dissertation

[JP1] **J. F. Munoz-Martin**, A. Perez, A. Camps, S. Ribó, E. Cardellach, J. Stroeve, V. Nandan, P. Itkin, R. Tonboe, S. Hendricks, M. Huntemann, G. Spreen, and M. Pastena, "Snow and ice thickness retrievals using GNSS-R: Preliminary results of the MOSAiC experiment," *Remote Sensing*, vol. 12, no. 24, p. 4038, Dec. 2020. [Online]. Available: https://doi.org/10.3390/rs12244038

[JP2] **J. F. Munoz-Martin**, L. Fernandez-Capon, J. Ruiz-de-Azua, and A. Camps, "The Flexible Microwave Payload-2: A SDR-Based GNSS-Reflectometer and L-Band Radiometer for CubeSats," *IEEE Journal of Selected Topics in Applied Earth Observations and Remote Sensing*, vol. 13, pp. 1298–1311, 2020. [Online]. Available: http://dx.doi.org/10.1109/jstars.2020.2977959

[JP3] A. Camps and **J. F. Munoz-Martin**, "Analytical computation of the spatial resolution in GNSS-R and experimental validation at L1 and L5," *Remote Sensing*, vol. 12, no. 23, p. 3910, Nov. 2020. [Online]. Available: https://doi.org/10.3390/rs12233910

[JP4] **J. F. Munoz-Martin**, R. Onrubia, D. Pascual, H. Park, A. Camps, C. Rüdiger, J. Walker, and A. Monerris, "Untangling the Incoherent and Coherent Scattering Components in GNSS-R and Novel Applications," *Remote Sensing*, vol. 12, no. 7, p. 1208, Apr 2020. [Online]. Available: http://dx.doi.org/10.3390/rs12071208

[JP5] **J. F. Munoz-Martin**, R. Onrubia, D. Pascual, H. Park, A. Camps, C. Rüdiger, J. Walker, and A. Monerris, "Experimental evidence of swell signatures in airborne L5/E5a GNSS-Reflectometry," *Remote Sensing*, vol. 12, no. 11, p. 1759, May 2020. [Online]. Available: https://doi.org/10.3390/rs12111759

[JP6] ——, "Single-Pass Soil Moisture Retrieval Using GNSS-R at L1 and L5 Bands: Results from Airborne Experiment," *Remote Sensing*, vol. 13, no. 4, p. 797, Feb. 2021. [Online]. Available: https://doi.org/10.3390/rs13040797

[JP7] ——, "Vegetation Canopy Height Retrieval using L1 and L5 Airborne GNSS-R," *IEEE Geoscience and Remote Sensing Letters*, 2021 (Submitted).

[JP8] **J. F. Munoz-Martin**, L. Fernandez, A. Perez, J. A. R. de Azua, H. Park, A. Camps, B. C. Domínguez, and M. Pastena, "In-orbit validation of the FMPL-2 instrument—the GNSS-R and L-Band Microwave radiometer payload of the FSSCat mission," *Remote Sensing*, vol. 13, no. 1, p. 121, Dec. 2020. [Online]. Available: https://doi.org/10.3390/rs13010121

[JP9] D. Llaveria, **J. F. Munoz-Martin**, C. Herbert, M. Pablos, H. Park, and A. Camps, "Sea ice concentration and sea ice extent mapping with l-band microwave radiometry and gnss-r data from the ffscat mission using neural networks," *Remote Sensing*, vol. 13, no. 6, p. 1139, Mar 2021. [Online]. Available: http://dx.doi.org/10.3390/rs13061139

[JP10] C. Herbert, **J. F. Munoz-Martin**, D. Llaveria, M. Pablos, and A. Camps, "Sea ice thickness estimation based on regression neural networks using l-band microwave radiometry data from the fsscat mission," *Remote Sensing*, vol. 13, no. 7, p. 1366, Apr 2021. [Online]. Available: http://dx.doi.org/10.3390/rs13071366

[JP11] **J. F. Munoz-Martin**, D. Llaveria, C. Herbert, M. Pablos, H. Park, and A. Camps, "Soil Moisture Estimation Synergy Using GNSS-R and L-Band Microwave Radiometry Data from FSSCat/FMPL-2," *Remote Sensing*, vol. 13, no. 5, p. 994, Mar 2021. [Online]. Available: http://dx.doi.org/10.3390/rs13050994

Relevant conference publications associated to this dissertation

[CP1] **J. F. Munoz-Martin**, N. Miguelez, R. Castella, L. Fernandez, A. Solanellas, P. Via, and A. Camps, "3Cat-4: Combined GNSS-R, L-Band Radiometer with RFI Mitigation, and AIS Receiver for a I-Unit Cubesat Based on Software Defined Radio," in *2018 IEEE International Geoscience and Remote Sensing Symposium, Valencia, Spain*, July 2018, pp. 1063–1066. [Online]. Available: https://doi.org/10.1109/IGARSS39084.2018.8519037

[CP2] A. Camps, A. Golkar, A. Gutierrez, J. A. R. de Azua, **J. F. Munoz-Martin**, L. Fernandez, C. Diez, A. Aguilella, S. Briatore, R. Akhtyamov, and N. Garzaniti, "FSSCat, the 2017 Copernicus Masters' "Esa Sentinel Small Satellite Challenge" Winner: A Federated Polar and Soil Moisture Tandem Mission Based on 6U Cubesats," in *IGARSS 2018 - 2018 IEEE International Geoscience and Remote Sensing Symposium, Valencia, Spain*, July 2018, pp. 8285–8287. [Online]. Available: https://doi.org/10.1109/IGARSS39084.2018.8518405

[CP3] J. R. de Azua, M. Sobrino, A. Navarro, H. Lleo, M. Sureda, M. Soria, A. Calveras, A. Camps, **J. F. Munoz-Martin**, L. Fernandez, M. Badia, D. Llaveria, C. Diez, A. Aguilella, A. Perez, and O. Milian, "3cat-4 mission: A 1-unit CubeSat for earth observation with a l-band radiometer and a GNSS-Reflectometer using Software Defined Radio," in *IGARSS 2019 - 2019*

IEEE International Geoscience and Remote Sensing Symposium. IEEE, Jul. 2019. [Online]. Available: https://doi.org/10.1109/igarss.2019.8898317

[CP4] **J. F. Munoz-Martin**, R. Onrubia, D. Pascual, H. Park, A. Camps, C. Rüdiger, J. Walker, and A. Monerris, "Untangling the GNSS-R coherent and incoherent components: Experimental evidences over the ocean," in *IGARSS 2020 - 2020 IEEE International Geoscience and Remote Sensing Symposium*, 2020, pp. 5925–5928. [Online]. Available: https://doi.org/10.1109/IGARSS39084.2020.9324005

[CP5] **J. F. Munoz-Martin**, R. Onrubia, D. Pascual, H. Park, A. Camps, C. Rüdiger, J. Walker, and A. Monerris, "First experimental evidence of Wind and Swell signatures in L5 GPS and E5A Galileo GNSS-R waveforms," in *IGARSS 2020 - 2020 IEEE International Geoscience and Remote Sensing Symposium*, 2020, pp. 3369–3372.

[CP6] **J. F. Munoz-Martin**, R. Onrubia, D. Pascual, H. Park, A. Camps, C. Rüdiger, J. P. Walker, and A. Monerris, "Parameter considerations for the retrieval of surface soil moisture from spaceborne GNSS-R," in *IGARSS 2021 - 2021 IEEE International Geoscience and Remote Sensing Symposium*. IEEE, Jul. 2021.

[CP7] A. Camps, **J. F. Munoz-Martin**, A. Pérez, E. Cardellach, S. Ribó, and M. Pastena, "FFSCAT mission: Preliminary results and ice products validation with MOSAiC campaign data," in *IGARSS 2020 - 2020 IEEE International Geoscience and Remote Sensing Symposium*, 2020, pp. 3341–3344. [Online]. Available: https://doi.org/10.1109/IGARSS39084.2020.9324355

[CP8] **J. F. Munoz-Martin**, L. Fernandez, J. R. de Azua, and A. Camps, "The Flexible Microwave Payload -2: Architecture and Testing of a Combined GNSS-R and L-Band Radiometer With RFI Mitigation Payload For Cubesat-Based Earth Observation Missions," in *IGARSS 2019 - 2019 IEEE International Geoscience and Remote Sensing Symposium*. IEEE, Jul. 2019. [Online]. Available: https://doi.org/10.1109/igarss.2019.8898402

[CP9] ——, "The Flexible Microwave Payload -2: Design, Implementation, and Optimization of a GNSS-R and Radiometry Processor for CubeSat-Based Earth Observation Missions," in *IGARSS 2019 - 2019 IEEE International Geoscience and Remote Sensing Symposium*. IEEE, Jul. 2019. [Online]. Available: https://doi.org/10.1109/igarss.2019.8899300

[CP10] ——, "The Flexible Microwave Payload -2: The Flexible Microwave Payload -2: A CubeSat-based GNSS-R instrument for Sea-Ice detection," in *2019 GNSS+R Symposium*, May 2019.

[CP11] A. Camps, **J. F. Munoz-Martin**, J. A. Ruiz-de-Azua, L. Fernandez, A. Perez-Portero, D. Llaveria, C. Herbert, M. Pablos, A. Golkar, A. Gutierrez, C. Antonio, J. Bandeiras, J. Andrade, D. Cordeiro, S. Briatore, N. Garzaniti, F. Nichele, R. Mozzillo, A. Piumatti, M. Cardi, M. Esposito, B. C. Dominguez, M. Pastena, G. Filippazzo, and A. Reagan, "FSSCAT mission description and first scientific results of the FMPL-2 onboard ^{3}Cat-5/A," in *IGARSS 2021 - 2021 IEEE International Geoscience and Remote Sensing Symposium*. IEEE, Jul. 2021.

[CP12] **J. F. Munoz-Martin**, L. Fernandez, A. Perez, H. Park, J. A. R. de Azúa, and A. Camps, "In-orbit validation of the FMPL-2 dual microwave payload onboard the FSSCAT mission," in *IGARSS 2021 - 2021 IEEE International Geoscience and Remote Sensing Symposium*. IEEE, Jul. 2021.

[CP13] **J. F. Munoz-Martin**, D. Llaveria, C. Herbert, M. Pablos, and A. Camps, "Soil moisture retrieval using the FMPL-2/FSSCAT GNSS-R and microwave radiometry data," in *IGARSS 2021 - 2021 IEEE International Geoscience and Remote Sensing Symposium*. IEEE, Jul. 2021.

Supplementary peer-reviewed journal publications during the Ph.D.

[SJP1] L. Fernandez, M. Sobrino, O. Milian, A. Aguilella, A. Solanellas, M. Badia, **J. F. Munoz-Martin**, J. A. R. de Azua, M. Sureda, and A. Camps, "Deployment mechanism for a L-band helix antenna in 1-Unit Cubesat," *Acta Astronautica*, Sep. 2020. [Online]. Available: https://doi.org/10.1016/j.actaastro.2020.09.005

[SJP2] H. Carreno-Luengo, A. Camps, P. Via, **J. F. Munoz-Martin**, A. Cortiella, D. Vidal, J. Jané, N. Catarino, M. Hagenfeldt, P. Palomo, and S. Cornara, "3Cat-2 An Experimental Nanosatellite for GNSS-R Earth Observation: Mission Concept and Analysis," *IEEE Journal of Selected Topics in Applied Earth Observations and Remote Sensing*, vol. 9, no. 10, pp. 4540–4551, Oct 2016. [Online]. Available: https://doi.org/10.1109/JSTARS.2016.2574717

[SJP3] H. Carreno-Luengo, A. Amézaga, D. Vidal, R. Olivé, **J. F. Munoz-Martin**, and A. Camps, "First Polarimetric GNSS-R Measurements from a Stratospheric Flight over Boreal Forests," *Remote Sensing*, vol. 7, pp. 13 120–13 138, 10 2015. [Online]. Available: https://doi.org/10.3390/rs71013120

[SJP4] A. Perez, **J. F. Munoz-Martin**, J. Querol, H. Park, and A. Camps, "Implementation of a Testbed for GNSS-R Payload Performance Evaluation," *IEEE Journal of Selected Topics in Applied Earth Observations and Remote Sensing*, vol. 13, pp. 2708–2715, 2020. [Online]. Available: https://doi.org/10.1109/jstars.2020.2997717

[SJP5] A. Perez-Portero, **J. F. Munoz-Martin**, H. Park, and A. Camps, "Airborne GNSS-R: A key enabling technology for environmental monitoring," *IEEE Journal of Selected Topics in Applied Earth Observations and Remote Sensing*, pp. 1–1, 2021. [Online]. Available: https://doi.org/10.1109/jstars.2021.3076003

[SJP6] M. Sureda, M. Sobrino, O. Milian, A. Aguilella, A. Solanellas, M. Badia, **J. F. Munoz-Martin**, L. Fernandez, J. A. R. de Azua, and A. Camps, "Design and testing of a helix antenna deployment system for a 1u CubeSat," *IEEE Access*, pp. 1–1, 2021. [Online]. Available: https://doi.org/10.1109/access.2021.3075660

Supplementary conference publications during the Ph.D.

[SCP1] A. Pérez, P. Fabregat, M. Badia, M. Sobrino, C. Molina, **J. F. Munoz-Martin**, L. Fernandez, L. Rayón, and J. Ramos, "Rita: Requirements and preliminary design of an L-Band microwave radiometer, optical imager, and RFI detection payload for a 3U CubeSat," in *IGARSS 2020 - 2020 IEEE International Geoscience and Remote Sensing Symposium*, 2020, pp. 5986–5989. [Online]. Available: https://doi.org/10.1109/IGARSS39084.2020.9324458

[SCP2] A. Perez-Portero, P. Fabregat, M. Badia, M. Sobrino, C. Molina, L. Fernandez, L. Rayón, A. Rodriguez, **J. F. Munoz-Martin**, J. Ramos-Castro, A.-H. Jallad, and Z. A. Aziz, "RITA: A 1U multi-sensor payload for the GRSSSAT contributing soil moisture, vegetation analysis and RFI detection," in *IGARSS 2021 - 2021 IEEE International Geoscience and Remote Sensing Symposium*, 2021, pp. 5986–5989.

[SCP3] A. Pérez, **J. F. Munoz-Martin**, and A. Camps, "Analysis on the feasability of airborne GNSS-R receivers for weather nowcasting and target detection," in *IGARSS 2020 - 2020 IEEE International Geoscience and Remote Sensing Symposium*, 2020, pp. 6274–6277. [Online]. Available: https://doi.org/10.1109/IGARSS39084.2020.9323637

Other activities during the Ph.D.

[CD1] Generalitat de Catalunya, Departament de Polítiques Digitals i Administració Pública, Grup de treball per a la definició de l'Estratègia NewSpace de Catalunya, "Estratègia NewSpace de Catalunya," Available: https://politiquesdigitals.gencat.cat/web/.content/Telecomunicacions/Newspace/Estrategia-NewSpace-de-Catalunya.pdf. Last visited: Mar 30. 2021, 2020.

[CD2] A. Perez, "Design, Implementation and Verification of Cubesat systems for Earth Observation," MSc. thesis from Technical University of Catalonia. Available: https://upcommons.upc.edu/bitstream/handle/2117/134850/Adrian_Perez_TFM.pdf. Last visited: Mar 3. 2021, 2019.

[CD3] A. Garcia, "Design and implementation of the software for an extensible network of satellite ground stations," BSc. thesis from Technical University of Catalonia. Available: https://upcommons.upc.edu/bitstream/handle/2117/328686/148815.pdf. Last visited: Mar 30. 2021, 2020.

[CD4] A. Camps, J. A. Ruiz-de-Azúa, A. Perez-Portero, L. Fernandez, J. F. Munoz-Martin, "Evolving capabilities and limitations of future CubeSat missions," Book chapter (in press).